Hybrid spin-nanomechanical systems in parametric interaction

Sven Rohr

To cite this version:

Sven Rohr. Hybrid spin-nanomechanical systems in parametric interaction. Physics [physics]. Grenoble University, 2014. English. NNT : . tel-01150728v1

HAL Id: tel-01150728
https://theses.hal.science/tel-01150728v1

Submitted on 11 May 2015 (v1), last revised 22 Nov 2016 (v2)

UNIVERSITÉ DE GRENOBLE

THÈSE

Pour obtenir le grade de

DOCTEUR DE L'UNIVERSITÉ DE GRENOBLE

Spécialité : **Physique**

Arrêté ministériel : 7 août 2006

Présentée par

Sven Rohr

Thèse dirigée par **Dr. Wolfgang Wernsdorfer**
et codirigée par **Dr. Olivier Arcizet**

préparée au sein **de l'Institut Néel**
et de **l'École Doctorale Physique**

Hybrid spin-nanomechanical systems in parametric interaction

Thèse soutenue publiquement le **15 décembre 2014**,
devant le jury composé de :

M. Jean-Philippe Poizat
DR CNRS, Institut Néel, Président
M. Jean-François Roch
DR CNRS, ENS Cachan, Rapporteur
M. Tobias Kippenberg
Professeur, EPF de Lausanne, Rapporteur
M. Patrick Maletinsky
Professeur, Université de Bâle, Examinateur
M. Wolfgang Wernsdorfer
DR CNRS, Institut Néel, Directeur de thèse
M. Olivier Arcizet
CR CNRS, Institut Néel, Co-Directeur de thèse

To my family,

who has been trying to cope with my antics for more than 27 years.

C'est en faisant n'importe quoi qu'on devient n'importe qui.

Rémi Gaillard

Acknowledgements

I think that life evolves in spirals. Just like we rethink thoughts of years ago, and we dream dreams of the past, we return to old places and meet again people we have met before. More than three years ago, I wrote an Email to Professor Jean-François Roch inquiring about a possible PhD position. He had to refuse a cooperation at that time and instead directed me towards Olivier Arcizet, which turned out to be very wise counsel. Now, at the end of my PhD, I meet Professor Roch when I defend my thesis, for he has luckily agreed to be part of the committee. I would like to use this occasion to thank him for what he has done for me in the past and for what he is doing for me in the present.

Likewise, I want to extend my gratitude to Professor Tobias Kippenberg for his willingness to read and evaluate this manuscript despite the large time constraints with which I have burdened him.

I furthermore would like to thank Professors Patrick Maletinsky and Jean-Philippe Poizat not only for their interest in my work and accepting to examine me during the defense, but also for their scientific contributions, which rendered the field of hybdrid mechanical systems an exciting domain to work in.

Finally, I also thank Professor Wolfgang Wernsdorfer, who has accepted me as a PhD student and signed countless administrative documents. Beyond bureaucratic efforts, I appreciate truly the trust I have received to follow a series of outstanding PhD students that have worked with him before.

Throughout the last three years, my work was funded by the Nanoscience foundation. I am grateful not only for its monetary contributions, but also for personal council concerning scientific outreach as well as profiting from living in Grenoble, which I have received from Alain Fontaine and Stéphanie Monfront

Here is another spiral coming back at me. I am writing these lines in a moment of enthusiasm. An equation solved, another curve fitted – something is working out. Tomorrow, I will go to the lab and present my results. There will be comments: “Why is it that way and not the other?”, “Take another measurement! The data quality can probably be improved.”, “Have you thought about such and such?”. I will first feel discouraged, but eventually grateful for having been told what every student should learn: to think my results through and take responsibility for what I do. I will go back to work, until another equation is solved, another curve fitted. Such are the spirals outlining the life of a scientist. It is important to stay optimistic to find the energy necessary to learn from mistakes. Then the spiral will turn outwards. At every new moment of discovery, the satisfaction will become more profound, the perception of nature’s beauty more awe-inspiring. Conversely, we will return to our lows with more confidence and the ability to endure hardships with higher morale and more discipline. During my PhD, we were making some measurements just to see how things are working out. We then stumbled upon an interesting effect, which took a lot of time to understand. We slowly developed a little theory, gradually improving it more and more. Eventually, the theory could even make experimental predictions. We then went back to the lab and tested those, demonstrating great agreement between the two. I lived through stages of perceived enlightenment only to be frustrated the next day. Curiosity and discipline got me back on my feet, the joy of learning keeping me constant company throughout the journey across the land of scientific plenty that has been my PhD. As I am regaling in looking back at the past years, I conclude that I have had all that science has to offer. With all my heart, I wish to thank the people that have made my stay at the institute either possible or agreeable or both. First and foremost my thanks go to Signe Seidelin and Olivier Arcizet, who first invited me to Grenoble, tutored me to secure funding and finally welcomed me very warmly upon my arrival in the laboratory. While a PhD is often stereotyped to be a very cumbersome phase of existence, I know that it is a high priority for you two to prove the opposite, and, as my case shows, you have been successful in doing so: unlike Robert Oppenheimer, I did not try to poison any of my supervisors. From a professional point of view much has to be said about Olivier. Suffice it to mention that I often felt like sitting on the shoulder of a giant, enjoying the view. I would like to thank you for having made two remarkable achievements. First, you have promoted me to heights that I believed unreachable for myself. Looking at this manuscript, I feel for the first time in my life proud of something I did. Second, you have provided me with a source of eternal inspiration. Your

dedication, vision, helpfulness, friendliness and humaneness will be a shining light for me wherever I go.

This work is the result of a collaboration between many people, all of which have contributed in different ways. Arnaud, I thank you for your camaraderie. On the winding trails to administrative success overgrown with the thorny scrub of bureaucracy, your initiative and deep understanding of the French way of life have been a razor-sharp machete, cutting me a path so that I may prevail as well. Alas, your attempts to introduce me to your culture have been of questionable outcome. During more than three years of living in France, I only have eaten exactly one Croissant and one Pain-au-Chocolat (during the breakfast that you offered me on my first week in Grenoble) and when I tell people that I like Francky Vincent, they shake their heads in disbelief.

Laure, our many conversations concerning personal affairs have been a great counterweight to the scientific madness going on in the lab. They rendered my working days more human and I often went home enlivened by what was sometimes banter, sometimes venting anger, often mutual appreciation. After all, amidst the noise of countless fans, despite national, cultural and gastronomic differences, the essence of friendship can be found in a dark room lit only by computer screens and reflections of light on dirty mirror surfaces.

Laure and Arnaud, you have been fantastic partners in crime. I am sure that both of you will continue to be good scientists, taking large gulps from the holy grail of knowledge ad infinitum. Yet, I hope you will always remain a little *thirsty.*

Eva, you have taught me to question my own results and my understanding of the subject at hand. To be honest, I was initially quite irritated by your many questions, which probably made working with me ... *not so easy.* Thank you for your persistence though. From your care for detail I eventually learned where to look for the devil when things have gone wrong.

Benjamin, it has been a real delight to work in the lab on your side. Your awareness of your call of duty and your resilience to (experimental) adversary have been nothing short of inspiring. In return, seeing you work so hard on extending the results of my project has been one of the most rewarding experiences during my PhD. While discussing and trying to convince the other of an idea sometimes made me feel like I was doing sciences, teaming up with you has also been a great personal experience.

Pierre, I have to thank you for your patience. I do not remember how often I asked you the same questions over and over. And I am sure you did not have enough chalk to mark on the wall the number of times I came into your office to disturb. However, I hope that eventually you agree with me that your efforts could be turned into some pretty physics in the final chapter of the thesis. Without you, the last fifty or so pages of this manuscript would be blank.

Aurélien, you almost showed me what a good German is: your degree of organization is exemplary. The only shortcoming I could notice is your French pronunciation of your German surname. I wish there would have been more time for me to fix this...

The atmosphere in our little group has been very delightful, friendly and supportive throughout, which made my PhD meaningful beyond purely intellectual pleasure. Nobody ever got angry or complained to me about what I consider to be my greatest blunder. In about fifty percent of my interactions I was nodding my head despite having understood almost nothing. Your patience for my abusing your language has been infinite and I appreciate it immensely.

The PhD students and Post-Docs at the institute have helped tremendously to make the daily grind memorable. I thank Jean-Francois and Paul for their lessons in Québecois, Matias, Romain and Christophe for shattering my ideas of a doctor's decency. I thank John, whose manners have entertained the whole institute and Fabien for helping me to not forget my mother tongue.

Matias, Stefan and Mark have set very high standards in the academic family. I thank you, brothers, for being a great inspiration and for the infinite jest that we lived to see together, either in the gym, in a bar, at a party, wherever.

Hanno, Farida, Johanna, Katrin, Carina have all been part of the deutsche Kommune that taught me a lot about my origins. Thank you for the many evenings we shared together and which always had a taste of home.

Omid, Hadi, Vito and Yani have rendered the life at the institute much more exotic and brought some sunlight into the institute's hallways. The same is true for Dipankar, who has moreover been an excellent (young) padawan that any teacher would be proud of.

Without the tremendous and selfless help of Tobias I would not have survived France. Thank you for a great friendship! Unfortunately, I feel like I have never been able to return the innumerable favors you paid me. I will try to make up for it in the future.

The last colleague on my list of gratitude is one to which I have a very special relationship. You, nameless NV defect, with whom the next 200+ pages are concerned. There are in the universe probably no two other electrons that have been tortured alike in the name of scientific venture. Despite all the noise I exposed you to, the microwaving and the constant surveillance with the all-seeing eye of the confocal microscope, you have stayed loyal to your big brother for more than two years. We have been getting dressed and undressed together in the heat of the laboratory and enjoyed a pretty good time altogether.

A little note on the formalities of being a student. I would also like to thank the university administration, for they have taught me an important lesson of life. I was at first utterly confused and at loss to explain the intense anger I felt on several occasions, where administrative procedures often prevented me from doing what I came here for: science. It seemed to me that obstacles where put in my way by a mischievous mastermind who sought to direct all its grief against me. It was in a moment of deep contemplation, however, that I came to understand that the obstacles I was confronted with originated not from some supernatural evil, but from a broken system of organization combined with the irresponsible behavior of a few individuals. Coming to accept that the encountered hardships and hindrances are not based on personal disrespect has been a character forming experience.

On a separate note, I would like to truly thank the Valoridoc team. When I was obliged to attend their courses, I initially mistook them as a further outgrowth of the aforementioned mastermind's wickedness. Luckily, I was soon proven wrong and found the insights gained during class useful on many levels. I wish them good luck in doing what they do.

During my time in France, I have received much support from home or elsewhere. It was not possible to meet with many friends as often as I would have wished. Yet, when we met again, it always felt as if we had not been separated for a single day. Cheers to Tim and Flo, Phil and Phil, Toni and Steven.

If Yannick, Xavier, Hedi or Sami ever find their names in here, they will know what for: thank you for having shared a huge adventure and for being unforgettable company on a lifelong journey!

I want to deeply thank Iza, a number terrorist with a baking obsession. The confidence and trust you had for me when you decided to come along to Grenoble fill me still with fondness and pride. Moreover, the infinite number of cakes coming out of your oven would not only have impressed Hilbert, but have also, beyond mathematical reality, been the highlight of many days for me.

I will be eternally grateful for having met Aline. As strangers in the night started what has amounted to having lived through a highest state of existence. Like Dante's Beatrice, you lead me through what was certainly the most joyful stage of my PhD. Loving you and loving who I am around you have made me feel a man.

Eventually, I thank my family, who does not understand a single bit about what I was doing. Yet, their love for me compelled them once to ask me to translate the title of this thesis into German. Of course, it did not make any sense to them either, but we all had a good laugh about it *zusammen – und das ist alles, was zählt.* I feel very lucky to have received from you all this uncompromising love and support.

I must especially thank my grandfather, who has fostered from a very young age my curiosity with unforgotten riddles, jokes and bits of Latin wisdom. "Salve magister, moritorus te salutat!" *Moriturus* is to be understood in the same sense as used by Paul Erdős, who spoke of mathematicians as dead after they had quit their profession. I am leaving behind me now the world of physics. Colleagues, friends, the fame, the money... But not all is lost, for there is comfort in the insights offered by someone who found himself empty handed after a life of restless seeking: “So we beat on, boats against the current, borne back ceaselessly into the past.” – Francis Scott Fitzgerald, THE GREAT GATSBY

Structure of this thesis

This thesis summarizes original research results regarding the dynamics of a single spin parametrically coupled to the motion of a nanomechanical resonator. The underlying work was performed between September 2011 and October 2014 in the group *Hybrid Quantum Nano Optomechanics* under the supervision of Dr. Olivier Ariczet at the Néel Institute in Grenoble, France. Our studies are rooted in the context of hybrid spin mechanical systems - a new class of devices in which single quantum systems are coupled to a macroscopic object. Such a system, built from the electron spin of a single nitrogen vacancy defect magnetically coupled to a silicon carbide nanowire, had already been set up in the host laboratory prior to this work and held promising opportunities for the exploration of novel effects arising from the mutual coupling of the two constituents. Harnessing its potential, however, required gaining detailed insights into the dynamics of the single spin as its energy is periodically modulated by the motion of the nanoresonator. To do so has been the goal of the PhD thesis that is presented here. The manuscript is structured as follows:

In Chapter 1 we provide a general introduction to the field of hybrid mechanical systems. In the first part, we motivate their relevance for modern day physics research and highlight especially their applicability for the generation of arbitrary quantum states of motion of macroscopic objects. Hoping to develop in the reader an appreciation of the versatility and technological challenge of working with hybrid mechanical devices, we furthermore review state-of-the-art experiments from around the world. In the second part, we present the hybrid spin-mechanical system that is at the center of this thesis. We introduce its constituent components, electron spin of a nitrogen vacancy defect and SiC nanowire, and outline earlier experiments that have successfully demonstrated functioning of the hybrid device.

We dedicate Chapter 2 to the establishment of a theoretical framework necessary to describe the hybrid interaction. We start by formalizing the (quantum) mechanical oscillator, its interaction with the environment, its response to externally applied forces and we discuss the optical readout of the nanowire displacement. Subsequently, we provide the formal description of the electron spin of the nitrogen vacancy defect, explain how it is affected by dissipation and decoherence effects and how its spin state can be prepared and detected optically. Eventually, we present the hybrid interaction in terms of a coupling Hamiltonian and develop a set of Bloch equations describing the evolution of the spin under the influence of the nanomechanical motion. Finally, we reduce our considerations to the parametric interaction, where the spin energy becomes a function of the oscillator position.

We have decided to first study the dynamics of a single spin during the parametric interaction on a test system, where the mechanical motion is emulated by radio frequency (RF) magnetic fields delivered to the electron spin by a waveguide system. On the one hand, the system's high spatial stability has allowed to accumulate data during long acquisition times. On the other hand, working with RF magnetic fields has enabled the tuning of the parametric interaction through a large parameter range. In Chapter 3 we describe the experimental setup and discuss two techniques to probe the spin's population. Using optically detected magnetic resonance spectroscopy, we probe the steady state spin population in the adiabatic and resolved sideband regime, corresponding to slow and fast mechanical motion with respect to the spin lifetime. The latter regime presents an important benchmark for hybrid systems, as it enables advanced manipulation protocols for the hybrid device. It is studied in further detail by measuring Rabi oscillations. We have come to observe a spin locking effect, where the dynamics of the spin become synchronized to the oscillator motion when the spin evolution frequency approaches the frequency of mechanical modulation. This effect, analogous to the Mollow triplet in quantum electrodynamics and bearing great importance in the realization of a mechanical measurement of spin forces, is analyzed in detail throughout the rest of this chapter and remains in the focus of the remainder of this work.

In Chapter 4 we present an advanced hybrid setup, especially developed to provide high spatial stability required when using large magnetic field gradients. An important novelty of this system arises from the two dimensional motion exhibited by the nanowire, resulting in a vectorial character of the spin-oscillator interaction. This additional richness is conquered by using experimental techniques to directly measure the two dimensional energy landscape of the electron spin in the strong magnetic field gradient. We show that the spin locking mechanism is also observed in the true hybrid device and demonstrate that the phononic Mollow triplet gains a vectorial character.

Finally, in Chapter 5 we explore the role of noise created by the random thermal motion of the mechanical oscillator in the hybrid spin-mechanical system. We do so by returning to the test system and injecting in the waveguide an incoherent RF signal emulating the oscillator's random Brownian motion. First, we show that the Mollow triplet can also be created by the thermally driven oscillator. Second, we study how the thermal noise perturbs the Mollow triplet created by a coherent energy modulation of the spin. Finally, we conclude our study with a last experiment demonstrating that the phononic Mollow triplet can be used to perform a spectroscopic measurement of the spin environment by detecting the Brownian motion of a mechanical mode near the mechanical drive frequency.

Contents

Chapter 1

Hybrid systems of nanomechanical oscillators and two level systems

In the first chapter of this thesis we are going to provide an introduction to hybrid spin mechanical systems for the general audience. We will start by reviewing the experimental effort that has been invested into the observation and generation of one of quantum physics most bizarre manifestations of the uncertainty principle: the perpetual twitch at zero energy of a microscopic yet visible object. This so called ground state of motion of a mechanical oscillator being the conceptual starting point of an entirely new domain of physics, we will continue by elucidating how the frontier between classical and quantum physics can be pushed further towards the macroscopic. To do so, it has been suggested to couple mechanical oscillators to one of quantum mechanics' hallmark ingredients – the quantum two level system. After a brief illustration of possible consequences of such a coupling, we will present recent experiments that have already successfully demonstrated the interaction between the two components.

In the second part of this introduction, we are going to describe the hybrid spin mechanical system that is in the focus of this thesis. Advantages of choosing a silicon carbide nanowire as a mechanical oscillator and a single nitrogen vacancy defect as a two level system will be highlighted. Earlier experiments preceding this thesis work have already demonstrated the parametric coupling between NV spin and oscillator motion on this device. Motivated by this success, we will outline how a measurement of the mechanical oscillator's dynamics can be used to detect the state of the two level system. Such an experiment requires profound knowledge of the behavior of the quantum two level system, which has been the stimulating drive of this work.

1.1 Non-classical states of motion

1.1.1 The motional ground state

Quantum mechanical oscillators

In [1], Landau and Lifshitz open their work with a remark pinpointing the profoundness of harmonic potentials. Assuming that a given one dimensional potential function $U(x)$ is continuous, it can be expanded around a minimum x_0 as

$$U(x-x_0) = U_0 + U_1(x-x_0) + U_2(x-x_0)^2 + O((x-x_0)^3).$$

The first term U_0 can always be absorbed as the zero of energy, while $U_1 = 0$ by definition. Hence, any physical object displaced by $\delta x = x - x_0$ around its rest position can be approximately described by a potential function that is quadratic in the displacement. The study of such potentials comprises a wide field of applications and the resulting dynamics, described by harmonic oscillations, can be found almost everywhere in nature. Examples range from the center of mass motion of galaxies over currents in RLC circuits to the motion of single atoms in molecules. The latter systems, however, are so small that they cannot be explained sufficiently in terms of classical physics, but rather a quantum treatment becomes necessary.

Heisenberg's principle of uncertainty can be viewed as a cornerstone postulate of quantum mechanics. It states that a simultaneous measurement of two conjugate variables describing an object can only be performed within the limit of a well defined imprecision. For a measurement of position x and momentum p of an object, their respective uncertainties, Δx and Δp, are limited by $\Delta x \Delta p \geq \frac{\hbar}{2}$, where $\hbar$ is Planck's constant h divided by 2π and equals $\hbar = 1.054 \times 10^{-34}$ Js. As a consequence, the object is always moving even at zero energy, giving rise to what is termed zero-point fluctuations. Entering this regime with a macroscopic object is an important benchmark for quantum mechanical experiments and offers a way to probe the frontiers between the classical and quantum world. There are, however, three important reasons why this is in general a difficult task. First, because the zero-point fluctuations are very small, as can be seen by inspecting the size of Planck's constant h. Second, at room temperature the object has a large thermal energy leading to additional motion much larger than quantum fluctuation. At last, an arbitrary macroscopic object consists of many atoms. Their collective motion is described by a single massive object, whose zero-point fluctuations consequently decrease with the number of involved particles.

Cooling single ions into their motional ground state

Despite their small size, single ions have provided physicists with an excellent playground to explore the weirdness of quantum mechanics early on. Indeed, advancement in this field of physics was awarded with several Nobel prizes [1]. Working with single ions is advantageous mainly due to two characteristics. First, their charge enables their confinement and isolation in an oscillating electromagnetic potential, which lead to the development of ion traps by physicists like Wolfgang Paul in the 1950s [2]. Second, the advent of laser light sources in the 1960s largely increased the spectroscopy toolbox, which provided the experimenters with great control over the ions. It was realized in the 1970s that a single ion's oscillating motion in a trap potential can be cooled down using laser light [3, 4]. The principal idea is that a laser beam impinging onto a single ion provides the particle with a momentum kick. Since photons are scattered arbitrarily in all directions, the net result is momentum transfer from the photons onto the ion in the direction opposite to its motion. Exploiting the Doppler effect, the radiation pressure force can slow down the atoms and hence decreases their temperature. The phenomenon was first observed in 1978 by Wineland, Drullinger, and Walls [5], who cooled a cloud of magnesium ions to less than 40 K using a technique called Doppler cooling. This being a great success in itself, the technique prevented cooling below a temperature limit set by the ions spectroscopic linewidth. In 1982 it was suggested that these limitations could be circumvented by setting up an electromagnetic trap whose oscillation frequency was much larger than the absorption linewidth of the ions [6]. In this configuration, called the Resolved Sideband (RSB) regime [7], an excited ion undergoes many oscillations in the trap potential before de-excitation. Wineland and his group in Boulder, Colorado, USA, overcame the experimental challenges for a first time in 1989 [8] and demonstrated cooling of a single mercury ion to its ground state of motion. Soon after, the cooling of collective modes of oscillation shared between several ions (called ion crystals) was demonstrated, revealing the quantum behavior of a group of particles [9, 10]. These advancements brought along the question whether quantum behavior could be demonstrated on larger objects as well. Like ion crystals in a trap, atoms in a solid also oscillate in discrete mechanical modes, called phonons. This is indeed a very desirable situation when aiming at generating macroscopic quantum behavior, since it avoids the problem of having to control each participating particle individually. Mechanical oscillators are the manifestation of such a collective behavior in a solid state system and they have therefore been identified as suitable

---

[1] for example to Hans Dehmelt and Wolfgang Paul in 1989 who were working with single ions and Steven Chu, Claude Cohen-Tannoudji and William Phillips in 1997, who worked on single atom experiments

candidates for the generation of macroscopic quantum states of motion.

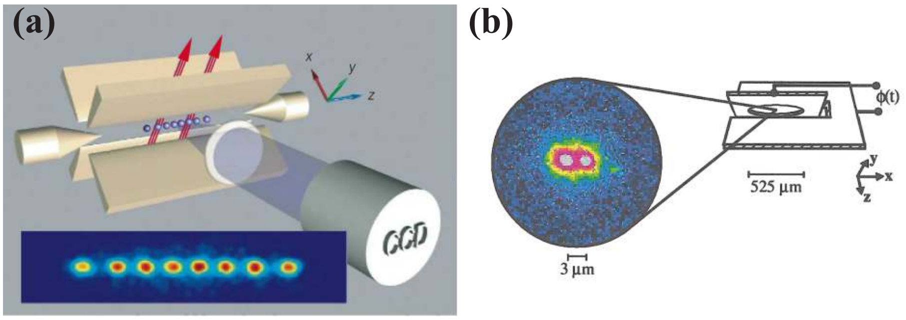

Figure 1.1: Trapped ion experiments. **(a)** An array of several laser cooled $^{40}\mathrm{Ca}^{+}$ ions is aligned in a Paul trap and imaged with a CCD camera by means of a fluorescence readout. Image source: [11]. **(b)** King and Wineland confined two $^{9}\mathrm{Be}^{+}$ ions in an elliptical Paul trap and cooled modes of their collective motion to the ground state [10].

Cooling mechanical oscillators into their motional ground state

The challenge of observing a device in its motional ground state mainly consists in extracting all its thermal energy $k_B\Theta$, where Θ is its temperature and $k_B = 1.38 \times 10^{-23}\mathrm{J/K}$ is the Boltzmann constant. In Chapter 2 we will see that the necessary temperature that needs to be achieved is $\Theta_{\mathrm{gs}} = \hbar\Omega_{\mathrm{m}}/k_B$. For a mechanical oscillator of resonance frequency $\Omega_{\mathrm{m}}/2\pi = 1\,\mathrm{MHz}$, the ground state temperature is $\Theta_{\mathrm{gs}} \approx 48\,\mu\mathrm{K}$, much colder than the microwave background of the universe and any realistic temperature achievable in a cryostat. The first physicists to ever reveal the quantum nature of a macroscopic object visible by the human eye were O'Connell and Cleland in 2010 [12]. In their groundbreaking experiment a unique system, consisting of a membrane with extremely high frequencies in the gigahertz range and a ground state temperature of about 100 mK, was cooled by using purely cryogenic techniques. However, more conventional oscillators have lower mechanical frequencies and cryogenic cooling techniques can hardly be expected to go below 10 mK in presence of probe fields. This is due to the reduction of heat capacity and cooling power in standard dilution refrigerators at low temperatures. The whole system thus becomes more susceptible to thermalization induced by the probe fields, limiting the lowest achievable temperature. These problems altogether motivate the use of active cooling techniques similar to those used for single ions, which were explored in the context of cavity optomechanics. Actively cooling mechanical oscillators only decreases the temperature of a single mode, leaving the environment unchanged. A. Heidmann and coworkers first demonstrated that the thermal motion of a cavity mirror can be cooled using an active feedback scheme [13]. The random Brownian motion of the mirror is detected and differentiated and serves to modulate the intensity of an additional laser beam with an acousto-optic modulator. This second laser is directed onto the cavity mirror and its radiation pressure provides a viscous force that is damping its thermal motion. Because this technique reduces temperature and leads to increased mechanical dissipation, it is termed cold damping. This active cooling technique has been demonstrated to achieve impressive cooling factors of more than 40 by Heidmann and later by more than a factor of 1000 by D. Rugar and D. Bouwmeester [14, 15]. However, the installation of an active feedback system is experimentally challenging, especially because this technique necessitates an extreme readout sensitivity and therefore large probe powers, which are hardly compatible with ultracryogenic experiments. For this reason, alternative strategies have been suggested, which make use of the optomechanical interaction [16–19]. Radiation pressure cooling of a movable mirror relies on the principle that the intracavity field exerts a force that has components oscillating in and out of phase with the mirror's motion. This phase delay is a consequence of the build-up time of the intracavity field and therefore depends on the detuning of the light field from cavity resonance. The force component out of phase with the oscillator motion appears like an additional damping, leading to a reduction of the effective temperature of the phonon mode of interest. This technique is the optomechanical analog of laser cooling of atoms, exploiting the parametric coupling between the cavity resonance and mechanical motion. The first experiments were implemented by the groups of A. Heidmann [17] and A. Aspelmeyer [18] and were quickly followed by those of other research groups [15, 20–22]. Since then, it has been demonstrated to work over a large variety of mass scales, ranging from nanomembranes of a few picograms in the group of Harris [23] to gram [24] and kilogram objects [25]. Such large experimental interest was accompanied by much theoretical support [26–29]. It was realized that, in analogy with trapped atom experiments, in case where the mechanical oscillation frequency is below the linewidth of the cavity transmission, the lowest temperature achievable is limited to the equivalent of a Doppler limit temperature [30]. Again, the situation can be remedied by going to the resolved sideband regime of the optomechanical interaction. First demonstrations of resolved sideband cooling were realized by the group of T. Kippenberg in 2009 [31, 32]. In their experiment a cryogenically precooled micro-toroid was used in which so called whispering gallery modes of the cavity were coupled to breathing modes of the toroid. A tapered optical fibre was brought into close proximity to the toroid's rim, such that the micro-toroid's evanescent field could couple to the fibre guided mode. The radiation pressure cooling in the resolved sideband regime brought the thermal occupation of the mechanical mode down to ~ 60 phonons. Soon after, in 2011, two groups of experimenters achieved sideband cooling to the ground state. Painter and Chan also used a tapered optical fibre to couple light into a suspended silicon beam serving as both, optical cavity and mechanical resonator, eventually obtaining phonon occupation of less than one [33]. Teufel and Lehnert from Boulder showed that the same principles apply in a microwave cavity using an electromechanical coupling scheme [34]. Because of the large coupling strength achieved, resolved sideband cooling was sufficient to freeze a mechanical oscillator down to its ground state, whose remaining thermal occupation of the mode was determined to be of only 0.34 phonons. Figure 1.2 gives a visual overview of experiments that have successfully cooled macroscopic mechanical oscillators into or close to their ground state of motion.

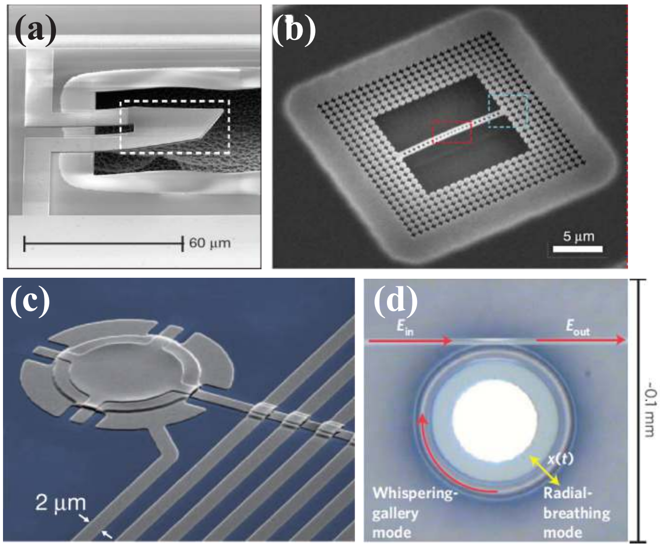

Figure 1.2: Mechanical oscillators observed in or close to their ground state of motion. **(a)** The GHz film bulk resonator of [12] can be cooled to its ground state using purely cryogenic techniques. **(b)** [33] used laser cooling to bring the occupation number of this silicon nanobeam down to 0.85 thermal phonons. **(c)** Resolved sideband cooling with MW photons was used to cool the aluminum membrane of [34] into its motional ground state. **(d)** The group of T. Kippenberg used resolved sideband cooling by coupling an evanescent field to a whispering gallery mode of a silica micro-toroid, which was cooled to a thermal occupation of first 60 [31], later 10 [32] and 1.7 phonons [35].

1.1.2 Non-classical states of motion of macroscopic objects

Preparation of an object in its ground state $|m = 0\rangle$ builds the basis for the generation of non-classical states of motion. Trapped ion experiments have provided exquisite demonstrations of such, where the generation of number states [36] or squeezed states [37] is now a task routinely accomplished in the laboratory.

Moreover, due to coupling of an internal state with two level character to a motional degree, arbitrary quantum states can be created. In the resolved sideband regime, where ion lifetimes exceed the duration of the motional period in the trap potential ($\Omega_{\mathrm{m}} > \Gamma_{\mathrm{ion}}$), transitions from $|g, m\rangle \to |e, m + k\rangle$ can be resolved spectrally. By irradiating the ion with a so called π pulse (coming for example from a laser source or a microwave antenna), it is then possible to entangle internal and motional degrees of freedom: for an uncoupled two level system (TLS), a π pulse can transfer population from the ground state $|g\rangle$ to the excited state $|e\rangle$ (or back from the excited state to the ground state) if its frequency matches the energy gap ($\delta = 0$).

$$|g\rangle \xrightarrow{\pi(\delta=0)} |e\rangle$$

For an ion bound in a trap potential, population can be transferred using a π-pulse that is detuned from resonance by the trap frequency $\Omega_{\mathrm{m}}/2\pi$ ($\delta = \pm\Omega_{\mathrm{m}}$). The energy difference will be compensated for by excitation or de-excitation of the ion's motion [36].

$$|g, m\rangle \xrightarrow{\pi(\delta=\pm\Omega_{\mathrm{m}})} |e, m \pm 1\rangle$$

The situation is depicted in Figure 1.3. If instead a $\pi/2$-pulse is used, that creates a superposition of the internal ground and excited states, internal and motional degrees become entangled:

$$|g, n\rangle \xrightarrow{\pi/2(\delta=\Omega_{\mathrm{m}})} \frac{1}{\sqrt{2}}(|g, n\rangle + |e, n + 1\rangle)$$

In combination with a controlled NOT (cNOT) operation[2], arbitrary entangled states can be created [11, 38]. The technique has not only been used to entangle single ions with their motional state [39] or internal states of other ions [40] but also to entangle motional degrees of two spatially separated ion pairs [41].

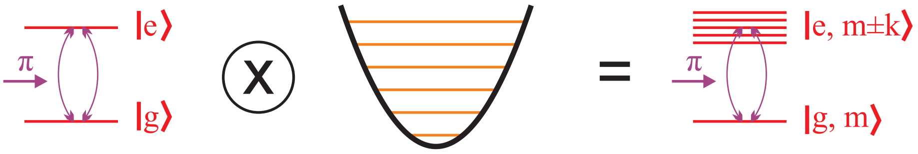

Figure 1.3: Entanglement generation with trapped ions. The energy of an ion's internal state is modified by the trap potential. In the resolved sideband regime, the internal state serves as an interface to excite or de-excite the ion's motional modes.

In a theoretical discussion given by Cirac and Zoller in 1995 [42] it is suggested that such entanglement protocols can be employed to create a quantum computer. Since the computational power of such a device largely depends on the size of the qubit network [43, 44], researchers have made an effort to demonstrate entangled states between larger ensembles of atoms. Wavefunctions describing a superposition of two maximally different states containing six particles have been engineered [45]. Such entangled states are called cat states, a homage to Schrödinger's famous thought experiment. So far their observation has been restricted to experiments containing only a small number of particles.

---

[2] A cNOT operation changes the state $|t\rangle$ of a target system, conditioned on the state $|c\rangle$ of a control system. For example, if both systems are qubits each with states $|0\rangle$ and $|1\rangle$, the cNOT operation changes $|c, t\rangle$ to $|c, c \oplus t\rangle$, where $\oplus$ denotes addition modulo 2. It has been shown by [38], that all quantum computing operations can be decomposed into cNOT gates combined with full qubit state rotations.

1.1.3 Mechanical hybrid systems

The experiments outlined above demonstrate that an interface is needed in order to control the coherence properties of quantum mechanical motion. Tian and Zoller [46] suggested that the coupling between internal and motional degrees of freedom can be extended to create non-classical motion of large scale objects. They propose a configuration in which a single ion is tightly confined in a trap potential. In a scenario where its motion is strongly coupled to the mechanical resonators that make up the trap, a quantum state of the ion can be mapped onto the motion of the resonators and vice versa. The interface is thus provided by the coupling to a quantum system in the mechanical hybrid device, see Figure 1.4. A natural, but not exclusive, choice for the quantum object is a quantum TLS, which can be used to create non-classical motion, following the above described strategy. In recent years a large toolbox to control the coherence properties of a wide range of qubits has been established. Hybrid systems can thus profit from a large variety of potential components to map their quantum state onto the mechanics, which can in principle be done in two different ways. In case where mechanical displacement leads to a change in energy of the qubit, the same protocols as for trapped ions can be used in hybrid mechanical systems. As an example, for operation in the resolved sideband regime, where the mechanical oscillation frequency surpasses the characteristic linewidth of the quantum system, it will be possible to perform sideband cooling of the mechanical resonator [47, 48]. In case where both components, oscillator and quantum system, can resonantly exchange single excitations, the Law-Eberly protocol [49] provides an algorithm to create any arbitrary motional quantum state. Such a state can in principle be composed out of an infinite superposition of states each with different amplitude and phase. Creation of a quantum state of a mechanical oscillator with a classical field, which is likewise described by a superposition of an infinite number of states, is problematic: On the one hand the interaction of the many levels that are involved is intractable, while on the other hand, the experimenter only has two control parameters, namely amplitude and phase of the classical field, at his disposal. The problem is resolved by invoking the nonlinear excitation behavior of a quantum TLS, whose evolution is restricted between two states, as an interface between classical and quantum object. Manipulation of the qubit's amplitude and phase with the amplitude and phase of the classical field is well described by the Jaynes - Cummings model, enabling arbitrary quantum state generation of the TLS. This quantum state can subsequently be mapped onto the mechanical oscillator by carefully timing the interaction length. An arbitrary quantum state of motion can thus be created bit by bit, as visualized in Figure 1.4. Such couplings have already been used between a phase qubit and a superconducting resonator [50] to create arbitrary quantum states of the MW field.

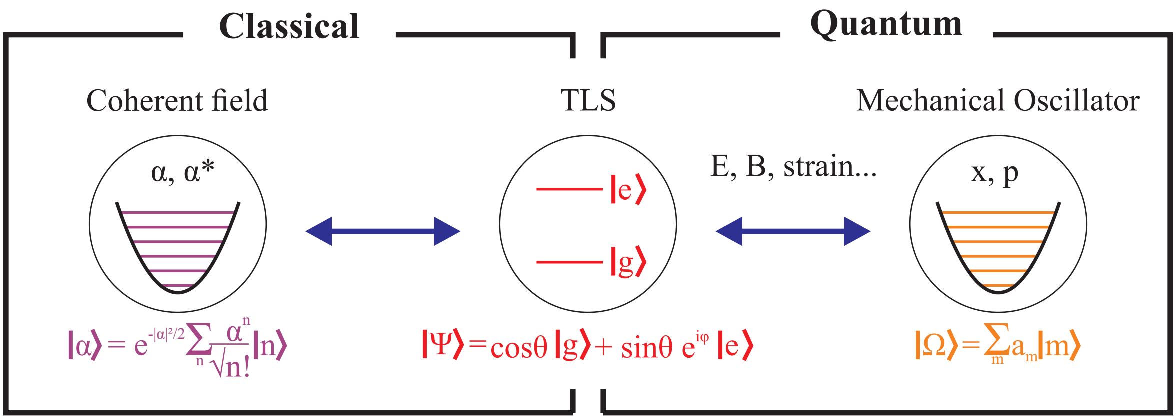

Figure 1.4: Mechanical hybrid systems. The two level system serves as an interface between an external classical field and the state of a quantum mechanical oscillator.

A historically important experiment was presented in 2004 by an IBM resarch team lead by Dan

Rugar, see Figure 1.5. They demonstrated the detection of a single electron spin with a macroscopic cantilever for the first time [51]. In this first hybrid spin-mechanical system an electromagnetic pulse sequence was applied to force the spin of a single electron trapped in a solid to oscillate at the mechanical resonance frequency. The spin magnetic moment then exerted a force on the cantilever tip holding a magnetic gradient structure. Despite such a force being naturally small, it induced a measurable shift in the mechanical resonance frequency. Detecting possible quantum states was however out of reach for the researchers, as the small coupling strength between the two components required long averaging times. Nonetheless, demonstrating single spin detection opened doors for new technological development aiming at improvement of the experimental apparatus. Increasing mechanical sensitivity as well as coherence times of the quantum systems has been a major focus since and several schemes have been proposed [52, 53].

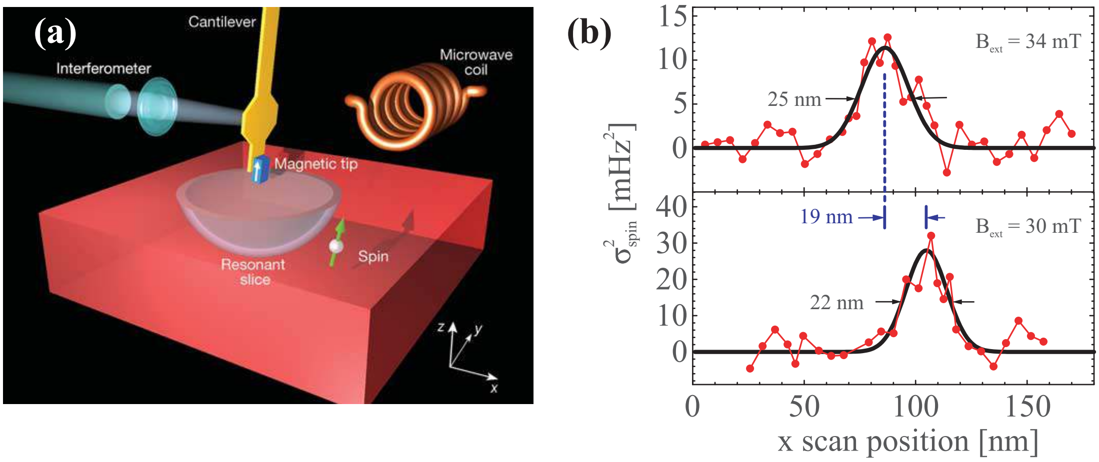

Figure 1.5: Detection of a single electron spin with a mechanical oscillator. **(a)** Setup of the hybrid system. A magnetic gradient structure is attached to the tip of a mechanical oscillator, whose motion is read out with an optical interferometer. A MW coil drives transitions of all spins contained in a *resonant slice*, which is set by an external magnetic field and the cantilever tip. **(b)**. The variance of the spin induced frequency shift as a function of the probe position with respect to the sample for two different external fields. Image source: [51]

O'Connell and Cleland [12] were the first to expose the coherence properties of a macroscopic oscillator in the quantum regime in 2010. In their experiment the aforementioned membrane was not only cooled to its motional ground state, but furthermore coupled to by a superconducting qubit in order to resonantly exchange individual excitations. A necessary requirement for such an interaction is that the coupling between the hybrid's components, parameterized by a frequency $g_x/2\pi$, takes place on a time scale much smaller than the decay time of the quantum states of oscillator and qubit. The rate Γ_{th} at which a motional quantum state decoheres largely depends on the mechanical dissipation rate Γ_{m} and the environmental temperature Θ: $\Gamma_{\mathrm{th}} = \Gamma_{\mathrm{m}} k_B \Theta / \hbar\Omega_{\mathrm{m}}$. Similarly for the quantum system, the so called decoherence rate Γ_2, usually varies between the different qubit types and also strongly depends on its environment. Creating non-classical states of motion thus requires a hybrid mechanical system with coupling mechanism such that

$$g_x > \Gamma_{\mathrm{th}}, \Gamma_2. \tag{1.1}$$

These requirements pose important hurdles in the development of mechanical hybrid systems and have also been a limiting factor in the experiment of O'Connell. Different architectures might profit from increased coherence times, while often the decrease in decoherence rates goes hand in hand with decreased coupling strength. At the present moment there exist many different proposals to combine mechanical oscillators and quantum systems. Potential applications are various. Transfer of a quantum state onto a macroscopic object would provide physicists with a new playground. It would allow them to generate and observe non-classical states of motion as well as to test fundamental quantum theory with macroscopic objects. At the same time, quantum systems intrinsically are extremely sensitive probes of their surroundings and can serve to transduce tiny forces onto the mechanical oscillator and vice versa [35, 54]. Sensing these forces thus allows detection in the quantum regime. Potential quantum computers might profit from the implementation of such hybrid systems, since their qubits – quantum systems like electronic or nuclear spins – can store quantum information while mechanical modes provide means of long range interactions between them [42, 55]. Promising advances towards these goals have been made in recent years. In the next section we are going to review some recently proposed hybrid mechanical systems.

1.1.4 Existing hybrid mechanical systems around the world

In this section we are going to review some of the hybrid mechanical systems that presently exist. We will see the large variety of mechanical oscillators, quantum systems and coupling mechanisms that have been employed in recent years.

Quantum ground state cooling and single-phonon control In this experiment performed in 2010 by O'Connell and Cleland in Santa Barbara [12] a suspended film bulk piezo resonator is cooled to its quantum ground state at about 100 mK with a dilution refrigerator. Due to the oscillator's large resonance frequency of around 6 GHz, no additional cooling techniques are required in order to extract all thermal phonons. The oscillator is made out of a piezo electric material, which means that its motion creates an electrical signal and vice versa. A superconducting phase qubit is coupled to the oscillator via an electrical circuit and serves as control and monitor for the mechanical motion. This man made two level system, built up of a Josephson junction shunted by a capacitor and an inductance, exhibits an energy splitting that can be tuned via a bias current between 5 and 10 GHz. O'Connell and Cleland show that the initially off-resonant qubit can be brought into its excited state and subsequently tuned into resonance. When the energy splitting of the qubit matches the energy splitting of the mechanical resonator, the two systems can resonantly exchange single excitations at the vacuum Rabi frequency $g_x/2\pi = 124\,\mathrm{MHz}$. Such a rather large frequency is necessary due to qubit lifetimes of only around 17 ns. Nonetheless, this experiment presents the world's first demonstration of a macroscopic object exhibiting non-classical motion. Because the interaction duration and strength are well controlled, the mechanical oscillator's phonon occupation can be set arbitrarily between zero and one. This success was made possible by an extremely cumbersome micro-fabrication process, which has since been adapted in similar systems [56].

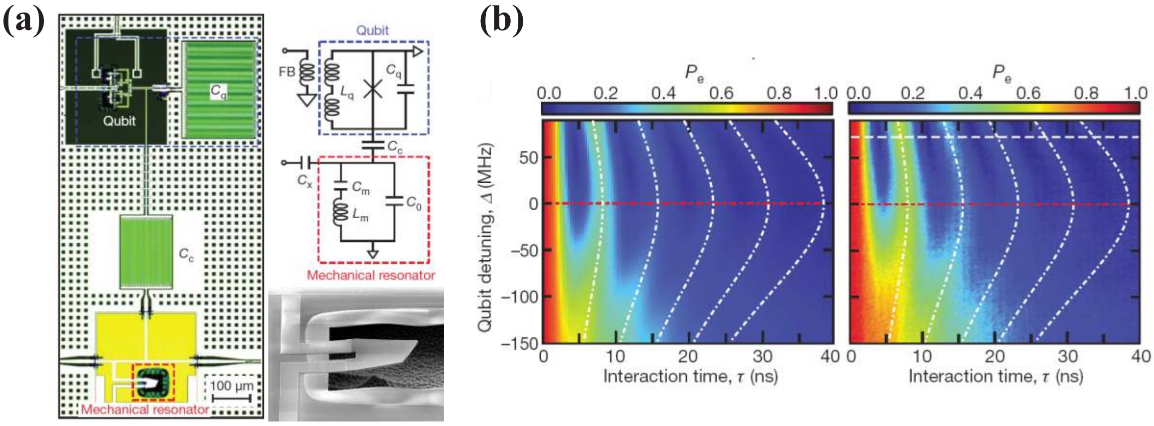

Figure 1.6: Quantum ground state cooling and single-phonon control. **(a)** Setup of the hybrid system consisting of a film bulk membrane and a tunable superconducting qubit coupled by a superconducting MW circuit. **(b)** The mechanical oscillator was controlled and read out using the quantum two level system. The coherent coupling was put into evidence by measuring Rabi oscillations of the excited state population (left: simulations, right: experiment). Image source: [12].

Optical coupling between an atom cloud and an oscillating membrane This hybrid optomechanical system presented by Camerer and Treutlein demonstrates the bidirectional interaction between a mechanical oscillator and an ensemble of cold atoms [57]. In the experiment atoms are cooled and confined by a magneto optical trap (MOT). At the same time a one dimensional optical lattice consisting of interfering laser beams is set up. This is made possible by creating standing waves of light due to reflection of one laser beam with a SiN oscillating membrane. In this configuration, displacement of the membrane shifts the optical lattice and leads to a restoring force onto the atoms. Simultaneously, the atoms' displacement through the optical lattice leads to a change of the radiation pressure that is exerted from the optical field onto the membrane, which presents itself as a restoring dipole force on the mechanical resonator. Due to this bidirectional effect, the optical lattice mediates interaction between the atoms and the reflecting membrane despite a large disparity in the masses of the two components (the oscillator being 10^8 times heavier than the atom cloud). This interplay becomes interesting when the trap frequency approaches the frequency of the membrane mechanical oscillations at around 270 kHz, despite a small coupling strength in the sub-Hz region. Camerer and Treutlein show that the effect of the atoms onto the membrane is an induced additional mechanical damping, while the motion of the atoms along the optical axis is heated by the membrane displacement.

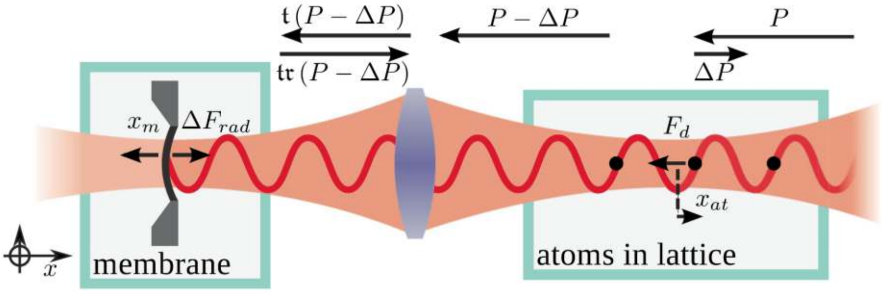

Figure 1.7: Optical coupling between an atom cloud and an oscillating membrane. The mechanical hybrid system of Camerer and Treutlein [57] couples a cloud of cooled atoms to the displacement of an oscillating membrane by means of an optical lattice. While a shift of the atom position modifies the radiation pressure force acting on the membrane, the membrane displacement results in a shift of the optical lattice.

Resonant coupling between a mechanical oscillator and a Bose-Einstein condensate This experiment by Hunger and Treutlein [58] uses two exotic ingredients: The motion of a micromechanical oscillator is coupled via a surface force to a Bose-Einstein condensate (BEC) of Rubidium atoms. In short, the BEC is held by a magnetic trap and placed about 1 μm above the cantilever. The cantilever motion with a resonance frequency of around 10 kHz can be driven and couples to the BEC by changing the trap potential due to surface affects. The perturbation becomes stronger with increasing oscillation amplitude. This leads to an excitation of atomic motion, as a consequence of which atoms can leave the trap potential. The authors show indeed that the number of atoms remaining in the trap is strongly correlated with mechanical drive frequency and amplitude. This result suggests that the small size of the BEC can be exploited to map the local amplitude of oscillation with large spatial resolution. However, due to the large difference in mass, only a small collective coupling constant of $g_x/2\pi < 1\,\mathrm{Hz}$ was achieved and no backaction could be detected from the BEC onto the mechanical oscillator.

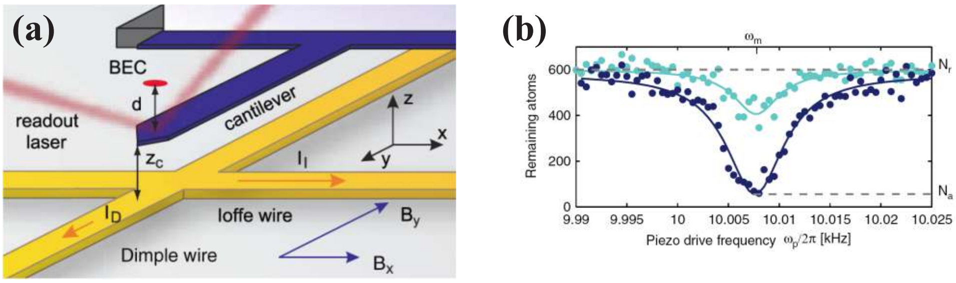

Figure 1.8: Resonant coupling between a mechanical oscillator and a Bose-Einstein condensate [58]. **(a)** A BEC couples via a surface force to the position of a cantilever, which modifies the trap potential. **(b)** The number of atoms remaining in the BEC after it is brought into interaction with the cantilever encodes drive frequency and strength of the cantilever motion.

Nanomechanical measurements of a superconducting qubit In this technologically extremely demanding experiment [59], the group of Roukes demonstrated a spectroscopy measurement of a Cooper Pair Box (CPB) with a nano electromechanical system (NEMS). A CPB is a quantum system made from two Josephson junctions connected by a superconducting loop which presents a non-harmonic charge potential. Due to the varying energy splitting between neighboring states, the ground and first excited states of the CPB form an effective two level system at cryogenic temperatures. The mechanical resonator is a flexural mode of a silicon nitride nano-resonator oscillating around $\Omega_\mathrm{m}/2\pi = 58$ MHz, whose displacement capacitivly couples to the qubit and changes its energy. The total Hamiltonian of the system in the charge eigenbasis is

$$H = \underbrace{\hbar\Omega_\mathrm{m} a^\dagger a}_{H_\mathrm{osc}} + \underbrace{E_\mathrm{el}\sigma_z + E_\mathrm{J}\sigma_x}_{H_\mathrm{CPB}} + \underbrace{\hbar g_z(a^\dagger + a)\sigma_z}_{H_\mathrm{int}} .$$

In the dispersive coupling regime where qubit and oscillator frequency are very different, the parametric interaction generates a force $-\nabla H_\mathrm{int}$ onto the mechanical oscillator, which leads to a qubit state dependent shift of the resonator's eigenfrequency. The coupling between the qubit and resonator can be engineered to be quite large with $g_z/2\pi \approx 0.3 - 2.3\,\mathrm{MHz}$ resulting in a change of $\Omega_\mathrm{m}/2\pi$ by up to $\Delta\Omega_\mathrm{m}/2\pi = 1.6$ kHz. However, coherence times in superconducting qubits are usually small and have been on the order of ns in this experiment. It has therefore not been possible to probe the coherent dynamics of the TLS in this experiment, but readout of $\Delta\Omega_\mathrm{m}$ has been used to detect the steady state population $\langle\sigma_z\rangle$, which constitutes a mechanically mediated spectroscopic measurement of the CPB.

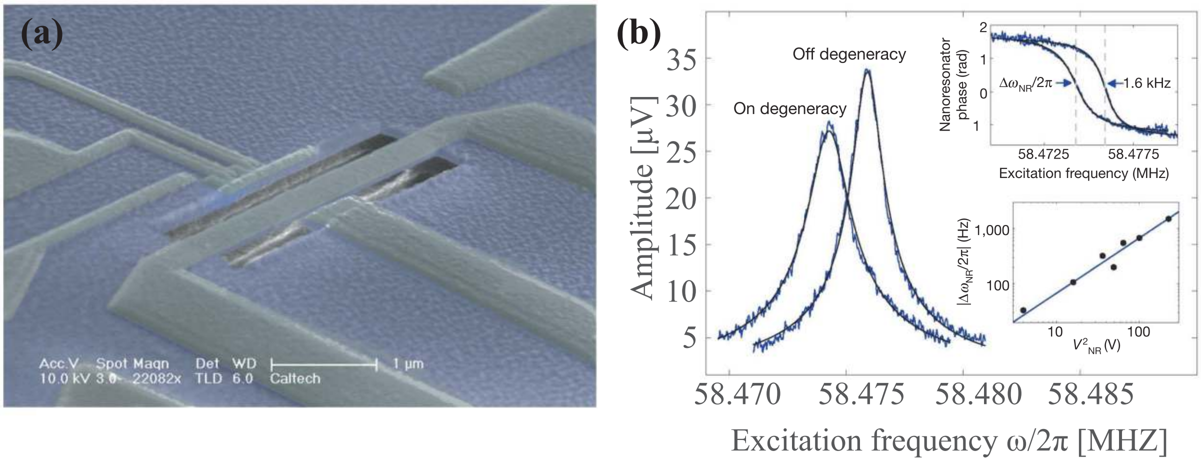

Figure 1.9: NEMS based qubit spectroscopy. **(a)** The mechanical oscillator here is the fundamental in-plane flexural mode of a Silicon-Nitride nanooscillator which couples capacitively to a CPB. **(b)** The qubit can be manipulated externally to change its occupation. Simultaneously, the qubit exerts a state dependent force, which shifts the effective resonance frequency of the mechanical oscillator. Image source: [59]

Charge induced mechanical damping by strong electro-mechanical coupling Shortly after Roukes, Bennet and Grütter of McGill university in Montreal [60] presented a mechanical hybrid system between an atomic force microscope (AFM) cantilever and an Indium-Arsenide quantum dot. In their device, motion of the cantilever at about 166 kHz periodically varies a capacitance between the cantilever tip and quantum dot and thus changes the energy of the electrons on the dot. This leads to oscillator position dependent tunneling rates for charges to hop on or off the dot, whose balance defines the steady state charge number. Conversely, capacitance and thus the charge dependent voltage in the circuit vary with the tip position. This gradient gives rise to a charge dependent force, which is felt by the oscillator and detectable either as frequency shift or additional damping. In astonishingly good agreement with theory, the experimenters show that indeed amplitude and gate voltage dependent damping is induced on the mechanical motion. The tunable coupling strength is on the order of 10 meV per electron on the dot translating to displacement of the resonator on the nm scale.

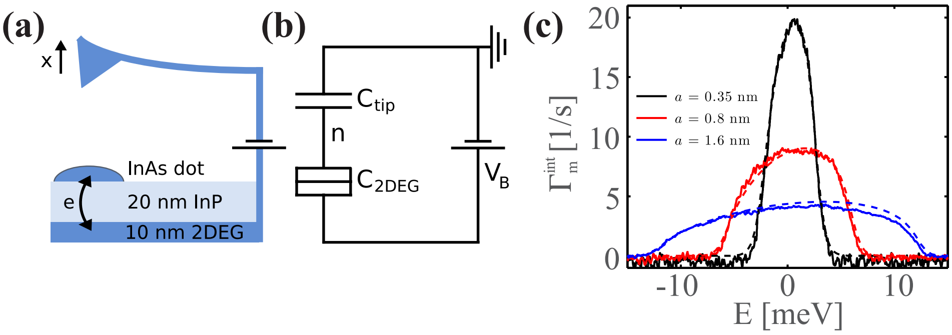

Figure 1.10: Charge induced mechanical damping. **(a)** Motion of the cantilever tip above a quantum dot changes the capacitance between the dot and the AFM cantilever tip, periodically varying the quantum dot energy. **(b)** Circuit diagram of the hybrid system. **(c)** Mechanical damping as a function of gating voltage induced by charges on the quantum dot. The charge number on the quantum dot is position and therefore amplitude dependent, resulting in an amplitude dependent charge induced mechanical damping. For large enough oscillation amplitudes the interaction enters a strong electromechanical coupling regime, where a difference of probabilities between electrons either hopping onto or off the quantum dot is evidenced by a damping behavior that is asymmetric with respect to the applied bias voltage. Image source: [60]

A quantum dot in a photon trumpet While the experiment by O'Connell and Cleland demonstrated a resonator and qubit in resonant interaction, the experiment by Yeo [61] demonstrates how a GaAs trumpet shaped nanowire, acting as a photonic waveguide and mechanical oscillator at the same time, could change the energy splitting of a two level system. The TLS in the experiment is a quantum dot which upon de-excitation emits photons in the optical range. The associated energy splitting is a function of local strain effects in the GaAs nanowire, which is periodically modified due to the oscillator's motion, again expressed by the parametric interaction Hamiltonian $H_{\text{int}} = \hbar g_z(a^\dagger + a)\sigma_z$. Since the wavelength of the emitted photons directly corresponds to the energy splitting of the quantum dot, a spectroscopic analysis of the measured fluorescence revealed the coupling between quantum dot and nanowire. The experimental parameters were such that the oscillation period of the mechanical resonator, around $\sim 2\,\mu$s, was much longer than the lifetime associated with excited quantum dot around $\sim 500\,$ps. The experiment therefore is deep in the so called adiabatic regime, which leads to slow modulation of the quantum dot energy splitting. As a consequence, the wavelength of the emitted photons was related to the phase of mechanical oscillation, see Figure 1.11. Yeo furthermore showed that the coupling strength between quantum dot and oscillator ($g_z/2\pi \approx 450\,$kHz) was very close to the frequency of mechanical modulation, $\Omega_{\text{m}}/2\pi = 530\,$kHz. Their system thus presents a very promising candidate for the ultra strong interaction regime, where $g_z > \Omega_{\text{m}}$. A consequence of such a large coupling is that the separation of the rest positions corresponding to opposing quantum states becomes larger than the zero-point fluctuations of the mechanical oscillator, a phenomenon at which we will take a closer look in Chapter 2.

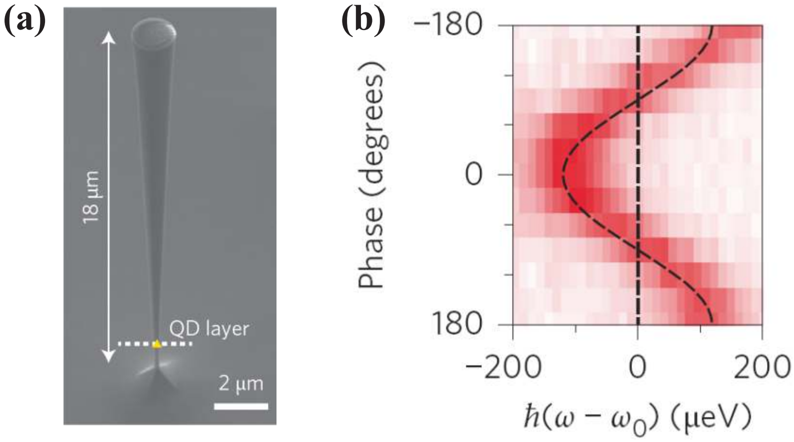

Figure 1.11: A quantum dot in a photon trumpet [61]. **(a)** The photon trumpet consists of a conically shaped photonic GaAs nanowire hosting an optically active InAs quantum dot. **(b)** Deflection of the trumpet creates strain in its matrix, which couples to the energy splitting of the quantum dot. In the adiabatic regime of slow mechanical oscillation, this shift was observed to encode the oscillation phase of the mechanical oscillator by means of emission spectroscopy.

Hybrid circuit quantum electrodynamics In a very recent experiment [56], Silanpää and colleagues of Finnish Aalto University couple a superconducting transmon qubit to a microwave cavity. The energy of the qubit is modulated with coupling strength $g_z/2\pi = 4.5\,\text{MHz}$ by a capacitively coupled Aluminum membrane oscillating at 72 MHz. At these modulation frequencies, much faster than the energy decay rates, the researchers work in the resolved sideband regime, where the imprint of the mechanical modulation is the appearance of motional sidebands in the energy spectra of this artificial two level system. Demonstrating time resolved control on the qubit state and sufficiently long lifetimes of the qubit, Silanpää and his group could access the spin dynamics and showed how these are modified in presence of driven mechanical motion.

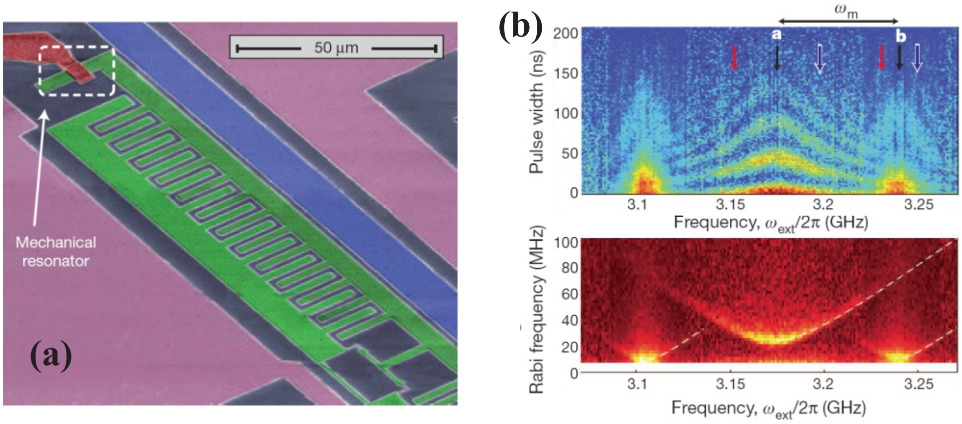

Figure 1.12: Hybrid circuit quantum electrodynamics [56]. **(a)** A 72 MHz mechanical resonator fabricated out of aluminum on a sapphire substrate capacitively couples to a ∼ 3 GHz transmon qubit. **(b)** Motion of the oscillator modulates the transmon energy splitting. The authors showed that Rabi oscillations could be driven on the motional sidebands of the qubit (top: temporal trace, bottom: Fourier trace).

1.2 A SiC nanowire - NV electronic spin hybrid mechanical system

In this part of the introduction we are going to present the device used in this work: a single solid state hybrid spin mechanical system with the potential to bidirectionally probe the spin state and mechanical motion at room temperature operation using magnetic field coupling. We are going to take a closer look at its components first. The electron spin of negatively charged NV defects in nanodiamonds and ultra light Silicon Carbide nanowires. Finally, we will present the first signatures of hybridization in this system, in which the TLS has been used to probe the oscillator dynamics.

1.2.1 Nitrogen vacancy defects in diamond

In our experiment, we are working with a solid state qubit provided by the electron spin of a so called Nitrogen Vacancy defect (NV) hosted in diamond. Diamond itself is a remarkable material, consisting of covalently bound carbon atoms forming two interpenetrating face centered cubic lattices with interatomic distances of 0.2 nm. This structure renders diamond not only chemically inert, but also one of the hardest materials in the world, expressed by the highest Debye temperature of all materials [62].

In addition to being one of the best thermal conductors, diamond is also a wide-gap semiconductor with its conduction band 5.43 eV above the valence band [63]. All these properties have ignited a large research interest in diamond, with applications as heat sinks, optical windows, cutting tools, large power electronics and so on. Because of the wide band gap, diamond is host to many optically active color defects of which more than 500 have been identified and many of these can be excited without excessive heating of the material. These defects arise due to naturally occurring impurities, like Boron or Nitrogen atoms. A so called Nitrogen vacancy color center (for short NV) is a defect that emerges when a single nitrogen atom replacing a carbon atom is situated next to a vacancy in the regular diamond lattice.

The NV defect has a well defined symmetry, denoted C_{3v}, which corresponds to a symmetry group formed by rotations by an angle $2n\pi/3$ around the NV axis and three mirror symmetries with respect to the planes defined by the rotation axis and one of the Carbon atoms of the tetrahedron. Yet, the regular structure at which electrons distribute is broken around the defect. While three of the five valence electrons of the nitrogen atom build bonds with the surrounding carbon atoms, two remain in a lone pair [64]. There are three electrons associated with the vacancy coming from its three neighboring carbon atoms. At a given time, any two of them form a quasi covalent bond, while the last electron remains unpaired, due to which the charge neutral NV^0 defect posses a $S = \frac{1}{2}$ net electron spin. An additional electron can be trapped in the vacancy, forming a negatively charged NV$^-$ defect with $S = 1$.

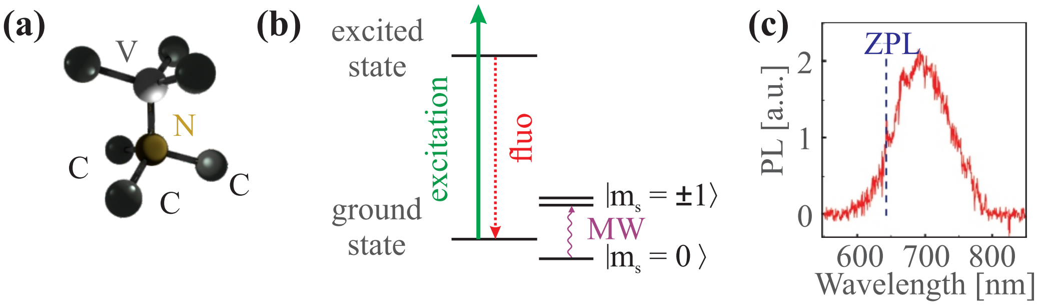

Figure 1.13: The Nitrogen Vacancy defect in diamond. **(a)** The NV defect consists of a Nitrogen impurity next to a vacancy in the diamond matrix. Its structure with broken tetrahedral symmetry gives rise to a $C_{3\nu}$ symmetry. **(b)** The orbital excited state of the NV defect can be stimulated by off-resonant excitation at 532 nm while fluorescence is emitted in the red. **(c)** Emission spectrum of a negatively charged NV defect with zero phonon line at 637 nm, corresponding to an energy gap of 1.945 eV. Image source: [65, 66].

The ability to detect individual NV defects with a confocal microscope [67] has established their nature as stable single photon source at room temperature operation [68, 69]. While the zero phonon emission line is slightly offset between the charge states, coupling with optical phonons leads to a broad emission spectrum at room temperature in both configurations. This broadening can however be suppressed in a low temperature environment and NV defects have been integrated in quantum cryptography [70, 71] and surface plasmon [72] experiments due to their reliable properties as single photon emitters. The charge state has important consequences on the optical and spin properties. While the $S = \frac{1}{2}$ system is energetically degenerate at zero magnetic field, the NV$^-$ has a well defined spin ground state and shows spin dependent photon emission [73, 74]. The fact that its spin state can be very efficiently read out and prepared using optical techniques has dramatically boosted research around the negatively charged defect. In this configuration, spin ground and excited states are separated by a large frequency gap of 2.87 GHz [75]. Microwave enabled manipulation and optical readout of a spin naturally trapped in a solid state system with coherence times in the ms range at room temperature [76] make the NV$^-$ a close to ideal quantum register. The negatively charged NV defect[3] [77–80] has thus found a wide variety of applications. Its sensitivity to magnetic fields due to the Zeeman effect turns the electron spin into a sensitive and nanozied magnetometer. A shift of the resonance frequency of 28 MHz/mT permits the detection of small magnetic fields within short acquisition times. NV defects occurring in small sized and bio-compatible nano-diamonds thus enable the construction of nanoscale magnetometers [81–84], but their employment in devices for electric field [85] sensing and temperature measurement in living cells [86] has also been demonstrated, see Figure 1.14.

---

[3] Indeed, almost all spin based experiments were performed with the negatively charged configuration. Throughout this thesis we are going to restrict our discussion to the NV$^-$ and use the term NV defect synonymously, unless stated otherwise.

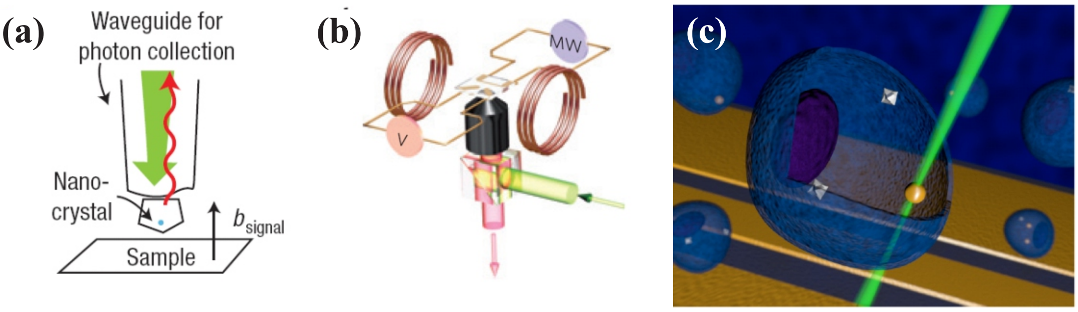

Figure 1.14: Applications of NV defects combine technological mastery over the host material diamond as well as the sensitivity of a single isolated quantum system. NV defects have recently been employed as probes for magnetic **(a)** and electric fields **(b)** as well as thermometers in living cells **(c)**. Image sources: [81, 85, 86].

Because of excellent spin and optical properties, NV defects have become extremely relevant in modern day solid state physics research. Advanced fabrication techniques combine with long term stability and precise control over the NV defect's quantum state to generate a workstation to push the frontiers of modern day technology. In order to illustrate these points we are going to outline here two experiments demonstrating the use of the NV defect as a probe for magnetic fields and as an entanglement generating qubit. This will allow us to introduce the experimental toolbox for manipulating NV defects, many elements of which we will see again later in this thesis.

Magnetometry with NV defects

In this paragraph we summarize the experimental techniques for the measurement of magnetic fields developed during the PhD thesis of Loïc Rondin [87] in the group of Vincent Jacques and Jean-François Roch of ENS Cachan. Magnetic field detection with NV defects is based on the Zeeman effect. For weak fields, the energy of the single spin changes with the magnitude of the projection of an externally applied magnetic field onto the spin axis. By performing a spectroscopy measurement, the resonance frequency of the spin can be related to the external magnetic field. In order to construct a magnetometer with high spatial resolution it is important to work with a probe of small spatial extension. To this end, the experimenters chose to use single NV defects hosted in small nanodiamonds with diameters of around 50 nm (a typical setup is shown in Figure 1.15 **(a)**). The experiment further profits from using an atomic force microscope (AFM) cantilever tip, whose position can be well controlled by means of a piezo stage. Nanodiamonds can be prepared on a substrate and those hosting a single NV defect can be identified with a confocal microscope. The AFM cantilever is subsequently functionalized by dipping its tip into a polymer which serves as a glue. Following this procedure, it can then be swept across the substrate to pick up the optically selected nanodiamond. By carefully detecting the evolution of the resonance frequency in a well controlled three dimensional magnetic field, the orientation of the NV defect with respect to the cantilever alignment can be inferred. This probe can then be swept across a sample and by detection of the position dependent resonance frequency the magnetic field can be measured with nanometric spatial resolution. Rondin and Jacques exploit the spin dependence of the emitted NV fluorescence in two different measurement strategies. In a first technique, the spin resonance can be measured directly at various positions and the magnetic field component along the NV axis can be mapped. In a second technique, the NV defect is continuously excited with off-resonant laser light at 532 nm, while the fluorescence emitted above 637 nm is detected. Simultaneously, a frequency modulated MW field rapidly alternating between two frequencies $\omega_1/2\pi$ and $\omega_2/2\pi$ is applied by a MW antenna. The MW signal is resonant with the spin only at certain positions above a measurement sample. Namely at those, where the magnetic field emerging from the sample shifts the spin frequency $\omega_0(B_{\text{ext}})/2\pi$ to match either one of the MW frequencies. In that case the MW drive manages to reduce the ground state population of the spin, as a result of which the difference of emitted fluorescence corresponding to the two MW frequencies increases. Then, by tracking this signal as the probe is swept across the sample, isomagnetic field lines can be detected.

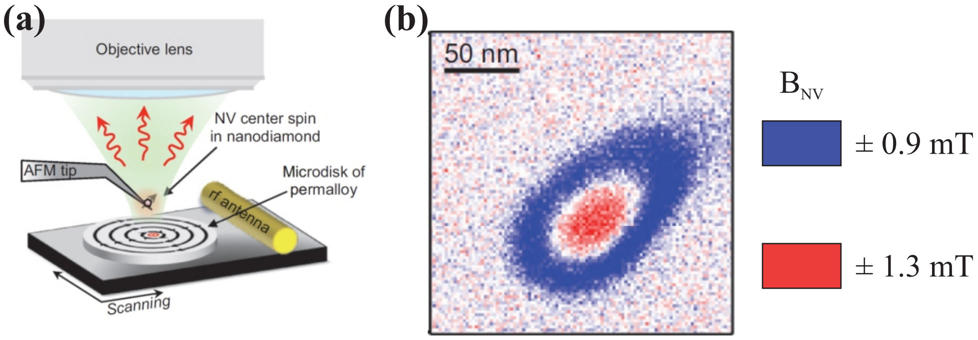

Figure 1.15: Magnetometry with NV defects. **(a)** Magnetometry setup showing the AFM cantilever tip holding a nanodiamond hosting a single NV spin and the confocal microscope used to detect the spin state dependent fluorescence of the NV defect. A RF antenna provides MW fields of two frequencies $\omega_1/2\pi$ and $\omega_2/2\pi$. Each frequency is resonant for a given projected magnetic field strengths, that depends on the relative position between NV and magnetic structure. When spin flips are induced the fluorescence collected from the NV reduces. **(b)** Dual-iso-magnetic field lines resulting from the difference of the fluorescence signal gated to the sample irradiation with the two MW frequencies. Image source: [88].

The measurement of magnetic fields with high spatial resolution is advantageous when investigating structures with large magnetic field gradients, such that the magnetic field amplitude rapidly changes over a small length scale. This is the case with vortex structures, where the magnetic field orientation changes from in-plane to out-of-plane over a strip of ~15 nm in the central region. In that case the method to detect iso-magnetic fields has provided quantitative determination of the stray fields of a ferromagnetic microdisk at the vortex core, as shown in Figure 1.15 **(b)**. Importantly, high quality sensing is achieved because the NV probe does not perturb the magnetic sample, which is in contrast to MFM techniques.

Entanglement between solid state qubits

An experiment of Pfaff, Robledo and Hanson emphasizes the NV defect's exploitability as a quantum state transducer [89,90]. At low temperatures (here ~8 K) the spin dependent transitions (labeled E_x for $|m_s = 0\rangle$ and A_1 for $|m_s = \pm 1\rangle$, denoting the orbital symmetry) to the optical excited state can be resolved spectrally, see Figure 1.16 **(a)**. Because there spin mixing can occur, continuous resonant excitation of E_x (A_1) leads to polarization of the spin in $|m_s = \pm 1\rangle$ ($|m_s = 0\rangle$) with fidelities above 90%, shown in Figure 1.16 **(b)**. Resonant optical excitation can also be used for spin readout. Since under excitation of the E_x transition photons can only be absorbed for the $|m_s = 0\rangle$ state, the detection of NV fluorescence (or its absence) strongly correlates with the NV's spin state, see Figure 1.16 **(c, d)**.

Moreover, the NV spin strongly interacts with its surroundings, which mostly consists of Carbon and Nitrogen atoms. Nearby nuclear spins of these atoms create a magnetic field that couples to the electron spin via dipole-dipole interactions. The coupling is especially prominent with the $I = 1$ nuclear spin of the ^{14}N atom that makes up the NV defect and with a nearest or next nearest ^{13}C nuclear spin. Notice that the coupling to a Nitrogen nuclear spin is unavoidable, since both isotopes (14 and 15) have a net nuclear spin, while the probability to couple to a nearby Carbon nuclear spin is a function of the random distribution of the ^{13}C isotope (with 1.1% natural abundance). Their effect is to shift the resonance frequency of the electron spin as is depicted in Figure 1.16 **(e)**. The spectrum shows that the energy of the NV defect is split into three resonances by roughly $0, \pm 2.2$ MHz due to the Nitrogen nuclear spin and by ± 6.4 MHz due to a nearest neighbor Carbon nuclear spin.

The authors chose to work with the nuclear spins as quantum registers because of their intrinsically weak coupling to the environment leading to naturally long coherence times, which is on the order of a few milliseconds compared to $\sim 1\,\mu$s for the NV spin. Because all three spin registers have different energy gaps, they can be addressed and manipulated separately using resonantly tuned radio frequency fields emitted by an antenna attached to the bulk diamond sample. By properly timing these fields, they can be used to drive Rabi oscillations of the nuclear spin states, as shown in Figure 1.16 **(f)**, enabling the following entanglement generation procedure: the nuclear spins are initialized in the state $|\mathrm{I_z^C} = \frac{1}{2}, \mathrm{I_z^N} = 0\rangle \equiv |00\rangle$ (conversely, $|\mathrm{I_z^C} = -\frac{1}{2}, \mathrm{I_z^N} = 1\rangle \equiv |11\rangle$), see Figure 1.16 **(g)**. This is achieved by first polarizing the electron spin in $|\mathrm{m_s} = \pm 1\rangle$ using optical pumping of the E_x transition. Subsequently, a MW pulse is applied to the spin that is resonant only for one combination of the nuclear spin's projection along the NV axis, namely the $|00\rangle$ configuration. Next, the nuclear spins are projected by measurement into the $|CN\rangle = |00\rangle$ configuration: Again the E_x transition is probed optically. If fluorescence is indeed emitted, the NV spin has been in the ground state and, consequently, the nuclear spins are in the $|CN\rangle = |00\rangle$ configuration (otherwise, the process is repeated until fluorescence can be detected). By applying a RF pulse to each nuclear spin, they can be brought into a superposition, see Figure 1.16 **(h)**. The NV defect comes again into play when it is used to entangle the nuclear spins. With the NV spin initially occupying its excited state, two MW pulses are applied, which rotate the spin to the ground state if $|CN\rangle = |00\rangle$ or $|CN\rangle = |11\rangle$. If now the state of the NV defect is measured, its quantum superposition state is projected into an eigenstate. If it is found to be rotated, the nuclear spins are evenly projected, but into a maximally entangled state, see Figure 1.16 **(i)**. The authors go on by measuring the correlations between the nuclear spins and demonstrate that the Bell inequalities are indeed violated, proving the non-existence of hidden variables. In conclusion, the experiment illustrates how the NV defect can be used as a so called ancilla qubit, an auxiliary qubit to create quantum correlations in a different system. Their use as a quantum bit transducer is thus general and not limited to mechanical hybrid systems.

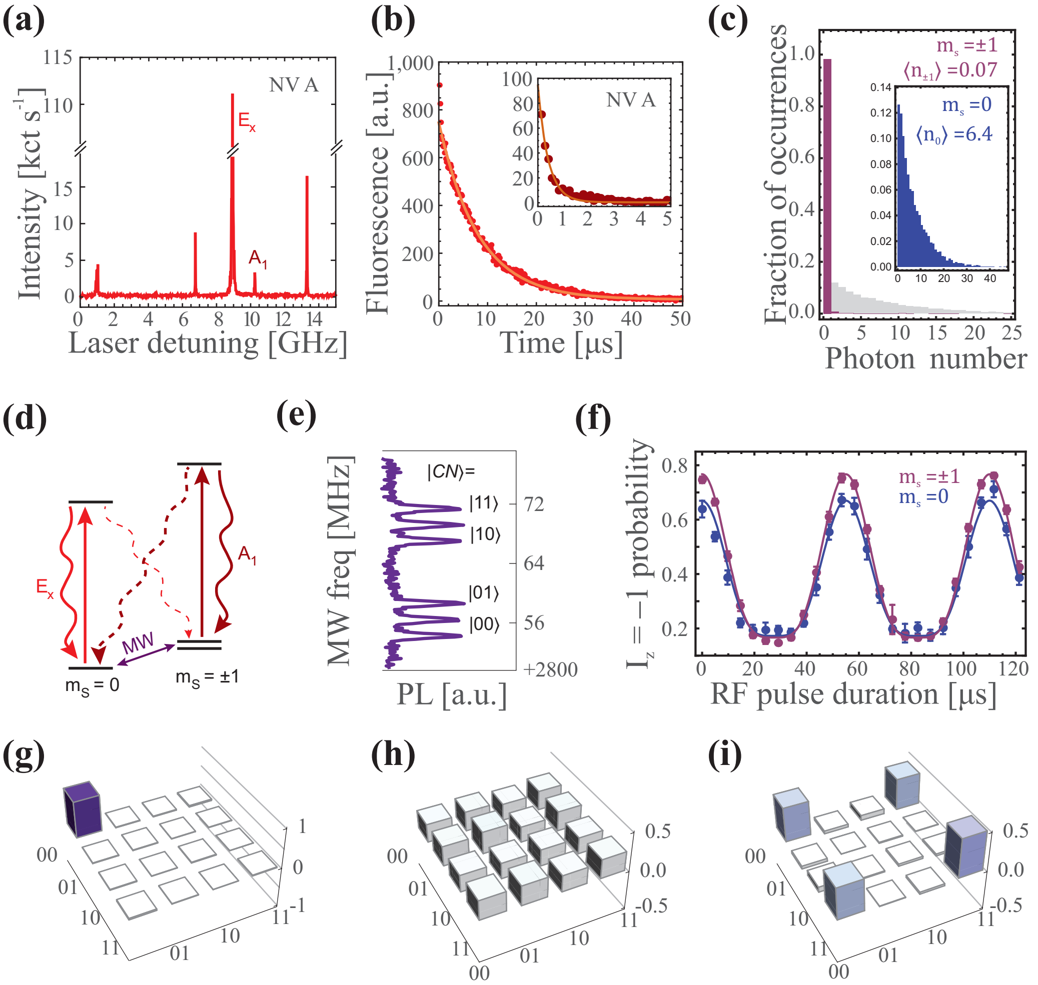

Figure 1.16: Entanglement between solid state qubits. **(a)** Spin dependent optical transitions become spectrally resolvable at low temperatures. E_x corresponds to the $|0\rangle$- and A_1 to the $|\pm1\rangle$-state. **(b)** Fluorescence measurement of the NV defect under continuous excitation of the E_x transition (the inset shows the A_1 transition). The exponential decay indicates that the spin state is mixed in the orbital excited state, which can be used to optically pump the spin state. **(c)** Single-shot readout of the spin state. If no photons are detected in a sampling window following excitation of the E_x transition, the spin has been in one of the two excited states (purple curve). If, on the contrary, the spin is in the ground state, a considerable amount of photons are detected (blue curve). **(d)** Diagram of the probed transitions, showing optical polarization channels (wavy arrows) and the MW induced spin transitions. **(e)** Spectroscopy of the NV spin showing splitting of the energy levels due to coupling with a ^{14}N nuclear spin (top and bottom triplet) and a ^{13}C nuclear spin (doublet structure). The ket vectors indicate the experimental subspace. **(f)** Rabi oscillations of the Nitrogen nuclear spin driven by a RF source, as a function of the electronic spin state. **(g)** Real part of the density matrix for the nuclear spins showing initialization in the $|00\rangle$ state by projective measurement of the NV spin. **(h)** Using different RF pulses for the nitrogen and carbon nuclear spin, a superposition state can be prepared. **(i)** The NV spin is then rotated into the ground state by application of two MW pulses tuned to the $|00\rangle$ or $|11\rangle$ transition. If the NV spin is afterward found to be in the ground state, the nuclear spins are projected into the Bell state of even parity. Image source: [89, 90].

NV defects in hybrid mechanical systems

Hybrid mechanical systems potentially profit from integrating NV defects because of their two level character with optical preparation and readout as well as long coherence times all at room temperature.

This, combined with their high sensitivity to magnetic fields, makes the strong coupling regime seem within reach [53]. Current developments promise to further push the boundaries of experimentally feasible realizations. Engineering of integrated devices is now possible, providing researchers with lighter and yet more sensitive devices. Nanomechanical oscillators can be directly produced from a single-crystal diamond sample. The high stiffness of diamond permits to access large oscillation frequencies. Consequently, as suggested in [47], a strain coupled hybrid system formed by a NV spin and a diamond mechanical oscillator was recently demonstrated to operate in the resolved sideband regime [91]. At the same time these oscillators have been shown to reach extremely high mechanical quality factors of $Q = 10^6$ [92]. Moreover, the ability to control the environment reduces coupling of the spin to surrounding impurities resulting in largely increased life- and coherence times of quantum states. Indeed, the observation of room temperature coherence times in the millisecond regime [76] translates to the feasibility of performing more than 1000 gate operations at MHz frequencies. These systems might further profit from implantation techniques that offer great spatial control over the position of artificially created NV defects or the ability to mill solid immersion lenses into the diamond matrix directly above single NV defects in order to increase the fluorescence collection efficiency. These developments are summarized in Figure 1.17.

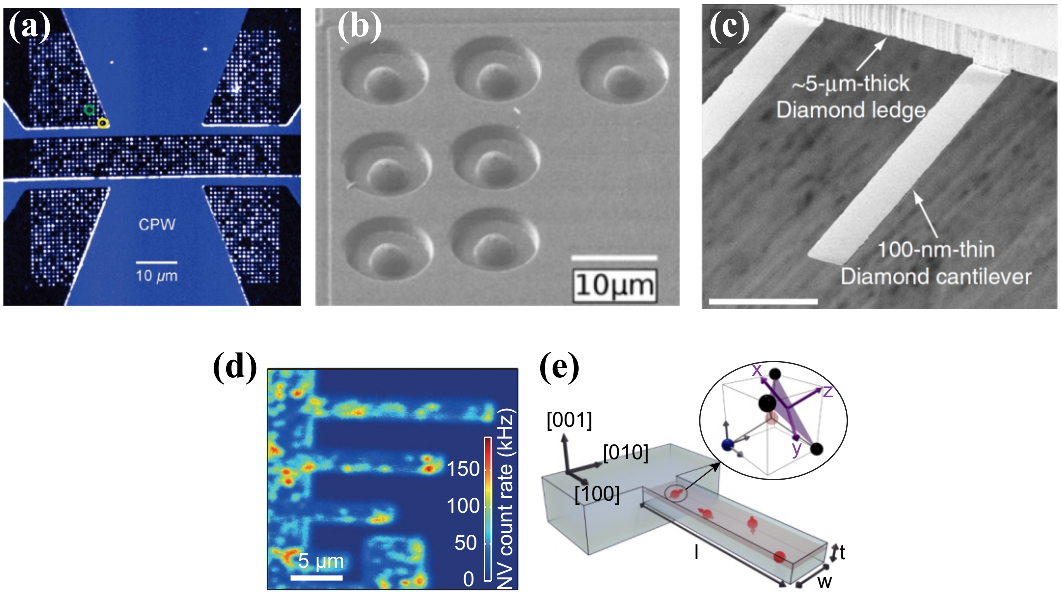

Figure 1.17: NV defects in integrated systems. **(a)** Implantation techniques with spatial control have been developed in the context of quantum network registers [93]. **(b)** Solid immersion lenses can be milled directly above a single NV defect and therefore increase the collection angle for fluorescence readout [94]. **(c)** High quality mechanical oscillators can be fabricated from monolithic diamond [92]. **(d)** These cantilevers can be prepared from diamond already hosting NV defects, as was done in [91]. **(e)** NV defects in these cantilevers are coupled to the oscillator motion due to time varying strain in the diamond matrix. Because of the material's large stiffness high oscillation frequencies can be achieved, facilitating operation in the resolved sideband regime [91].

1.2.2 SiC nanowires as mechancial oscillators

We propose working with monocrystalline Silicon Carbide nanowires, batch produced from a bottom-up fabrication process [95, 96]. These nanowires can be glued to a tungsten support tip and thus be navigated and nano-positioned through free space, which is of crucial importance when exploring large magnetic field gradients necessary to couple their motion to a single NV defect. Observed dimensions of length and thickness of the cylindrical nanowires range between 10 - 100 μm and 50 - 300 nm, respectively. A typical nanowire is shown in Figure 1.18 **(a)**. Importantly, the oscillator motion can be excited using electrostatic forces or a piezo drive connected to the support tip. Because of the material's wide band gap, the nanowires are resilient to damage induced by optical irradiation, which enables optical readout of their motion, as indicated in Figure 1.18 **(b)**.

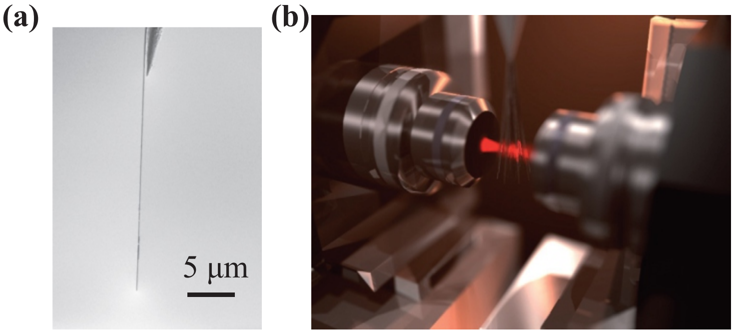

Figure 1.18: SiC nanowires. **(a)** A typical SiC nanowire clamped to a Tungsten support tip. **(b)** The nanowire displacement can be detected optically with sensitivities reaching ≈ fm/Hz$^{0.5}$ [97].

Extremely low masses on the order of tens of fg and low mechanical dissipation rates on the order of a few tens of Hz turn SiC nanowires into extremely sensitive probes with a force sensitivity of several aN/Hz$^{0.5}$ at 300 K. In order to exploit SiC nanowires as ultrasensitive force sensors, a cavity free optical detection setup was developed in our laboratory during the PhD project of Arnaud Gloppe [97]. Indeed, the shot noise limited displacement detection (near the standard quantum limit) of the nanowire's thermal motion was realized with an extremely large signal-to-noise ratio of 72 dB. Figure 1.19 shows a typical mechanical spectrum obtained for a nanowire of length $l = 52\,\mu$m and diameter $d = 150\,$nm. Visible are the first three thermally driven oscillation modes with frequencies 113, 473 and 1160 kHz. Due to oscillation frequencies in the 100 kHz range and the low mass of the mechanical resonator, the root mean square thermal oscillation amplitudes and zero-point fluctuations are on the nm and pm scale, respectively. The latter figure is an important benchmark for the strong coupling regime of hybrid interaction. For the coupling strength $g_z/2\pi$ to reach 100 kHz with zero-point fluctuations of ≈ 10 pm, magnetic field gradients on the order of 10^6 T/m will be required, which is experimentally feasible [98].

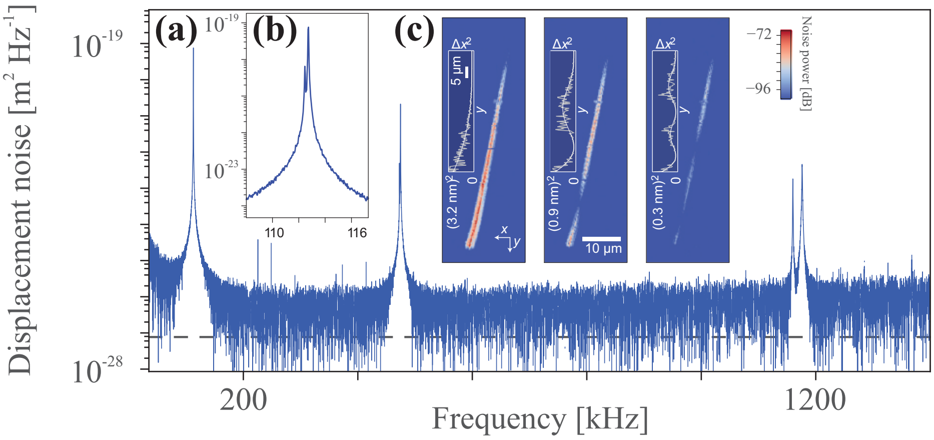

Figure 1.19: Mechanical vibration spectrum of a SiC nanowire. **(a)** The first three longitudinal modes of oscillation are visible. **(b)** Zoom onto the first resonance revealing two peaks corresponding to two orthogonal displacement modes due to asymmetries in the nanowire shapes and clamping conditions. **(c)** Geometric profile of the first three oscillation modes. Image source: [97]

The singly clamped SiC nanowires can be functionalized by attaching nanodiamonds hosting single

NV defects or magnetic structures to the free moving end. The nanowire motion can then be coupled to the spin by displacement through a magnetic field gradient. In the next section we will show how such a setup has been successfully used to read out the mechanical motion of the nanowire by means of a spectroscopic measurement of the NV spin.

1.2.3 Coupling of a single NV defect to a SiC nanowire

A first experiment in 2011 demonstrated a hybrid system made from a single NV defect attached to the free moving tip of a SiC nanowire operating at room temperature and ambient pressure [99]. Figure 1.20 **(a)** shows a fluorescence map in which the supporting tungsten tip, the SiC nanowire and the single NV can be seen. The essential parts of the measurement setup are shown in Figure 1.20 **(b)**. The mechanical drive was induced by either an electrostatic force or a piezo drive actuating mechanical motion with tunable amplitude and drive frequency. The nanowire position was coupled to the NV spin by means of a large magnetic field gradient. A confocal microscope was used to read out red fluorescence emitted by the NV defect during 532 nm excitation. Simultaneously, a MW magnetic field provided by a nearby antenna could be used to drive transitions of the NV spin and realize steady state ESR spectroscopy.

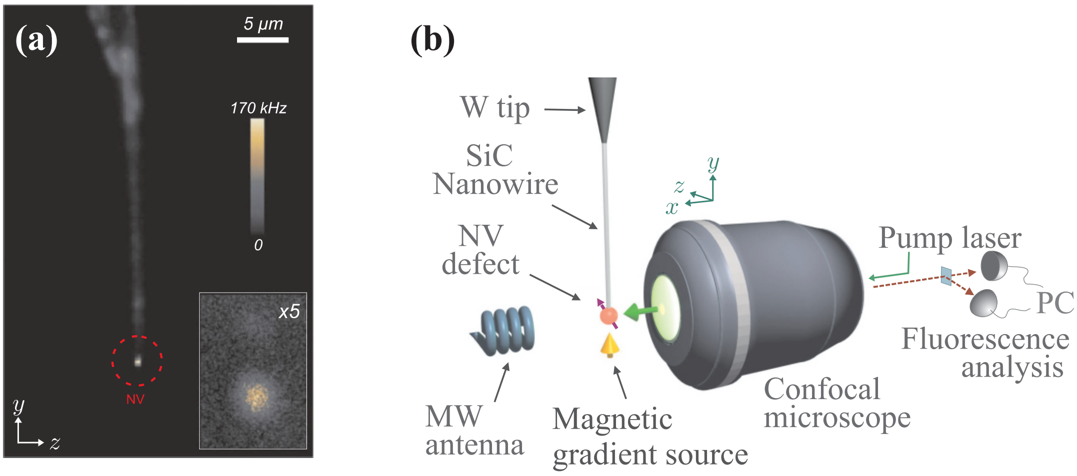

Figure 1.20: A SiC nanowire - NV spin hybrid system. **(a)** Fluorescence scan of the hybrid system showing the SiC nanowire and the emission of a NV defect attached to the bottom end of the wire. **(b)** Essential components of the measurement setup.

The first characterization of the coupling of the NV defect to the nano-mechanical motion was obtained when measuring the autocorrelation function of the NV fluorescence, which yields the statistical probability of measuring a single photon with delay τ after the detection of a first photon. At rest, such a measurement demonstrated single emitter character of the NV defect: a dip at zero delay reaching below half the value obtained at large delay times signifies that only one photon is emitted at a time. This signature is altered when performing the same measurement while driving the mechanical motion. Since the nanowire periodically moves the NV defect across the detection area in front of the confocal microscope, the autocorrelation function is modulated at the half period. The modified autocorrelation function can be analyzed in terms of motional amplitude and mechanical oscillations can thus be calibrated in terms of drive strength.

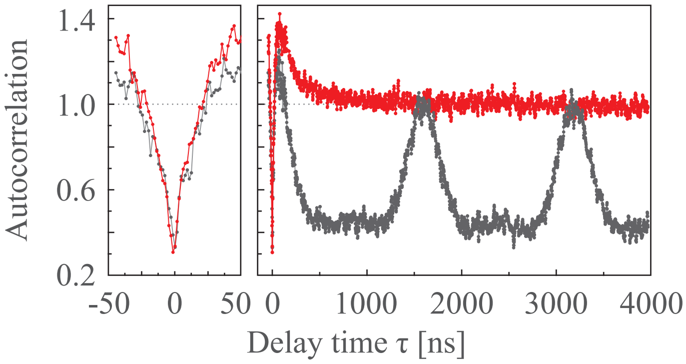

Figure 1.21: Autocorrelation function of the emitted NV fluorescence. The red curve corresponds to the SiC nanowire at rest, while the grey curve represents the case of driven mechanical motion. Clearly visible is the modulation at half the mechanical period. The panel on the left hand side represents a zoom onto short delay times.

The single spin character of the NV defect can likewise be utilized to detect mechanical motion. Due to the presence of a magnetic field gradient, a spatially dependent Zeeman effect changes the energy of the spin as a function of position. Applying a resonant electrostatic force drives the mechanical oscillator into motion, so that the NV defect experiences varying magnetic field strength across its trajectory. The MW antenna is used to perform a spectroscopy measurement: a continuous MW current creates a magnetic field that can drive the spin when its frequency matches the Zeeman shifted energy gap. A sweep of the MW frequency allows to identify the resonance frequency by means of a steady state spin ground state population measurement (called ESR for electron spin resonance measurement) with the confocal microscope. Such a measurement of the resonance also allows to determine two important experimental parameters: first, from the shift of spin resonance frequency as a function of displacement the magnetic gradient can be determined. It was found to be on the order of 10^4 T/m, which parametrically shifts the spin resonance frequency by 2.8 MHz for a 10 nm displacement. Second, it was possible to resolve the linewidth of the spin, which was broadened by the mechanical oscillations. The fundamental mode of the mechanical oscillator was found to be around 625 kHz, which puts the hybrid interaction in the adiabatic regime, where the mechanical period is much larger then the spin lifetime. Broadening of the ESR linewidth as a result of driving the resonator into motion, can be explained by averaging the spin energy over the trajectory of mechanical oscillations, see Figure 1.22 **(a, b)**. Finally, measurement of the spin linewidth also permits to deduce the mechanical oscillator's response to the drive frequency, which is shown in Figure 1.22 **(c)**.

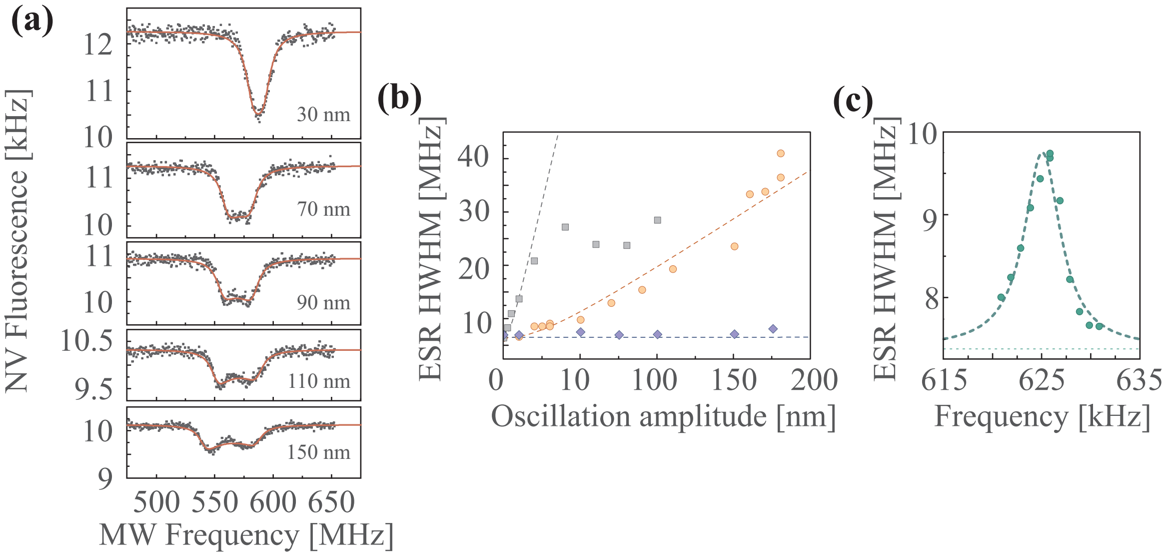

Figure 1.22: Spin readout of the mechanical motion. **(a)** ESR spectra taken for different resonant drive strength of the mechanical motion. **(b)** Broadening of the spin linewidth as the oscillation amplitude of the resonantly driven oscillator increases with magnetic field gradients 0.1 (blue), 6700 (yellow) and 45000 T/m (grey). **(c)** The spin linewidth changes as the mechanical drive frequency is swept across resonance of the first oscillation mode.

Modification of the autocorrelation function and spin linewidth prove that in this hybrid system the NV spin can indeed be used to read out the mechanical motion. Several effects beyond these first signatures can be envisioned. For example working at larger magnetic field gradients can enable the strong coupling regime of the hybrid interaction. Furthermore, a more careful detection of the spin linewidth in absence of a mechanical drive might allow probing the oscillator's root mean square displacement due to its thermal excitation. Next to such thermometry measurements, it seems realistic to enter the resolved sideband regime, which becomes possible when using mechanical resonators with larger oscillation frequency and spins with increased lifetimes. This would open doors to advanced spin manipulation protocols, leading up to effects like sideband cooling of the mechanical motion. One strong advantage of this hybrid system is the ability to independently monitor and control both constituents, which allows to perform bidirectional measurements. Conversely to using the spin as a mechanical probe, it is also thinkable to do the inverse and perform mechanical measurements to read out the spin state and its dynamics. Anticipated signatures are spin state dependent shifts of the oscillator's rest position as well as spin induced drive of the mechanical motion.

1.3 Conclusion

1.3.1 Goals of this thesis

At my arrival in the host group, the experiments described in the second part of this chapter had been successfully demonstrated on the SiC nanowire -NV defect hybrid device. However, after having shown how the steady state spin populations are altered due to the mechanical motion in the adiabatic regime, control of dynamical spin evolution remained an important ingredient to add to the hybrid system toolbox. The goal of this PhD thesis has therefore been the development of the experimental tools and the theoretical comprehension necessary to drive transitions of a single spin as its energy is modulated by mechanical motion. Moreover, at this stage, further exploration of novel signatures of the hybrid interaction demanded going to the spin-mechanical resolved sideband regime, which had so far not been explored. Because here the spin energy is not fixed, dynamics of the spin can be anticipated to be much more complex.

On the one hand, this fact in itself motivates its experimental study. From a technical point of view, the resolved sideband regime puts sharp conditions on the experimental apparatus. Hence, it was decided that an initial study of this regime was more easily facilitated by using a test system, in which the parametric interaction with the spin is emulated by RF magnetic fields. Such a test system was developed from a quartz plate on which a waveguiding structure could be lithographed. Single NV defects can first be spin coated on the substrate and selected afterward. In order to investigate the time evolution of single driven NV spins, a setup had to be developed and implemented that allowed precise control and sequencing of well timed MW and optical pulses. In combination with high long term stability of this system (thermal drifts are almost absent and due to its long lifetime, the same NV defect – essentially consisting out of one Nitrogen and three Carbon atoms fixed in space – has been studied for over 18 months) single spin dynamics in the resolved sideband regime could be studied with great accuracy.

On the other hand, the novelty of our results and the increasing attention paid to this field of research demands that the observed phenomena are explained and interpreted in terms of very physical arguments. In fact, at the onset of this PhD thesis, there existed no single dispersively coupled hybrid setup that could demonstrate coherent control over driven spin dynamics, a situation that has changed throughout the last three years [56, 91, 100, 101]. Thus, to ensure versatile applicability of our results, we have developed a proper formalization of the hybrid interaction. Therefore, while our findings are obtained (and will be presented here) in the context of the SiC nanowire - NV spin setup, they remain valid for a wide range of hybrid systems. A further advantage of such formalization is that all of the ideas developed throughout this thesis can be supported by numerical simulations of the spin dynamics. This has often allowed us to anticipate numerically relevant signatures before their experimental confirmation.

During our study, we have also observed a mechansim that synchronizes the spin dynamics to the mechanical energy modulation. Given the great relevance of such a phenomenon with respect to the measurement of spin dependent forces (the effect of a force exerted at the resonance frequency of a mechanical oscillator may potentially surpass a static force by many orders of magnitude), we have since dedicated much effort to the effect that we have (somewhat loosely) coined *spin locking*. On the theory side, a picture was developed which allows to interpret the driven spin dynamics subjected to the hybrid interaction in terms of a double dressing of the NV spin. The model is in great agreement with experimental results obtained with the waveguide-based test system. This has motivated the construction of a hybrid setup that is able to operate in the spin dynamical resolved sideband regime (which differs from the ESR resolved sideband regime, because of the absence of optical broadening). The demands on the mechanical stability necessitated much innovation which mainly originated from the expertise of Benjamin Pigeau. However, a considerable part of the experimental concept had already been established and accelerated the construction and implementation phase. This is only partly so because of the previous development of spin manipulation protocols. Of great importance to the success of the hybrid setup is the work of Arnaud Gloppe and Laure Mercier de Lépinay, who developed, in parallel to the work presented here, an ultra sensitive optical readout of the nanowire motion and a software interface during their PhD projects [102], respectively.

Unavoidably, any realistic hybrid system is subject to thermal noise, whose role becomes more and more important as the external driving force of mechanical motion becomes smaller. Ultimately we are interested in probing mechanical motion driven by a single spin. In such a regime the random thermal motion of the resonator will have important consequences on the spin coherence and might therefore compromise the efficiency of the *spin locking* mechanism. To anticipate the role of thermal motion, we have extended the RF waveguide-based test system to a platform that permits us to study the influence of noise on the spin dynamics. This has allowed us to experimentally explore a spin coherence protection mechanism that is mediated by the spin locking effect and which can be understood in terms of the previously developed picture of double dressing.

1.3.2 Summary

Ground breaking trapped ion and atom experiments have revealed the quantum physical aspects in the behavior of small objects. Ground state cooling, generation of arbitrary quantum states and the creation of quantum correlations between clusters of several particles have become well established experimental techniques. These developments motivate looking for similar signatures in larger, and eventually, macroscopic objects. Hybrid systems between mechanical oscillators and a single quantum system have been suggested as, and already proven to be, potential devices that offer the necessary properties required to achieve such an ambitious goal. We have seen a wide variety of existing and operational devices. By magnetically coupling the motion of a SiC nanowire to a single NV defect electron spin, we here propose to realize a hybrid system that can potentially operate in the resolved sideband regime. SiC nanowires can be engineered to have large aspect ratios. Due to their low masses and the material's very high Young modulus, large oscillation frequencies and amplitudes can be observed. This facilitates the observation of zero-point fluctuations on the one hand. On the other hand, these oscillators become very susceptible force sensors, rendering them useful to detect the small forces exerted by a quantum system. NV defects have gained much popularity throughout a wide range of scientific communities due to their exceptional properties as single photon sources and solid state qubits. Here we profit from optical preparation and readout and MW control of the spin state together with exceptional coherence times at room temperature. Coupling of the spin energy to the mechanical motion of the SiC nanowire has so far been witnessed in spectroscopy measurements.

The goal of this thesis is to gain insights in the alteration of the spin dynamics as its energy is modulated by mechanical motion and to thus advance the experimental protocols to control the hybrid device. In order to establish a knowledge base for the concepts developed in this thesis, we will present the necessary theoretical formalism in the next chapter.

Chapter 2

Formalization of the hybrid coupling mechanism

In this chapter we introduce the formalism required to describe the coupling of a single NV defect to the position of a mechanical oscillator. We introduce the quantum description of the mechanical oscillator coupled to a reservoir, its energy quantization, the zero-point motion and the Brownian motion at finite temperatures. Subsequently, we present the properties of the electronic spin of the negatively charged nitrogen vacancy center and its coupling to external magnetic fields. The mechanisms of dissipation and decoherence of the qubit are then introduced prior to discussing its photophysical properties enabling spin polarization and optical readout of the spin state. We continue by describing the magnetic coupling between both components of the hybrid spin-mechanical system and introduce the resonant and parametric regimes. This permits introducing spin dependent forces, the key element enabling the creation of non-classical states of motion through the hybrid coupling. We then investigate the spin evolution when coupled to a classical mechanical oscillator. It is described by a master equation enabling the derivation of Bloch equations for the coupled spin-oscillator dynamics.

2.1 Harmonic oscillators

2.1.1 Mechanical states of motion

In this part we are going to present the theoretical description of the quantized and classical mechanical oscillator and its coupling to a thermal bath and an external force.

Energy quantization of a harmonic oscillator

We start this section by presenting the energy quantization and deriving zero-point fluctuations, which is an important benchmark for the estimation of the hybrid spin-mechanical coupling in the quantum regime. Suppose a point-like classical particle of mass M and total energy E_{tot} is confined to a harmonic potential of $U(x) = \frac{k}{2}x^2$, where k is called the spring constant. The dynamics of such a particle, that is the relation between its position x and momentum p, are then governed by a periodic conversion of potential energy $U(x)$ into kinetic energy $E_{\mathrm{kin}} = \frac{p^2}{2M}$ and vice versa. Its total energy is thus

$$E_{\mathrm{tot}} = \frac{p^2}{2M} + \frac{k}{2}x^2. \tag{2.1}$$

The transition from the classical to the quantum scenario is made via the correspondence principle. This entails transforming the classical variables into their quantum operator counter parts, $x \rightarrow \hat{X}$ and $p \rightarrow \hat{P}$, all by ensuring that the Heisenberg uncertainty principle holds true. Using the following commutation relation between position and momentum operator

$$[\hat{X},\hat{P}] = i\hbar, \tag{2.2}$$

where $\hbar$ is the reduced Planck constant. The expression for the total energy of the system (2.1) thus becomes Hamiltonian $\hat{H}$ [103]:

$$\hat{H} = \frac{\hat{P}^2}{2M} + \frac{k}{2}\hat{X}^2. \tag{2.3}$$

We now introduce the creation ($\hat{a}^\dagger$) and annihilation ($\hat{a}$) operators of the phonon field related to the mode of oscillation at a frequency $\Omega_\mathrm{m} \equiv \sqrt{\frac{k}{M}}$:

$$\hat{a} = \sqrt{\frac{M\Omega_\mathrm{m}}{2\hbar}}\left(\hat{X} + i\frac{\hat{P}}{M\Omega_\mathrm{m}}\right), \quad \hat{a}^\dagger = \sqrt{\frac{M\Omega_\mathrm{m}}{2\hbar}}\left(\hat{X} - i\frac{\hat{P}}{M\Omega_\mathrm{m}}\right). \tag{2.4}$$

The position and momentum operators then become

$$\hat{X} = \sqrt{\frac{\hbar}{2M\Omega_\mathrm{m}}}(\hat{a} + \hat{a}^\dagger), \quad \hat{P} = \frac{\sqrt{2M\hbar\Omega_\mathrm{m}}}{2i}(\hat{a} - \hat{a}^\dagger). \tag{2.5}$$

The operators $\hat{a}$ and $\hat{a}^\dagger$ have commutation relations of their own, coined the canonic commutation relationship for the Boson ladder operators,

$$[\hat{a},\hat{a}^\dagger] = 1. \tag{2.6}$$

Using those, we can rewrite the Hamiltonian in (2.3):

$$\hat{H} = \hbar\Omega_\mathrm{m}\left(\hat{a}^\dagger\hat{a} + \frac{1}{2}\right). \tag{2.7}$$

In the classical case the term $\hbar\Omega_\mathrm{m}a^\dagger a$ is equivalent to the total energy of the system. Due to energy quantization, however, an additional term $\hbar\Omega_\mathrm{m}/2$ appears and corresponds to the ground state energy of the quantum mechanical oscillator. This energy is intrinsic to the oscillator corresponding to its so called zero-point energy. Here, $\hat{a}^\dagger\hat{a} = \hat{m}$ is the phonon number operator at frequency Ω_m, whose eigenstates are the Fock states $|m\rangle$ of phonon number m, such that

$$\hat{m}|m\rangle = m|m\rangle. \tag{2.8}$$

From the above expressions, we see that the same Fock states are eigenstates of H and that thus the associated energy is

$$\hat{H}|m\rangle = E_m|m\rangle = \hbar\Omega_\mathrm{m}(m + \frac{1}{2})|m\rangle. \tag{2.9}$$

The result shows that the mechanical oscillator has a quantized energy ladder of ground state energy $\hbar\Omega_\mathrm{m}/2$ and harmonic rung spacing of $\hbar\Omega_\mathrm{m}$, see Fig. (2.1). The non-zero ground state energy is reminiscent of the Heisenberg uncertainty principle ($\Delta\hat{X}\Delta\hat{P} \geq \frac{\hbar}{2}$). Considering that the energy is evenly distributed in the vacuum state, the position of the oscillator is Gaussian distributed around $X = 0$ with a spatial spreading

$$\delta x_\mathrm{q} = \sqrt{\frac{\hbar}{2M\Omega_\mathrm{m}}}. \tag{2.10}$$

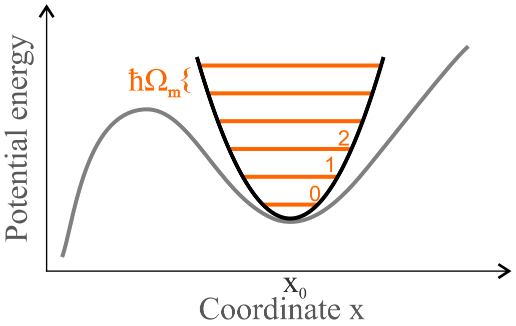

Figure 2.1: A potential energy function can be approximated as a quadratic potential $U(x)$ around its minimum at x_0. The quantized oscillator potential exhibits energy levels at $\hbar\Omega_\mathrm{m}(m+\frac{1}{2})$.

Notice: A completely analogous procedure can be performed for electromagnetic fields. The electric and magnetic field vectors (**E** and **B**, respectively) can be expressed in terms of operators $\hat{b}$ and $\hat{b}^\dagger$, such that $E \propto (\hat{b}+\hat{b}^\dagger)$ and $B \propto (\hat{b}-\hat{b}^\dagger)$. This transformation leads to a quantized energy ladder associated with the photon number operator $\hat{n}=\hat{b}^\dagger\hat{b}$. We will later use this result to describe radiofrequency and microwave electromagnetic fields.

Coupling to the environment

We now look at the coupling of the oscillator to the environment in order to understand its thermalization at low temperatures. A dissipative mechanical oscillator will always be coupled to an environment with finite temperature Θ. Such interaction will lead to thermalization of the mechanical oscillator and, at thermal equilibrium, the phonon number occupation will follow a Bose-Einstein distribution. The oscillator is then described by the density matrix

$$\rho = \frac{1}{Z} e^{-\frac{\hat{H}}{k_B\Theta}}, \tag{2.11}$$

where k_B is the Boltzmann constant and Z is the partition function normalizing the density matrix, defined as

$$Z = \sum_{m=0}^{\infty} e^{-(m+\frac{1}{2})\frac{\hbar\Omega_\mathrm{m}}{k_B\Theta}} = \frac{e^{-\frac{\hbar\Omega_\mathrm{m}}{2k_B\Theta}}}{1-e^{-\frac{\hbar\Omega_\mathrm{m}}{k_B\Theta}}}. \tag{2.12}$$

We then find the energy of the thermally excited oscillator to be

$$\langle H\rangle = \mathrm{Tr}\left\{\rho H\right\} = \hbar\Omega_\mathrm{m}\left(\bar{m}_\mathrm{th}+\frac{1}{2}\right) \tag{2.13}$$

with mean phonon number

$$\bar{m}_\mathrm{th} = \frac{1}{e^{\frac{\hbar\Omega_\mathrm{m}}{k_B\Theta}}-1}. \tag{2.14}$$

Classically, the equipartition theorem predicts that there will be an average energy of $k_B\Theta/2$ in each degree of freedom. With contributions from the potential and kinetic energy, the classical oscillator thus has an average energy of $\langle E_\mathrm{classic}\rangle = k_B\Theta$, which drops to zero at zero temperature. The difference in energy between the classical and quantum oscillator is shown in Figure 2.2.

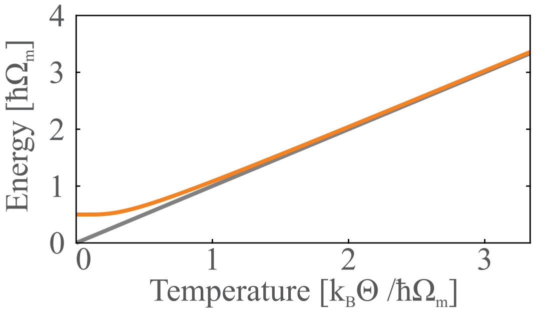

Figure 2.2: Energy of the quantized oscillator as a function of temperature Θ. The gray curve is the classical energy, which diverges from the energy of the quantized oscillator (orange) at low temperature.

Mechanical susceptibility

We now proceed to introduce the mechanical susceptibility of the oscillator in order to understand the resonator's response to an external force. Newton's second law of motion describes the dynamical evolution of a mechanical oscillator due to an external force F_{ext}:

$$\ddot{x}(t) = -\Omega_{\mathrm{m}}^2 x(t) - \Gamma_{\mathrm{m}}\dot{x}(t) + \frac{1}{M}F_{\mathrm{ext}}(t), \tag{2.15}$$

where Γ_{m} is the oscillator damping rate. The response of the oscillator to F_{ext} is then given by a transfer function $\chi[\Omega]$, called the mechanical susceptibility, whose Fourier transform[1] is

$$\chi[\Omega] = \frac{1/M}{\Omega_{\mathrm{m}}^2 - \Omega^2 - i\Omega\Gamma_{\mathrm{m}}} \tag{2.16}$$

and relates oscillator displacement to an external force via

$$x[\Omega] = \chi[\Omega]F_{\mathrm{ext}}[\Omega]. \tag{2.17}$$

The frequency dependence of $\chi[\Omega]$ is depicted in Figure 2.3. Its argument reflects the dephasing of the oscillator response to the excitation force. The mechanical susceptibility allows us to characterize the oscillator's response to any external force. In this thesis we are going to consider two cases, namely a monochromatic, coherent force resulting in coherent mechanical motion and a broadband, incoherent force modeling thermal excitation of the mechanical oscillator.

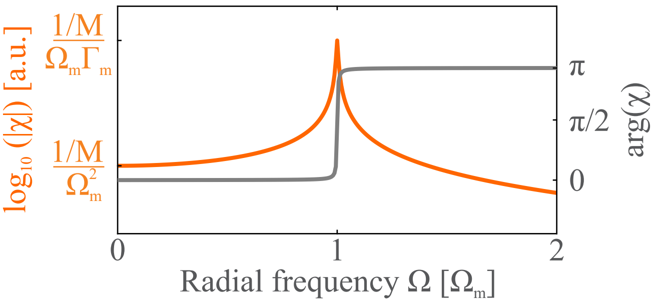

Figure 2.3: Mechanical susceptibility. $|\chi[\Omega]|$ gives the amplitude response (orange) and $\arctan\left(\frac{\mathrm{Im}(\chi)}{\mathrm{Re}(\chi)}\right)$ the dephasing (grey) between the driven mechanical response and the excitation force.

---

[1] Fourier transforms are defined according to $x[\Omega] = \int \mathrm{d}\tau\, x(\tau)\, e^{i\Omega\tau}$ and $x(\tau) = \frac{1}{2\pi}\int \mathrm{d}\Omega\, x[\Omega]\, e^{-i\Omega\tau}$.

Thermal states of motion

Here we introduce the thermal noise of the oscillator, which will help us in Chapter 5 to understand the effect of the resonator's Brownian motion on the spin dynamics in case of parametric coupling. Considering the dynamics of the quantized oscillator, thermalization with the surrounding bath is mediated by the quantum mechanical analogue of the Langevin force, $\hat{F}^{\mathrm{q}}_{\mathrm{th}}$, with commutation relations

$$[\hat{F}^{\mathrm{q}}_{\mathrm{th}}[\Omega], \hat{F}^{\mathrm{q}}_{\mathrm{th}}[\Omega']] = 2\pi\delta(\Omega + \Omega')2\hbar M\Gamma_{\mathrm{m}}\Omega_{\mathrm{m}}. \tag{2.18}$$

It has a Gaussian probability distribution with $\left\langle \hat{F}_{\mathrm{th}} \right\rangle = 0$ and a frequency spectrum defined as

$$\left\langle \hat{F}^{\mathrm{q}}_{\mathrm{th}}[\Omega]\hat{F}^{\mathrm{q}}_{\mathrm{th}}[\Omega'] \right\rangle = 2\pi\delta(\Omega + \Omega')S^{\mathrm{q}}_{\mathrm{F_{th}}}. \tag{2.19}$$

After [104,105] the fluctuation - dissipation theorem establishes the relation between energy dissipation of the oscillator and the spectrum of the Langevin force inducing fluctuations via

$$S^{\mathrm{q}}_{\mathrm{F_{th}}}[\Omega] = -\hbar \left| \mathrm{Im}\left(\frac{1}{\chi[\Omega]}\right)\right| \coth\left(\frac{\hbar|\Omega|}{2k_B\Theta}\right) = \hbar M\Gamma_{\mathrm{m}}|\Omega| \coth\left(\frac{\hbar|\Omega|}{2k_B\Theta}\right). \tag{2.20}$$

This excitation leads to a displacement noise spectral density of

$$S^{\mathrm{q}}_{x}[\Omega] = \int_{-\infty}^{\infty} \langle x_{\mathrm{q}}(t), x_{\mathrm{q}}(t+\tau)\rangle \, e^{i\Omega\tau}\, \mathrm{d}\tau = |\chi[\Omega]|^2 S^{\mathrm{q}}_{\mathrm{F_{th}}}[\Omega], \tag{2.21}$$

which, in the limit of sufficiently large quality factors $Q = \Omega_{\mathrm{m}}/\Gamma_{\mathrm{m}}$, becomes

$$S^{\mathrm{q}}_{x}[\Omega] = \frac{2\Gamma_{\mathrm{m}}\hbar\Omega_{\mathrm{m}}/M}{(\Omega_{\mathrm{m}}^2 - \Omega^2)^2 + \Omega^2\Gamma_{\mathrm{m}}^2}\left(\bar{m}_{\mathrm{th}} + \frac{1}{2}\right). \tag{2.22}$$

The zero-point fluctuations of the quantum mechanical oscillator at $\langle m \rangle = 0$ verify the relation

$$\delta x_{\mathrm{q}}^2 = \frac{1}{2\pi}\int_{-\infty}^{\infty} \mathrm{d}\Omega\, S^{\mathrm{q}}_{x}[\Omega] = \frac{\hbar}{2M\Omega_{\mathrm{m}}}, \tag{2.23}$$

as expected. The above expressions have their classical analogues in the high temperature limit, where $k_B\Theta \approx \hbar\Omega_{\mathrm{m}}(\bar{m}_{\mathrm{th}} + \frac{1}{2})$. The spectral density of the classical Langevin force $F^{\mathrm{q}}_{\mathrm{th}}$ then takes the form

$$S^{\mathrm{th}}_{\mathrm{F}}[\Omega] = 2M\Gamma_{\mathrm{m}}k_B\Theta \tag{2.24}$$

yielding a thermal spectral density of mechanical oscillations proportional to the equilibrium temperature

$$S^{\mathrm{th}}_{x}[\Omega] = \int_{-\infty}^{\infty} \langle x_{\mathrm{th}}(t), x_{\mathrm{th}}(t+\tau)\rangle \, e^{i\Omega\tau}\, \mathrm{d}\tau = |\chi[\Omega]|^2 S^{\mathrm{th}}_{\mathrm{F}}[\Omega] = \frac{2\Gamma_{\mathrm{m}}k_B\Theta/M}{(\Omega_{\mathrm{m}}^2 - \Omega^2)^2 + \Omega^2\Gamma_{\mathrm{m}}^2}. \tag{2.25}$$

The classical variance of the displacement becomes

$$\Delta x_{\mathrm{th}}^2 = \frac{1}{2\pi}\int_{-\infty}^{\infty} \mathrm{d}\Omega\, S^{\mathrm{th}}_{x}[\Omega] = \frac{k_B\Theta}{M\Omega_{\mathrm{m}}^2}. \tag{2.26}$$

We notice two key values for S_x^{th}:

$$\begin{aligned} S_x^{\mathrm{th}}[0] &= \frac{2\Gamma_{\mathrm{m}} k_B \Theta / M}{\Omega_{\mathrm{m}}^4} = \frac{2\Gamma_{\mathrm{m}}}{\Omega_{\mathrm{m}}^2}\Delta x_{\mathrm{th}}^2, \\ S_x^{\mathrm{th}}[\Omega_{\mathrm{m}}] &= \frac{2 k_B \Theta / M}{\Omega_{\mathrm{m}}^2 \Gamma_{\mathrm{m}}} = \frac{2}{\Gamma_{\mathrm{m}}}\Delta x_{\mathrm{th}}^2. \end{aligned}$$

Their ratio can be expressed by the mechanical quality factor as $S_x^{\mathrm{th}}[\Omega_{\mathrm{m}}]/S_x^{\mathrm{th}}[0] = Q^2$.

The corresponding phase - space distribution of the thermal state is shown in Figure 2.4 and presents a variance growing linearly with temperature.

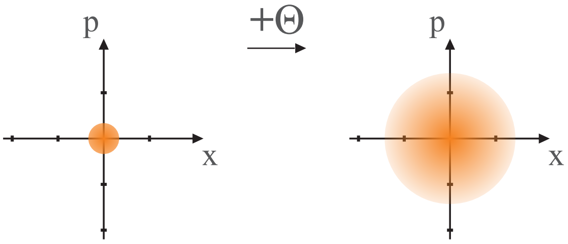

Figure 2.4: Thermal states. As the temperature is increased, the phase - space distribution of a thermal state stays centered around zero, while its width increases radially.

In terms of orders of magnitude, for a mechanical oscillator of mass $M = 10$ fg and $\Omega_{\mathrm{m}}/2\pi = 6$ MHz at 0 and 300 K one has

$$\begin{aligned} \delta x^{\mathrm{q}} &= \sqrt{\frac{\hbar}{2M\Omega_{\mathrm{m}}}} = 374\,\mathrm{fm}, \\ \Delta x_{\mathrm{th}} &= \sqrt{\frac{k_B\Theta}{M\Omega_{\mathrm{m}}^2}} = 540\,\mathrm{pm}. \end{aligned}$$

At room temperature, the Brownian motion of the oscillator is three orders of magnitude larger than its zero-point fluctuations.

Coherent states of motion

We consider next the coherent state of motion, which not only describes classical monochromatically driven motion of the oscillator (as will be considered in Chapters 3 and 4) but also the coherent MW electromagnetic field used to drive transitions of the NV spin. A coherent state $|\alpha\rangle$ of the oscillator with complex amplitude α is described by a normalized infinite superposition of Fock states:

$$|\alpha\rangle = e^{-|\alpha|^2/2} \sum_{m=0}^{\infty} \frac{\alpha^m}{\sqrt{m!}} |m\rangle. \tag{2.27}$$

These states are eigenstates of the field lowering operator $\hat{a}$:

$$\hat{a}|\alpha\rangle = \alpha|\alpha\rangle. \tag{2.28}$$

Key features of the coherent state are mean and variance of the phonon (photon) number, which are characteristic of a Poissonian distribution:

$$\langle m \rangle = \langle \alpha|\hat{m}|\alpha\rangle = \langle \alpha|\hat{a}^\dagger \hat{a}|\alpha\rangle = \langle \alpha|\alpha^* \alpha|\alpha\rangle = |\alpha|^2 \tag{2.29}$$

$$\Delta m^2 \equiv \left\langle m^2 \right\rangle - \langle m \rangle^2 = |\alpha|^2 = \langle m \rangle\,. \tag{2.30}$$

Furthermore, coherent states are simultaneously minimum uncertainty states for the position and momentum distributions

$$\Delta\hat{X} = \sqrt{\frac{\hbar}{2M\Omega_{\mathrm{m}}}} \quad \text{and} \quad \Delta\hat{P} = \sqrt{\frac{M\hbar\Omega_{\mathrm{m}}}{2}}. \tag{2.31}$$

are the same as those of the vacuum state $|0\rangle$ and thus Heisenberg limited. After introduction of the displacement operator $D(\alpha) = e^{\alpha\hat{a}^\dagger - \alpha^*\hat{a}}$, one also has

$$D(\alpha)|0\rangle = |\alpha\rangle, \tag{2.32}$$

which allows us to look at coherent states as displaced vacuum states, see Figure (2.5). The application of $D(\alpha)$ thus corresponds to an increase of field amplitude of a mode a, while the phase distribution gets reduced at large drive. For example, ideal laser light in the absence of technical noise can be described by a coherent state. For coherent states, the ratio $\Delta m/\langle m\rangle$ scales as $1/\sqrt{\langle m\rangle}$ and thus the amplitude becomes better defined for large photon or phonon numbers. Hence, for a coherent, monochromatic drive of frequency $\Omega_{\mathrm{d}}/2\pi$ one can describe the position of the classical oscillator as

$$x_{\mathrm{coherent}}(t) = A\cos\left(\Omega_{\mathrm{d}}t + \phi\right), \tag{2.33}$$

where amplitude A and phase ϕ are related to the driving force according to expression (2.17).

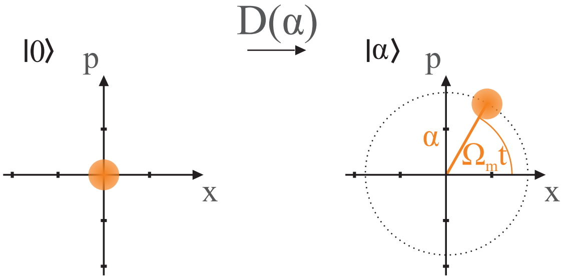

Figure 2.5: Coherent states. Application of the displacement operator $D(\alpha)$ shifts the phase space distribution of the vacuum state by amplitude α away from the origin.

2.1.2 Vibrational eigenmodes of singly clamped SiC nanowires

In this section we are concerned with the motion specific to the mechanical oscillators that will be used in the experiments of Chapter 4. We will be working with singly clamped, cylindrical SiC nanowires with generally large aspect ratios. Typically, the length L is on the order of several tens of μm and diameter d on the order of a few hundred nm. In order to determine the eigenmodes of oscillation we will approximate the nanowires to be perfectly cylindrical and homogeneous. The rotational symmetry reduces the problem to considering a single displacement direction. As the wire bends in one direction, it experiences compression to one side and dilation to the other. We call the *neutral surface* the surface at which both effects annihilate each other and define the deflection $\mathbf{u}(y,t)$ of the nanowire as the deflection of the neutral surface along the wire axis $\mathcal{O}y$, shown in Figure 2.6.

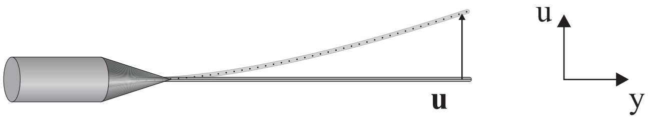

Figure 2.6: Displacement vector $\mathbf{u}(y)$.

Under these conditions and assuming the absence of shear, $\mathbf{u}(y,t)$ obeys the Euler-Bernouilli [106] equation:

$$\rho\frac{\partial^2}{\partial t^2}u + \frac{D}{d}\left(\frac{\partial^2}{\partial y^2}\right)^2 u = 0. \tag{2.34}$$

Here, D is defined in terms of the material's Young modulus E and Possion ratio σ as $D = \frac{Ed^3}{12}(1-\sigma^2)$ and ρ in this case is the material's density. For SiC, these values are $E \approx 400\,\mathrm{GPa}$ and $\rho = 3210\,\mathrm{kg/m^3}$. Searching for the eigenmodes, we look for separable, stationary solutions of the form $\mathbf{u_n}(y,t) = \mathrm{Re}\left(\mathbf{u_{n,y}}(y)e^{i\Omega_{\mathrm{m},n}t}\right)$. From equation (2.34) we then obtain the dispersion relation

$$\Omega_{\mathrm{m},n} = k_n^2\sqrt{\frac{D}{d\rho}}, \tag{2.35}$$

defining the eigenfrequency $\Omega_{\mathrm{m},n}$ of the n^{th} mode of oscillation in terms of the acoustic wave numbers k_n, which are found by solving for the spatial part of $u(y,t)$. We impose the general form

$$u_y(y) = A_n\cos(k_n y) + B_n\sin(k_n y) + C_n\cosh(k_n y) + D_n\sinh(k_n y)$$

and demand that the boundary conditions are met. These conditions arise from the clamping, requiring zero deflection and slope at $y = 0$, as well as zero bending moment and zero change of torque at the end point $y = L$ [106]. We thus have

$$u_y(0) = 0, \quad \frac{\partial u_y}{\partial y}(0) = 0, \quad \frac{\partial^2 u_y}{\partial y^2}(L) = 0, \quad \frac{\partial^3 u_y}{\partial y^3}(L) = 0.$$

Consequently, the wave numbers k_n fulfill the relationship

$$-\cos(k_n L) = \frac{1}{\cosh(k_n L)}. \tag{2.36}$$

The solutions to the above equation are shown in Figure 2.7 **(a)**. Notice the quadratic dependence of $\Omega_{\mathrm{m},n}$ on k_n, which becomes increasingly periodically spaced as n grows large. The validity of this model has been verified with a finite element simulation in our group [107]. We find typical eigenfrequencies of $(\Omega_1, \Omega_2, \Omega_3)/2\pi = (0.22, 1.38, 3.81)\,\mathrm{MHz}$ for the first three modes of a cylindrical nanowire with $L = 30\,\mu\mathrm{m}$ and $d = 100\,\mathrm{nm}$. We remark that the oscillation frequencies scale as $\Omega_{\mathrm{m},n} \propto d/L^2$. This implies that working with a high frequency fundamental mode of oscillation requires a short nanowire. Using the same geometry as before, to bring the oscillation frequency of the first mode to $\Omega_1/2\pi = 6\,\mathrm{MHz}$, the nanowire has to be cut from $L = 30\,\mu\mathrm{m}$ to $L = 5.7\,\mu\mathrm{m}$.

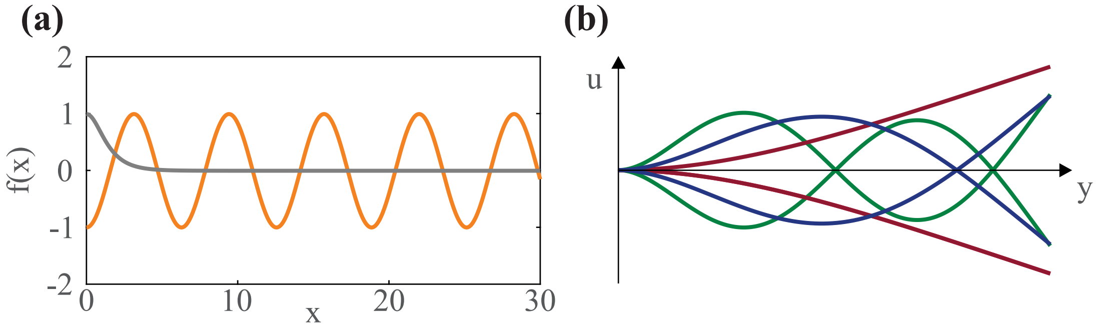

Figure 2.7: Eigenmodes of the nanowire. **(a)** The n^{th} intersection of $\frac{1}{\cosh(k_n L)}$ (black) with $-\cos(k_n L)$ (orange) corresponds to the value $x = Lk_n$. **(b)** Spatial profiles of the first three vibrational modes. Red: $k_1 L = 1.87$, Blue: $k_2 L = 4.69$, Green: $k_3 L = 7.86$.

2.1.3 Optical displacement detection

In our laboratory, an optical detection scheme for the displacement of the nanowire was developed during the PhD of A. Gloppe, in which the mechanical oscillations modulate the transmitted intensity of a tightly focused laser beam, which can be detected with a quadrant photo diode [97]. In this way the oscillation perpendicular to the optical axis $\mathcal{O}z$ can be detected. If the cylindrical symmetry of the nanowire is broken, for example due to impurities or non-uniform clamping, the two mode degeneracy is lifted and two perpendicular directions of oscillation emerge, one of them being potentially aligned along $\mathcal{O}z$. However, the optical detection scheme can in principle be expanded using a second probe laser and quadrant photodiode. It is then possible to measure the physical displacement of the mechanical oscillator $\delta\mathbf{r}_{\text{opt}}$, which can be expanded in the base of the nanoresonator's eigenmodes $\mathbf{u_n}$. The measured deformations can be written as

$$\delta\mathbf{r}_{\text{opt}} \equiv \sum_n a_n(t)\mathbf{u_n}(y) \tag{2.37}$$

in order to describe the dynamical displacement of the oscillator in the non-stationary regime with the modal time dependencies $a_n(t)$. The total energy of the mechanical oscillator is the sum of the energies of all modes:

$$E = \sum_n \left(\frac{\dot{a}_n^2}{2M_n} + \frac{1}{2} M_n \Omega_{\text{m},n}^2 a_n^2 \right), \tag{2.38}$$

which introduces the dynamical masses for each mode

$$M_n = \rho \int \mathrm{d}^3\mathbf{r}\, \mathbf{u_n}^2(y). \tag{2.39}$$

We consider the time evolution of each mode, which is described by a set of individual dynamical equations:

$$\ddot{a}_n(t) = -\Omega_{\text{m},n}^2 a_n(t) - \Gamma_{\text{m},n}\dot{a}_n(t) + \frac{1}{M_n}\left(F_{\text{th},n}(t) + \langle \mathbf{f_{ext}}(\mathbf{r},t), \mathbf{u_n}(\mathbf{r})\rangle\right), \tag{2.40}$$

where $\langle \mathbf{f_{ext}}(\mathbf{r},t), \mathbf{u_n}(\mathbf{r})\rangle$ denotes the overlap of the external force with volume density $\mathbf{f_{ext}}(\mathbf{r},t)$ with the mode profile via the integral $\int \mathrm{d}^3\mathbf{r}\, \mathbf{f_{ext}}(\mathbf{r},t).\mathbf{u_n}(\mathbf{r})$. Here we have furthermore introduced the Langevin force $F_{\text{th},n}$ experienced by the n^{th} mode. Requiring that the dissipation-fluctuation theorem holds for each mode, we have a thermal force spectral density [108]

$$S_{\text{F}_\text{n}}^{\text{n}}[\Omega] = \hbar \left| \operatorname{Im}\left(\frac{1}{\chi_n[\Omega]}\right) \right| \coth\left(\frac{\hbar|\Omega|}{2k_B\Theta}\right). \tag{2.41}$$

We obtain the displacement amplitude:

$$a_n[\Omega] = \chi_n[\Omega]\left(F_{\text{th},n}[\Omega] + \langle \mathbf{f_{ext}}(\mathbf{r},t), \mathbf{u_n}(\mathbf{r})\rangle\right). \tag{2.42}$$

The measured deformation of the oscillator is then given by

$$\delta\mathbf{r}_{\text{opt}}[\Omega] = \sum_n \chi_n[\Omega]\left(F_{\text{th},n} + \langle \mathbf{f_{ext}}(\mathbf{r},t), \mathbf{u_n}(\mathbf{r})\rangle\right)\mathbf{u_n}(\mathbf{r_0}). \tag{2.43}$$

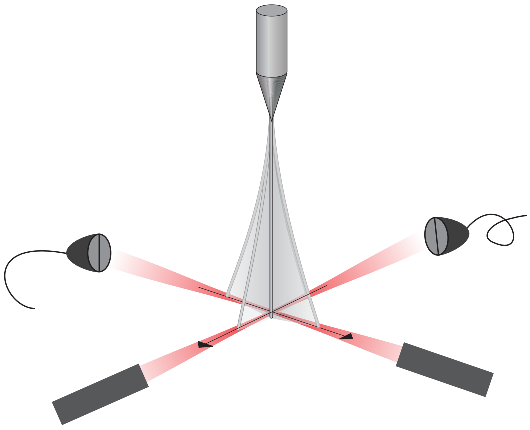

Figure 2.8: Optical displacement detection. A laser is tightly focused onto the nanowire tip, whose vibrations perturb the beam. A quadrant photo diode is used to detect the time dependent intensity distribution of each quadrant, which is demodulated to measure the oscillation spectrum. A second beam and QPD can additionally be employed to fully capture the two dimensional nanowire motion.

2.1.4 A local force acting on the nanowire

We now consider the special case of a force acting on the nanowire, exhibiting a spatial distribution smaller than the characteristic size of the eigenmode profile. This corresponds, for example, to the case of the feedback force from a single NV spin. If such a local force described by $\mathbf{f_{ext}} = \delta^3(\mathbf{r} - \mathbf{r_0})\mathbf{F_{ext}}$ is applied to the mechanical oscillator at position $\mathbf{r_0}$, the overlap between mode and external force, $\langle \mathbf{f_{ext}}(\mathbf{r}, t), \mathbf{u_n}(\mathbf{r})\rangle$, then simplifies, such that

$$\delta\mathbf{r}_{\mathrm{opt}}[\Omega] = \sum_n \chi_n[\Omega] \left(F_{\mathrm{th},n} + \mathbf{F_{ext}}.\mathbf{e_n} u_n(\mathbf{r_0})\right) u_n(\mathbf{r_0}).\mathbf{e_n}, \tag{2.44}$$

where the unit vector $\mathbf{e_n}$ denotes the mode displacement direction, $\mathbf{u_n}(\mathbf{r_0}) \equiv u_n(\mathbf{r_0})\mathbf{e_n}$. The effect of the force on the eigenmodes will be maximized if it is applied at a point of large oscillation amplitude. This leads to the definition of an effective mass:

$$M_n^{\mathrm{eff}} = \frac{M_n}{\mathbf{u_n}^2(\mathbf{r_0})} = \rho \frac{\int \mathrm{d}^3\mathbf{r}\, \mathbf{u_n}^2(\mathbf{r})}{\mathbf{u_n}^2(\mathbf{r_0})}. \tag{2.45}$$

We next define an effective mechanical susceptibility as [108]

$$\chi_n^{\mathrm{eff}} = \frac{1/M_n^{\mathrm{eff}}}{\Omega_{\mathrm{m},n}^2 - \Omega^2 - i\Gamma_{\mathrm{m},n}\Omega}, \tag{2.46}$$

so that

$$\delta\mathbf{r}_{\mathrm{opt}}[\Omega] = \sum_n \chi_n^{\mathrm{eff}}\Omega] \left(\delta F_{\mathrm{th},n} + \mathbf{F_{ext}}.\mathbf{e_n}\right) \mathbf{e_n}. \tag{2.47}$$

The effective Langevin force experienced by each mode

$$\delta F_{\mathrm{th},n} = \frac{F_{\mathrm{th},n}}{u_n(\mathbf{r_0})}, \tag{2.48}$$

still verifies the fluctuation-dissipation theorem with the effective susceptibility:

$$S^{\mathrm{n}}_{\delta \mathrm{F_{th,n}}}[\Omega] = \hbar \left| \operatorname{Im}\left(\frac{1}{\chi_n^{\mathrm{eff}}}\right) \right| \coth\left(\frac{\hbar\Omega}{2k_B\Theta}\right). \tag{2.49}$$

The force profile that is relevant for our hybrid spin-mechanical system is a local force applied by a single spin attached at the moving extremity of the nanowire. In that case, the overlap of the force with the mode profile is largest for $n = 1$ and the effective mass is $M_1^{\mathrm{eff}} \approx \frac{M}{4}$, which represents the physical mass that the spin will have to move.

2.2 Spin Hamiltonian of the NV defect

The nitrogen atom of the charge neutral NV^0 center possesses five valence electrons, three of which bond covalently to the surrounding carbon atoms. The remaining two electrons are not bound and build a *lone pair*. Three electrons are situated in the vacancy and thus the NV^0 is a spin 1/2 system. Trapping of one extra electron, however, turns the negatively charged NV^- center into a spin 1 system [109], [110], to which we will restrict the following considerations. The ground state configuration of the NV spin is described by a symmetric (triplet) spin wave function which combines with an antisymmetric orbital wave function. In this section we will look at the Hamiltonian describing the ground state spin and see how NV defects can experimentally be turned into an effective two level system.

2.2.1 Global Hamiltonian

The NV defect possesses a natural quantization axis along the N-V direction due to its C_{3v} symmetry. We define an XYZ coordinate system around this quantization axis, which we choose to be the **z**-direction, see Figure 2.9 **(a)**. A measurement of the spin angular momentum along **z**, labeled S_z, will result in $S_z = m_s\hbar$, where $m_s = 0, \pm 1$. The eigenvectors are $|m_s\rangle$, which are eigenstates of the spin 1 Pauli operator $\hat{\sigma}_z$, such that $\hat{\sigma}_z|m_s\rangle = m_s|m_s\rangle$. For these conventions, $|0\rangle$ and $|\pm1\rangle$ are referred to as the spin ground and excited states, respectively. With $|\uparrow\rangle/|\downarrow\rangle$ denoting the electron spin's up/ down configuration, the spin triplet eigenstates are

$$\begin{aligned} |0\rangle &= \frac{1}{\sqrt{2}}(|\uparrow\downarrow\rangle + |\downarrow\uparrow\rangle) \\ |{+1}\rangle &= |\uparrow\uparrow\rangle \\ |{-1}\rangle &= |\downarrow\downarrow\rangle \end{aligned}$$

Spin - spin interactions cause a relatively large zero field splitting of $D/2\pi = 2.87\,\mathrm{GHz}$ between the states $|0\rangle$ and $|\pm1\rangle$, enabling spin manipulation with microwave (MW) electromagnetic fields. Additional strain in the diamond matrix can distort the C_{3v} symmetry of the NV defect. These two effects are summarized in the conventional Hamiltonian H_{NV} for the S = 1 electron spin associated with the NV defect's orbital ground state [111]:

$$H_{\mathrm{NV}}/\hbar = D\sigma_z^2 + E(\sigma_x^2 - \sigma_y^2), \tag{2.50}$$

where the spin 1 Pauli matrices are defined as

$$\hat{\sigma}_x = \frac{1}{\sqrt{2}}\begin{pmatrix} 0 & 1 & 0 \\ 1 & 0 & 1 \\ 0 & 1 & 0 \end{pmatrix}, \hat{\sigma}_y = \frac{i}{\sqrt{2}}\begin{pmatrix} 0 & -1 & 0 \\ 1 & 0 & -1 \\ 0 & 1 & 0 \end{pmatrix}, \hat{\sigma}_z = \begin{pmatrix} 1 & 0 & 0 \\ 0 & 0 & 0 \\ 0 & 0 & -1 \end{pmatrix}, \tag{2.51}$$

obeying the commutation relations $[\sigma_i, \sigma_j] = i\varepsilon_{ijk}\sigma_k$. Transverse strain effects in the diamond matrix are parametrized by E and vary between different samples as a function of the homogeneity of the crystal lattice. It is generally much smaller than D and extends between a few tens of kHz for ultra pure diamond samples and several MHz in nanodiamonds. Thus, the $|m_s\rangle$ states are generally not eigenstates of H_{NV}. Longitudinal (along the **z**-axis) strain effects shift the excited states' energy relative to the ground state and can thus be absorbed into D. The energy diagram and a typical measurement of the spin energy is presented in Fig. 2.9.

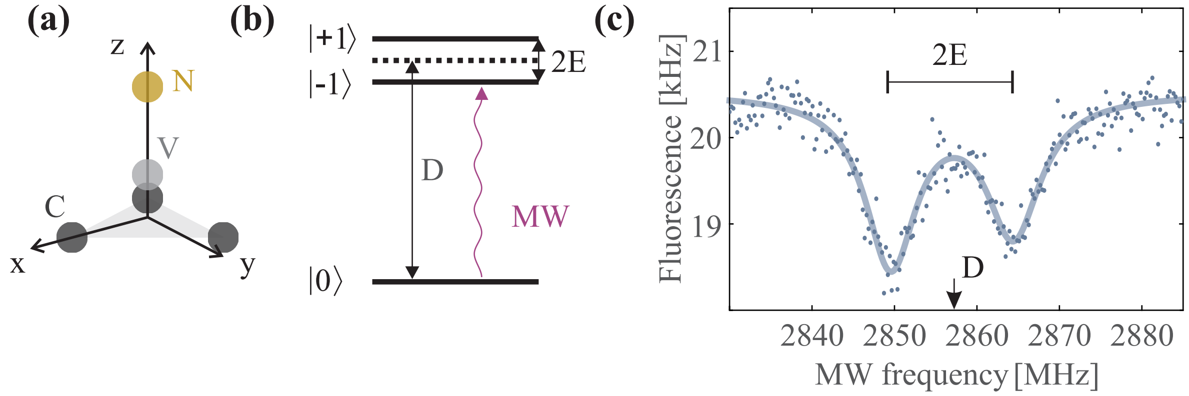

Figure 2.9: Energy of the NV spin. **(a)** Convention of the NV coordinate system. **(b)** Energy diagram of the perturbed eigenstates probed by MW irradiation. **(c)** Spectroscopic measurement of the NV spin. For nanodiamonds E can be on the order of several MHz (here, $E/2\pi \approx 7.5\,\text{MHz}$). Strain along the spin axis leads to a shift of $D/2\pi$ from 2870 MHz to 2857 MHz. The solid line is a fit of the experimental data to a sum of two Lorentzian lineshapes.

2.2.2 Magnetic coupling

Due to the Zeeman effect, the energy of the spin can be varied by an external magnetic field $\mathbf{B}$, which is described by the Hamiltonian

$$H_{\mathrm{B}} = -g\mu_B \mathbf{B}.\boldsymbol{\sigma}, \tag{2.52}$$

where $g \approx 2$ is the electron's Landé factor [112], $\mu_B = 9.274 \times 10^{-24} J/T$ is the Bohr magneton and $\boldsymbol{\sigma}$ is the vector of the spin 1 Pauli matrices. The minus sign in Hamiltonian (2.52) ensures that a spin aligned with the magnetic field has less energy than a spin that is anti-aligned. Notice that the spin is sensitive to magnetic fields in all directions. Strong fields in the transverse directions result in a mixing of the $|m_s\rangle$ eigenstates leading to nonlinear behavior of the associated energies, see Fig 2.10.

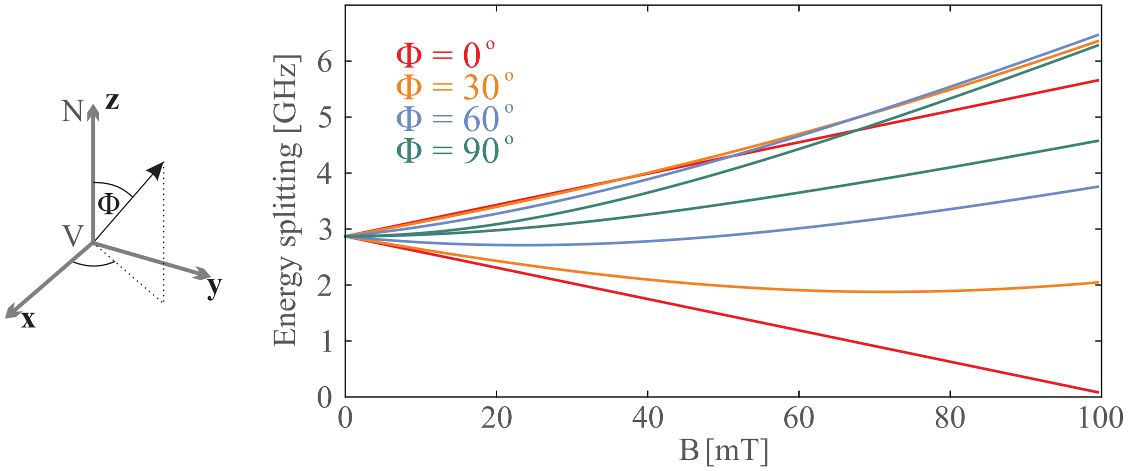

Figure 2.10: Zeeman effect. A magnetic field applied along the quantization axis leads to linear splitting of the spin energies ($\Phi = 0°$), whereas fields with transverse components ($\Phi > 0°$) lead to a mixing of the eigenstates, resulting in nonlinear energy shifts.

2.2.3 Hyperfine coupling

A closer look at experimental NV spin spectra with higher frequency resolution reveals a substructure of the resonance peaks, see Fig. 2.11. This substructure can be explained by hyperfine coupling of the nuclear spin I of the nitrogen atom with the electron spin S mediated by dipole-dipole interactions. The interaction depends on the isotope of the present nitrogen atom as well as the electron's orbital state and can be modeled by H_{nuclear}:

$$H_{\text{nuclear}}/\hbar = \mathbf{I}.\mathbf{A}\boldsymbol{\sigma}, \tag{2.53}$$

Here, $\mathbf{A}$ is a coupling tensor that has received a considerable amount of theoretical [113, 114] as well as experimental [115–119] attention. In this work we are only concerned with the orbital ground state of the NV defect, for which the $\mathbf{z}$ projections of the ^{14}N's $I = 1$ nuclear spin splits the electron spin resonances into three peaks due to couplings $A_{\|}^{14}\sigma_z I_z$. It has been determined that their separation is given by $A_{\|}^{14}/2\pi = -2.16$ MHz, whereas the $I = 1/2$ nuclear spin of the ^{15}N atom splits the resonances into two, separated by $A_{\|}^{15}/2\pi = 3.03$ MHz (the natural abundance of ^{14}N isotope is larger than 99% compared to ^{15}N).

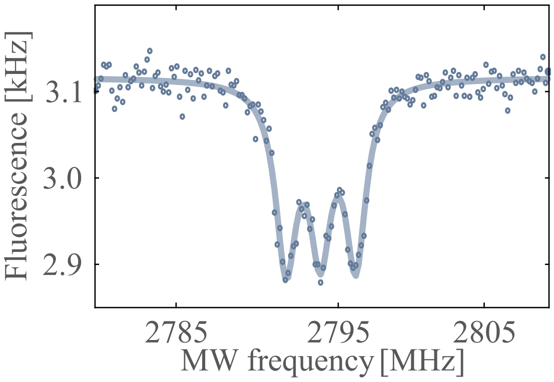

Figure 2.11: Splitting of the NV resonance by 2.16 MHz due to hyperfine coupling with the ^{14}N nuclear spin. To reveal the hyperfine structure, optically detected magnetic resonance (ODMR) measurements are performed at lower optical and MW power in order to avoid power broadening, see sections 2.4.2 and 3.3.

Importantly, polarization of the nuclear spin has been observed experimentally. Because of the smaller zero field splitting $D_{\text{es}}/2\pi = 1.42$ GHz [120] in the excited states, the frequency splitting between $|m_s = 0\rangle$ and the orbitally excited $|m_s = -1\rangle$ state becomes very small when working at magnetic fields $\mathbf{B} \approx (0, 0, 51\text{mT})$ [116, 117], see Figure 2.12. This facilitates nuclear-electron spin flip-flops enabled by an interaction term $A_{\perp}\sigma_z I_{\pm}$ occurring when the NV spin is promoted to the excited orbital state under optical illumination. Due to the NV's photophysics as outlined in section 2.4, these couplings result in a very effective polarization (> 90%) of the nuclear spin in the $|I_z = +1\rangle$ (^{14}N) [116] or $|I_z = -\frac{1}{2}\rangle$ (^{15}N) [117] state.

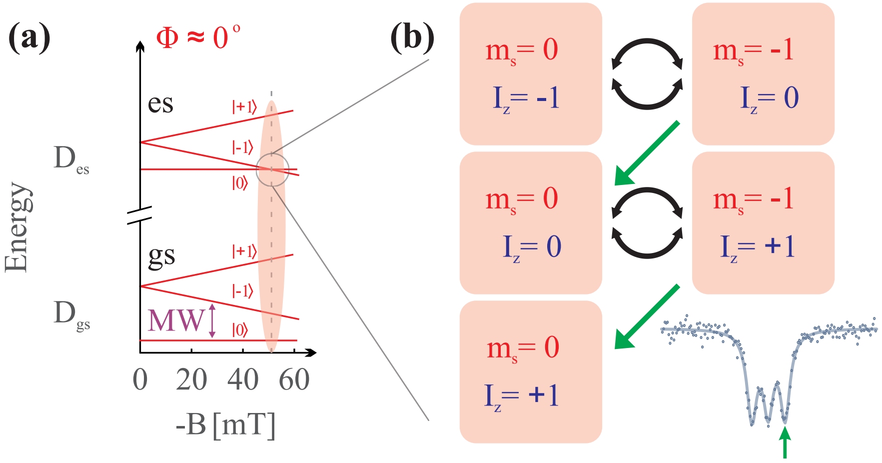

Figure 2.12: Self polarization of the ^{14}N nuclear spin. **(a)** A magnetic field splits the states $|-1\rangle$ and $|+1\rangle$ far apart from each other, allowing to address a two level subspace (purple double arrow) by MW frequency selection. Indicated by the red oval is the region in which the excited state level anti-crossing (ESLAC) leads to self polarization of the nuclear spin. **(b)** Spin flip-flops between the ^{14}N nuclear spin and the excited state electron spin occur at the ESLAC, indicated by black arrows. Optical pumping re-polarizes the electron spin in $|0\rangle$ (green arrows), leading to a pumping of the nuclear spin in $|I_z = +1\rangle$. Notice that the mechanism applies for the $\{|0\rangle, |-1\rangle\}$ subspace, which requires a negative magnetic field.

2.2.4 Reduction of the NV spin to an effective two level system

Diagonalizing the total global Hamiltonian

Taking into account effects of strain, external magnetic fields and the hyperfine structure of the NV defect, we arrive at a total global Hamiltonian $H_0 = H_{\mathrm{NV}} + H_{\mathrm{B}} + H_{\mathrm{nuclear}}$, whose eigenstates are generally mixtures of $|m_s\rangle$:

$$H_0/\hbar = D\hat{\sigma}_z^2 + E(\hat{\sigma}_x^2 - \hat{\sigma}_y^2) - \frac{g\mu_B}{\hbar}\mathbf{B}.\boldsymbol{\sigma} + A\mathbf{I}.\boldsymbol{\sigma}. \tag{2.54}$$

If now a sufficiently large magnetic field is aligned carefully along the **z** axis, such that $B_z \gg \frac{\hbar E}{g\mu_B}, B_x, B_y$, we can neglect all transverse terms in the Hamiltonian $H_{\mathrm{NV}} + H_{\mathrm{B}}$. Furthermore, when working at the ESLAC, the nuclear spin can be polarized, as discussed in section 2.2.3. The polarization technique requires optical illumination of the NV defect, but nuclear spin states are typically long-lived ($\sim$ ms) and, unless stated otherwise, optical pumping is interrupted for no longer than several μs in our experiments. For our purposes, we can thus assume complete polarization of the nuclear spin. In this case, H_{nuclear} is static and can be treated as a renormalization of the magnetic field along **z**. We have thus created a system of three eigenstates $|m_s\rangle$, which are all split far away from each other, see Fig. 2.13. This situation allows us to turn the NV defect into an effective spin 1/2 TLS by restricting ourselves to the subspace $\{|m_s = 0\rangle, |m_s = 1\rangle\}$, which is split in frequency by $\omega_0/2\pi$ (equivalent to ≈ 1.44 GHz at $B_z = 51$ mT).

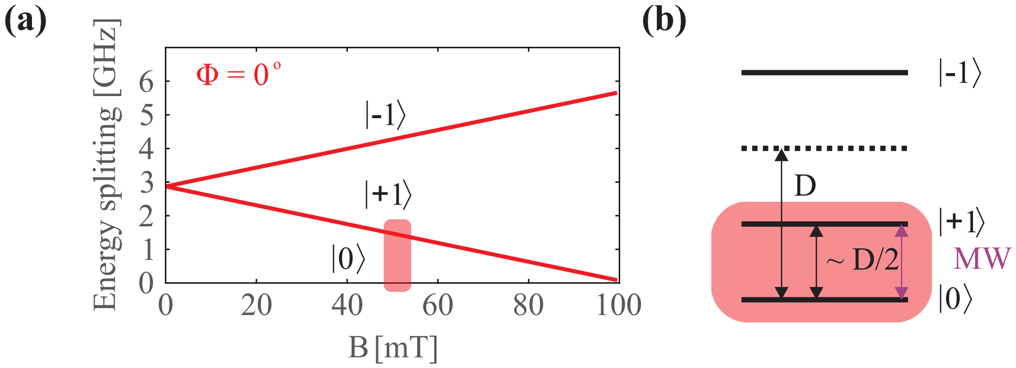

Figure 2.13: Working point for a longitudinal magnetic field. **(a)** A magnetic field aligned with the NV axis splits the states $|-1\rangle$ and $|+1\rangle$ via the Zeeman effect. Indicated by the red oval is the region in which the the excited state level anti crossing (ESLAC) leads to polarization of the nuclear spin. **(b)** We can restrict our study to the $\{|0\rangle, |+1\rangle\}$ subspace MW by frequency selection ($\omega/2\pi \sim 1.4\,\text{GHz}$).

The two level system

In a formal representation, we assign the states $|0\rangle$ of energy $E_0 = 0$ to $|m_s = 0\rangle$ and $|1\rangle$ of energy $E_1 = \hbar\omega_0$ to $|m_s = 1\rangle$. Any superposition $|\Psi\rangle$ of these states can be expressed as:

$$|\Psi\rangle = \cos\theta|0\rangle + \sin\theta e^{i\varphi}|1\rangle \tag{2.55}$$

The angles φ and θ are interpreted as azimuthal and polar angles, respectively, mapping the state $|\Psi\rangle$ on the so called Bloch sphere, see Figure 2.14. φ describes the superposition phase, whose evolution is related to the spin's energy ($\varphi = \frac{E_1 - E_0}{\hbar}t + \varphi_0 = \omega_0 t + \varphi_0$ in the Schrödinger picture), while θ reflects the population of each of the spin states.

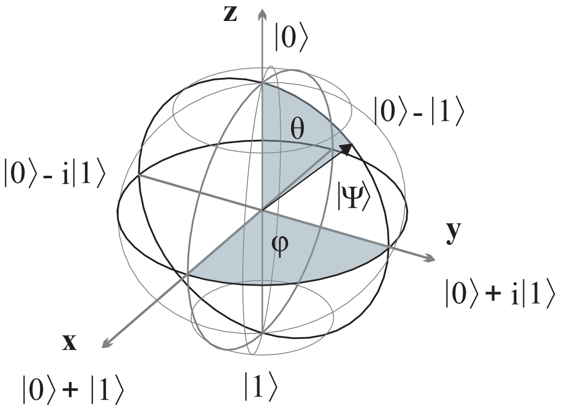

Figure 2.14: Conventions of the Bloch sphere.

Transitions between the states $|0\rangle$ and $|1\rangle$ can be induced by the raising and lowering operators

$$\sigma_+ = |1\rangle\langle 0| = \begin{pmatrix} 0 & 1 \\ 0 & 0 \end{pmatrix} \text{ and } \sigma_- = |0\rangle\langle 1| = \begin{pmatrix} 0 & 0 \\ 1 & 0 \end{pmatrix}, \tag{2.56}$$

which can be expressed in terms of the spin 1/2 Pauli operators:

$$\sigma_\pm = \frac{1}{2}(\sigma_x \pm i\sigma_y). \tag{2.57}$$

Experimentally, spins are flipped by a near resonant transverse magnetic field. For simplicity, we consider purely linear polarization of a microwave magnetic field along the **x** axis with classical amplitude B_x and radial frequency ω,

$$\mathbf{B}^{\mathbf{MW}}(t) = B_x^{\mathrm{MW}} \cos(\omega t)\hat{\mathbf{x}}, \tag{2.58}$$

which couples to the spin via Eq. (2.52):

$$H_{\mathrm{MW}} = g\mu_B B_x^{\mathrm{MW}} \cos(\omega t)\sigma_x = \hbar\Omega_{\mathrm{R,x}} \cos(\omega t)\sigma_x, \tag{2.59}$$

where the Rabi frequency $\Omega_{\mathrm{R}}/2\pi$ parametrizes the coupling strength,

$$\Omega_{\mathrm{R}} = \frac{g\mu_B}{\hbar} B_x^{\mathrm{MW}}. \tag{2.60}$$

Although all experiments in this work make use of purely classical, coherent MW irradiation, it will be useful to introduce the quantum description of the field in terms of the mode raising and lowering operators $\hat{b}^\dagger$ and $\hat{b}$, respectively. The Hamiltonian of the mode is $H_\omega = \hbar\omega \left(b^\dagger b + \frac{1}{2}\right)$, and the spin-MW field interaction Hamiltonian is

$$H_{\mathrm{MW}} = \hbar\Omega_{\mathrm{R}}^{\nu} \cos(\omega t)(b^\dagger + b)\sigma_x, \tag{2.61}$$

where $\Omega_{\mathrm{R}}^{\nu}$ is the vacuum Rabi frequency. For a coherent field $|\beta_x\rangle$ with amplitude β_x and mean photon number $\bar{n}_{\mathrm{coh}} = |\beta_x|^2$ we have the following relationship between the vacuum and coherent Rabi frequency:

$$\Omega_{\mathrm{R}} = \Omega_{\mathrm{R}}^{\nu}\sqrt{\bar{n}_{\mathrm{coh}}}. \tag{2.62}$$

The effect of the MW field in the Bloch sphere representation is to induce rotations of the vector representing $|\Psi\rangle$ around the **x**- axis: $\theta \to \Omega_{\mathrm{R}}\tau + \theta_0$, the usual Rabi precession.

2.3 Dissipation and decoherence processes

A proper understanding of energy dissipation and decohence is important for the establishment of a quantum master equation describing the spin dynamics. In this section we look at how coupling to the environment affects the general TLS and how the underlying mechanisms apply to the particular case of the NV spin

Any realistic two level system is coupled to an environment modeled by arbitrarily fluctuating fields coming from spin impurities randomly distributed in the vicinity of the NV defect. Rather than tracking the origins of each of these field fluctuations individually, their collective effect is summarized into what is called the spin bath. Relevant for the NV defect is the coupling to this environment via magnetic fields, see Hamiltonian (2.52). We will model this interaction via the coupling Hamlitonian

$$V = g\mu_B \mathbf{R}.\boldsymbol{\sigma}, \tag{2.63}$$

where **R** describes the magnetic field bath. We make the following assumptions on **R**. First, the bath is taken to be a very large reservoir when compared to the NV spin and that the state of the bath is therefore not modified by coupling to the NV defect. The density matrix describing the bath in the interaction picture, $\tilde{\rho}_{\mathrm{R}}$, is therefore stationary, $\tilde{\rho}_{\mathrm{R}}(t) = \tilde{\rho}_0$. Next, we assume that the bath is described by a stationary process, meaning that there is no coupling between the different states that make up the bath. We can then write ρ_{R} as a statistical mixture of eigenstates of the bath Hamiltonian. In the experimentally relevant case, the bath is occupying a thermal state. We therefore have

$$\rho_{\mathrm{R}} = \sum_r p_r |r\rangle\langle r|, \tag{2.64}$$

where the weights p_r are given by the Boltzman distribution $p_r = \frac{1}{Z} e^{-\frac{\hbar\omega_r}{k_B\Theta}}$, where $\hbar\omega_r$ is the energy associated with the state $|r\rangle$. Furthermore, the average value of the field emerging from the reservoir is assumed to have a fixed value, which we will take to be zero. The influence of the bath on the spin dynamics is then given by higher moments of R. We model these bath fluctuations to have a very short correlation time τ_c compared to the timescale $1/\Gamma$ at which the spin evolves[2].

2.3.1 Dissipation

The reservoir fluctuations couple to the spin along both, its longitudinal and transverse components, see equation (2.63). As we have seen in the above section, transverse coupling affects the spin population. Field fluctuations perpendicular to the spin axis thus bring the spin into thermal equilibrium with the bath. The equilibrium population is found from the Boltzmann factor. For a TLS with energy splitting $\hbar\omega_0$, denoting the ground/ excited state population by $P_{0/1}$, we have

$$\frac{P_1}{P_0} = e^{-\frac{\hbar\omega_0}{k_B\Theta}} \approx 1 \quad \text{at 300 K.} \tag{2.65}$$

Hence, at room temperature, the spin is equally likely occupying both states $|0\rangle$ and $|1\rangle$, the stationary populations thus being $P_0^{\mathrm{st}} = P_1^{\mathrm{st}} = 1/2$. Any polarization of the spin is decaying according to:

$$\frac{\mathrm{d}}{\mathrm{d}t} P_1(t) = -\Gamma_{1\to 0} P_1 + \Gamma_{0\to 1} P_0. \tag{2.66}$$

Notice that in the above equation $\Gamma_{1\to 0}$ and $\Gamma_{0\to 1}$ closely resemble the Einstein coefficients, with $\Gamma_{0\to 1}$ representing absorption processes, while $\Gamma_{1\to 0}$ combines spontaneous and stimulated emission. Denoting Γ_{sp} the spontaneous emission rate, we have

$$\Gamma_{0\to 1} = \bar{n}_{\mathrm{th},\omega_0}\Gamma_{\mathrm{sp}} \quad \text{and} \quad \Gamma_{1\to 0} = (\bar{n}_{\mathrm{th},\omega_0} + 1)\Gamma_{\mathrm{sp}}, \tag{2.67}$$

where $\bar{n}_{\mathrm{th},\omega_0}$ is the mean photon number of the mode resonant with the spin. We see that the rates $\Gamma_{1\to 0}$ and $\Gamma_{0\to 1}$ are the same at high temperature when considering that the steady state populations are equal. It is conventional to define the spin dissipation rate Γ_1 as:

$$\Gamma_1 \equiv \Gamma_{1\to 0} + \Gamma_{0\to 1}. \tag{2.68}$$

With this convention the population evolves as

$$P_1(t) = \left(P_1(0) - \frac{\Gamma_{0\to 1}}{\Gamma_1} \right) e^{-\Gamma_1 t} + \frac{\Gamma_{0\to 1}}{\Gamma_1}.$$

Here, Γ_1 emerges from Fermi's Golden rule type arguments, with $\Gamma_{1\to 0} \propto |\langle 0|V|1\rangle|^2$. The rates $\Gamma_{1\to 0}$ and $\Gamma_{0\to 1}$ are therefore proportional to the transverse magnetic noise spectral density of the spin bath, $S_{\delta\omega_\perp}[\Omega]$, evaluated at $\Omega = \omega_0$ and $-\omega_0$, respectively [121], where we define

$$S_{\delta\omega_\perp}[\Omega] = \left(\frac{g\mu_B}{\hbar} \right)^2 \int_{-\infty}^{\infty} \mathrm{d}\tau \, \langle \delta R_\perp(\tau) \delta R_\perp(0) \rangle \, e^{i\omega\tau}. \tag{2.69}$$

In the following we will assume that the radiation of the bath is isotropic, such that $S_{\delta\omega_\perp}[\Omega] = 2S_{\delta\omega_\parallel}[\Omega]$. With this convention, we have

$$\Gamma_1 = \pi S_{\delta\omega_\perp}[+\omega_0] + \pi S_{\delta\omega_\perp}[-\omega_0], \tag{2.70}$$

as long as we are working at large temperature. We remark that the above considerations are the result of a perturbative treatment of the bath coupling. They are valid as long as

$$\Gamma_1 \tau_c \ll 1, \tag{2.71}$$

a condition that is sometimes referred to as motional narrowing condition [122].

---

[2] The spin-bath coupling closely resembles the situation of a heavy particle immersed in a gas undergoing Brownian motion. The particle is experiencing a Langevin force with zero average value. The momentum exchange takes place on a very short time scale over which a collision occurs and perturbs the heavy particle very little. By the same token, a friction force acts to dissipate the particle's energy at a comparatively slow rate Γ.

2.3.2 Decoherence

We define Γ_2 as the total decoherence rate. It receives contributions from various processes. First, energy removal from the spin will naturally perturb any superposition phase between the states $|0\rangle$ and $|1\rangle$. This takes place at a rate which is the half sum of $\Gamma_{0\to 1}$ and $\Gamma_{1\to 0}$, equal to $\Gamma_1/2 = (\bar{n}_{\mathrm{th},\omega_0}+1/2)\Gamma_{\mathrm{sp}}$. Furthermore, the phase of the superposition evolves as

$$\varphi(t) = \int_0^t \omega_0(\tau)\,\mathrm{d}\tau. \tag{2.72}$$

The spin resonance frequency $\omega_0/2\pi$ is a function of time due to longitudinal bath fluctuations with spectral density $S_{\delta\omega_\parallel}$ and leads to a random accumulated phase $\Delta\varphi$. If the noise source is Gaussian distributed[3], the average accumulated phase can be related to the mean square of the phase:

$$\left\langle e^{i\Delta\varphi}\right\rangle = e^{-\frac{1}{2}\left\langle\Delta\varphi^2\right\rangle}. \tag{2.73}$$

At the same time, the noise process can be considered as a random walk process. In case of a flat spectral density, such a process is equivalent to diffusion described by the Langevin equation. As a result, $\left\langle\Delta\varphi^2\right\rangle$ scales with t and we can write

$$\left\langle e^{i\Delta\varphi}\right\rangle = e^{-\frac{1}{2}\left\langle\Delta\varphi^2\right\rangle} = e^{-\Gamma_\varphi t}. \tag{2.74}$$

The Bloch-Redfield theory [123] relates the pure dephasing rate, Γ_φ, to the noise spectral density:

$$\Gamma_\varphi = \pi S_{\delta\omega_\parallel}[\Omega = 0]. \tag{2.75}$$

Evaluation of the longitudinal noise spectral density at zero frequency reflects the fact that the underlying noise events correspond to processes in which the bath changes from one state $|r_1\rangle$ to another state $|r_2\rangle$ of the same energy, without changing the energy of the two level system.

The two effects are summarized in the decoherence rate Γ_2:

$$\Gamma_2 = \frac{1}{2}\Gamma_1 + \Gamma_\varphi. \tag{2.76}$$

Again, these considerations are true as long as the motional narrowing condition is met: $\Gamma_2\tau_c \ll 1$. Notice that τ_c can be very different for the case of dissipation and decoherence, as the spectral functions $S_{\delta\omega_\perp}[\Omega = \omega_0]$ and $S_{\delta\omega_\parallel}[\Omega = 0]$ might be dominated by different physical processes at frequencies 0 and ω_0. In the Bloch sphere representation, the effect of the two rates can be understood as a tendency of the state vector to fall onto the equatorial plane (Γ_1) or a randomization of the state vector in the equatorial plane (Γ_2), see Figure 2.15.

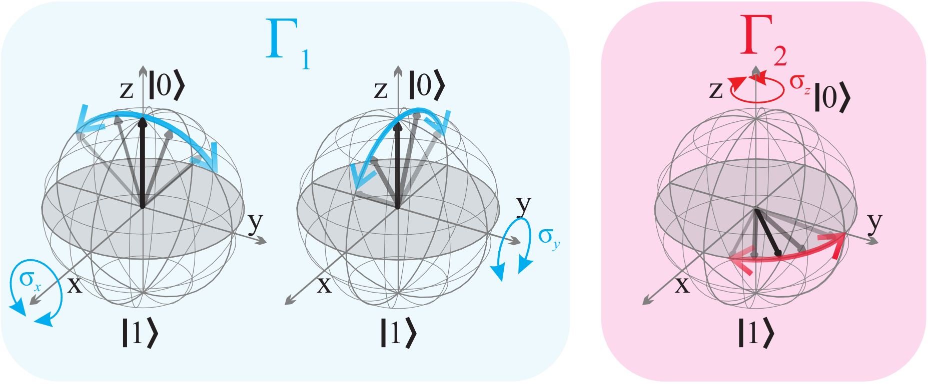

Figure 2.15: The effect of external noise on spin populations (Γ_1) and coherences (Γ_2).

---

[3] As long as a large number of individual independent noise sources contributes to the total fluctuations, the central limit theorem assures that the noise source is indeed Gaussian.

We recall that we supposed here that the reservoir is stationary, Gaussian, Markovian and spectrally flat around the frequencies of interest. We will now justify these assumptions.

2.3.3 Dissipation rates of NV spin qubits

Solid state quantum systems have been proposed as an attractive candidate for data storage devices in quantum computers [67, 124–126]. Not only are they spatially well confined but also intrinsically scalable. As such, NV defects have attracted huge interest in recent years for two reasons [127–129]. First, its photophysical properties permit optical spin preparation and optical readout of the spin state (see section 2.4). Second, NV defects have been demonstrated to exhibit long life- and coherence times at room temperature.[4] Spontaneous dissipation rates, which in atoms amount to $\sim$ 100 MHz – 10 GHz, can be expected to play a negligible role in MW qubits, because the radiation energy density scales as ω^3 and is therefore relatively low in the GHz range. Instead, dissipation processes in solids are dominated by environmental interactions. Compared to other host materials, diamond exhibits a low vibrational density of states below $\sim 1\,\mathrm{THz}$, due to which spin - phonon interactions are suppressed in the orbital ground state of the electron. This creates a low transverse noise spectral density $S_{\delta\omega_\perp}[\Omega]$ around the spin transition frequency $\omega_0/2\pi$, causing the relatively long spin relaxation times. Experimentally measured values for the lifetimes are on the order of several ms at room temperature in ultra pure bulk diamond samples [131], but can be extended to $T_1 \sim 200\,\mathrm{s}$ at 10 K.

2.3.4 Decoherence rates of NV spin qubits

Because spin-phonon interactions play a minor role, dephasing effects are dominated by random fluctuations of the local magnetic field created by impurities in the environment. The spin bath is mainly made up of the $I = 1/2$ nuclear spin of naturally abundant ^{13}C atoms or $S = 1/2$ spins associated with the excess electron of nitrogen impurities, called P1 centers [132]. Both impurities have comparably small Larmor frequencies of around 300 kHz and $\sim 100\,\mathrm{MHz}$ [127, 133], respectively, and are thus too far detuned from the NV resonance to directly induce spin transitions. This limits their influence to pure dephasing. Owing to the small size of the proton Bohr magneton, the NV defect is only affected by ^{13}C atoms when they occupy a site in close vicinity. They limit the spin coherence in the absence of P1 centers [134, 135]. In nitrogen rich samples, the bath is dominated by the dipolar long range interaction of nitrogen impurities [136].

The P1 bath has been studied and characterized by the group of Ronald Hanson from the Delft University of Technology [137]. Due to strong flip - flop interactions that can occur among the electron donors, the bath has a finite correlation time τ_c related to the densities of the impurities and their coupling strength [127]. However, it turns out that their effect on the single NV defect can be described by an effective mean field of a large number of individual, randomly distributed spin 1/2 fluctuators. This is because the long range interaction results in equal coupling amplitudes between the NV spin and the individual bath spins as well as among the bath spins. Contributions from the single NV to the bath are therefore negligible compared to the many interactions in the large reservoir. An analysis of a series of spin echo experiments on a single NV defect yielded that the fluctuations of the local field can therefore be described by an Ornstein - Uhlenbeck process [138], which is caused by a bath that is stationary (meaning that there is weak backaction from the spin onto the bath), Markovian (meaning that the effect of the bath on the spin is independent of its history due to incoherent contributions coming from a large number of spins) and Gaussian at once [137, 139]. All in all, the magnetic field $B(t)$ with amplitude $\delta B(t)$ seen by the NV defect is described by an auto-correlation function

$$\langle \delta B(0)\delta B(t)\rangle = b^2 e^{-\frac{t}{\tau_c}}, \tag{2.77}$$

---

[4] In [130], the authors report the observation of coherence times at cryogenic temperatures exceeding 10 s for a Nitrogen electron donor in an ultra pure silicon crystal. This achievements puts solid state qubits on equal footing with, for example, trapped ion based systems.

where b is the width of the amplitude's Gaussian distribution. Such a bath has a Lorentzian spectral density

$$S_{\delta\omega_\perp}[\Omega] = b^2\tau_c \frac{(\frac{1}{\tau_c})^2}{(\frac{1}{\tau_c})^2 + \Omega^2} \tag{2.78}$$

and is coined *slow*, since the induced dephasing is due to frequencies smaller than $1/\tau_c$. In [137], the authors measured the coupling strength b to be on the order of a few MHz, while the observed correlation time τ_c amounted to a few tens of μs. The spectral density at zero frequency $b^2\tau_c$ therefore was around $\lesssim 1\,\text{MHz}$.

Diamond types The sample used in the above experiment was a nanodiamond made from a type Ib crystal containing less than 200 ppm nitrogen atoms (an overview of the impurity concentration in the various types of diamond is offered in table 2.1). This density of impurities can be decreased in order to improve the coherence times of NV defects. Record values have been achieved in [76], where a crystal was grown by chemical vapor deposition (CVD) in a well maintained atmosphere of low nitrogen concentration. These crystals are then subjected to an implantation process, where the sample is bombarded with nitrogen atoms, which creates vacancies as well as nitrogen impurities. Subsequent heating allows the vacancies to redistribute and NV defects are created [140]. The result was the observation of an extremely long coherence time of $T_2 = 1.8\,\text{ms}$ at room temperature[5]. These so called type IIa crystals have an impurity density of about 10^{-2} ppb, are however difficult to produce and thus expensive. An alternative way for creating NV defects is by heating graphite in a high pressure environment. This technique, called high pressure - high temperature (HPHT), produces type Ia crystals with larger concentrations of impurities (several hundreds ppm [141, 142]). Additional irradiation with free electrons creates vacancies in the diamond lattice, which redistribute after an additional heating step. The resulting NV defects have larger decoherence rates than their counterparts in the type IIa crystals. However, their advantage is that HPHT samples can have a very large concentration of NV defects, which permits the creation of nanodiamonds of sub-micron diameters in which individual NV defects can be found. In these nanodiamonds additional decoherence of the NV defect can be due to their proximity to the crystal surface [143]. NV defects in nanodiamonds have been proven incredibly useful in magnetometry applications [82, 87], where the small size of the probe can be exploited to perform nanometer scale resolution magnetic imaging. In general, these magnetometers have a field sensitivity that strongly depends on T_2, which is why large experimental effort has been dedicated to overcome these limitations. Multipulse techniques, where a series of spin manipulations decouple the spin from its environment, have been shown to increase coherence times by factors related to the number of pulses employed in such a sequence [137, 144, 145]. Despite the complexity of these spin manipulation protocols, they have been demonstrated to successfully increase magnetic field sensitivities [146, 147]. To conclude, the spin bath in HPHT nanodiamonds fulfills the requirement of being Gaussian, stationary and Markovian from our considerations above as long as the NV defect is sufficiently far away from the surface. However, the Lorentzian form of (2.78) entails flatness of $S_{\delta\omega_\parallel}[\Omega]$ only for $\Omega > 1/\tau_c$, a concern that we will have to keep in mind.

---

[5] The value was obtained by a so called Ramsey or free induction decay (FID) measurement, in which the value for T_2 comprises inhomogeneous as well as homogeneous broadening.

Diamond types		
type	label	impurities
type I	a b	rich in N, < 3000 ppm less rich in N, < 500 ppm
type II	a b	very low in N very low in N, rich in B

Table 2.1: Impurity concentrations in various diamond types.

2.4 Photophysics of the NV defect

In this section we are going to quickly review the photophysics of the NV defect, since it plays an important role in spin detection and manipulation.

2.4.1 Molecular level structure of the NV defect

The negatively charged NV defect can be excited via an optical dipole transition, making the defect behave as an isolated molecule trapped in a crystal. The transition has a zero phonon line (ZPL) at 638 nm. However, due to interactions of the excited state with optical phonons, the observed absorption and emission spectra are stokes shifted [73, 148]. The NV defect can thus be excited in a window ranging from 450 nm to 650 nm, while de-excitation is observed in a $\approx$ 100 nm range around a 670 nm peak, see Figure 2.16 **(a)**. This effect enables spectral distinction of pump and fluorescent light. Remarkably, the NV defect proves to be very photo stable and shows neither bleaching nor blinking. Upper state lifetimes of $\sim 10\,\text{ns}$ [149] make this single photon source relatively bright. All of these features are available at room temperature operation and NV defects have therefore been employed as bio-compatible markers [150].

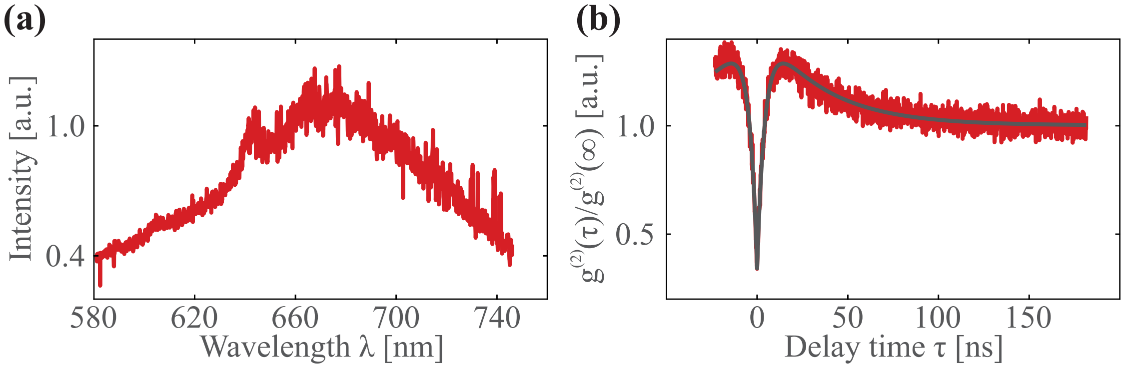

Figure 2.16: Optical properties of the negatively charged NV defect in nanodiamonds. **(a)** A typical emission spectrum of the NV defect with ZPL close to 638 nm. **(b)** A typical autocorrelation function of the emitted NV fluorescence as a function of time delay τ. The dip at zero delay goes below 0.5, verifying the single photon source character of the NV defect. The grey line represents a fit to $g^{(2)}(\tau) = a_0 - a_1\exp(-\gamma_1\tau) - a_2\exp(-\gamma_2\tau)$, corresponding to parasitic fluorescence offset, antibunching and overshoot signatures due to population trapping in the metastable state (see Figure 2.17), respectively.

Orbital ground and excited states are spin triplets and optical transitions among them preserve the spin state [151]. The upper state is an orbital doublet (E_x, E_y), which is averaged out at room temperature, resulting in an effective zero field splitting of $D_{\text{es}}/2\pi \approx 1.42\,\text{GHz}$ [120]. Spin - orbit interactions lead to inter system crossing (ISC) to the singlet state, which is predominant for $|m_s = \pm 1\rangle$ [67, 152]. Details of the singlet state orbital structure are not fully understood and remain subject of ongoing debate between experimentalists and theorists. It has however been demonstrated that two levels ${}^1E$ and ${}^1A_1$ are involved [153, 154], which show a radiative transition in the infra red around 1042 nm, as depicted in Figure 2.17 **(a)**. The non-radiative decay from ${}^1A_1$ to ${}^3A$ is temperature dependent [154] with lifetimes ranging from 200 to 400 ns and happens predominantly into the $|m_s = 0\rangle$ state [67], leading to spin polarization with fidelity of more than 80 % [118, 155]. In this thesis we are not sensitive to the singlet's structure and will therefore condense it into a single metastable state with a lifetime of about 200 ns, see Figure 2.17 **(b)**.

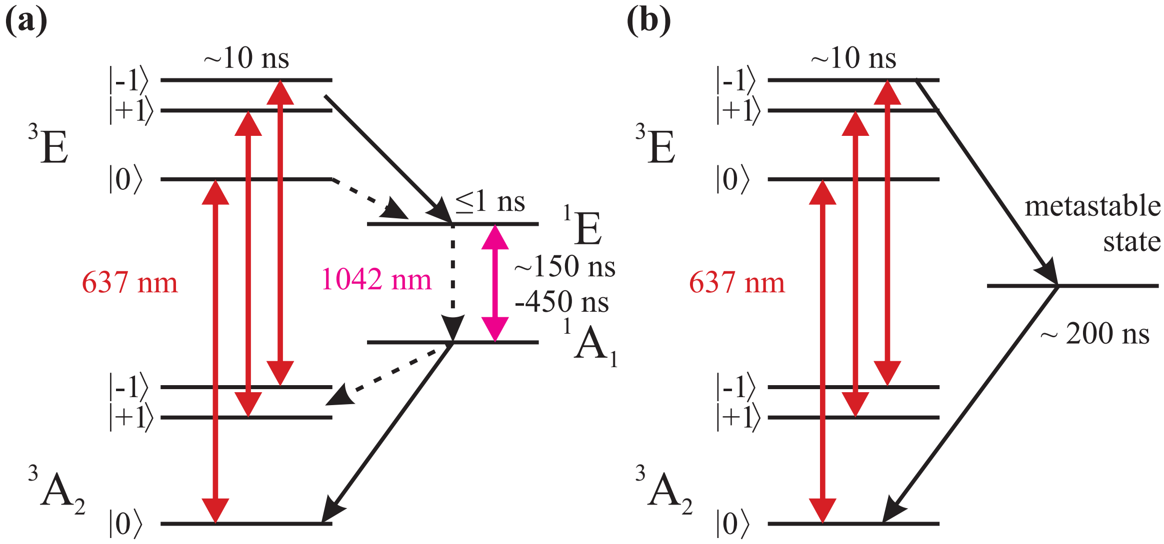

Figure 2.17: Energy diagram of the NV defect. **(a)** The level diagram shows radiative (red arrows) and non-radiative (black arrows) transitions. The principal non-radiative pathways are indicated by solid arrows. There exist however finite branching ratios, indicated by the dashed arrows, that allow transitions from the ${}^3E$ ground to the ${}^1E$ metastable level as well as from the metastable ${}^1A_1$ level to the ${}^3A_2$ excited state. The exact structure of the singlet state is still under debate. Figure after [154]. **(b)** Simplified scheme: The singlet state consists of a single level, with lifetimes on the order of 200 ns. Furthermore, we prevent population of the metastable state from $|0\rangle$ and model spin polarization from the metastable state into the ground state to be perfect.

2.4.2 Optically detected magnetic resonance

These features of the NVs photophysics can be exploited to perform optical readout of the spin state. While transitions from E to A always fluoresce for the $|m_s = 0\rangle$ spin state, there is a finite probability to fall into the metastable state from $|m_s = \pm 1\rangle$. Such a transition is not associated with photon emission around 670 nm. The amount of detected fluorescence can thus be related to the spin state. At the same time, continued pumping of the ${}^3E \leftrightarrow {}^3A_2$ transition leads to polarization of the spin, which can be used for preparation of the electron spin in the ground state. Optical polarization of the spin state is modeled by introducing an optical pumping rate Γ_p that depends on the optical power P_opt and saturation power P_sat (reflecting the single photon source character of the NV defect) [156]:

$$\Gamma_\mathrm{p} = \Gamma_\mathrm{p}^\infty \frac{s}{s+1} \tag{2.79}$$

with

$$s \equiv \frac{P_\mathrm{opt}}{P_\mathrm{sat}}. \tag{2.80}$$

Since optical pumping depends on the excited spin state population, the relaxation rate $\Gamma_{1\to0}$ is modified in the presence of optical pumping to $\Gamma_{1\to0} \to \Gamma_{1\to0} + \Gamma_\mathrm{p}$ and the spin dissipation rate becomes $\Gamma_1 \to \tilde{\Gamma}_1 = \Gamma_1 + \Gamma_\mathrm{p}$. At the same time, optical polarization destroys any coherences present in the system. This introduces dependence of the optical power in Γ_2, such that $\Gamma_2 \to \tilde{\Gamma}_2 = \Gamma_2 + \Gamma_\mathrm{c}$, where $\Gamma_\mathrm{c} = \Gamma_\mathrm{c}^\infty \frac{s}{s+1}$. The parameters Γ_p^∞ and Γ_c^∞ vary between different NV defects. Polarization of the spin into the ground state is induced via the singlet state. Γ_p^∞ is therefore given by the inverse lifetime of the metastable state, which is on the order of $(200\,\mathrm{ns})^{-1}$. It has been shown experimentally that optical excitation from the ground to the excited state preserves spin coherence [157]. Currently, it is not clear whether or not spin coherence is preserved via a transition from the excited state to the ground state. Via the relation $\Gamma_2 = \Gamma_1/2 + \Gamma_\varphi$, a minimum estimate for Γ_c^∞ is $\Gamma_\mathrm{c}^\infty \geq \Gamma_\mathrm{p}^\infty/2$.

2.5 Coupling Hamiltonian

Having established the formal description of oscillator and spin, we will now turn to the formalization of their coupling. We consider a setup in which the NV defect is attached to the tip of the nanowire and displaced through a magnetic field gradient. We first investigate the position dependent energy of the spin giving rise to a spin dependent force. Thereafter, we consider two experimental configurations resulting in either parametric or resonant coupling between oscillator and spin and discuss the reasons for having chosen to work with a parametric coupling mechanism.

2.5.1 Spin forces

As we have seen, the spin couples to magnetic fields via the Zeeman effect, see equation (2.52), giving rise to a spin-oscillator energy $E_{\mathrm{spin-osc}} = -g\mu_B \boldsymbol{\sigma}.\boldsymbol{B}(\boldsymbol{r_0} + \delta\mathbf{r})$. One can expand $\boldsymbol{B}(\boldsymbol{r_0} + \delta\mathbf{r})$ at first order in the oscillator vibrations $\delta\mathbf{r}(t)$, $\boldsymbol{B}(\boldsymbol{r_0} + \delta\mathbf{r}) \simeq \boldsymbol{B}(\boldsymbol{r_0}) + (\delta\mathbf{r}.\boldsymbol{\nabla})\,\mathbf{B}\big|_{\mathbf{r_0}}$, so that we can write

$$E_{\mathrm{spin-osc}} = E^0_{\mathrm{spin-osc}} - g\mu_B \boldsymbol{\sigma}.(\boldsymbol{\delta r}.\boldsymbol{\nabla})\mathbf{B}\big|_{\boldsymbol{r_0}} \tag{2.81}$$

The static term $E^0_{\mathrm{spin-osc}} \equiv -g\mu_B \boldsymbol{\sigma}.\boldsymbol{B}(\mathbf{r_0})$ represents the Zeeman shift at the mean oscillator position $\boldsymbol{r_0}$. Position fluctuations in the presence of magnetic field gradients give rise to an interaction energy $E_{\mathrm{int}} = -\hbar\lambda_{ij}\delta r_j \sigma_i$. The strength of the gradient is directly proportional to the coupling strength λ_{ij}, which we define as

$$\hbar\lambda_{ij} = g\mu_B \partial_i B_j. \tag{2.82}$$

The position dependent energy of the spin gives rise to a vectorial force $\mathbf{F_{spin}} = -\boldsymbol{\nabla} E_{\mathrm{int}}$, with components

$$\mathbf{F_{spin}}.\mathbf{e_i} = \frac{\partial}{\partial(\delta r_i)} g\mu_B \partial_j B_i \sigma_i \delta r_j = g\mu_B \sigma_i \partial_m B_i. \tag{2.83}$$

We thus arrive at a general expression for the force exerted by the spin onto the mechanical force:

$$\mathbf{F_{spin}} = g\mu_B \sum_{i=x,y,z} \sigma_i \boldsymbol{\nabla} B_i. \tag{2.84}$$

Because the spread of the spin wavefunction is much smaller than the mechanical oscillator, $\mathbf{F_{spin}}$ presents a local force, as was discussed at the end of section 2.1. As a result a spin induced mechanical displacement will be measurable as

$$\boldsymbol{\delta r_{\mathrm{opt}}}[\Omega] = \sum_i \chi_i^{\mathrm{eff}}[\Omega] \left(\mathbf{F_{spin}}.\mathbf{e_i} + \delta F_i^{\mathrm{th}} \right) \mathbf{e_i}. \tag{2.85}$$

2.5.2 Interaction Hamiltonian

We are now going to restrict the mechanical motion to be described by a single oscillation mode along the $\mathbf{z}$-direction. Such a situation is typical for cantilevers with a large ratio between width and thickness. The displacement vector then simply becomes $\delta\mathbf{r} \equiv \delta x \mathbf{u_z}$, in which case the form of the spin force simplifies to $\mathbf{F_{spin}} = \sum_i g\mu_B \sigma_i \partial_z B_i$. We obtain the interaction Hamiltonian H_{int} by quantizing the interaction energy $E_{\text{int}} = -\sum_i g\mu_B \delta x \left(\sigma_i \partial_z B_i\right)$:

$$H_{\text{int}} = -\sum_i g\mu_B \delta x^{\mathrm{q}} \left(a + a^\dagger\right) \left(\sigma_i \partial z B_i\right) = -\sum_i \hbar g_i \sigma_i \left(a + a^\dagger\right), \tag{2.86}$$

where the coupling strength g_i is defined in terms of the gound state wavefunction spread δx^{q} as

$$\hbar g_i \equiv g\mu_B \delta x^{\mathrm{q}} \partial_z B_i\big|_{\mathbf{r_0}} = g\mu_B \sqrt{\frac{\hbar}{2M_{\text{eff}}\Omega_{\text{m}}}} \partial_z B_i\big|_{\mathbf{r_0}}. \tag{2.87}$$

The term $\boldsymbol{\sigma}.\partial_z\mathbf{B}$ appearing in Hamiltonian (2.86) treats variations of the magnetic field in the **x**- or **z**- directions on different footings due to the different roles of the σ_x and σ_z operators. While changes of the magnetic field along a direction transverse to the spin can induce state transitions in the TLS, changes of the parallel component will modulate the spin's energy. The magnitude of these two effects, called resonant and dispersive coupling, respectively, can be tuned by alignment of the magnetic field gradient with respect to the spin and oscillation direction. Assuming that the spin **z**-axis is aligned with $\mathbf{u_z}$, as shown in Figure 2.18 **(a)** we can consider two configurations.

Longitudinal gradient We can align the gradient such that only the longitudinal component is varied along the direction of motion ($\partial_z B_z \neq 0$, $\partial_z B_x = \partial_z B_y = 0$), as shown in Figure 2.18 **(b)**. The Maxwell equations require that the magnetic field has zero divergence, $\boldsymbol{\nabla}.\boldsymbol{B} = \mathbf{0}$. Necessarily, we then have non zero contributions of $\partial_x B_x + \partial_y B_y \neq 0$. As the displacement is restricted to the **z**-direction, these terms do not add to either H_{int} or $\mathbf{F_{spin}}$.

Transverse gradient When $\partial_z B_x \neq 0$, displacement along **z** modifies the transverse field components seen by the NV (shown in Figure 2.18 **(c)**). Since $\boldsymbol{\nabla} \wedge \mathbf{B} = \mathbf{0}$ and $\partial_z B_x \neq 0$, $\partial_x B_z \neq 0$ is required. However, if there is no displacement in the **x** direction, it does not contribute to the force along **z**. However, this term will be responsible for a force along **x**.

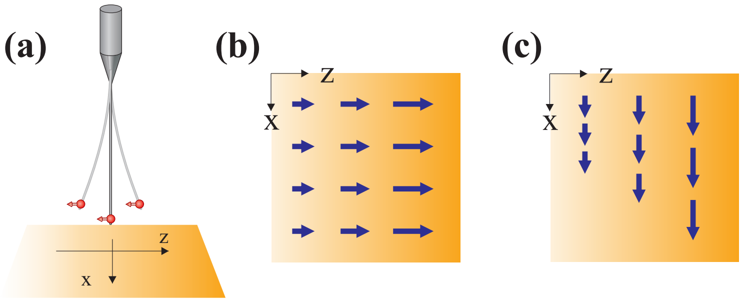

Figure 2.18: Selection of different coupling mechanisms. **(a)** The spin axis and oscillation direction are aligned, $\mathbf{z} \parallel \mathbf{e_z}$. **(b)** Magnetic field configuration with $\partial_z B_z \neq 0$. **(c)** Magnetic field configuration with $\partial_z B_x \neq 0$.

It is thus experimentally possible to tune the coupling between a parametric and resonant interaction. We will now discuss the effects characteristic of each configuration.

Parametric coupling

The parametric coupling between oscillator and spin,

$$H_{\text{int}} = -\hbar g_z \sigma_z (a + a^\dagger), \tag{2.88}$$

is analogous to the optomechanical interaction, where a movable endmirrors modifies the resonance frequency of an optical cavity. The resolved sideband regime is reached when the oscillation frequency $\Omega_{\mathrm{m}}/2\pi$ is larger than the spin linewdith Γ_{spin} (or the cavity decay rate κ). Sidebands will then appear in the energy spectra of the spin, indicating absorption and emission processes mediated by phonon-assisted off-resonant MW transitions. Under these conditions, pumping spin transitions on the lower (higher) frequency sideband allows cooling (heating) of the mechanical oscillator [48] as phonons are sucked out of (pumped into) the resonator. The experimental feasibility has been successfully demonstrated on trapped ions [8] and optomechanical cavities [31]. Moreover, it is possible to conduct a Stern-Gerlach like experiment, where originally spin state and position of a beam of atoms become correlated. In the typical scenario [158] a beam of spin polarizable neutral atoms enters through a slit a region of a magnetic field gradient perpendicular to the direction of motion. The propagation direction of the atoms traversing the magnetic field gradient deviates as a function of the spin state. A consecutive position measurement of the atoms incident on a screen away from the slit then detects the spin state. The situation is shown in Figure 2.19 **(a)**. In the case of the mechanical oscillator, see Figure 2.19 **(b)**, the spin state dependent force $\mathbf{F_{spin}}$ deflects the mechanical oscillator. The net difference in force

$$\Delta F_{\mathrm{spin}} = F_{\mathrm{spin}}(\uparrow) - F_{\mathrm{spin}}(\downarrow) = \frac{\hbar g_z}{\delta x^{\mathrm{q}}} = g\mu_B \partial_z B_z \tag{2.89}$$

traduces to a position difference

$$\Delta x^{\mathrm{stat}}_{\mathrm{spin}} = x^{\mathrm{stat}}(\uparrow) - x^{\mathrm{stat}}(\downarrow) = \Delta F_{\mathrm{spin}}\chi[\Omega = 0] = \frac{\hbar g_z}{\delta x^{\mathrm{q}} M \Omega_{\mathrm{m}}^2} = \delta x^{\mathrm{q}} \frac{2g_z}{\Omega_{\mathrm{m}}}. \tag{2.90}$$

One directly sees that in case where $g_z > \Omega_{\mathrm{m}}$, the spin dependent separation of the oscillator positions is larger than its zero-point fluctuations. In the cavity QED domain, this regime is called the ultra strong coupling regime. Notice that the spin force only depends on the strength of the magnetic field gradient, for which a value of $\partial_z B_z = 10^6\,\mathrm{T/m}$ is realistic [51]. The spin force then yields $\Delta F_{\mathrm{spin}} \approx 20\,\mathrm{aN}$. Furthermore, the protocol measures the spin population, which decays with a lifetime $1/\Gamma_1$, typically much larger than the oscillation period. Hence, to perform the above experiment, operation in the resolved sideband regime is not necessary, and thus one can chose an oscillator with low oscillation frequency. Working with state-of-the-art nanoresonators, featuring $M_{\mathrm{eff}} = 1\,\mathrm{fg}$ and $\Omega_{\mathrm{m}}/2\pi = 100\,\mathrm{kHz}$, the spin force induced separation of the mechanical oscillator yields $\Delta x^{\mathrm{stat}}_{\mathrm{spin}} \approx 44\,\mathrm{pm}$, which is comparable with its zero-point fluctuations of $\delta x^{\mathrm{q}} \approx 280\,\mathrm{fm}$. Simultaneously, a coupling strength of $g_z/2\pi \approx 8\,\mathrm{kHz}$ is achieved, opening interesting perspectives in terms of weak measurements [159].

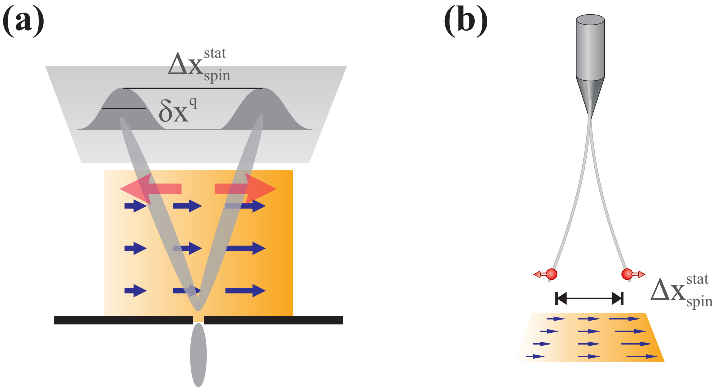

Figure 2.19: Stern-Gerlach experiment. **(a)** In the original experiment, a beam of silver atoms traverses a magnetic field gradient. The atoms are deflected depending on their spin state. The separation $\Delta x^{\mathrm{stat}}_{\mathrm{spin}}$ of the atoms incident on a screen is dependent on the gradient $\partial_z B_z$. The measurement is considered a strong measurement, if the wave function spread is smaller than the separation, $\delta x_{\mathrm{q}} < \Delta x^{\mathrm{stat}}_{\mathrm{spin}}$. **(b)** Stern-Gerlach like experiment with a spin-hybrid mechanical oscillator. The rest position becomes a function of the spin state with magnetic field gradient dependent separation $\Delta x^{\mathrm{stat}}_{\mathrm{spin}}$.

The shot noise limited cavity-free optical detection scheme developed in our laboratory [97] allows room temperature displacement measurement of a SiC nanowire with force sensitivity $S_{\mathrm{F}} = 30\,\mathrm{aN}/\sqrt{\mathrm{Hz}}$ and position sensitivity of $S_{\mathrm{x}} = 10\,\mathrm{fm}/\sqrt{\mathrm{Hz}}$, enabling observation of the above mentioned effects in a dedicated experiment.

These favorable conditions incite to think about more exotic regimes of the hybrid interaction. In particular, superpositions of the spin state (i.e. $|\Psi\rangle = \frac{1}{\sqrt{2}}(|0\rangle + |1\rangle)$) translate to superpositions of two forces applied onto the resonator which can lead to a spatial superposition if the superposition lifetime is longer than the mechanical period. Such a state of the hybrid system is experimentally difficult to observe because of the short coherence time, which depends inversely on the separation $\Delta x^{\mathrm{stat}}_{\mathrm{spin}}$ and is given by [160–162]

$$\tau_\rho = Q\frac{\hbar}{k_B\Theta}\left(\frac{\delta x^{\mathrm{q}}}{\Delta x^{\mathrm{stat}}_{\mathrm{spin}}}\right)^2 = Q\frac{\hbar}{k_B\Theta}\left(\frac{\Omega_{\mathrm{m}}}{2g_z}\right)^2. \tag{2.91}$$

For the above mechanical oscillator we find that the coherence of the superposition state is preserved for only about 40 ns at room temperature, which is the reason why the observation of macroscopic cat states remains a challenge of modern-day experiments. However, at 300 mK and it can reach 40 μs, surpassing the oscillator period of 10 μs.

In this class of experiments, it is important to rule out the role of thermal noise, which is superposed to the spin related signatures and can also lead to additional decoherence. However, the "on/off" character of the force, which can be activated independently with MW pulses, proposes novel strategies to resolve the mechanical displacement induced by the qubit. If one measures the motion of the mechanical oscillator in real time, a flip of the spin at t_0 changes the force and the nanoresonator goes through transitory oscillations around a new rest position, which is reached at t_1 ($t_1 - t_0 \sim 1/\Gamma_{\mathrm{m}}$), see Figure 2.20. This measurement protocol, when realized at room temperature, suffers from the thermal motion of the mechanical oscillator with a spreading of $\Delta x_{\mathrm{th}} = 540\,\mathrm{pm}$, which is much larger than the position shift. However, by repeating the protocol one averages the oscillator trajectories over its Brownian motion, which is not correlated with the spin manipulation protocol. To facilitate the measurement, the resonator can be actively cooled using cold damping, which reduces the rms position noise and degrades the quality factor. The latter effect is not problematic here since one does not seek to measure a stationary force, but instead a transitory behavior. On the contrary, this acceleration of the decay rate permits a faster stabilization and a faster repetition rate. The ~ 80 dB of signal-to-noise observed experimentally ($\Omega_{\mathrm{m}}/2\pi = 100$ kHz, $Q = 10^4$), renders possible a reduction of the mode effective temperature by four orders of magnitude, reaching ≈ 30 mK, while preserving an effective quality factor of $Q_{\text{eff}} = Q/10^4 = 10$, allowing repetition of the measurement every 100 ms. Thus, the effective thermal spreading is reduced to $\Delta x_{\text{th}}^{\text{eff}} = 1\,\text{pm}$, which is approximately 20 times larger than $\Delta x_{\text{spin}}^{\text{stat}}$, so that $20^2 = 400$ iterations will be required to average the thermal noise below the spin related trajectory. This corresponds to 40 s averaging time, which is within experimental reach. Summarizing, it seems realistic to observe the spin recoil in a room temperature experiment, using large magnetic field gradients and active cooling of the resonator. However, the resulting averaging time (40 s) is clearly larger than the spin lifetime ($T_1 \sim$ ms at best). This situation is dramatically modified at low temperature, where the mechanical thermal noise decreases and the spin lifetime increases. As such it should be possible, using a real-time window averaging of the oscillator position to detect mechanically spin flips of the qubit. Since the position operator $\hat{x}$ commutes with the interaction Hamiltonian H_{int}, measuring the hybridized oscillator position does not perturb the spin state. Such a protocol would represent a QND and single shot measurement of the spin population.

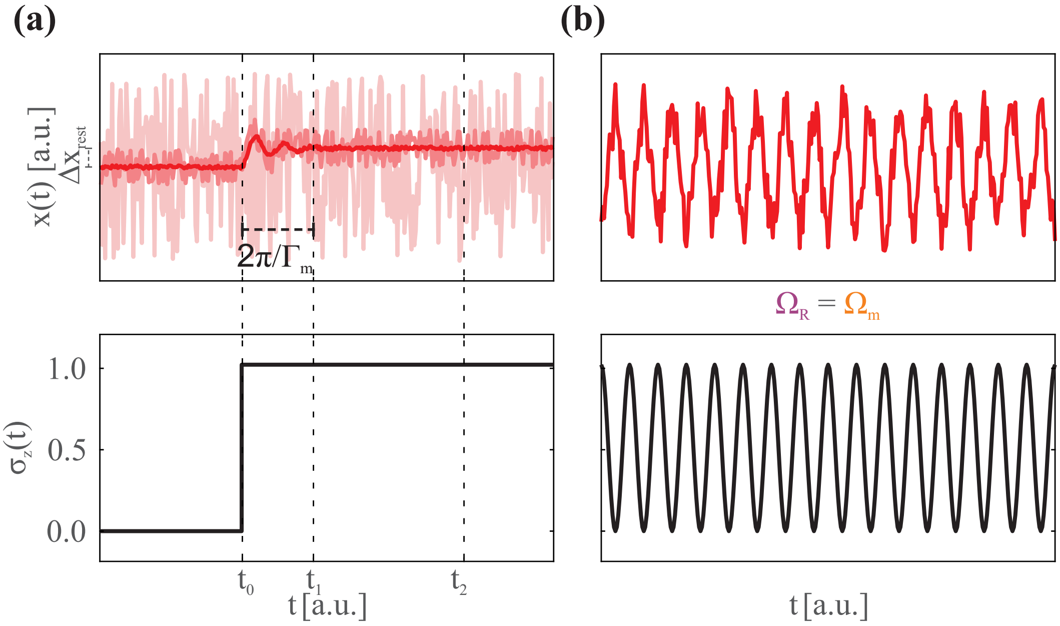

Figure 2.20: Potential spin force measurement protocols. **(a)** Static case. Swapping of the spin state at t_0 leads to a new zero position for the mechanical oscillator after the transitory regime at t_1. By repeating the protocol the incoherent thermal or quantum motion gets averaged out and only the coherent signal persists. **(b)** Dynamic case. When the Rabi frequency is tuned to match the mechanical frequency, $\Omega_{\text{R}} = \Omega_{\text{m}}$, the force on the mechanical oscillator is increased by the Q factor. The coherent amplitude can become comparable to the incoherent, thermal amplitude of the mechanical motion.

Moreover, operation in the resolved sideband regime allows to measure a dynamical spin force. In that case, the force F_{spin} is oscillating at the Rabi frequency $\Omega_{\text{R}}/2\pi$. At the *resonance* condition, $\Omega_{\text{R}} = \Omega_{\text{m}}$, the force is increased by the quality factor Q.

$$\Delta x_{\text{spin}}^{\text{dyn}}[\Omega_{\text{R}}] = \Delta F_{\text{spin}} \cos \Omega_{\text{R}} t \chi[\Omega_{\text{m}}] = Q \Delta x_{\text{spin}}^{\text{stat}}. \tag{2.92}$$

The enhancement by the quality factor can be enormous, as values of $Q > 10^5$ are readily achievable when using the SiC nanowires of this thesis in vacuum environments. For sufficiently large quality factors, the amplitude due to a dynamical spin feedback force can thus approach the nanometer scale and compares positively with the oscillator's thermal motion, as seen in section 2.1. Synchronizing spin oscillations at $\Omega_{\text{R}} = \Omega_{\text{m}}$, however, imposes considerable experimental difficulties. In this thesis we will show how these can be solved by a mechanism that we term *spin locking*.

Resonant coupling

The hallmark signature of a resonant coupling process,

$$H_{\text{int}} = -\hbar g_x \sigma_x (a + a^\dagger), \tag{2.93}$$

is the transfer of coherence between two different quantum systems. Such interaction has been widely studied between a single atom and a light field in cavity quantum electrodynamics. The ability to map the same effects onto a hybrid spin-mechanical system bears the potential to coherently manipulate macroscopic objects and to generate arbitrary non-classical states of motion as already realized in [12, 50]. In this case, phonons play the role of photons and the single atom is replaced by a single spin. As opposed to the Stern-Gerlach like experiment from above, protocols exploiting the coherent interaction compete against the coherence time of the quantum system. In the strong coupling regime, we require that the coupling occurs on a timescale shorter than mechanical dissipation ($1/\Gamma_{\text{m}}$) or quantum state decay ($1/\Gamma_{\text{TLS}}$). As large mechanical quality factors are available, the requirement that $g_x > \Gamma_{\text{m}}$ is easily met. More challenging is the condition for small decoherence rates and large coupling strength $g_x > \Gamma_{\text{TLS}}$, and, as the interaction with the environment provokes large decoherence rates, many experiments employing artificial qubits are performed at cryogenic temperatures. Another problem is the necessity to match the resonance frequency of mechanical oscillator with the frequency of the TLS. While mechanical oscillators with frequencies in the GHz range have been realized in hybrid setups [12], these oscillators suffer from small oscillation amplitudes and therefore weak coupling strength. Yet, by proper engineering of the here proposed hybrid device, these issues can be overcome. In principle it is possible to change the spin frequency $\omega_0/2\pi$ by application of a magnetic field. At $B_z \approx 100\,\text{mT}$ the $|m_s = 1\rangle$ and $|m_s = 0\rangle$ state are split by only a few MHz, see Figure 2.21 **(b)**. From an experimental point of view, this regime is difficult to achieve as the high external magnetic field required puts considerable constraints on the stability and control of the setup. Alternatively, it has been demonstrated that higher order coupling terms can induce a resonant interaction between the $|m_s = -1\rangle$ and $|m_s = 1\rangle$ states in strain coupled hybdrid architectures [163]. These two-phonon processes slightly loosen the resonance condition to $\Delta\omega_0 = 2\Omega_{\text{m}}$, while tuning the frequency splitting of the spin excited states is simultaneously less demanding. However, since the coupling is described by $H_{\text{int}} = -\hbar g_x \sigma_x^2 (a + a^\dagger)$, it will not be observable in our system.

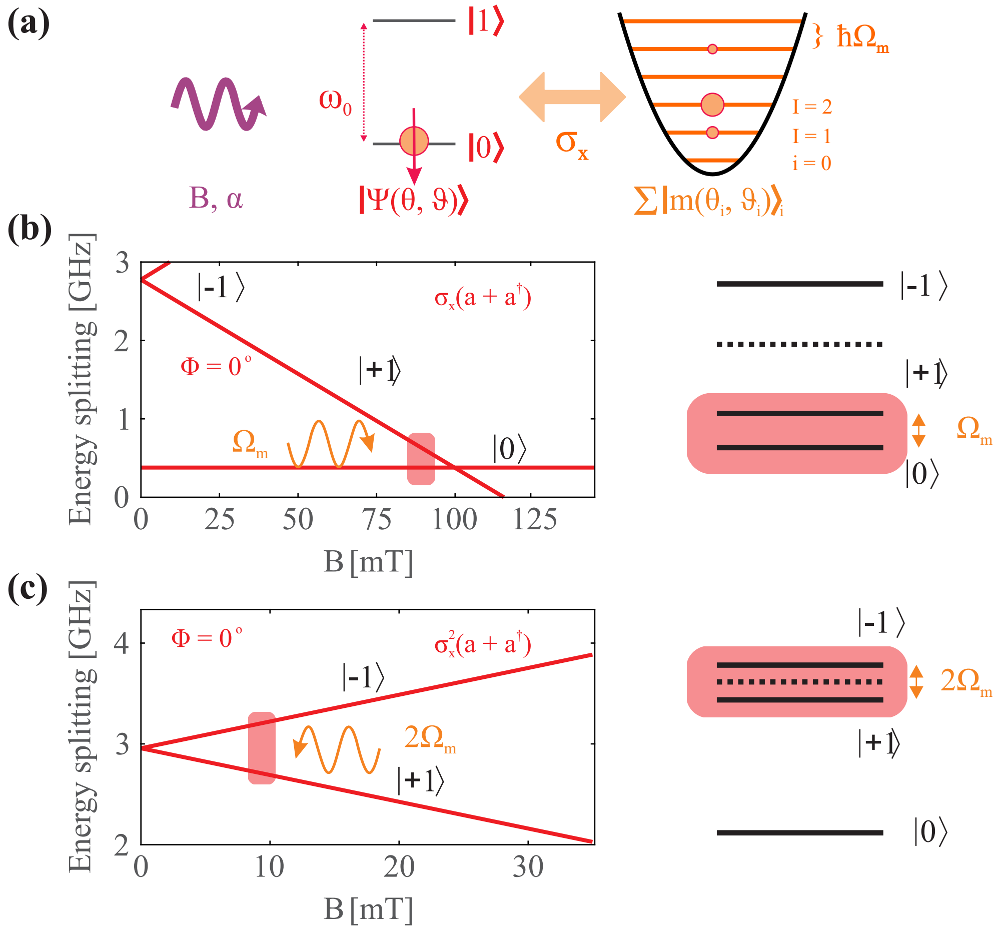

Figure 2.21: Resonant coupling. **(a)** The nonlinearity of the two level system presents an interface to coherently manipulate the multilevel mechanical oscillator with a coherent field. Arbitrary quantum states can thus be created in terms of superpositions of Fock states with arbitrary phases and amplitudes as was done in ccQED experiments. **(b)** In order to make the interaction resonant, spin and oscillator frequency need to match. This can be achieved by applying a large magnetic field, so that the splitting between spin ground and excited states becomes very small. **(c)** Alternatively, the subspace $\{|m_s = -1\rangle, |m_s = +1\rangle\}$ can be chosen to serve as a TLS, manipulation of which involves two-phonon processes. Such processes are however only observable in strain coupled systems, as they require terms proportional to σ_x^2.

The resonant interaction between spin and oscillator offers a fantastic playground for various modern day experiments. While several routes are possible, experimental realization is demanding on the two level system as well as the mechanical oscillator. In this thesis, however, we will demonstrate that we can turn a parametrically coupled spin-hybrid mechanical system into a resonantly coupled one by dressing the spin with a MW field. The dressed spin has an energy splitting that can be tuned into resonance with the mechanical oscillator by changing the intensity of the MW field, while at the same time roles of the σ_x and σ_z operators inverse. Both effects then conspire together to activate resonant coupling processes, even though NV spin and mechanical oscillator stay largely detuned in frequency.

Conclusion In Figure 2.22 we summarize the experimental configurations that allow either parametric or resonant coupling in the hybrid spin-mechanical system. Throughout this thesis, the mechanical oscillator will be purely classical and all the coupling effects that we consider here are due to the parametric interaction as described above. The classical amplitude of mechanical motion will therefore induce a shift $\delta\omega_0/2\pi$ in the resonance frequency $\omega_0/2\pi$ of the spin. In magnetic field gradients of 10^6T/m, oscillation amplitudes of 1 nm amount to a coupling strength of $\approx \delta\omega_0/2\pi = 28$ MHz.

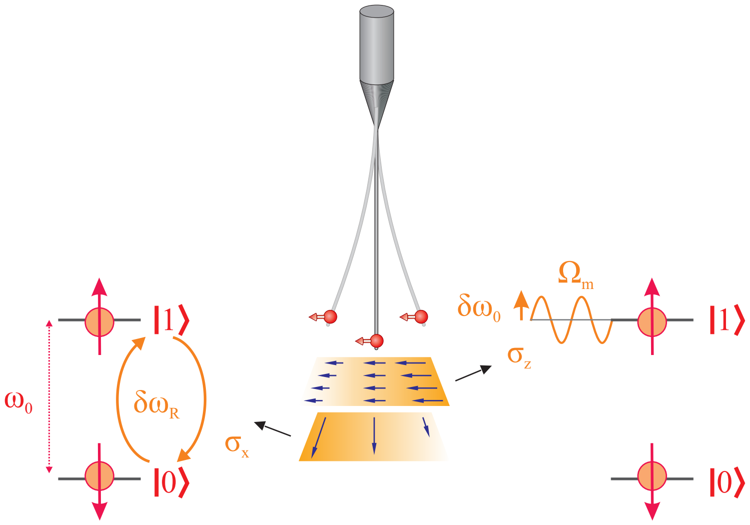

Figure 2.22: Coupling mechanism. The spin's axis is aligned with the direction of oscillation, while the magnetic field gradient has components along the transverse and longitudinal directions. Modulation of the transverse magnetic field (bottom layer) leads to resonant coupling and might induce spin transitions at a Rabi frequency $\delta\omega_R/2\pi$ (as indicated on the left hand side), while modulation of the longitudinal component (top layer) parametrically changes the energy of the two level system, described by $\delta\omega_0$ on the right hand side.

2.6 Spin evolution

The goal of this section is to establish a set of Bloch equations that we will use to describe the evolution of the coupled spin-oscillator system. We start by considering a spin 1 coupled to a mechanical oscillator. We then go on by restricting the problem to a two level subspace, for which we establish a quantum master equation. The quantum master equation can be reduced to a set of coupled equations in terms of spin and oscillator coordinates. Finally, we deduce a set of Bloch equations describing the spin dynamics in the hybrid system.

2.6.1 A spin 1 system coupled to a mechanical oscillator

We will now consider the magnetic field coupling of a spin 1 system to a single mechanical mode in a most generic approach. Assuming that the mechanical oscillator is classical its position can be described by the time dependent variable $\delta\mathbf{r}$. We consider the quantum master equation for the density matrix ρ:

$$i\hbar\dot{\rho} = [H, \rho] + i\hbar\dot{\rho}_{\mathrm{relax}}, \tag{2.94}$$

where the Hamiltonian H is defined as

$$H = \hbar\omega_0\sigma_z^2 - g\mu_B\left(\mathbf{B_0} + \mathbf{B}_{\mathrm{MW}}(t) + \boldsymbol{\mu}(\delta\mathbf{r})\right)\cdot\boldsymbol{\sigma}. \tag{2.95}$$

Notice that the entries of the vector $\boldsymbol{\sigma}$ are the Pauli operators (2.51) and that (2.95) includes the coupling term

$$\boldsymbol{\mu}(\delta\mathbf{r})\cdot\mathbf{e_i} = \delta r_j\partial_j B_i. \tag{2.96}$$

The average value of a generic observable A can be calculated using

$$\langle A\rangle(t) = \mathrm{Tr}\left\{A\rho(t)\right\} = \sum_{i,j} A_{ij}\rho_{ji}(t) \tag{2.97}$$

with

$$\rho_{nm}(t) \equiv \langle n|\rho|m\rangle = \mathrm{Tr}\left\{|m\rangle\langle n|\rho\right\} = \langle P_{n\to m}\rangle(t),$$

where we have introduced the projector $P_{n\to m} \equiv |n\rangle\langle m|$. We then have:

$$\langle \dot{A}(t)\rangle = \frac{1}{i\hbar}\mathrm{Tr}\left\{A[H,\rho]\right\} + \dot{A}_{\mathrm{relax}},$$

which, using the identity $\mathrm{Tr}\left\{ABC\right\} = \mathrm{Tr}\left\{CAB\right\}$, can be simplified[6] to:

$$\langle \dot{A}(t)\rangle = \frac{1}{i\hbar}\langle [A,H](t)\rangle + \dot{A}_{\mathrm{relax}}. \tag{2.98}$$

The generic evolution of the spin density matrix elements is described by:

$$\dot{\rho}_{ij}(t) = \sum_{n,m} M_{ijnm}\rho_{nm} + \dot{\rho}_{ij}^{\mathrm{relax}}. \tag{2.99}$$

In the base $\{\rho_{11}, \rho_{00}, \rho_{10}, \rho_{01}, \rho_{-1-1}, \rho_{0-1}, \rho_{-10}, \rho_{1-1}, \rho_{-11}\}$, the evolution matrix M reads:

$$M = \begin{pmatrix}
0 & 0 & i\beta_x-\beta_y & -i\beta_x-\beta_y & 0 & 0 & 0 & 0 & 0 \\
0 & 0 & -i\beta_x+\beta_y & i\beta_x+\beta_y & 0 & i\beta_x-\beta_y & -i\beta_x-\beta_y & 0 & 0 \\
i\beta_x+\beta_y & -i\beta_x-\beta_y & -i(\beta_z\sqrt{2}+\omega_0) & 0 & 0 & 0 & 0 & i\beta_x-\beta_y & 0 \\
-i\beta_x+\beta_y & i\beta_x-\beta_y & 0 & i(\beta_z\sqrt{2}+\omega_0) & 0 & 0 & 0 & 0 & -i\beta_x-\beta_y \\
0 & 0 & 0 & 0 & 0 & -i\beta_x+\beta_y & i\beta_x+\beta_y & 0 & 0 \\
0 & i\beta_x+\beta_y & 0 & 0 & -i\beta_x-\beta_y & -i(\beta_z\sqrt{2}-\omega_0) & 0 & -i\beta_x+\beta_y & 0 \\
0 & -i\beta_x+\beta_y & 0 & 0 & i\beta_x-\beta_y & 0 & i(\beta_z\sqrt{2}-\omega_0) & 0 & i\beta_x+\beta_y \\
0 & 0 & i\beta_x-\beta_y & 0 & 0 & -i\beta_x-\beta_y & 0 & -2i\beta_z\sqrt{2} & 0 \\
0 & 0 & 0 & -i\beta_x+\beta_y & 0 & 0 & i\beta_x-\beta_y & 0 & 2i\beta_z\sqrt{2}
\end{pmatrix} \tag{2.100}$$

where we have used the β_i components of $\boldsymbol{\beta} = -\frac{g\mu_B}{\hbar\sqrt{2}}(\mathbf{B_0} + \mathbf{B}_{\mathrm{MW}} + \boldsymbol{\mu}(\delta\mathbf{r}))$.

The force $\mathbf{F}_{\mathrm{spin}}$ experienced by the resonator only depends on the spin operators σ_i, whose time evolution is connected to linear combinations of the ρ_{nm} elements and is calculated using equation (2.98). In order to compute the dynamics of σ_i, we have to estimate $\mathrm{Tr}\left\{[\sigma_i, B_j\sigma_j]\rho\right\} = i\epsilon_{ijk}B_j\langle\sigma_k\rangle = i(\mathbf{B}\wedge\boldsymbol{\sigma})_i$. Generally, $i(\mathbf{B}\wedge\boldsymbol{\sigma})_i$ describes a precession of $\boldsymbol{\sigma}$ around a magnetic field $\mathbf{B}$. However, as a consequence of the zero field splitting, the dynamics of the spin 1 vector does not only depend on the components of $\boldsymbol{\sigma}$. Instead, we need to consider that $\sigma_z^2 = \sigma_z - 2|-1\rangle\langle -1|$. We therefore have: $[\sigma_x, \sigma_z^2] = -i\sigma_y + \sqrt{2}\left(|0\rangle\langle -1| - |-1\rangle\langle 0|\right)$ and $[\sigma_y, \sigma_z^2] = i\sigma_x - i\sqrt{2}\left(|0\rangle\langle -1| + |-1\rangle\langle 0|\right)$. Consequently, one obtains:

$$\frac{d\boldsymbol{\sigma}}{dt} = \left(\omega_0\mathbf{e_z} + \frac{g\mu_B}{\hbar}\left(\mathbf{B_0} + \mathbf{B}_{\mathrm{MW}}(t) + \boldsymbol{\mu}(\delta\mathbf{r})\right)\right)\wedge\boldsymbol{\sigma} + \dot{\boldsymbol{\sigma}}_{\mathrm{relax}} + \dot{\boldsymbol{\sigma}}_{-1} \tag{2.101}$$

and

$$\ddot{\delta\mathbf{r}} = -\boldsymbol{\Omega}^{\mathbf{2}}\cdot\delta\mathbf{r} - \Gamma\dot{\delta\mathbf{r}} + \frac{1}{M_{\mathrm{ef}}}\left(\delta\mathbf{F}^{\mathbf{th}} + g\mu_B\sigma_i\boldsymbol{\nabla}B_i\right), \tag{2.102}$$

where we have separated the contribution of the coherences originating from the $|-1\rangle$ state:

$$\dot{\boldsymbol{\sigma}}_{-1} = -\sqrt{2}\omega_0\begin{pmatrix} i\left(\rho_{-10} - \rho_{0\,-1}\right) \\ \rho_{-10} + \rho_{0\,-1} \\ 0 \end{pmatrix}.$$

The last step is useful because it allows us to consider a subspace for the evolution of a TLS instead of a three level system. Such a simplification reduces the size of the parameter space and permits a straightforward interpretation of the evolution of the spin populations and coherences on the Bloch sphere. This step is justified under the experimental conditions described in section 2.2.4.

---

[6] $\mathrm{Tr}\left\{A[H,\rho]\right\} = \mathrm{Tr}\left\{[A,H]\rho\right\} = \langle [A,H](t)\rangle$

2.6.2 Quantum Master equation for a spin 1/2 system coupled to a mechanical oscillator

Hamiltonian in $\{|0\rangle, |1\rangle\}$ the subspace: To take into account the two level system character of the NV spin, we chose to work with the subspace $\{|0\rangle, |1\rangle\}$ of (2.100). In that case, the evolution of the density matrix is

$$\frac{d}{dt}\begin{pmatrix} \rho_{11} \\ \rho_{00} \\ \rho_{10} \\ \rho_{01} \end{pmatrix} = \begin{pmatrix} 0 & 0 & i\beta_x - \beta_y & -i\beta_x - \beta_y \\ 0 & 0 & -i\beta_x + \beta_y & i\beta_x + \beta_y \\ i\beta_x + \beta_y & -i\beta_x - \beta_y & -i(\beta_z\sqrt{2} + \omega_0) & 0 \\ -i\beta_x + \beta_y & i\beta_x - \beta_y & 0 & i(\beta_z\sqrt{2} + \omega_0) \end{pmatrix} \cdot \begin{pmatrix} \rho_{11} \\ \rho_{00} \\ \rho_{10} \\ \rho_{01} \end{pmatrix} + \dot{\rho}_{\text{relax}} \tag{2.103}$$

Notice, that due to the restriction of the $\{|0\rangle, |1\rangle\}$ subspace, all entries of the term $\dot{\boldsymbol{\sigma}}_{-1}$ in (2.102) are zero. To be able to map the evolution of ρ on the Bloch sphere, we express Hamiltonian (2.95) in terms of the vector $\boldsymbol{\sigma}^\star$ with entries

$$\sigma_x^\star = \frac{1}{2}\begin{pmatrix} 0 & 1 \\ 1 & 0 \end{pmatrix}, \sigma_y^\star = \frac{i}{2}\begin{pmatrix} 0 & \text{-1} \\ 1 & 0 \end{pmatrix}, \sigma_z^\star = \frac{1}{2}\begin{pmatrix} 1 & 0 \\ 0 & \text{-1} \end{pmatrix}, \sigma_0^\star = \frac{1}{2}\begin{pmatrix} 1 & 0 \\ 0 & 1 \end{pmatrix}, \tag{2.104}$$

which are proportional to the spin 1/2 Pauli matrices. We thus arrive at

$$H = \hbar\omega_0(\sigma_z^\star + \sigma_0^\star) - g\mu_B B_x^\star \sigma_x^\star - g\mu_B B_y^\star \sigma_y^\star - g\mu_B B_z^\star(\sigma_z^\star + \sigma_0^\star), \tag{2.105}$$

whose structure is equivalent to a true spin 1/2 Hamiltonian when using new magnetic fields

$$B_{x,y}^\star = \sqrt{2}B_{x,y} = \sqrt{2}\left(B_0^{x,y} + B_{\text{MW}}^{x,y} + \mu_{x,y}(\delta\mathbf{r})\right), \tag{2.106}$$

$$B_z^\star = B_z = B_0^z + B_{\text{MW}}^z + \mu_z(\delta\mathbf{r}). \tag{2.107}$$

Notice that the $\mu_{x,y}$ components are only connected to the $B_{0x,y}$ components according to definition (2.96). The term $\hbar\omega_0\sigma_0^\star$ represents an energy offset and does not change the spin dynamics. It will thus be omitted in the suite. Conversely, the term $g\mu_B B_z^\star \sigma_0^\star$ may vary in space and it can not be suppressed. The three first spin 1/2 components satisfy the commutation relations

$$[\sigma_i^\star, \sigma_j^\star] = i\epsilon_{ijk}\sigma_k^\star,$$

which are similar to the ones of the spin 1 $\boldsymbol{\sigma}$ operators. Consequentially, the dynamical evolution of $\boldsymbol{\sigma}^\star$ will be described in terms of a cross product with the effective field $\mathbf{B}^\star$. Therefore, $\boldsymbol{\sigma}^\star$ can directly be mapped onto the Bloch sphere. Additionally, since $\sigma_0^\star$ commutes with all the spin operators, it does not play any role in the spin dynamics.

Spin force in the $\{|0\rangle, |1\rangle\}$ subspace: Concerning the spin force, we have

$$\mathbf{F_{spin}} = g\mu_B \sigma_i^\star \boldsymbol{\nabla} B_{0i}^\star + \frac{g\mu_B}{2}\boldsymbol{\nabla} B_{0z}^\star, \tag{2.108}$$

by inspection of Hamiltonian (2.105). The terms $\sigma_i^\star \boldsymbol{\nabla} B_{0i}^\star$ and the subspace restriction of $\sigma_i \boldsymbol{\nabla} B_{0i}$ are equal for $i = x, y$, so that the transverse components are representation independent. However this is not the case for the z direction. This discrepancy is compensated for by the second term on the right hand side. This contribution represents a static force which ensures that the total force stays unchanged, but it does not impact the resonator dynamics. While we restrict the spin 1 to a spin 1/2 subspace, we have to keep in mind that the ground state $|m_s = 0\rangle$ does not exert a spin-dependent force. In conclusion, we have shown that the spin 1 dynamics can be restricted to a two dimensional subspace by transformations of the effective control fields in order to preserve a SU(2)-like dynamics.

Quantum Master equation in the $\big\{|0\rangle, |1\rangle\big\}$ subspace: With Hamiltonian (2.105) we rewrite the quantum master equation in terms of a Liouville operator $\mathcal{L}_\Gamma(\rho)$ [48]:

$$\dot{\rho} = -\frac{i}{\hbar}[H, \rho] + \mathcal{L}_\Gamma(\rho). \tag{2.109}$$

The Liouville operator describing energy dissipation by the spin 1/2 is usually expressed in terms of the Pauli matrices:

$$\begin{aligned}\mathcal{L}_\Gamma(\rho) = &\frac{\Gamma_\perp}{2}(\bar{n}_{\text{th}} + 1)(2\sigma_-\rho\sigma_+ - \sigma_+\sigma_-\rho - \rho\sigma_+\sigma_-) \\ &+ \frac{\Gamma_\perp}{2}(\bar{n}_{\text{th}})(2\sigma_+\rho\sigma_- - \sigma_-\sigma_+\rho - \rho\sigma_-\sigma_+) \\ &+ \frac{\Gamma_\parallel}{2}(\sigma_z\rho\sigma_z - \rho).\end{aligned} \tag{2.110}$$

By defining the raising and (lowering) operator $\sigma_+^\star = \sigma_x^\star + i\sigma_y^\star$ ($\sigma_-^\star = \sigma_x^\star - i\sigma_y^\star$), we express the Liouville operator $\mathcal{L}_\Gamma(\rho)$ in terms of $\boldsymbol{\sigma}^\star$:

$$\begin{aligned}\mathcal{L}_\Gamma(\rho) = &\frac{\Gamma_{1\to 0}}{2}(2\sigma_-^\star\rho\sigma_+^\star - \sigma_+^\star\sigma_-^\star\rho - \rho\sigma_+^\star\sigma_-^\star) \\ &+ \frac{\Gamma_{0\to 1}}{2}(2\sigma_+^\star\rho\sigma_-^\star - \sigma_-^\star\sigma_+^\star\rho - \rho\sigma_-^\star\sigma_+^\star) \\ &+ 2\Gamma_\varphi(\sigma_z^\star\rho\sigma_z^\star - \rho).\end{aligned} \tag{2.111}$$

We thus find the form of $\dot{\rho}_{\text{relax}}$ in the $\{|0\rangle, |1\rangle\}$ base:

$$\dot{\rho}_{\text{relax}} = \begin{pmatrix} -\frac{\Gamma_1}{2}(\rho_{11} - \rho_{00}) & -\Gamma_2\rho_{01} \\ -\Gamma_2\rho_{10} & +\frac{\Gamma_1}{2}(\rho_{11} - \rho_{00}) \end{pmatrix} \tag{2.112}$$

and, equivalently,

$$\dot{\boldsymbol{\sigma}}^\star_{\text{relax}} = \begin{pmatrix} -\Gamma_2 & 0 & 0 & 0 \\ 0 & -\Gamma_2 & 0 & 0 \\ 0 & 0 & -\Gamma_1 & 0 \\ 0 & 0 & 0 & 0 \end{pmatrix} .\boldsymbol{\sigma}^\star \tag{2.113}$$

The evolution of the coupled system is then found from

$$\frac{d\boldsymbol{\sigma}^\star}{dt} = \Big(\omega_0\mathbf{e_z} + \frac{g\mu_B}{\hbar}\left(\mathbf{B_0}^\star + \mathbf{B}^\star_{\text{MW}}(t) + \boldsymbol{\mu}^\star(\delta\mathbf{r})\right)\Big) \wedge \boldsymbol{\sigma}^\star + \dot{\boldsymbol{\sigma}}^\star_{\text{relax}} \tag{2.114}$$

and

$$\ddot{\delta\mathbf{r}} = -\mathbf{\Omega^2} \cdot \delta\mathbf{r} - \Gamma\dot{\delta\mathbf{r}} + \frac{1}{M_{\text{eff}}}\left(\delta\mathbf{F}^{\text{th}} + g\mu_B\sigma_i^\star\boldsymbol{\nabla}B^\star_{0i} + \frac{g\mu_B}{2}\boldsymbol{\nabla}B^\star_{0z}\right). \tag{2.115}$$

Remark: The Quantum Master equation above ignores the fact that thermalization of the spin leads to non-zero population in the $|m_s = -1\rangle$ state and the spin therefore leaves the subspace $\big\{|0\rangle, |1\rangle\big\}$. This is, however, an effect that occurs on a timescale $1/\Gamma_1$. In the rest we will assume that such processes are much slower than decoherence processes, which will dominate the spin dynamics.

2.6.3 The Bloch equations

It is usual practice to introduce the Bloch vector

$$\mathbf{b} = \begin{pmatrix} \langle\sigma_x^\star\rangle \\ \langle\sigma_y^\star\rangle \\ \langle\sigma_z^\star\rangle \end{pmatrix}, \tag{2.116}$$

which evolves according to

$$\frac{d\mathbf{b}}{dt} = U \cdot \mathbf{b} + \left.\frac{d\mathbf{b}}{dt}\right|_{\text{relax}}. \tag{2.117}$$

We now assume that the MW field has negligible longitudinal components. Then, the evolution matrix U is expressed as

$$U = \begin{pmatrix} 0 & -\omega_0 - \frac{g\mu_B}{\hbar}\left(B_0^z + \mu_z(\delta\mathbf{r})\right)) & \sqrt{2}\frac{g\mu_B}{\hbar}(B_0^y + \mu_y(\delta\mathbf{r})) + \Omega_R^y(t) \\ \omega_0 + \frac{g\mu_B}{\hbar}\left(B_0^z + \mu_z(\delta\mathbf{r})\right)) & 0 & -\sqrt{2}\frac{g\mu_B}{\hbar}(B_0^x + \mu_x(\delta\mathbf{r})) - \Omega_R^x(t) \\ -\sqrt{2}\frac{g\mu_B}{\hbar}(B_0^y + \mu_y(\delta\mathbf{r})) - \Omega_R^y(t) & \sqrt{2}\frac{g\mu_B}{\hbar}(B_0^x + \mu_x(\delta\mathbf{r})) + \Omega_R^x(t) & 0 \end{pmatrix} \tag{2.118}$$

and

$$\left.\frac{d\mathbf{b}}{dt}\right|_{\text{relax}} = \begin{pmatrix} -\Gamma_2 b_x \\ -\Gamma_2 b_y \\ -\Gamma_1 b_z \end{pmatrix}. \tag{2.119}$$

We will now make the time dependence of the magnetic fields explicit. As a first step, we are going to assume that the photon field is described by a classical coherent state oscillating at a single frequency ω. We then align the MW field in the $\mathbf{x}$-direction and substitute the MW field amplitude by the effective Rabi frequency:

$$\begin{aligned} \frac{g\mu_B}{\hbar} B^y_{\text{MW}}(t)\sqrt{2} &= 0, \\ \frac{g\mu_B}{\hbar} B^x_{\text{MW}}(t)\sqrt{2} &= \Omega_R^x \cos\omega t. \end{aligned}$$

We expand the linearly polarized MW field in terms of counter propagating left- and right circularly polarized fields and make the rotating wave approximation in order to simplify the calculations. This approximation neglects off-resonant terms that correspond to processes of a photon being absorbed upon spin transition into the ground state and a photon being emitted upon spin transition into the excited state. The details of the calculation are given in Appendix B. The co-rotating part of the Bloch vector $\tilde{\mathbf{b}}$ is then expressed in terms of $\{u, v, w\}$, with u and v representing the real and imaginary parts of the co-rotating coherences, respectively, and w half the population difference.

Finally, in a frame rotating with the MW field, the NV spin dynamics are described by the following system of equations:

$$\begin{pmatrix} \dot{u} \\ \dot{v} \\ \dot{w} \end{pmatrix} = \begin{pmatrix} -\Gamma_2 & \delta - \delta\omega_0(t) & -2\delta\omega_{\text{R}}(t)\sin\omega t \\ -\delta + \delta\omega_0(t) & -\Gamma_2 & -\Omega_{\text{R}} - 2\delta\omega_{\text{R}}(t)\cos\omega t \\ 2\delta\omega_{\text{R}}(t)\sin\omega t & \Omega_{\text{R}} + 2\delta\omega_{\text{R}}(t)\cos\omega t & -\Gamma_1 \end{pmatrix} \begin{pmatrix} u \\ v \\ w \end{pmatrix} \tag{2.120}$$

Here, $\delta\omega_0$ and $\delta\omega_{\text{R}}$ represent the parametrized modulation strength of the mechanical oscillator in the longitudinal and transverse direction, respectively:

$$\hbar\delta\omega_0(t) = -g\mu_B \partial_j B_z \delta r_j(t) \tag{2.121}$$

and

$$\hbar\delta\omega_{\text{R}}(t) = -\sqrt{2} g\mu_B \partial_j B_x \delta r_j(t). \tag{2.122}$$

Notice that the rotating wave approximation has not been performed on the mechanically driven transverse components of $\delta\omega_{\text{R}}(t)$.

2.6.4 Parametric coupling

Spin evolution in the parametrically coupled hybrid system

Throughout this thesis, we will be interested in the purely parametrically coupled hybrid system as shown in Figure 2.23. It can be described by a single mechanical mode, whose displacement direction is aligned along the spin axis, along which a sufficiently large magnetic field gradient $\partial_z B_z$ is applied (the Zeeman effect creates a frequency shift of about 28 MHz/mT). Under these conditions, and with a coherent MW field along the **x**-direction, we have

$$\begin{pmatrix} \dot{u} \\ \dot{v} \\ \dot{w} \end{pmatrix} = \begin{pmatrix} -\Gamma_2 & \delta - \delta\omega_0(t) & 0 \\ -\delta + \delta\omega_0(t) & -\Gamma_2 & -\Omega_R \\ 0 & \Omega_R & -\Gamma_1 \end{pmatrix} \begin{pmatrix} u \\ v \\ w \end{pmatrix}. \tag{2.123}$$

Note that we do not take into account any spin related back action onto the resonator. If needed, on should take into account equation (2.115).

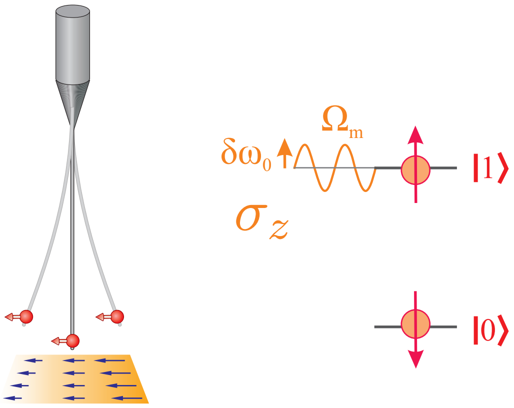

Figure 2.23: Parametric coupling of the spin-hybrid mechanical system described by the energy shift $\delta\omega_0(t)$.

Numerical evaluation of the Bloch equations

The system of coupled differential equations can be solved numerically using a fourth order Runge-Kutta (RK4) algorithm [164]. The initial vector $\tilde{\mathbf{b}}(t = t_0)$ is supposed to be known at $t_0 = 0$. Then, a weighted average change over an incremental time step of size h is calculated for each of the quantities u, v, w , yielding $\tilde{\mathbf{b}}(t = t_0 + h)$. $\tilde{\mathbf{b}}(t = t_0 + h)$ is then re-injected as a new initial vector. The convergence of the algorithms largely depends on choosing a small enough step size h, which needs to be much smaller than the inverse of the largest frequency appearing in the Bloch equations.

Simulated values

In our experiment, we have chosen to work with mono crystalline HPHT nanodiamonds. It is possible to identify single NV defects whose surroundings are free of ^{13}C atoms. The concentration of nitrogen impurities in these samples is on the order of several 100 ppm, which justifies assuming that the above considerations for the bath are valid for our samples. Furthermore, for small enough correlation times τ_c, the bath is spectrally flat at frequencies $\Omega = 0$ and $\Omega = \omega_0$, validating our assumptions for the rates Γ_1 and Γ_2 of section 2.2.4. For simulations of the Bloch equations (2.120) in a room temperature environment, we are therefore choosing a relaxation rate to be on the order of $\Gamma_1 \approx 10\,\text{kHz}$ and for the decoherence rate $\Gamma_2 \approx 1\,\text{MHz}$.

Chapter 3

Parametric coupling of a single spin qubit to a radio frequency magnetic field

In this chapter we focus on the parametric interaction between a single spin parametrically coupled to a nanomechanical oscillator. In such an interaction, the energy splitting of the two level system is modulated by the vibrations of the resonator. Here, we start by emulating such a coupling by immersing a single spin in a radiofrequency magnetic field. At first we will describe the experimental apparatus of this test experiment, which facilitates the implementation of standard procedures of NV spin manipulation and readout. We are then going to study the effect of monochromatic energy modulation on the microwave driven NV spin dynamics with two different techniques. As a first step, we investigate the steady state regime of the spin population by means of a spectroscopic measurement and introduce and explore two relevant regimes of modulation: the adiabatic and resolved sideband regimes. Our results are analyzed and compared using the Bloch equations presented in Chapter 2. In a second series of experiments we then investigate the time evolution of the spin dynamics. Analysis of the results can be done by an interpretation of the Bloch equations with the so called Bloch-Redfield theory. Our system can operate in a regime where the frequencies of mechanical oscillation and microwave driven spin precession match: $\Omega_{\mathrm{R}} \simeq \Omega_{\mathrm{m}}$. In this situation we observe that the spin dynamics is significantly modified by the emulated mechanical motion. In particular, the spin dynamics become locked onto the oscillator dynamics. The effect will be explained in terms of a double dressing of the spin with the two orthogonal microwave and radiofrequency fields and, alternatively, by studying the Bloch equations describing the dressed spin, which will be introduced here. We conclude the chapter with a discussion of potential consequences of this synchronization for real hybrid systems.

3.1 Emulating oscillator dynamics with radio frequency fields

In Chapter 1 we have motivated the study of hybrid spin-mechanical systems. The richness of the qubit dynamics proposes several strategies for the generation of non-classical states. In the NV spin-SiC nanowire device, typical frequencies of mechanical oscillations are in the 100 kHz - 10 MHz range, while the splitting of the spin frequency is $\omega_0/2\pi \sim$ GHz. Thus, we focus on a dispersive coupling scheme, in which the mechanical motion modulates the energy of the TLS's eigenstates rather than inducing rotations of the spin states. The experimental demonstration of such parametric interaction between spin and oscillator was outlined in section 1.2. It has lead to a broadening of the spin resonance in the adiabatic regime, where spin decay rates are much larger than the mechanical frequency. However, we would now like to go beyond the adiabatic case and enter the resolved sideband regime, where spin manipulation could be used to create non-classical states of motion of the macroscopic mechanical oscillator, see section 1.1.2. In order to achieve large coupling strength, it is necessary to employ large magnetic field gradients. Thus, a slight mechanical drift can generate a large qubit frequency shift, as well as important misalignment of spin and magnetic gradients in the experiment. For example, using $\nabla B = 10^6$ T/m, the magnetic field can vary by 1 T due to 1 μm thermal drift, causing a change of spin frequency by 30 GHz. This puts important limitations on achievable integration times and renders data analysis complicated. We have therefore decided to build a test system, which avoids experimental drifts and allows to study the dynamics of a spin in parametric interaction over a wide range of experimental parameters. A schematic description of our test system is depicted in Figure 3.1. The principle idea is that the mechanical oscillations are emulated by a time varying magnetic field. Instead of changing the spin energy by displacing the NV defect through a magnetic field gradient (creating a spatially dependent Zeeman effect), the magnetic field is changed in time: RF magnetic fields created by an oscillating current in a nearby waveguiding structure lead to a time dependent Zeeman effect.

Principle: Depositing several nanodiamonds hosting single NV defects on a quartz plate allows addressing optically (employing a confocal microscope) individual defects presenting a large distribution in orientation and spin lifetimes. The waveguide simultaneously carries MW and RF currents. These currents are created with waveform generators that allow tuning their respective frequencies and amplitudes over a wide parameter range. In principle any mechanical oscillation with arbitrary resonance frequency and drive strength can thus be emulated. In the next section we are going to further detail the different elements of the setup.

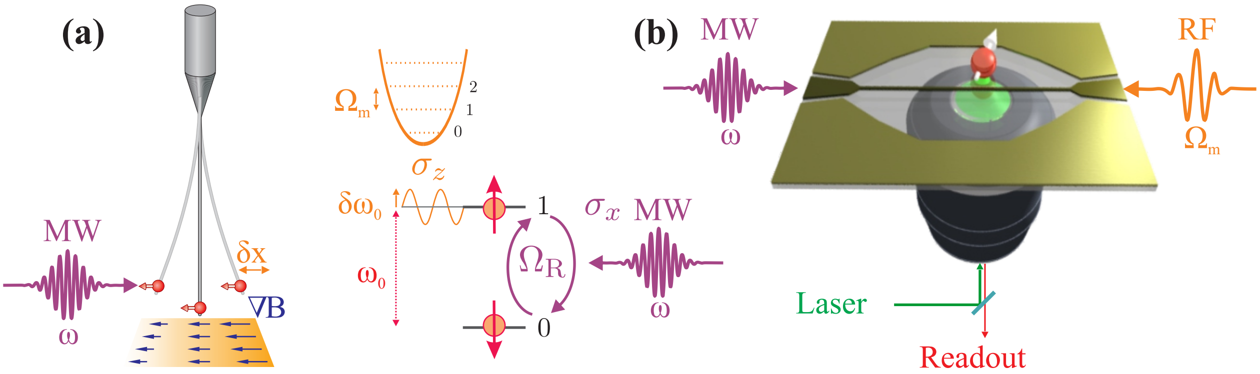

Figure 3.1: Emulating the hybrid parametric coupling on a test system. **(a)** The qubit energy is mechanically modulated at $\Omega_\mathrm{m}/2\pi$ with amplitude $\delta\omega_0/2\pi$ proportional to the vibration amplitude δx. Spin transitions are driven with a MW field of frequency $\omega/2\pi$ and strength $\Omega_\mathrm{R}/2\pi$, the Rabi frequency. **(b)** On a test system, currents provide MW and RF magnetic fields to the spin, generating Rabi transitions and energy modulation, respectively. A confocal microscope allows addressing individual NV defects that have been spin coated on the quartz plate beforehand.

3.2 Setup

In this section we are going to describe the individual building blocks of the experiment.

3.2.1 Nanodiamonds

The NV defects that we are using are hosted in HPHT grown monocrystaline nanodiamonds. Such diamonds are commercially available as an industrial polishing solution and were purchased from the company Microdiamant. The particular solution contains 20 g of diamond per kg of the liquid. Our samples are specified to be of 50 nm average diameter, which is rather large, so that there is limited surface degradation of the spin properties [87]. The solution strongly is diluted with de-ionized water to $\sim 50:1$ and exposed to an ultrasound bath for 15 minutes in order to lift off residual debris from the nanodiamonds' surface. These residuals may add parasitic fluorescence to the optical readout but can be eliminated by intense laser illumination. The solution is subsequently spin coated (at 4000 turns per minute for 30 seconds) onto the quartz plate with a coplanar waveguide to carry MW and RF fields to the location of the NVs. Single NV defects can subsequently be identified with the confocal microscope.

3.2.2 Electromagnetic waveguide

The coplanar waveguide structure is the central piece of the experimental apparatus and is depicted in Figure 3.2 **(a)** and **(b)**. Its design has to incorporate an optical window to address the NV defects with the confocal microscope. In order to be able to generate magnetic fields of sufficiently large amplitudes, large current densities are required to pass through the waveguide, which puts limitations on its dimensions. On the other hand, both end terminals need to be impedance matched to 50 Ohm in order to ensure proper transmission of the MW currents around 1.45 GHz and 2.87 GHz (the ESLAC and natural resonance frequency of the NV defect, respectively) and prevent end reflections which may reduce the local current strength. Starting at the terminals, the width of the waveguide is reduced while adapting the gap size to the ground mass to keep the impedance fixed at 50 Ohm. The impedance calculations are performed with the software TXline. However, in order to integrate an optical window in the design and permit efficient spin-coating, it is necessary to increase the gap size. At this point the width of the waveguide is reduced to 27 μm, which locally increases current density. In order keep transmission losses low, the length of the central part is kept at 1 mm.

The waveguide was fabricated in-house at the NanoFabrication facility using laser lithography and lift-off techniques (resist: microposit S1818, G2 positive photoresist). The whole structure is mainly created out of a 150 nm Gold layer, which provides the necessary electric conductance. A first thin layer of Titanium is patterned onto the 0.2 mm thick quartz plate to ensure proper adhesion of the waveguide to the surface and an additional layer of Platinum is sandwiched between the Gold and Titanium layer in order to prevent diffusion of the two materials, see Figure 3.2 **(c)**. The MW transmission has been measured with a Vector Network Analyzer and is shown in Figure 3.2 **(d)**. At 1.45 GHz, the loss is around 2 dBm and at 2.87 GHz around 4.5 dBm. A 17 Ohm DC resistance was measured across the waveguide, dominated by the constriction. The magnetic field created by low frequency currents was modeled using the Biot-Savart law. We estimate that the magnetic field at 5 μm distance from the central conductor is pointing in the direction of the surface vector with strength 13.7 mT/A. The current is supplied by a waveform generating voltage source with 50 Ohm output impedance. Taking into account the 50 Ohm end termination of the circuit, a magnetic field of 0.235 mT/V is created by the waveguide, where the voltage is here the output voltage demanded from the waveform generator.

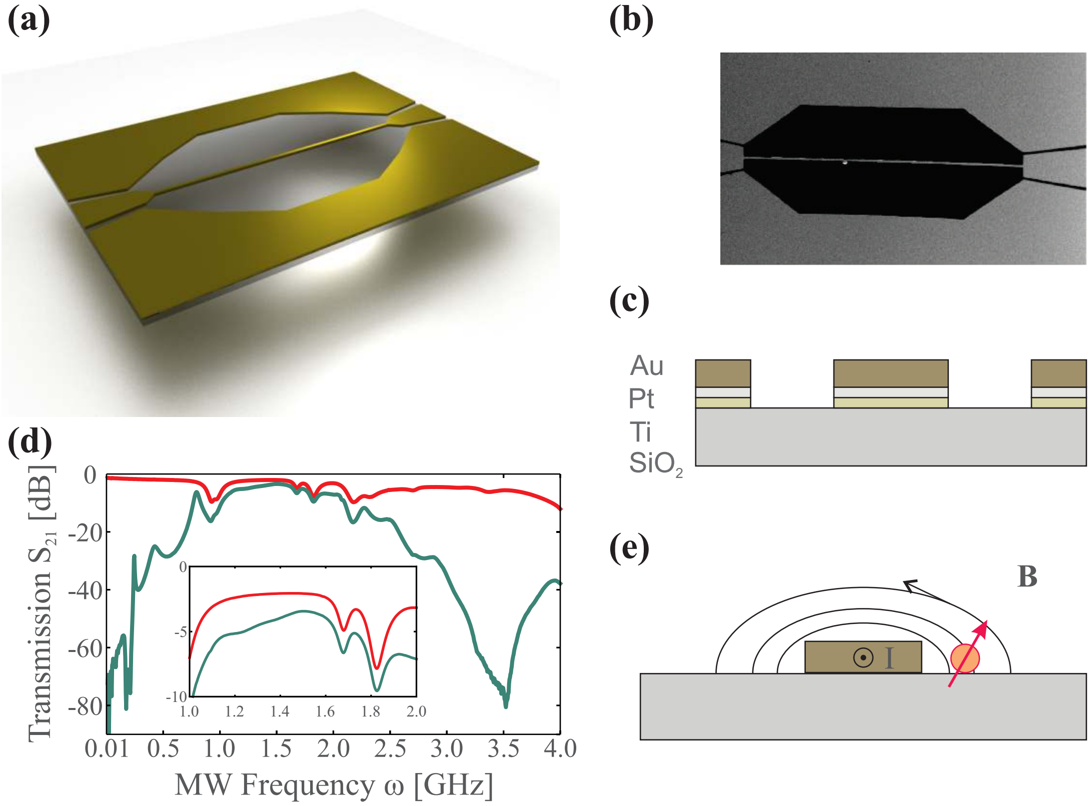

Figure 3.2: Description of the waveguide. **(a)** Schematic view onto the coplanar waveguide. The central constriction across the optical window is 27 μm thick. **(b)** SEM image of the waveguide showing the constriction across the optical window. **(c)** Vertical composition: SiO_2: 200 μm, Ti: < 5 nm, Pt: < 5 nm, Au: 15 nm. **(d)** Transmission of the waveguide measured with a vector network analyzer. The red curve presents the transmission across the waveguide and sample holder. The green curve presents the transmission across waveguide, sample holder and two bias tees (see section 3.2.3). *Inset:* Zoom on the region near 1.45 GHz. **(e)** Vertical cut across the waveguide indicating the magnetic field created by a current across the constriction. Also indicated is a single NV defect with arbitrary orientation.

3.2.3 Sample holder and electrical wiring

Once the nanodiamonds are deposited on the sample, NV defects are identified with the confocal microscope. To do so, the lithographed quartz plate is mounted on a sample holder supporting the SMA connectors to the signal sources. It is positioned by a XYZ translational stage such that the sample surface is perpendicular to the optical axis of the confocal microscope. The translational stage with micrometric screws permits alignment in each direction with 10 μm precision. The sample holder allows to connect current signals to the waveguide, which is done by microbonding the central waveguide and ground plane to two SMA connectors of the sample holder. The microbonds together with some additional adhesive tape well fix the sample and permit to quickly exchange the specimen if necessary.

Microwave signals are generated by a Rohde & Schwarz SMBV 100A Vector Signal Generator (operating between -60 dBm and + 30 dBm output power from 9 kHz to 6 GHz) and can optionally be amplified using a ZHL-42 Amplifier from Mini-Circuits. MW signals are turned on and off rapidly using a fast TTL controlled ZASWA-2-50DR++ coaxial High Isolation Switch with 5 ns rise/fall time (also from Mini-Circuits). TTL pulses with short rise time are provided by the 300 MHz PulseBlasterESR-PRO arbitrary waveform generator (AWG) from the company SpinCore. Radio frequency and DC signals are generated by a 2 port Agilent 33500 Function generator and can be injected from both directions into the waveguide in order to increase magnetic field strength. RF and MW signals are combined using a in-house built bias tee, designed by Christophe Hoarau. These devices have specific MW transmission properties. Since we are working at either 1.45 GHz or 2.87 GHz, two sets of them are available. Figure 3.2 **(d)** shows the entire transmission losses with one bias tee connector on each port, amounting to less than 4 dBm at 1.45 GHz. The bias tee elements furthermore permit efficient protection of the MW source from RF voltages. All signals are converted into currents by terminating them with a 50 Ohm resistor. The wiring circuit diagram is depicted in Figure 3.3.

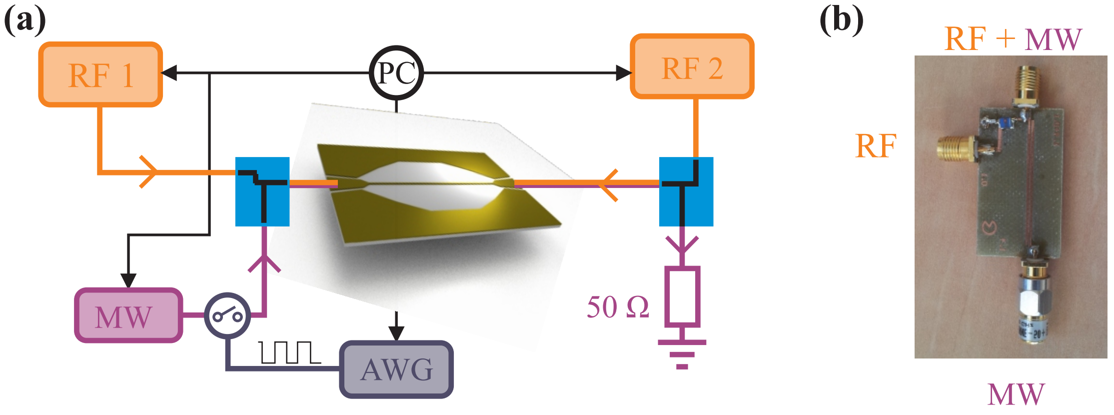

Figure 3.3: Wiring to the waveguide. **(a)** All MW, RF and pulse sources are interfaced by a single PC that is in charge of spin manipulation. Blue rectangles are the bias tees. **(b)** Photograph of the bias tee.

3.2.4 Confocal microscope

The home built confocal microscope setup, shown in Figure 3.4, is essentially based on a 532 nm diode pumped solid-state frequency doubled Nd:YaG laser (model *GEM* from Laser Quantum, 200 mW maximum output power). The beam (0.9 mm diameter) is focused onto the sample via a Zeiss microscope objective with 63x magnification, numerical aperture of 0.85 ($\approx 60°$), working distance of 200 μm and compensated for the 170 μm thick quartz plate. The transmission of the achroplan objective covers $90 - 95\,\%$ of the NV fluorescence window. After beam shaping and polarization control, the light can be injected either directly or through a second path that enables fast intensity switching of the laser via a MT200 acousto-optic modulator (AOM) from Opto-Electronic. A flip mirror is used in order to select the beam, depending on the type of experiment. A telescope increases the beam width in order to maximize the overlap of the beam spot and the microscope objective opening. The fluorescence light spanning a range from 630 nm to 750 nm is thus collected via the same microscope objective and separated via a 580 nm dichroic mirror from the pump beam. It is subsequently filtered by a highpass and a 532 nm notch filter. Finally, the filtered fluorescence is sent onto a fiber coupled single photon counting avalanche photo diode (APD) with 32 ns dead time from Perkin & Elmer and dark count rate around 200/300 Hz. In addition to the monochromatic light, white light can be superposed on the incoming path through a backpolished mirror narrowly coated around 532 nm. This serves to image the sample with the help of a CCD camera positioned in the fluorescence path (Watec 101N+). The sample position is coarsely aligned with a translational stage. The NV search is performed by moving the microscope objective with a XYZ piezo stage from Mad City Lab (PDQ75). XYZ voltage signals are amplified via the Nano-Drive 85 from Mad City Labs. The fluorescence imaging is realized with a Nanonis Scanning Probe Microscopy control system, which simultaneously detects the fluorescence and controls the position of the microscope objective. This enables three dimensional raster scans of the fluorescence across the sample as well as tracking of a single NV defect in space.

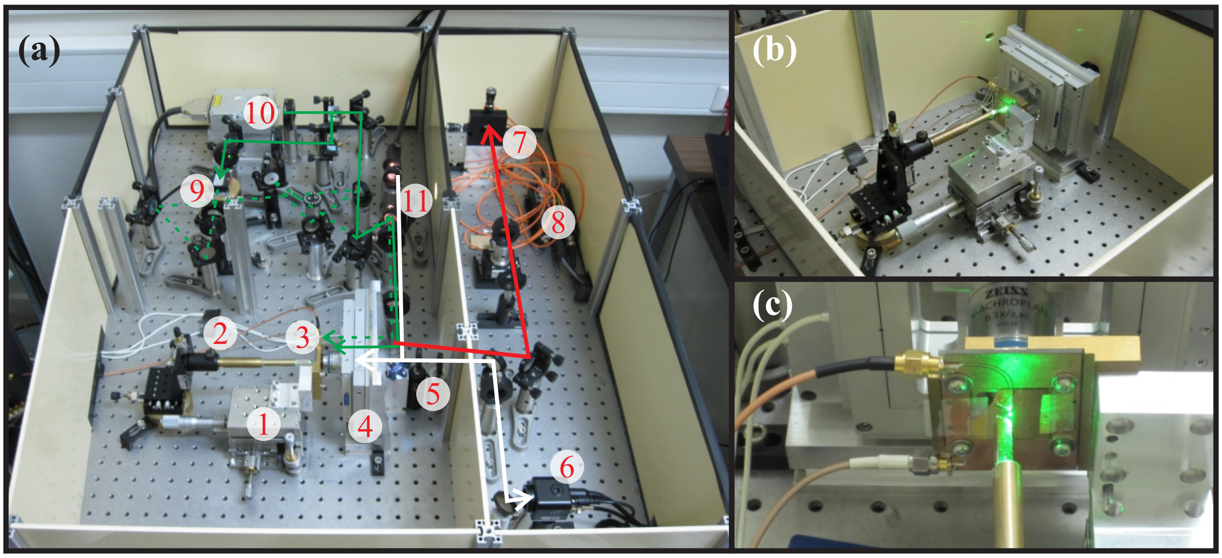

Figure 3.4: Experimental setup. **(a)** Phoptograph of the optical table. 1) Manual translational stage. 2) External magnet. 3) Waveguide sample holder. 4) XYZ piezo stage with the microscope objective. 5) Optical filters. 6) CCD camera. 7) Optical fiber coupler. 8) APD. 9) AOM. 10) GEM laser. 11) White light injection. The green arrows indicate the laser pathways, the red arrow is indicates the fluorescence pathway, the white arrow the white light pathway. **(b)** Closeup photograph of the XYZ piezo stage holding the microscope objective and the XYZ stage holding the waveguide sample. **(c)** Closeup photograph of the waveguide holder (in front of the microscope objective) and an external magnet. The experiment is fully interfaced and can be controlled remotely.

Raster scan An XY raster scan across the sample can be used to detect NV defects spin-coated onto the lithographed quartz plate. While the green laser light is continuously focused onto the sample, the position of the microscope objective is swept. NV defects in the focal spot are optically excited and their fluorescence is detected by the APD. For ~ 1 mW of injected laser power, NV defects appear as bright spots of collected fluorescence with count rates between a few kHz up to a few hundred kHz. A scan of the 75 μm x 75 μm piezo range yields a fluorescence map that permits localizing a large number of centers with respect to the waveguide. The waveguide fluoresces in our detection band due to the Gold material, which allows visualizing its borders on the raster scans, see Figure 3.5. The map shows isolated spots as well as islands of fluorescence. These are due to a large density of nanodiamonds as well as parasitic fluorescence from residues in the solution which have not been laser bleached. Figure 3.5 also shows the NV defect that is used throughout the text. The raster scan imaging has been used to measure its distance from the waveguide to be 5 μm.

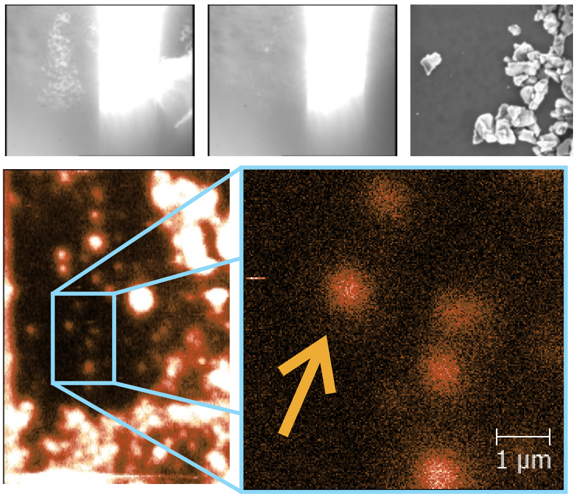

Figure 3.5: Raster scan. *Top row:* The first two images are taken with the CCD camera. The picture on the left shows an impurity to the right of the waveguide that has been used for orientation. The center picture shows the region around the NV defect used in this thesis. The SEM image on the right shows single nanodiamonds, taken from a different sample. *Bottom row:* A raster scan taken with the confocal microscope. The image on the right shows the NV defect on which all measurements of Chapters 3 and 5 were performed. It is approximately 5 μm away from the waveguide.

Single NV tracking The controller allows tracking of single NV defects in order to compensate mechanical drifts (mainly originating from temperature variations). After having identified isolated spots on the raster scans as in Figure 3.5, the microscope objective can be directed onto what is presumably a single NV defect. Isolated NV defects exhibit a near Gaussian detection profile with typical width of $\Delta w = 400\,\mathrm{nm}$, as seen in Figure 3.6. The LabView controlled tracking program ensures that the NV stays in the detection volume. It records the average fluorescence emitted in a time interval that is typically chosen to be 10 ms. The position is then changed by 10 nm in the $\mathbf{x}$-direction and the result of a new fluorescence measurement is compared to the previous one. The objective is then moved to the coordinate corresponding to the larger fluorescence count. This cycle is repeated for all three directions and has proven to be very reliable, effectively keeping track of the same NV defect over the period of several weeks. An adaptive step size has been implemented to progressively reduce the correction size when the NV is well positioned. It furthermore allows a fast intensity recovery in case of a sudden position drift. The tracking routine is permanently used and does not affect subsequent measurements.

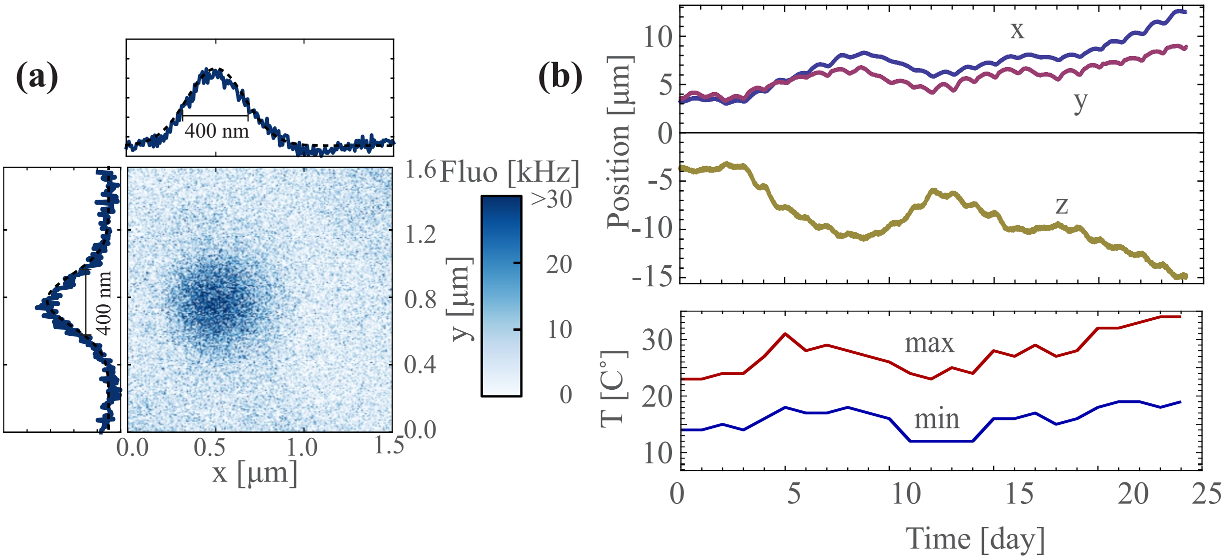

Figure 3.6: Raster scan of a single NV defect. **(a)** The single NV defect is clearly visible in the fluorescence microscope as a bright spot with width $\Delta w = 400$ nm. **(b)** The tracking runs continuously over a period of several weeks. Clearly visible are the correlations between piezo position and temperature measured at a local weather station (source: XXX).

3.2.5 Autocorrelation measurement of NV defects

In order to ensure that the bright spot identified with the confocal microscope is a single photon emitter, an autocorrelation function of the fluorescence can be recorded. Ambiguities arising from the fact that two NV defects might be hosted in the same nanodiamond or the possibility of detecting a cluster of nanodiamonds can thus be removed.

3.2.6 Optical saturation of NV defects

The fluorescence of NV defects depends on the optical pump power at 532 nm and saturates for large values. This is a consequence of the finite lifetime of the excited state which puts a limit on the maximum fluorescence rate. This is because only one photon at a time can be radiated while the excitation is off-resonant and does therefore not induce stimulated emission. The knowledge of this saturation behavior is important for a proper understanding of the ODMR experiments that will be described later (see section 3.3).

The photodynamics can be modeled by the seven level system shown in Figure 3.7 **(a)**, where we have depicted the spin triplet states on the left and a singlet state $|s\rangle$ on the right. Transitions from the $^3A_2$ to the ^3E state can be excited off-resonantly. From there it relaxes back to the orbital ground state within approximately $1/\Gamma_{^3\mathrm{E}} \sim 10$ ns, emitting fluorescence. For low optical power P_{opt} there is only a small chance for the NV defect to absorb a photon and small fluorescence rates will be observed. However, when the power is increased beyond a threshold value P_{sat}, a pump photon is absorbed almost instantly after the electron has relaxed to the ground state $^3A_2$. In this case, the photon emission rate is limited by the lifetime $\Gamma_{^3\mathrm{E}}$. This behavior can be modeled by a saturation parameter s, where $s = \frac{P_{\mathrm{opt}}}{P_{\mathrm{sat}}}$ as defined in Chapter 2 and the total detected fluorescence rate is

$$\Gamma_{\mathrm{fluo}} = \eta \Gamma_{^3\mathrm{E}} \frac{s}{s+1}. \tag{3.1}$$

Here, η parameterizes the total detection efficiency, which arises from the limited solid detection angle, injection losses and imperfections of photon detection by the APD. This simple picture, however, neglects the presence of the metastable state $|s\rangle$, from which no radiative transitions to the ground state are observed. It is mainly populated by decay from the excited spin states and has a relatively long lifetime. Population of $|s\rangle$ might therefore largely decrease the fluorescence rate, an effect that we will absorb in η. When increasing the pump power, parasitic background emission also increases. Such background photons can be modeled by a classical source with an emission rate proportional to the pump power. To determine the optical saturation power P_{opt}, we take raster scans as presented in Figure 3.5 for the NV defect of interest for several values of optical pump power. The NV fluorescence is obtained by adjusting the images to a spatially flat background and a two dimensional Gaussian profile. To ensure a stable pump intensity we found it more adequate to run the laser at full output power and subsequently attenuate with a $\lambda/2$-waveplate combined with a beam cube, rather than varying the pump current of the laser. Figure 3.7 shows data of fluorescence readings. A fit of the data with expression (3.1) yields a typical value for the saturation power, $P_{\mathrm{sat}} = 125\,\mu$W and saturation fluorescence of 33.8 kHz. The value is in agreement with [156], where a saturation power of $P_{\mathrm{sat}} = 250\,\mu$W was measured.

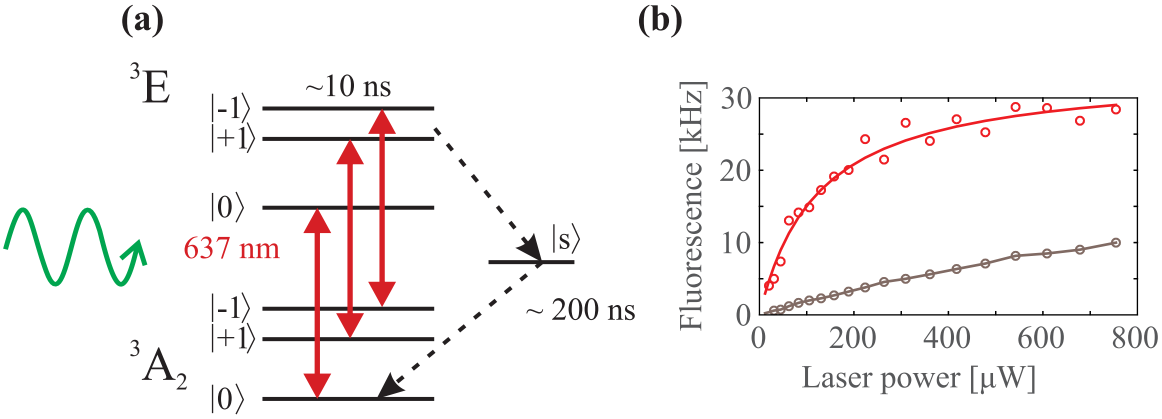

Figure 3.7: Optical saturation. **(a)** 7 level scheme of the NV defect. The transition from the ^3E to the $^3A_2$ states is radiative and red fluorescence can be detected. The cycling frequency is however limited by the lifetime of the upper state, which leads to a saturation of the transition. Further effects involving the population of the metastable state $|s\rangle$ result in a decrease in the total fluorescence rate that can be observed. **(b)** Measurement of the fluorescence as a function of applied laser power. The red dots show the NV fluorescence with clear saturation behavior. From a fit to expression (3.1) (red solid line) we find a saturation power of $P_{\mathrm{sat}} = 125\,\mu$W with saturated fluorescence rate $\mathrm{F}_{\mathrm{sat}} = 33.8\,$kHz. Here, we have subtracted parasitic background fluorescence (dark curve), which shows a linear increase with the laser power.

3.2.7 Summary of the setup

The complete setup is depicted below on Figure 3.8.

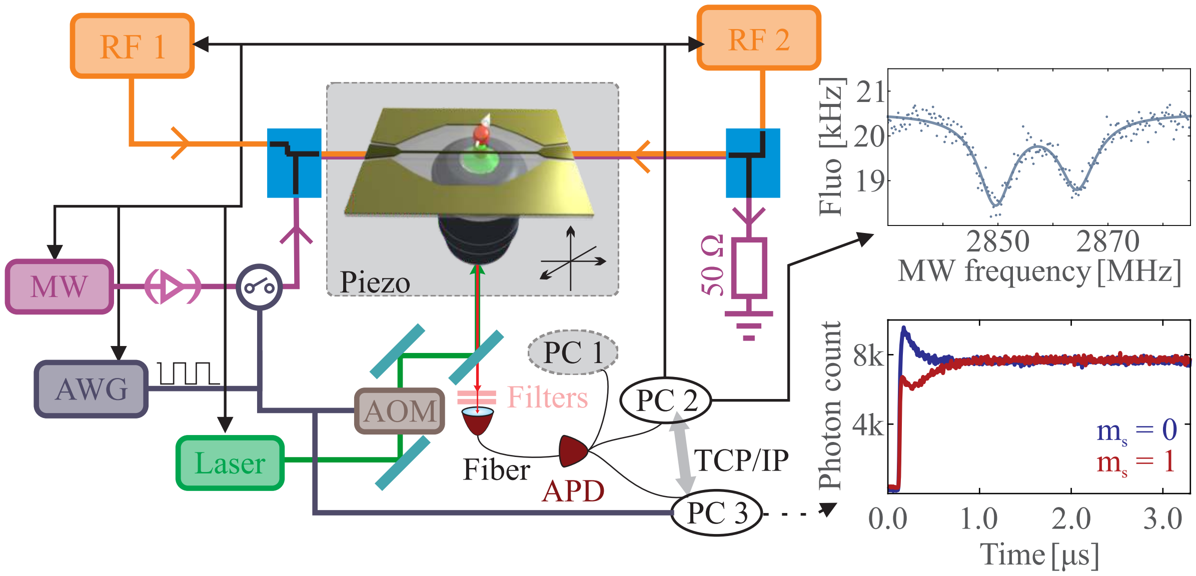

Figure 3.8: Setup of the experiment. A first computer, PC 1, correlates the NV fluorescence and the piezo position to track single defects or to perform raster scans (see Figure 3.5). A second PC controls MW, RF and laser irradiation. Pulse sequencing is done via an arbitrary waveform generator, which is also programmed by PC 2. Fluorescence and MW frequency are correlated to yield the ODMR measurements described in section 3.3. At last, PC 3 performs a time resolved fluorescence measurement. The details are described in section 3.5.

3.3 ODMR based spin spectroscopy

The confocal microscope allows us to address and track individual NV defects. We present here the optically detected magnetic resonance (ODMR) measurement. This form of electron spin resonance (ESR) detection is specific to the negatively charged NV defect and will provide us with information about spin energy splitting, lifetimes and orientation. The underlying principle is that the emitted fluorescence is spin state depend. Spin spectroscopy is realized by detecting the average fluorescence under continuous optical excitation while sweeping the frequency of an applied MW magnetic field. If the microwave field is resonant with the spin transition, the spin is flipped and the fluorescence decreases due to a change in the average population. The details are explained in section 2.4.

3.3.1 Experimental realization

Description of the measurement procedure

The functioning of the ODMR measurement is depicted in Figure 3.9. A SMBV-100A microwave generator is prepared to execute a sweep of MW frequency across the spin resonance frequency at fixed output power. The MW generator is fed the desired sweep start and sweep end frequency as well as the frequency step. The MW trigger is adjusted such that an external TTL rising signal shifts the output frequency step by step to the end frequency. A PCIe 6323 data acquisition card from National Instruments prepares the TTL signal with as many pulses as desired frequency bins and with a TTL period corresponding to the requested fluorescence averaging time. Typical values are 300 frequency steps at 30 ms photon accumulation time for each bin. The TTL signal output triggers the SMBV-100A to increment the MW signal frequency. Synchronously, the TTL signal serves to gate a time binned counting measurement of the photons detected by the APD. The counting operates in a pause-trigger mode, such that the fluorescence rate is only measured during a TTL low level. This ensures that no NV fluorescence is recorded at times when the MW frequency is changed, avoiding a transient regime that can degrade the quality of the ODMR signal. After one sweep, the cycle is repeated to acquire a representative average. The protocol is controlled via a LabView interface, which allows data retrieval. Depending on the measurement condition, 10 averages can be enough to well resolve the ESR frequency. However, due to the tracking program, data acquisition time is virtually unlimited.

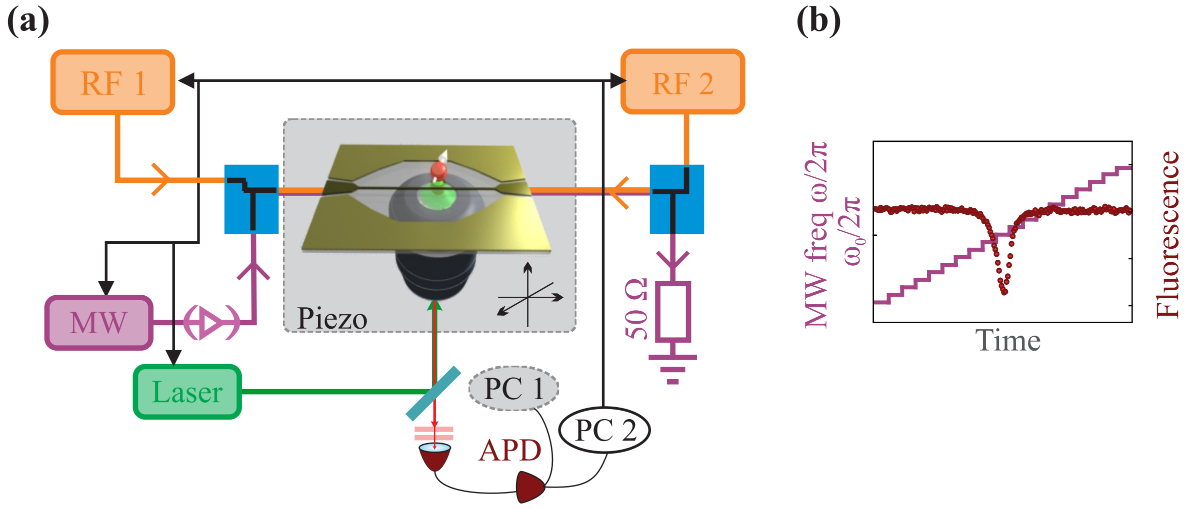

Figure 3.9: ODMR measurement. **(a)** Setup used to perform the ESR measurement. PC 1 is tracking a single NV defect. PC 2 controls the MW generator and correlates a fluorescence reading to the applied frequency. **(b)** Photon counts are taken for each frequency value applied by the MW generator. The dark red curve shows a typical ODMR measurement for a large number of averages.

The ODMR measurement also permits to verify whether or not the measured emitter is a NV$^-$ defect. Resonance frequency and lifetime can be compared to peak position and linewidth, which is expected to be around 2.87 GHz and several MHz in the absence of any magnetic fields. We perform ODMR measurements on several different emitters on the sample in order to identify NV defects suitable for our experiments. We choose modest microwave powers on the order of 10 dBm and look for those specimen close to the waveguide that show ESR contrast of more than 10 % while maintaining a small linewidth (which can be broadened by strain effects and coupling to environmental spins). We can thus identify those NV defects that couple well to the MW magnetic field, as is demonstrated in Figure 3.10 for the NV defect shown in Figure 3.5. The spectrum in **(a)** hints at several facts. The contrast is approximately 20%, which is reasonably close to the maximally attainable. The strain splitting of the $|m_s\rangle$ states is quite large in this nanodiamond ($E \approx 7.5$ MHz). This does not pose a problem, since we will be using a large magnetic field along the spin axis to reach the ESLAC. The linewidth is on the order of 6 MHz, indicating that there is no broadening due to coupling to nearby impurities like ^{13}C nuclear spins. Here, the main broadening mechanism is the intrinsic coupling to the ^{14}N nuclear spin, giving rise to a triplet structure of the ESR resonance. However, spectra are usually power broadened, merging the triplet into a single peak. Figure 3.5 **(b)** shows an other ODMR measurement taken at low MW and optical power. This reveals the triplet structure due to the hyperfine coupling. The splitting was found to be $A_{\parallel}^{14} = 2.15\,\text{MHz}$, in agreement with the literature [116].

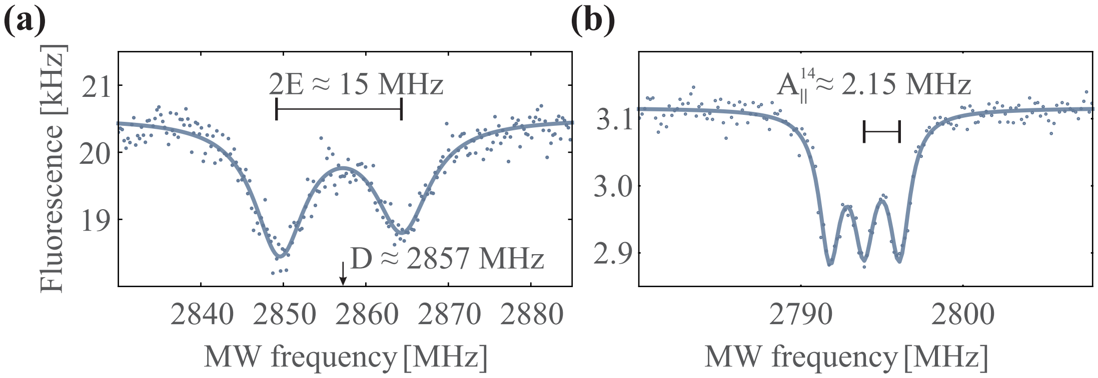

Figure 3.10: ODMR measurements. **(a)** The ODMR measurement reveals a large strain splitting in the absence of an external field. **(b)** An external magnetic field shifts the resonance frequency. Due to low MW and optical power, power broadening of the resonances is almost absent and thus the hyperfine splitting is exposed.

ESLAC

The excited state level anti crossing occurs for an external magnetic field of 51 mT along the spin axis. At this point, the N nuclear spin can be polarized through its interactions with the electron spin. As a consequence, the triple peak structure, that is resolved in ODMR measurements when operating at low MW and optical powers, disappears. This is seen in Figure 3.11. At that point the linewidth of the spin reduces from 3 × 2.2 MHz to 2.2 MHz. Experimentally, to reach the ESLAC, the external field is increased by approaching a permanent magnet in several steps while observing the fluorescence (the MW generator is turned off). Misalignment of the field leads to state mixing, which decreases the fluorescence rate. After each step an ODMR measurement is taken to survey the resonance shift. The hyperfine structure disappears from the ODMR spectra when the resonance frequency reaches $\omega_0/2\pi \approx 1.45\,\text{GHz}$.

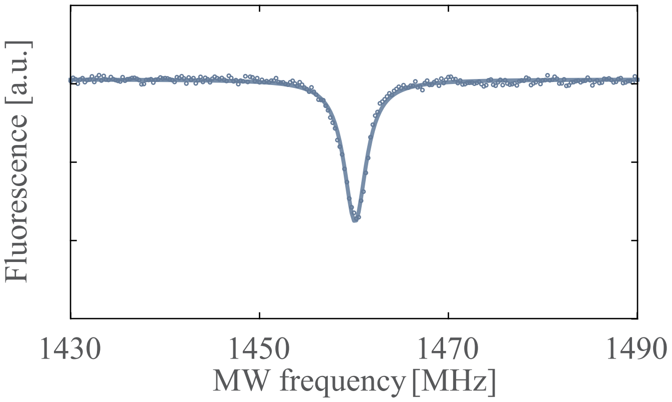

Figure 3.11: Polarization of the nuclear spin at the ESLAC.

3.3.2 Orientation of the selected NV defect

We have thus identified a single NV defect with good optical and MW response. Next, we describe two measurements to determine first the NV orientation with respect to the optical axis and second its response to the RF magnetic fields generated by the waveguide.

Orientation of the NV defect with respect to the optical axis

Since we have no direct control over the direction of the NV axis, the required sensitivity of the investigated NV to both, MW and RF fields, demands a favorable orientation of the defect. It has been measured using a permanent magnet whose field strength was calibrated independently. The magnet was displaced along the optical axis as well as in a perpendicular direction and ODMR spectra were taken at each position. The detected frequency shifts as a function of field strength were adjusted with two angles θ and φ as defined in Figure 3.12 **(a)**. From the data shown in Figure 3.12 **(b)** we determine the angles to be $\theta = 59°$ and $\varphi = 78°$. The remaining uncertainty on these values is lifted through the waveguide calibration explained in the next section, where we infer a polar angle of $\theta = 56°$.

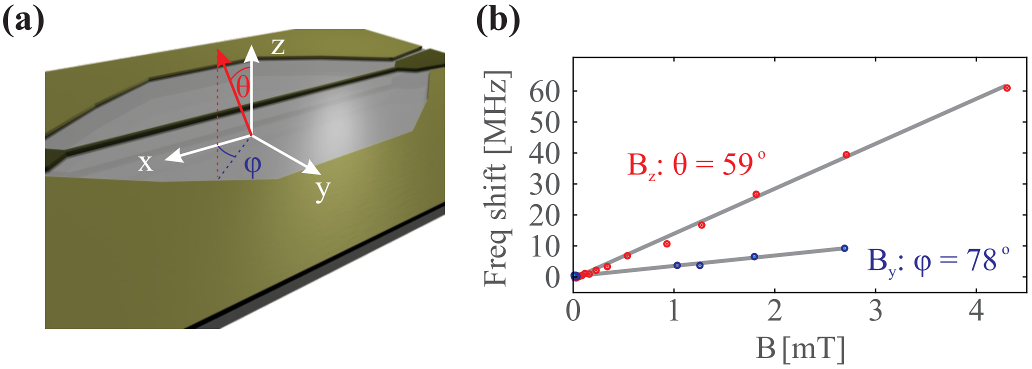

Figure 3.12: Orientation of the investigated NV defect. **(a)** Conventions for the angles θ and φ. **(b)** The frequency shift for a magnetic field applied along the **z** and **y**-axis.

Sensitivity to RF magnetic fields

Apart from good MW and ODMR properties, we also require a strong response to the magnetic field created by RF currents. MW and RF fields generated by the waveguide have the same orientation with respect to the optical axis but couple differently to the spins due to their different frequencies. While field components parallel to the NV axis shift the spin's energy, components perpendicular to the spin axis induce transitions when the resonance condition is met. We therefore distinguish between four components of the magnetic fields, where the orientations $(\perp, \|)$ are with respect to the direction of the NV axis:

- $\mathrm{B}_{\|}^{\mathrm{RF}}$: Magnetic fields oscillating slowly at frequency $\Omega_{\mathrm{m}}/2\pi$ along the direction of the NV periodically modulate the spin energy with amplitude $\hbar\delta\omega_0$ due to the Zeeman effect.

- $\mathrm{B}_{\perp}^{\mathrm{RF}}$: Magnetic fields oscillating in a direction perpendicular to the spin could induce spin flips. However, since the mismatch between Ω_{m} and ω_0 is large, the RF fields are far from resonance. We can thus neglect this effect of the transverse RF components. Sufficiently strong transverse fields can also lead to a mixing of the eigenstates, leading to a correction of the spin energy. This can lead to an additional linear and quadratic modulation of the spin energy at RF frequencies. The perturbative effect was found to be negligible for the NV used in the test experiment (Chapter 3 and 5) but is taken into account for the NV spin- SiC nanowire hybrid system of Chapter 4.

- $\mathrm{B}_{\|}^{\mathrm{MW}}$: These fields modulate the spin energy at MW frequencies. On the relevant timescales of spin evolution, which is set by $(\Omega_{\mathrm{R}}, \Gamma_1, \Gamma_2)$ in the rotating frame, energy modulation at $\omega/2\pi$ is much too rapid to be followed by the spin. We thus also neglect the effect of parallel MW fields.

- $\mathrm{B}_{\perp}^{\mathrm{MW}}$: MW fields perpendicular to the spin direction induce spin transitions when close to resonance, $|\delta| = |\omega - \omega_0| \lesssim \Gamma_{\mathrm{spin}}$, where Γ_{spin} is the experiment dependent linewidth.

We can measure the response of the above NV defect to RF magnetic fields by applying a DC current through the waveguide and measuring the resultant Zeeman shift of the spin with the ODMR spectroscopy technique. First a permanent magnet applies a weak magnetic field of a few mT along the optical axis in order to shift the $|m_s = \pm 1\rangle$ peaks apart from each other. We then turn on a DC signal with one RF generator connected to each of the two RF input ports and vary the signal strength between -2.5 V and + 2.5 V in 0.5 V steps for each output (see Figure 3.13 **(a)** for the conventions used here). ESR spectra are recorded at each point and fitted with a Lorentzian lineshape function, see Figure 3.13 **(b)**. The shift of the resonance frequency $\delta\omega_0/2\pi$ as a function of DC voltage V is shown in Figure 3.13 **(c)**. Fitting $\delta\omega_0/2\pi(V)$ with a second order polynomial reveals that the main contribution is linear as expected. Quadratic contributions, which might arise from misalignment of the magnetic field with the NV axis or spurious electric fields, are negligible, as depicted in Figure 3.13 **(d)**. Knowing that $g\mu_B/h \simeq 28\,\mathrm{MHz/mT}$, we determine $\mathrm{B}_{\|}^{\mathrm{RF}} \approx 0.13\,\mathrm{mT/V}$ and a frequency shift of $\delta\omega_0/2\pi = 3.6\,\mathrm{MHz}$ per volt injected from input port one.

Modeling the magnetic field with the Biot - Savart law predicts a magnetic field strength of 0.235 mT/V for the NV $5\,\mu$m away from the waveguide (see 3.2.4 and Figure 3.5). The measured frequency shift of $\delta\omega_0/2\pi = 3.6\,\mathrm{MHz}/V$ then corresponds to an angle $\theta = 56°$, which is in very good agreement with the measured value of $\theta = 59°$.

A similar value of 3.8 MHz/V is obtained for the shifts due to the second port. The slight difference can be explained either by a spurious impedance that draws currents to either side of the waveguide constriction. Additional mismatch can be due to the fact that the signal of one output port was swept fast and the other one slowly. Drifts of the distance between the permanent magnet and sample can then lead to shifts of the resonance leading to a larger impact on the slowly swept direction. Being able to modulate along two directions enables us to superpose two RF signals. On the one hand, this strategy can be used to compensate quadratic shifts, which is not necessary here (but was important when working with an other NV defect on a different sample). On the other hand, adding the two RF signals allows us to generate a larger modulation strength. Since the measured shift of $\delta\omega_0/2\pi = 3.6\,\mathrm{MHz}/V$ has proven to be sufficiently large for our experiments, we have injected the RF signal only through the first port.

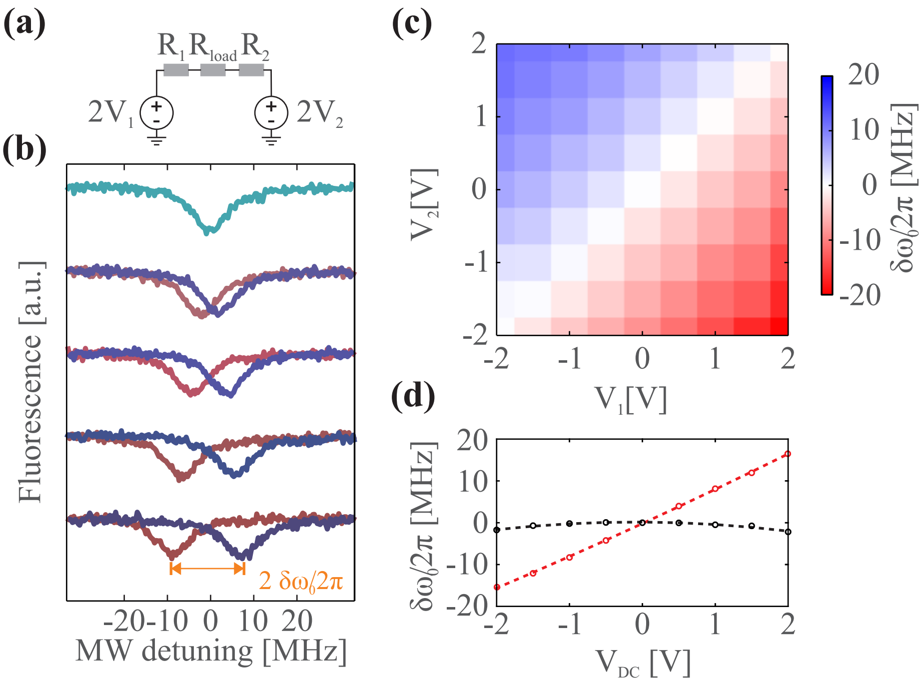

Figure 3.13: Measurement of the NV sensitivity to RF fields. **(a)** The wiring of the sample with resitance $R_{\text{load}} = 17$ Ohm to the two RF sources 1 and 2 with input impedances $R_1 = R_2 = 50$ Ohm. The voltage values V_1 and V_2 correspond to half the voltage that is applied by the RF generator. The actual voltage dropped across the 17 Ohm waveguide resistance is $\frac{2V}{R_1+R_2+R_{\text{load}}}R_{\text{load}} \sim 0.3\times$ the value stated in the text. **(b)** ODMR spectra showing the shift of the spin resonance frequency due to voltages applied by a single generator. The values are $V_2 = 0$ V, $V_1 = 0.0$, ± 0.5, ± 1.0, ± 1.5, ± 2.0 V from top to bottom. **(c)** The map shows the shift of resonance frequency for both voltage sources. **(d)** Linear (red) and quadratic (black) contributions of the shift. Quadratic contributions can be neglected here.

To conclude, we have identified a single NV defect that shows satisfying optical properties as well as a good MW and RF field response.

3.3.3 Modelization of ESR spectra

ODMR spectroscopy provides a measurement of the two level system's average population when irradiated by optical and MW fields. As already mentioned, the observed contrast and ESR linewidth are strongly dependent on the strength on the probe fields. Here, we investigate how the experimental parameters affect the optically detected ESR spectra using modified Bloch equations to account for the role of the pump light.

Bloch equations and steady state spin population

The model is developed in further detail in [156]. In absence of mechanical oscillations, the Bloch equations (2.123) of Chapter 2 are adapted to:

$$\begin{pmatrix}\dot{u}\\ \dot{v}\\ \dot{w}\end{pmatrix} = \begin{pmatrix}-\tilde{\Gamma}_2 & \delta & 0\\ -\delta & -\tilde{\Gamma}_2 & -\Omega_{\text{R}}\\ 0 & \Omega_{\text{R}} & -\Gamma_1-\Gamma_{\text{p}}\end{pmatrix}\begin{pmatrix}u\\ v\\ w\end{pmatrix} - \frac{1}{2}\begin{pmatrix}0\\ 0\\ \Gamma_{\text{p}}\end{pmatrix}, \tag{3.2}$$

where the optical repolarization is described by the additional population pumping rate $\Gamma_{\text{p}} = \Gamma_{\text{p}}^{\infty}\frac{s}{s+1}$ (with $s = \frac{P_{\text{opt}}}{P_{\text{sat}}}$), such that $\Gamma_{1\to 0} \to \Gamma_{1\to 0}+\Gamma_{\text{p}}$. This change also leads to a redefinition of the decoherence rate, which we absorb in $\tilde{\Gamma}_2$ (see the discussion in section 2.4.2). Notice that an additional source term appears on the right hand side due to the optical pumping. The equations can be used to study ESR spectra, for which it is assumed that the dynamics has reached a steady state. Introducing the effective lifetime $\tilde{\Gamma}_1 = \Gamma_1 + \Gamma_\mathrm{p}$, one obtains

$$w^\mathrm{st} = -\frac{\Gamma_\mathrm{p}}{2}\frac{\tilde{\Gamma}_2^2 + \delta^2}{(\tilde{\Gamma}_2^2 + \delta^2)\tilde{\Gamma}_1 + \Omega_\mathrm{R}^2\tilde{\Gamma}_2}, \tag{3.3}$$

which can be recast into

$$w^\mathrm{st} = -\frac{1}{2}\frac{\Gamma_\mathrm{p}}{\tilde{\Gamma}_1}\left(1 - \frac{\Omega_\mathrm{R}^2}{\Omega_\mathrm{R}^2 + \tilde{\Gamma}_2\tilde{\Gamma}_1} \times \frac{\tilde{\Gamma}_2(\tilde{\Gamma}_2 + \frac{\Omega_\mathrm{R}^2}{\tilde{\Gamma}_1})}{\delta^2 + \tilde{\Gamma}_2(\tilde{\Gamma}_2 + \frac{\Omega_\mathrm{R}^2}{\tilde{\Gamma}_1})}\right) \tag{3.4}$$

in order to yield a Lorentzian line shape for the spectrum of w^st:

$$w^\mathrm{st} = w_\infty^\mathrm{st}\left(1 - C_w \times \frac{\Gamma_\mathrm{eff}^2}{\delta^2 + \Gamma_\mathrm{eff}^2}\right).$$

Here,

$$w_\infty^\mathrm{st} \equiv -\frac{1}{2}\frac{\Gamma_\mathrm{p}}{\Gamma_1 + \Gamma_\mathrm{p}} = -\frac{1}{2}\frac{1}{1 + \frac{\Gamma_1}{\Gamma_\mathrm{p}^\infty}\left(1 + \frac{P_\mathrm{sat}}{P_\mathrm{opt}}\right)} \tag{3.5}$$

can be understood as the population difference for a MW drive far off resonance. We note that, as expected, $w_\infty^\mathrm{st} \xrightarrow{P_\mathrm{opt}\to 0} 0$ in the absence of light and $w_\infty^\mathrm{st} \xrightarrow{P_\mathrm{opt}\to\infty} -\frac{1}{2}\frac{1}{1+\frac{\Gamma_1}{\Gamma_\mathrm{p}^\infty}}$ for large optical pumping. Full polarization is achieved when $\Gamma_\mathrm{p} \gg \Gamma_1$. The linewidth Γ_eff (HWHM) and contrast C_w both depend on microwave power Ω_R^2 ($\propto (B_\perp^\mathrm{MW})^2$) and optical power P_opt:

$$\Gamma_\mathrm{eff} = \tilde{\Gamma}_2\sqrt{1 + \frac{\Omega_\mathrm{R}^2}{\tilde{\Gamma}_1\tilde{\Gamma}_2}}, \tag{3.6}$$

$$C_w = \frac{\Omega_\mathrm{R}^2}{\Omega_\mathrm{R}^2 + \tilde{\Gamma}_1\tilde{\Gamma}_2}. \tag{3.7}$$

We note that the contrast behaves as expected. In the absence of MW power it falls to zero, $C_w \xrightarrow{\Omega_\mathrm{R}\to 0} 0$, while, for a very strong drive, maximum contrast is achieved $C_w \xrightarrow{\Omega_\mathrm{R}^2 \gg \tilde{\Gamma}_1\tilde{\Gamma}2} 1$. Increase of linewidth and saturation of the contrast with Ω_R^2 is a power broadening effect, which starts to play a role when $\Omega_\mathrm{R} \gtrsim \sqrt{\tilde{\Gamma}_1\tilde{\Gamma}_2}, \tilde{\Gamma}_1$. In general, spectra of w reflect a competition between MW and optical photons. Effective contrast can only be achieved when absorption of a MW photon induces a spin flip, which is balanced by subsequent optically induced re-polarization. In Figure 3.14 the contrast C_w is shown as a function of the optical saturation parameter s and MW drive strength Ω_R for typical values of $\Gamma_1, \Gamma_2, \Gamma_p^\infty, \Gamma_c^\infty$. Notice, while the contrast can be important for small values of s, w_∞^st approaches zero as the spin is almost not polarized by optical pumping. To obtain a meaningful signal, many photons need to be collected and thus data acquisition will take a very long time in this regime.

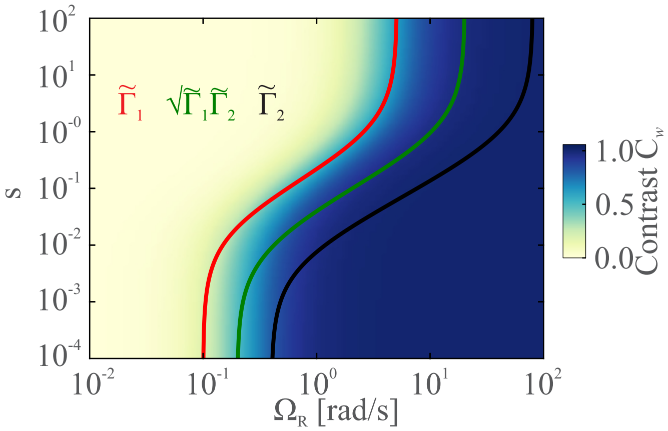

Figure 3.14: ESR contrast C_w as a function of MW drive and laser saturation calculated from expression (3.7). The contrast increases and saturates at MW powers verifying $\Omega_R > \sqrt{\tilde{\Gamma}_1\tilde{\Gamma}_2}$, a quantity strongly affected by optical broadening. For a given MW power, it is interesting to note that there exists an optimum power that maximizes the ODMR contrast.

Measurement of fluorescence parameters

The contrast of ODMR measurements relates to the above model as follows. The emitted fluorescence at a given MW frequency is

$$F[\delta] = (f_0\rho_{00} + f_1\rho_{11})\frac{s}{s+1} = (f_0 - f_1)(1 - 2w^{\mathrm{st}})\frac{s}{s+1}, \tag{3.8}$$

where f_0 and f_1 are the fluorescence rates of the spin in the ground or excited state, respectively. Since these rates differ by $\sim 30\%$, the fluorescence becomes spin dependent with fluorescence contrast

$$C^{\mathrm{ODMR}} = \frac{F(\delta = \infty) - F(\delta = 0)}{F(\delta = \infty)} = \mu C_w, \tag{3.9}$$

with

$$\mu \equiv -\frac{(f_0 - f_1)w_\infty^{\mathrm{st}}}{(f_0 + f_1) + w_\infty^{\mathrm{st}}(f_1 - f_0)} \xrightarrow{\Gamma_{\mathrm{p}} \gg \Gamma_1} \frac{f_0 - f_1}{2f_0} \tag{3.10}$$

Acquiring ODMR spectra for a wide range of parameters Ω_R and s allows us to determine the rates Γ_c^∞ and Γ_p^∞ as well as μ. This necessitates a calibration of Ω_R with the applied MW power via Rabi measurements, which is detailed in section 3.5.2. The experimental data presented in Figure 3.15 is grouped into two sets, corresponding to small and larger values of s. Each group is fitted with a least square algorithm in order to find a common set of the parameters (Γ_c^∞, Γ_p^∞, μ). The data shows good agreement for Γ_p^∞, the inverse metastable state lifetime, as well as for μ, which describes the optical distinction between spin ground and excited state. However, there is less agreement for the value Γ_c^∞. The measurement suffers from variation of the laser power during data acquisition, which overrides the calibration values used for s (see section 3.2.6). Moreover, the model that is employed makes important assumptions on the orbital properties of the NV defect, namely power independent transition rates f_0 and f_1, as well as perfect spin polarization for a transition from the metastable to the ground state. These ideas have recently been reviewed by the group of Jacques [74] and Drezet [165] and incorporating their findings might lead to a more conclusive result. Nonetheless, the data shows how the interplay between MW and optical photons influences the contrast seen in ODMR measurement. For modest MW powers (~ 18 dBm) large values of detected contrast have been measured ($> 20\%$), illustrating the efficient coupling of the waveguided MW field to the spin, when compared to antenna-like MW sources, which usually require MW amplifiers.

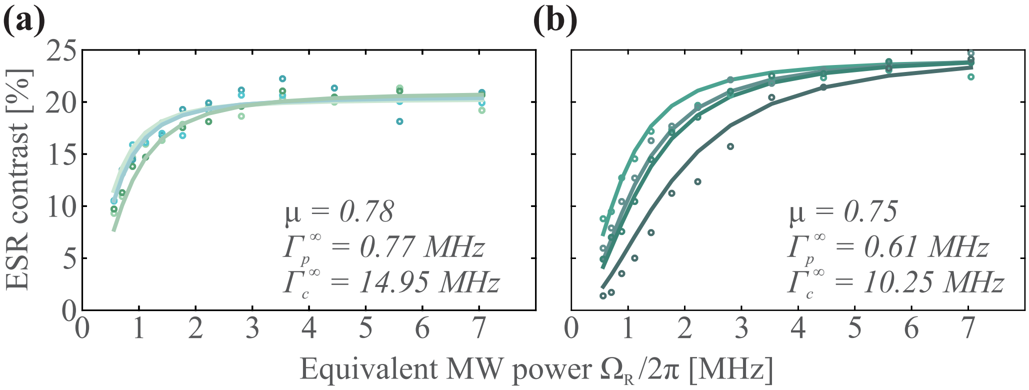

Figure 3.15: Measurement of the parameters μ, Γ_p^∞, Γ_c^∞. Curves correspond to values of s, which are {0.17, 0.19, 0.2, 0.28} (from bright to dark) in **(a)** and to {0.5, 0.8, 1.0, 2.5} in **(b)**.

In conclusion, we have seen how laser pump and MW output power affect ODMR spectra. While reducing laser pump power avoids optical broadening of the ESR spectra, it also increases the required measurement time. The signal-to-noise ratio scales with $\sqrt{N}$, where N is the number of detected photons per time bin, which is proportional to the detected fluorescence rate. When ESR spectra are detected in order to quickly determine the spin resonance frequency, we can work at large fluorescence rates and compensate for the reduced contrast by using sufficient MW power. When ESR spectra are detected in order to study sideband features or broadening of the resonance due to modulation with the RF field, we choose reduced fluorescence and MW power resulting in averaging times of several hours.

3.4 ODMR spectroscopy of a parametrically modulated NV spin

We now use ODMR spectroscopy to investigate the spin qubit in parametric interaction with a monochromatic RF field. We first focus on the adiabatic regime and then on the resolved sideband regime. In both situations we also present ODMR measurements synchronized to the RF oscillation phase in order to illustrate the time dependence of the parametrically modulated qubit spectrum.

3.4.1 Adiabatic ODMR spectra

We start our study of energy modulated spin spectra in the adiabatic regime similar to [99] by setting $\Omega_\mathrm{m}/2\pi = 20\,\mathrm{kHz}$. The RF generator is set to produce a sinusoidal signal at $\Omega_\mathrm{m}/2\pi = 20\,\mathrm{kHz}$, which is well below the spin linewidth, $\Omega_\mathrm{m} \ll \Gamma_\mathrm{eff}$. This produces a magnetic field $B_\parallel^{RF}(t)$

$$B_\parallel^{RF}(t) = B_\parallel^{RF}\cos(\Omega_\mathrm{m} t), \tag{3.11}$$

which will lead to a time dependent energy modulation of the spin, $\omega_0(t) = \omega_0 + \delta\omega_0(t)$, with:

$$\delta\omega_0(t) = \delta\omega_0\cos(\Omega_\mathrm{m} t), \tag{3.12}$$

A series of ODMR spectra are acquired for RF output voltage amplitudes varying between $0\,\mathrm{V_{pp}}$ and $4\,\mathrm{V_{pp}}$. The result is shown in Figure 3.16. We observe the anticipated broadening of the resonance for increased oscillation amplitudes, see Figure 3.16 **(a)**. In this adiabatic regime, the energy modulation is much slower than the internal spin dynamics. The resulting ODMR spectra can therefore be modeled as a sum of realizations, each of which exhibiting a different resonance frequency. At each consecutive instance of the RF oscillation, the spin's energy is slightly changed and the corresponding ODMR spectrum shows a slight frequency shift. The sum of all these frequency translated spectra reflects the temporal distribution of qubit energy values explored by the spin, which is given by $\omega_0(t)$. According to this picture, we fit the spectra with the expression

$$\frac{F[\delta]}{\mu C_w} = \frac{\Omega_\mathrm{m}}{2\pi} \int_0^{2\pi/\Omega_\mathrm{m}} \frac{\Gamma_\mathrm{eff}^2 \, \mathrm{d}t}{(\delta - \delta\omega_0 \cos(\Omega_\mathrm{m} t))^2 + \Gamma_\mathrm{eff}^2}. \tag{3.13}$$

The results of the fits are presented in Figure 3.16 **(b)**. They show very good agreement with a DC calibration similar to the one presented in section 3.3.2, where we measured $\delta\omega_0/2\pi = 4\,\mathrm{MHz/V}$. This underlines the absence of RF cut-off in the DC to 20 kHz frequency range.

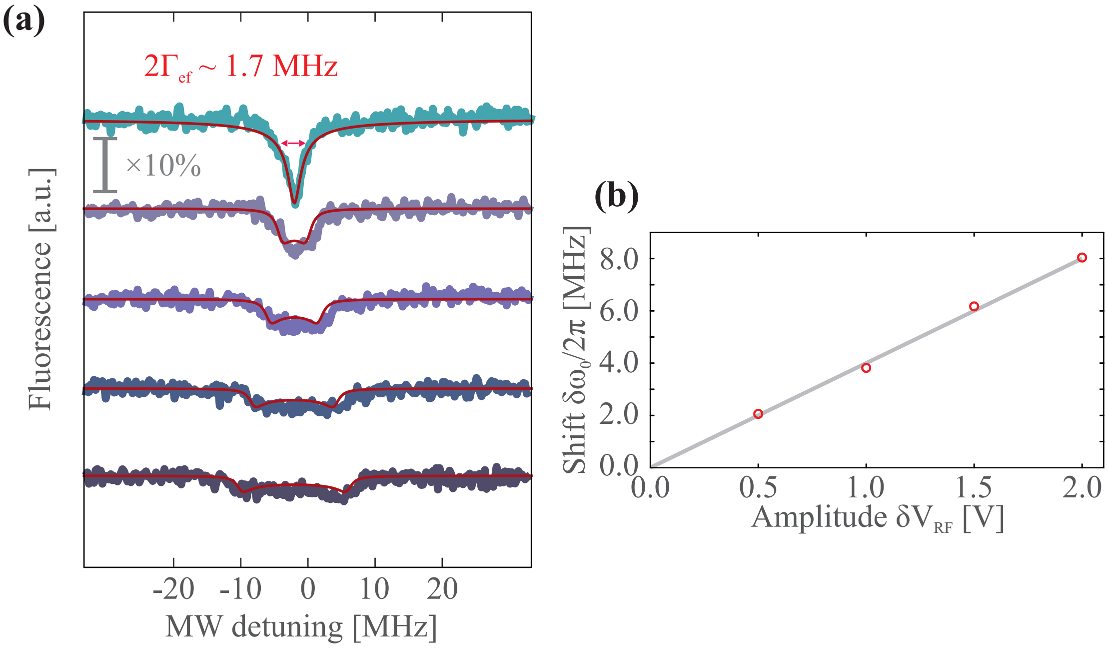

Figure 3.16: ODMR spectroscopy of a NV defect irradiated by an adiabatic field for increasing RF strength. **(a)** The data are adjusted using expression (3.13), the only free parameter being $\delta\omega_0$. Contrast ($C = 0.11$) and linewidth ($\Gamma_\mathrm{eff} = 0.85\,\mathrm{MHz}$) of the unmodulated spectrum ($0\mathrm{V}_\mathrm{pp}$) are retrieved from a Lorentzian fit and injected into expression (3.13). **(b)** The obtained values are found to be ($\delta\omega_0/2\pi$, δV_RF) = (2.06 MHz; 0.5 V), (3.82 MHz; 1 V), (6.17 MHz; 1.5 V), (8.04 MHz; 2 V) and are in excellent agreement with the calibration $\delta\omega_0/2\pi = 4\,\mathrm{MHz/V}\delta\mathrm{V}_\mathrm{RF}$.

3.4.2 Time dependent ODMR spectra in the adiabatic regime

The above ODMR spectra are taken without any synchronization with respect to the RF phase. Thus the entire frequency distribution $\delta\omega_0(t)$ is explored by the spin. It is, however, possible to take snapshots of the RF field oscillation, by synchronizing the photon counting sequence to the RF phase. To do so, a fast switch is connected between the APD and the NI data acquisition card. It is controlled by an external TTL signal. The switch lets the signal from the APD pass for the TTL up state and blocks the signal for the TTL down state. The TTL signal with 20% duty cycle is generated by the second output port of the RF generator, using the rectangular waveform mode with the same period and phase as the sinusoidal RF signal. This procedure gates the ODMR measurement to be accumulated only during the time window corresponding to the 20% duty cycle of the RF phase. The instantaneous qubit resonance depends on the relative phase between the RF field and the TTL signal. Figure 3.17 shows a series of the snapshots for varying relative phase between RF oscillation and TTL with a stepsize of 5°. As expected, the fluorescence dip indicating the position of the resonance frequency varies sinusoidally with the phase delay. This result confirms the above interpretation of the

ODMR spectra in the adiabatic regime as a sum over all realizations of the parametrically modulated qubit resonance frequency $\omega_0 + \delta\omega_0(t)$.

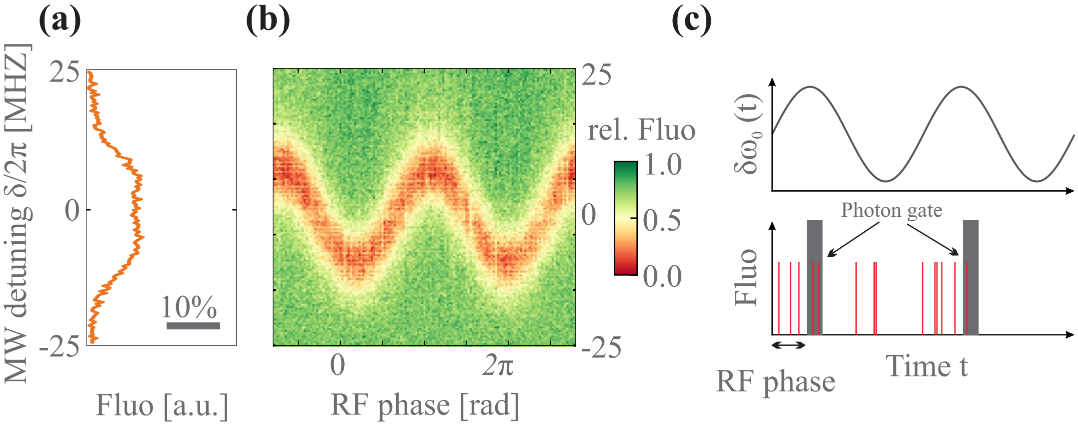

Figure 3.17: Time dependence of ODMR spectra in the adiabatic regime. **(a)** An ESR spectrum shows the broadening of the resonance due to adiabatic energy modulation at 20 kHz. **(b)** A series of ESR measurements is gated to the oscillation phase. This resolves the time dependence of the spin energy, which follows the sinusoidal modulation. **(c)** Measurement scheme. During the ESR measurement, the MW frequency is swept. While the spin energy is modulated (*top*), photons are emitted continuously. However, they are detected only during fixed intervals of the RF duty cycle (*bottom*).

3.4.3 ODMR spectroscopy in the resolved sideband regime

We now turn to the case where the modulation frequency surpasses the spin linewidth ($\Omega_\text{m} > \Gamma_\text{spin}$) and repeat the measurements of the section above. We do expect a different outcome because now the energy modulation of the spin takes place much more rapidly than its internal dynamics. The modulation frequency is set to $\Omega_\text{m}/2\pi = 8\,\text{MHz}$. Again we record ODMR spectra for different values of the RF amplitude, see Figure 3.18 **(a)**. This time we do not observe a broadening of the peak, but instead we see additional sidebands appearing at frequencies $(\omega_0 \pm \Omega_\text{m})/2\pi$. Since the spin energy is modulated at a period which surpasses the spin's lifetime, the spin dynamics is too slow to follow the applied modulation. The appearance of sidebands is usually associated with a frequency modulation process, such as in FM radio signals but also in other parametrically coupled systems, for example in optomechanics [31]. In our case the spin Larmor pulsation ω_0 is modulated by $\delta\omega_0$ at a frequency $\Omega_\text{m}/2\pi$. A quantum treatment of frequency modulation was presented in [166]. We can consider the Hamiltonian $H_\text{spin} + H_\text{osc}$ with $H_\text{spin} = \hbar\omega_0\sigma_z$ and $H_\text{osc} = \hbar\Omega_\text{m}a^\dagger a$. The eigenstates of this system are the states $|\epsilon, m\rangle$ ($\epsilon = 0/1$ being the ground/ excited state here and m the RF photon or phonon number) and their energies are shown in Figure 3.18 **(b)**. In such a system, the MW induces transitions between $|0\rangle \leftrightarrow |1\rangle$ without changing the phonon number, because σ_x does not couple states of different phonon number m. The situation changes due to the hybrid interaction term, $H_\text{int} = \hbar g_z\sigma_z\left(a^\dagger + a\right)$. Its effect is to induce transitions within each column shown in Figure 3.18 **(b)**. Such coupling creates new eigenstates $|\epsilon, \tilde{m}\rangle$. By a first order perturbation theoretical approach, we have

$$|\epsilon, \tilde{m}\rangle = |\epsilon, m\rangle + \frac{\epsilon g_z}{\Omega_\text{m}}\sqrt{m+1}|\epsilon, m+1\rangle - \frac{\epsilon g_z}{\Omega_\text{m}}\sqrt{m}|\epsilon, m-1\rangle. \tag{3.14}$$

MW irradiation can now induce transitions between the new eigenstates $|+, \tilde{m}\rangle \leftrightarrow |-, \tilde{m}\rangle$ and therefore change the phonon number, resulting in the absorption spectra exhibiting sidebands. As higher order perturbations become important, the eigenstates become contaminated by other states $|\epsilon, m \pm n\rangle$ and the number of sidebands is no more restricted to $n = 0, \pm 1$. Indeed, if we experimentally increase the oscillation amplitude, we find that second order sidebands appear, see Figure 3.18 **(c)**.

These sidebands can be interpreted like the ones observed in trapped ion experiments: the red sideband at $\delta = -\Omega_\mathrm{m}$ corresponds to the process of absorbing a low frequency detuned MW photon and extracting a photon of frequency $\Omega_\mathrm{m}/2\pi$ out of the RF field. Inversely, a resonance peak at $\delta = +\Omega_\mathrm{m}$ marks the absorption of a large frequency detuned MW photon by the spin accompanied by pumping a photon of frequency $\Omega_\mathrm{m}/2\pi$ into the RF field. The fast periodic energy modulation of the spin affects the evolution of the spin coherences, which can be shown to evolve as $\sim \sum_n J_n \left(\frac{\delta\omega_0}{\Omega_\mathrm{m}}\right) e^{i(\omega_0 t + n\Omega_\mathrm{m} t)}$, where J_n is the n^th-order Bessel function. Via Fermi's golden rule, the spin transition probability is proportional to $|\langle i|\sigma_x|f\rangle|^2$. The sidebands thus correspond to multiphoton absorption events with relative probabilities proportional to $J_n^2 \left(\frac{\delta\omega_0}{\Omega_\mathrm{m}}\right)$.

This dependency was experimentally verified by fitting the ODMR spectra with a Lorentzian lineshape function for each sideband. Since the spectral peaks are differently broadened, the total power emitted in each peak is more correctly reflected by the peak area A_n. We then compare the squares of the Bessel functions with the product of the contrast C_n and linewidth Γ_eff found from the fitting function $A_n \propto C_n \delta\nu_n \propto J_n^2 \left(\frac{\delta\omega_0}{\Omega_\mathrm{m}}\right)$, see Figure 3.18 **(d)**. We allow for four free parameters to fit the area of the five sidebands up to second order. These include a rescaling factor for the area individual for each function and a single parameter to accommodate an uncertainty in our calibrated energy shift $\delta\omega_0(\delta \mathrm{V}_\mathrm{RF})/2\pi = 4.00\,\mathrm{MHz/V}\delta V_\mathrm{RF}$. The result is shown in Figure 3.18 **(d)**. In general the squared Bessel functions reproduce the tendency of the sideband evolution with increased modulation amplitude. However, the fits require different prefactors for each sideband (see caption of Figure 3.18), which is hard to justify. At this point we turn to the Bloch equations (3.2) and simulate the sideband evolution *in silico* in order to obtain a better description of the experimental data.

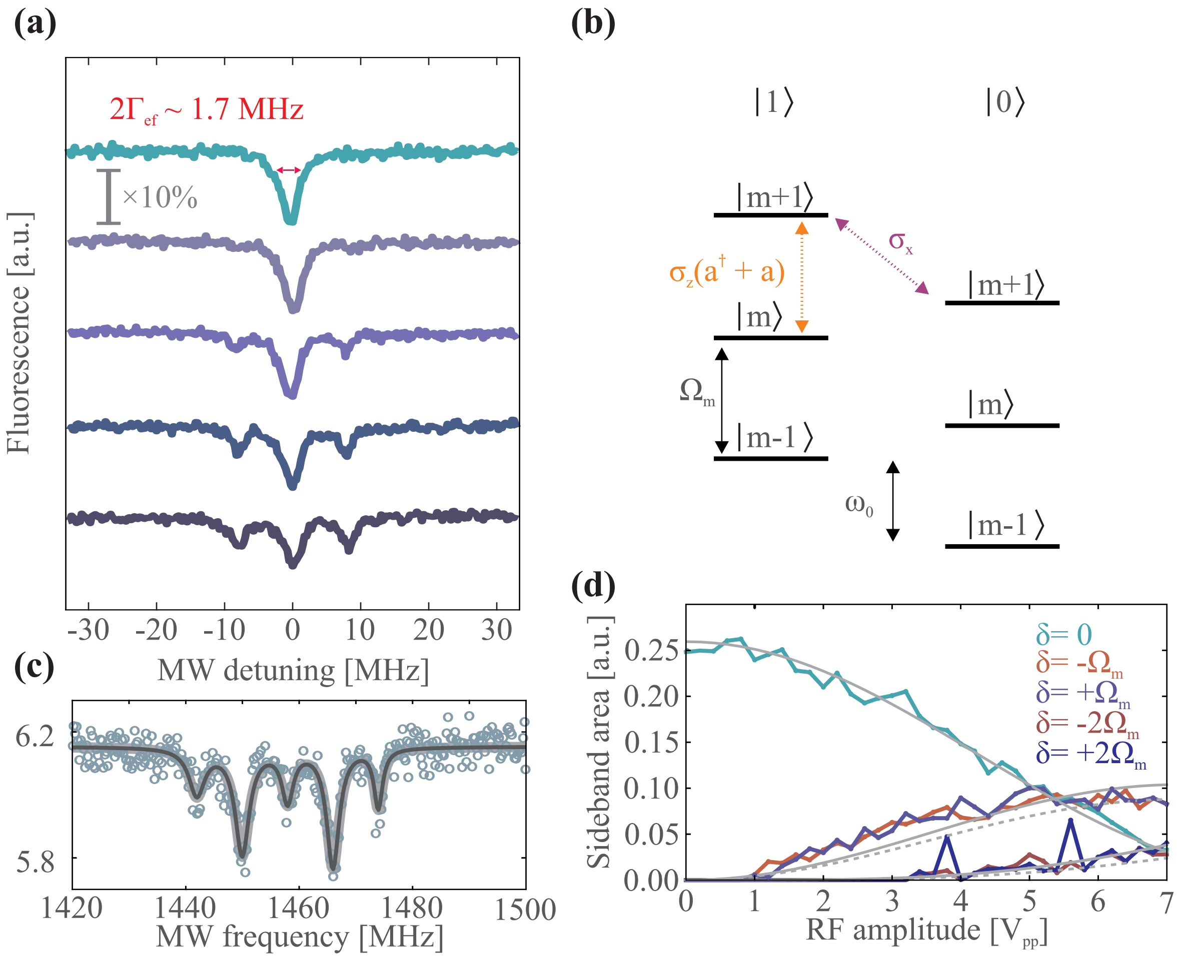

Figure 3.18: ODMR spectroscopy in the RSB regime taken on the same NV as in Figure 3.16. **(a)** RSB spectra $\delta V_{\mathrm{RF}} = (0., 0.5, 1.0, 1.5, 2.0)$ V. **(b)** The uncoupled energies due to $H_{\mathrm{spin}} + H_{\mathrm{osc}}$. The MW, whose action is described by σ_x and couples the spin ground and excited states, leaving the phonon number unchanged. The mechanical interaction emulated by the RF field couples states of the same column only, leading to new eigenstates contaminated by states of different RF photon (phonon) number states, see text. Under these conditions, the MW field can probe transitions of different phonon number, resulting in sidebands in the absorption spectra. **(c)** Spectrum taken at $\Omega_{\mathrm{m}}/2\pi = 8\,\mathrm{MHz}$ and $\delta V_{\mathrm{RF}} = 3.5\,\mathrm{V}$ exhibiting very prominent second order sidebands. **(d)** The solid grey lines represent fits to $a_n J_n^2\left(c \times \frac{\delta\omega_0}{\Omega_{\mathrm{m}}}\right)$, with correction factor $c = 2.04$ and $a_0 = 0.26$, $a_1 = 0.31$, $a_2 = 0.41$. The dashed lines represent curves $a_0 J_n^2\left(c \times \frac{\delta\omega_0}{\Omega_{\mathrm{m}}}\right)$. While they reproduce the experimental data reasonably well, our simulations show that power broadening affects each sideband differently.

3.4.4 Simulations of the steady state spin population in the resolved sideband regime

Simulating ODMR spectra in the resolved sideband regime requires obtaining the MW drive frequency dependent steady state population $w^{\mathrm{st}}[\omega]$. We therefore evaluate numerically equations (3.2) for $t \gg 1/\Gamma_2$ and average $w_{t\gg 1/\Gamma_2}(t)$ over a period much larger than $1/\Gamma_2$. The simulations readily reproduce the sideband spectra that were observed experimentally. For reasons of computational duration, we limit our calculations to the first two sidebands. The numerically obtained spectra are fitted with a sum of up to five Lorentzian lineshape functions. For each sideband we then retrieve the relative area A_n. As for the experimental case, fitting $A_n(\delta\omega_0)$ with the squared Bessel functions

$J_n^2\left(\frac{\delta\omega_0}{\Omega_\mathrm{m}}\right)$ does not provide a satisfying result. We therefore inspect the analytic expression for the area A of the resonance in absence of modulation, using equations (3.7) and (3.6):

$$A = C_w\Gamma_\mathrm{eff} = \frac{1}{2\pi}\frac{\Omega_\mathrm{R}^2}{\Omega_\mathrm{R}^2+\tilde{\Gamma}_2\tilde{\Gamma}_1}\tilde{\Gamma}_2\sqrt{1+\frac{\Omega_\mathrm{R}^2}{\tilde{\Gamma}_1\tilde{\Gamma}_2}}. \tag{3.15}$$

We see that the general form of A presents a nontrivial dependence on the MW power Ω_R^2. From our above considerations of frequency modulation, the appearance of sidebands, which leads to an effective change of the Rabi strength for each transition according to

$$\Omega_\mathrm{R}^n = \Omega_\mathrm{R} J_n\left(\frac{\delta\omega_0}{\Omega_\mathrm{m}}\right), \tag{3.16}$$

results in a modification of the effective magnetic dipole strength. The above expression will be verified experimentally in the next section by measuring Rabi oscillations on each transition. Injecting it in the power broadened sideband area A_n yields

$$A_n = \frac{1}{2\pi}\frac{\Omega_\mathrm{R}^2 J_n^2\left(\frac{\delta\omega_0}{\Omega_\mathrm{m}}\right)}{\Omega_\mathrm{R}^2 J_n^2\left(\frac{\delta\omega_0}{\Omega_\mathrm{m}}\right)+\tilde{\Gamma}_2\tilde{\Gamma}_1}\tilde{\Gamma}_2\sqrt{1+\frac{\Omega_\mathrm{R}^2 J_n^2\left(\frac{\delta\omega_0}{\Omega_\mathrm{m}}\right)}{\tilde{\Gamma}_1\tilde{\Gamma}_2}}. \tag{3.17}$$

This equation well fits the numerically obtained sideband areas, see Figure 3.19.

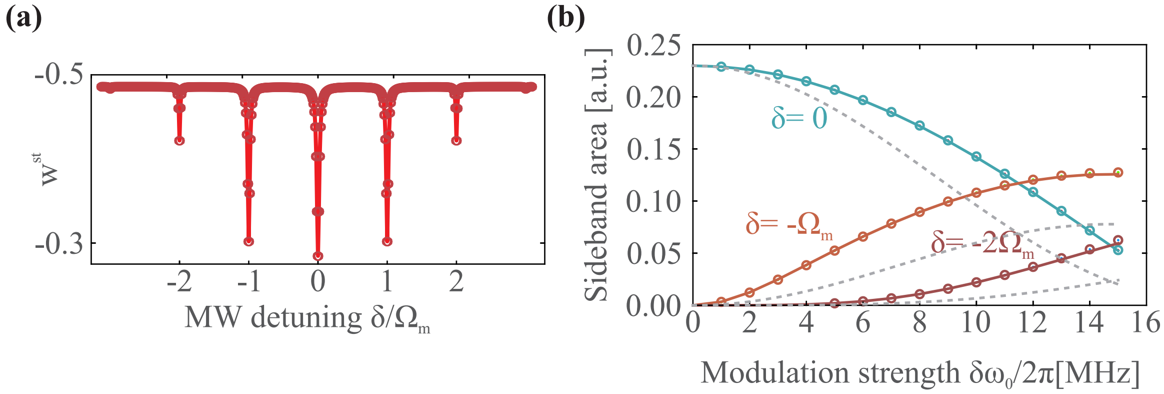

Figure 3.19: Simulated RSB spectra. **(a)** A typical ESR spectrum obtained from the simulations ($\Omega_\mathrm{m}/2\pi = 8\,\mathrm{MHz}$, $\delta\omega_0/2\pi = 10\,\mathrm{MHz}$). Dots are numerical data points and the solid line is a fit to a lineshape function with seven Lorentzian peaks. **(b)** Sideband areas for the carrier and the two first lower sidebands extracted from simulations. Dots are data points, solid lines are expression (3.17). The grey dashed lines indicate the functions $A_0(0)J_n^2\left(\frac{\delta\omega_0}{\Omega_\mathrm{m}}\right)$.

We use expression (3.17) to fit the experimentally obtained sideband areas. The results are presented in Figure 3.20. Doing so requires knowledge of μ, which was determined above to be $\mu = 0.78$ (see Figure 3.15). The MW power for these measurements was set to 0 dBm, which corresponds to relatively small MW powers to avoid excessive broadening. The result is presented in Figure 3.20 with fitting parameters $\tilde{\Gamma}_1 = 0.19$ MHz, $\tilde{\Gamma}_2 = 2.34$ MHz and $\Omega_\mathrm{R}/2\pi = 0.12\,\mathrm{MHz}$. These values for $\tilde{\Gamma}_1$ and $\tilde{\Gamma}_2$ seem reasonable in view of the low light power used ($s \approx 0.2$) and the values obtained for Γ_p^∞ and Γ_c^∞. The value for the Rabi frequency Ω_R is slightly off from a factor of four with respect to the value from the MW power calibration, see section 3.5.2. Overall however, the data is in good agreement with the model and all three curves can be fitted with the same set of parameters, which represents an improvement to the fits in Figure 3.18.

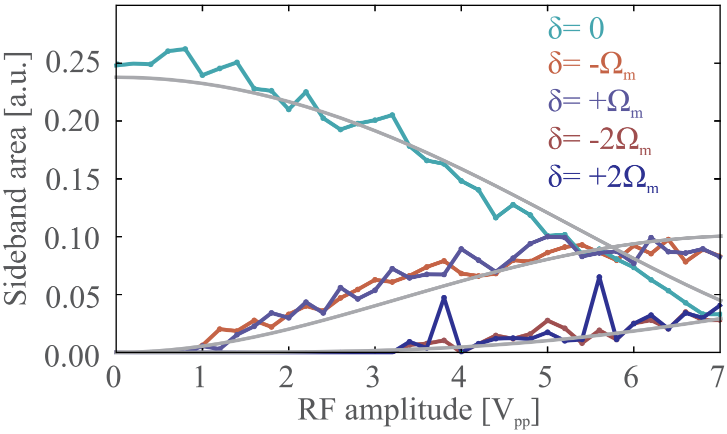

Figure 3.20: Adjustement of the ODMR spectra in the RSB regime using expression (3.17) with: $\tilde{\Gamma}_1 = 0.19$ MHz, $\tilde{\Gamma}_2 = 2.34$ MHz, $\Omega_R/2\pi = 0.12\,$MHz, $\mu = 0.78$.

3.4.5 Time dependence of ODMR spectra in the resolved sideband regime

As in the case of adiabatic modulation, we can gate the photon detection to the RF oscillation phase. Here we have chosen to inject a modulation frequency of $\Omega_m/2\pi = 15\,$MHz and a gate duty cycle of 20%. The result, shown in Figure 3.21, is qualitatively different from the adiabatic case. Here we see no variation of the resonance frequency along with the gating phase. Again, the RF oscillation period is much shorter than the intrinsic spin lifetime. Because of the different time scales, the spin does not have enough time to adiabatically follow the energy modulation. This is in contrast to the adiabatic case, where the ODMR measurement represented a sum over statistical realizations of the spin resonance frequency due to the slowly changing spin energy. The resolved sideband regime of the parametric interaction is important for true hybrid mechanical systems, where the RF modulation is replaced by mechanical motion. In particular, it allows accessing phonon sidebands which is fundamental in spin based coding protocols [48, 53].

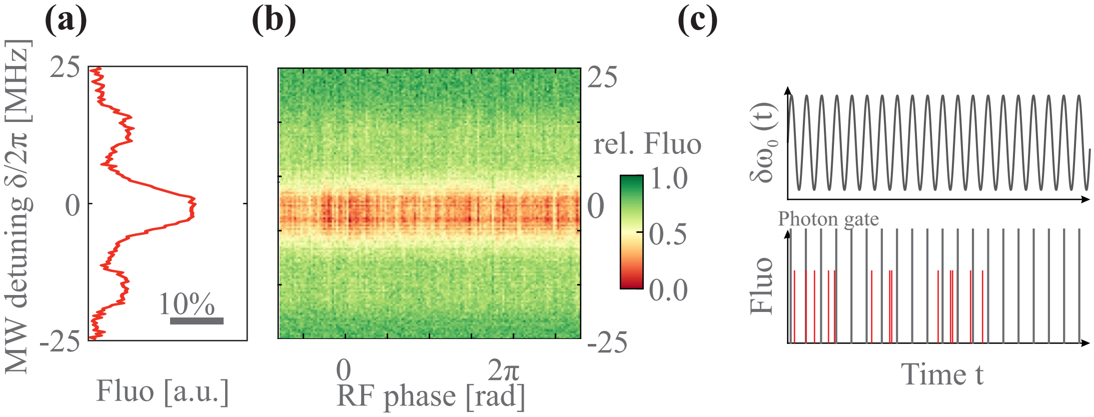

Figure 3.21: Time dependence of ODMR spectra in the resolved sideband regime. **(a)** ESR spectra exhibit sidebands at the modulation frequency $\Omega_m/2\pi = 15\,$MHz. **(b)** As in Figure 3.17, a series of ESR measurements is gated to the oscillation phase. The data exposes the fact that the spin cannot follow adiabatically the energy modulation. **(c)** Measurement scheme. The curves represent qualitatively the change of the timescales in the measurement protocol.

Summary The results of the ODMR measurements with monochromatic energy modulation emulating the displacement of the spin through a magnetic field gradient by a mechanical oscillator are summarized in Figure 3.22. A static displacement of the spin results in a shift of its resonance frequency due to the Zeeman effect. For an oscillating RF field emulating the motion of a mechanical oscillator, we can identify two regimes. If the modulation frequency is smaller than the spin decay rate, the spin experiences an adiabatic change of its transition frequency that leads to a broadening of the ODMR spectra. If the mechanical frequency exceeds the spin decay rate, the ODMR spectra exhibit sidebands separated from the carrier peak by integer multiples of the RF frequency. These signatures have been sought after in the hybrid mechanical systems community because they demonstrate that the device is operating in a parameter space where spin and resonator can be coupled in order to generate non-classical states of motion[1]. Being able to emulate the resolved sideband regime of a parametrically coupled hybrid mechanical system, we now proceed to study the underlying spin dynamics.

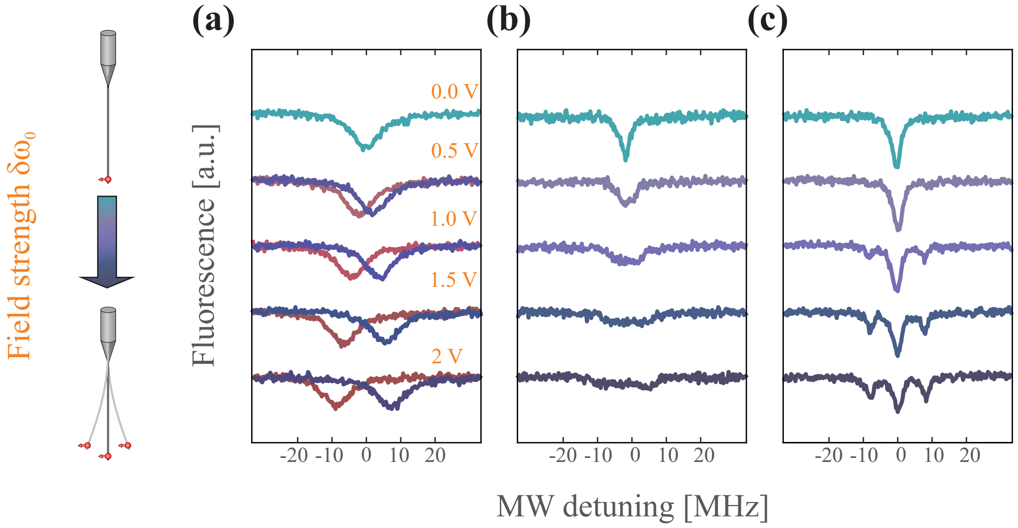

Figure 3.22: ODMR spectra of a single spin parametrically coupled to a mechanical oscillator. **(a)** Static displacement, $\Omega_{\mathrm{m}} = 0$. **(b)** Periodic oscillation in the adiabatic regime, $\Gamma_{\mathrm{spin}} > \Omega_{\mathrm{m}}$. **(c)** Periodic oscillation in the resolved sideband regime, $\Gamma_{\mathrm{spin}} < \Omega_{\mathrm{m}}$.

3.5 Measuring spin dynamics

The investigation of spin dynamics consists in studying of the evolution of the ground and excited state populations in presence of MW and RF driving fields. In a two level system, the driving of transitions between the two qubit states creates an interplay between absorption and (spontaneous and stimulated) emission, which results in a cycling of the spin populations known as Rabi oscillations, see Figure 3.23. In this section we introduce the measurement of Rabi oscillations as a general tool to probe the time resolved dynamics of a single spin driven by a MW field.

---

[1] Tessier and Maletinksy have recently presented the first experimental demonstration of a strain coupled hybrid mechanical system working in this regime [91].

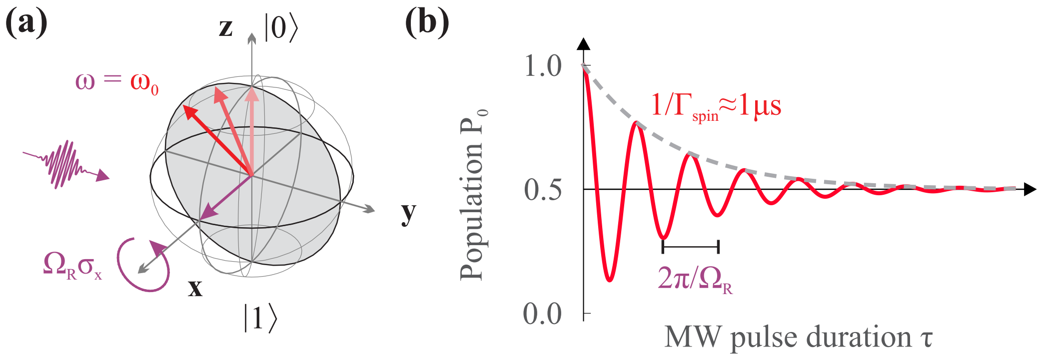

Figure 3.23: MW driven cycling of the ground state population. **(a)** Bloch sphere representation. A near resonant MW field polarized along the **x**-direction rotates the Bloch vector around the x axis. **(b)** A time resolved population measurement reveals Rabi oscillations at frequency $\Omega_\mathrm{R}/2\pi$ with characteristic decay time $1/\Gamma_\mathrm{spin}$.

3.5.1 Experimental realization

Measurement principle In order to measure the spin's evolution under MW driving, we need to be able to detect the spin population after a MW signal of variable length, strength and frequency has been applied. The idea is to send an optical pulse to the NV defect and measure the thereupon emitted fluorescence. Since the amount of emitted optical photons is spin state dependent (the fluorescence rate is $\sim 30\%$ higher in the ground state $|0\rangle$ than in the excited state $|1\rangle$, see section 3.3), we can deduce the spin population from time resolved photon counting during optical excitation of the NV following the MW/RF pulse sequence. The principle measurement protocol is outlined in Figure 3.24.

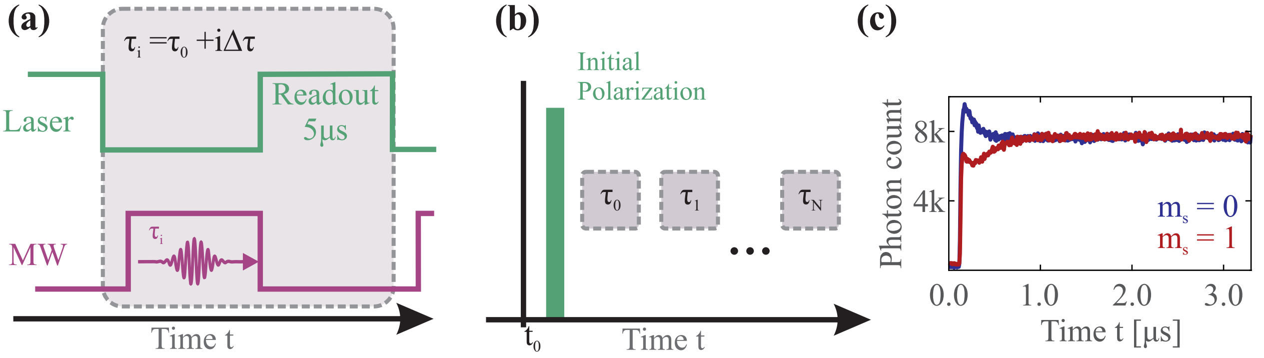

Figure 3.24: Measurement protocol for the detection of Rabi oscillations. **(a)** A $5\,\mu$s laser pulse polarizes the spin in the ground state. A subsequent MW pulse of duration τ_i is used to rotate the spin state and followed by an optical readout pulse. The grey box indicates the i^{th} element in the sequence. **(b)** A first pulse is used to measure the ground state population. A series of elements described in **(a)** is then swept to obtain the desired pulse number of different pulse durations. **(c)** Photons are counted and accumulated for each element of the sequence resulting in different fluorescence patterns. The spin state detection is explained in the next section and in Figure 3.25.

Measurement setup While the MW strength and frequency can be controlled by the signal generator, our setup needs to be adapted in order to create well timed MW and optical signals and to synchronize the optical readout of the spin state after its manipulation. Since we expect coherence times on the order of a few microseconds, (see section 2.3) it is sufficient to resolve the spin dynamics on a 10 ns timescale. We thus use the PulseBlaster 300 card from SpinCore that can create TTL logic gates with pulse rise times of 3 ns and minimum pulse duration of $\tau_0 = 20\,\text{ns}$. The card has four output BNC connectors, each of which can be programmed independently and synchronized to the same on-board clock. We use three of these ports in order to:

a) gate a MW switch in order to let the continuous MW signal provided by the MW generator pass only at the desired instances for a well defined duration τ_i.

b) gate the acousto-optic modulator (AOM) installed on the indirect beam path in order to create well timed optical pulses. These pulses mediate readout of the spin state following a MW burst (duration $\tau_0 + i\Delta\tau$) but also serve to repolarize the spin in its ground state in order to prepare it for the subsequent MW pulse (duration $\tau_0 + (i+1)\Delta\tau$).

c) synchronize a fast time resolved fluorescence reading to the pulse sequence. At the beginning of each execution, a trigger of 20 ns duration is sent to a fast time-of-flight card P7889 from FastComTec with 100 ps resolution, recording an array of photon arrival times.

The setup is shown below in Figure 3.25 **(a)**. The TTL generating PulseBlaster 300 card is programmed to produce a sequence of N blocks as shown in Figure 3.24 **(a)** and **(b)**. In each of these blocks, the spin is exposed to a MW pulse of minimum length $\tau_0 = 20\,\text{ns}$ (set by the minimal length of the PulseBlaster card) followed by 5 μs of laser light irradiation. There is a 300 ns gap between the laser pulse falling edge and the next block, which has proven to be critical for the data quality. In these 300 ns, population trapped in the singlet state is given time to fall back into the ground state. For measurements of Rabi oscillation we choose the laser power to operate in the saturated regime in order to be less sensitive to laser power fluctuations. We typically detect NV fluorescence rates around 30 kHz. One sweep of the sequence, which varies in duration as a function of MW pulse step size $\Delta\tau$ and maximum pulse number N, lasts between 2 and 20 ms and thus only about 300 photons are collected. The protocol is therefore executed 1.4×10^6 times in order to obtain a statistically meaningful photon count with sufficiently averaged signal. Depending on the protocol, a measurement for a single Rabi curve lasts typically between 40 and 150 minutes. In order to accurately determine the resonance frequency of the spin, an ODMR spectrum is recorded and fitted before each measurement of Rabi oscillations. We have fully automated this procedure, which permits efficient acquisition of a large number of Rabi measurements over the course of several days without being sensitive to MW detuning induced by thermal drifts. A representative trace of time correlated photon counts is shown in Figure 3.25 **(b)**, where data was accumulated in 6.4 ns long time bins for a period of over 7 days. The integrated fluorescence bursts differ in the shape of their front edge. If the MW pulse prepared the spin in the ground state $|m_s = 0\rangle$, the pulse exhibits a steep edge with a large overshoot, before the average fluorescence drops to a steady state value, reflecting a nonzero probability to occupy the metastable state. For a MW pulse preparing the spin in the excited state $|m_s = -1\rangle$, less fluorescence is emitted subsequently and the observed edge shows a smaller photon count. For the spin state measurements we are only interested in the first 300 ns of each of these fluorescence pulses. The pulse front area is normalized by the integrated photon count in the last 1 μs of the pulse yielding a spin state specific fluorescence count. A plot of these normalized counts against the preceding MW pulse duration yields Rabi oscillations of the NV electron spin as shown in Figure 3.25 **(c)**.

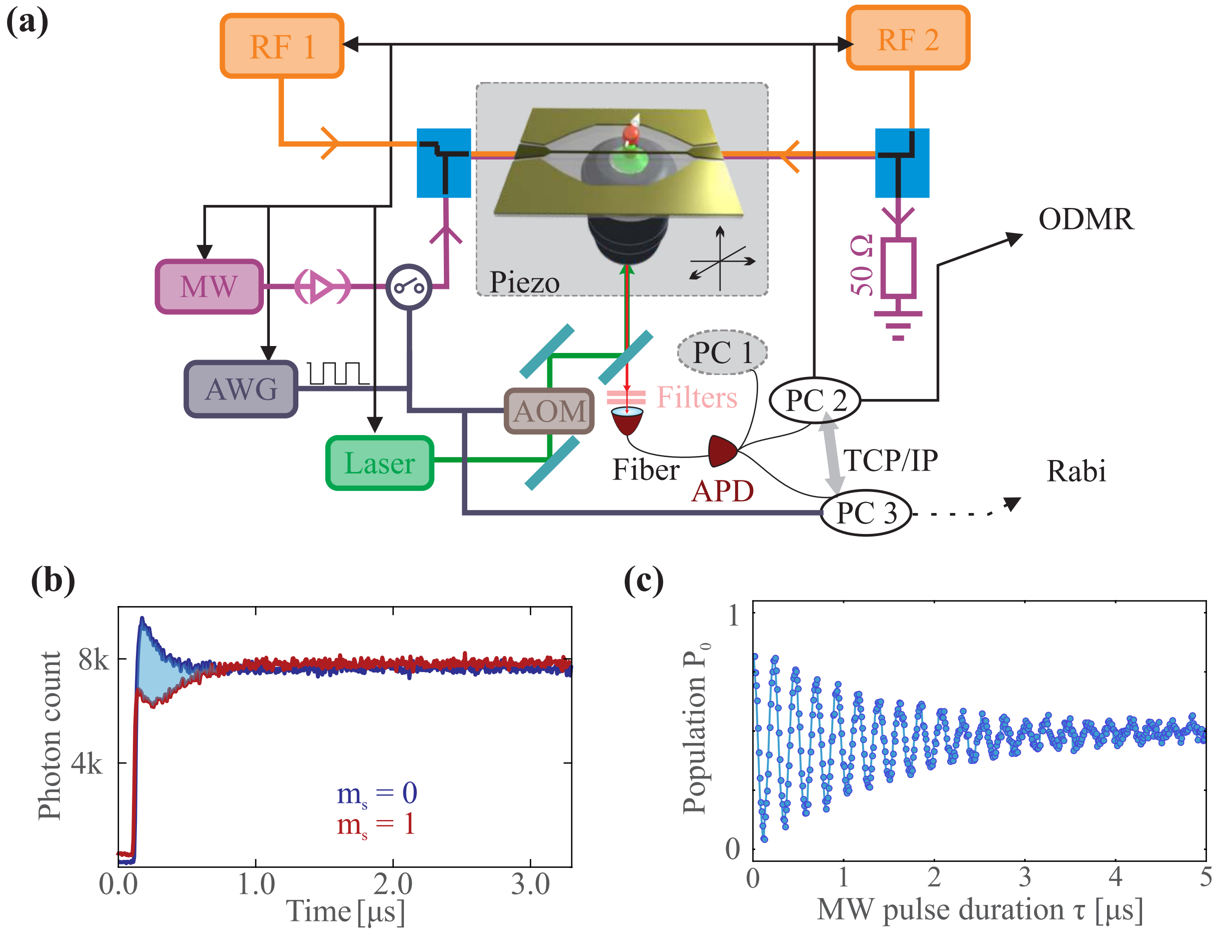

Figure 3.25: Setup for Rabi measurements. **(a)** A fluorescence measurement from the avalanche photo diode (APD) is shared between three different PCs. PC 1 tracks the position of the NV center by adjusting the piezo stage holding the microscope objective. PC 2 performs the ODMR measurements, infers the spin resonance frequency $\omega_0/2\pi$ and sets the desired MW output frequency $\omega/2\pi$. Subsequently, the arbitrary waveform generator (AWG) is programmed to measure Rabi oscillation with N pulses of duration $\tau_{i=1...N}$. The AWG opens and closes the MW switch and the acousto-optic modulator (AOM) in accordance with the pulse sequence shown in Figure 3.24. Via TCP/IP communication, PC 3 is then activated to start the time resolved fluorescence count which is synchronized to the Rabi pulse sequence by means of the AWG. **(b)** The detected time resolved fluorescence reading is spin state dependent. The initial pulse area difference (blue shaded region) thus encodes the spin state corresponding to the previously applied MW burst. The accumulation time for this particular measurement was on the order of days for both curves. **(c)** This difference, normalized by the fluorescence contained in the last 1 μs of the pulse (not shown), is plotted against MW pulse duration to yield a measurement of Rabi oscillations.

3.5.2 Characterization of MW coupling

The frequency of Rabi oscillations as seen in Figure 3.25 is proportional to the magnetic field amplitude perpendicular to the NV axis, $B_\perp^{\mathrm{MW}}$, and therefore proportional to $\sqrt{P_{\mathrm{MW}}}$, where P_{MW} is the output power of the MW generator. In order to calibrate the Rabi frequency $\Omega_{\mathrm{R}}/2\pi$, we acquire a series of Rabi measurements while varying P_{MW}. A typical result is presented in Figure 3.26 **(a)**. The values of Rabi frequencies are extracted by fitting the temporal traces with a single oscillation. The MW generator produces an output of up to 30 dBm, but the MW switch input is limited to 24 dBm. The

MW power on the sample can be increased by an additional signal amplifier, which is specified to not be operated at more than -5 dBm input power. The calibration data in Figure 3.26 **(b)** shows traces for a setup with and without amplifier installed. It was found that operation without the amplifier showed less drift in the MW power seen by the NV and thus ensures a more stable Rabi frequency. Typical operation of the setup was thus chosen to be realized without amplifier, at MW output powers P_{MW} between 10 and 20 dBm, producing Rabi frequencies between 1 and 7 MHz (which are sufficiently rapid with respect to the observed Rabi decay rate, $\Omega_{\mathrm{R}} > \Gamma_{\mathrm{spin}}$). These measured Rabi frequencies are in good agreement with the determined spin orientation of $\theta = 59°$, when taking into account the waveguide transmission losses (see section 3.2.2 and Figure 3.2).

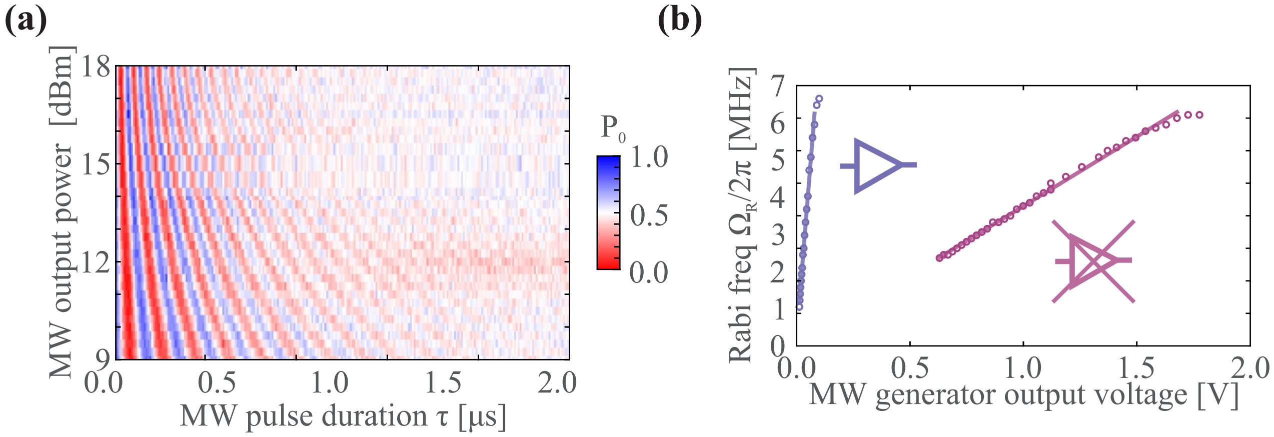

Figure 3.26: Characterization of the MW coupling. **(a)** The data shows Rabi oscillations for various output powers of the MW generator without amplifier. **(b)** The data from **(a)** can be fitted in order to extract the Rabi frequency, which is a function of the MW power.

In absence of energy modulation, the characterization of the Rabi frequency allows us to rotate the spin on the Bloch sphere by any polar angle (the technique does not allow us to control the phase of the superposition). In principle, we always use optical polarization followed by a well timed MW pulse at the necessary output power. The efficiency ϵ of MW photon absorption can also be deduced. The measured Rabi frequency is the number of photons absorbed per second. Assuming that all the injected power P_{MW} is converted into a flux Φ photons of frequency $\omega/2\pi = 1.45\,\mathrm{GHz}$, we have

$$\epsilon = \frac{\Omega_{\mathrm{R}}}{2\pi\Phi} \approx \frac{\Omega_{\mathrm{R}}\hbar\omega}{2\pi P_{\mathrm{in}}} = 2.2 \times 10^{-16}.$$

3.5.3 Lifetime measurement of the NV spin

We conclude this section by performing a measurement of the spin lifetime T_1. We use the newly acquired control over the spin state and adapt the technique proposed in [131]: first, the spin is prepared in the ground or excited state, using either optical polarization or optical polarization followed by a fast MW π-pulse, respectively. After a variable delay time we perform a time resolved fluorescence measurement, as was done for the detection of Rabi oscillations. During the delay time, the spin relaxes from one of the m_s eigenstates to its steady state population, which is $P_0 = P_1 = 0.5$ at room temperature. We detect the difference in population between relaxation from the ground and excited state for various delay times, see Figure 3.27 **(a)**. We fit the data with a single exponential decay and thus deduce the spin relaxation time. The result is depicted in Figure 3.27 **(b)**. We observe a relaxation time of $T_1 = 173\,\mu\mathrm{s}$, corresponding to $\Gamma_1 = 6\,\mathrm{kHz}$. This value is in agreement with our considerations in section 2.3 and demonstrates that the decay time of Rabi oscillations is dominated by Γ_2-processes.

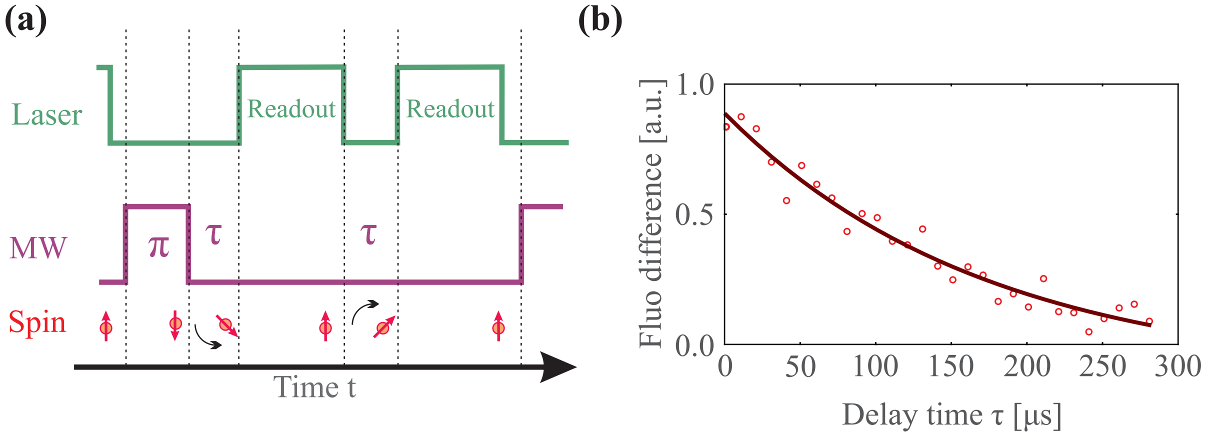

Figure 3.27: Lifetime measurement of the NV spin. **(a)** Lifetime measurement protocol. The spin is alternately prepared in the ground or excited state and read out after a variable delay time τ. **(b)** Plot of the detected fluorescence versus delay time τ. A fit to a single exponential decay reveals a decay rate $\Gamma_1 = 6\,\mathrm{kHz}$, corresponding to a lifetime of $1/\Gamma_1 = 173\,\mu\mathrm{s}$.

3.5.4 Dependence of Rabi oscillations on the MW frequency

We now present Rabi oscillations as a function of the frequency of the MW field in absence of RF parametric modulation. The data is shown in Figure 3.28 **(a)**. Rabi oscillations were obtained for 18 dBm MW pulses between $0\,\mu\mathrm{s}$ and $1.8\,\mu\mathrm{s}$ in $10\,\mathrm{ns}$ steps in the absence of an external magnetic field. The data's complexity is therefore enriched by hyperfine coupling of the NV defect to the ^{14}N nuclear spin. We take it into account by assuming relatively long lived nuclear spins compared to the largest MW pulse of $1.8\,\mu\mathrm{s}$ in $10\,\mathrm{ns}$, so that one can assume that at each sweep of the Rabi sequence the nuclear spin is in a random projection. We simulate the experimental data by numerically solving the Bloch equations (2.123) for three different resonance frequencies $\omega_0/2\pi = (2870 \pm 0, 2.2)\,\mathrm{MHz}$ and adding the results incoherently. When driving Rabi oscillations the laser is turned off during the spin evolution. Hence $s = 0$ and the decay rates reduce to $\tilde{\Gamma}_1 = \Gamma_1$ and $\tilde{\Gamma}_2 = \Gamma_2$, since $\Gamma_\mathrm{p} = \Gamma_\mathrm{c} = 0$. Furthermore, the resonance frequency is fixed in absence of RF modulation, $\omega_0(t) = \omega_0$. This simplifies equation (2.123) to:

$$\begin{pmatrix} \dot{u} \\ \dot{v} \\ \dot{w} \end{pmatrix} = \begin{pmatrix} -\Gamma_2 & \delta & 0 \\ -\delta & -\Gamma_2 & -\Omega_\mathrm{R} \\ 0 & \Omega_\mathrm{R} & -\Gamma_1 \end{pmatrix} \begin{pmatrix} u \\ v \\ w \end{pmatrix} \tag{3.18}$$

With the initial conditions being $(u, v, w) = (0, 0, -1/2)$, the results of numerical simulations (see Figure 3.28 **(b)**) are in good qualitative agreement with the experimental data. Small details like the hyperfine coupling induced substructure of the Rabi beats as well as the outside fringes agree between experiment and theory. For increasing detuning from the resonance frequency, the pattern shows an increasing oscillation frequencies and decay rates. Moreover, in both cases the population does not decay to $P_0 = 0.5$ on the same time scale for large detunings ($\delta > \Omega_\mathrm{R}$) as at resonance ($\delta = 0$). This can be explained with the fact that for large values of δ the population is only sensitive to Γ_1-like processes. We now further analyze the Bloch equations (2.123) in order to properly explain this observation.

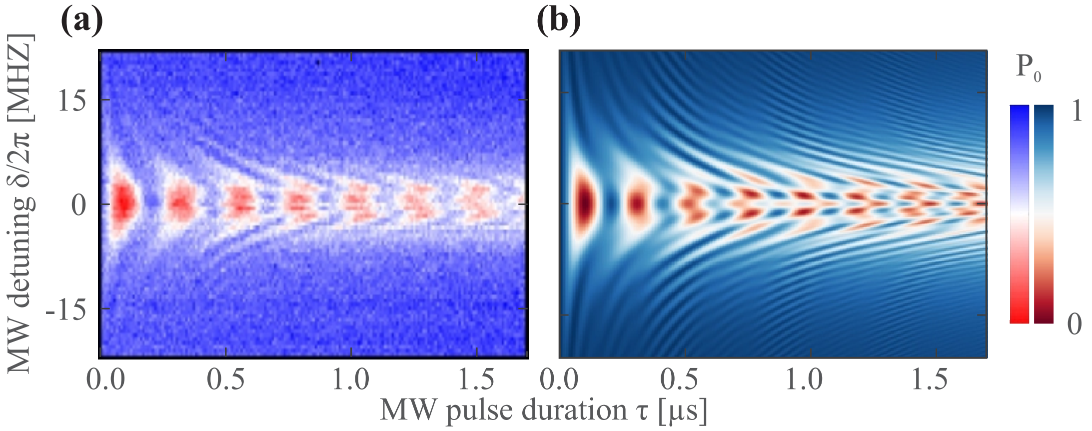

Figure 3.28: Detuned Rabi oscillations. **(a)** The experimental results show additional complexity due to the interaction with the ^{14}N nuclear spin. As the detuning is increased, the frequency as well as the decay rate of oscillation is increased. Far from resonance, the population is not decaying on the timescale shown here. This is because the MW has no effect on the spin, which decays at a rate $\sim \Gamma_1 = 66\,\mathrm{kHz}$, as was found in section 3.5.3.

3.5.5 Bloch-Redfield theory

Understanding of the driven spin evolution is simplified when thinking in the MW rotating frame, which was first suggested by [123]. The spin is initially polarized in the ground state and thus aligned with the $\mathbf{z}$-axis as shown in Figure 3.29 **(a)**. A magnetic field of strength Ω_R at frequency $\omega = \omega_0$ polarized along the $\mathbf{x}$ axis is applied, driving rotations of the Bloch vector around $\mathbf{x}$ at the Rabi frequency $\Omega_\mathrm{R}/2\pi$, see **(b)**. This situation changes when the MW field becomes detuned from the spin resonance such that $\delta \neq 0$. Inspecting equation (3.18), where the rotating wave approximation has been made, we see that the Bloch vector describes a pseudo spin 1/2 system immersed in an *effective magnetic field* aligned along $\mathbf{s} = \Omega_\mathrm{R}\hat{\mathbf{x}} + \delta\hat{\mathbf{z}}$ and strength $\hbar\Omega_\mathrm{R}^\mathrm{eff} = \hbar\sqrt{\Omega_\mathrm{R}^2 + \delta^2}$. This effective Rabi frequency can be regarded as the pseudo spin's Larmor frequency and increases with detuning of the MW field. The tilt between the $\mathbf{x}$-axis and the new rotation axis $\mathbf{s}$ leads to a decrease of contrast of the Rabi oscillations, as the Bloch vector's projection onto the $\mathbf{z}$-axis does not pass by the poles of the Bloch sphere anymore.

At the beginning of the Rabi sequence, however, the spin has been polarized in the ground state. From there, the Bloch vector falls into the plane perpendicular to $\mathbf{s}$, giving rise to an additional non-oscillating, exponentially decaying component of the population observed for nonzero detuning.

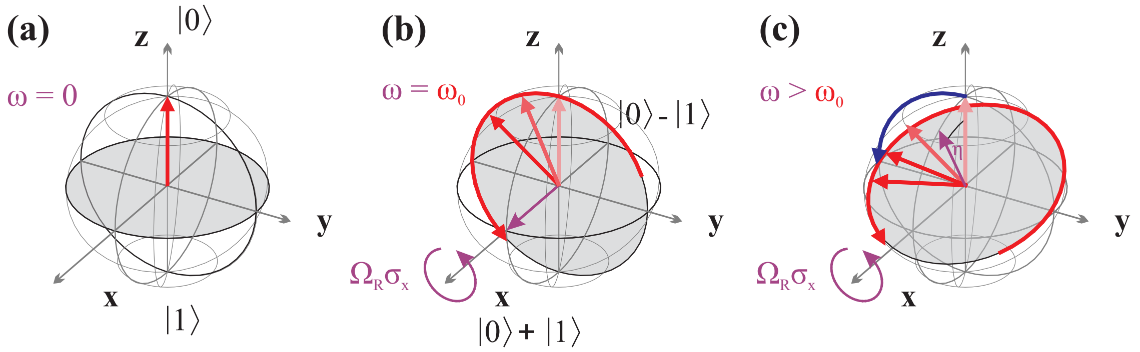

Figure 3.29: Bloch-Redfield theory and the effective field description. **(a)** Representation of the ground state $|0\rangle$ polarized spin (red arrow) in the Bloch sphere. **(b)** By application of a resonant ($\delta = \omega - \omega_0 = 0$) MW field along the $\mathbf{x}$-axis, rotations of the spin in the $(\mathbf{y}, \mathbf{z})$-plane are induced. These rotations are called Rabi precessions. In the frame rotating with ω, the effective field is given by $\mathbf{s} = \Omega_{\mathrm{R}} \hat{\mathbf{x}}$, shown as the purple arrow. In the rotating frame, the motion of the spin is described by a rotation around $\mathbf{s}$ and can then be interpreted as the Larmor precession of a pseudo spin with a quantization axis along $\mathbf{x}$ and energy splitting $\hbar\Omega_{\mathrm{R}}$. **(c)** When the applied MW field is detuned from resonance, the effective field is pointing away from the $\mathbf{x}$-axis, such that $\mathbf{s} = \Omega_{\mathrm{R}}\hat{\mathbf{x}} + \delta\hat{\mathbf{z}}$, with angle $\eta = \arctan(\Omega_{\mathrm{R}}/\delta)$ and amplitude $\Omega_{\mathrm{R}}^{\mathrm{eff}} = \sqrt{\Omega_{\mathrm{R}}^2 + \delta^2}$. The motion of the spin then describes a rotation around $\mathbf{s}$ as before (red circular arrow). Due to initial polarization in $|0\rangle$, an additional component arises, corresponding to the spin falling from the plane normal to $\mathbf{x}$ to a plane normal to $\mathbf{s}$ (blue circular arrow).

These dynamics are described by the expression

$$P_0(\tau) = A_1 \exp\left(-\Gamma_{\mathrm{static}}\tau\right) + A_2 \exp\left(-\Gamma_{\mathrm{spin}}\tau\right) \cos\left(\Omega_{\mathrm{R}}^{\mathrm{eff}}\tau\right) + \frac{1}{2}, \tag{3.19}$$

where $\Omega_{\mathrm{R}}^{\mathrm{eff}} = \sqrt{\Omega_{\mathrm{R}}^2 + \delta^2}$ is the effective Rabi frequency of the oscillating component with amplitude A_2 and decay rate Γ_{spin}, and the non-oscillating component has amplitude A_1 and decay rate Γ_{static}. The initial conditions impose that $P_0(\tau = 0) = 1 = A_1 + A_2 + 1/2$. The constant $1/2$ reflects the steady state value, around which the population is oscillating. As already discussed, the amplitude[2] A_2 of the oscillating population is reduced due to a tilt of $\mathbf{s}$ by angle $\eta = \arctan(\Omega_{\mathrm{R}}/\delta)$:

$$A_2 = \frac{\sin^2(\eta)}{2} = \frac{1}{2}\frac{\Omega_{\mathrm{R}}^2}{\Omega_{\mathrm{R}}^2 + \delta^2}. \tag{3.20}$$

It follows for the amplitude A_1 that

$$A_1 = \frac{\cos^2(\eta)}{2} = \frac{1}{2}\frac{\delta^2}{\Omega_{\mathrm{R}}^2 + \delta^2}. \tag{3.21}$$

It remains to determine the decay constants Γ_{static} and Γ_{spin}. They can be obtained by reasoning in terms of the dissipation and decoherence rates for the pseudo spin, taking into account the effect of the noise spectral densities $S_{\delta\omega_{\parallel}}[\Omega]$ and $S_{\delta\omega_{\perp}}[\Omega]$ after geometric rotation by the angle η and considering that the pseudo spin becomes sensitive to noise phenomena at Ω_{R} [121]. Projecting the noise sources $S_{\delta\omega_{\parallel}}[\Omega]$ and $S_{\delta\omega_{\perp}}[\Omega]$ onto $\mathbf{s}$ shifts the contributions of the noise to yield the effective spin relaxation (Γ_{static}) and de-phasing (Γ_{spin}) rates of the pseudo spin. Notice that, since $\mathbf{s}$ lies in the $(\mathbf{x}, \mathbf{z})$-plane,

---

[2] The factor 1/2 arises because the oscillation is limited between 0 and 1, while the squares arise from the fact that the Bloch sphere projections give wave function amplitudes and need to be squared in order to reflect a probability.

only the $\mathbf{x}$-component of $S_{\delta\omega_\perp}[\Omega]$ changes to $\frac{\cos^2\eta}{2}S_{\delta\omega_\perp}[\Omega]$, while the $\hat{\mathbf{y}}$ component stays the same, $\frac{1}{2}S_{\delta\omega_\perp}[\Omega]$. We have[3]

$$\Gamma_{\text{static}} = \Gamma_\nu \sin^2\eta + \Gamma_1 \frac{1+\cos^2\eta}{2}, \tag{3.22}$$

$$\Gamma_{\text{spin}} = \frac{1}{2}\Gamma_\nu \sin^2\eta + \Gamma_\varphi \cos^2\eta + \Gamma_1 \frac{3-\cos^2\eta}{4}, \tag{3.23}$$

which introduces the dephasing at the Rabi frequency $\Gamma_\nu = \pi S_{\delta\omega_\parallel}[\Omega_{\text{R}}^{\text{eff}}]$. These expressions are in quantitative agreement with the numerical evaluation of our simulations and show that the coherence time of Rabi oscillations, $1/\Gamma_{\text{spin}}$, is larger than the coherence time of the NV spin, $1/\Gamma_2$. For the simplified simulated spin bath with a flat spectral density $S_{\delta\omega_\parallel}[\Omega] = S_{\delta\omega_\parallel}$ we have $\Gamma_\varphi = \Gamma_\nu$, which at $\delta = 0 \rightarrow \eta = \pi/2$ leads to $\Gamma_{\text{spin}} = \frac{\Gamma_1+\Gamma_2}{2}$ (we have used $\Gamma_2 = \Gamma_1/2 + \Gamma_\varphi$). The results are summarized in Figure 3.31. Such a flat spectral density does not properly describe the true experimental spin bath, which can be assumed to have a Lorentzian spectral density, see section 2.3. In this case, however, it is still true that $\Gamma_\nu < 2\Gamma_\varphi + \Gamma_1$, and we can consequently expect improvement of the coherence time of Rabi oscillations when going from smaller to larger Rabi frequencies.

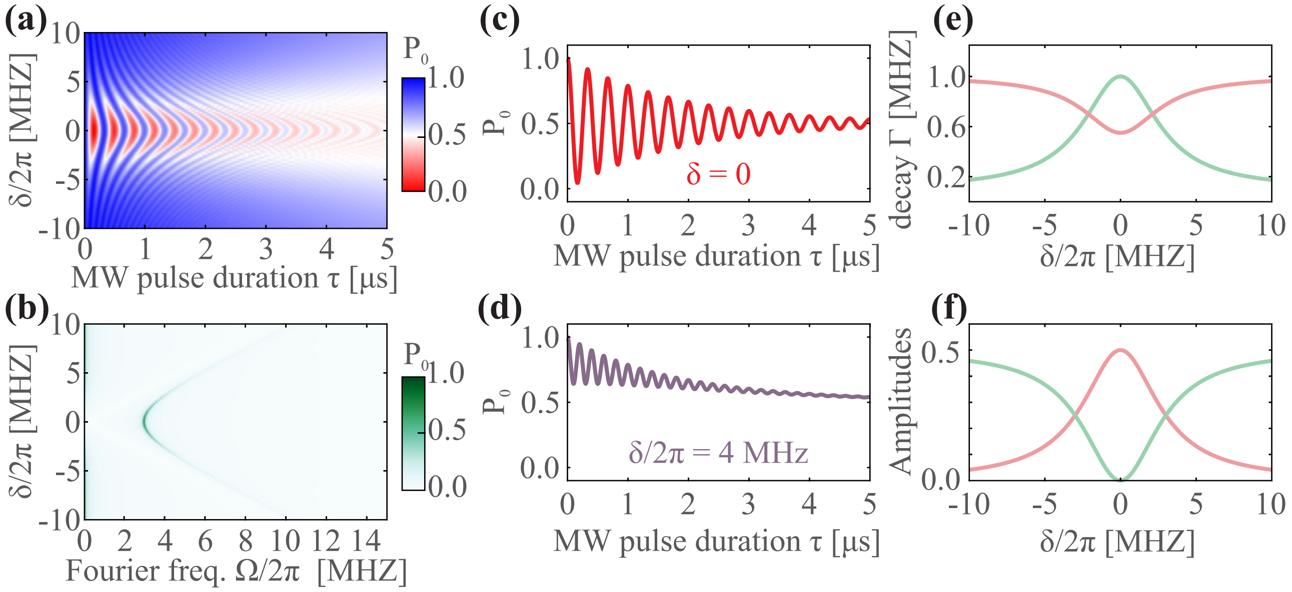

Figure 3.30: Simulated Rabi oscillations in the absence of hyperfine coupling. **(a)** Temporal traces of Rabi oscillations where the MW frequency $\omega/2\pi$ has been varied along the vertical axis. **(b)** Fourier transform of the data in **(a)**. The component at $\Omega = 0$ was cut out in order to increase the contrast for the component at $\Omega = \Omega_{\text{R}}^{\text{eff}}$. **(c)** Rabi oscillation for zero detuning. **(d)** Rabi oscillation for $\delta/2\pi = 4$ MHz. For $\delta \neq 0$ an additional exponential decay is visible. **(e)** Analytic expressions (3.22) and (3.23) of the decay rates Γ_{static} (green) and Γ_{spin} (red). **(f)** Analytic expressions (3.21) and (3.20) of the amplitudes A_1 (green) and A_2 (red). Here, we have chosen $\Gamma_1 = 0.1$ MHz, $\Gamma_2 = 1.0$ MHz, $\Omega_{\text{R}}/2\pi = 3.0$ MHz.

We analyze the experimental data in Figure 3.28 with the expressions established in this section, setting $\Omega_{\text{R}}/2\pi = 4\,\text{MHz}$ and choosing Γ_{static}, Γ_{spin} and δ as free parameters in order to define a single effective detuning value for all three resonance frequencies corresponding to different orientations of the hyperfine spin. Because of small values of Γ_1 and small amplitudes of the static component around resonance, the exponential decay described by Γ_{static} was neglected near $\delta \approx 0$. By evaluating the

---

[3] Notice the link between the dissipation (Γ_{static}) and decoherence rate (Γ_{spin}) of the pseudo spin with the dissipation (Γ_1) and decoherence rate (Γ_2) of the original NV spin. We have $\Gamma_2 = \Gamma_1/2 + \Gamma_\varphi$ and $\Gamma_{\text{spin}} = \Gamma_{\text{static}}/2 + \Gamma_{\varphi'}$, with $\Gamma_{\varphi'} = \Gamma_1 \sin^2(\eta)/2 + \Gamma_\varphi \cos^2(\eta)$ and in the limit of $\Omega_{\text{R}} \rightarrow 0$ we recover $\Gamma_{\text{static}} \rightarrow \Gamma_1$ and $\Gamma_{\text{spin}} \rightarrow \Gamma_2$.

evolution of Γ_{spin} with detuning δ we find a dephasing rate of $\Gamma_\varphi \approx 21\,\text{MHz}$, as shown in Figure 3.30. Imposing a Lorentzian spectral density of a NV spin bath dominated by P1 centers, we deduce from equation (2.78) a correlation time of $\tau_c \approx 1\,\mu\text{s}$. This value is in agreement with considerations from section 2.3, but we need to emphasize that the expressions (3.22) and (3.23) are assuming a flat spectral density over a range of $\approx \Gamma_2$, which is not a given for frequencies near $1/\tau_c$. However, the value found for $\Gamma_\varphi \approx 21\,\text{MHz}$ seems very large. Especially when considering the linewidth of ESR measurements in section 3.4, which is limited by Γ_φ (in absence of power broadening, compare to expression (3.6)) and was found to be about 1 MHz, see Figure 3.16. This discrepancy arises because the above considerations have ignored drifts of the effective Rabi frequency leading to an overestimated decay rate. This variation of Ω_{R} arising from thermal drifts (changing the circuit impedance and the spin resonance frequency by small misalignment of the external magnetic field) poses a major problem when using the Rabi protocol for noise detection, as the preceding analysis demonstrates. In section 3.7.8 we will encounter the *spin locking* mechanism, which circumvents the difficulties arising from drifts of the Rabi frequency.

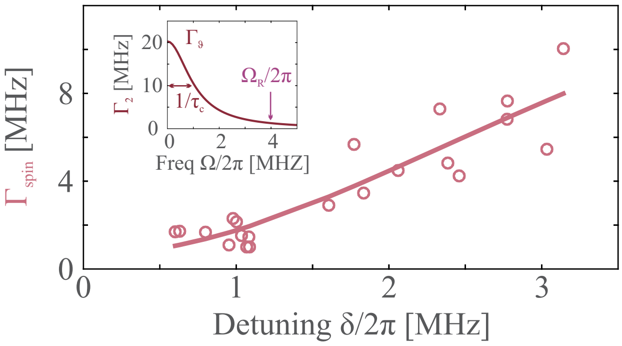

Figure 3.31: Experimentally obtained values for the decay of the oscillating part of Rabi oscillations of the measurement presented in Figure 3.28 with Rabi frequency $\Omega_{\text{R}}/2\pi = 4\,\text{MHz}$. The inset shows the deduced spectrum of the decoherence rate Γ_2, neglecting Γ_1 effects and assuming a Lorentzian bath. The pure dephasing rate was found to be $\Gamma_\varphi = 20.8$ MHz corresponding to $\tau_c \approx 1\,\mu\text{s}$.

3.6 Spin locking onto the parametrically modulating RF field

We have presented the required experimental techniques to study Rabi oscillations in presence of monochromatic energy modulation. In this section we are going to compare the dynamics of the driven spin between the static and the resolved sideband regime and show that we can lock the spin dynamics onto the RF field.

3.6.1 Rabi spectroscopy in the resolved sideband regime

The ODMR spectra of section 3.4.3 have revealed resolved sidebands as a consequence of fast modulation of the spin's energy. We have interpreted these sidebands as signatures of multi-photon absorption and emission processes and therefore expect to see similar signatures when performing Rabi spectroscopy. We execute the same measurement of Rabi oscillations for various MW detunings as shown in Figure 3.28 in the presence of a RF signal oscillating at $\Omega_{\text{m}}/2\pi = 15\,\text{MHz}$ with oscillation amplitude $\delta V = 2.5\,\text{V}$. MW frequencies are swept between $\pm 20\,\text{MHz}$ around the qubit resonance at rest ($\omega_0/2\pi = 2.79\,\text{GHz}$ here). The experimental result is presented and compared to the numerical solution of the Bloch equations in Figure 3.32. The latter are obtained by solving equations (2.123), replacing $\delta\omega_0(t)$ by $\delta\omega_0 \cos(\Omega_{\text{m}} t + \alpha)$ and averaging over the initial phase α. One can clearly see that it is possible to drive long lived Rabi oscillations when pumping on the motional sidebands at $\omega = \omega_0 \pm 0, \Omega_{\text{m}}$.

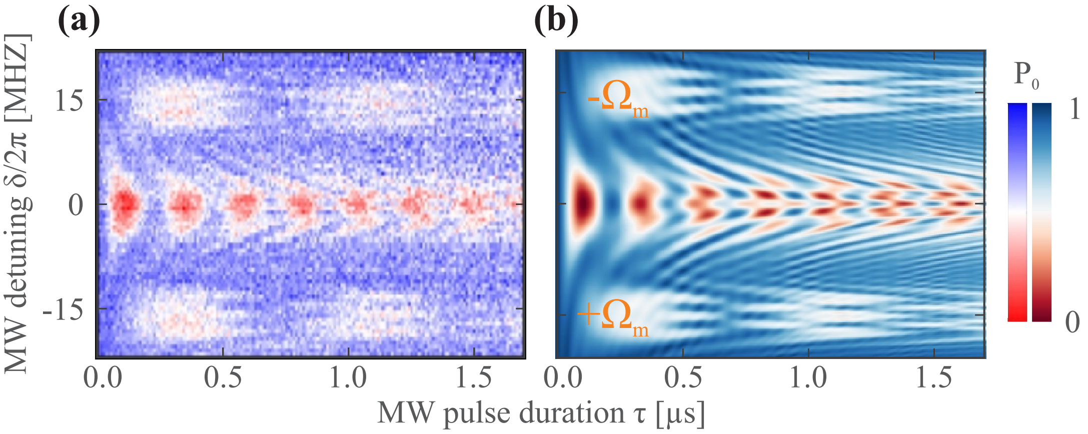

Figure 3.32: Detuned Rabi oscillations with modulation in the resolved sideband regime, $\Omega_\mathrm{m}/2\pi = 15\,\mathrm{MHz}$. **(a)** Experimental data. **(b)** Simulation data.

In section 3.4.4, the sideband area was found by substituting $\Omega_{\mathrm{R},n}^2$ by $\Omega_\mathrm{R}^2 J_n^2\left(\frac{\delta\omega_0}{\Omega_\mathrm{m}}\right)$ in equations (3.17). Here, we justify this step using Rabi spectroscopy, verifying that the effective Rabi frequency of a given sideband is

$$\Omega_{\mathrm{R},n} = \Omega_\mathrm{R} J_n\left(\frac{\delta\omega_0}{\Omega_\mathrm{m}}\right). \tag{3.24}$$

This assumption is tested by varying MW output power Ω_R, oscillation frequency $\Omega_\mathrm{m}/2\pi$ and amplitude $\delta\omega_0$ when measuring Rabi oscillations at $\omega = \omega_0 \pm 0, \Omega_\mathrm{m}$. The results are shown in Figure 3.33 and present remarkable agreement with equation (3.24).

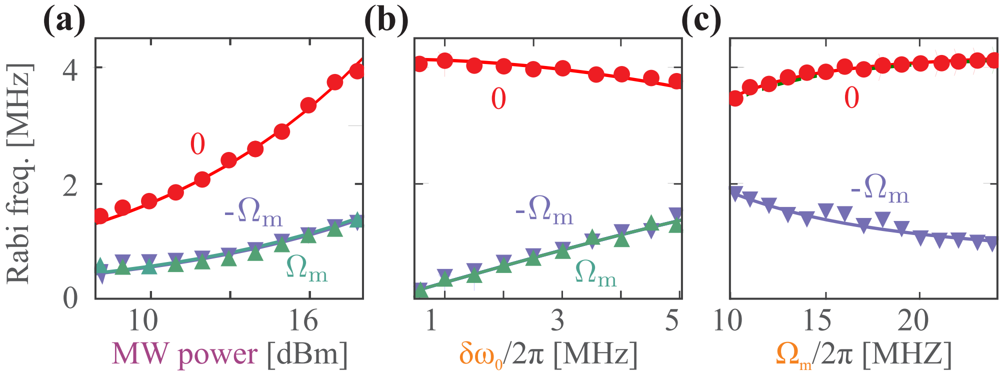

Figure 3.33: Rabi spectroscopy. Solid lines are the expected Rabi frequencies according to expression (3.24). **(a)** Sweep of the MW power. **(b)** Sweep if the modulation frequency. **(c)** Sweep of the oscillation amplitude.

The analysis of Rabi maps presented in Figure 3.32 shows that when the RF frequency is larger than the characteristic linewidth of the Rabi oscillations (which is a function of the MW strength Ω_R, see equation (3.20), it is possible to think of the sideband peaks appearing the the ESR spectra as newly allowed transitions, featuring a reduced coupling strength. It is thus interesting here to adapt the reasoning developed in section 3.5.5 to the spin dynamics in the presence of RF field modulation. Rabi oscillations on the n^th mechanical sideband present a reduced cycling frequency $\Omega_\mathrm{R} J_n\left(\frac{\delta\omega_0}{\Omega_\mathrm{R}}\right)$. For large modulation frequencies, $\Omega_\mathrm{m} \gg \Omega_\mathrm{R}$, this captures the spin dynamics in the resolved sideband regime. However, this image is expected to be wrong when the characteristic frequency of spin evolution becomes comparable to the sideband separation: $\Omega_\mathrm{m} \approx \Omega_\mathrm{R}$. In that case pumping Rabi oscillations on the zeroth order sideband, called the carrier, also off-resonantly pumps Rabi oscillations of the first order sidebands. We now investigate the regime, important for hybrid systems, where the spin dynamics and the mechanical oscillator evolve at similar frequencies.

3.6.2 Observation of spin locking onto the parametrically coupled RF field.

A prominent manifestation of the complex spin dynamics is shown in Figures 3.34 and 3.35. Figure 3.34 **(a)** shows data for unmodulated Rabi oscillations with $\Omega_{\mathrm{R}}/2\pi = 4.3\,\mathrm{MHz}$. This is in contrast to **(b)**, which shows Rabi oscillations where we have added RF modulation at the Rabi frequency, such that $\Omega_{\mathrm{R}}/2\pi = \Omega_{\mathrm{m}}/2\pi = 6\,\mathrm{MHz}$ and $\delta\omega_0/2\pi \approx 3.6\,\mathrm{MHz}$. Notice that the latter case is deep in the resolved sideband regime[4]. A strong beating is observed, as well as a large increase of the characteristic decay time ($\Gamma_{\mathrm{spin}} = 0.65\,\mathrm{MHz}$ here).

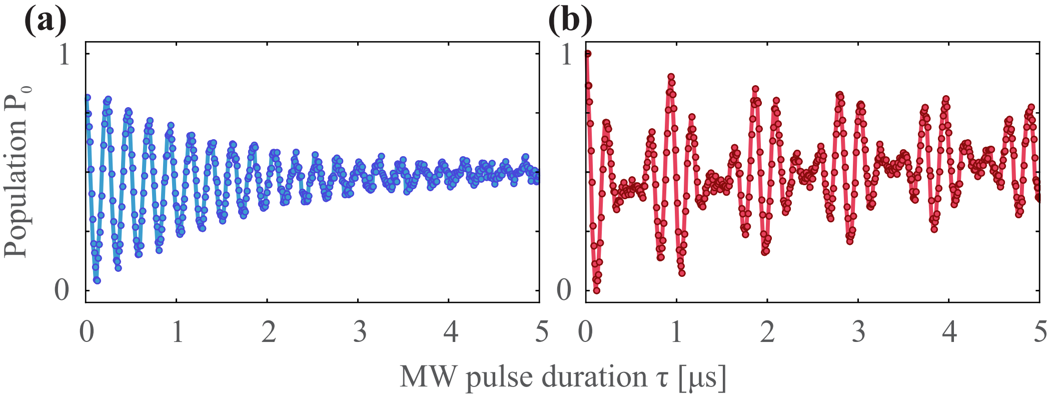

Figure 3.34: Rabi oscillations in absence **(a)** and in presence **(b)** RF modulation tuned to the Rabi frequency, $\Omega_{\mathrm{m}} = \Omega_{\mathrm{R}}$.

The Fourier transforms[5] of both temporal traces are shown in Figure 3.35. In absence of RF modulation, we observe a low frequency decay and a single peak as explained above. This signature changes dramatically in presence of RF parametric modulation. We observe a triplet structure consisting of a central peak at the modulation frequency $\Omega_{\mathrm{m}}/2\pi$ and two sidebands at $(\Omega_{\mathrm{m}} \pm \delta\omega_0/2)/2\pi$. Careful inspection of Figure 3.35 reveals even more interesting details. A small peak at $\delta\omega_0/4\pi$ as well as an interference dip between the central and the sideband peaks are visible. Moreover, the central peak seems much narrower than in the unmodulated case, which corresponds to a larger coherence time evidenced in the temporal trace. The remainder of this chapter is dedicated to explaining this intriguing feature of the dynamics of a parametrically modulated spin. In order to further explore the signatures of Figure 3.35, we perform three additional measurements, varying the microwave power ($\Omega_{\mathrm{R}}/2\pi$), the oscillation amplitude ($\delta\omega_0/2\pi$) and the mechanical frequency ($\Omega_{\mathrm{m}}/2\pi$).

---

[4] The observation of several oscillations implies that $\Omega_{\mathrm{R}} > \Gamma_{\mathrm{spin}}$. Since $\Omega_{\mathrm{m}} = \Omega_{\mathrm{R}}$, we have $\Omega_{\mathrm{m}} > \Gamma_{\mathrm{spin}}$, the condition for operation in the resolved sideband regime.

[5] Here we use the DFT convention of the Numerical Python package *Numpy* [167]. Fourier coefficients are defined as $A_k = \sum_{m=0}^{n-1} a_m \exp\left\{-2\pi i \frac{mk}{n}\right\} \quad k = 0, ..., n-1$. Unless stated otherwise, we will give the absolute values $|A_k|$. Notice that the population P_0 oscillates around the steady state value of $P_0 = \frac{1}{2}$, which yields a constant value of $P_0[\Omega = 0] = \frac{1}{2}$, representing the mean value of $P(\tau)$. Throughout this work, this constant term has been suppressed in all plots of Fourier spectra for reasons of visibility of the regions where $\Omega > 0$.

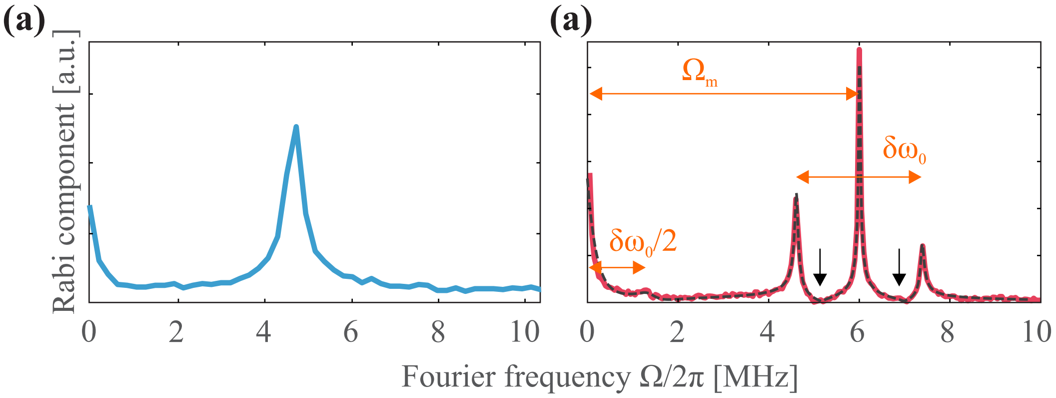

Figure 3.35: The Fourier transforms of the Rabi oscillations of Figure 3.34 in absence **(a)** and in presence **(b)** RF modulation tuned to the Rabi frequency, $\Omega_\mathrm{m} = \Omega_\mathrm{R}$.

3.6.3 Triple peak structure and spin locking

We investigate here the dependence of the triplet structure on the spin precession frequency ($\Omega_\mathrm{R}/2\pi$) and demonstrate that our observation can be viewed as a locking onto the RF tone. We choose a modest RF voltage amplitude of $\delta V = 0.75\,\mathrm{V}$, which creates a frequency shift $\delta\omega_0/2\pi = 2.7\,\mathrm{MHz}$ and measure resonant Rabi oscillations ($\omega = \omega_0$) for varying MW power in order to generate Rabi frequencies $\Omega_\mathrm{R}/2\pi$ between 2 MHz and 7 MHz across $\Omega_\mathrm{m}/2\pi = 6\,\mathrm{MHz}$. The temporal traces are shown for reasons of completeness in Figure 3.36, but the signatures are more conclusive in the frequency space and the Fourier transformed data are presented in Figure 3.37. The lower left branch represents the Rabi peak rising towards larger frequencies as the MW power is increased. However, it avoids a crossing at $\Omega_\mathrm{m}/2\pi$ for a MW power that generates Rabi oscillations at 6 MHz in absence of energy modulation. As the power is increased beyond $\Omega_\mathrm{R} = \Omega_\mathrm{m}$, the branch reverses but with reduced visibility. On the other hand an upper branch appears around $\Omega_\mathrm{R} \approx \Omega_\mathrm{m}$, gaining in intensity and curving towards larger frequencies as the MW power is further increased. These two branches represent the sidebands of Figure 3.35 **(b)** around the central peak, which emerges very early, for MW powers corresponding to $\sim 3\,\mathrm{MHz}$. It gains maximum intensity around $\Omega_\mathrm{R} = \Omega_\mathrm{m}$ but still persists at larger drive strength. We interpret the latter signature as a *spin locking effect*: the RF frequency representing the periodic mechanical motion becomes mapped onto the spin dynamics even at drive strength that usually do not produce Rabi oscillations at the resonator's *eigenfrequency*. The synchronization region here appears to be centered around $\Omega_\mathrm{R} = \Omega_\mathrm{m}$ in with a width of $\approx \delta\omega_0$.

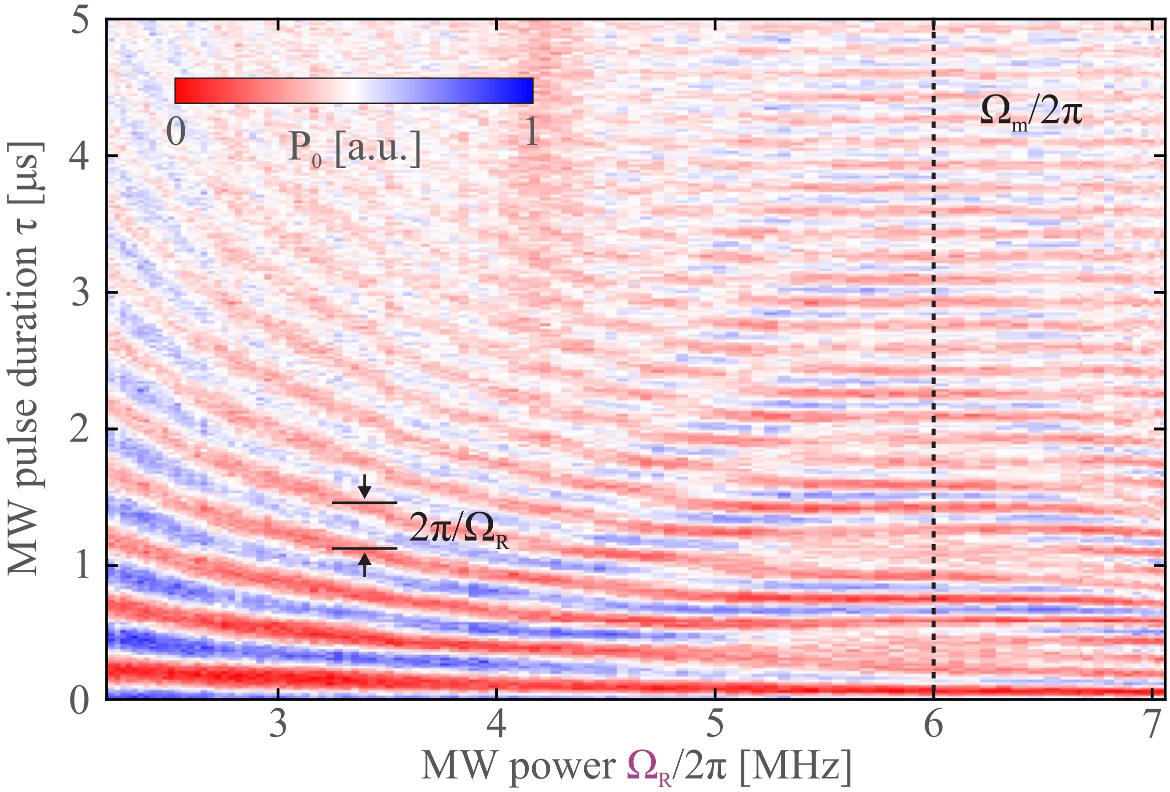

Figure 3.36: Sweep of the Rabi frequency across the mechanical frequency. The temporal map shows the initial acceleration of Rabi oscillations until the synchronization region is reached. Close to $\Omega_\mathrm{R}/2\pi = \Omega_\mathrm{m}/2\pi = 6\,\mathrm{MHz}$ a constant oscillation is visible and beating patterns emerge.

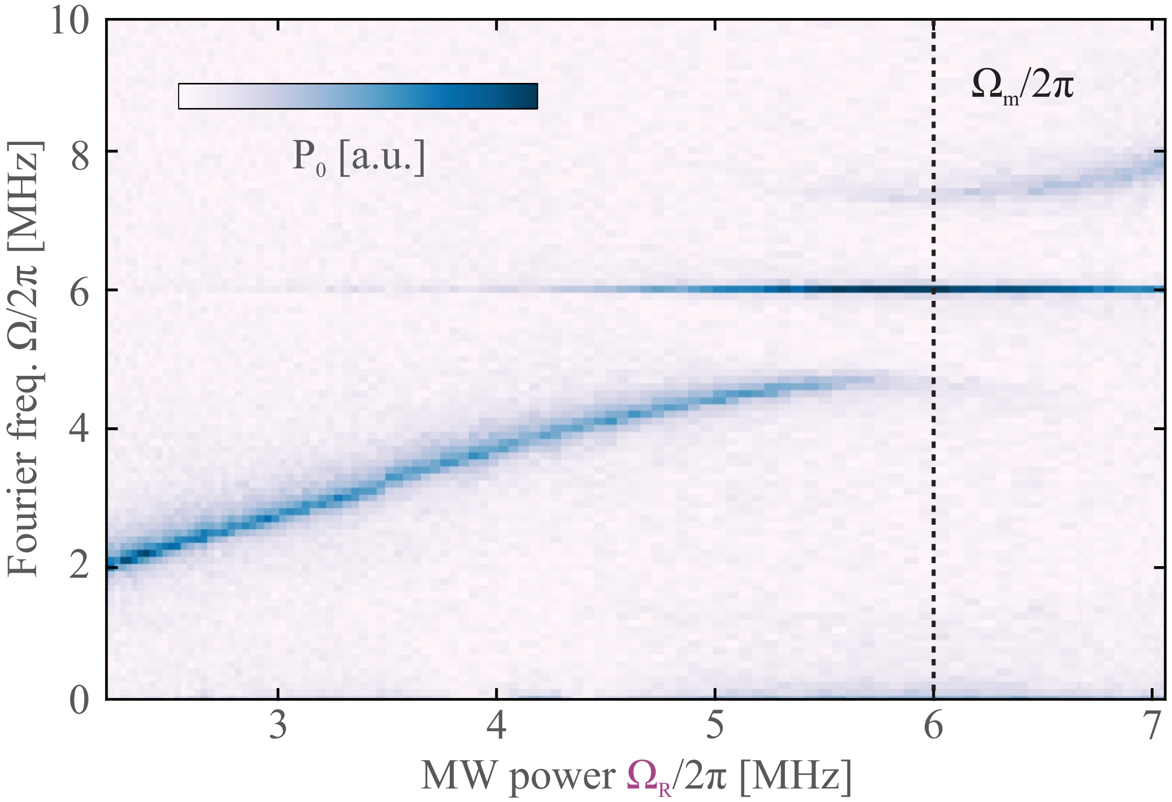

Figure 3.37: Sweep of the Rabi frequency across the mechanical frequency. The Fourier map shows an anti-crossing of the Ω_R-component close to Ω_m. The central component oscillating at $\Omega_\mathrm{m}/2\pi$ emerges for $\Omega_\mathrm{R} < \Omega_\mathrm{m}$ and stays isolated, suppressing frequency components in its vicinity.

In order to better understand the strength of the vertical anticrossing between the upper and the lower branch, we measure Rabi oscillations at the spin locking condition $\Omega_\mathrm{R} \simeq \Omega_\mathrm{m} = 2\pi \times 5\,\mathrm{MHz}$ and increase the amplitude of the RF field. The data, shown in Figure 3.38 **(a)**, demonstrates that the gap size between the sidebands is $\delta\omega_0$, meaning that not only the oscillation frequency but also the amplitude is imprinted on the spin dynamics. We furthermore see that the sidebands of the triple peak only separate from the central component once the RF amplitude is sufficiently large, such that the separation beats the central component's linewidth. This is the case when $\delta\omega_0 > \Gamma_\mathrm{spin}$, since the width of each Fourier component represents the decay rate of the corresponding oscillation. It can therefore be said that the spin dynamics are in a *strong coupling regime of the parametric interaction*. Here we use the term *strong coupling* in reference to cavity QED experiments, where it is usually employed in the context of resonant coupling.

In Figure 3.38 **(b)**, we operate with a fixed Rabi frequency, $\Omega_\mathrm{R}/2\pi = 5\,\mathrm{MHz}$ and choose a RF amplitude of $\delta\omega_0/2\pi = 2.7\,\mathrm{MHz}$. This time we vary the RF frequency across the Rabi frequency. Even though conceptually not different from the measurement presented in Figure 3.37 it aids the understanding of the underlying physics. For small values of the RF frequency, we see that the dynamics are governed by two peaks, at the frequency of the field and the Rabi oscillation. When the RF frequency approaches the frequency of spin dynamics, a coupling occurs, causing a splitting of the observed components. If the RF frequency is further increased, the components become again clearly separable into the RF/ phonon field and Rabi component.

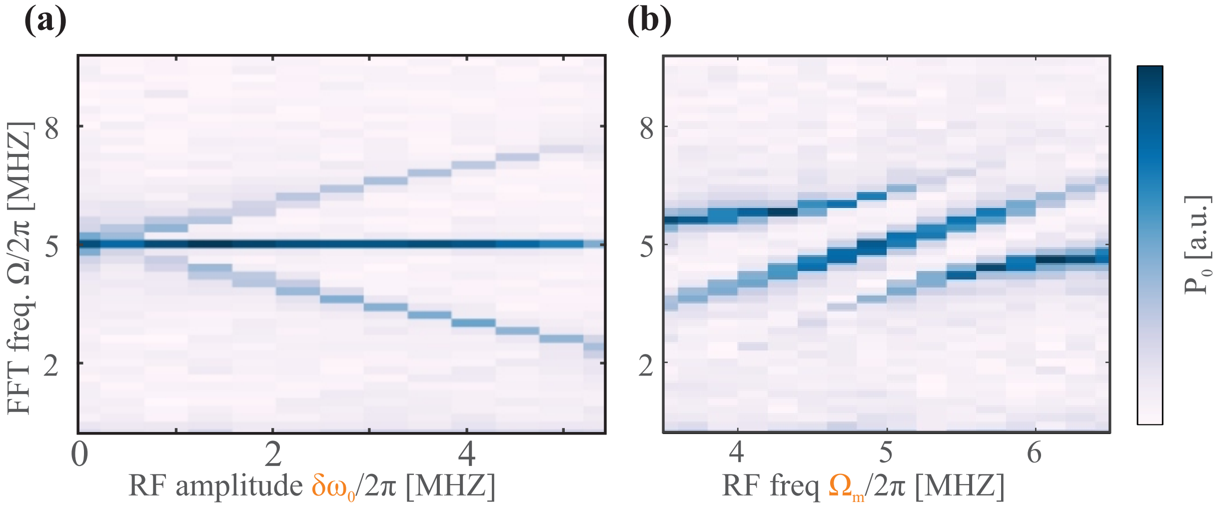

Figure 3.38: Investigation of the triplet structure. **(a)** The amplitude $\delta\omega_0$ is varied at the spin locking condition $\Omega_{\mathrm{R}} = \Omega_{\mathrm{m}}$. A triplet signature emerges once the sideband separation is larger than the linewidth of each component, $\delta\omega_0 > \Gamma_{\mathrm{spin}}$. **(b)** Sweep of the mechanical frequency. A coupling signature arises as soon as Ω_{m} approaches Ω_{R}. Such a signature is strongly analogous to a resonant interaction between a single atom and a cavity field [159].

The experiments described above all show the emergence of a well protected central component oscillating at the mechanical frequency. Like a phase lock loop, the spin, here behaving as the slave, becomes locked onto the master (the classical RF field) and variations of the MW power do not affect the effective Rabi frequency close to $\Omega_{\mathrm{m}}/2\pi$. A window of suppressed frequencies emerges and the spin dynamics become locked onto the the mechanical oscillator. Naturally, the question of the relative phase between spin and oscillator arises. Since experimentally we do not control the phase between RF field and Rabi oscillations, we will later show theoretically that the component of the population rotating at Ω_{m} is indeed synchronized to the mechanical oscillations. The term *spin locking* is also used in the Nuclear Magnetic Resonance (NMR) language, where it describes an experimental protocol to suppress dephasing processes in a spin ensemble. Quite similarly to the case here, this is achieved by means of application of an external field rotating at the Larmor frequency of the spins. We will later clarify the link between the two variations of the spin locking protocol. Furthermore, the presented data are reminding of the interaction between an atom and a near resonant electromagnetic field in a cavity [159] and exhibit a strong similarity to the Mollow triplet [168]. In the following, we will formalize the described phenomena and justify this analogy.

3.6.4 Explanation in terms of a doubly dressed qubit

We formalize here the two-tone interaction (MW and RF field) with the NV qubit in terms of a double dressing of the spin. We begin by considering the effect of the quasiresonant MW field on the spin enabling a first dressing. Then, we investigate the role of the RF field emulating the mechanical motion. We find that by probing the MW dressed spin with the phonon field we can explain the triple peak features and anti-crossing in the FFT spectra. Reversely, this picture also leads to an explanation of the Bessel-like dependence of the effective Rabi frequency.

Dressing the spin with the MW field

Using the matrices

$$\hat{\sigma}_x = \begin{pmatrix} 0 & 1 \\ 1 & 0 \end{pmatrix}; \hat{\sigma}_y = \begin{pmatrix} 0 & -i \\ i & 0 \end{pmatrix}; \hat{\sigma}_z = \begin{pmatrix} 1 & 0 \\ 0 & 0 \end{pmatrix}, \tag{3.25}$$

we consider the total Hamiltonian:

$$H_{\text{tot}} = H_0 + H_{\text{MW}} + H_{\text{int}} \tag{3.26}$$

with

$$H_0 = \hbar\omega_0\hat{\sigma}_z + \hbar\Omega_{\text{m}}\hat{a}^\dagger\hat{a} + \hbar\omega\hat{b}^\dagger\hat{b}, \tag{3.27}$$

$$H_{\text{MW}} = \frac{\hbar\Omega_{\text{R}}^v}{2}(\hat{b}^\dagger + \hat{b})(\sigma^+ + \sigma^-), \tag{3.28}$$

$$H_{\text{int}} = \hbar g_z(\hat{a}^\dagger + \hat{a})\sigma_z. \tag{3.29}$$

The generic eigenstates of H_0 are $|m_s, N, M\rangle$, where $m_s = 0, 1$ is the spin state, N the photon number and M the phonon number[6]. Their eigenenergies are (setting the ground state ($|0, 0, 0\rangle$) energy $(\hbar\omega + M\hbar\Omega_{\text{m}})/2$ to 0):

$$E_{|m_s,N,M\rangle}/\hbar = m_s\hbar\omega_0 + N\hbar\omega + \hbar\Omega_{\text{m}}. \tag{3.30}$$

The following considerations are valid in the *secular limit* where $\Omega_{\text{R}} \gg \Gamma$ and where $\langle N\rangle \gg \Delta N \gg 1$. We first consider H_{MW}, which does not affect the phonon field. Using the rotating wave approximation, which corresponds to dropping the off-resonant terms[7] in H_{MW} ($\hat{b}^\dagger\sigma^+$ and $\hat{b}\sigma^-$), we obtain

$$H_{\text{MW}}^{\text{RWA}} = \frac{\hbar\Omega_R^v}{2}(\hat{b}^\dagger\sigma^- + \hat{b}\sigma^+). \tag{3.31}$$

The coupling term of the so called *Jaynes-Cummings model* [159] corresponds to interactions where a spin excitation is traded for a MW field excitation. It only couples between sets of states $\{|0, N\rangle, |1, N-1\rangle\}$. We therefore introduce the multiplicities ($N \geq 1$)

$$\mathcal{E}(N) = \{|1, N-1\rangle, |0, N\rangle\}. \tag{3.32}$$

The total + MW Hamiltonian (neglecting the phonon field) is an infinite tensor product

$$H_{\text{tot}} + H_{\text{MW}}^{\text{RWA}} = \bigotimes_N H^{(N)}, \tag{3.33}$$

reflecting the coupling of the TLS to each Fock state of the coherent field. If $\delta \equiv \omega - \omega_0$ is the MW detuning, we have the Hamiltonian $H^{(N)}$ acting in the subspace $\mathcal{E}(N)$:

$$H^{(N)}/\hbar = \begin{pmatrix} N\omega - \delta & \frac{\Omega_{\text{R}}^v\sqrt{N}}{2} \\ \frac{\Omega_{\text{R}}^v\sqrt{N}}{2} & N\omega \end{pmatrix}. \tag{3.34}$$

Diagonalization of the Hamiltonian leads to new eigenstates $|\pm_N\rangle$ with energies

$$E_{|\pm_N\rangle}/\hbar = N\omega - \frac{\delta}{2} \pm \frac{1}{2}\sqrt{\delta^2 + N{\Omega_{\text{R}}^v}^2} \tag{3.35}$$

featuring a splitting of

$$\Delta_N = \sqrt{\delta^2 + N{\Omega_{\text{R}}^v}^2}. \tag{3.36}$$

We find the new eigenstates by making the linear transformation

$$\begin{pmatrix} |+_N\rangle \\ |-_N\rangle \end{pmatrix} = \begin{pmatrix} \cos\theta_N & \sin\theta_N \\ -\sin\theta_N & \cos\theta_N \end{pmatrix} \begin{pmatrix} |1, N-1\rangle \\ |0, N\rangle \end{pmatrix}, \tag{3.37}$$

---

[6] We change to using capital letters N and M denoting photon and phonon number for aesthetic reasons.

[7] This is justified as long as $\Omega_{\text{R}}^v\sqrt{N} = \Omega_{\text{R}} \ll \omega_0$.

using

$$\tan 2\theta_N = -\frac{\Omega_\mathrm{R}^v \sqrt{N}}{\delta} \quad \text{with} \quad \theta_N \in [0, \pi/2] \tag{3.38}$$

and

$$\cos\theta_N = \sqrt{\frac{1-\delta/\Delta_N}{2}}, \tag{3.39}$$

$$\sin\theta_N = \sqrt{\frac{1+\delta/\Delta_N}{2}}. \tag{3.40}$$

The new eigenstates,

$$\begin{aligned} |+_N\rangle &= \cos\theta_N |1, N-1\rangle + \sin\theta_N |0, N\rangle, \\ |-_N\rangle &= -\sin\theta_N |1, N-1\rangle + \cos\theta_N |0, N\rangle \end{aligned} \tag{3.41}$$

are called the *dressed* states. Their energies are shown below in Figure 3.39. Importantly, the interaction between MW and spin causes an energy splitting of Δ_N in $\mathcal{E}_N$, giving rise to the *Jaynes-Cummings energy ladder* with sets of rungs $\Big\{|-_N\rangle, |+_N\rangle\Big\}$. If the MW field is described by a large amplitude coherent field $|\alpha\rangle = e^{-|\alpha|^2/2} \sum\limits_{n=0}^{\infty} \frac{\alpha^n}{\sqrt{n!}} |n\rangle$, the photon distribution is given by $P(N) = e^{-|\alpha|^2} \frac{\alpha^{2N}}{N!}$, which is centered around $\bar{N} = |\alpha|^2$ with width $\Delta N = \sqrt{\bar{N}}$. The variation of the rung spacing Δ_N does not vary significantly over the photon distribution. Then, for a large coherent drive strength ($\bar{N} \gg 1$) the splitting can be described by the classical field amplitude, $\Omega_\mathrm{R}^v \sqrt{\langle N \rangle} = \Omega_\mathrm{R}^v |\alpha| = \Omega_\mathrm{R}$, so that $\Delta_N = \sqrt{\Omega_\mathrm{R}^2 + \delta^2}$ for $N - \bar{N} \ll \Delta N$. This resonant coupling effect is also called *dressing* of the qubit with the MW field. The resulting energy diagram is illustrated in Figure 3.39.

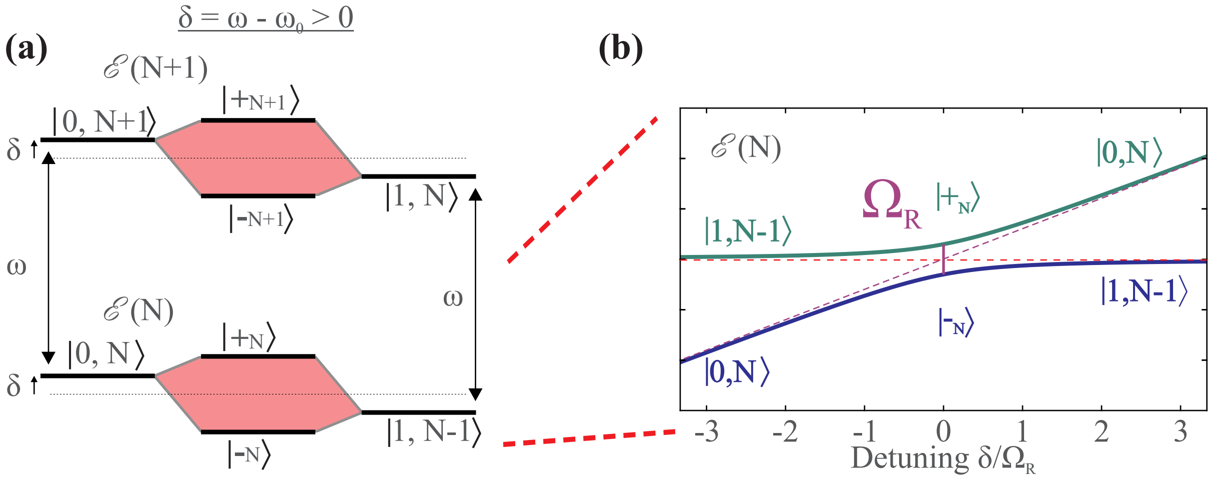

Figure 3.39: Energy diagram of the qubit dressed by the MW field. **(a)** Neighboring multiplicities $\mathcal{E}_N$ and $\mathcal{E}_{N+1}$ are separated by $\hbar\omega$ and give rise to the Jaynes-Cummings energy ladder. **(b)** Within one multiplicity, the uncoupled states $|1, N-1\rangle$ and $|0, N\rangle$ become coupled by a near resonant MW field. At $\delta = 0$ their splitting corresponds to the Rabi frequency $\Delta_N = \hbar\Omega_\mathrm{R}$.

As a remark, it is interesting to note that the dressed states correspond to a rotation of the eigenstates by an angle $2\theta_N$ in the Bloch sphere (see the expressions in (3.41)). Notice that the angle θ_N is closely related to the angle η described by the effective field of the Bloch-Redfield theory of section 3.5.5 and that the strength of the effective field corresponds to the splitting Δ_N. Before investigating the role of the phonon field, it is important to calculate the effect of the σ_z operator, describing the parametric interaction, on the dressed states. Within one multiplicity $\mathcal{E}(N)$, it can be expressed in the basis $\{|+_N\rangle, |-_N\rangle\}$ by:

$$\sigma_z|_{\mathcal{E}(N)} = \begin{pmatrix} \cos^2\theta_N & -\cos\theta_N\sin\theta_N \\ -\cos\theta_N\sin\theta_N & \sin^2\theta_N \end{pmatrix} = \begin{pmatrix} \cos^2\theta_N & -\frac{1}{2}\sin 2\theta_N \\ -\frac{1}{2}\sin 2\theta_N & \sin^2\theta_N \end{pmatrix}. \tag{3.42}$$

This point shows that the σ_z operator now has some non-trivial action on the new dressed eigenstates: the phonon field described by H_{int} can induce transitions among the dressed states (notice that σ_z does not couple states between different multiplicities).

Dressing the MW dressed states with the phonon field

Effect of the phonon field on the MW dressed states In the picture of dressed states the role of longitudinal and transversal magnetic field components are interchanged, as, for near resonant pumping, the dressed spin is polarized along an axis in the equatorial plane of the Bloch sphere. This is a consequence to having rotated the eigenvectors onto the equator of the original Bloch sphere, see equation (3.41). Hence, a magnetic field along the **z**-direction oscillating at frequency $\Omega_\text{m}/2\pi$ can induce transitions between the dressed states if the field is resonant with their energy splitting $\hbar\Delta_N = \hbar\Omega_\text{R}$. In order to explain the dressing of MW dressed states with the RF field, we proceed as before, starting in the eigenbasis of the MW dressed states. We add the phonon field and the generic eigenstates are now of the form $|\pm_N, M\rangle$. Since the hybrid interaction Hamiltonian,

$$H_{\text{int}} = \hbar g_z(\hat{a}^\dagger + \hat{a})\sigma_z,$$

does not couple multiplicities with different photon number N but permits raising or lowering phonon number M, its effect can be studied between dressed states combined with adjacent phonon number states only, as

$$H_{\text{int}}^{N,\Delta M=\pm 1} \propto \tag{3.43}$$

$$\begin{array}{c} \\ |-_N, M+1\rangle \\ |+_N, M\rangle \\ |-_N, M\rangle \\ |+_N, M-1\rangle \\ |-_N, M-1\rangle \\ |+_N, M-2\rangle \end{array} \begin{array}{c} \begin{array}{cccccc} |-_N, M+1\rangle & |+_N, M\rangle & |-_N, M\rangle & |+_N, M-1\rangle & |-_N, M-1\rangle & |+_N, M-2\rangle \end{array} \\ \begin{pmatrix} 0 & -\frac{\sqrt{M+1}}{2}\sin 2\theta_N & \sqrt{M+1}\sin^2\theta_N & 0 & 0 & 0 \\ -\frac{\sqrt{M+1}}{2}\sin 2\theta_N & 0 & 0 & \sqrt{M}\cos^2\theta_N & -\frac{\sqrt{M}}{2}\sin 2\theta_N & 0 \\ \sqrt{M+1}\sin^2\theta_N & 0 & 0 & -\frac{\sqrt{M}}{2}\sin 2\theta_N & \sqrt{M}\sin^2\theta_N & 0 \\ 0 & \sqrt{M}\cos^2\theta_N & -\frac{\sqrt{M}}{2}\sin 2\theta_N & 0 & 0 & \sqrt{M-1}\cos^2\theta_N \\ 0 & -\frac{\sqrt{M}}{2}\sin 2\theta_N & \sqrt{M}\sin^2\theta_N & 0 & 0 & -\frac{\sqrt{M-1}}{2}\sin 2\theta_N \\ 0 & 0 & 0 & \sqrt{M-1}\cos^2\theta_N & -\frac{\sqrt{M-1}}{2}\sin 2\theta_N & 0 \end{pmatrix} \end{array}.$$

Having realized that the action of σ_z can induce spin flips in the dressed state basis, it is natural to invoke a dressing of the dressed states with the phonon field. Allowed transitions between neighboring multiplicities are shown in Figure 3.40 **(a)**, which also highlights that due to the interaction Hamiltonian dressed state populations can leave a given multiplicity (here shown as orange boxes):

$$\mathcal{F}(N, M) = \Big\{|+_N, M-1\rangle, |-_N, M\rangle\Big\}. \tag{3.44}$$

However, the inter-multiplicity transition are due to fast rotating coherences and we can neglect their contribution by means of a second rotating wave approximation[8], this time on the phonon field oscillating at $\Omega_\text{m}/2\pi$. We are then left with only the intra-multiplicity transitions, shown in Figure 3.40 **(b)**.

---

[8] This approximation is valid as long as $g_z\sqrt{M} \ll \Omega_\text{R}$, see section 3.6.5.

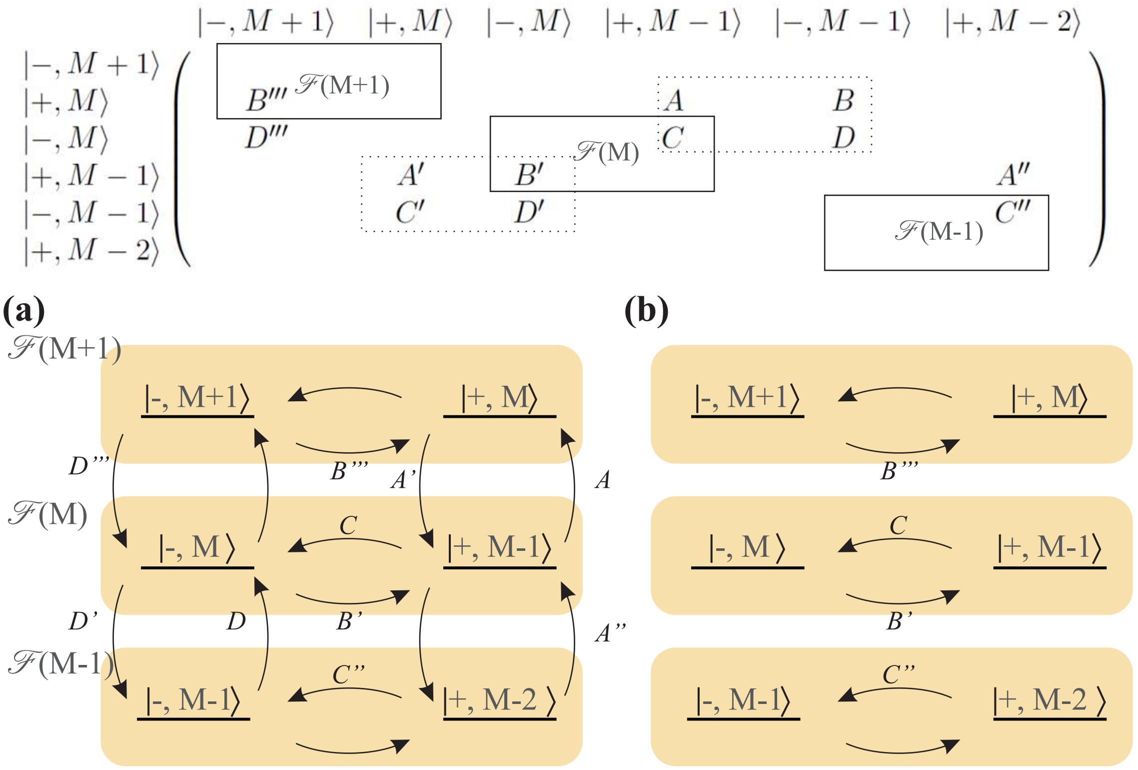

Figure 3.40: Effect of the hybrid Hamiltonian on the $|\pm\rangle$ basis. The label N for the photon number was omitted as there is no coupling between the multiplicities $\mathcal{E}_N$. The above table presents the matrix elements of the $(\hat{a}^\dagger + \hat{a})\sigma_z$ interaction Hamiltonian. The multiplicities $\mathcal{F}(M \pm 0, 1)$ are indicated by the boxes, indicating the intra-multiplicity transitions. The dotted frames indicate inter-multiplicity transitions due to the second dressing. Notice that these are two fold. The transition C' corresponds to an energy penalty of $2\hbar\Omega_\mathrm{m}$ and is typically omitted by the RWA of the Jaynes-Cummings model. Contributions of such terms lead to the Bloch-Siegert corrections discussed in the next section. Transitions A' and D' occur with an energy penalty $\hbar\Omega_\mathrm{m}$. They correspond to the vertical couplings shown in **(a)** and do not, as opposed to C', change the state of the singly dressed spin. Panel **(b)** highlights the intra-multiplicity transitions, which are left after the rotating wave approximation.

Then, the interaction Hamiltonian can be approximated by its restriction to the intra-multiplicities, so that

$$H^{(\mathrm{N})}_{\mathrm{int}} = \frac{\hbar g_z}{2}\left(\hat{a}^\dagger|-_N\rangle\langle+_N| + \hat{a}|+_N\rangle\langle-_N|\right) \tag{3.45}$$

in the $\mathcal{F}(N,M)$ basis, having uncoupled energies

$$E_{|\pm_N,M\rangle}/\hbar = N\omega - \frac{\delta}{2} \pm \frac{1}{2}\sqrt{\delta^2 + N{\Omega^v_R}^2} + M\Omega_\mathrm{m}. \tag{3.46}$$

One has then to consider $H^{(N,M)} = H^{(N)} + H^{(M)}_{\mathrm{int}}$ acting on in the multiplicity $\mathcal{F}(N,M)$, which can be reduced to

$$H^{(N,M)}/\hbar = \begin{pmatrix} \Delta_N - \Omega_\mathrm{m} & g_{N,M}/2 \\ g_{N,M}/2 & 0 \end{pmatrix}, \tag{3.47}$$

where an energy offset of $\hbar(N\omega - \delta/2 - \Delta_N.2 + M\Omega_\mathrm{m})$ has been subtracted and $g_{N,M}$ is defined as

$$g_{N,M} \equiv -\frac{g_z\sqrt{M}}{2}\sin 2\eta_N = -\frac{g_z\sqrt{M}}{2}\frac{\Omega^v_\mathrm{R}\sqrt{N}}{\Delta_N}. \tag{3.48}$$

Since Hamiltonian (3.47) has the same form as Hamiltonian (3.34), we can directly write down eigenenergies $E_{|\pm_{N,M}\rangle}$ and eigenstates $|\pm_{N,M}\rangle$ in terms of $\{|+_N, M-1\rangle, |-_N, M\rangle\}$. We find

$$E_{|\pm_{N,M}\rangle} = N\omega - \frac{\delta}{2} + M\Omega_\mathrm{m} - \frac{\Omega_\mathrm{m} - \Delta_N}{2} \pm \frac{1}{2}\Delta_{N,M}, \tag{3.49}$$

where

$$\Delta_{N,M} \equiv \sqrt{(\Omega_\mathrm{m} - \Delta_N)^2 + g_{N,M}^2} \tag{3.50}$$

and (following the procedure from the section above)

$$|+_{N,M}\rangle = \cos\theta_{N,M}|+_N, M-1\rangle + \sin\theta_{N,M}|-_N, M\rangle, \tag{3.51}$$

$$|-_{N,M}\rangle = -\sin\theta_{N,M}|+_N, M-1\rangle + \cos\theta_{N,M}|-_N, M\rangle \tag{3.52}$$

and

$$\tan 2\theta_{N,M} = -g_{N,M}/(\Omega_\mathrm{m} - \Delta_N) \quad \text{with} \quad \theta_{N,M} \in [0, \pi/2]. \tag{3.53}$$

We see now that $\Omega_\mathrm{m} - \Delta_N$ plays the role of δ for the singly dressed qubit. For a large MW and RF drive, $\sqrt{N}\Omega_\mathrm{R}^v \to \Omega_\mathrm{R}$, $\sqrt{M}g^v \to \delta\omega_0$, the splitting becomes $\Delta_{N,M} \to \Delta_\mathrm{Mollow}$, with

$$\Delta_\mathrm{Mollow} = \sqrt{\left(\Omega_\mathrm{m} - \sqrt{\delta^2 + \Omega_\mathrm{R}^2}\right)^2 + \left(\frac{\delta\omega_0}{2}\right)^2 \frac{\Omega_\mathrm{R}^2}{\delta^2 + \Omega_\mathrm{R}^2}}. \tag{3.54}$$

In case of resonant pumping $\delta = 0$, it simplifies to:

$$\Delta_\mathrm{Mollow} = \sqrt{(\Omega_\mathrm{m} - \Omega_\mathrm{R})^2 + \left(\frac{\delta\omega_0}{2}\right)^2}. \tag{3.55}$$

Frequencies of Rabi oscillations

As discussed earlier in this section, the frequencies present in the Rabi oscillations correspond to the energy differences between the doubly dressed states. The eigenstates of neighboring multiplicities $\mathcal{F}_{N,M}$ are coupled by the σ_z operator. Transitions featuring $\Delta M = \pm 1$ occur as follows:

$|+_{N,M+1}\rangle \leftrightarrow |-_{N,M}\rangle$ oscillating at $\Omega_\mathrm{m} + \Delta_{N,M}$

$|-_{N,M+1}\rangle \leftrightarrow |-_{N,M}\rangle$ oscillating at Ω_m

$|+_{N,M+1}\rangle \leftrightarrow |+_{N,M}\rangle$ oscillating at Ω_m

$|-_{N,M+1}\rangle \leftrightarrow |+_{N,M}\rangle$ oscillating at $\Omega_\mathrm{m} - \Delta_{N,M}$

$|+_{N,M}\rangle \leftrightarrow |-_{N,M}\rangle$ oscillating at $\Delta_{N,M}$

Table 3.1: Frequencies of Rabi oscillations and the corresponding transitions between the doubly dressed states.

These frequencies indeed well reproduce the observed components in the Fourier spectra of Rabi oscillations. This is demonstrated in Figure 3.41 **(a)**, which shows the same measurement as Figure 3.37 but with the above frequencies superposed, using $\delta\omega_0/2\pi = 2.7\,\mathrm{MHz}$. There is good agreement with the components oscillating at $\Omega_\mathrm{m}, \Omega_\mathrm{m} \pm \Delta_{N,M}$. However, there are two remarks to make. First, the position of the anticrossing between the upper and the lower branches does not seem to coincide with the MW power corresponding to $\Omega_\mathrm{R} = \Omega_\mathrm{m}$. Second, it seems as if the component oscillating at

$\Delta_{N,M}$ is completely absent in this measurement (whereas it is slightly visible in Figure 3.35). The absence of Rabi oscillations at $\Delta_{N,M}$ demands that we develop a more exact picture of the underlying physics, which will eventually allow us to understand the individual weights of each component. Before we do so, we consider the first remark concerning the position of the anticrossing.

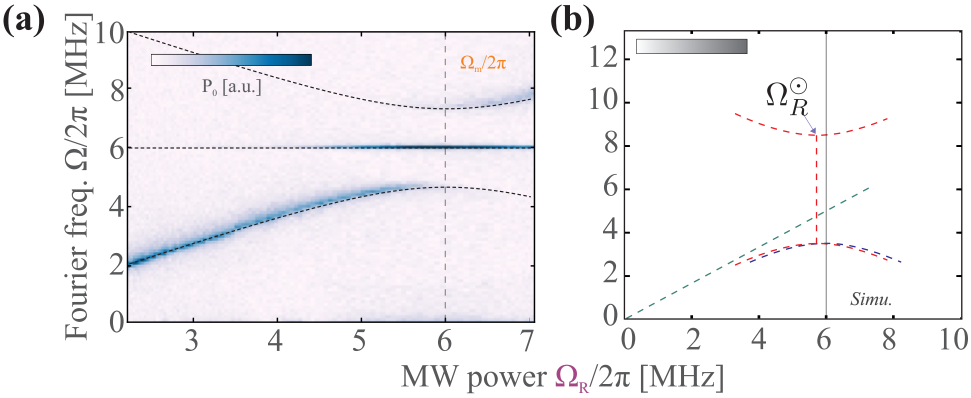

Figure 3.41: Frequencies of Rabi oscillations. **(a)** The experimental data is compared to the expressions in table 3.1. **(b)** Simulations showing how the oscillation frequencies are modified by the Bloch-Siegert shift. The blue trace indicates components due to unperturbed energies, whereas the red traces indicate those due to the Bloch-Siegert shift.

3.6.5 Bloch - Siegert shifts

The Bloch-Siegert shift of a TLS's resonance frequency towards larger energies is due to the counter-rotating terms of the applied field and start to play a role as soon as the coupling strength becomes comparable to the qubit energy splitting ($\Omega_\mathrm{R} \sim \omega_0$ or $\delta\omega_0 \sim \Omega_\mathrm{R}$). Indeed, in our system coupling strengths on the order of the dressed qubit's energy splitting, ($\delta\omega_0 \approx \Omega_\mathrm{R}$), are easily obtainable. We therefore explore the Bloch-Siegert shift due to the phonon field, which is indeed visible in our simulations and experimental data shown in Figure 3.42. We consider $\delta = 0$ in the following. The application of the phonon field at Ω_m increases the splitting of the dressed qubit, as seen by the co-propagating phonon field, to $\Delta_N(\Omega_\mathrm{R}) \to \Delta_N^{\mathrm{BS}}$. That is, as we are sweeping the MW power in measurements like the one of Figure 3.37, and therefore increasing the Rabi frequency, the Bloch-Siegert corrected frequency at which the spin is rotating, Δ_N^{BS}, is ahead of Ω_R. The resonance condition for the phonon field, $\Delta_N^{\mathrm{BS}} = \Omega_\mathrm{m}$, is therefore met for smaller drive power than otherwise expected: $\Omega_\mathrm{R} < \Omega_\mathrm{m}$. We denote $\Omega_\mathrm{R}^{\odot}$ the value of the parametrized MW power at which $\Delta_N^{\mathrm{BS}} = \Omega_\mathrm{m}$. According to [169] the minimum splitting between the perturbed energy eigenstates occurs at $\Omega_\mathrm{R} = \Omega_\mathrm{R}^{\odot}$, with

$$\Omega_\mathrm{R}^{\odot} \equiv \Omega_\mathrm{m} - \frac{\left(\frac{\delta\omega_0}{4}\right)^2}{\Omega_\mathrm{m}} - \frac{5\left(\frac{\delta\omega_0}{4}\right)^4}{4\,\Omega_\mathrm{m}^3} - \frac{61\left(\frac{\delta\omega_0}{4}\right)^6}{32\,\Omega_\mathrm{m}^5}. \tag{3.56}$$

On the other hand, we also observe a shift to larger MW powers for the absorption peak of the central component. We find from numerical simulations that its position can be well predicted by inverting the expression for $\Omega_\mathrm{R}^{\odot}$ [169]. Denoting Ω_R^{*} the MW power at which the central peak exhibits its maximum, we have

$$\Omega_\mathrm{R}^{*} \equiv \Omega_\mathrm{R} + \frac{\left(\frac{\delta\omega_0}{4}\right)^2}{\Omega_\mathrm{R}} + \frac{\left(\frac{\delta\omega_0}{4}\right)^4}{4\,\Omega_\mathrm{R}^3} - \frac{36\left(\frac{\delta\omega_0}{4}\right)^6}{32\,\Omega_\mathrm{R}^5}. \tag{3.57}$$

Even though it is clear that this shift arises from higher order contributions of the parametric hybrid interaction coupling the MW dressed states, its interpretation has been difficult and remains an open question. Nonetheless, the above expressions are in quantitative agreement with simulations and in qualitative agreement with experimental data, see Figure 3.42.

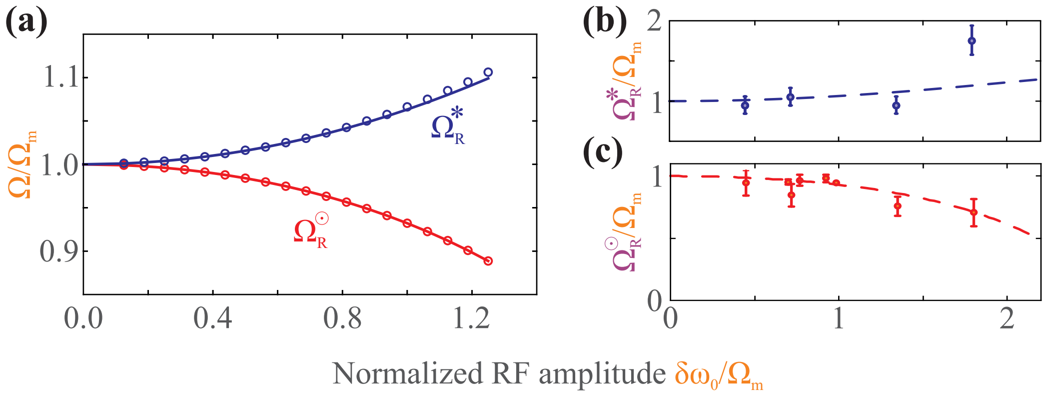

Figure 3.42: Effect of the Bloch - Siegert shift. The MW power required for reaching the minimum splitting ($\Omega_R^{\odot}$, red) and the maximum spectral density (Ω_R^*, blue) at Ω_m depends on the RF drive amplitude. **(a)** The dots are data points obtained from numerical simulations and fat solid lines are the analytic expressions given above. **(b)** The component Ω_R^* inferred from a series of measurements similar to the one shown in Figure 3.37. The amplitude data of the Fourier transforms is subject to considerable noise, rendering the experimental result non-conclusive. These type of measurements are extremely time consuming and thus we have not pursued this road any further. **(c)** The shift of the minimum splitting to lower MW powers, here $\Omega_\mathrm{R}^{\odot}$, shows decent agreement between the analytic expression and the experimentally measured data.

3.7 Interpretation of Rabi oscillation spectra in terms of emission detection of the dressed spin

In this section we further analyze the experimental observations. It is important to recall that the singly dressed qubit is aligned along the **x**-axis of the Bloch sphere representing the original spin qubit. As we have seen, the roles of the σ_x and σ_z operator for the dressed spin are interchanged and the mechanical oscillator moving along the **z**-axis couples resonantly to the dressed states. The singly dressed qubit therefore experiences irradiation from the coherent phonon field oscillating at Ω_m. Hence, we can attempt to describe the evolution of the dressed spin by a quantum master equation. Here, we introduce Bloch equations for the MW dressed qubit coupled to the RF field. This allows analyzing the spin locking signatures: in particular, we here find the dependence of the weights of the Mollow triplet peaks on the oscillation amplitude and phase.

3.7.1 The reduced density matrix for the dressed qubit

We consider the evolution of σ_z:

$$\begin{aligned}\langle\sigma_z(t)\rangle &= \mathrm{Tr}\left\{\rho\sigma_z\right\}\\ &= \sum_{\substack{\alpha=\pm\\ \beta=\pm\\ M\\ N}} \langle\alpha_N|\rho|\beta_M\rangle \underbrace{\langle\beta_M|\sigma_z|\alpha_N\rangle}_{\mathrm{A}}.\end{aligned} \tag{3.58}$$

Considering an example for A:

$$\begin{aligned}A = \langle +_M|\sigma_z|-_N\rangle &= (\cos\theta_M\langle 1, M-1| + \sin\theta_M\langle 0, M|)\,\sigma_z\,(-\sin\theta_M|1, M-1\rangle + \cos\theta_M|0, M\rangle)\\ &= -\cos\theta_M\sin\theta_N\langle 1|\sigma_z|1\rangle\delta_{N,M}\\ &= -\cos\theta_N\sin_N\delta_{N,M},\end{aligned}$$

we see that all parts of the sum with $N \neq M$ vanish. Thus,

$$\begin{aligned}\langle\sigma_z(t)\rangle &= \sum_{\substack{\alpha=\pm\\ \beta=\pm\\ N}}\langle\alpha_N|\rho|\beta_N\rangle\langle\beta_N|\sigma_z|\alpha_N\rangle\\ &= \sum_N \mathrm{Tr}\left\{\rho^{(N)}\sigma_z\big|_{\mathcal{E}(N)}\right\},\end{aligned}\tag{3.59}$$

where $\rho^{(N)}$ is the density matrix of the N^{th} multiplicity,

$$\rho^{(N)} = \begin{pmatrix}\rho^N_{++} & \rho^N_{+-}\\ \rho^N_{-+} & \rho^N_{--}\end{pmatrix}.\tag{3.60}$$

In particular, we find that

$$\langle\sigma_z(t)\rangle = \sum_N \cos^2\theta_N\rho^{(N)}_{--} + \sin^2\theta_N\rho^{(N)}_{++} - \cos\theta_N\sin\theta_N(\rho^{(N)}_{+-} + \rho^{(N)}_{-+}),\tag{3.61}$$

which reduces to

$$\begin{aligned}\langle\sigma_z(t)\rangle &= \frac{1}{2}\sum_N(\rho^{(N)}_{--} + \rho^{(N)}_{++}) - \frac{1}{2}\sum_N(\rho^{(N)}_{+-} + \rho^{(N)}_{-+})\\ &= \frac{1}{2}(\pi_- + \pi_+) - \frac{1}{2}(\sigma_{+-} + \sigma_{-+}) \qquad (3.62)\\ &= \frac{1}{2} - \frac{1}{2}(\sigma_{+-} + \sigma_{-+}). \qquad (3.63)\end{aligned}$$

in case of resonant pumping. Here we have defined the reduced populations $\pi_\pm = \sum_N \rho^{(N)}_{\pm\pm}$ and coherence $\sigma_{+-} = \sum_N \rho^{(N)}_{+-}$, which illustrates[9] that we can introduce an effective two level system which describes the MW dressed qubit. Equation (3.62) signifies that spectra of **Rabi oscillations can be understood as the spectra of excitations emitted and absorbed by the dressed spin** in interaction with its environment (Γ_{spin}) and the mechanical oscillator $\delta\omega_0$. We can therefore expect to be able to interpret spectra of Rabi oscillations in terms of phenomena similar to spectra of photons emitted by a single atom irradiated by a light field.

3.7.2 Quantum master equation for the dressed qubit

In the dressed state basis, the interaction Hamiltonian $H_{\mathrm{int}} = \hbar g_z\sigma_z\left(a^\dagger + a\right)$ can be written as

$$H^{(N)}_{\mathrm{int}} = \frac{1}{2}\hbar g_z\left(\mathbb{I}^{(N)} - \sigma^{(N)}_x\right)\left(a^\dagger + a\right)\tag{3.64}$$

for resonant pumping[10], $\delta = 0$. The first term does not affect the dynamics while the second term can induce transitions due to its transverse character in the dressed state basis. If a large enough MW

---

[9] The full derivation of the dressed qubit is given in [122].

[10] Throughout this section we will assume that the MW is in resonance with the spin, $\delta = 0$, unless stated otherwise.

field is applied ($\bar{N} \gg \Delta N \gg 1$), which is the case in most experimental conditions when operating with a NV spin qubit, the variation of θ_N over the dominantly populated multiplicities is negligible, so that all the reduced Hamiltonians evolve in the same way. As such, we can restrict our analysis to one single multiplicity: The global density matrix ρ follows the evolution equation

$$\dot{\rho} = \frac{1}{i\hbar}[H_0 + H_{\mathrm{int}}, \rho] + \dot{\rho}_{\mathrm{relax}} \tag{3.65}$$

with

$$H_0 + H_{\mathrm{int}} = \sum_N \Big(|{+_N}\rangle\langle{+_N}| E_{+_N} + |{-_N}\rangle\langle{-_N}| E_{-_N} \Big) + \hbar g_z \left(a^\dagger + a \right) \sigma_z. \tag{3.66}$$

For a classical RF drive $\hbar g_z \left(a^\dagger + a\right) \sigma_z \to \hbar\delta\omega_0 \cos(\Omega_{\mathrm{m}} t + \alpha)\sigma_z$ (where α is now the initial phase of the RF field), so that for example

$$\begin{aligned}
\dot{\rho}^N_{+-} &\equiv \langle{+_N}|\dot{\rho}|{-_N}\rangle \\
&= \frac{1}{i\hbar}\langle{+_N}|[H_0, \rho]|{-_N}\rangle - i\delta\omega_0 \cos\left(\Omega_{\mathrm{m}} t + \alpha\right) \langle{+_N}|\sigma_z \rho - \rho\sigma_z|{-_N}\rangle + \dot{\rho}^N_{+-,\mathrm{relax}} \\
&= -i\frac{E_{+_N} - E_{-_N}}{\hbar}\rho^N_{+-} + i\frac{\delta\omega_0}{2}\cos(\Omega_{\mathrm{m}} t + \alpha)\left(\rho^N_{--} - \rho^N_{++}\right) + \dot{\rho}^N_{+-,\mathrm{relax}}.
\end{aligned}$$

3.7.3 Bloch equations describing the dressed qubit evolution

In order to find $\dot{\rho}^N_{\mathrm{relax}}$, we have to identify adequate transition rates. We invoke the reasoning from section 3.5.5 and arrive at the energy dissipation rate Γ_{static} and decoherence rate Γ_{spin} for the dressed spin, see equations (3.22) and (3.23). In order to simplify the following calculations, we approximate Γ_{static}, which is dominated by Γ_2, as $\Gamma_{\mathrm{static}} \approx 2\Gamma_{\mathrm{spin}}$. We thus arrive at a set of Bloch equations for the dressed states

$$\begin{aligned}
\dot{\rho}^N_{+-} &= -i\Omega_{\mathrm{R}}\rho^N_{+-} - i\frac{\delta\omega_0}{2}\cos(\Omega_{\mathrm{m}} t + \alpha)\left(\rho^N_{++} - \rho^N_{--}\right) - \Gamma_{\mathrm{spin}}\rho^N_{+-}, \\
\dot{\rho}^N_{-+} &= +i\Omega_{\mathrm{R}}\rho^N_{+-} + i\frac{\delta\omega_0}{2}\cos(\Omega_{\mathrm{m}} t + \alpha)\left(\rho^N_{++} - \rho^N_{--}\right) - \Gamma_{\mathrm{spin}}\rho^N_{-+}, \\
\dot{\rho}^N_{++} &= i\frac{\delta\omega_0}{2}\cos(\Omega_{\mathrm{m}} t + \alpha)\left(\rho^N_{-+} - \rho^N_{+-}\right) - 2\Gamma_{\mathrm{spin}}\rho^N_{++}.
\end{aligned} \tag{3.67}$$

By summing over N, we arrive at the Bloch equations of the fictitious spin:

$$\begin{aligned}
\dot{\sigma}_{+-} &= -i\Omega_{\mathrm{R}}\sigma_{+-} - i\frac{\delta\omega_0}{2}\cos(\Omega_{\mathrm{m}} t + \alpha)\left(\pi_{++} - \pi_{--}\right) - \Gamma_{\mathrm{spin}}\sigma_{+-}, \\
\dot{\sigma}_{-+} &= +i\Omega_{\mathrm{R}}\sigma_{-+} + i\frac{\delta\omega_0}{2}\cos(\Omega_{\mathrm{m}} t + \alpha)\left(\pi_{++} - \pi_{--}\right) - \Gamma_{\mathrm{spin}}\sigma_{-+}, \\
\dot{\pi}_{++} &= i\frac{\delta\omega_0}{2}\cos(\Omega_{\mathrm{m}} t + \alpha)\left(\sigma_{-+} - \sigma_{+-}\right) - 2\Gamma_{\mathrm{spin}}\pi_{++}.
\end{aligned} \tag{3.68}$$

It is a standard technique to solve these equations by means of a rotating wave approximation. In that case we express (3.68) in terms of the coherences in the frame rotating at the mechanical oscillator frequency, defining

$$\tilde{\sigma}_{-+} = \sigma_{-+} e^{-i\Omega_{\mathrm{m}} t - i\alpha},$$

for which the Bloch equations in the rotating frame are

$$\begin{aligned}
\dot{\tilde{\sigma}}_{+-} &= -i(\Omega_{\mathrm{R}} - \Omega_{\mathrm{m}})\tilde{\sigma}_{+-} - i\frac{\delta\omega_0}{4}\left(\pi_{++} - \pi_{--}\right) - \Gamma_{\mathrm{spin}}\tilde{\sigma}_{+-}, \\
\dot{\tilde{\sigma}}_{-+} &= +i(\Omega_{\mathrm{R}} - \Omega_{\mathrm{m}})\tilde{\sigma}_{-+} + i\frac{\delta\omega_0}{4}\left(\pi_{++} - \pi_{--}\right) - \Gamma_{\mathrm{spin}}\tilde{\sigma}_{-+}, \\
\dot{\tilde{\pi}}_{++} &= i\frac{\delta\omega_0}{4}\left(\tilde{\sigma}_{-+} - \tilde{\sigma}_{+-}\right) - 2\Gamma_{\mathrm{spin}}\pi_{++}.
\end{aligned} \tag{3.69}$$

We then define the Bloch vector $\mathbf{b}_\alpha$

$$\mathbf{b}_\alpha = \begin{pmatrix} u_\alpha \\ v_\alpha \\ w_\alpha \end{pmatrix} = \begin{pmatrix} (\tilde{\sigma}_{-+} - \tilde{\sigma}_{+-})/2 \\ (\tilde{\sigma}_{-+} - \tilde{\sigma}_{+-})/2i \\ (\pi_{++} - \pi_{--})/2 \end{pmatrix}, \tag{3.70}$$

so that

$$\begin{aligned} \sigma_{-+} &= e^{i\Omega_\mathrm{m} t + i\alpha}(u_\alpha + iv_\alpha), \\ \sigma_{+-} &= e^{-i\Omega_\mathrm{m} t - i\alpha}(u_\alpha - iv_\alpha), \\ \frac{\sigma_{+-}(t) + \sigma_{-+}(t)}{2} &= u_\alpha(t)\cos(\Omega_\mathrm{m} t + \alpha) - v_\alpha(t)\sin(\Omega_\mathrm{m} t + \alpha). \end{aligned}$$

The evolution equation of the Bloch vector is

$$\begin{pmatrix} \dot{u}_\alpha \\ \dot{v}_\alpha \\ \dot{w}_\alpha \end{pmatrix} = M\mathbf{b}_\alpha = \begin{pmatrix} -\Gamma_\mathrm{spin} & (\Omega_\mathrm{m} - \Omega_\mathrm{R}) & 0 \\ -(\Omega_\mathrm{m} - \Omega_\mathrm{R}) & -\Gamma_\mathrm{spin} & -\delta\omega_0/2 \\ 0 & \delta\omega_0/2 & -2\Gamma_\mathrm{spin} \end{pmatrix} \begin{pmatrix} u_\alpha \\ v_\alpha \\ w_\alpha \end{pmatrix}. \tag{3.71}$$

Notice that the dependence on the initial phase α is hidden in the initial conditions at $t = 0$. Since the spin is always prepared in the ground state $|0\rangle$ by optical pumping, we have

$$\rho^{(N)}(t=0) = \frac{1}{2}\begin{pmatrix} 1 & 1 \\ 1 & 1 \end{pmatrix}, \tag{3.72}$$

and

$$\begin{aligned} u_\alpha(t=0) &= \frac{1}{2}\left(\frac{e^{-i\alpha}}{2} + \frac{e^{i\alpha}}{2}\right) = \frac{\cos\alpha}{2}, \\ v_\alpha(t=0) &= \frac{1}{2i}\left(\frac{e^{-i\alpha}}{2} - \frac{e^{i\alpha}}{2}\right) = -\frac{\sin\alpha}{2}, \\ w_\alpha(t=0) &= 0. \end{aligned}$$

We will restrict the following considerations to the resonant condition, where $\Omega_\mathrm{m} = \Omega_\mathrm{R}$. We then look for solutions like

$$\begin{pmatrix} u_\alpha \\ v_\alpha \\ w_\alpha \end{pmatrix}(t) \propto e^{\lambda t}$$

and find solutions to λ by solving the eigenvalue problem $\det(M - \lambda\mathbb{I}) = 0$. The eigenvalues are

$$\lambda_0 = -\Gamma_\mathrm{spin}, \tag{3.73}$$

$$\lambda_\pm = -\frac{3}{2}\Gamma_\mathrm{spin} \pm \frac{1}{2}\sqrt{\Gamma_\mathrm{spin}^2 - \delta\omega_0^2}, \tag{3.74}$$

for which the Bloch vector evolves as

$$u_\alpha(t) = \frac{\cos\alpha}{2}e^{-\Gamma_\mathrm{spin} t}, \tag{3.75}$$

$$v_\alpha(t) = -\frac{\sin\alpha}{2}e^{-\frac{3}{2}\Gamma_\mathrm{spin} t}\left(\cosh\left(\frac{1}{2}\sqrt{\Gamma_\mathrm{spin}^2 - \delta\omega_0^2 t}\right) + \frac{\Gamma_\mathrm{spin}}{\sqrt{\Gamma_\mathrm{spin}^2 - \delta\omega_0^2}}\sinh\left(\frac{1}{2}\sqrt{\Gamma_\mathrm{spin}^2 - \delta\omega_0^2 t}\right)\right), \tag{3.76}$$

$$w_\alpha(t) = \frac{\delta\omega_0}{2}\sin\alpha\frac{e^{-\frac{3}{2}\Gamma_\mathrm{spin} t}}{\sqrt{\Gamma_\mathrm{spin}^2 - \delta\omega_0^2}}\sinh\left(\frac{1}{2}\sqrt{\Gamma_\mathrm{spin}^2 - \delta\omega_0^2 t}\right). \tag{3.77}$$

We note that for large enough amplitudes $\delta\omega_0$, the character of the evolution changes from an exponential decay to exponentially decaying oscillations. When $\delta\omega_0 > \Gamma_{\mathrm{spin}}$,

$$\cosh\left(\frac{1}{2}\sqrt{\Gamma_{\mathrm{spin}}^2 - \delta\omega_0^2 t}\right) \to \cos\left(\frac{1}{2}\sqrt{\delta\omega_0^2 - \Gamma_{\mathrm{spin}}^2 t}\right),$$

$$\frac{1}{\sqrt{\Gamma_{\mathrm{spin}}^2 - \delta\omega_0^2}}\sinh\left(\frac{1}{2}\sqrt{\Gamma_{\mathrm{spin}}^2 - \delta\omega_0^2 t}\right) \to \frac{1}{\sqrt{\delta\omega_0^2 - \Gamma_{\mathrm{spin}}^2}}\sin\left(\frac{1}{2}\sqrt{\delta\omega_0^2 - \Gamma_{\mathrm{spin}}^2 t}\right).$$

The Rabi precessions are then

$$\begin{aligned}\langle\sigma_z^\alpha\rangle(t) &= \sum_N \left(\frac{1}{2} - \frac{\rho_{+-}^N(t) + \rho_{-+}^N(t)}{2}\right)\\ &= \frac{1}{2} - \big(\cos(\Omega_{\mathrm{m}}t + \alpha)\,u_\alpha(t) - \sin(\Omega_{\mathrm{m}}t + \alpha)\,v_\alpha(t)\big),\end{aligned} \tag{3.78}$$

where it is clear that u_α is the component oscillating in phase with the mechanical motion and v_α the quadrature:

$$\begin{aligned}\langle\sigma_z^\alpha\rangle(t) = \frac{1}{2}\Bigg\{&1\\ &- e^{-\Gamma_{\mathrm{spin}}t}\cos\alpha\cos(\Omega_{\mathrm{m}}t + \alpha)\\ &- e^{-\frac{3}{2}\Gamma_{\mathrm{spin}}t}\sin\alpha\sin(\Omega_{\mathrm{m}}t + \alpha)\left[\cosh\left(\frac{1}{2}\sqrt{\Gamma_{\mathrm{spin}}^2 - \delta\omega_0^2 t}\right)\right.\\ &\left.\qquad + \frac{\Gamma_{\mathrm{spin}}}{\sqrt{\Gamma_{\mathrm{spin}}^2 - \delta\omega_0^2}}\sinh\left(\frac{1}{2}\sqrt{\Gamma_{\mathrm{spin}}^2 - \delta\omega_0^2 t}\right)\right]\Bigg\},\end{aligned} \tag{3.79}$$

which we can reexpress as:

$$\begin{aligned}\langle\sigma_z^\alpha\rangle(t) = \frac{1}{2}\Bigg\{&1\\ &- e^{-\Gamma_{\mathrm{spin}}t}\cos\alpha\cos(\Omega_{\mathrm{m}}t + \alpha)\\ &- \frac{1}{2}e^{-\frac{3}{2}\Gamma_{\mathrm{spin}}t}\sin\alpha\sin(\Omega_{\mathrm{m}}t + \alpha)\left[e^{\frac{1}{2}\sqrt{\Gamma_{\mathrm{spin}}^2 - \delta\omega_0^2}t}\left(1 + \frac{\Gamma_{\mathrm{spin}}}{\sqrt{\Gamma_{\mathrm{spin}}^2 - \delta\omega_0^2}}\right)\right.\\ &\left.\qquad + e^{-\frac{1}{2}\sqrt{\Gamma_{\mathrm{spin}}^2 - \delta\omega_0^2}t}\left(1 - \frac{\Gamma_{\mathrm{spin}}}{\sqrt{\Gamma_{\mathrm{spin}}^2 - \delta\omega_0^2}}\right)\right]\Bigg\}.\end{aligned} \tag{3.80}$$

With our definition of the σ_z operator, the population $P_0^\alpha = 1 - \langle\sigma_z^\alpha\rangle(t)$ is evolving as

$$\begin{aligned}P_0^\alpha(t) = \frac{1}{2}\Bigg\{&1\\ &+ e^{-\Gamma_{\mathrm{spin}}t}\cos\alpha\cos(\Omega_{\mathrm{m}}t + \alpha)\\ &+ \frac{1}{2}e^{-\frac{3}{2}\Gamma_{\mathrm{spin}}t}\sin\alpha\sin(\Omega_{\mathrm{m}}t + \alpha)\left[e^{\frac{1}{2}\sqrt{\Gamma_{\mathrm{spin}}^2 - \delta\omega_0^2}t}\left(1 + \frac{\Gamma_{\mathrm{spin}}}{\sqrt{\Gamma_{\mathrm{spin}}^2 - \delta\omega_0^2}}\right)\right.\\ &\left.\qquad + e^{-\frac{1}{2}\sqrt{\Gamma_{\mathrm{spin}}^2 - \delta\omega_0^2}t}\left(1 - \frac{\Gamma_{\mathrm{spin}}}{\sqrt{\Gamma_{\mathrm{spin}}^2 - \delta\omega_0^2}}\right)\right]\Bigg\}.\end{aligned} \tag{3.81}$$

3.7.4 Comparison with the experimental observations

Experimentally, our measurement protocols are not synchronized to the RF phase, so that we have to average over α in order to recover the observed spin dynamics:

$$P_0(t) = \frac{1}{2\pi} \int_0^{2\pi} \mathrm{d}\alpha \, P_0^\alpha(t). \tag{3.82}$$

With

$$\langle \cos(\Omega_\mathrm{m} t + \alpha) \cos\alpha \rangle_\alpha = \frac{\cos\Omega_\mathrm{m} t}{2} \quad \text{and} \quad \langle \sin(\Omega_\mathrm{m} t + \alpha) \sin\alpha \rangle_\alpha = \frac{\cos\Omega_\mathrm{m} t}{2},$$

we get

$$\begin{aligned} P_0(t) =& \frac{1}{2} \\ &+ \frac{1}{4} e^{-\Gamma_\mathrm{spin} t} \cos\Omega_\mathrm{m} t \\ &+ \frac{1}{8} e^{-\frac{3}{2}\Gamma_\mathrm{spin} t} \cos\Omega_\mathrm{m} t \left[e^{\frac{1}{2}\sqrt{\Gamma_\mathrm{spin}^2 - \delta\omega_0^2}\, t} \left(1 + \frac{\Gamma_\mathrm{spin}}{\sqrt{\Gamma_\mathrm{spin}^2 - \delta\omega_0^2}} \right) \right. \\ &\left. \qquad + e^{-\frac{1}{2}\sqrt{\Gamma_\mathrm{spin}^2 - \delta\omega_0^2}\, t} \left(1 - \frac{\Gamma_\mathrm{spin}}{\sqrt{\Gamma_\mathrm{spin}^2 - \delta\omega_0^2}} \right) \right]. \end{aligned} \tag{3.83}$$

For sufficiently large amplitudes, $\delta\omega_0 > \Gamma_\mathrm{spin}$, the expression simplifies to

$$\begin{aligned} P_0(t) = & \frac{1}{2} + \frac{1}{4} e^{-\Gamma_\mathrm{spin} t} \cos(\Omega_\mathrm{m} t) \\ & + \frac{1}{8} e^{-\frac{3}{2}\Gamma_\mathrm{spin} t} \cos\left(\left(\Omega_\mathrm{m} + \frac{\delta\omega_0}{2} \right) t \right) \\ & + \frac{1}{8} e^{-\frac{3}{2}\Gamma_\mathrm{spin} t} \cos\left(\left(\Omega_\mathrm{m} - \frac{\delta\omega_0}{2} \right) t \right) \end{aligned} \tag{3.84}$$

The three peaks of the Mollow triplet are present in the above equation, as well as their weights, widths and relative phases (which is preserved despite averaging over the mechanical phase α). Notice that the constant term reflects the mean value of Rabi oscillations: $P_0(t \to \infty) = P_1(t \to \infty) = \frac{1}{2}$. By transforming expression (3.84) into its Fourier space we can write down the analytic form of the *phonon Mollow triplet*:

$$2\pi P_0[\Omega] = \frac{1}{2}\delta[\Omega] + \frac{A_-}{\Gamma_\mathrm{coh} + i(\Omega - \Omega_\mathrm{m} + \Delta_{N,M})} + \frac{A_0}{\Gamma_\mathrm{pop} + i(\Omega - \Omega_\mathrm{m})} + \frac{A_+}{\Gamma_\mathrm{coh} + i(\Omega - \Omega_\mathrm{m} - \Delta_{N,M})} \tag{3.85}$$

$$= \frac{1}{2}\delta[\Omega] + \frac{\frac{1}{8}}{\frac{3}{2}\Gamma_\mathrm{spin} + i(\Omega - \Omega_\mathrm{m} + \frac{\delta\omega_0}{2})} + \frac{\frac{1}{4}}{\Gamma_\mathrm{spin} + i(\Omega - \Omega_\mathrm{m})} + \frac{\frac{1}{8}}{\frac{3}{2}\Gamma_\mathrm{spin} + i(\Omega - \Omega_\mathrm{m} - \frac{\delta\omega_0}{2})}. \tag{3.86}$$

In equation (3.85) we have explicitly separated the parts that are due to the evolution of either the reduced coherences or populations of the dressed states. The second line fully captures amplitude, frequency and relative phase of each component at the spin locking condition and is in perfect agreement with the simulation results. Expression (3.85) was used to fit the experimentally measured phonon Mollow triplet as shown in Figure 3.43. For the shown data set, we obtain

Amplitudes:
$A_0 = 0.19, \quad A_- = 0.17, \quad A_+ = 0.10$

Frequencies:
$\Omega_\mathrm{m}/2\pi = 6.0$ MHz, $\quad (\Omega_\mathrm{m} - \Delta_{N,M})/2\pi = 4.6$ MHz, $\quad (\Omega_\mathrm{m} + \Delta_{N,M})/2\pi = 7.4$ MHz

Linewidths:
$\Gamma_\mathrm{pop}/2\pi = 17.8$ kHz, $\quad \Gamma_{\mathrm{coh},-}/2\pi = 32.5$ kHz, $\quad \Gamma_{\mathrm{coh},+}/2\pi = 66.8$ kHz

We see that the ratio of the amplitudes and linewidths between the central peak and sidebands do not correspond exactly to those predicted by theory. Partially, this can be attributed to a nonzero detuning δ of the applied MW field. Another reason for this discrepancy is that experimentally the noise spectral density is not flat in the region between $\Omega_\mathrm{m} - \frac{\delta\omega_0}{2}$ and $\Omega_\mathrm{m} + \frac{\delta\omega_0}{2}$. We will discuss the consequences in more detail in section 5.5 of Chapter 5.

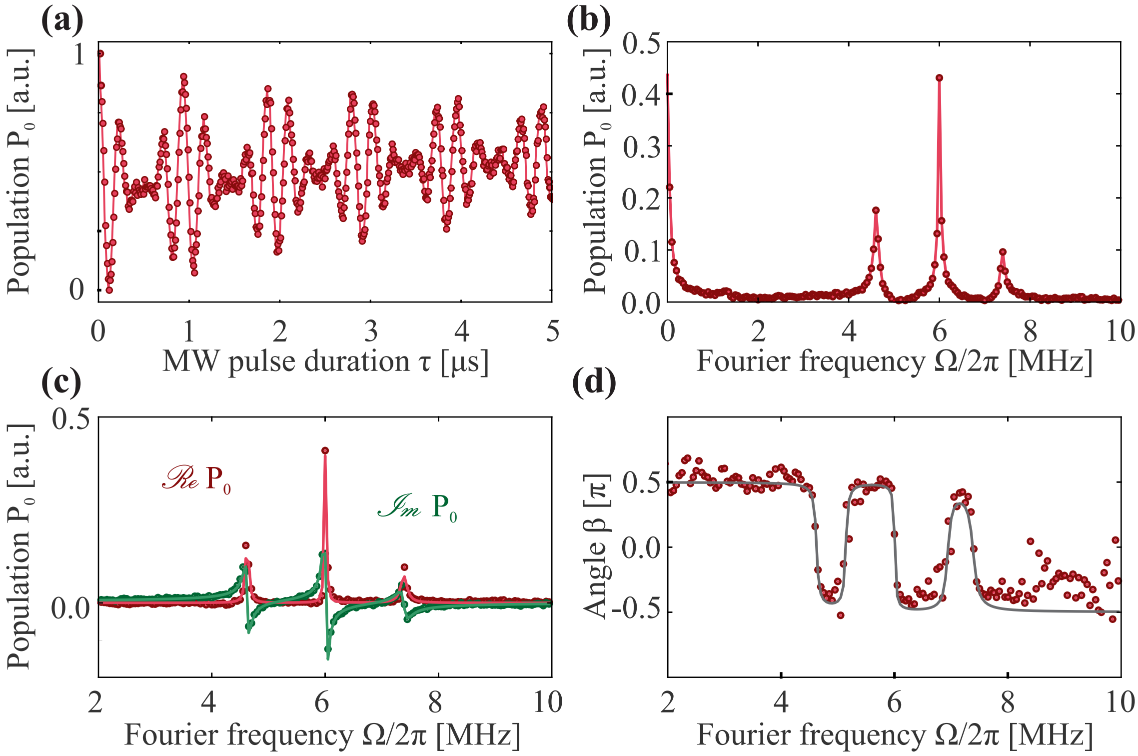

Figure 3.43: Phonon Mollow triplet. **(a)** Temporal trace of the same Rabi measurement as shown in Figure 3.34. **(b)** Absolute values of the discrete Fourier transform of **(a)** The curve is the same as already shown in Figure 3.35. The solid lines in **(a)** and **(b)** are guides to the eye. **(c)** Real (red) and imaginary (green) parts of the Fourier transform of **(b)** fitted to expression (3.85) (solid lines). **(d)** Phase of the Mollow triplet. Red points represent data, the grey solid line represents the phase obtained from expression (3.85) with the fitting values obtained from **(c)**.

3.7.5 Weak and strong coupling of the parametric interaction

Expression (3.85) describes Rabi spectra taken at the resonance or *spin locking condition* $\Omega_\mathrm{m} - \Omega_\mathrm{R} = 0$. This corresponds to the experiment shown in Figure 3.38 **(a)** in which the coupling strength $\delta\omega_0$ is gradually increased. The emergence of the triplet structure with augmenting oscillation amplitude is visible. Since the separation of the sidebands is directly related to the coupling strength, we expect that the individual components are distinguishable once the parameterized oscillation amplitude is larger than the peak linewidth: $\delta\omega_0 \gtrsim \Gamma_\mathrm{spin}$. Such a condition is usually called a strong coupling condition, which applies here to the interaction of the phonon field with respect to the MW dressed spin. In principle, however, the interaction of the spin with the phonon field is parametric. We therefore coin

$$\left(\delta\omega_0, \Omega_\mathrm{R} \approx \Omega_\mathrm{m}\right) \gtrsim \Gamma_\mathrm{spin}, \tag{3.87}$$

the strong interaction regime of the parametric coupling.

Transition from the weak to the strong coupling regime In order to understand the transition from the weak to the strong coupling regime, we inspect (3.83). The vector $\mathbf{b}(t)$ can generally be expressed in terms of superpositions of functions $c_{i,j}\exp(\lambda_i t)\exp(i\Omega_\mathrm{m} t)$, where $j \in \{u, v, w\}$ labels the component of the Bloch vector and λ_i is the i^th ($i \in \{0, +, -\}$) eigenvalue of the matrix M:

$$\begin{aligned} \lambda_0 &= -\Gamma_\mathrm{spin}, \\ \lambda_\pm &= -\frac{3}{2}\Gamma_\mathrm{spin} \pm \frac{1}{2}\sqrt{\Gamma_\mathrm{spin}^2 - \delta\omega_0^2}. \end{aligned} \tag{3.88}$$

These eigenvalues provide the time dynamics of the qubit in the (doubly) rotating mechanical oscillator frame (spinning at Ω_m). In the limit of large coupling strength they become

$$\begin{aligned} \lambda_0(\delta\omega_0 \gg \Gamma_\mathrm{spin}) &= \Gamma_\mathrm{spin}, \\ \lambda_\pm(\delta\omega_0 \gg \Gamma_\mathrm{spin}) &= \frac{3}{2}\Gamma_\mathrm{spin} \pm i\frac{\delta\omega_0}{2}. \end{aligned} \tag{3.89}$$

with respective amplitudes

$$\begin{aligned} c_{\bar{u},0} &= \frac{1}{4}, \\ c_{\bar{v},\pm} &= \frac{1}{8}. \end{aligned} \tag{3.90}$$

We also see that the three frequencies are degenerate for $\delta\omega_0 < \Gamma_\mathrm{spin}$, since all λ_i are then purely real and the time evolution of $\mathbf{b}(t)$ is described by exponential decay of its components. In the limit of small coupling strength the eigenvalues are

$$\begin{aligned} \lambda_0(\delta\omega_0 \ll \Gamma_\mathrm{spin}) \approx \lambda_+(\delta\omega_0 \ll \Gamma_\mathrm{spin}) &\approx -\Gamma_\mathrm{spin}, \\ \lambda_-(\delta\omega_0 \ll \Gamma_\mathrm{spin}) &\approx -2\Gamma_\mathrm{spin}. \end{aligned} \tag{3.91}$$

This regime corresponds to the weak coupling limit and defines a bandwidth Γ_spin below which the coupling strength $\delta\omega_0$ is not large enough to couple the states $|-_N, M\rangle$ and $|+_N, M-1\rangle$ and causes an energy shift between them. In that case spectra of Rabi oscillations exhibit only a single peak at $\Omega = \Omega_\mathrm{m} = \Omega_\mathrm{R}$. Increasing $\delta\omega_0$ in this regime does thus not lead to a frequency splitting but to a change in the decay rates of the components of $\mathbf{b}(t)$ - a phenomenon also encountered in the weak driving limit of the interaction between an atom and a laser field. In our case the increased decay rates will lead to a reduction of peak height in the Fourier spectra of Rabi oscillations. Their evolution is shown below in Figure 3.44 together with the corresponding amplitudes.

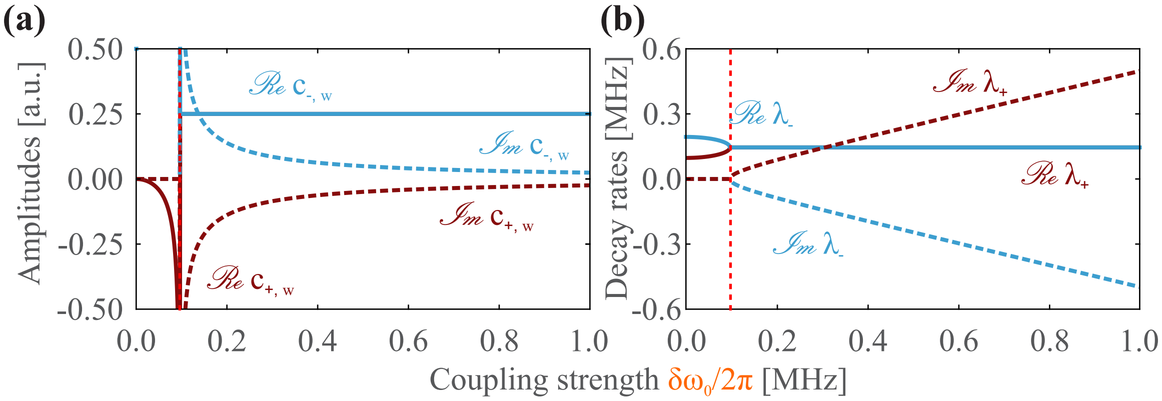

Figure 3.44: Amplitudes and eigenvalues. $\Gamma_{\mathrm{spin}} = 0.609\,\mathrm{MHz}$ here. **(a)** Real (solid lines) and imaginary (dashed lines) parts of the amplitudes. Notice that their divergence towards $\pm\infty$ around $\delta\omega_0 \approx \Gamma_{\mathrm{spin}}$ cancels out. **(b)** Real (decay rates, solid lines) and imaginary (frequencies, dashed lines) parts of the eigenvalues.

Now we consider the height of the central component of the Mollow triplet in Fourier space, $\sigma_z[\Omega = \Omega_{\mathrm{m}}]$, explicitly. We then have three Lorentzian components at frequencies $i\Omega_{\mathrm{m}} + \lambda_i$ and the real part of $\sigma_z[\Omega = \Omega_{\mathrm{m}}]$ is the sum of respective amplitudes of (u, v, w) divided by their width:

$$\begin{aligned}\sigma_z[\Omega = \Omega_{\mathrm{m}} = \Omega_{\mathrm{R}}, \delta\omega_0] =& \frac{1}{4}\frac{1}{\Gamma_{\mathrm{spin}}} + \\ & \frac{1}{8}\left(1 - \frac{\Gamma_{\mathrm{spin}}}{\sqrt{\Gamma_{\mathrm{spin}}^2 - \delta\omega_0^2}}\right)\frac{1}{\frac{3}{2}\Gamma_{\mathrm{spin}} + \frac{1}{2}\sqrt{\Gamma_{\mathrm{spin}}^2 - \delta\omega_0^2}} + \\ & \frac{1}{8}\left(1 + \frac{\Gamma_{\mathrm{spin}}}{\sqrt{\Gamma_{\mathrm{spin}}^2 - \delta\omega_0^2}}\right)\frac{1}{\frac{3}{2}\Gamma_{\mathrm{spin}} - \frac{1}{2}\sqrt{\Gamma_{\mathrm{spin}}^2 - \delta\omega_0^2}}. \end{aligned} \tag{3.92}$$

Initially, for as long as $\delta\omega_0 < \Gamma_{\mathrm{spin}}$, $\sigma_z[\Omega = \Omega_{\mathrm{m}}]$ experiences a decrease because of line broadening due an increase of the decay rates. Then, at $\delta\omega_0 \geq \Gamma_{\mathrm{spin}}$, the respective decay rates reach their maximum but the different components of the Mollow triplet separate, leading to a further decrease of $\sigma_z[\Omega = \Omega_{\mathrm{m}}]$. We investigate the nature of the transition into the strong coupling regime with our simulations. Indeed, we find that an initial decrease in the height of the Fourier peak is followed by a leveling to half the unperturbed value, as is expected from the expression for A_0. Expression (3.92) can be recast into:

$$\frac{\sigma_z[\Omega = \Omega_{\mathrm{m}} = \Omega_{\mathrm{R}}, \delta\omega_0]}{\sigma_z[\Omega = \Omega_{\mathrm{m}} = \Omega_{\mathrm{R}}, 0]} = \frac{1}{2}\left(1 + \frac{\Gamma_{\mathrm{spin}}}{\Gamma_{\mathrm{spin}} + \delta\omega_0^2/8\Gamma_{\mathrm{spin}}}\right). \tag{3.93}$$

Equation (3.93) is shown in Figure 3.45 **(a)**, where it is compared to numerical data. The agreement is reasonably good, until for large values of the coupling strength, $\delta\omega_0 \approx \Omega_{\mathrm{m}}$, Bloch-Siegert shifts start to play a role and the height of the Fourier peak decreases. Figure 3.45 **(b)** compares the same expression to the experimental data shown in Figure 3.38. We observe a strong disagreement between the two curves. It can be accounted for by the surprising fact that the width of the central component has experienced narrowing due to the spin locking effect, which will be explained in section 3.7.8, see Figure 3.45 **(c)**. By normalizing the absolute value of the central peak with the experimentally measured width, we eventually obtain good agreement between the experimentally inferred central amplitude and expression (3.93).

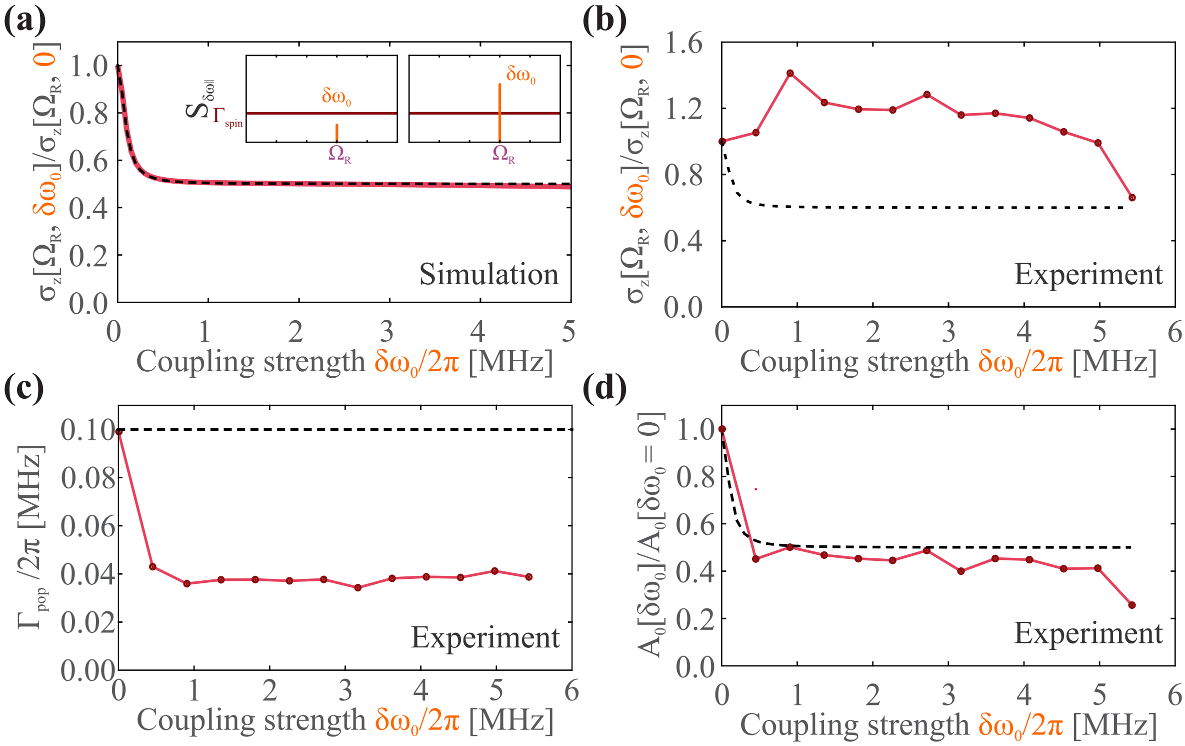

Figure 3.45: Transition to the strong coupling regime. **(a)** Simulations. *Inset:* Monochromatic oscillations are indistinguishable to the spin as long as their amplitudes are small compared to the noise spectral density. **(b)** Experimental data of Figure 3.38. We plot the magnitude of the central component, $\sigma_z[\Omega = \Omega_\mathrm{m}]$ (red curve) and compare it to expression (3.93), noting strong disagreement between the two. **(c)** This can be explained with the narrowing of the central peak observed at the spin locking condition. The red curve shows the experimental values, while the black dashed line indicates the expected analytic value, which does not change with the oscillation amplitude, $\delta\omega_0/2\pi$. **(d)** By accounting for this narrowing we eventually observe good agreement between the analytic expressions and experimental data. Here, we assume a central peak of the form $\sigma_z[\Omega = \Omega_\mathrm{m}] = \frac{A_0(\delta\omega_0)}{\Gamma(\delta\omega_0)}$. Taking $\Gamma(\delta\omega_0)$ from **(c)**, we obtain $A_0(\delta\omega_0)$, which behaves as expected.

Rabi oscillations as a spectrum analyzer The dynamics of the mechanical oscillator become spectrally resolvable in the strong coupling regime. By analysis of the peak position in the Rabi Fourier spectra, mechanical oscillation amplitude and frequency can be determined (moreover, the oscillation phase is also encoded in the Rabi spectra, as we will see in the section 3.7.6). This is not restricted to the hybrid setup and remains true for any RF signal along the spin's longitudinal axis, as we clearly demonstrate here. Thus, Rabi oscillations can serve to perform a spectral analysis of the electromagnetic spin environment. Notice that here, the advantage to detecting a flat and slowly changing noise spectral density as in section 3.5.5 is the ability to detect fast oscillating, monochromatic signals. Our spectrum analyzer is characterized by expression (3.93), which informs us about the progression of the hybrid interaction from the weak to the strong coupling regime. Simultaneously, by comparing the oscillation amplitude $\delta\omega_0$ to the Rabi oscillation coherence time $1/\Gamma_\mathrm{spin}$, we obtain the relationship between signal strength and measurement bandwidth. Moreover, since the height of the (central) Fourier peak is inversely proportional to the linewidth, $\sigma_z[\Omega = \Omega_\mathrm{R}] = \frac{1}{\Gamma_\mathrm{pop}}$, we expect

$$\frac{\sigma_z[\Omega = \Omega_\mathrm{R}, \delta\omega_0]}{\sigma_z[\Omega = \Omega_\mathrm{R}, 0]} - \frac{1}{2} = \frac{\Gamma_\mathrm{spin}}{\Gamma_\mathrm{spin} + \delta\omega_0^2/8\Gamma_\mathrm{spin}} = \frac{2\Gamma_\mathrm{spin}^2}{2\Gamma_\mathrm{spin}^2 + \delta\omega_0^2/4} = \frac{1}{1 + \left(\frac{\delta\omega_\mathrm{RMS}}{2\Gamma_\mathrm{spin}}\right)^2}. \tag{3.94}$$

The last term in the above expression underlines the analogy to a spectrum analyzer. While the level of a monochromatic signal is proportional to the energy contained in the signal ($\frac{\delta\omega_0^2}{2}$), the level of noise depends on the bandwidth used in the measurement. The maximum bandwidth of a Rabi oscillation measurement is closely related to the longitudinal noise. As a consequence, the transition into the strong coupling regime of the parametric interaction is a function of the square of the amplitudes, rather than the amplitude itself, as shown in Figure 3.46.

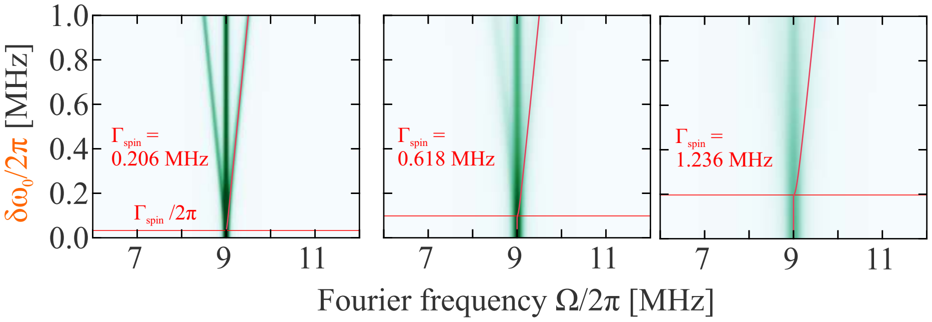

Figure 3.46: Transition into the strong coupling regime, shown for three values of $\Gamma_{\mathrm{spin}}/2\pi$ (red horizontal line). The vertical red line is the imaginary part of the eigenvalue λ_+ and well describes the splitting of the single central peak into the phonon Mollow triplet. **(a)** $\Gamma_{\mathrm{spin}} = 0.203\,\mathrm{MHz}$. **(b)** $\Gamma_{\mathrm{spin}} = 0.609\,\mathrm{MHz}$. **(c)** $\Gamma_{\mathrm{spin}} = 1.218\,\mathrm{MHz}$.

3.7.6 Phase of the mechanical oscillator

Expression (3.85) ignores the oscillation phase of the mechanical oscillator. This approach is justified, because experimentally the measurement protocols were not synchronized to the oscillation phase and the here presented data therefore shows Rabi oscillations that are averaged over all initial positions of the mechanical oscillator. In the numerical evaluation of equations (3.18) the time dependence of

$$\delta\omega_0(t) = \delta\omega_0 \cos(\Omega_{\mathrm{m}} t + \alpha)$$

demands that we average over the phase α, which describes the initial phase between mechanical oscillation and spin polarization, which, at $t = 0$ always is $P_0 = 1$. Figure 3.47 **(a)** shows the influence of α on the real part of Rabi spectra when the Rabi frequency Ω_{R} is swept across Ω_{m}. In the synchronization region $|\Omega_{\mathrm{R}} - \Omega_{\mathrm{m}}| \lesssim \delta\omega_0$ the relative weights of each component of the phonon Mollow triplet shifts as a function of α, leading to complementary suppression or enhancement of the sidebands and central peak. We investigate this interplay at the resonance condition $\Omega_{\mathrm{R}} = \Omega_{\mathrm{m}}$ in Figure 3.47 **(b)**, where we compare the weights with expression (3.81). Expanding

$$\begin{aligned}
\cos\alpha\cos(\Omega_{\mathrm{m}} t + \alpha) &= \cos(\Omega_{\mathrm{m}} t)\cos^2\alpha - \sin(\Omega_{\mathrm{m}} t)\sin\alpha\cos\alpha \quad \text{(central peak)},\\
\sin\alpha\sin(\Omega_{\mathrm{m}} t + \alpha) &= \cos(\Omega_{\mathrm{m}} t)\sin^2\alpha + \sin(\Omega_{\mathrm{m}} t)\sin\alpha\cos\alpha \quad \text{(sidebands)},
\end{aligned}$$

we identify the in-phase and quadrature components of $P_0(t)$. Invoking that temporal sin-components are transformed to a negative imaginary component in Fourier space, we have

$$\begin{aligned}
2\pi\sigma_z[\Omega = \Omega_{\mathrm{m}}, \Omega_{\mathrm{R}} = \Omega_{\mathrm{m}}](\alpha) &= \frac{1}{2}\frac{1}{\Gamma_{\mathrm{spin}}}\cos\alpha(\cos\alpha + i\sin\alpha),\\
2\pi\sigma_z[\Omega = \Omega_{\mathrm{m}} \pm \frac{\delta\omega_0}{2}, \Omega_{\mathrm{R}} = \Omega_{\mathrm{m}}](\alpha) &= \frac{1}{4}\frac{1}{\frac{3}{2}\Gamma_{\mathrm{spin}}}\sin\alpha(\sin\alpha - i\cos\alpha).
\end{aligned} \tag{3.95}$$

Apart from a slight difference that can be attributed to the Bloch-Siegert effect, expression (3.95) well reproduces the numerical data.

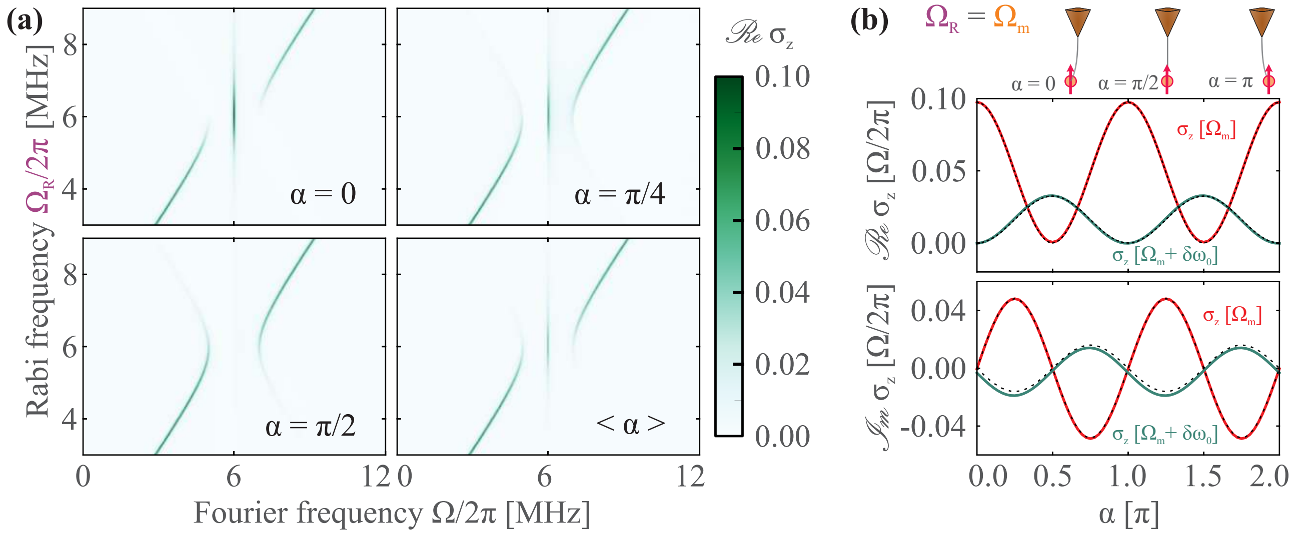

Figure 3.47: Phase dependence of the triplet structure for the simulation data. **(a)** Sweeps of the Rabi frequency for different initial phases α of the mechanical oscillator, clearly showing the complementary suppression or enhancement of the central peak and the sidebands. **(b)** The real and imaginary Fourier components of the central peak (red) and the sidebands (green), compared to the analytic expressions (3.95).

The Bloch equation approach of section 3.7.3 showed that the initial phase α can be interpreted as a rotation angle between real and imaginary parts of the coherences, leading to new respective initial conditions at the beginning of the Rabi protocol for each component. By averaging α over the interval $[0; 2\pi[$, we see that that the imaginary parts fall to zero and the real parts fall to

$$\begin{aligned} A_0[\Omega_\mathrm{R} = \Omega_\mathrm{m}](\langle\alpha\rangle) &= A_0, \\ A_\pm[\Omega_\mathrm{R} = \Omega_\mathrm{m}](\langle\alpha\rangle) &= A_\pm. \end{aligned} \tag{3.96}$$

This phase dependence of the Rabi oscillations is of great importance with respect to spin forces exerted onto the mechanics. From the above consideration, we conclude that, at the spin locking condition $\Omega_\mathrm{R} = \Omega_\mathrm{m}$, the Ω_m-component of σ_z is oscillating in phase with the mechanical oscillation, for we have

$$\arg\left(\sigma_z[\Omega_\mathrm{m}]\right) = \arctan\left(\frac{\mathrm{Im}\,(\sigma)_z\,[\Omega_\mathrm{m}]}{\mathrm{Re}\,(\sigma_z[\Omega_\mathrm{m}])}\right) = \arctan\left(\frac{\mathrm{Im}\,(A_0)}{\mathrm{Re}\,(A_0)}\right) = \arctan\left(\frac{\sin\alpha}{\cos\alpha}\right) = \alpha. \tag{3.97}$$

Thus, a feedback force $F_\mathrm{fb}[\Omega_\mathrm{m}] \propto \nabla B \sigma_z[\Omega_\mathrm{m}]$ acting on the mechanical oscillator will induce a shift of the mechanical resonance frequency. Furthermore, these findings show that magnitude of the $\sigma_z[\Omega]$-component can be tuned by means of synchronization of Rabi oscillations to the initial oscillation phase α.

3.7.7 Interpretation of the triple peak spectra in terms of a phonon Mollow triplet

As we have seen above in section 3.7.5, we can identify a strong coupling regime for the mechanical oscillator. The mechanical displacement along the **z**-axis couples resonantly to the dressed states thereby modifying the pseudo qubit's energy, which results in a new Jaynes-Cummings energy ladder in terms of photon number N and phonon number M. On the other hand, spontaneous emission of the dressed qubit is not induced via transverse (σ_x), but rather by longitudinal (σ_z) processes. As already discussed in section 3.5.5, the rate at which the environment induces transitions between the dressed dressed states is given by the decay rate of Rabi oscillations, Γ_spin. The same mechanism is now responsible for inducing transitions between the multiplicities $\mathcal{F}_{N,M}$. As for the case of an atom coupled to a resonant coherent light field, these transitions can be interpreted as a cascade through the Jaynes-Cummings energy ladder. Thus, we can understand Rabi oscillations as a measurement of the time evolution of the doubly dressed spin as it cascades down the photon-phonon energy ladder. The frequency components that we observe in the Rabi oscillations therefore correspond to the energies associated with jumps (permitted by the selection rules of the σ_z-operator) between two eigenstates. Moreover, Fourier spectra of Rabi oscillations not only allow us to identify the energies associated with jumps of the spin from rung to rung. By considering the relative height and width of each component, we can also identify the corresponding weight and timescale for each transition, see Figure 3.48. This interpretation is in close analogy to the fluorescence cascade emitted by a laser dressed atom leading to the observation of the Mollow triplet [122]. In contrast to the Bloch equation ansatz, the radiation cascade interpretation describes an average over all initial oscillator phases α, which accurately describes the experimental case (see section 3.7.6). On the other hand it allows us to obtain analytic expressions for the various components of the triplet at nonzero detuning $\Omega_\mathrm{m} - \Omega_\mathrm{R}$. In the following we are going to present the ideas that lead to an analytic prediction for the widths and weights of the various components of the *phonon Mollow triplet* as we observe it in the spectra of Rabi oscillations. The full calculations are found in Appendix C.

Phonon Mollow triplet due to double dressing of the spin Fourier specra of Rabi oscillations,

$$\langle \sigma_z[\Omega] \rangle = \int_0^T \langle \sigma_z(t) \rangle \, e^{i\Omega t} \, \mathrm{d}t, \tag{3.98}$$

reflect a linear measurement of the time evolution of the spin at different frequency components Ω. Jumps between multiplicities $\mathcal{F}_{N,M}$ changing M are induced at rates related to Γ_spin, which reflects the coherence rate of Rabi oscillations and can be interpreted as the lifetime of the singly dressed spin. Jumps between different $\mathcal{F}_{N,M}$ changing N occur due to spontaneous emission of the NV qubit at timescales $1/\Gamma_1$. The experimental observation $\Gamma_2 \gg \Gamma_1$ therefore allows us to prioritize the cascade through the phonon energy ladder and fixing N to its mean value $\langle N \rangle$. The different peaks of the Mollow triplet correspond to different transitions from one multiplicity to the next. To find the relative weights, we can define transition rates at which the environment excites jumps through the phonon ladder, associated with the various frequency components:

$$\Omega_\mathrm{m} + \Delta_{N,M}\colon\ 2\Gamma_{+\to-} = 2\Gamma_\mathrm{spin} |\langle +_{N,M+1} | \sigma_z | -_{N,M} \rangle|^2 = 2\Gamma_\mathrm{spin} \cos^4 \theta_{N,M} \sin^2 \theta_N \cos^2 \theta_N$$

$$\Omega_\mathrm{m}\colon\ 2\Gamma_{+\to+} = 2\Gamma_\mathrm{spin} |\langle +_{N,M+1} | \sigma_z | +_{N,M} \rangle|^2 = 2\Gamma_\mathrm{spin} \sin^2 \theta_{N,M} \cos^2 \theta_{N,M} \sin^2 \theta_N \cos^2 \theta_N$$

$$\Omega_\mathrm{m}\colon\ 2\Gamma_{-\to-} = 2\Gamma_\mathrm{spin} |\langle -_{N,M+1} | \sigma_z | -_{N,M} \rangle|^2 = 2\Gamma_\mathrm{spin} \sin^2 \theta_{N,M} \cos^2 \theta_{N,M} \sin^2 \theta_N \cos^2 \theta_N$$

$$\Omega_\mathrm{m} - \Delta_{N,M}\colon\ 2\Gamma_{-\to+} = 2\Gamma_\mathrm{spin} |\langle -_{N,M+1} | \sigma_z | +_{N,M} \rangle|^2 = 2\Gamma_\mathrm{spin} \sin^4 \theta_{N,M} \sin^2 \theta_N \cos^2 \theta_N$$

$$\Delta_{N,M}\colon\ 2\tilde{\Gamma}_{+\to-} = 2\Gamma_\mathrm{spin} |\langle +_{N,M} | \sigma_z | -_{N,M} \rangle|^2 = 2\Gamma_\mathrm{spin} \sin^2 \theta_{N,M} \cos^2 \theta_{N,M} (\cos^2 \theta_N - \sin^2 \theta_N)^2.$$

Requiring that the total sum of all transitions equals 1/2, we find for the individual weights

$$A_0 = 4 \sin^2 \theta_{N,M} \cos^2 \theta_{N,M} \sin^2 \theta_N \cos^2 \theta_N, \tag{3.99}$$

$$A_- = 2 \sin^4 \theta_{N,M} \sin^2 \theta_N \cos^2 \theta_N, \tag{3.100}$$

$$A_+ = 2 \cos^4 \theta_{N,M} \sin^2 \theta_N \cos^2 \theta_N, \tag{3.101}$$

$$A_\Delta = 2 \sin^2 \theta_{N,M} \cos^2 \theta_{N,M} (\cos^2 \theta_N - \sin^2 \theta_N)^2, \tag{3.102}$$

Notice that these considerations inform us why the $\Delta_{N,M}$-component has been absent in the measurement shown in Figure 3.37. It depends on the detuning between the MW and spin frequency. Only a nonzero detuning permits its observation. In this measurement, each vertical line was averaged for about two hours while the MW frequency was tuned to resonance before each acquisition, such that $\delta = 0$. On the other hand, the data measured in Figure 3.35 was acquired over a period of several days without readjustment of the MW frequency, such that drift of the spin resonance was much more likely to occur, resulting in a nonzero detuning. In the experimentally relevant case, where $\delta = 0$, we are therefore left with the three components $\Omega = \Omega_\mathrm{m}, \Omega_\mathrm{m} \pm \Delta_{N,M}$. We find

$$\begin{aligned} A_0 =& \sin^2\theta_{N,M}\cos^2\theta_{N,M}, \\ A_- =& \frac{1}{2}\sin^4\theta_{N,M}, \\ A_+ =& \frac{1}{2}\cos^4\theta_{N,M}. \end{aligned} \tag{3.103}$$

We can motivate an expression for the width of the central line Γ_pop by considering that it reflects the rate of relative change of the populations, which is associated with the emission and absorption of transitions different from Ω_m:

$$\Gamma_\mathrm{pop} = \Gamma_{+\to-} + \Gamma_{-\to+}. \tag{3.104}$$

On the other hand, the sidebands reflect transitions between multiplicities that do change the relative population, which are broadened by radiative damping on the one hand and coherence transfer on the other. We have

$$\Gamma_\mathrm{coh} = \frac{1}{2}(\Gamma_{-\to-} + \Gamma_{+\to+} + \Gamma_{-\to+} + \Gamma_{+\to-}) + \sqrt{\Gamma_{+\to+}\Gamma_{-\to-}}. \tag{3.105}$$

With the expressions found above, we have

$$\begin{aligned} \Gamma_\mathrm{pop} =& 2\Gamma_\mathrm{spin}\left(\sin^4\theta_{N,M} + \cos^4\theta_{N,M}\right), \\ \Gamma_\mathrm{coh} =& 2\Gamma_\mathrm{spin}\left(\frac{1}{2} + \sin^2\theta_{N,M}\cos^2\theta_{N,M}\right). \end{aligned} \tag{3.106}$$

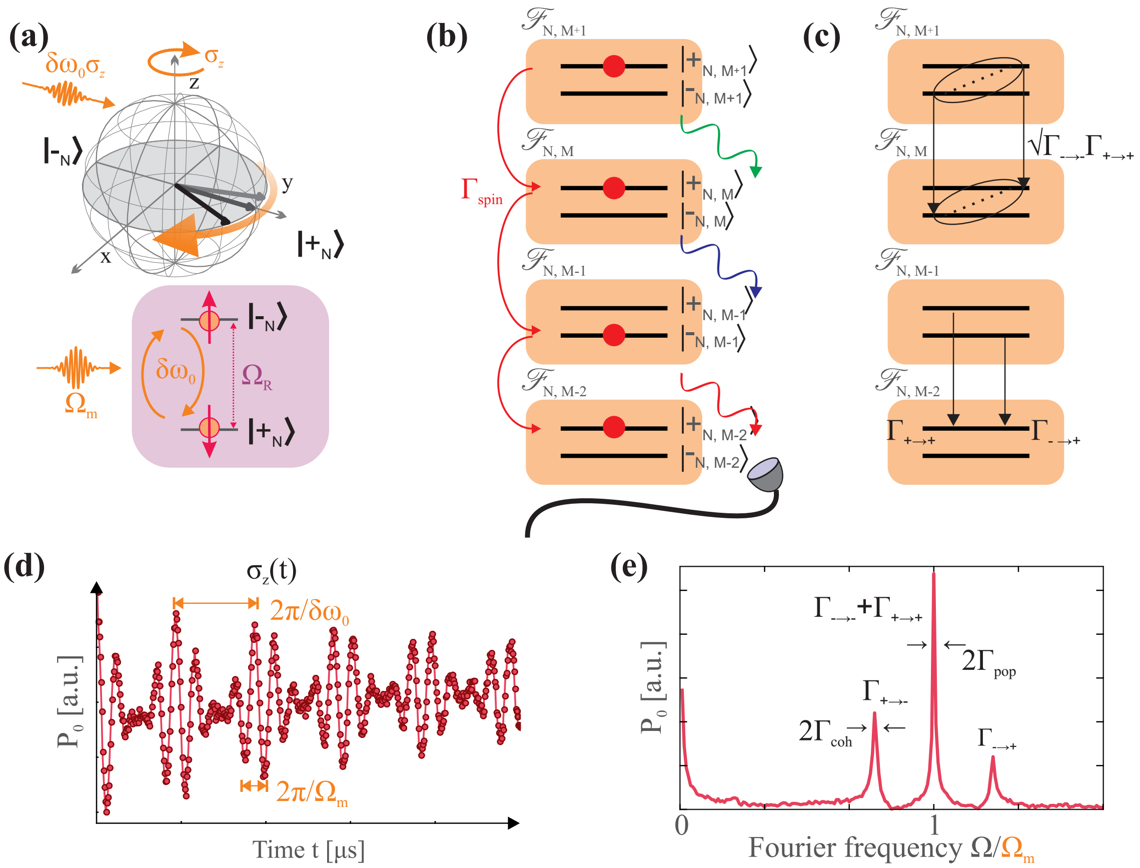

Figure 3.48: The phonon Mollow triplet. **(a)** Diagram illustrating the second dressing through the phonon field. **(b)** Cascade through the phonon Jaynes-Cummings ladder due to interaction with the environment. **(c)** Illustration of the various decay rates. $\sqrt{\Gamma_{-\to+}\Gamma_{+\to-}}$ is the contribution due to coherence transfer between the multiplicities. **(d)** The cascade gives rise to different oscillation frequencies. **(e)** Summary of the different transition rates yielding the individual weights and widths of the Mollow triplet components.

These considerations, summarized in Figure 3.48, readily reproduce the results for the widths and amplitudes found via the Bloch equation approach in case of large drive strength. Noticing that at $\Omega_\mathrm{R} = \Omega_\mathrm{m}$ the decay rates are $\Gamma_\mathrm{pop} = \Gamma_\mathrm{spin}$ and $\Gamma_\mathrm{coh} = \frac{3}{2}\Gamma_\mathrm{spin}$, we verify the agreement with equation (3.89) and (3.90):

$$\begin{aligned}
&\mathrm{Re}\left(\lambda_0(\delta\omega_0 \gg \Gamma_\mathrm{spin})\right) = -\Gamma_\mathrm{spin} = -\Gamma_\mathrm{pop},\\
&\mathrm{Re}\left(\lambda_\pm(\delta\omega_0 \gg \Gamma_\mathrm{spin})\right) = -\frac{3}{2}\Gamma_\mathrm{spin} = -\Gamma_\mathrm{coh},\\
&A_0 = \frac{1}{4}, \qquad A_\pm = \frac{1}{8}.
\end{aligned}$$

Eventually, using the above expressions in equation (3.85) we find a fully analytic form of the *phonon Mollow triplet*. We performed a series of simulations in which we are comparing the numerically obtained Rabi spectra with the analytic form of the phonon Mollow triplet at $\delta = 0$. Figure 3.49 shows the results for $\Omega_\mathrm{m}/2\pi = 10\,\mathrm{MHz}$, $\delta\omega_0/2\pi = 2\,\mathrm{MHz}$, $\delta/2\pi = 0\,\mathrm{MHz}$ and $\Gamma_\mathrm{spin} = 0.203\,\mathrm{MHz}$. In order to improve the match between theory and simulation outcome, we invoked the Bloch-Siegert shift and adapted the resonance condition $\Omega_\mathrm{R} \approx \Omega_\mathrm{m} \to \Omega_\mathrm{R} \approx \Omega_\mathrm{R}^*$.

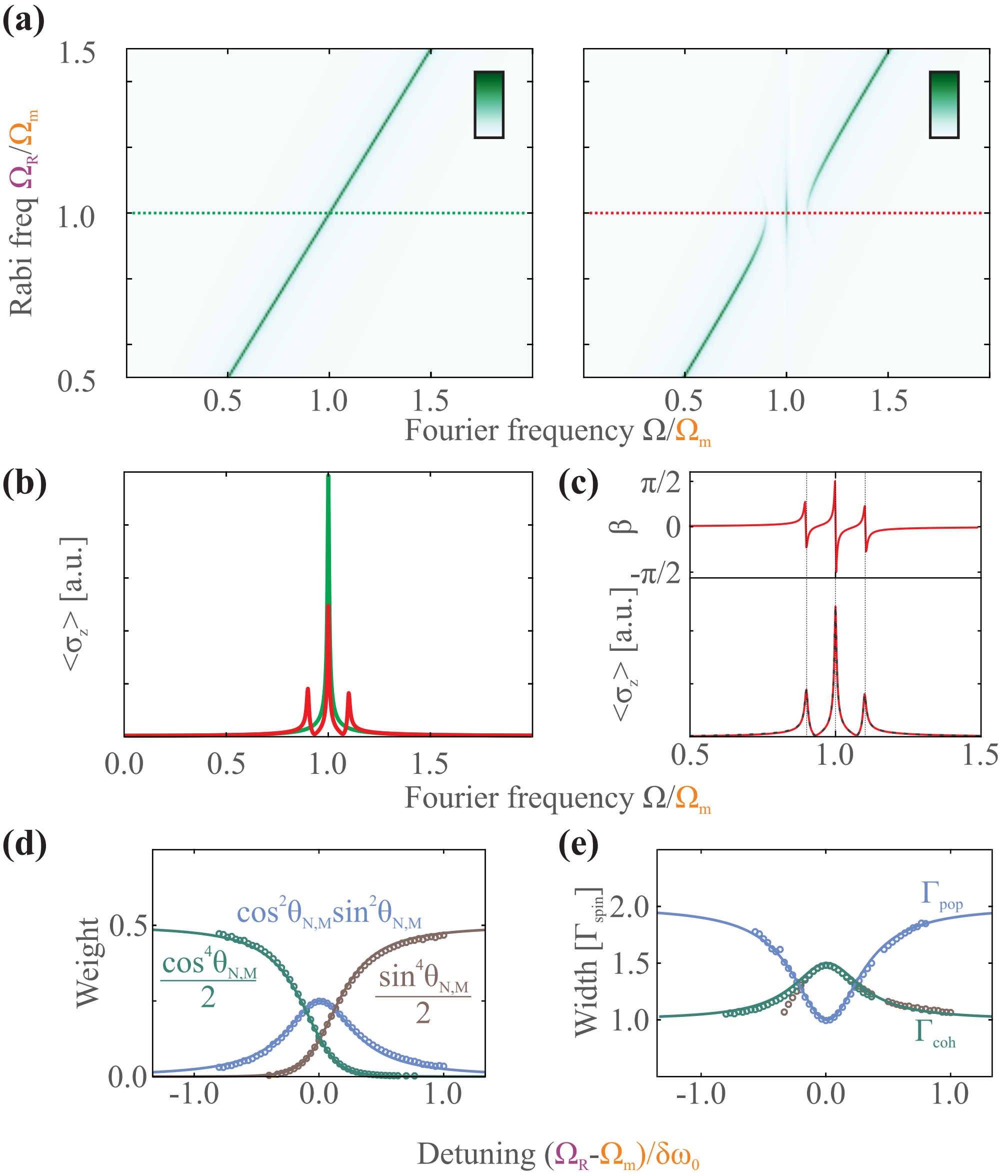

Figure 3.49: **(a)** FFT maps without and with anti-crossing at $\Omega_\mathrm{R} = \Omega_\mathrm{m}$ and $\delta\omega_0/2\pi = 2$MHz. **(b)** Phonon Mollow triplet compared to unperturbed cut along the lines indicated in **(a)**. **(c)** Fit of the phonon Mollow triplet with three coherently added Lorentzians, as in equation (3.85) . **(d)** Weight of each Lorentzian. Analytic expressions (3.103) (solid lines) compared to values from the simulations (dots). **(e)** Widths of each Lorentzian. Simulation data (dots) compared to Γ_pop and Γ_coh of expression (3.106).

3.7.8 Protection of spin coherence

When inspecting Figure 3.35, we observe that the central peak of the Mollow triplet, seen in **(b)**, is in fact much narrower than the single peak observed in **(a)**. This alteration can in principle be attributed to the different noise spectral density at two different Rabi frequencies, which were here 4.5 and 6 MHz. In order to verify this assumption we repeat a Rabi measurement with and without modulation at a drive strength $\Omega_\mathrm{m}/2\pi = 6\,\mathrm{MHz}$, see Figure 3.50 **(a)**. Here we clearly observe that the coherence time increases considerably under the spin locking conditions. This is additionally evidenced by a direct comparison of the corresponding Fourier spectra in **(b)**. Fitting the two curves to Lorentzian lineshapes, we extract two different values for Γ_spin.

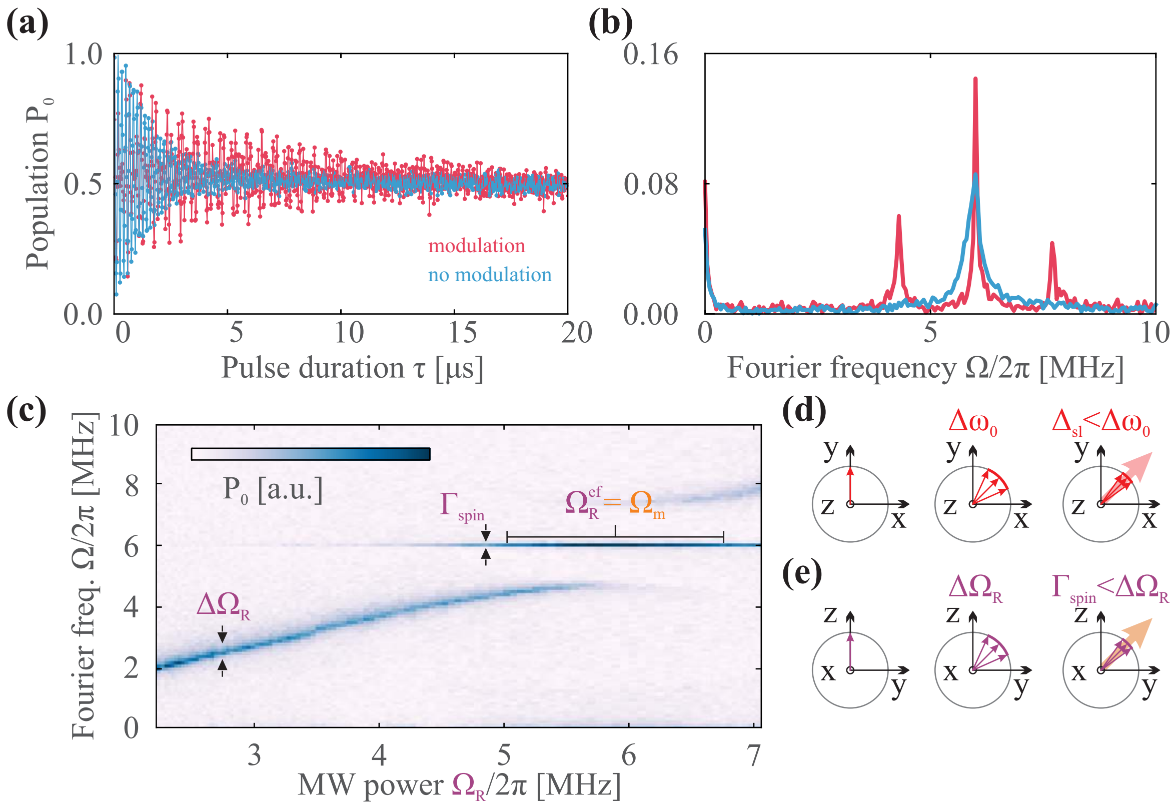

Figure 3.50: Locking of the Rabi frequency. The temporal traces of Rabi oscillations in **(a)** show an increase of the coherence time when the spin energy is modulated at $\Omega_\mathrm{m} = \Omega_\mathrm{R}$. The Fourier spectra in **(b)** therefore show a triplet with a central component much narrower than the single Rabi peak. Fitting both curves to Lorentzian lineshapes yields a reduction of the linewidth by more than a factor three from $\Gamma_\mathrm{spin} = 2\pi \times 80\,\mathrm{kHz}$ to $\Gamma_\mathrm{spin} = 2\pi \times 25\,\mathrm{kHz}$. In **(c)** spin locking in the dressed state basis demonstrates the stability of the Rabi frequency with varying MW drive power Ω_R over the locking region. **(d)** Spin locking protocol as it is used in NMR experiments. The magnetization $\mathbf{m}$ (red arrow) is turned into the equatorial $(\mathbf{x},\mathbf{y})$-plane, where it precesses freely. The Bloch vector is spreading out due to the frequency distribution of width $\Delta\omega_0$ in the spin ensemble. If an external field oscillating at ω_0 is added, the Bloch vector is forced to follow, which suppresses inhomogeneous dephasing processes and therefore reduces the spreading to Δ_sl. **(e)** The same is true for the dressed spin evolving in its equatorial plane, which is here the $(\mathbf{x},\mathbf{y})$-plane. The external RF field oscillates at $\Omega_\mathrm{m} = \Omega_\mathrm{R}$. This spin locking suppresses effects of the variation $\Delta\Omega_\mathrm{R}$ and, for sufficiently large amplitudes $\delta\omega_0$, reduces the width of the central peak to the true Γ_spin (arising from the spin bath) as indicated in **(c)**.

The effect that so far we have loosely called *spin locking*, protects the Rabi oscillations from decoherence. In fact, the situation is very similar to the spin locking protocol known from the field of NMR [123]. In typical experiments on large spin ensembles, the magnetization $\mathbf{m}$ provided by an external field $\mathbf{B_0}$ is projected onto the equator of the Bloch sphere by a $\pi/2$-pulse. The free evolution of $\mathbf{m}$ is described by an in-plane rotation at the Larmor frequency $\omega_0 = B_0 g \mu_B/\hbar$. However, inhomogeneous broadening mechanisms, for example due to a spatially inhomogeneous field B_0, the Larmor frequency ω_0 varies throughout the sample, giving rise to the width $\Delta\omega_0$. This will cause the magnetization $\mathbf{m}$ to spread out. This dephasing due to inhomogeneous broadening can be overcome by means of application of a magnetic field in the equatorial plane, oscillating at the ensemble's Larmor frequency (the so called Hartmann-Hahn condition). In the frame rotating at ω_0, the freely precessing magnetization then sees a static field and tends to align with it. Consequentially, an increase of the dephasing time in the laboratory frame can be detected by means of a Ramsey measurement, see

Figure 3.50 **(d)**. If the strength of the spin lock field is larger than $\Delta\omega_0$, the broadening becomes homogeneous and is limited by transverse relaxation processes.

In case of the MW driven spin experiencing energy modulation at the Rabi frequency, it is the singly dressed spin, rotating in the equatorial plane of the dressed spin's Bloch sphere, that experiences spin locking due to the monochromatic field $\delta\omega_0 \cos\Omega_\mathrm{m} t$. Inhomogeneous broadening processes that lead to a spread $\Delta\Omega_\mathrm{R}$ in the Rabi frequency $\Omega_\mathrm{R}/2\pi$ can thus be overcome.

This is clearly evidenced in Figure 3.50 **(c)**: close to the spin locking condition, $\Omega_\mathrm{R} \approx \Omega_\mathrm{m}$, the spin gets locked onto the frequency of the oscillator and the central component of the triplet at Ω_m does not shift for large variations of the drive strength Ω_R. This locking effect is beneficial as long as broadening of the Rabi peaks is less than the monochromatic field strength: $\Delta\Omega_\mathrm{R} < \delta\omega_0$. In our experiment, thermal effects at room temperature operation lead to slight drifts of the position of the external magnetic field, shifting the spin resonance frequency $\omega_0/2\pi$. This causes a detuning of the effective dressed spin energy splitting, $\Omega_\mathrm{R}^\mathrm{eff} = \sqrt{\Omega_\mathrm{m}^2 + (\omega - \omega_0)^2}$. While these thermal drifts occur on a long time scale, averaging data acquisition over several tens of minutes makes our Rabi measurement sensitive to these fluctuations. The monochromatic energy modulation lifts this dependency on the MW power and frequency. In the case of spin locking, the detuning δ is absent in the expression for the position of the central component of the triplet, see equation (3.85). Notice that this is not the case for the sidebands, whose position depends on $\Delta_\mathrm{Mollow}(\delta)$, see expression (3.54). Concerning the component evolving at Ω_m, the coherence time of Rabi oscillations is then limited by the magnetic noise induced by the bath on the one hand and variations of the oscillator frequency on the other hand, while the latter effect is negligible in case of a monochromatic modulation source. The dressed spin then sees the *true* Γ_spin, which is due to the finite spectral density of the electromagnetic environment[11]. We therefore stress that by locking onto a classical system with well controlled properties the quantum system has become insensitive to the experimental noise sources.[12]. This procedure then presents a resource with the help of which the data quality of the noise sensing protocol of section 3.5.5 can be dramatically improved. Employment of the spin locking protocol is therefore fundamental when using Rabi oscillations as an analyzer of the true environmental noise spectral density.

3.7.9 The doubly dressed spin picture in the limit of a weak MW drive

The goal of this section is to establish the connection between the picture of the doubly dressed spin and the modification of the effective Rabi frequency by Bessel functions in case where $\Omega_\mathrm{R} \ll \Omega_\mathrm{m}$. The problem is considered in the context of NMR in [122]. We will here give a recapitulation and then motivate that it also holds for the doubly dressed spin. In the context of NMR, one starts with a single spin 1/2 system with eigenstates $|\pm\rangle$, which is irradiated by a transverse radiofrequency field in the absence of an external magnetic field ($\omega_0 = 0$):

$$H(\omega_0 = 0) = \hbar\Omega_\mathrm{m} a^\dagger a + \lambda\sigma_x \left(a^\dagger + a\right), \tag{3.107}$$

where σ_x is the usual Pauli matrix for the spin 1/2 case. H is diagonal in the σ_x-basis. Using $\epsilon = \pm$, we write:

$$\begin{aligned} H_\epsilon &= \hbar\Omega_\mathrm{m}\tilde{a}^\dagger\tilde{a} + \frac{\epsilon}{2}\lambda\left(a^\dagger + a\right) \\ &= \hbar\Omega_\mathrm{m}\left(a^\dagger + \frac{\epsilon\lambda}{2\hbar\Omega_\mathrm{m}}\right)\left(a + \frac{\epsilon\lambda}{2\hbar\Omega_\mathrm{m}}\right) - \frac{\lambda^2}{4\hbar\Omega_\mathrm{m}}. \end{aligned}$$

---

[11] The sidebands do not experience the same degree of protection, which is why $\Gamma_\pm > 3\Gamma_0/2$ for the fitting values retrieved from the data in Figure 3.43.

[12] A similar effect has recently been discussed by the authors of [145], where it was shown that the coherence time of Rabi oscillations can be extended by application of a series of mutually orthogonal fields, each at the spin locking condition of the preceding one.

Making use of the displacement operator $D(\alpha) = \exp\left(\alpha^* a - \alpha a^\dagger\right)$, with $\alpha = -\epsilon\lambda/2\hbar\Omega_\mathrm{m}$, H_ϵ is displaced to

$$\tilde{H} = \hbar\Omega_\mathrm{m} a^\dagger a - \frac{\lambda^2}{4\hbar\Omega_\mathrm{m}}, \tag{3.108}$$

which has eigenenergies

$$E_m = m\hbar\Omega_\mathrm{m} - \frac{\lambda^2}{4\hbar\Omega_\mathrm{m}} \tag{3.109}$$

and degenerate eigenstates

$$|\widetilde{\epsilon_x, m}\rangle = e^{-\frac{\epsilon\lambda(a^\dagger - a)}{2\hbar\Omega_\mathrm{m}}} |\epsilon_x, m\rangle, \tag{3.110}$$

where $|\epsilon_x\rangle$ are the spin eigenstates in the σ_x-basis. The degeneracy of the states $|\widetilde{\epsilon_x, m}\rangle$ is lifted by application of an external static magnetic field along the spin direction, $H_z = \hbar\omega_0\sigma_z$. Using a first order perturbative treatment, the action of H_z is given by its projection onto the eigenstates $|\widetilde{\epsilon_x, m}\rangle$:

$$\begin{aligned} \langle\widetilde{\epsilon_x, m}|H_z|\widetilde{\epsilon_x, m}\rangle &= 0, \\ \langle\widetilde{+_x, m}|H_z|\widetilde{-_x, m}\rangle &= \frac{\hbar\omega_0}{2}\langle m|e^{\frac{\lambda}{\hbar\Omega_\mathrm{m}}\left(a^\dagger - a\right)}|m\rangle. \end{aligned} \tag{3.111}$$

Notice that the last term gives the energy splitting between the spin eigenstates in the presence of a weak static field and a coherent drive field. The expression $\langle m|e^{\frac{\lambda}{\hbar\Omega_\mathrm{m}}\left(a^\dagger - a\right)}|m\rangle$ can thus be interpreted as a Landé factor of the dressed spin. In case of a coherent field, it can be shown that this Landé factor can be approximated by the zeroth order Bessel function $\langle m|e^{\frac{\lambda}{\hbar\Omega_\mathrm{m}}\left(a^\dagger - a\right)}|m\rangle \approx J_0\left(\frac{2\Omega_1}{\Omega_\mathrm{m}}\right)$, where $\Omega_1 = \lambda\sqrt{\bar{m}}/\hbar$ is the coherent field strength.

The above arguments are also valid for the MW dressed spin experiencing energy modulation due to the RF field. In that case $\lambda\sigma_x\left(a^\dagger + a\right)$ of (3.107) becomes replaced by the interaction Hamiltonian expressed in the dressed state basis, see equation (3.64):

$$\lambda\sigma_x\left(a^\dagger + a\right) \rightarrow \frac{1}{2}\hbar g_z \sigma_x^{(N)}\left(a^\dagger + a\right),$$

resulting in a Landé factor of the dressed spin, $J_0\left(\frac{\delta\omega_0}{\Omega_\mathrm{m}}\right)$. The MW Hamiltonian H_MW plays the role of H_z in the rotating frame. Notice that the spin 1/2 degeneracy if lifted by an external field, which splits the sublevels by $\hbar\omega_0$. Likewise, the MW field can be thought to lift the degeneracy of the states $|\pm_N\rangle$, inducing an energy splitting of $\hbar\Omega_\mathrm{R}$ between them. By analogy, we have $\omega_0 \rightarrow \Omega_\mathrm{R}$. We remark that the perturbative treatment leading to expression (3.111) enforces the condition $\Omega_\mathrm{R} \ll \Omega_\mathrm{m}$, which is in agreement with our experimental observation: modulation of the Rabi frequency in terms of Bessel functions was observed for small MW powers. By detuning the MW frequency such that $\delta = k\Omega_\mathrm{m}$, we can access higher order resonances. The dressed spin Landé factor then evaluates to $\langle m|e^{\frac{\lambda}{\hbar\Omega_\mathrm{m}}\left(a^\dagger - a\right)}|m-k\rangle = J_k\left(\frac{\delta\omega_0}{\Omega_\mathrm{m}}\right)$ [166]. Finally, in the limit $\Omega_\mathrm{R} \approx \Omega_\mathrm{m}$, the dressed state approach produces the Mollow triplet picture presented in the preceding sections.

3.8 Conclusion

Monochromatic modulation of the spin energy leads to a wide range of consequences. Studying the average spin energy in the steady state regime by measuring ODMR spectra has revealed the existence of an adiabatic regime where the change of energy occurs on a time scale much larger than the spin lifetime and the spin resonances become broadened. Conversely, fast periodic energy variation leads to frequency modulation of the spin, whose spectra thereupon exhibit resolved sidebands.

We have subsequently investigated the dynamics of the MW driven spin. These can be interpreted with the help of an effective field theory, in which a pseudo two level system is created, whose energy splitting is proportional to the frequency of driven evolution. In the resolved sideband regime, the spin can be driven at frequency detunings that correspond to integer multiples of the modulation frequency. For small enough strength of the MW drive, the Rabi frequency associated with each of those resonances is modulated by Bessel functions.

The dynamics of the driven spin become strongly altered when the modulation and drive frequency match, which was studied here at a resonant MW drive. Beating signatures between several frequencies appear in the spin's time evolution and the spectra of Rabi oscillations are marked by a symmetric triplet structure. This phenomenon, which we have labeled a Mollow triplet in analogy to experiments from atom physics, is the result of a twofold dressing of the spin with first the MW and second the RF field. Remarkably, the central component of the triplet locks the spin dynamics to the modulation frequency of the mechanical oscillator. In order to adequately describe these signatures, we have presented two approaches. On the one hand, Bloch equations of the dressed spin irradiated by a resonant field were considered, which lead to explanations at the *spin locking* condition. On the other hand, a study of the time evolution of the doubly dressed eigenstates has given insights to the strong coupling regime even when the Rabi and modulation frequencies do not match.

The effect that we call *spin locking* here is reminiscent to the spin locking effect known from NMR and applies to the dressed spin in our case. An increase of decay time of Rabi oscillations was observed, as the evolution of the spin becomes insensitive to variations of the MW power, which are dominated by thermal drifts.

These effects have important consequences and their observation in a hybrid device would constitute a significant development in this field of physics. They show how the spin dynamics can be tuned to evolve at the frequency at which a mechanical oscillator exhibits its maximum mechanical susceptibility. Under these conditions, forces of the spin exerted onto the mechanical oscillator can be resolved with a sensitivity exceeding the one of a static force by many orders of magnitude. At the same time, as Rabi oscillations become more coherent, spin forces become condensed in a smaller frequency interval.

For these reasons, we dedicate the next chapter to the observation of the *spin locking* effect in a NV spin - SiC nanowire hybrid system.

Chapter 4

Parametric coupling of a single spin qubit to a nanomechanical oscillator

In this chapter we are going to present an experimental realization of a hybrid spin mechanical system consisting of a SiC nanowire and a single NV spin. We first start with describing the overall experimental setup, the mechanical resonator and its functionalization with the NV spin. Second, we will explain how the mechanical displacement is measured and third, we describe the microwave guide and the magnetic structure that is used to couple the spin to the mechanical motion.

The second part of this chapter is dedicated to detailing the complex alignment between spin orientation, mechanical displacement and magnetic gradient directions. We will show how first the orientation of the NV defect is found and then how the MW and static magnetic fields are aligned. Second we calibrate the magnetic field strength and eventually determine the strength of the parametric coupling when the SiC nanowire is displacing the spin through an inhomogeneous magnetic field gradient in any direction.

As an additional feature to the RF waveguiding system of Chapter 3, the SiC nanowire exhibits a mechanical susceptibility, which is enriched by the fact that mechanical resonances are split into two orthogonal polarizations of slightly different frequencies. The last section is thus dedicated to the description of spin dynamics while the hybrid interaction gains in complexity due to the vectorial aspect of the coupling. We will start this part by considering the impact of the two-directional displacement of the oscillator. By initially fixing the excitation of the resonator to one single mechanical polarization, we continue in order to show that the Mollow triplet of the MW dressed spin dynamics can indeed be observed in this system, all while confirming the dependencies on MW field strength and oscillation amplitude as was found in the previous chapter. We then invoke experimentally the resonator's mechanical susceptibility. In the presence of a second mechanical mode, the oscillation direction changes as the mechanical drive frequency is swept and we will show how the Mollow triplet signature is affected. Finally, we present the observation of modifications of the spin dynamics due to coupling terms that are quadratic in the mechanical displacement.

4.1 Experimental setup

In this section we will explain how a spin mechanical hybrid device can be created by functionalizing a SiC nanowire with a single NV defect (a sketch of such a device is shown in Figure 4.1). Furthermore, we will describe how the mechanical motion is detected and excited. Afterward, we will discuss the waveguide and magnetic gradient used to manipulate the spin and couple its dynamics to the oscillator motion, respectively.

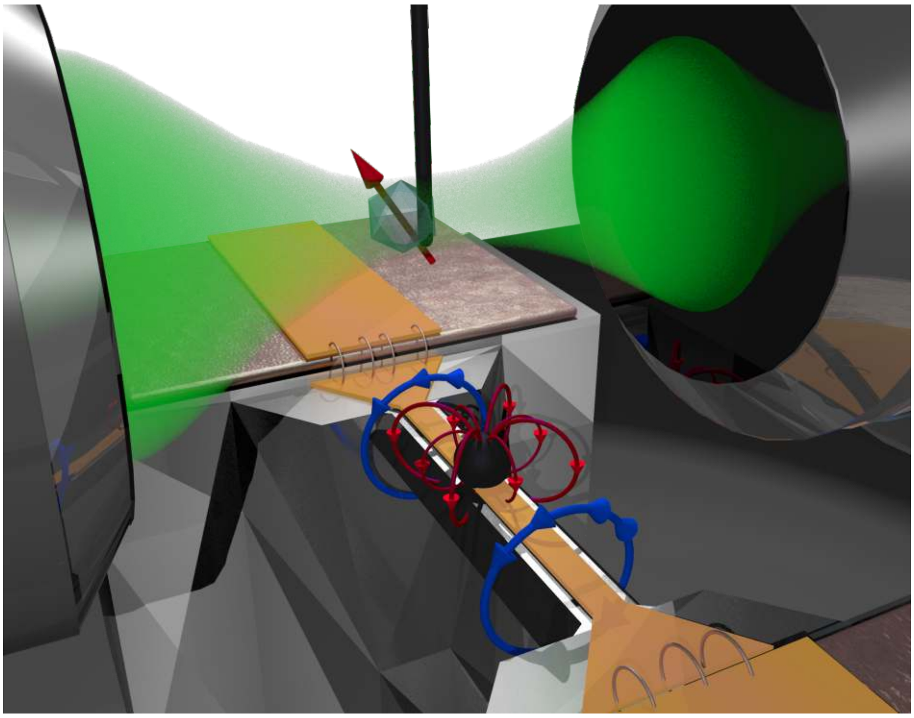

Figure 4.1: Sketch of the core part of the dispersively coupled hybrid spin mechanical system consisting of a SiC nanowire and a single NV defect immersed in a strong magnetic field gradient.

4.1.1 Overall experiment

The setup is shown in Figure 4.1, presenting a conceptual graphic and in Figure 4.3 in form of photographs. The experiment has been entirely developed from scratch, in a joint work with B. Pigeau and L. Mercier de Lépinay. The challenge was to combine in a volume of a few microns, the functionalized nanowire, the magnetic field gradient source, the microwave antenna and the electrostatic actuation. The difficulty was further aggravated by the necessity to have control on the orientation of the NV defect, magnetic field, oscillation directions and electrostatic force actuation. Also, an extremely high stability was required to operate the system: in a magnetic field gradient of 10^5 T/m, moving by 1 μm shifts the static field experienced by the NV spin by 100 mT, and represents a 3 GHz frequency shift, which is impossible to handle experimentally. Requiring a drift of less than 3 MHz imposes a stability of 1 nm over the measurement duration, which can last for hours. The strategy adopted was to keep the functionalized nanowire fixed in space and to organize the experiment around it. We have developed a overhanging MW waveguide, supporting a magnetic microstructure providing the strong magnetic field gradient. It is also used to apply an electrostatic force to drive the spin-functionalized nanowire into motion. The optical microscope objective was mounted on piezo actuators to track the NV defect in space. The whole experiment was mounted in a homemade vacuum chamber. Note that the results reported here, except for determination of the vibration orientations, were obtained at ambient pressure. However, the chamber nonetheless played a crucial role in ensuring a stable operation of the system.

Optical setup

The overall layout of the optical table is sketched in Figure 4.2. The laser source employed for fluorescence measurements and optomechanical readout is a 532 nm diode pumped solid-state frequency doubled Nd:YaG laser (model *Torus* from Laser Quantum, 200 mW maximum output power). While the *GEM* model employed in the test setup of Chapter 3 is a longitudinal multimode laser, this low noise, single frequency light source was found appropriate to ensure a great pump intensity stability and presented weak intensity noise. A confocal microscope arrangement is also implemented, the main novelty being the use of the reflected and transmitted intensities on quadrant photodiodes to read out the vibrations of the functionalized nanowire. Two injection paths are also employed. On a direct path, laser beam diameter and polarization can be controlled. An indirect path serves to adjusted and modulate the laser intensity with an AOM. The latter is controlled either by a network analyzer (Agilent E5061B) for optical force excitation or by an arbitrary TTL pulse generator (PulseBlaster 500 card from SpinCore) in order to allow ns timing of optical pulses. The laser enters the vacuum chamber through an optical window (covered with a broadband anti-reflection coating) and is reflected by a dichroic mirror located inside the cavity. Preventing the pump beam and fluorescence channel to traverse the same optical window ensures that no additional parasitic fluorescence is detected. The laser is focused onto the functionalized nanowire and the emitted NV fluorescence is collected through a high numerical aperture microscope objective (model EC plan - NEOFLUAR 100 ×0.75 from Zeiss), with a 4 mm working distance. The fluorescence exiting the chamber by an optical port is then filtered to select the NV emission band, subsequently split into two paths by a polarizing beam splitter and detected by two APDs. An active splitter based on logic gates, developed by C. Hoarau, duplicates the photon counts with variable delays. The different outputs are interfaced to a Nanonis scan controller, which controls the laser position, to a PCIe 6323 board (National Instruments) for ESR measurements and to a FastComTec MCS6A card for time resolved fluorescence detection, needed for the measurement of Rabi oscillations. The two APDs also permits to realize autocorrelations measurements of the emitted fluorescence. A white light source and a CCD camera (Watec 101N+) can optionally be used for coarse alignment of the nanowire, waveguide and magnetic gradient source. The reflected intensity is collected through a 90/10 non-polarizing beam splitter which is placed on the injection path, and focused on a quadrant photodiode amplifier developed by D. Lepoittevin. Similarly a second microscope objective can be installed facing the injection objective to collect the transmitted light. The DC output of both detectors can be used for fine positioning of the experiment, while the differential HF output serves for readout of the nanowire vibrations.

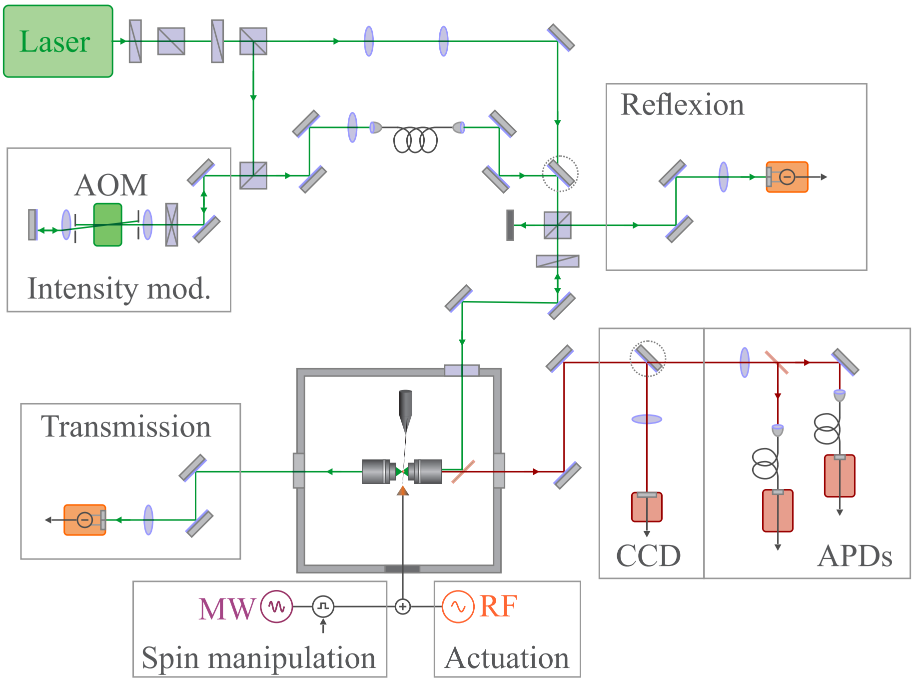

Figure 4.2: Experimental setup. MW manipulation and optical excitation of the NV defect and spin readout are identical to the setup of the test system. A novelty here is the usage of two APDs, allowing correlation measurements of the NV fluorescence and optical detection of the nanowire displacement, which is outlined in section 4.1.3.

Microwave - Radiofrequency apparatus

Spin manipulation is enabled by a MW antenna which also holds the magnetic gradient source that will be described in greater detail in section 4.1.5. It is brought in the vicinity of the functionalized nanowire by means of a closed loop Physik Instrument Nanocube, moving by $100 \times 100 \times 100\,\mu$m. The MW source is a SMB100A Signal Generator from Rohde & Schwarz. Its intensity is externally modulated by a fast microwave switch from Minicircuit (ZASWA-2-50DR++, coaxial High Isolation Switch) which is TTL controlled by the PulseBlaster card that governs the time sequence of dynamical spin measurements. When needed, a 25 W MW amplifier from Amplifier Research was used. Two vacuum feed-throughs with SMA connections are employed to bring MW and RF signal in and out of the vacuum chamber. A 50 Ohm 2W load was placed on the output port, to avoid power dissipation inside the chamber. The waveguide was also used for electrostatic actuation of the nanowire motion, which is described in section 4.1.4.

Micro-positioning and position control

As already mentioned, the functionalized nanowire serves as a spatial reference in the experiment. It is mounted on a coarse XYZ translation stage (Microcontrole, 562) equipped with piezo motors (Picomotors, vacuum compatible from Newport) that serves for coarse positioning of the nanowire on the optical axis. The injection objective is mounted on a XYZ piezostage (733.DD from Physik Instrument, vacuum compatible version) with a $30 \times 30 \times 10\,\mu$m scan range. A Nanonis scan engine serves for imaging the system and tracking the NV fluorescence in time to compensate the thermal drifts with respect to the optical axis. The piezo stage holding MW waveguide and magnetic structure is mounted on a second XYZ translation stage, that also supports the translational stage holding the nanowire. As such, after a preliminary alignment phase, where the motorized stages are involved, the nanowire ends within the scan range of the optical microscope, while the magnetic gradient source can be micro-positioned in the vicinity of the functionalized nanowire. Once this configuration is reached, all of the positioning parameters can be derived from physical measurements and optical monitoring is not needed anymore. The piezo stage holding the magnetic field gradient is controlled by a National Instrument (PCIe6323) board interfaced by a homemade scanning software. One computer is dedicated to the microscope objective position control, realized through the Nanonis scan engine, including the homemade tracking routine. A second computer is dedicated to MW control and magnetic gradient positioning. Furthermore, it holds the PulseBlaster Pro card that synchronizes the time resolved fluorescence measurements.

Vacuum chamber

The chamber has been realized according to a homemade design, incorporating a large internal volume to host several massive translation stages as well as numerous optical and electrical accesses, built such that it can sit directly on the optical table. It is machined in a monolithic aluminum block, see Figure 4.3, and was anodized to maintain a high surface quality over time. A 300 l/s turbopump (Agilent/Varian) allows to reach 10^{-6} mbar under continuous pumping, but in order to avoid excessive vibrations, the pump is stopped during sensitive measurements. In that case, a static pressure below 10^{-2} mbar can be maintained during several days.

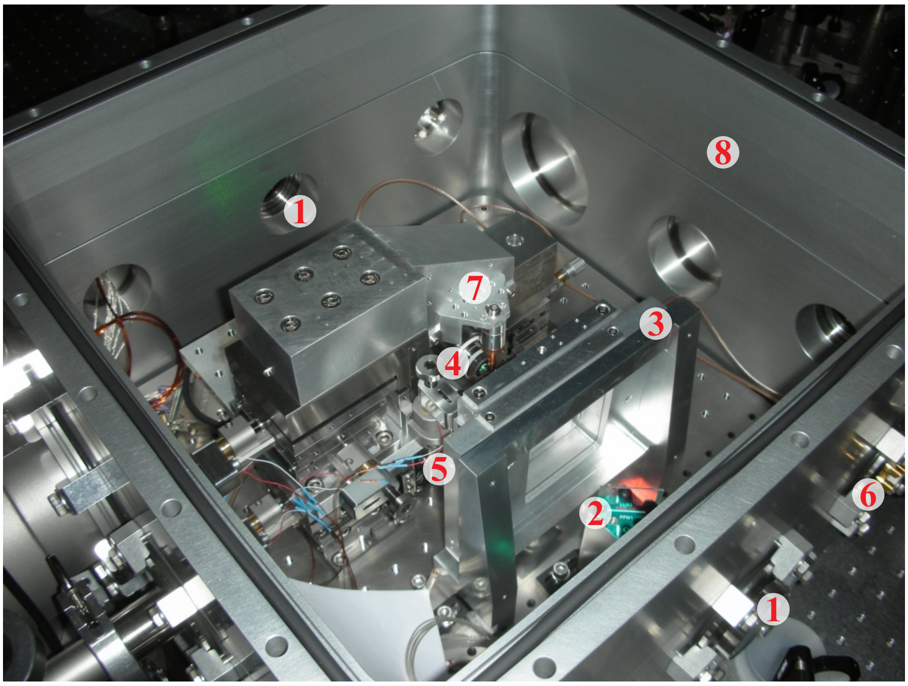

Figure 4.3: Photograph of the setup. **1** Optical windows. **2** Dichroic mirror. **3**Mount for microscope objective (injection and reflection). **4** Microscope objective (transmission). **5** Physik Instrument Nanocube holding antenna. **6** SMA connecters for MW. **7** XYZ coarse translation. **8** Vacuum chamber.

4.1.2 SiC nanowires functionalized with a NV spin qubit

Long SiC nanowires with large aspect ratios and oscillation frequencies in the 100 kHz-10 MHz range exhibit large zero point fluctuations. In mechanical hybrid systems, these resonators might therefore serve as potential candidates to enter a regime of strong spin-mechanical interaction at the level of a few motional quanta. Here, however, we seek to demonstrate the previously seen Mollow triplet phenomena of the driven NV spin dynamics in the hybrid setup and to expose aspects of vectorial coupling in the system. Hence, we are interested in working in the spin dynamical resolved sideband regime, where we observe a mechanical oscillation frequency that surpasses the spin decay rates. Consequently, we have chosen to work with rather short and massive nanowires. Figure 4.4 shows a scanning electron microscope image of a 102 μm long SiC nanoresonator that was selected from a batch of available samples provided by the collaborating group *Physique des nanostructures et emission de champ* from the Institut Lumière Matière in Lyon [95,96]. The nanowire used in our measurements has a length of 6 μm and a width of 150 nm and is not shown.

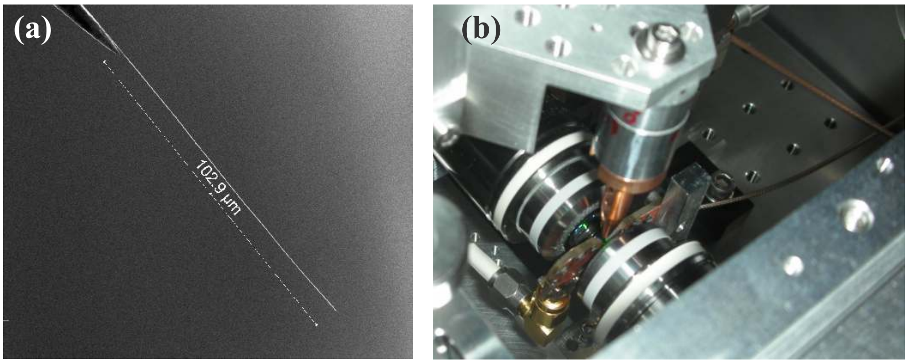

Figure 4.4: SiC nanowire control. **(a)** SEM image of a SiC nanowire. The dimensions of this sample are $L = 102\,\mu$m and $d = 190$ nm. **(b)** Photograph of the sample holder (made from copper) holding the tungsten tip with the SiC nanowire in the focal point of the confocal microscope.

In order to attach a single NV defect to the tip of the SiC nanowire, we use the arrangement of the position controllers for the nanowire and waveguide of the hybrid setup. The nanowire is mounted in the copper sample holder which is fixed to the translational stage. A drop of the nanodiamond solution (see section 3.2.1) is deposited on a Silicon wafer which is put on the same piezo stage that otherwise holds the waveguide. White light illumination of the detection volume of the confocal microscope and the CCD camera facilitate navigation of the drop of NV solution, which is steered upward until its surface is penetrated by the nanowire. We then direct green laser light onto the nanowire tip. This creates heat convection favoring a flow of nanodiamonds near the resonator. A small optical–tweezers–like effect might also play a role [170]. In order to limit the number of nanodiamonds attaching themselves to the wire by a surface effect, the process is interrupted after a few seconds by moving the wire out of the solution. We then use the confocal microscope and the ability to perform fluorescence scans in the vertical $(\mathbf{x}, \mathbf{y})$-plane dissecting the nanowire, as shown in Figure 4.5 **(a)**. If NV defects have attached to the nanowire, they become visible as bright spots in these measurements. By measuring an autocorrelation function of the light emitted from the fluorescence spots, their single photon source character can be verified, see Figure 4.5 **(b)**. Ultimately, an ODMR measurement and detection of the spin resonance near 2.87 GHz verifies that the emitters are indeed negatively charged NV defects (see Figure 4.5 **(c)**). If no NV defect is found, the process is repeated. Despite this approach being completely heuristic, the NV yield is usually quite high and after a few iteration a single NV defect can be attached to the nanowire extremity.

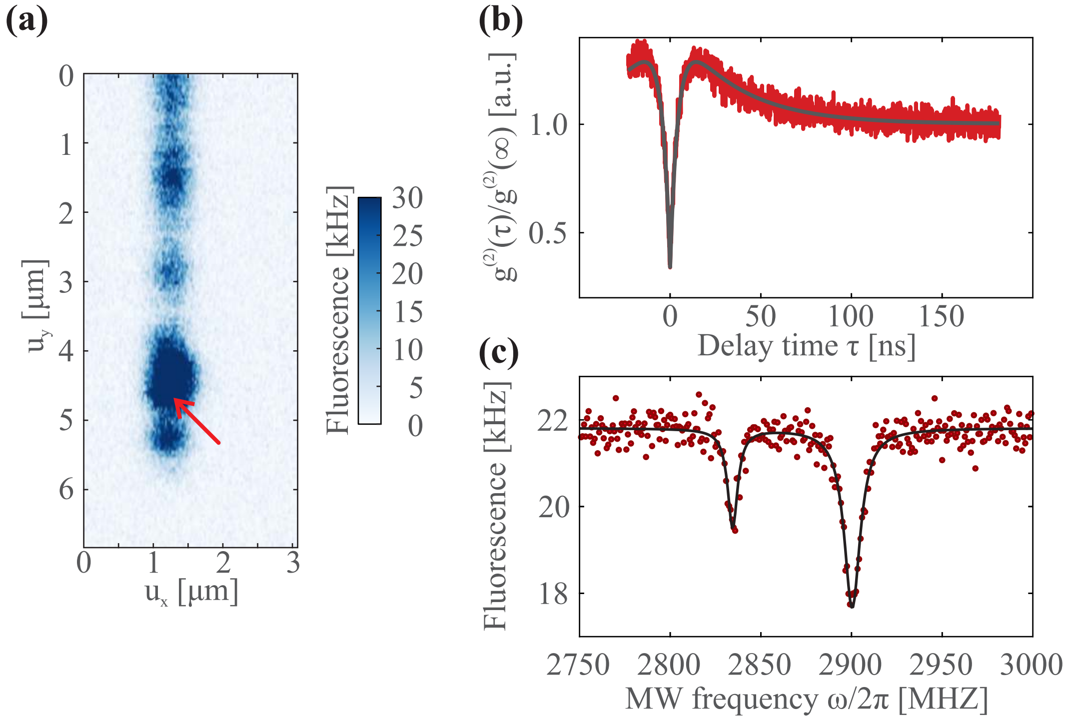

Figure 4.5: Characterization of fluorescence centers attached to the SiC nanowire. **(a)** Fluorescence image of the functionalized nanowire. The bright spots are fluorescence sources attached to the nanowire. The spot marked by the red arrow corresponds to the NV defect of the hybrid device. **(b)** Autocorrelation function of the fluorescence emerging from the position marked by the red arrow in **(a)**. The dip below 0.5 verifies single photon source character. **(c)** ODMR measurement of the single photon emitter ultimately verifying the presence of a single NV defect. We observe a large separation of the two ESR peaks due to strong strain splitting as well as a weak magnetic fields. The solid line indicates the fit to a sum of two Lorentzian lineshape.

4.1.3 Measurement of the nanowire motion

Despite the sub-wavelength diameter of the SiC nanowire, its vibrations can be efficiently read out optically. This is facilitated by the existence of Mie resonances which enhance the scattering cross section of the nanowires. In turn, they interact more efficiently with the tightly focused laser beam used for pumping the NV defect. The latter is then also used to monitor the nanomotion of the functionalized SiC nanowire. As a consequence of the material's large bandgap, optical intensities of up to 100 μW can be employed without inflicting thermal damage on the sample. Moreover, at such optical powers no heating signatures could be observed on the nanowire's Brownian motion. In the experimental setup we move the tightly focused beam from the 532 nm laser across the nanowire. The transmitted or reflected beam is recollected and directed onto a quadrant photodiode (QPD), which converts the optical intensity impinging on each quadrant into a voltage signal (see Figure 4.6 **(a)**). As the beam position is slowly swept across the QPD, the DC difference signal of the two quadrants $V_\ominus(\mathbf{r_0})$ changes as a function of the relative position $\mathbf{r_0}$ between the beam waist and the nanowire. Figure 4.6 **(b)** represents $V_\ominus(\mathbf{r_0})$. When the nanowire vibrates, its extremity being positioned at $\mathbf{r_0} + \delta\mathbf{r}(\mathbf{t})$, it generates a differential intensity fluctuation $V_\ominus(\mathbf{r_0} + \delta\mathbf{r}(\mathbf{t}))$ whose dynamical contribution

$$\delta V_\ominus(t) = \delta\mathbf{r}(\mathbf{t}) \cdot \boldsymbol{\nabla} V_\ominus|_{\mathbf{r_0}} \tag{4.1}$$

contains all information about the oscillation.

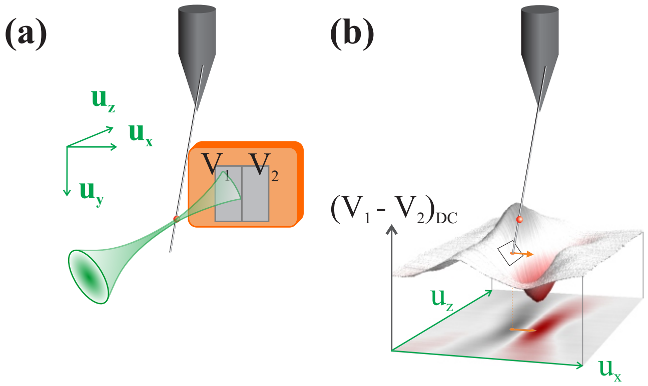

Figure 4.6: Readout of the nanowire motion. **(a)** The waist of the laser beam is swept across the nanowire, which diffuses the beam impinging on the QPD. **(b)** The position dependent slope of the DC difference signal is used to calibrate the sensitivity of an AC displacement measurement.

From formula (4.1), it is important to notice that the scalar measurement realized with the differential output of the dual photodiode is indeed a projective measurement of the 2D dynamics of the nanowire extremity. We can thus introduce a projective measurement vector $\boldsymbol{\beta} \equiv \beta \mathbf{e}_\beta = \boldsymbol{\nabla} V_\ominus|_{\mathbf{r_0}}$ which can be determined using the measured static transmission or reflection maps $V_\ominus(\mathbf{r_0})$. The 2D displacement $\delta\mathbf{r}$ of the nanowire can be expressed in terms of the two polarizations of the fundamental longitudinal eigenmode of the nanowire, oriented along $\mathbf{e_i}$. The mechanical displacement's Fourier decomposition is

$$\delta\mathbf{r}[\Omega] = \sum_{i=1,2} \chi_i[\Omega](\delta\mathbf{F}[\Omega] \cdot \mathbf{e_i} + \delta F_i^{\mathrm{th}})\mathbf{e_i}, \tag{4.2}$$

with $\chi_i[\Omega]^{-1} = M_i(\Omega_i^2 - \Omega^2 - i\Omega\Gamma_i)$ being the mechanical susceptibility of the i^{th} mode. Each mode is subjected to an external vectorial force $\delta\mathbf{F}$ and to the Langevin force δF_i^{th}, generating the nanowire's 2D Brownian motion.

In the following, we will be using the measured projected displacement $\delta\mathbf{r}_\beta(t) \equiv \delta\mathbf{r}(t) \cdot \mathbf{e}_\beta$ whose fluctuations can be expressed as

$$\delta\mathbf{r}_\beta[\Omega] = \sum_{i=1,2} \chi_i[\Omega](\delta\mathbf{F}[\Omega] \cdot \mathbf{e_i} + \delta F_i^{\mathrm{th}})(\mathbf{e_i} \cdot \mathbf{e}_\beta). \tag{4.3}$$

The HF output of the differential photodiode contains information about the spatial fluctuations. In absence of external driving forces, one can use a spectrum analyzer to monitor the Brownian motion of the nanowire. The spectral density $S_{F_i}^{\mathrm{th}}$ of each Langevin force component is given by

$$S_{F_i}^{\mathrm{th}}[\Omega] = -\frac{2k_B T}{\Omega} \,\mathrm{Im}\left(\frac{1}{\chi_i[\Omega]}\right) = 2M_i\Gamma_i k_B T. \tag{4.4}$$

Some typical spectra of the projected Brownian motion $S_{\delta\mathbf{r}_\beta}[\Omega]$ are represented in Figure 4.7, both in air and at low pressure (10^{-3} mbar). They yield important information about the mechanical properties, such as oscillation frequency, effective mass and damping rates. The spectra shown in Figure 4.7 also reveal that the two polarizations of the fundamental longitudinal mode are not frequency degenerate. They oscillate along two orthogonal directions as determined below, which are set by the asymmetry of the nanowire geometry. Using equations (4.3) and (4.4), one finds that they can be adjusted by the following expression:

$$S_{\delta\mathbf{r}_\beta}[\Omega] = S_{V_\ominus}[\Omega]/\beta^2 = \sum_{i=1,2} \frac{2k_B\Gamma_i T/M_i}{\left(\Omega_i^2 - \Omega^2\right)^2 + \Omega^2\Gamma_i^2} |\mathbf{e_i} \cdot \mathbf{e}_\beta|^2. \tag{4.5}$$

Thus, the height of both thermal noise peaks depends on the orientation of the measurement vector. Each peak is maximized individually when its corresponding eigendirection is aligned with $\mathbf{e}_\beta$. The maximal signal-to-background ratio is obtained by positioning the nanowire is a region of strong differential intensity gradients.

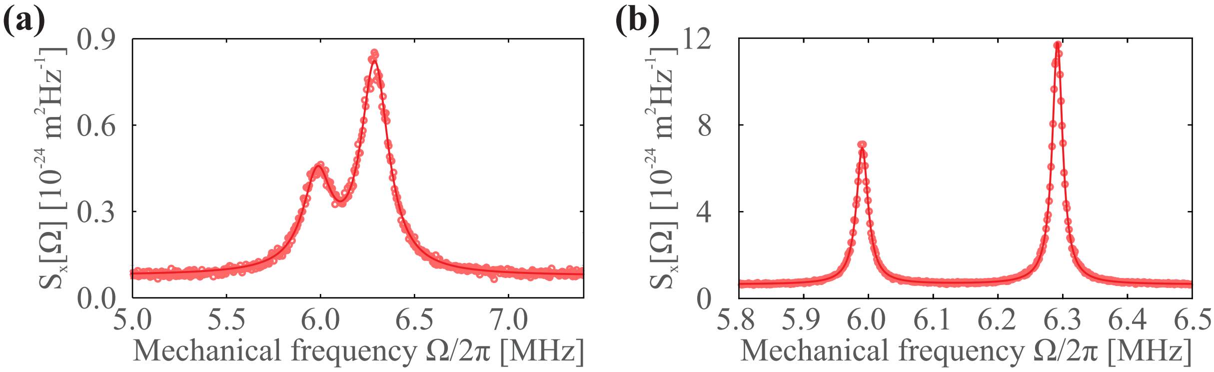

Figure 4.7: Measurement of the thermal noise of the nanowire, at room pressure (left) and low pressure (right: 0.001 mbar). The two peaks correspond to the two polarizations of the nanowire, whose degeneracy is lifted by the geometric asymmetry of the system. Both curves are adjusted with two thermal noise mechanical Lorentzian curves, following expression (4.5), which allows to derive the frequencies and damping rates of both eigenmodes. Their effective masses and orientations can be deduced from the reproduction of similar measurement at different locations within the optical waist, which allows varying the measurement vector β (see text). The visible increase of the mechanical quality factors at low pressure is due to the reduction of acoustic damping.

Reproducing this measurement for different measurement vector orientations $\mathbf{e}_\beta$, following the procedure developed in [97, 102], allows to determine the vibration orientations $\mathbf{e_i}$, as well as the mechanical damping rates and effective masses, assuming that no static heating occurs. Variation of the measurement vector can be realized by moving to different positions within the optical waist. The cartography of the measurement vector is reproduced in Figure 4.8. A sequence of 10×10 measurements performed on a $3.5 \times 1.7\,\mu$m grid allowed to determine the perpendicular orientations of the eigenmodes being rotated by 10 degrees with respect to the optical axis $\mathbf{u_z}$, as is shown in Figure 4.10. The adjusted oscillation frequencies are $\Omega_1/2\pi = 5.99$ MHz, $\Omega_2/2\pi = 6.29$ MHz of both modes, their mechanical damping rates are $\Gamma_1/2\pi = 0.19$ MHz, $\Gamma_2/2\pi = 0.18$ MHz in air and the effective mass is $M = 1.5\,\mathrm{pg}$. These large mechanical frequencies are very close to the one emulated in Chapter 3 and should therefore allow operation in the resolved sideband regime of the driven spin dynamics. Notice that the mechanical spectra were obtained under ambient pressure. At lower pressure, the reduced friction causes the mechanical decay rates to decrease by about a factor of ten to $\Gamma_1/2\pi = 22\,\mathrm{kHz}$ and $\Gamma_2/2\pi = 19\,\mathrm{kHz}$. These values correspond to an intrinsic quality factor of $Q \approx 300$ which is far from the best values achieved on similar nanowires (approx. 10 000). However since here we were not interested in the dynamical back action of the spin onto the resonator, and since the oscillation amplitudes achieved were sufficient, this was not considered as a limitation. All experiments that will be shown in the suit were therefore executed under ambient conditions.

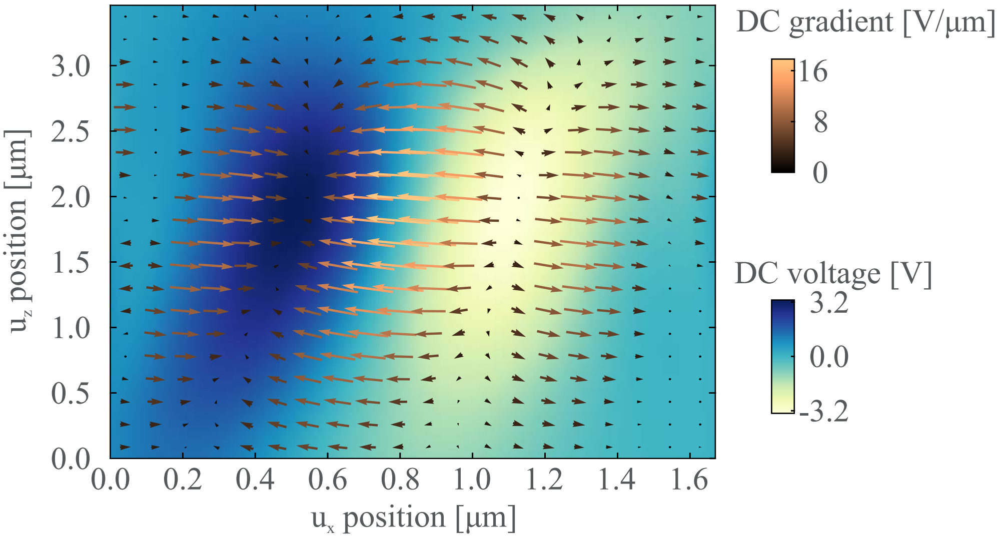

Figure 4.8: AC displacement calibration in the $(\mathbf{u_x}, \mathbf{u_z})$-plane. The local two dimensional gradient is shown in terms of the vector field $\boldsymbol{\beta}(u_x, u_y, u_z)$. u_y is fixed to the NV position on the nanowire.

4.1.4 Mechanical excitation of the nanowire motion

Mechanical motion of the SiC nanowire can be excited by two means. The first one is by modulating the input voltage of a piezo stack placed on the nanowire support at a drive frequency $\Omega_\mathrm{d}/2\pi$. The modulation voltage is provided by an Agilent 33250A signal generator, amplified by a high speed high voltage amplifier (WMA-300 from Falco Systems) with an output limited between -150 V and 150 V. A complication arises due to resonances of the piezo excitation with the drive frequency, which render the calibration of the nanowire driving force difficult. Alternatively, an electrostatic force $\mathbf{F}$ can be used to actuate the nanowire. It is connected to the spatial dependence of the capacitance C between the nanowire and the waveguide which is at a potential V: $\mathbf{F} = -\frac{V^2}{2}\boldsymbol{\nabla}C$. Again, RF voltages are supplied by the Agilent 33250A signal generator. Because the electrostatic force is proportional to V^2, it is necessary to apply a voltage offset V_0 around which the tension is modulated (amplitude δV). After amplification, the signal is injected in the waveguide circuit, for which we use two bias tees as employed for combining RF fields in the test system. Opening the circuit on the RF port of the exit bias tee ensures that no currents are drawn (see Figure 4.9). Since the circuit transmission is relatively flat at low RF frequencies, the amplitude of the electrostatic driving force is independent of the drive frequency $\Omega_\mathrm{d}/2\pi$. As such it can be expanded as

$$\mathbf{F}(t) \approx -\frac{V_0^2}{2}\boldsymbol{\nabla}C - V_0\delta V(t)\boldsymbol{\nabla}C. \tag{4.6}$$

The first term represents a time independent force that creates a static deflection of the nanowire towards the waveguide. The second term represents a time varying force $\delta\mathbf{F}(t)$ that serves to resonantly drive the nanowire.

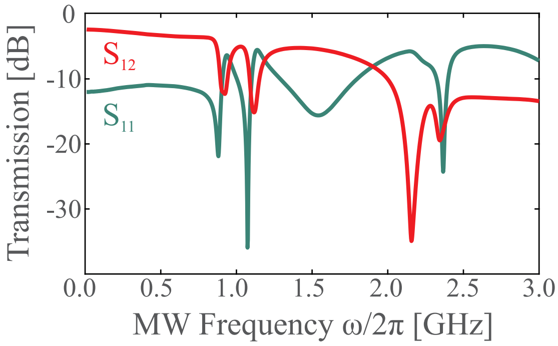

Figure 4.9: Measurement of the waveguide transmission S_{12} (red) and reflection S_{11} (green).

The direction $\mathbf{e_F}$ of the dynamical electrostatic driving force $\delta\mathbf{F}(t) = \delta F \cos\Omega_\mathrm{d} t\, \mathbf{e_F}$ must be precisely calibrated in order to understand the orientation and magnitude of the induced displacement, the latter of which strongly depends on force's projection onto the two modes $(\mathbf{e_1}, \mathbf{e_2})$, see Figure 4.10 **(a)**. This is done by exploiting the vectorial force sensitivity of the nanowire, granted by the frequency non-degeneracy between both eigenmodes, and sweeping the electrostatic force frequency $\Omega_\mathrm{d}/2\pi$ across the two polarizations. Simultaneous measurement of the induced projected displacement with a vector network analyzer yields the electrostatic response function of the nanowire,

$$\frac{\delta r_\beta}{\delta F}[\Omega_\mathrm{d}] = \sum_{i=1,2} \chi_i[\Omega_d](\mathbf{e_i}\cdot\mathbf{e}_\beta)(\mathbf{e_i}\cdot\mathbf{e_F}), \tag{4.7}$$

where we have assumed that the thermal noise has a negligible contribution. The amplitude of a typical response measurement is represented in Figure 4.10 **(b)**. Since the measurement vector is known, an adjustment with $\left|\sum_{i=1,2}\chi_i[\Omega_d](\mathbf{e_i}\cdot\mathbf{e}_\beta)(\mathbf{e_i}\cdot\mathbf{e_F}) + \chi^\mathrm{bck}_\mathrm{elec}\right|^2$ permits to infer the magnitude and the orientation of the force vector [97]. Note that a small coherent background added by electrostatic parasites to the differential photocurrent must be taken into account in order to obtain perfect agreement. The resulting force vector is shown in Figure 4.10**(a)**. It is oriented at 50° of the first polarization, pointing towards the waveguide. The deviation with respect to the optical axis can be explained by the presence of the magnetic bead and the nearby tungsten tip holding the nanowire.

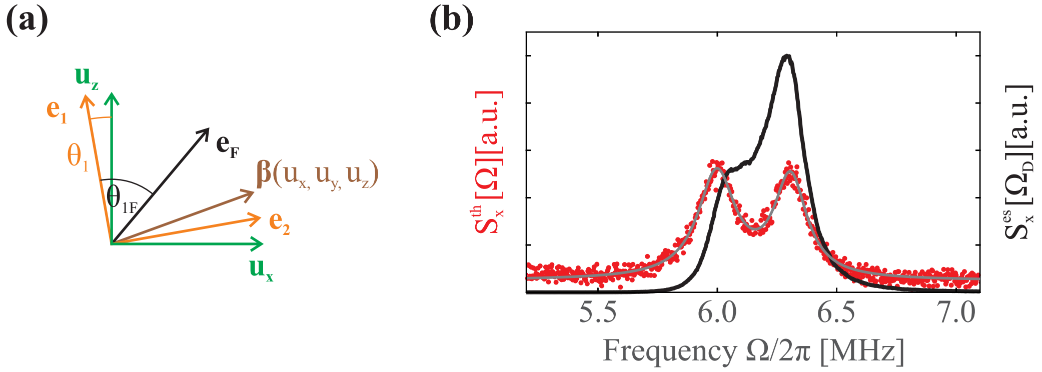

Figure 4.10: Application of an external driving force. **(a)** Diagram showing the random orientation of the mechanical modes, optical axis, measurement vector and the external electrostatic force. **(b)** Measurement of the nanowire's Brownian motion (red) compared to its response to the electrostatic force with the same value of $\boldsymbol{\beta}$

4.1.5 Suspended waveguide and magnetic gradient structure

For this experiment, a specific waveguide has been developed (with the help of Laure Mercier de Lépinay, Aurlien Kuhn and the Nanofab team) in order to permit an efficient optical access compatible with the large numerical aperture objectives used in our experiment. It also supports the magnetic gradient source. The waveguide used in this hybrid setup, schematically shown in Figure 4.11 **(a)**, is based on the same principles as the waveguide of the test system of Chapter 3. A 500 μm thick Silicon substrate supports a 400 nm silicon nitride insulator and a 200 nm thick gold layer (and 1 nm Ti as an adhesion layer) which carries electrical signals shaped into a central constriction of 40 μm in width and 1 mm in length, where the local current densities are increased to provide large magnetic fields. In order to permit optical access to the NV defect and nanowire just above the structure, KOH dry etching along the Si crystal's (111) direction was used to render the bulk cross section trapezoidal, which widens the opening angle to 54.7°, which is steeper than the 48° angle of the laser beams focused by our 0.75 NA microscope objectives, see Figure 4.11 **(b)**. The waveguide is micro-bonded onto a PCB board and connected to the MW and RF circuit by SMA connectors. The whole structure is mounted on a remote controlled piezo-stage which enables high precision position control in all XYZ directions.

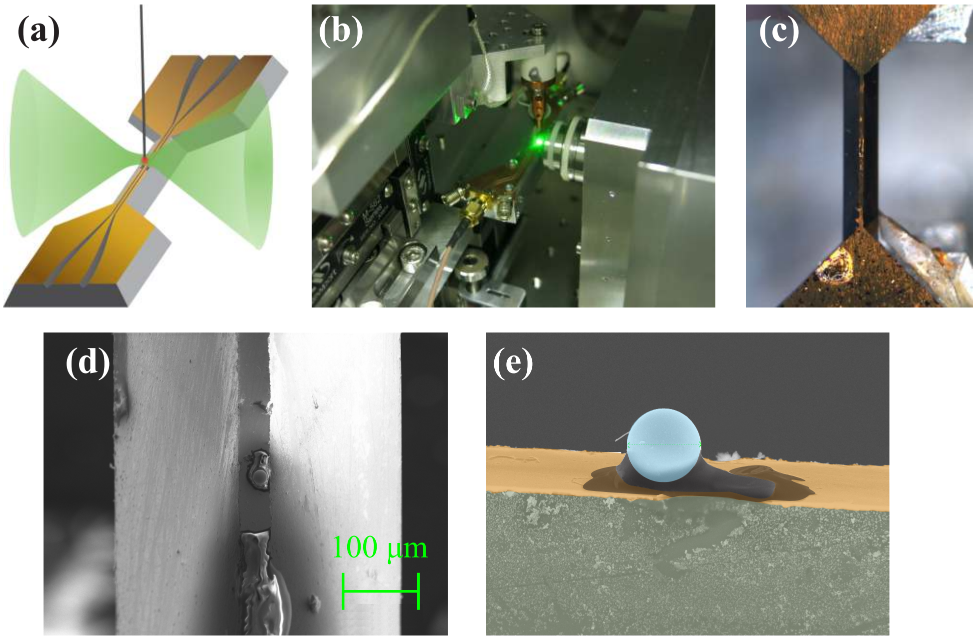

Figure 4.11: Waveguide and magnetic structure. **(a)** Graphical sketch illustrating the wide opening anlge offered by the MW waveguide to improve optical access to the nanowire and NV defect. **(b)** Photograph showing the waveguide in the close proximity of the microscope objective. **(c)** Image taken with an optical microscope showing the ∼ 1 mm long constriction of the waveguide from above. **(d)** SEM image showing the same. Clearly visible are the trapezoidal cross-section of the waveguide and the magnetic bead in the center. **(e)** False color SEM image with an angled view of the micro-bead. The diameter of the bead is about 18 μm.

In order to achieve a good and stable control on the spin dynamics at the working point position in the magnetic field gradient, it was decided to attach the magnetic field gradient source to the waveguide. The magnetic structures employed are commercially available (MQP-S-11-9-20001-060 isotropic powder from Magnequench) spherical beads made from a NdFeB with a diameter of several μm. Their typical coercive field is approximately 0.55 T. Using a strong external magnetic field provided by a 2 T magnet, the magnetic dipole can be oriented along a desired direction which will be adjusted to the measured NV orientation. In order to obtain large magnetic field gradients, the working distance to the NV defect is small, comparable to the bead's radius and requires a very stable positioning as explained above. SEM images of the magnetic bead deposited onto the waveguide edge are shown in Figures 4.11 **(c)** and **(d)**. The deposition of the micro-bead onto the waveguide is realized with micro-manipulators combined with a high quality optical microscope featuring a precise and convenient scanning table. Working at a constant magnetic field amplitude and direction then requires adequate positioning of the waveguide. While this might reduce coupling to the MW fields, we have not been limited by this restriction due to a 25 W MW amplifier from Amplifier Research which was also able to compensate for the small residual impedance mismatch. Attaching the magnetic bead directly onto the waveguide furthermore reduces the number of elements close to the microscope objectives and thus simplifies spatial access to the optical detection region. The overall experiment was stable over a few hours before the static magnetic field has to be realigned. On shorter timescales, residual vibrations as well as thermal drifts slightly shift the resonance frequency $\omega_0/2\pi$. This leads to inhomogeneous broadening of the spin resonance, resulting in the observation of Gaussian lineshapes in the spin spectra. Since the thermal drifts become relevant to the spin only for large enough magnetic field gradients, the inhomogeneous broadening is only observed when working at lower spin energies. As the ELSAC is approached, the line profile thus gradually changes from Lorentzian to Gaussian, see Figure 4.12.

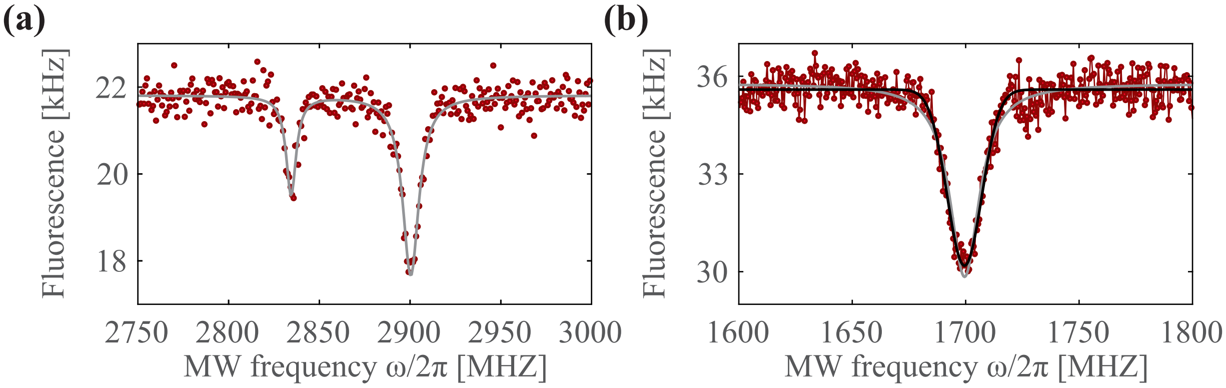

Figure 4.12: ODMR measurements of the NV spin. **(a)** Far away from the magnetic structure, the spin couples only weakly to the oscillator position and the $|+1\rangle$ and $|-1\rangle$ eigenstates are mainly split due to strain effects in the nanodiamond. The gray line is a fit two a sum of two Lorentzian lineshapes. **(b)** Closer to the magnetic structure, the magnetic field and magnetic field gradient increase, shifting the $|+1\rangle$ eigenstate close to the ESLAC ($B_{\|}^{\mathrm{ext}} \approx 51$ mT). ESR spectra, taken over several minutes, are then experiencing additional broadening due to thermal drifts, which slowly shift the spin resonance frequency $\omega_0/2\pi$ in an inhomogeneous manner. The gray line indicates a fit to a Lorentzian lineshape, while the black curve is a fit to a Gaussian lineshape. The difference in fluorescence is due to different optical powers.

4.2 Alignment of the setup

The preceding description of the experimental setup has introduced the many components that are at play, giving rise to a large parameter space. In this section we will discuss the constraints for the alignment of the NV defect and how its position can be adjusted in the magnetic field gradient emerging from the magnetic bead.

4.2.1 Alignment of the NV defect

The orientation of the NV defect can be measured using the same procedure as described in section 3.3.2. The waveguide is moved relatively far away from the NV defect such that the influence of the magnetic field from the NdFeB micro-bead becomes negligible. An external magnetic field with a well known orientation is then approached from the $\mathbf{u_x}$- and the $\mathbf{u_z}$-direction while ODMR spectra are taken to track the shift of the resonance frequency. Once the polar and azimuthal angles are determined, the sample holder of the nanowire is rotated such that the $\mathbf{z}$-direction of the spin is aligned as close as possible with the optical axis $\mathbf{u_z}$, see Figure 4.13 **(a)**. In this configuration the two optical dipoles of the NV center, which are lying in the plane perpendicular to the NV axis, are almost transverse to the optical axis. This ensures that a maximum amount of the emitted fluorescence is collected by the confocal microscope. This step is of crucial importance for achieving reasonable averaging times.

4.2.2 Alignment of the MW field

In order to achieve an efficient manipulation of the spin, the MW magnetic field needs to exhibit a strong component transverse to the spin direction. Because of spatial restrictions, the waveguide is oriented such that the MW current flows in the $\mathbf{u_x}$-direction, perpendicular to the optical axis. As can be seen in Figure 4.13, a transverse component is present as soon as the NV position is slightly displaced from right above the waveguide along the optical axis. By measuring the contrast of ODMR spectra and the frequency of Rabi oscillations, it is possible to infer the local strength of the transverse component of the MW magnetic field. We found that by using the MW amplifier, fast Rabi precessions are observable even at waveguide distances of more than 20 μm. However, in order to not operate at too large MW powers we decided to work slightly in front of the waveguide, as illustrated in Figure 4.13, maximizing the transverse field component. Once in place, the MW amplifier can be operated at 44 dBm gain while most of the power is dissipated in the 50 Ohm resistor (with a 2 Watt limit) connected outside of the cavity. Simultaneously, this working point permits to produce an efficient electrostatic force, which would cancel in case where the NV is positioned above the waveguide.

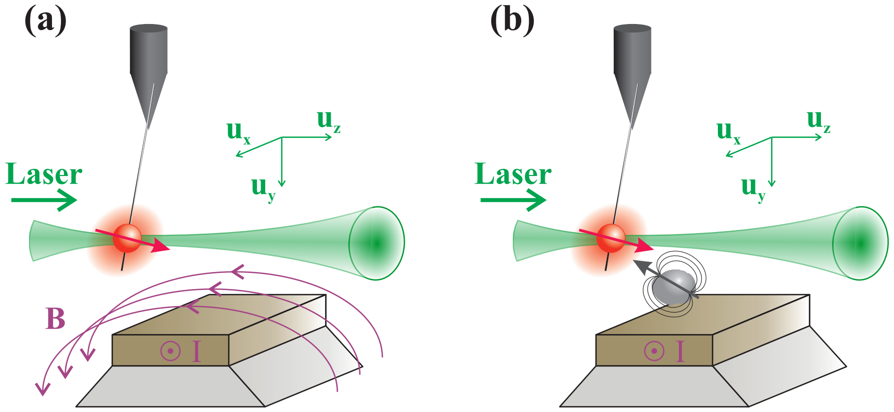

Figure 4.13: NV alignment. **(a)** The nanowire is rotated such that the spin $\mathbf{z}$-direction is as close as possible parallel to the optical axis $\mathbf{u_z}$. The optical dipoles of the NV, lying in the NV $(\mathbf{x},\mathbf{y})$-plane, then efficiently emit fluorescence in the solid angle detected by the confocal microscope. Moving the nanowire in the $(\mathbf{u_x},\mathbf{u_z})$-plane changes the coupling to the MW magnetic field. **(b)** Coupling to the magnetic dipole can be increased or decreased by moving the waveguide in the $\mathbf{u_x}$-direction. First, the bead is brought into the $(\mathbf{u_y},\mathbf{u_z})$-plane intersecting with the optical axis. Next, the magnetic field at the NV position is adjusted by motion in the $(\mathbf{u_x},\mathbf{u_z})$-plane.

4.2.3 Orientation of the oscillation directions

As explained above, we measured the vibration axis $\mathbf{e_1}$ to be tilted by 10° with respect to the optical axis $\mathbf{u_z}$. Finally, the constraints on the vibration direction can be lifted by adjusting the drive frequency, as long as the force vector is not aligned along one of the vibration axes. Indeed, the presence of the micro-bead (see Figure 4.13 **(b)**) distorts the iso-voltages of the electrostatic potential, such that the orientation of the electrostatic force can be changed by moving the waveguide along $\mathbf{u_x}$. In the following part, we are interested in the vectorial character of the hybrid coupling, which does not necessitate optimization of the coupling strength along one particular direction.

4.2.4 Magnetic field alignment

The NV defect is now aligned such that, on the one hand, a large amount of fluorescence is collected and, on the other hand, that it shows good coupling to the MW magnetic field. By moving the waveguide in the $\mathbf{u_x}$-direction (see Figure 4.13 **(b)**), we can approach the NdFeB bead, which increases the magnetic field and the local magnetic gradient. In order to go to the ESLAC regime, where the nuclear spin becomes polarized, the bead is moved to lie in the $(\mathbf{u_x}, \mathbf{u_y})$-plane that coincides with the optical axis. Following this step, the projection of the magnetic dipole field along the NV axis has to be increased to about 51 mT. It is important to ensure that transverse components of the magnetic field stay small in order to avoid both, level mixing and fluorescence decrease. Hence, by surveying the emitted fluorescence as the magnetic structure is brought closer, the ESLAC can be reached. In our laboratory, we used this principle, which is essentially the same as was used in section 3.3, to developed a procedure that allowed us to rapidly bring the NV spin to the ESLAC regime. Raster scans of the NV fluorescence are taken by fixing the confocal microscope to the NV position and sweeping the position of the NdFeB bead in the vertical $(\mathbf{u_x}, \mathbf{u_y})$-plane by moving the waveguide with help of the piezo controllers. Such slices inform us qualitatively about how much the spin energy eigenstates (in the presence of an external magnetic field) are different from the eigenstates of σ_z, for which the fluorescence is maximized. Typical maps are shown in Figure 4.14. The rearmost image corresponds to a large distance between the magnetic dipole and the NV ($\approx 24\,\mu$m). It shows an area of maximum fluorescence in the central part, indicating the region where the magnetic field emerging from the bead is mainly oriented along the NV $\mathbf{z}$-direction. After such a scan, the magnetic bead is moved in the $(\mathbf{u_x}, \mathbf{u_y})$-plane to the position of maximum fluorescence. Subsequently the u_z distance is lowered. Another fluorescence scan in the $(\mathbf{u_x}, \mathbf{u_y})$-plane is performed to optimize magnetic field alignment at the new z position. Closer to the bead, the NV defect sees a larger magnetic field but also larger gradients in the transverse directions, leading to a reduced size of the maximum fluorescence spots, see Figure 4.14. An ODMR measurement verifies the resonance frequency $\omega_0/2\pi$ of the NV spin at that precise location. The previous steps are repeated until $\omega_0/2\pi \approx 1.45\,$GHz. Due to high spatial control of the piezo motors, the procedure is very robust as long as rough orientation of the NV and magnetic dipole are known and the NV can be aligned at the ESLAC condition on a timescale of 10 minutes.

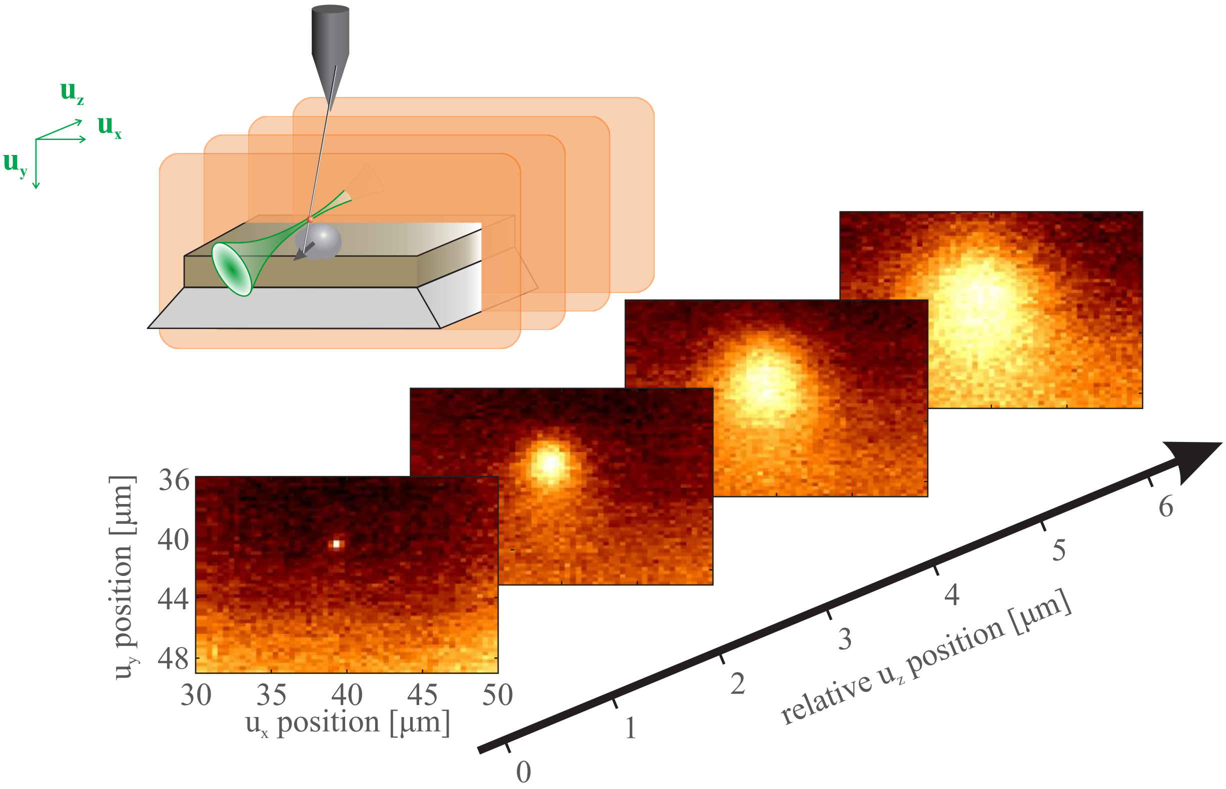

Figure 4.14: Magnetic field alignment. The fluorescence maps are obtained by locking the confocal microscope onto the NV fluorescence and moving the waveguide supporting the NdFeB micro-bead in the vertical $(\mathbf{u_x}, \mathbf{u_y})$-plane. Closer to the bead, at a reduced u_z distance, the transverse gradients $\partial_x \mathbf{B}$ and $\partial_y \mathbf{B}$ are larger, which reduces the size of the maximum fluorescence area.

4.3 Determination of the vectorial parametric coupling strength

As introduced in Chapter 2, the hybrid coupling Hamiltonian is $H_{\text{int}} = -g\mu_B \boldsymbol{\sigma}.\left(\delta\mathbf{r}.\boldsymbol{\nabla}\right)\mathbf{B}\big|_{\boldsymbol{r_0}}$ and the corresponding modulation strength is $\hbar\delta\omega_0 = \delta\mathbf{r}.\boldsymbol{\lambda}$ with $\boldsymbol{\lambda} = \hbar\boldsymbol{\nabla}\omega_0\big|_{\boldsymbol{r_0}}(\boldsymbol{r_0})$. The dynamical coupling strength $\boldsymbol{\lambda}$ can thus be extrapolated from the knowledge of the spatial dependence of the spin energy $\hbar\omega_0$. In other words, the knowledge of iso-spin energy contours will allow the determination of the vectorial coupling strength $\boldsymbol{\lambda}$. To do so, we apply a fixed MW frequency $\omega/2\pi$ and scan the position of the magnetic bead. For every position $\boldsymbol{r_0}$ where $\omega_0(\mathbf{r_0}) = \omega$, a reduction of fluorescence is observed, which permits finding positions of iso-spin energies. This technique, also called *resonant slicing* in magnetic resonance imaging, was already employed in NMR [51] and, more recently, used in NV based magnetometry [87], as was briefly discussed in Chapter 1. In Figure 4.15 we show such measurements, scanning the magnetic bead in the $(\mathbf{u_x}, \mathbf{u_y})$-plane at various MW frequencies. As the spin axis is roughly parallel to the $\mathbf{u_z}$-direction, and the magnetic dipole of the bead is roughly oriented as indicated in Figure 4.13 **(b)**, we see dark rings describing iso-energy contours, where the spin energy is $E_{\text{NV}} = \hbar\omega$. Likewise for scans in the $(\mathbf{u_x}, \mathbf{u_z})$-plane, where instead of rings, the iso-energy contours describe *parachute* like arches, see Figure 4.16.

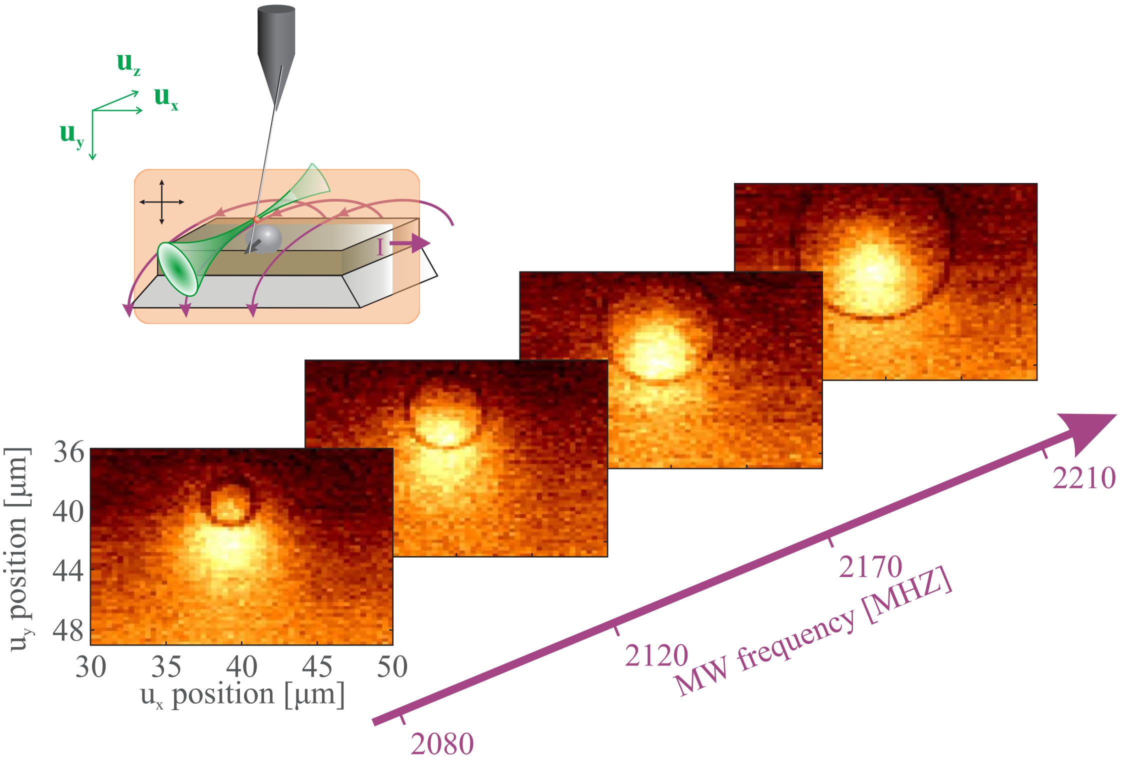

Figure 4.15: Measurement of the position dependent coupling strength. A monochromatic MW tone ω flips the spin state and reduces the NV fluorescence where $E_{\text{NV}} = \hbar\omega$. Iso-energy contours are visible as rings for scans in the $(\mathbf{u_x}, \mathbf{u_y})$-plane.

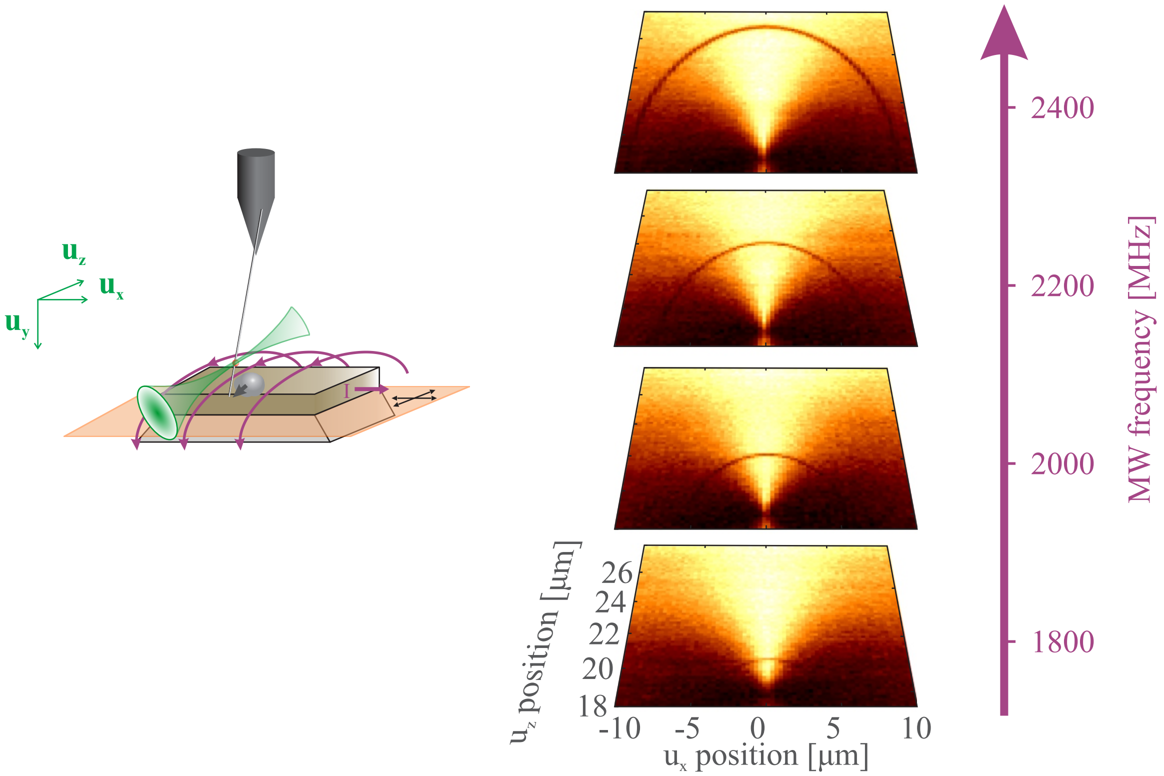

Figure 4.16: Measurement of the position dependent coupling strength. A monochromatic MW tone ω flips the spin state and reduces the NV fluorescence where $E_{\mathrm{NV}} = \hbar\omega$. Iso-energy contours are visible as parachutes for scans in the $(\mathbf{u_x}, \mathbf{u_z})$-plane.

These iso-energy contours directly inform us about the spatial dependence of the spin energy gradient, which is used for the calibration of the coupling strength $\delta\omega_0$. An analysis of the gradients of the iso-energy contours is shown in Figure 4.17. Closer inspection indicates that gradients on the order of $\sim$ MHz/nm are available, which corresponds to a magnetic field gradient of $\sim 3 \times 10^4\,\mathrm{T/m}$. This coupling strength represents a $g_z/2\pi \approx 40\,\mathrm{Hz}$ for zero-point fluctuations $\delta x^{\mathrm{q}} \approx 40\,\mathrm{fm}$ of the resonator. The Brownian motion extends over $\Delta x_{\mathrm{th}} = \sqrt{k_B \Theta / M\Omega_{\mathrm{m}}^2} \approx 170\,\mathrm{pm}$, which corresponds to a thermal motion coupling strength of $\delta\omega_{\mathrm{th}}/2\pi \approx 140\,\mathrm{kHz}$. The role of Brownian motion in the hybrid interaction will be neglected here and its study is delayed Chapter 5).

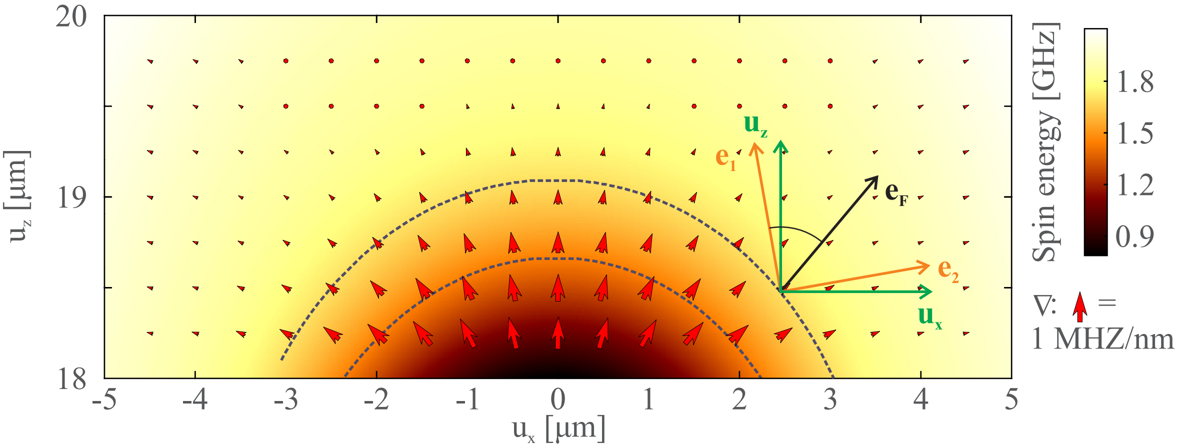

Figure 4.17: Magnetic coupling strength as a function of the micro-bead position interpolated from measurements in Figure 4.16. The map in the background was obtained by interpolating the resonant slice measurements of Figure 4.16 and visualizes directly the position dependent spin energy in terms of $\omega_0/2\pi$. The optical and oscillation axes are as indicated. The working point $u_x = 0$ corresponds to alignment of the spin axis with the dipole magnetic field which maximizes the fluorescence. The spin resonance is set to $\omega_0/2\pi = 1.7\,\text{GHz}$ (indicated by the top dashed line), slightly above the ESLAC at $\omega_0/2\pi \approx 1.45\,\text{GHz}$ (lower dashed line), which decreases the influence of thermal drifts.

4.4 Observation of the Mollow triplet

The necessary ingredients to demonstrate the Mollow triplet of the driven spin dynamics along with the spin locking protocol are thus available to us. In this section, we will expose the experimental observation of the locked spin dynamics that we obtained with the hybrid setup. Before doing so, however, it is necessary to extend the Mollow triplet signatures to take into account the two dimensional character of the system, as the two perpendicular oscillation modes give rise to vectorial coupling of the hybrid components.

4.4.1 Two-directional displacement of the spin

If a driving force $\delta\mathbf{F}$ is tuned close to the mechanical resonance frequencies of the fundamental mode family, higher order modes can be neglected. The displacement $\delta\mathbf{r}(t) \equiv \mathrm{Re}\left(\delta\mathbf{r}[\Omega]e^{-i\Omega t}\right)$ caused by a driving force $\delta\mathbf{F}$ is:

$$\delta\mathbf{r}[\Omega] = \sum_{i=1,2} \chi_i[\Omega]\left(\delta\mathbf{F}.\mathbf{e_i} + \delta F_i^{\mathrm{th}}\right)\mathbf{e_i}. \tag{4.8}$$

The displacement is indicated in Figure 4.18.

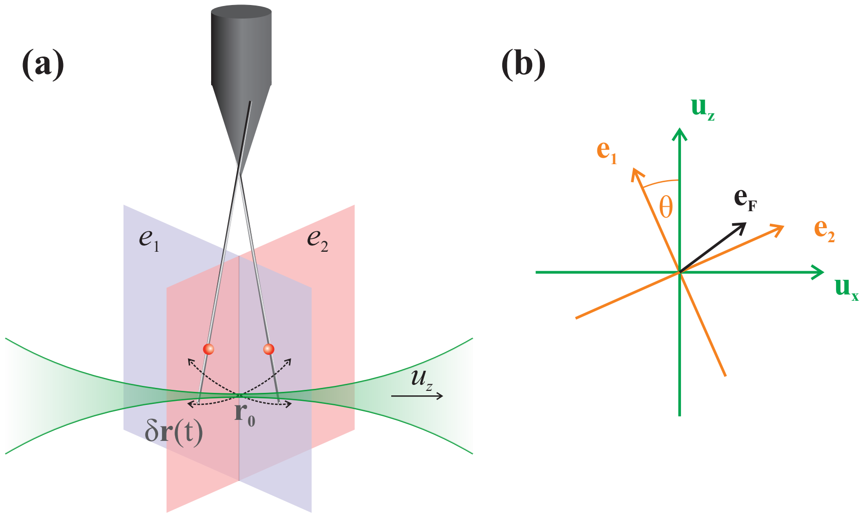

Figure 4.18: Two dimensional motion of the nanowire. **(a)** The oscillator displacement is described by two perpendicular modes, each describing an independent one dimensional mechanical oscillator. **(b)** As long as the force vector $\mathbf{e_F}$ is not parallel to one of the eigenmodes, the orientation direction can be tuned via the drive frequency $\Omega_{\rm d}/2\pi$.

Depending on the orientation and the magnitude of the iso-spin energy gradient, the parametric modulation can thus be varied, according to

$$\delta\omega_0^{(1)}(t) = \delta\mathbf{r}(t)\boldsymbol{.}\boldsymbol{\nabla}\omega_0\big|_{\mathbf{r_0}}. \tag{4.9}$$

We can write

$$\delta\omega_0[\Omega] = \sum_{i=1,2} \chi_i[\Omega](\delta\mathbf{F}.\mathbf{e_i})(\mathbf{e_i}.\boldsymbol{\nabla}\omega_0) + \delta\omega_{\rm th}^i, \tag{4.10}$$

where

$$\delta\omega_{\rm th}^i \equiv \chi_i[\Omega]\delta F_{\rm th}^i(\mathbf{e_i}.\boldsymbol{\nabla}\omega_0), \tag{4.11}$$

which represents the fluctuations of the spin energy due to the thermal motion along the $\mathbf{e_i}$-direction. $\delta\omega_{\rm th}^i$ is responsible for longitudinal noise, with spectral density

$$S_{\delta\omega_{\rm th}^i}[\Omega_{\rm m}] = |\chi_i[\Omega]|^2 S_{F_{\rm th}}^i|\mathbf{e_i}.\boldsymbol{\nabla}\omega_0|^2, \tag{4.12}$$

which will be neglected in the rest of this section. We will return to the consequences of such an additional noise source in Chapter 5. Here, we will first choose a fixed drive frequency $\Omega_{\rm d}/2\pi$ on resonance with mode $\mathbf{e_2}$, so that the induced coherent displacement of a few nm will be significantly larger than the thermal noise and is presumably aligned with $\mathbf{e_2}$. While the above considerations describe motion along two directions, we will for now restrict ourselves to mechanical oscillation along one single direction. This is justified as long as the applied driving force has a fixed frequency $\Omega_{\rm d}/2\pi$ and an amplitude that is large compared to the thermal force.

4.4.2 Sweep of the Rabi frequency across the mechanical resonance

We move the magnetic bead to the ESLAC position following the above described procedure and drive mechanical motion of the SiC nanowire in resonance with the fundamental mode $\mathbf{e_2}$ at $\Omega_{\rm d}/2\pi = \Omega_{\rm m}/2\pi = 6.3\,$MHz using electrostatic excitation with $V_{\rm es} = (2 + 1.8\cos\Omega_{\rm d}t)\,$V. Rabi oscillations of the NV spin are driven as explained in section 3.5. Data is accumulated for approximately 5 minutes acquisition time before an automated ODMR measurement determines the resonance frequency $\omega_0/2\pi$ and the MW frequency is reset to resonance, $\omega = \omega_0$. This step is necessary to compensate for residual mechanical drifts, which were estimated to be on the order of a few MHz/h. Each Rabi curve is obtained from accumulation of five to ten iterations, so that each Rabi measurement lasts for about 30 minutes. After such averaging time, the data quality is sufficient to perform a decent FFT. We use this procedure to sweep the Rabi frequency across the mechanical resonance. The result is shown in Figure 4.19. The data exhibits strong congruence with the results and model of Chapter 3. We find that $\delta\omega_0/2\pi \approx 5.8$ MHz, which corresponds to an oscillation amplitude of 11 nm, as inferred from the analysis in section 4.3 and the knowledge of the local parametric coupling strength $\boldsymbol{\nabla}\omega_0.\mathbf{e_2} = 0.5$ MHz/nm at the NV position. The central component is clearly visible and both, the lower and upper branches of the anti-crossing, follow the parabolas $\Omega_\mathrm{R}^\mathrm{eff} = \Omega_\mathrm{m} \pm \sqrt{(\Omega_\mathrm{m}^2 - \Omega_\mathrm{R}^2) + \delta\omega_0^2/4}$ as indicated by the red curves. A slight divergence of the lower branch can be attributed to uncertainties in the calibration of $\Omega_\mathrm{R}(P_\mathrm{MW})$. A fourth component encircled by the green ellipse is also visible, whose origin is explained in section 4.5.

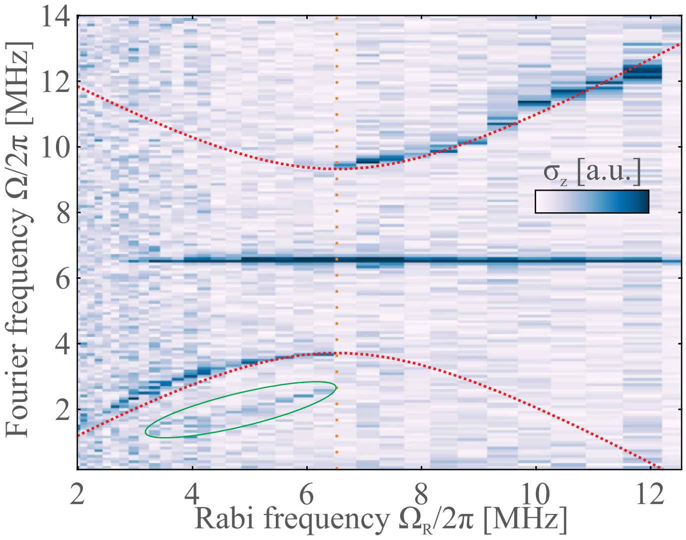

Figure 4.19: Sweep of the Rabi frequency $\Omega_\mathrm{R}/2\pi$ across the driving frequency $\Omega_\mathrm{d}/2\pi \approx \Omega_\mathrm{m}/2\pi$ (resonant with $\mathbf{e_2}$) with $\delta\omega_0/2\pi \approx 5.8$ MHz. Red curves are the expected lower and upper branch of the Rabi frequency. The green ellipse encircles a fourth component that appears here as a result of nonlinear coupling, explained section 4.5.

We furthermore observe a strong increase of Rabi oscillation coherence times in the spin locking regime, as already discussed in Chapter 3. Figure 4.20 shows Rabi oscillations in absence and presence of driven mechanical motion. Increase of the decay time is visible as well as a narrowing of the Rabi peaks in the Fourier spectra. We also notice that the mechanical sidebands are smaller in amplitude than expected. This can be attributed to the thermal motion of the oscillator that superposes itself to the monochromatic energy modulation. We will delay the investigation of this effect to section 5.5 of Chapter 5, which explores in detail how the Mollow triplet is affected by the additional incoherent motion.

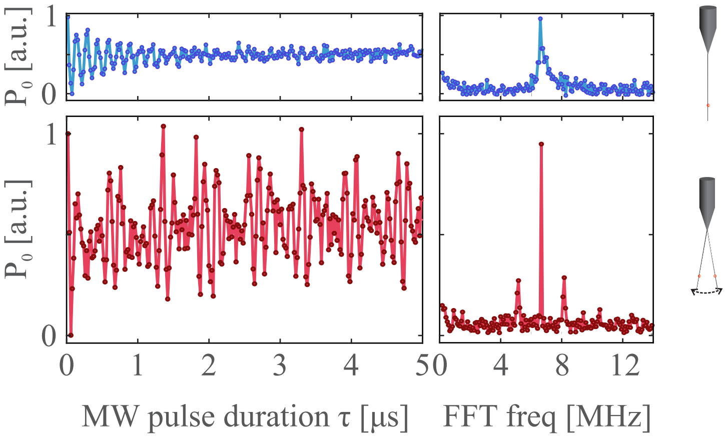

Figure 4.20: Spin locking in the hybrid setup. Blue curves show Rabi oscillations in absence of mechanical motion, red curves in presence of mechanical motion at the spin locking condition. Narrowing of the central peaks is clearly visible (from ~ 150 kHz to ~ 15 kHz, $\delta\omega_0/2\pi = 3$ MHz, $\delta r \sim 6$ nm).

4.4.3 Sweep of the mechanical oscillation amplitude

We subsequently sweep the amplitude of the force in order to further verify the consistency of the spin dynamics with the Mollow triplet model. We choose again to drive mechanical motion on the e_2 mode, this time using the piezo drive. We increase the drive amplitude from 0 V to 3 V. The separation of the Mollow triplet sidebands $\delta\omega_0/2\pi$ reach approximately 5 MHz at maximum drive, see Figure 4.21. By comparison with the magnetic gradient at the oscillator position as determined in section 4.3, we conclude that the oscillator displacement along $\mathbf{e_2}$ is varied between 0 nm and 10 nm, which is in agreement with the drive efficiency measured above. We also observe a faint component at $\Delta_{N,M} \sim \delta\omega_0/2$, which appears due to a MW detuning δ caused by thermal drifts.

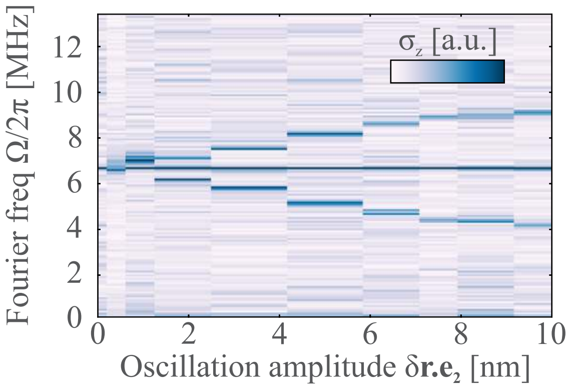

Figure 4.21: Sweep of the mechanical oscillation amplitude using piezo excitation. The measurement verifies the linear dependency of the sideband separation on the oscillation amplitude. In the vicinity of the intra-multiplicity component $\Delta_{N,M} \sim \delta\omega_0/2$ a darker color background indicates detuning noise cause by residual thermal drifts.

4.4.4 Investigation of the spin locking phenomenon in the two dimensional plane

We furthermore explore the vectorial coupling of the oscillator motion to the spin dynamics. By sweeping the frequency of the electrostatic driving force, $\Omega_d/2\pi$, across both mechanical modes e_1 and e_2, the oscillation trajectory of the SiC nanowire varies in the $(\mathbf{e_1}, \mathbf{e_2})$-plane, which allows exploring the vectorial nature of the interaction. Moreover, the oscillation amplitude changes as the frequency dependent mechanical susceptibility of each mode is probed. To directly measure this effect on the spin dynamics, we sweep the drive frequency $\Omega_\mathrm{d}/2\pi$, while adjusting the Rabi frequency $\Omega_\mathrm{R}/2\pi$ to always match the spin locking condition $\Omega_\mathrm{d} = \Omega_\mathrm{m} = \Omega_\mathrm{R}$ during the entire frequency sweep. The separation of the Mollow triplet sidebands then informs us directly about the dependence of the linear parametric coupling strength $\delta\omega_0^{(1)}$ on the mechanical susceptibilities of the two modes and the magnetic field gradient topology. Such a measurement is shown in Figure 4.22, where the electrostatic drive amplitude before the amplifier was set to 2.8 V with 2 V offset. As expected, the central component of the Mollow triplet is linearly increasing with Ω_d. Simultaneously, the separation of the Mollow triplet sidebands varies with Ω_d. Comparing the data to a measurement of the thermal noise displacement spectral density, see Figure 4.10 **(b)**, clearly illustrates that the sideband separation increases as the drive frequency approaches the respective resonance frequencies of the mechanical modes.

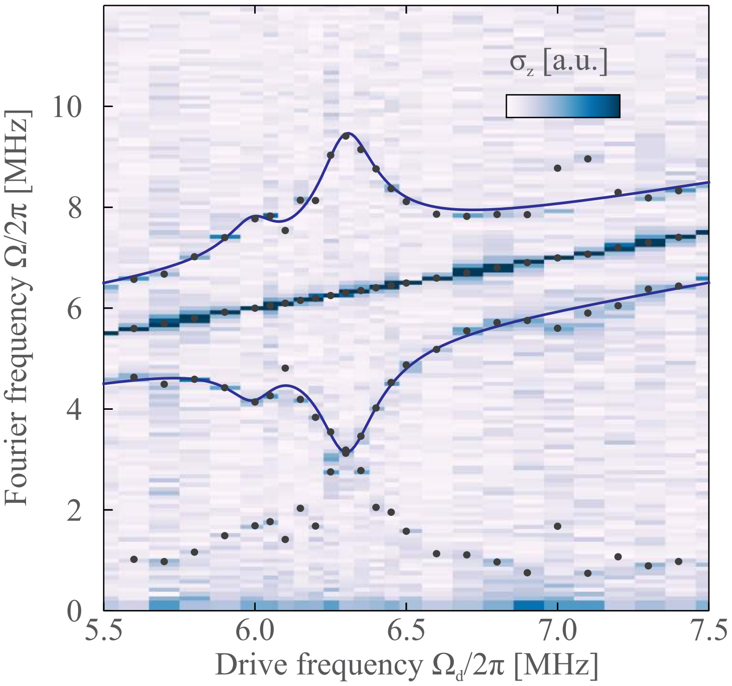

Figure 4.22: Sweep of the mechanical drive frequency $\Omega_\mathrm{d}/2\pi$, while adjusting the Rabi frequency to $\Omega_\mathrm{R} = \Omega_\mathrm{d}$. Visible is the linear increase of the central Mollow component with Ω_d and a variation of the sideband separation as a function of the mechanical drive frequency. The data is fitted with expression (4.15). We have imposed the values for $\Omega_{1,2}$, $\Gamma_{1,2}$, M and $\mathbf{e_F}$, as found from the measurements described above. We find that $\mathbf{e_1}.\boldsymbol{\lambda} \approx \cos 70°$, yielding a potential working point $(x_0, z_0) = (2.5, 18.5)\,\mu$m, in rough agreement with the value expected from the experimental settings.

To fully understand the vectorial character of the observed signatures and their dependence on the oscillator trajectory, it is necessary to closely inspect the driven trajectories and their evolution with the drive frequency, as described by $\delta\mathbf{r}(t) \equiv \mathrm{Re}\left(\delta\mathbf{r}[\Omega]e^{-i\Omega t}\right)$ and equation (4.8). One obtains

$$\begin{aligned}\delta\mathbf{r}(t) &= \sum_{i=1,2} \mathrm{Re}\left(\chi_i[\Omega]\left(\delta\mathbf{F}.\mathbf{e_i}\right)e^{-i\Omega t}\right)\mathbf{e_i} \equiv \sum_{i=1,2} \delta r_i(t)\mathbf{e_i} \\ &= \sum_{i=1,2} \left(\delta\mathbf{F}.\mathbf{e_i}\right)|\chi_i[\Omega]|\cos\left(\Omega t - \phi_i[\Omega]\right)\mathbf{e_i}, \end{aligned} \tag{4.13}$$

where the dephasing $\phi_i[\Omega]$ is given by $\chi_i[\Omega] = |\chi_i[\Omega]|e^{i\phi_i}$, so that

$$\phi_i[\Omega] = \arctan\left(\frac{\Omega\Gamma_i}{\Omega_i^2 - \Omega^2}\right). \tag{4.14}$$

It is important to notice, that when the damping rates Γ_i are comparable to the frequency splitting $\Omega_2 - \Omega_1 \approx 2\pi \times 300\,\text{kHz}$, the induced trajectories are elliptical in the $(\mathbf{e_1}, \mathbf{e_2})$-plane, since the vibrations projected along the $\mathbf{e_i}$-directions can acquire any dephasing. In vacuum, when the Q factor is increased, this is not the case anymore, and we retrieve quasi linear oscillation trajectories. Interestingly, it is then possible to suppress coupling to the qubit, by choosing a drive frequency for which the nanomotion is tangential to the iso-spin energy contours (notice that this, however, does not suppress parametric coupling of the oscillator's thermal motion). We take advantage of the elliptical trajectories to explore the vectorial character of the parametric coupling of the two dimensional oscillation with the qubit.

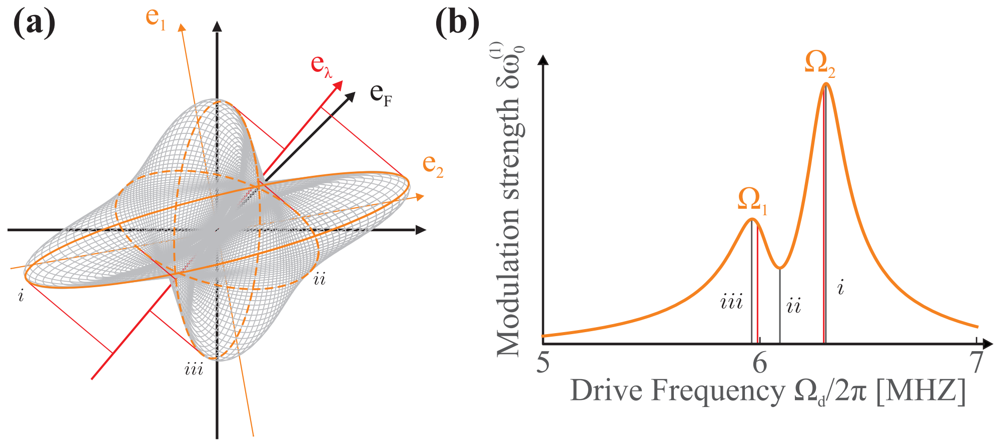

Figure 4.23: Driven oscillation trajectories. **(a)** In gray: trajectories obtained while driving the hybridized nanowire at various drive frequencies across the two fundamental mechanical polarizations, for a force vector at 45° with respect to the $\mathbf{u_x}$-axis. In orange are highlighted three trajectories corresponding to the extrema of the measured parametric modulation strength $\delta\omega_0^{(1)}$, shown in **(b)**, which is derived geometrically using the maximum of the ellipsoid's projection onto $\mathbf{e}_\lambda$. Note that in the situation of low mechanical quality factors, the maximum coupling strength is not obtained at the exact mechanical resonance frequencies which are highlighted in orange. Simulated values are $\Gamma_{1,2}/2\pi = (190, 170)$ kHz, $\Omega_{1,2}/2\pi = (5.99, 6.3)$ MHz.

Figure 4.23 **(a)** illustrates the trajectories of the driven nanowire in the horizontal plane. Their elliptical character is clearly visible. The linear parametric modulation strength $\delta\omega_0^{(1)}$ reads

$$\begin{aligned}\delta\omega_0^{(1)}(t) &= \sum_{i=1,2} \text{Re}\left(\chi_i[\Omega](\delta\mathbf{F}.\mathbf{e_i})(\mathbf{e_i}.\boldsymbol{\nabla}\omega_0)e^{-i\Omega t}\right) \\ &= \left|\sum_{i=1,2} \chi_i[\Omega](\delta\mathbf{F}.\mathbf{e_i})(\mathbf{e_i}.\boldsymbol{\nabla}\omega_0)\right| \cos\left(\Omega t - \phi[\Omega]\right), \end{aligned} \tag{4.15}$$

where the phase $\phi[\Omega]$ is the argument of the expression within the absolute value sign, which is the parametric modulation strength. The corresponding magnitude of the parametric modulation strength in represented in Figure 4.23 **(b)**. The signatures are in qualitative agreement with the experimental data shown in Figure 4.22.

Experimentally, we observe a remanent signature of the Mollow triplet even at large detunings of the drive frequency. This represents a parasitic effect due to the use of the electrostatic actuation, generating a modulation strength of $\delta\omega_0^{\text{bck}}/2\pi \approx 1.8\,\text{MHz}$. It is noteworthy that it disappears in case of piezo electric actuation, which does not generate residual currents, see Figure 4.24. Section 4.5 is dedicated to the interpretation of this parasitic signal.

Taking into account this parasitic component, we adjust the experimental data using

$$\delta\omega_0^{(1)}[\Omega] = \left| \sum_{i=1,2} \chi[\Omega]\,(\delta\mathbf{F}.\mathbf{e_i})\,(\mathbf{e_i}.\boldsymbol{\nabla}\omega_0) + \delta\omega_0^{\mathrm{bck}} \right|, \tag{4.16}$$

where $\delta\omega_0^{\mathrm{bck}}$ is a frequency independent complex term with amplitude $\left|\delta\omega_0^{\mathrm{bck}}\right| = 1.86\,\mathrm{MHz}$ and phase 99°. The fit shows very good agreement with the experimental data, as can be seen in Figure 4.22.

Several pairs of values of force and gradient $(\delta F, \nabla\omega_0)$ yield a satisfying fit of the experimental data. To verify the consistency with our measurements, we impose that the spin resonance frequency is fixed to $\omega_0/2\pi = 1.7\,\mathrm{GHz}$, which corresponds to a position along the contour indicated in Figure 4.17. We furthermore impose the orientation of the force vector, with an angle of 50° with respect to $\mathbf{e_1}$, resulting in a potential working point $(x_0, z_0) = (2.5, 18.5)\,\mu\mathrm{m}$, as highlighted in Figure 4.17. This position is in rough agreement with the one experimentally chosen. Notice that the measurement position is subject to the combined constraints of maximized fluorescence and preserving $\omega_0/2\pi = 1.7\,\mathrm{GHz}$, allowing a spatial tolerance for mechanical drifts within a $1\,\mu\mathrm{m}^2$ region. Agreement with the experimentally chosen position can potentially be improved by a larger precision on the measurement of $\mathbf{e_F}$, which was difficult due to non-trivial position dependence of the electric parasitic noise on the QPDs. The true position of the NV in the gradient is probably closer to the optical axis (and hence a smaller value x_0) as this is in agreement with the large amount of detected fluorescence NV during execution of the experiment.

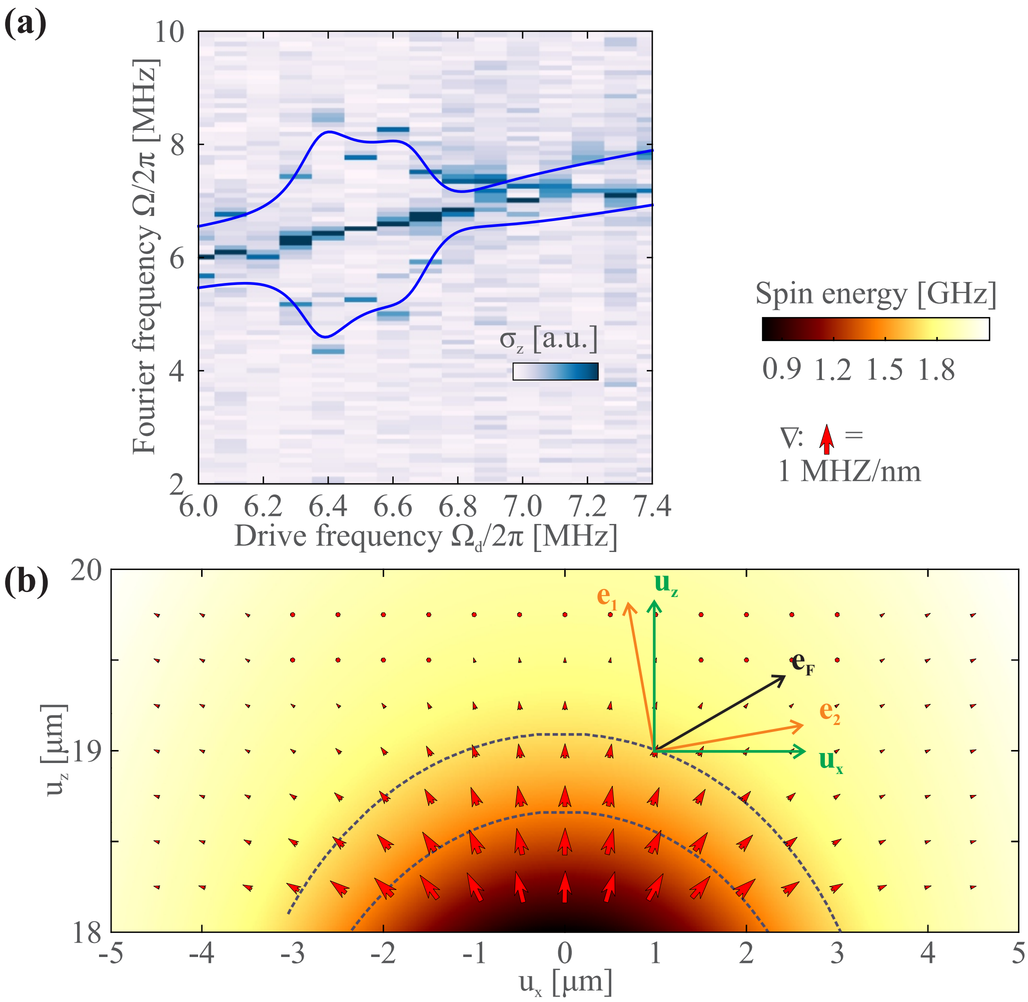

Figure 4.24: Sweep of the piezo-electric drive frequency $\Omega/2\pi$. **(a)** The measurement shows the same signature as in Figure 4.22. However, due to the complicated piezo response, we observe a more complicated frequency dependence of the oscillation amplitude. The blue lines are fits of equation (4.15) to the data, yielding an angle between $\mathbf{e_1}$ and $\boldsymbol{\lambda}$ of 28°. Notice the shift of the resonances, which was observed due to a permanent alteration of the nanowire during experimental data collection and can be explained by debris from the environment randomly accumulating on the resonator. **(b)** The resulting working point $(x_0, z_0) = (1.0, 19.0)\,\mu$m is indicated on the spin energy surface. $\mathbf{e_F}$ for the piezo drive was assumed to be at 70° with $\mathbf{e_1}$, inferred from the setup geometry and orientation of the piezo excitation crystal.

4.5 Quadratic coupling

We have seen that the linear coupling strength $\delta\omega_0^{(1)}$ achievable in our hybrid system can overpass the strength observed in the test experiment. It is thus natural to investigate higher order coupling mechanisms and we will now describe the experimental signatures as well as the two mechanisms which are at play: the nanomotion of the oscillator in a parabolic spin energy surface and a quadratic Zeeman shift due to a modulated residual transverse magnetic field.

4.5.1 Experimental observation

We now return to the observation of the additional component observed in Figure 4.19 (encircled in green). In order to increase the visibility of the phenomenon in this data set, we repeat a measurement of the Rabi frequency sweep at larger electrostatic driving amplitudes. The data is shown in Figure 4.25.

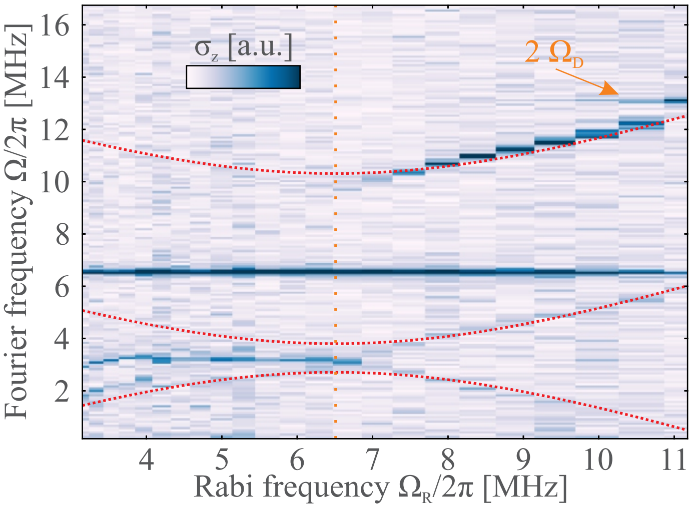

Figure 4.25: Sweep of the Rabi frequency $\Omega_\mathrm{R}/2\pi$ across the mechanical drive frequency $\Omega_\mathrm{d}/2\pi = \Omega_\mathrm{m}/2\pi = 6.29\,\mathrm{MHz}$, $\delta\omega_0/2\pi \approx 7.0$ MHz. A lower component $\sqrt{(\Omega_\mathrm{R}-\Omega_\mathrm{m})^2+\delta\omega_0^2/4}$ crosses with $\Omega = \Omega_\mathrm{m} - \sqrt{(\Omega_\mathrm{R}-\Omega_\mathrm{m})^2+\delta\omega_0^2/4}$ and therefore presents a strong deviation from the theoretical parabolic behavior that is indicated by the dotted lines. Another component becomes visible at $\Omega = 2\Omega_\mathrm{d}$.

We observe indeed again a fourth component $\Omega = \Delta_{N,M}$, that seems to join the lower branch around $\Omega_\mathrm{R}/2\pi = 5\,\mathrm{MHz}$ but then diverges and bends towards Ω_d as Ω_R increases. Also, a strong deviation from the parabolic prediction of equation (3.55) is visible. At the same time, where Ω_R approaches $2\Omega_\mathrm{d}$, a component at twice the modulation frequency starts to appear.

4.5.2 Quadratic parametric modulation

This behavior can be explained by an additional contribution to the spin energy modulation quadratic in the drive field,

$$\omega_0(t) = \omega_0 + \delta\omega_0(t) = \omega_0 + \delta\omega_0^{(1)} \cos\Omega_\mathrm{d} t + \delta\omega_0^{(2)} \cos^2\Omega_\mathrm{d} t, \tag{4.17}$$

which becomes important for strong driving amplitudes. Numerical simulations including this additional contribution show that the intramultiplicity component $\Delta_{N,M}$ appears, as well as a spin synchronization on the $2\Omega_\mathrm{d}$ tone, see Figure 4.26. The effect of the higher order term can be understood in terms of a dc energy shift and an oscillation at $2\Omega_\mathrm{d}$, for we have

$$\delta\omega_0^{(2)} \cos^2\Omega_\mathrm{d} t = \delta\omega_0^{(2)} \frac{1+\cos 2\Omega_\mathrm{d} t}{2}, \tag{4.18}$$

which effectively explains appearance of a component at $2\Omega_\mathrm{d}$. Notice that there also appears an anti-crossing slightly below $2\Omega_\mathrm{d}$. For a single tone Ω_m, higher order anti-crossings only occur at odd multiples of Ω_m [122, 169]. The anti-crossing at $2\Omega_\mathrm{d}$ of size $\delta\omega_0^{(2)}/2$ can therefore be ascribed to a second modulation frequency. Moreover, the offset term induces an effective detuning of the MW with the unperturbed resonance ω_0 of $\delta = \delta\omega_0^{(2)}/2$. Consequently, offresonant pumping leads to appearance of the component at $\Omega = \Delta_{N,M}$ in the Fourier spectra (see the selection rules (3.99)), as already mentioned above.

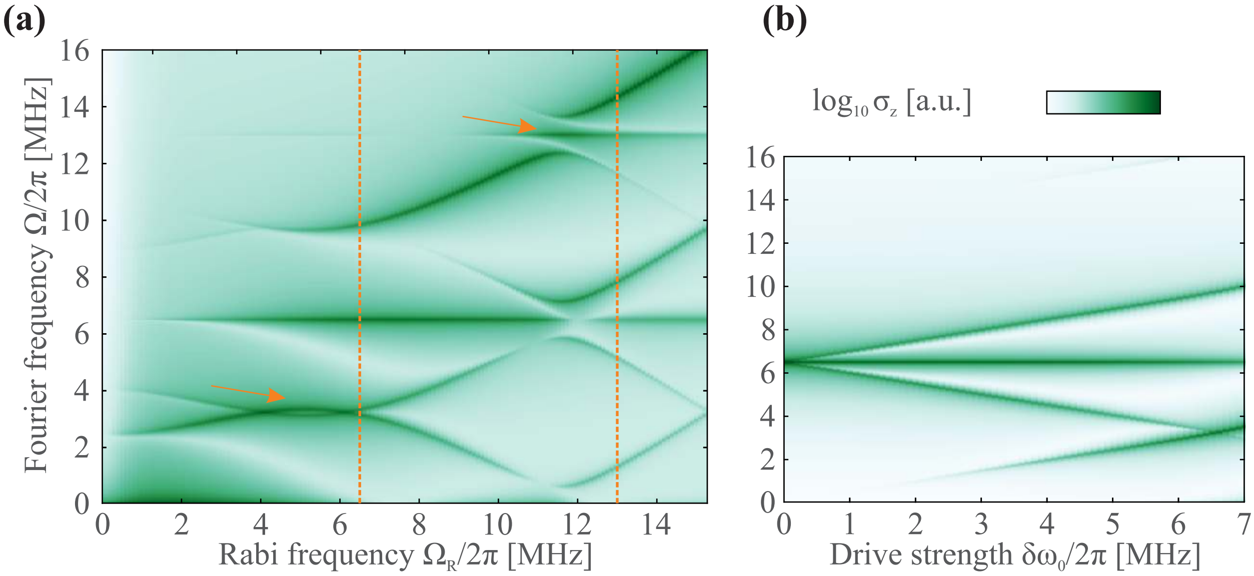

Figure 4.26: Simulation data with $\Omega_\mathrm{d}/2\pi = 6.5\,\mathrm{MHz}$ and $\delta\omega_0^{(2)} = a\delta\omega_0^2$, with nonlinearity $a = 0.22\,\mathrm{MHz}^{-1}$. **(a)** Simulated sweep of the Rabi frequency $\Omega_\mathrm{R}/2\pi$ across the mechanical drive frequency, $\delta\omega_0/2\pi = 7.0$ MHz and $\delta\omega_0^{(2)} = a\delta\omega_0^2 = 0.7\delta\omega_0$. The lower component $\Omega = \Delta_{N,M}$ and $\Omega = 2\Omega_\mathrm{d}$ become visible due to the quadratic contribution. Notice that the branch $\Omega_\mathrm{R} - \Delta_{(N,M)}$ crosses with the branch $\Delta_{N,M}$. **(b)** Sweep of the oscillation amplitude. For the nonlinearity $a = 0.22\,\mathrm{MHz}^{-1}$ the quadratic component does not significantly influence the spin dynamics in the simulated parameter range corresponding to the measurement in Figure 4.21.

4.5.3 Origin of the nonlinearity

We discuss here the origin of the contribution quadratic in the drive field. Motion of the nanowire at $2\Omega_\mathrm{d}$ as a potential explanation for the energy modulation at twice the mechanical frequency can be excluded: because of the small mechanical susceptibility far away from the resonance frequency, displacement due to an additional driving force $F_\mathrm{es}[2\Omega_\mathrm{d}]$ is negligible. We therefore seek the origin of the nonlinearity elsewhere.

Quadratic motional hybrid coupling

Due to the strong spatial variations of the magnetic field and the important oscillation amplitudes that are achieved, one has to take into account higher order terms in the expansion of the position sensitive Zeeman effect:

$$\omega_0(\mathbf{r}) \approx \omega_0(\mathbf{r_0}) + \delta\mathbf{r}.\boldsymbol{\nabla}\omega_0\big|_{\mathbf{r_0}} + \frac{1}{2}\left(\delta\mathbf{r}.\boldsymbol{\nabla}\right)^2\omega_0\big|_{\mathbf{r_0}}. \tag{4.19}$$

The last term is quadratic in the oscillation $\delta\mathbf{r}(t)$ and originates from a Hamiltonian

$$H_\mathrm{int}^{(2)} = \hbar\lambda^{(2)}\sigma_z\hat{x}^2. \tag{4.20}$$

This quadratic coupling term plays a fundamental role since it commutes with the oscillator energy, $\propto \hat{x}^2$, and permits a QND measurement of the resonator excitation spectrum through spin spectroscopy. In our situation, the quadratic modulation can be expressed as

$$\delta\omega_0^{(2)}(t) = \frac{1}{2}\sum_{i,j=1,2}\delta r_i(t)\delta r_j(t)\partial_{ij}^2\omega_0\big|_{\mathbf{r_0}}. \tag{4.21}$$

Using

$$\delta r_i(t) \equiv \delta \mathbf{r}(t).\mathbf{e_i} = \mathrm{Re}\left(\delta \mathbf{r}[\Omega].\mathbf{e_i} e^{-i\Omega t}\right) = |\delta r_i[\Omega]| \cos\left(\Omega t - \phi_i[\Omega]\right)$$

with $\phi_i[\Omega] = \arg\left(\delta r_i[\Omega]\right)$, we have

$$\delta\omega_0^{(2)}(t) = \frac{1}{2} \sum_{i,j=1,2} |\delta r_i[\Omega] \delta r_j[\Omega]| \cos\left(\Omega t - \phi_i[\Omega]\right) \cos\left(\Omega t - \phi_j[\Omega]\right) \partial^2_{ij}\omega_0\big|_{\mathbf{r_0}}. \tag{4.22}$$

The product of the cosines can be reexpressed as $\cos\left(2\Omega_\mathrm{m} - \phi_i - \phi_j\right) + \cos\left(\phi_i - \phi_j\right)$, where the second term corresponds to a static shift of the spin resonance frequency,

$$\begin{aligned}\Delta\omega_0 &= \frac{1}{2} \sum_{i,j=1,2} |\delta r_i[\Omega] \delta r_j[\Omega]| \cos\left(\phi_i[\Omega] - \phi_j[\Omega]\right) \\ &= \frac{1}{2} \mathrm{Re}\left(\sum_{i,j=1,2} \delta r_i[\Omega] \delta r_j[\Omega] \partial^2_{ij}\omega_0\big|_{\mathbf{r_0}}\right), \end{aligned} \tag{4.23}$$

and the first term represents the modulation strength at twice the drive frequency. It can be written as

$$\delta\omega_0^{(2)} = \frac{1}{2} \mathrm{Re}\left(\sum_{i,j=1,2} \delta r_i[\Omega] \delta r_j[\Omega] \partial^2_{ij}\omega_0\big|_{\mathbf{r_0}} e^{-i(2\Omega t - \phi_i - \phi_j)}\right) \tag{4.24}$$

$$= \delta\omega_0^{(2)} \cos\left(2\Omega t - \phi[\Omega]\right) \tag{4.25}$$

with Fourier representation

$$\delta\omega_0^{(2)}[\Omega] = \frac{1}{2} \left| \sum_{i,j=1,2} \chi_i[\Omega] \chi_j[\Omega] \left(\delta\mathbf{F}.\mathbf{e_i}\right) \left(\delta\mathbf{F}.\mathbf{e_j}\right) \partial^2_{ij}\omega_0\big|_{\mathbf{r_0}} \right|. \tag{4.26}$$

This expression permits to estimate the strength of quadratic coupling to the nanomotion once the force vector $\delta\mathbf{F}$ and the gradient direction $\boldsymbol{\lambda}$ as well as the second order spatial derivatives of the spin energy surface $\omega_0(\mathbf{r_0})$ are known. The latter is indeed described by a curvature matrix

$$\boldsymbol{\zeta}(\mathbf{r_0}) = \begin{pmatrix} \zeta_{11} & \zeta_{12} \\ \zeta_{21} & \zeta_{22} \end{pmatrix} \equiv \left.\begin{pmatrix} \partial^2_{11}\omega_0 & \partial^2_{12}\omega_0 \\ \partial^2_{21}\omega_0 & \partial^2_{22}\omega_0 \end{pmatrix}\right|_{\mathbf{r_0}}, \tag{4.27}$$

which is symmetric and can be diagonalized to infer the directions of the principal curvatures of the surface, which represent the directions $\mathbf{e}_{\boldsymbol{\alpha}}$, $\mathbf{e}_{\boldsymbol{\alpha+\pi/2=\beta}}$ of maximum and minimum curvature, respectively. The curvature matrix then becomes

$$\boldsymbol{\zeta}(\mathbf{r_0}) = \begin{pmatrix} \zeta_\alpha & 0 \\ 0 & \zeta_\beta \end{pmatrix}, \tag{4.28}$$

with eigenvalues

$$\zeta_{\alpha,\beta} = \frac{1}{2}\left(\zeta_{xx} + \zeta_{zz}\right) \pm \sqrt{\left(\zeta_{xx} - \zeta_{zz}\right)^2 + 4\zeta_{xz}^2} \tag{4.29}$$

and eigenvectors

$$\mathbf{e}_{\boldsymbol{\alpha}} = \frac{1}{\sqrt{\zeta_{xz}^2 + \left(\zeta_\alpha - \zeta_{xx}\right)^2}} \begin{pmatrix} \zeta_{xz} \\ \zeta_\alpha - \zeta_{zz} \end{pmatrix}, \tag{4.30}$$

$$\mathbf{e}_{\boldsymbol{\beta}} = \frac{1}{\sqrt{\zeta_{xz}^2 + \left(\zeta_\beta - \zeta_{zz}\right)^2}} \begin{pmatrix} \zeta_\beta - \zeta_{zz} \\ \zeta_{xz} \end{pmatrix}. \tag{4.31}$$

The quadratic coupling matrix $\boldsymbol{\zeta}(\mathbf{r_0})$ is shown in Figure 4.27. It is obtained by spatially differentiating the measured map of $\omega_0(\mathbf{r_0})$ seen in Figure 4.17. Also shown are the orientations of the principal curvatures, $\mathbf{e}_{\boldsymbol{\alpha}}$ and $\mathbf{e}_{\boldsymbol{\beta}}$, along which the quadratic contributions are maximum, and their magnitudes ζ_α and ζ_β. In order to observe large quadratic couplings, it is necessary to tune the nanomotion of the qubit along one of the principal orientations. To obtain an estimation of typical magnitudes in our measurement, we evaluated formula (4.26) at different points of the measurement area, conditioned to yield the observed linear parametric coupling terms as well as to fulfill $\omega_0/2\pi \approx 1.7\,\mathrm{GHz}$ (see Figure 4.17). The resulting strength is found to be in the $\delta\omega_0^{(2)}/2\pi = (20-150)\,\mathrm{kHz}$ range, strongly dependent on the measurement position.

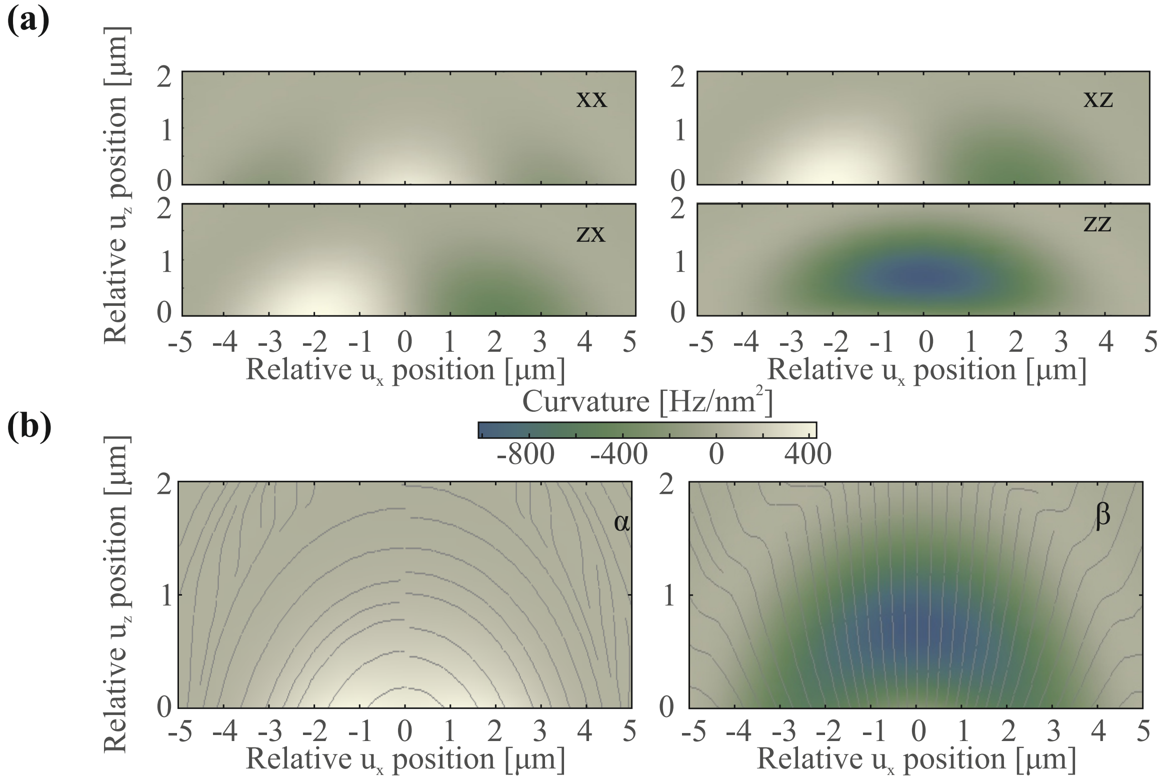
(a)
xx
xz
zx
zz
Relative u_z position [µm]
Relative u_x position [µm]
Curvature [Hz/nm^2]
-800
-400
0
400
(b)
α
β
Relative u_z position [µm]
Relative u_x position [µm]
-5 -4 -3 -2 -1 0 1 2 3 4 5
0 1 2

Leakage currents

Alternatively, the quadratic contribution of the energy modulation can also be created by magnetic fields generated by leakage currents traveling though the waveguide. This is possible despite the open circuit for the RF pathway because of a residual resistance of the waveguide and an impedance arising from about two meters of coaxial cables combined with large voltage signals ($\sim 150V$) used for the electrostatic actuation of the nanowire motion. While we do not have precise knowledge about the exact circuit elements, we model an equivalent circuit as shown in the diagram of Figure 4.28 **(a)**. We estimate that with a RF potential reaching up to 150 V, a total capacitance of $C = 100\,\text{pF}$ from the coaxial cables and a waveguide and amplifier resistance of $R_{\text{WG}} \approx 6$ Ohm and $R_{\text{A}} \approx 50$ Ohm, currents on the order of 100 mA are realistic. The magnetic field created by these currents can amount to several mT, inducing rather large frequency shifts at the position of the NV spin.

The angle Φ between these RF magnetic fields and the NV axis, as shown in Figure 4.28 **(b)**, plays an important role as it determines the slope of the spin energy with the magnetic field around the modulation point. In our experiment, a strong field of about $41\,\text{mT}$ is applied along the spin **z**-direction, necessary to achieve $\omega_0/2\pi = 1.7\,\text{GHz}$. In Figure 4.28 **(c)** we show plots of the spin energy against an additional magnetic field B_{RF} created by the parasitic currents for various angles. For $\Phi = 90°$, a parabola clearly indicates the quadratic shift, while the linear component becomes more important as the external field B_{RF} becomes more aligned with B_z. This tendency is shown in Figure 4.28 **(d)**. In the experimental case, we presume an angle Φ close to 90°. This assumption is for once supported by the good ESR contrast, indicating that the MW magnetic field orientation, which is the same as for the RF magnetic fields, is close to transverse to the NV spin. On the other hand, for $B_{\text{RF}} = 1\,\text{mT}$ created by the parasitic current, the linear shift observed in Figure 4.22 for large detunings, $\delta\omega_0^{\text{bck}}$, is relatively small with $\delta\omega_0^{\text{bck}}/2\pi \approx 1.7\,\text{MHz}$. The small linear component indicates strong misalignment with the longitudinal spin direction and therefore a large transverse component. For $\Phi = 87°$, 1 mT of modulation amplitude generates a linear and quadratic modulation strength of $\delta\omega_0/2\pi = 1.7\,\text{MHz}$ and $\delta\omega_0^{(2)}/2\pi \approx 550\,\text{kHz}$, respectively. The latter value is sufficiently large to explain the size of the splitting observed at the anitcrossing with the $2\Omega_{\text{d}}$ tone of Figure 4.28.

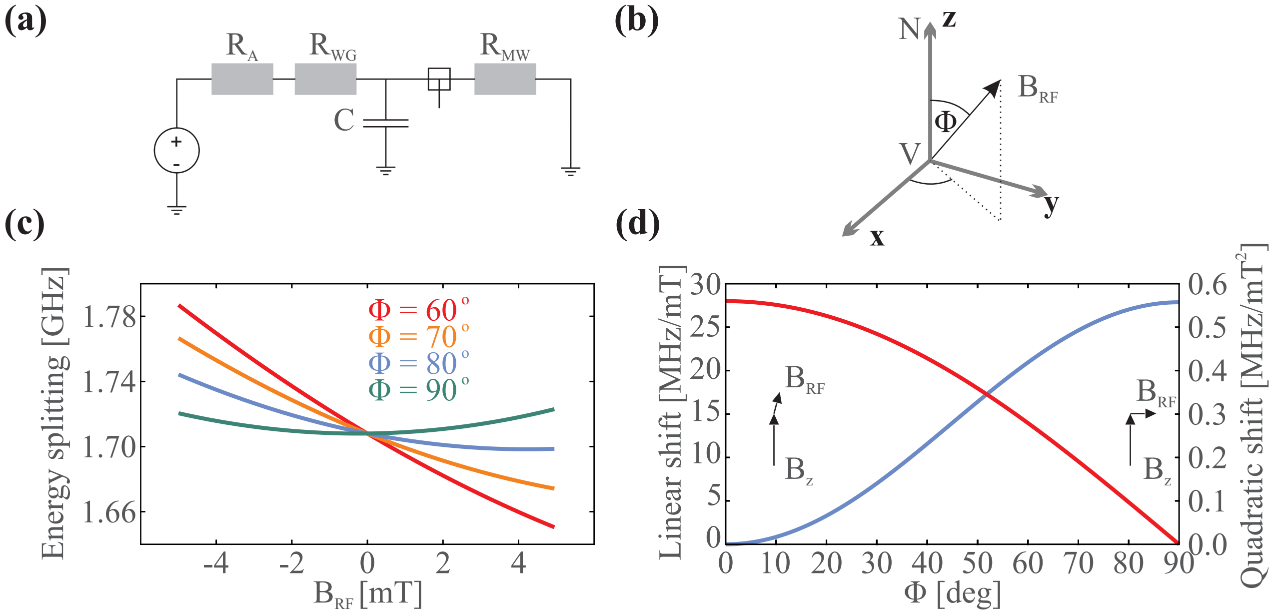

Figure 4.28: Leakage currents and quadratic RF energy modulation. **(a)** The equivalent circuit diagram taking into account the amplified voltage source, resistances of waveguide and amplifier and the coaxial cable's capacitance C. **(b)** Vector diagram defining Φ. **(c)** Change of the spin energy as a function of an additional magnetic field B along the indicated direction. The curves were obtained by calculating the eigenvalues of Hamiltonian (2.52). **(d)** Angular dependence of the linear and quadratic energy modulation terms, obtained from adjusting the curves in **(c)** to a second order polynomial.

Finally, it is a realistic scenario that both of the effects discussed are at play here. The influence of leakage currents can be verified by a measurement using the piezo-electric drive of the nanowire motion. Such a measurement has however proven difficult because of the complicated frequency dependent response behavior of the force to the actuation. Exact determination of the nature of the quadratic coupling will be subject of further study.

4.6 Conclusion

In this chapter we have demonstrated a functioning hybrid spin-mechanical system built from a SiC nanowire and a single NV electron spin hosted in a nanodiamond attached to the nanowire extremity. Optical readout of the nanowire motion and spin manipulation via a specifically designed waveguide granting a large access angle for a confocal microscope can be used independently to monitor and control both components of the hybrid system. The position of the nanowire is encoded in the spin energy once immersed in a large magnetic field gradient. While the spatial variation of the spin energy can be complex in the strongly varying magnetic landscape, we have presented a reliable technique to identify a reproducible working point for spin manipulation protocols which maximizes readout contrast and gives access to large magnetic field gradients. Moreover, cartography of the spin energy variation around the working point permits the determination of the vectorial parametric coupling strength. This is an important prerequisite for the proper understanding of directional coupling of spin and oscillator. We have verified that the principles of the driven spin dynamics in presence of mechanical motion adhere to the theoretical description established in Chapter 3, permitting the observation of the so called phononic Mollow triplet. The experimentally observed signatures of spin synchronization have however gained in richness, due to both, the vectorial and bidimensional character of the coupling inherent to the existence of two orthogonal eigenmodes which can be simultaneously addressed and the introduction of a quadratic contribution to the energy modulation.

Until now, we have neglected the incoherent thermal motion and, so far, all experimental signatures have been analyzed purely in the context of monochromatic motion of the oscillator. Indeed, it has been surprising to observe such close correspondence between the measurements performed with the test system and the hybrid experiment. Generally, the incoherent thermal motion can play a significant role in hybrid nanomechanical systems due to the ultralow mass of the resonator that enhances the spatial spreading of its thermal noise. In particular, one experimental feature visible in the measurement of Figure 4.22, motivates a deeper investigation of the role of thermal noise in the spin locking mechanism: at $\Omega_\mathrm{m}/2\pi = \Omega_\mathrm{R}/2\pi \approx 7\,\mathrm{MHz}$ we observe an unexpected feature in the Mollow triplet structure. While the lower Mollow sideband seems to be pushed to lower frequencies, the upper component almost disappears. This astonishing feature occurs exactly where the lower sideband is expected to overlap with the resonance frequency of the $\mathbf{e_1}$-mechanical mode. This signature therefore is potentially related to a coupling to the oscillator's thermal motion, which we expect to be on the order of $\sim 100\,\mathrm{kHz}$. In order to better understand this effect, we will now study the influence of the thermal noise on the Mollow triplet.

Chapter 5

Role of Brownian motion

We have seen various signatures of a mechanical oscillator parametrically coupled to a single NV defect. So far, the mechanical oscillations could be well described by coherent, monochromatic motion with quasi infinite correlation time. However, at the end of Chapter 4 we have also seen a striking modification of the Mollow triplet signature when one of the triplet sidebands coincides with a thermally driven mechanical mode. In this chapter we will go beyond monochromatic, coherent oscillator motion and we will look at the alteration of the Mollow triplet in the presence of mechanical noise. In order to do so, we return to the test system of Chapter 3, where along with a coherent, monochromatic RF field, we can also inject an additional signal, emulating the noise of an oscillator's Brownian motion. We then investigate the response of the phonon Mollow triplet to Brownian noise peaked at one of the sideband frequencies as well as the central component. In the latter case, we observe a certain immunity of the spin to the additional decoherence source and we will explain the protection of coherence invoking the doubly dressed state picture.

We then proceed to show that the double dressing signatures can also be observed for a purely Brownian drive and we will investigate the influence of temperature and mechanical dissipation on the thermal Mollow triplet. The latter study has also motivated us to revisit the resolved sideband experiments of Chapter 3, where the Rabi frequency is small compared to the mechanical resonance frequency, $\Omega_{\mathrm{R}} \ll \Omega_{\mathrm{m}}$. Results concerning numerical and experimental investigations of ODMR spectra and Rabi oscillations for a strong thermal drive are given in the appendices.

5.1 Motivation

When concerned with the study of hybrid spin-mechanical devices, the ubiquity of thermal noise in mechanical systems naturally motivates us to consider its effects on the parametrically coupled spin. Here it is desirable to reduce data acquisition times necessary to distinguish spin induced coherent from incoherent thermal motion in a lock-in detection scheme [98]. Working at small phonon occupation numbers in cryogenic environments to suppress the incoherent thermal displacement is thus a commonplace strategy. For the system presented in the previous chapter, exhibiting an effective mass of the SiC nanowire, $M \approx 1\,\mathrm{pg}$ and an oscillation frequency $\Omega_{\mathrm{m}}/2\pi \approx 6\,\mathrm{MHz}$, we have a typical thermal mean phonon occupation number of

$$\bar{m}_{\mathrm{th}} = \frac{1}{e^{\frac{\hbar\Omega_{\mathrm{m}}}{k_B\Theta}} - 1} \approx 165000$$

and, according to expression (2.26), a root mean square displacement of

$$\Delta x_{\mathrm{th}} = \sqrt{\frac{k_B\Theta}{M\Omega_{\mathrm{m}}^2}} = 170\,\mathrm{pm}.$$

In a magnetic field gradient of $\nabla B = 3 \times 10^4\,\mathrm{T/m}$, the Brownian motion couples to the spin with a rms coupling strength of $\delta\omega_{\mathrm{th}}/2\pi \approx 140\,\mathrm{kHz}$, as mentioned before. This value is roughly one order of magnitude less than the coupling strength obtained by coherently driving the mechanical oscillations for the setup of chapter 4 and so we can expect a noticeable influence on the experimental signatures. In this chapter we will thus aim at answering the question how the Brownian motion affects the Mollow triplet signature. Furthermore, the Brownian oscillator with finite correlation time $1/\Gamma_{\mathrm{m}}$ and asymmetric (around a nonzero peak frequency $\Omega_{\mathrm{m}}/2\pi$) spectral density $S_x^{\mathrm{th}}[\Omega]$ presents a somewhat novel noise source coupled to a single quantum two level system. In order to better understand the role of Brownian motion in the experiments that were presented in this thesis so far, we will now return to the test system of Chapter 3.

5.2 Experimental setup

Working with radio frequency fields instead of a true mechanical system will allow us to tune the emulated thermal noise through several coupling regimes. Throughout this chapter we will restrict all our considerations to a scalar coupling to only one polarization of the oscillator motion (for example $\mathbf{e_1}$), corresponding to $\boldsymbol{\lambda}.\mathbf{e_1} = \lambda$ and $\boldsymbol{\lambda}.\mathbf{e_2} = 0$. In that case, we define the scalar quantity

$$\delta\omega_{\mathrm{th}} = 2\pi\lambda\Delta x_{\mathrm{th}} = 2\pi\lambda\sqrt{\frac{k_B\Theta}{M\Omega_{\mathrm{m}}^2}}, \tag{5.1}$$

which is the parametric coupling strength between spin and thermal motion, summarizing the influence of oscillator mass M, frequency $\Omega_{\mathrm{m}}/2\pi$ as well as bath temperature Θ in one parameter. From a physical point of view, variation of $\delta\omega_{\mathrm{th}}$ can therefore be considered as changing the bath temperature. The incoherent coupling strength's independence of the mechanical dissipation rate Γ_{m} is an elegant demonstration of the fluctuation-dissipation theorem. From the thermal noise spectral density (2.25) we deduce the thermal coupling spectral density

$$\begin{aligned} S_{\delta\omega_\parallel}^{\mathrm{th}}[\Omega] \equiv \frac{1}{2}\left(2\pi\lambda\right)^2 S_x^{\mathrm{th}}[\Omega] &= \frac{\left(2\pi\lambda\right)^2 \Gamma_{\mathrm{m}} k_B\Theta/M}{(\Omega_{\mathrm{m}}^2 - \Omega^2)^2 + \Omega^2\Gamma_{\mathrm{m}}^2} \\ &= \frac{\delta\omega_{\mathrm{th}}^2\Gamma_{\mathrm{m}}\Omega_{\mathrm{m}}^2}{(\Omega_{\mathrm{m}}^2 - \Omega^2)^2 + \Omega^2\Gamma_{\mathrm{m}}^2}, \end{aligned} \tag{5.2}$$

with two reference values

$$S_{\delta\omega_\parallel}^{\mathrm{th}}[0] = \frac{\delta\omega_{\mathrm{th}}^2\Gamma_{\mathrm{m}}}{\Omega_{\mathrm{m}}^2}, \tag{5.3}$$

$$S_{\delta\omega_\parallel}^{\mathrm{th}}[\Omega_{\mathrm{m}}] = \frac{\delta\omega_{\mathrm{th}}^2}{\Gamma_{\mathrm{m}}} = Q^2 S_{\delta\omega_\parallel}^{\mathrm{th}}[0]. \tag{5.4}$$

In order to emulate such coupling experimentally, we have to inject a signal with spectral density (5.2) in the RF waveguide of our test system, subject to the condition that the full phase-space of Brownian motion is explored.

The latter can be witnessed in the time domain and is a second prerequisite for the generation of proper Brownian motion. We introduce the quadratures of the signal. By decomposing $x(t)$ into

$$x(t) = X_1(t)\cos\Omega_{\mathrm{m}}t + X_2(t)\sin\Omega_{\mathrm{m}}t, \tag{5.5}$$

and mixing the signal, we obtain the two quadratures of motion, X_1 and X_2. They can be extracted using low frequency filtering[1]:

$$\begin{aligned} X_1(t) =& \frac{2}{T} \int\limits_{t}^{t+T} \mathrm{d}\tau \, x(\tau) \cos \Omega_\mathrm{m} \tau, \\ X_2(t) =& \frac{2}{T} \int\limits_{t}^{t+T} \mathrm{d}\tau \, x(\tau) \sin \Omega_\mathrm{m} \tau. \end{aligned} \tag{5.6}$$

The two quadratures $X_1(t)$ and $X_2(t)$ experience random jumps on a time scale of $\sim 1/\Gamma_\mathrm{m}$ and therefore describe the mechanical oscillator's random walk through the phase-space diagram associated with the Brownian motion, shown in Figure 5.2 **(c)**. As opposed to the coherent case, the two quadratures $\{X_1(t), X_2(t)\}$ present a Gaussian distribution of width Δx centered at zero in the thermal case (compare with Figure 2.4).

5.2.1 Modification of the setup

The experimental setup is described in Figure 5.1 **(a)**. The ability to inject a coherent **(b)** as well as incoherent **(c)** signal simultaneously allows us to tune the competition between the two in a well controlled manner. The waveguiding structure therefore presents a unique platform for the experimental study of a single two level system as a spectrum analyzer. In principle, the arbitrary waveform generator allows the emulation of various spin bath scenarios, ranging from telegraph noise due to a few random fluctuators [171] over Gaussian colored noise due to many random fluctuators [172] to 1/f noise which is ubiquitous in superconducting qubits [121]. Here we will provide a set of proof-of-principle measurements on the example of the experimentally relevant Brownian noise as discussed above.

---

[1] In order to be insensitive to the fast oscillations but sensitive to the much slower amplitude decay, T is chosen such that $2\pi/\Omega_\mathrm{m} \ll T < 2\pi/\Gamma_\mathrm{m}$. This corresponds to a low pass filter cutting off frequencies above $\sim 1/T$.

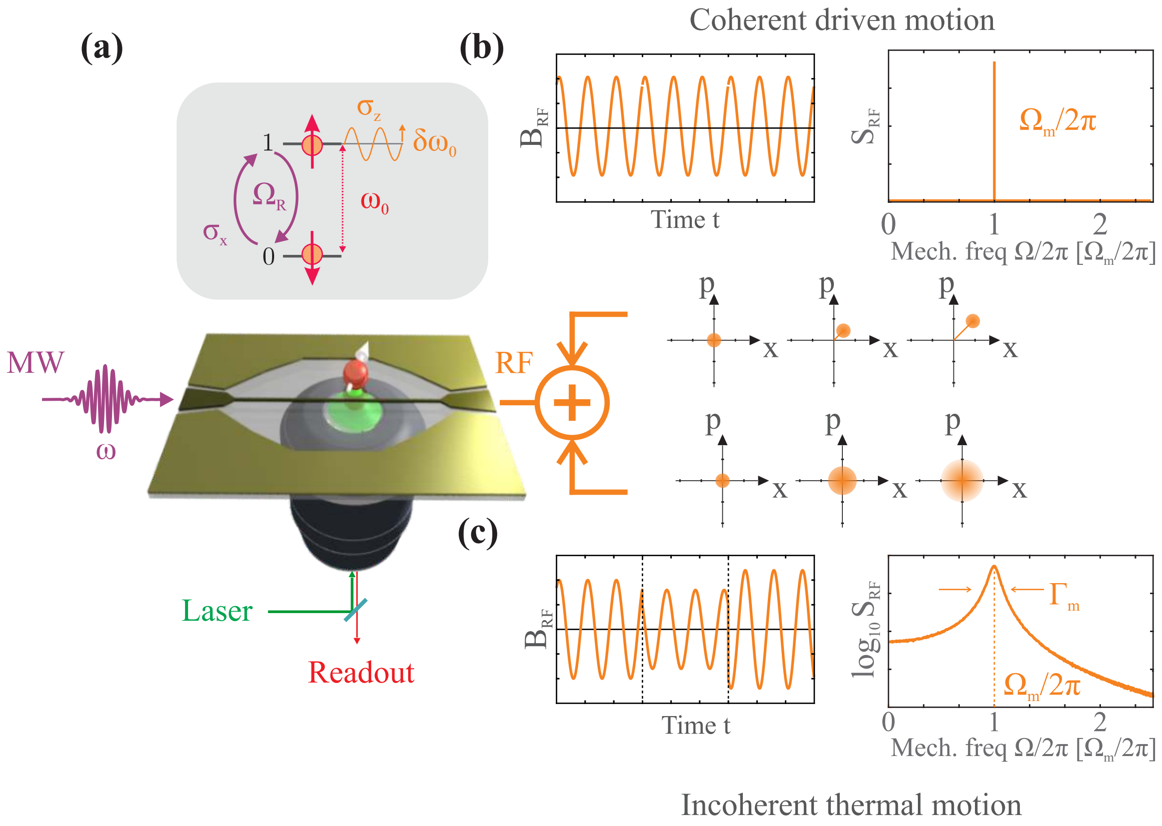

Figure 5.1: Experimental setup. **(a)** We use the test system of Chapter 3, driving spin transitions with a MW field and modulating the spin energy with an RF field. We inject a coherent **(b)** as well as an incoherent **(c)** signal in the waveguide, emulating the mechanical oscillator's monochromatically driven and thermal motion, respectively.

5.2.2 Simulated Brownian motion

The C based program performing these calculations and creating a single column ".txt" file is detailed in Appendix E. It is based on the realization of real physical Brownian motion: a spectrally flat random white force $\delta F[\Omega]$ is driving a mechanical oscillator with susceptibility $\chi[\Omega]$. By performing a Fourier transform of $x[\Omega] = \delta F[\Omega]\chi[\Omega]$, we emulate Brownian motion with the proper spectrum and Gaussian quadrature distribution. We create a table $X(i)$ of data points of successive positions x_i, such that the spectral decomposition of the auto-correlation function $a_X(j)$,

$$a_X(j) = \langle X(i+j)X(i)\rangle \tag{5.7}$$

agrees with the spectral density $S^{\mathrm{th}}_{\delta\omega_\parallel}[\Omega]$. We choose a time step of $dt = 4\,\mathrm{ns}$ resulting in a sampling frequency of 250 MHz, which is well above all other frequencies of interest (and also far from ω_0). This justifies a continuous treatment of the variable $X(i)$, such that $X(i) \to X(t)$. Finally, the table $X(t)$ is normalized to $\Delta X = 1$, which simplifies its handling in terms of the freely adjustable parameter $\delta\omega_{\mathrm{th}}$, such that $\delta\omega(\delta V, t) = \delta\omega_{\mathrm{th}}(\delta V)X(t)$.

The challenge in obtaining good agreement with a truly Brownian signal lies in the size of the created table $X(t)$, which needs to be sufficiently large in order to "explore" the full parameter space characterizing the thermal motion. This point is made clear by adopting the following picture of the oscillator's incoherent motion: the mechanical resonator is vibrating at its natural frequency $\Omega_m/2\pi$. At a given instance it is hit randomly by a particle of the surrounding gas. Exchange of momentum between the two causes the oscillator to experience a change in amplitude as well as phase of the oscillation, see Figure 5.2 **(a)**. To fully capture the average rate of collisions Γ_m it is necessary to acquire a large enough trace $X(t)$, such that the emulation of large Q values necessitates large file sizes.

We first verify numerically that our list $X(t)$ yields a spectral density (5.2). The Fourier transform of a calculated auto-correlation table a_X is shown in Figure 5.2 **(b)**, demonstrating very good agreement between the numerical data and the analytic expressions. Notice that the fits correspond to a conversion of the spectra $S_x^{\mathrm{th}}[\Omega]$ from radial frequency to frequency space $S_x^{\mathrm{th}}[f]$, such that

$$S_x^{\mathrm{th}}[f] = \frac{\frac{1}{\pi}\left(\frac{\Gamma_{\mathrm{m}}}{2\pi}\right) f_{\mathrm{m}}^2}{(f^2 - f_{\mathrm{m}}^2)^2 + f^2\left(\frac{\Gamma_{\mathrm{m}}}{2\pi}\right)^2}. \tag{5.8}$$

Here we have used the normalization of $X(t)$ to $\Delta X^2 = \frac{k_B \Theta}{M\Omega_{\mathrm{m}}^2} \equiv 1$. Typical traces for Q = 100 and Q = 200 at $\Omega_{\mathrm{m}}/2\pi = 6\,\mathrm{MHz}$ are shown in Figure 5.2 **(c)** and verify sufficient phase-space exploration by the tables $X(t)$.

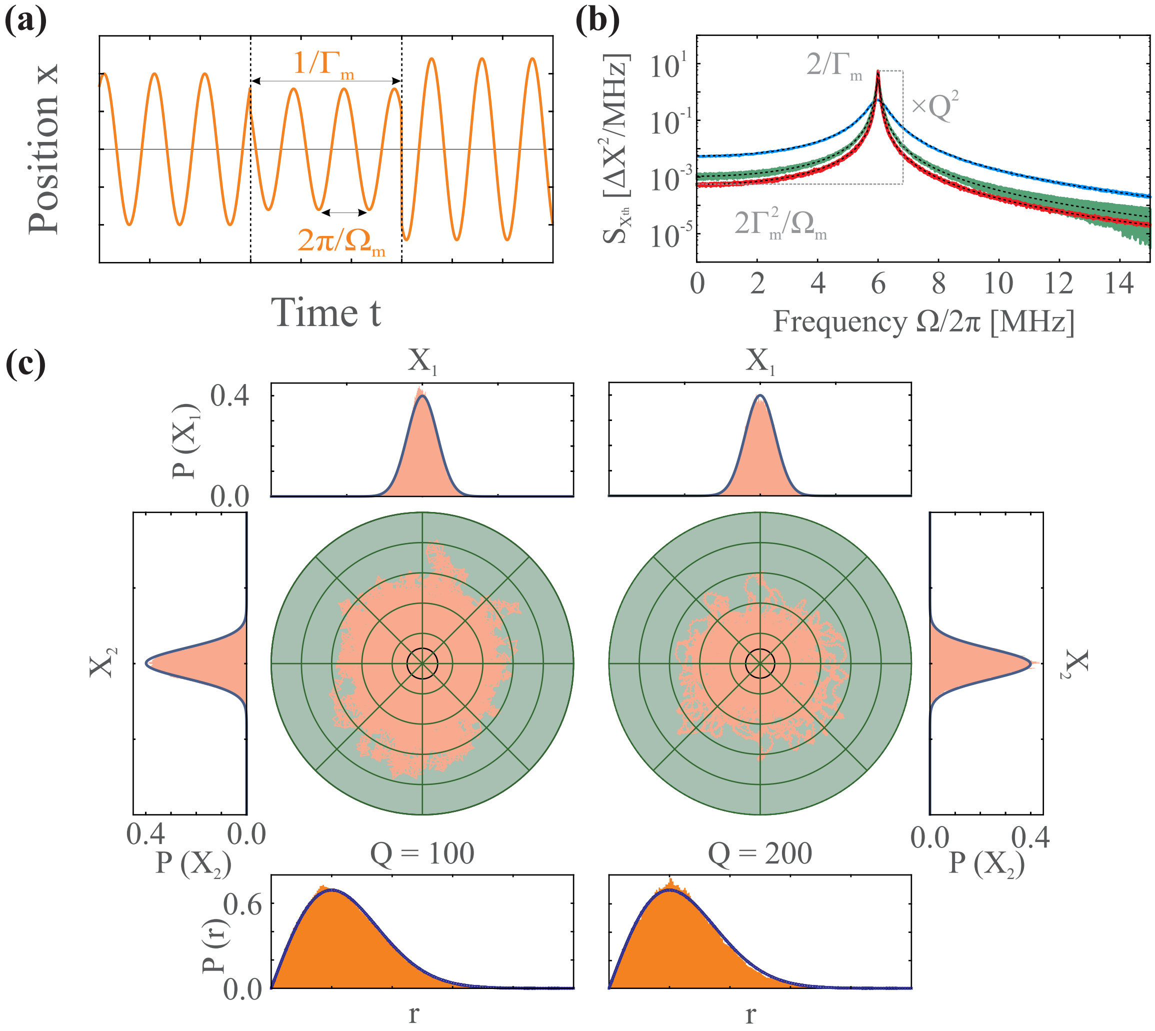

Figure 5.2: Numerically simulated Brownian motion. **(a)** Conceptualization of a Brownian temporal trace. Random momentum kicks occur at times indicated by the vertical dashed lines, indicating changes of phase and amplitude of the oscillator motion. **(b)** Spectra of simulated Brownian motion with quality factors Q = 10 (red), 50 (green), 100 (blue). The black dashed lines indicate fits to expression (5.8). **(c)** Phase-space of the simulated Brownian motion. Expressions for the solid lines in the histograms are $\frac{1}{\sqrt{2\pi\Delta x_{\mathrm{th}}^2}}e^{-\frac{1}{2}\frac{X_{1,2}^2}{\Delta x_{\mathrm{th}}^2}}$ for X_1 and X_2 or $\frac{r}{\Delta x_{\mathrm{th}}^2}e^{-\frac{1}{2}\frac{r^2}{\Delta x_{\mathrm{th}}^2}}$ for $r = \sqrt{X_1^2 + X_2^2}$. Care must be taken when choosing the filtering time T in (5.6) in order to avoid sampling at integer multiples of the mechanical frequency. Here we have chosen $T = 2\pi/37\Gamma_{\mathrm{m}}$.

5.2.3 Experimental characterization of the emulated Brownian motion

The same tables $X(t)$ can be fed to an arbitrary waveform generator in order to create a series of voltage points modulating the spin's energy according to $S^{\mathrm{th}}_{\delta\omega_{\|}}[\Omega]$. The Agilent 33500 Function generator can be programmed to cycle through a list of voltage values containing up to 16 Mpts. The maximum sampling rate 250 Mpts/s is in congruence with the time step chosen in the simulations. At such a rate we have more than 40 pts per oscillation period for an emulated mechanical oscillator at $\Omega_{\mathrm{m}}/2\pi = 6\,\mathrm{MHz}$. These conditions also imply that the maximum duration of the trajectory is $\frac{16\,\mathrm{Mpts}}{250\,\mathrm{Mpts/s}} = 64\,\mathrm{ms}$, a limitation that renders the emulated signal imperfect and compromises its randomness. However, the largest pulse duration during a Rabi measurement, limited by the decoherence rate Γ_{spin} is $\tau_{\mathrm{max}} = 20\,\mu\mathrm{s}$, which is 3200 times smaller that the Brownian trace and we therefore estimate the effect of the pseudo randomness to be negligible on the time scale of the Rabi measurement. The full exploration of the available phase-space by the emulated mechanical oscillator is experimentally verified by feeding the digitized RF signal to the Agilent MXA-N9020A signal analyzer, measuring the spectral density $S_\mathrm{V}[f]$. We fit the experimental curves to expression

$$S_{\mathrm{V,fit}}[f] = \frac{A_{\mathrm{BM}}^{\mathrm{RF}} g}{(f^2 - f_0^2)^2 + f^2 g^2} \tag{5.9}$$

with the three free parameters amplitude $A_{\mathrm{BM}}^{\mathrm{RF}}$, resonance frequency f_0 and linewidth g. Comparing the extracted values to the expected $S_{\delta\omega_\parallel}^{\mathrm{th}}[\Omega]$, we find agreement with the resonance frequency to within 1% and within 25% for the linewidth, which ultimately verifies the emulation of a thermally excited mechanical resonator over a frequency range of at least $2\Omega_\mathrm{m}/2\pi$. Integration of S_V yields the voltage variance $(\mathrm{V_{rms}})^2$, which is in very good quantitative agreement with the applied output voltage on the RF generator and obeys the relationship between the set peak-to-peak voltage and detected rms voltage $\mathrm{V_{rms}} = \mathrm{V_{pp}}/2\sqrt{2}$. We can therefore proceed with the calibration obtained for $\delta\omega_0(\mathrm{V_{pp}}/2)$ in the case of monochromatic energy modulation of Chapter 3 and use the simple relationship $\delta\omega_{\mathrm{th}} = \frac{\delta\omega_0}{\sqrt{2}}$ for our experiments.

Alternatively, the root mean square voltage contained in the signal $X(t)$ can be measured with an oscilloscope. Typical traces of $X(t)$ corresponding to the mechanical spectra are shown in Figure 5.3 **(b)**. The $2\,\mu$s time window allows identification of the principal oscillation frequency $\Omega_\mathrm{m}/2\pi$ and elegantly demonstrate the effect of the two different mechanical decay rates. Measured over a large enough time window, the oscilloscope can directly determine the rms voltage, which is in agreement with the aforementioned evaluation. These calibration measurements are crucial in verifying proper signal output by the AWG, which normalizes the numerical input data such that a maximum voltage of ±5 V is not surpassed.

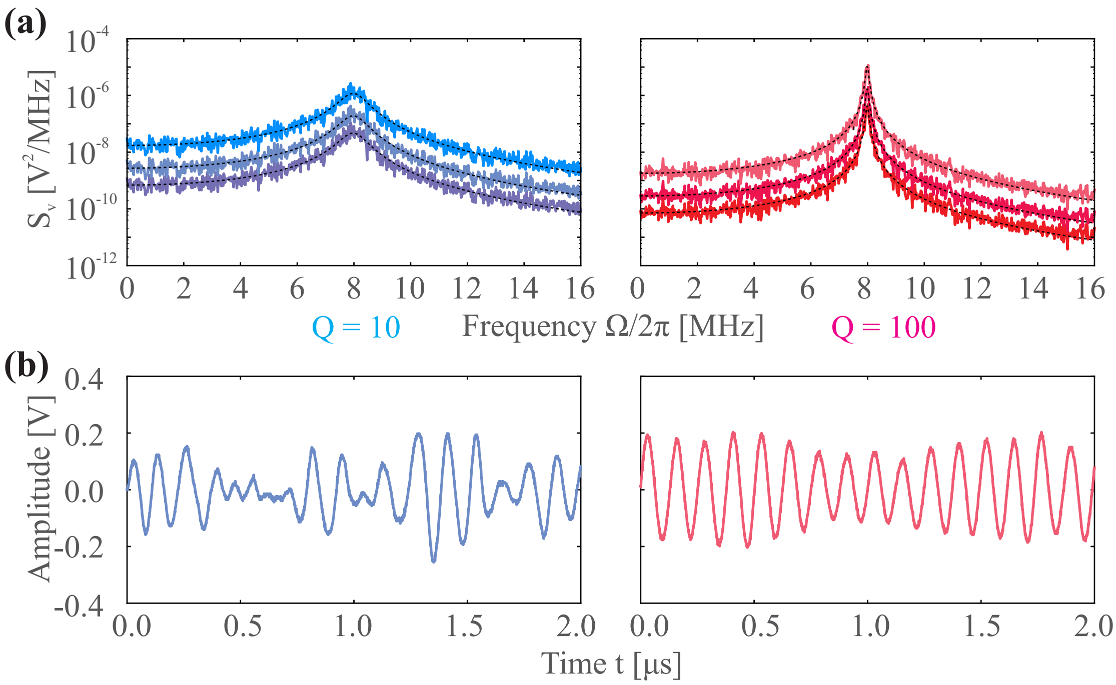

Figure 5.3: Simulated Brownian motion as injected in the RF waveguide. **(a)** The mechanical spectra S_V were obtained for two different quality factors and input peak-to-peak voltages of $\mathrm{V_{pp}} = 100$, 200, 500 mV (bottom to top). The log scale representation emphasizes that an increase of the input power as controlled by the AWG shifts the entire spectrum by a constant factor without changing the shape. The total area below each curve of the same input power but different Γ_m is the same. The temporal traces in **(b)** show "Brownian motion" of the RF voltage measured with an oscilloscope. A smaller quality factor Q leads to more frequent changes of the instantaneous amplitude and phase of the signal.

5.3 Experimental consequences

Above we have seen that thermal excitation of a mechanical oscillator leads to randomization of the frequency and amplitude of motion. In fact, the picture that we developed in terms of the oscillator and its environment experiencing random momentum exchanges, allows us to treat amplitude and frequency distribution separately: after each interaction, occurring at an average rate of $1/\Gamma_\mathrm{m}$, the mechanical oscillator is placed in a new oscillation regime, which is described by a new effective amplitude and phase. The instantaneous amplitude is therefore independent of the frequency distribution governed by the quality factor Q. We are now going to discuss potential consequences of such a motion on the dispersively coupled spin.

5.3.1 Frequency distribution

The phase coherence of mechanical oscillation is preserved over a time scale of $1/\Gamma_\mathrm{m}$. In order for the spin to detect such dephasing it necessarily needs to be sensitive for at least as long. We are therefore identifying two regimes. Let $1/\Gamma$ reflect the time scale [2] over which the spin's coherence is preserved. For $1/\Gamma < 1/\Gamma_\mathrm{m}$, mechanical dephasing processes are too slow for the spin to follow. The spin will then experience close-to-coherent energy modulation. In this regime the spin therefore acts as a broadband detector for mechanical oscillations. On the other hand, if $\Gamma_\mathrm{m} \gg \Gamma$ the spin acts as a narrow band detector and the variation of the noise spectral density $S^{\mathrm{th}}_{\delta\omega_\parallel}[\Omega]$ around Ω_m over the interval Γ_m will play a role.

---

[2] Generally, Γ is specific to the measurement in question. In case of Rabi oscillations, we have $\Gamma = \Gamma_\mathrm{spin}$.

5.3.2 Amplitude distribution

The phase-space diagrams of Figure 5.2 **(c)** show that the two quadratures $X_1(t)$ and $X_2(t)$ are two independent variables with a Gaussian distribution. The instantaneous amplitude of oscillation

$$r(t) = \sqrt{X_1^2(t) + X_2^2(t)} \tag{5.10}$$

therefore follows a so called circular distribution $p^{\mathrm{th}}(r)$ [173] given by

$$p^{\mathrm{th}}(r) = \int\limits_{\mathcal{R}^2} \mathrm{d}X_1 \mathrm{d}X_2\, \delta\left(r - \sqrt{X_1^2 + X_2^2}\right) p(X_1)p(X_2). \tag{5.11}$$

Using

$$p(X_1)p(X_2) = \frac{1}{\sqrt{2\pi}\Delta x} e^{-\frac{1}{2}\frac{X_1^2}{\Delta x^2}} \frac{1}{\sqrt{2\pi}\Delta x} e^{-\frac{1}{2}\frac{X_2^2}{\Delta x^2}},$$

and changing to polar coordinates (ρ, θ), such that

$$p^{\mathrm{th}}(r) = \int\limits_{\mathcal{R}^2} \rho\, \mathrm{d}\rho\, \mathrm{d}\theta\, \delta\left(r - \rho\right) \frac{1}{2\pi\Delta x^2} e^{-\frac{1}{2}\frac{\rho^2}{\Delta x^2}}, \tag{5.12}$$

we obtain

$$p^{\mathrm{th}}(r) = \frac{r}{\Delta x^2} e^{-\frac{1}{2}\frac{r^2}{\Delta x^2}}. \tag{5.13}$$

The mean value and standard deviation of the instantaneous amplitude are

$$\langle r \rangle = \int\limits_0^\infty \mathrm{d}r\, r p_{\Delta x}(r) \quad = \sqrt{\frac{\pi}{2}}\Delta x, \tag{5.14}$$

$$\left\langle r^2 \right\rangle = \int\limits_0^\infty \mathrm{d}r\, r^2 p_{\Delta x}(r) = 2\Delta x^2, \tag{5.15}$$

$$\Delta r = \sqrt{\langle r^2 \rangle - \langle r \rangle^2} \quad = \sqrt{2 - \frac{\pi}{2}}\Delta x. \tag{5.16}$$

The quantities $\langle r \rangle$ and Δr both increase with the temperature Θ. In terms of amplitude distribution, we see that the thermal excitation is very different from the coherent excitation even in the near monochromatic limit where $\Gamma_{\mathrm{m}} \ll \Gamma_{\mathrm{spin}}$. While increase of the mean phonon number of a coherent state leads to an improved ratio $\frac{\langle r \rangle}{\Delta r} \propto \sqrt{\langle r \rangle}$, the ratio between mean amplitude and amplitude deviation is independent of the drive strength for the Brownian oscillator, $\frac{\langle r \rangle}{\Delta r} = \sqrt{\frac{\pi/2}{2-\pi/2}}$. Consequentially, we can assume that the same spread in oscillation amplitude leads to a similar distribution of $\delta\omega_0$. The probability distribution for the parametrically coupled spin energy modulation amplitude $\delta\omega_0$ is therefore anticipated to be

$$p^{\mathrm{th}}(\delta\omega_0) = \frac{\delta\omega_0}{\delta\omega_{\mathrm{th}}^2} e^{-\frac{1}{2}\frac{\delta\omega_0^2}{\delta\omega_{\mathrm{th}}^2}}, \tag{5.17}$$

with $\delta\omega_{\mathrm{th}} = 2\pi\lambda\Delta x_{\mathrm{th}}$.

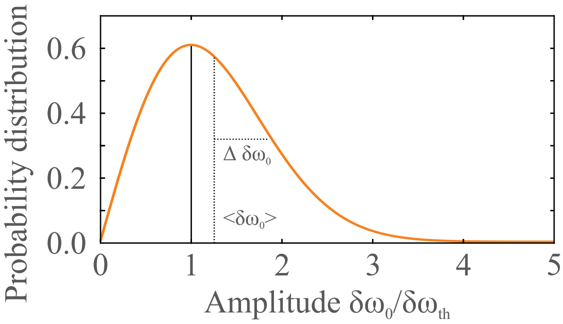

Figure 5.4: Probability distribution of the parametric spin energy modulation amplitude $\delta\omega_0$ arising from a thermally activated oscillator.

5.4 Brownian motion at the resonance condition: The thermally excited phonon Mollow triplet

In the above section we have established a picture which allows us to anticipate how thermal mechanical motion is going to affect the parametrically coupled spin. While the oscillator's amplitude distribution gives rise to a distribution of the spin energy modulation amplitude, the oscillator's frequency distribution sets apart parametric coupling in the dissipative (low Q) case from the near-monochromatic (large Q) case with respect to the spin linewidth. In this section we will look at how the phonon Mollow triplet signatures of the spin dynamics are altered due to the Brownian behavior of the oscillator.

We first investigate a sweep of the Rabi frequency across the mechanical resonance frequency by means of numerical simulations[3]. Figure 5.5 shows the result in three cases of $Q = 500$, 100, 10 at $\delta\omega_{\mathrm{th}}/2\pi = 1.5\,\mathrm{MHz}$ and $\Gamma_{\mathrm{spin}} = 0.5\,\mathrm{MHz}$. Here we have chosen to work at $\delta\omega_{\mathrm{th}}/2\pi = 1.5\,\mathrm{MHz}$ and $\Omega_{\mathrm{m}}/2\pi = 12\,\mathrm{MHz}$ in order to reduce higher order effects due to larger values of $\delta\omega_{\mathrm{th}}$. The corresponding mechanical decay rates are thus $\Gamma_{\mathrm{m}}/2\pi = 0.024$, 0.12, 1.2 MHz, rendering the mechanical oscillations narrow, intermediate and broadband compared to the spin linewidth, respectively. We see that for $Q = 500$ and $Q = 100$ the familiar signatures of the Mollow triplet are visible. A separate central component at $\Omega = \Omega_{\mathrm{m}}$ can be identified. However, the typical signature of an avoided level crossing is absent. In contrast, when the mechanical dissipation Γ_{m} surpasses the qubit decoherence rate Γ_{spin}, a broadening of the spin precession spectrum as well as a reduction of its amplitude are observed. Here, the typical signature of a spin precession frequency locked to the mechanical frequency is missing.

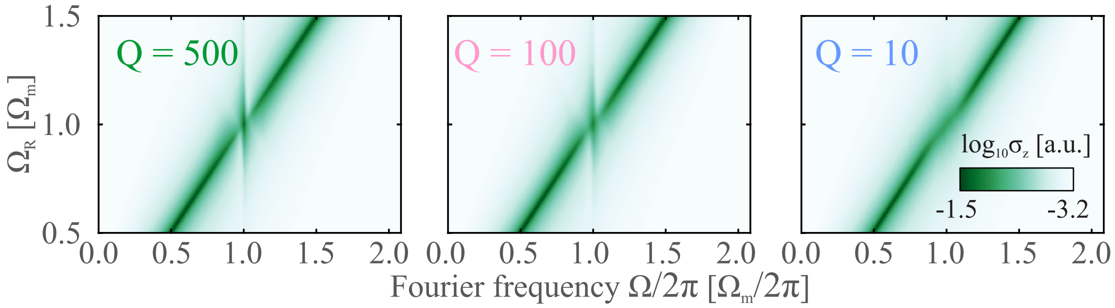

Figure 5.5: Sweep of the Rabi frequency showing the spin locking mechanism modified by the thermal drive for three different quality factors. Here, $\Gamma_{\mathrm{m}} = 0.5\,\mathrm{MHz}$ and $\Gamma_{\mathrm{m}}/2\pi = 0.024, 0.12$ and 1.2 MHz.

We take a closer look at horizontal cuts at the resonance condition $\Omega_{\mathrm{R}} = \Omega_{\mathrm{m}}$ of the above Fourier maps in Figure 5.6. Example traces of Rabi oscillation spectra of the thermally excited phononic

---

[3] Notice that for sufficiently long traces of Brownian motion no averaging over the initial oscillator phase α is necessary.

Mollow triplet for $\delta\omega_{\text{th}}/2\pi = 2\,\text{MHz}$ are shown. For $Q = 500$, the central peak is very prominent, but instead of the expected sidebands a broad pedestal is exhibited to the feet of the central peak. The same is visible for $Q = 100$, but here the central peak appears broader and smaller in spectral amplitude. In case of $Q = 10$, only a single Lorentzian peak appears.

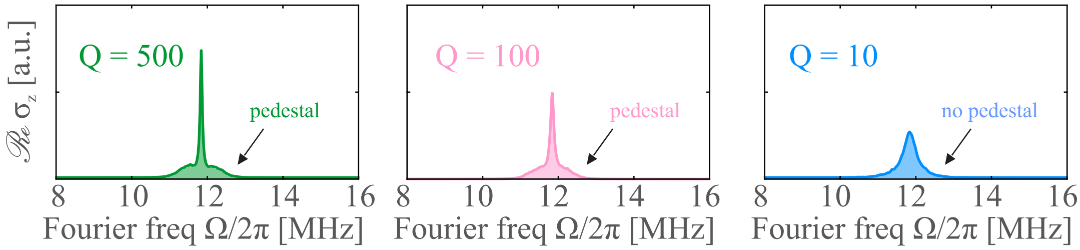

Figure 5.6: Numerically simulated Mollow triplets at various quality factors Q. Here we have chosen $\delta\omega_{\text{th}}/2\pi = 2\,\text{MHz}$ and $\Gamma_{\text{spin}} = 0.203$ MHz for visual reasons.

In order to verify these predictions on the modification of the phononic Mollow triplet spectra by the thermal oscillator, we experimentally measure Rabi oscillations at the resonance condition $\Omega_{\text{R}}/2\pi = \Omega_{\text{m}}/2\pi = 6\,\text{MHz}$ for two mechanical oscillators with $Q = 500$ and $Q = 10$. The data shown in Figure 5.7 well agrees qualitatively with the simulation data of Figure 5.6. In case of a large quality factor a sharp single peak protrudes above a pedestal. Increasing the oscillator's coupling strength leaves the component at Ω_{m} unaltered, but the pedestal spreads out more and more. Inversely, in case of the bad quality factor, only a single peak is visible, losing in height and gaining in width as $\delta\omega_{\text{th}}$ is increased.

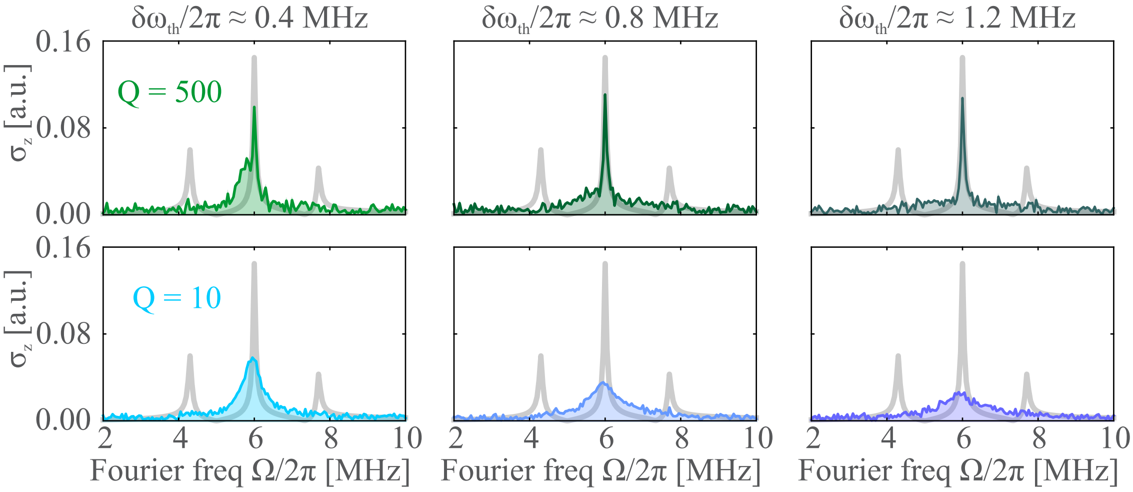

Figure 5.7: Experimentally measured phonon Mollow triplets due to Brownian motion of an emulated mechanical oscillator. The top row of large quality factors shows the evolution with the coupling strength $\delta\omega_{\text{th}}$ in case where the mechanical dissipation rate Γ_{m} is inferior to the spin decoherence rate Γ_{spin}, reflected by the linewidth of Rabi spectra. For small coupling strength $\delta\omega_{\text{th}}/2\pi = 0.4$, the synchronization signature is not yet fully established, but a pedestal is visible, as seen in the simulations. As $\delta\omega_{\text{th}}$ increases, the linewidth of the central peak stays unaltered, while the pedestal spreads out. The bottom row shows the evolution of Rabi spectra where the mechanical dissipation is superior to the spin decoherence. A single peak is visible, which loses in height and gains in width as $\delta\omega_{\text{th}}$ is increased. The gray curves in the background correspond to the Mollow triplet presented in Figure 3.35 ($\delta\omega_0/2\pi = 3.6\,\text{MHz}$) and are shown for purpose of comparison.

In order to explain these signatures, we will distinguish between small and large mechanical dissipation.

Large Q oscillator We start by considering the large Q limit. For $\Gamma_\mathrm{m} \ll \Gamma_\mathrm{spin}$ almost all of the mechanical power is contained within the spin linewidth:

$$P_\mathrm{m}^\mathrm{spin}(\Gamma_\mathrm{m}) \propto (2\pi\lambda)^2 \int\limits_{\Omega_\mathrm{m}-\Gamma_\mathrm{spin}}^{\Omega_\mathrm{m}+\Gamma_\mathrm{spin}} \mathrm{d}\Omega \frac{1}{\pi} S_x^\mathrm{th}[\Omega] \simeq \delta\omega_\mathrm{th}^2. \tag{5.18}$$

The mechanical noise then appears as near-monochromatic over the spin lifetime. Therefore, for each realization of the noise, Mollow sidebands should be visible in the Fourier spectra at the spin locking condition, $\Omega_\mathrm{m} \approx \Omega_\mathrm{R}$. However, the oscillation amplitude is distributed according to $p^\mathrm{th}(\delta\omega_0)$ and thus the sidebands are averaged over the amplitude distribution, forming the pedestal in Figure 5.7.

The dependence of the central peak position on the mechanical oscillation amplitude is different from the sidebands'. For small amplitudes, $\delta\omega_0 < \Gamma_\mathrm{spin}$ no spin locking occurs and Rabi spectra simply exhibit a component at $\Omega = \Omega_\mathrm{R}$ (which is here set to match Ω_m). However, under spin locking conditions, the position of the central component is dictated by Ω_m. As mechanical dissipation broadens the mechanical frequency by Γ_m (FWHM), a broadening of the components of the Mollow triplet can be expected as the Rabi protocol is averaged over many realizations of the Brownian motion. For different quality factors we can therefore anticipate different steady state values towards which $\sigma_z[\Omega_\mathrm{m}]$ converges at large temperatures when the criteria $\delta\omega_\mathrm{th} \ll \Gamma_\mathrm{spin}$ is fulfilled.

We can therefore average the Fourier transform of expression (3.83) over the distribution (5.13):

$$\sigma_z^\mathrm{BM}[\Omega] = \int\limits_0^\infty \mathrm{d}\delta\omega_0\, p^\mathrm{th}(\delta\omega_0) P_0[\Omega, \delta\omega_0], \tag{5.19}$$

while taking into account that spectral broadening of the central peak occurs for large mechanical oscillation amplitudes with $\Gamma_0 \to \Gamma_\mathrm{spin} + \Gamma_\mathrm{m}$. Expression (5.19) is compared to simulation results in Figure 5.8 and is found to be in very good agreement with the numerical data as long as the quality factor stays large.

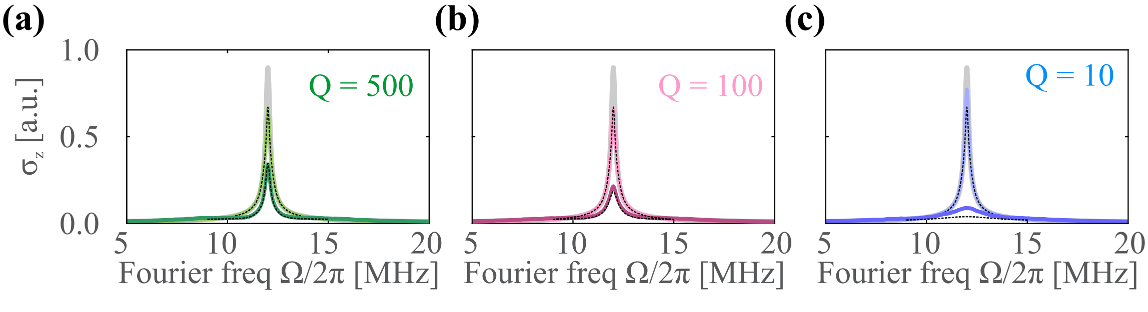

Figure 5.8: Thermal noise amplitude averaging of the Mollow triplet at $\Omega_\mathrm{m}/2\pi = 12$ MHz with $\Gamma_\mathrm{spin}/2\pi = 0.5$ MHz. Gray curves: $\delta\omega_\mathrm{th}/2\pi = 0$ MHz, light curves: $\delta\omega_\mathrm{th}/2\pi = 0.2$ MHz, dark curves: $\delta\omega_\mathrm{th}/2\pi = 4.0$ MHz. For a mechanical oscillator with large quality factor ($Q = 500$ in **(a)** and $Q = 100$ in **(b)**) we obtain very good agreement between formula (5.19) (black dashed lines) and the simulation data. **(c)** The averaging approach fails for small mechanical quality factors ($Q = 10$). Light blue curve: $\delta\omega_\mathrm{th}/2\pi = 0.4$ MHz, dark blue curve: $\delta\omega_\mathrm{th}/2\pi = 4.0$ MHz.

The phonon distribution of the thermal state is thus encoded in the sidebands of the thermally excited Mollow triplet. We find that both, their position and width now depend on the noise amplitude. This is in contrast to the Mollow triplet in presence of coherent mechanical motion, where the width of the sidebands Γ_coh was unaffected by the field strength $\delta\omega_0$.

Low Q oscillator In the case of large mechanical dissipation, the mechanical modulation is incoherent over the spin coherence time, presenting a nearly flat noise spectral density $S^{\mathrm{th}}_{\delta\omega_{\parallel}}[\Omega]$ around Ω_{m}. The thermal noise can thus be viewed as a Markovian noise source, leading to an increase of the spin decay rate via a contribution to Γ_ν (see equations (3.23) and (5.4)): $\Gamma_\nu = \pi S_{\delta\omega_{\parallel}}[\Omega_{\mathrm{R}}]$. This leads to an additional broadening of the central component Γ_0 (noting that $S^{\mathrm{th}}_x[\Omega_{\mathrm{m}}] = \delta\omega^2_{\mathrm{th}}/\Gamma_{\mathrm{m}}$):

$$\Gamma_0 \to \tilde{\Gamma}_{\mathrm{spin}} = \Gamma_{\mathrm{spin}} + \frac{\delta\omega^2_{\mathrm{th}}}{2\Gamma_{\mathrm{m}}}. \tag{5.20}$$

In the dressed state picture, this situation resembles an increased stimulated incoherent emission of the MW dressed spin due to the oscillator motion[4]. Notice that the above expressions are true for flat spectra and sufficiently low noise power, which is satisfied as long as the motional narrowing condition, $\Gamma_{\mathrm{spin}}, \delta\omega_{\mathrm{th}} \ll \Gamma_{\mathrm{m}}$, holds. Then, we can describe Rabi oscillations by a single component at $\Omega = \Omega_{\mathrm{R}} = \Omega_{\mathrm{m}}$ with increased exponential decay:

$$\sigma_z[\tau] = a_0 e^{-\Gamma_0\tau}\cos\Omega_{\mathrm{m}}\tau + \frac{1}{2} \approx \frac{1}{2} e^{-\left(\Gamma_{\mathrm{spin}} + \frac{\delta\omega^2_{\mathrm{th}}}{2\Gamma_{\mathrm{m}}}\right)\tau}\cos\Omega_{\mathrm{m}}\tau + \frac{1}{2}. \tag{5.22}$$

We test this assumption by performing numerical simulations of low Q Rabi oscillations and fit the linewidth Γ_0 of the central peak to expression (5.22). The inferred linewidth Γ_0 is shown in Figure 5.9 **(a)**. Clearly, at large temperatures the dependence of Γ_0 on $\delta\omega_{\mathrm{th}}$ is not quadratic anymore and deviations become more pronounced at large values of Q. In Figure 5.9 **(b)** we present a close-up showing the good agreement of (5.22) (dashed lines) with Γ_0 (solid lines) at small temperatures.

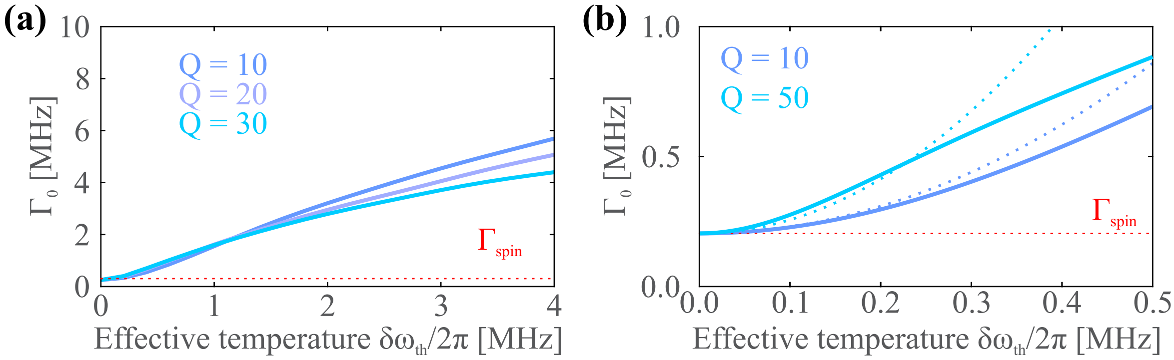

Figure 5.9: Linewidth Γ_0 of the central Mollow peak versus effective temperature for several values of Q. **(a)** The emulated mechanical frequency is $\Omega_{\mathrm{m}}/2\pi = 12\,\mathrm{MHz}$ and $\Gamma_{\mathrm{m}}/2\pi = 1.2,\ 0.6,\ 0.4$ MHz and $\Gamma_{\mathrm{spin}} = 0.203$ MHz. **(b)** Close-up with the indicated quality factors compared to expression 5.22. The agreement decreases with increasing $\delta\omega_{\mathrm{th}}$ and Q.

These considerations in terms of mechanically added noise at the Rabi frequency well describe the initial evolution of Γ_0 with $\delta\omega_{\mathrm{th}}$ of small Q oscillators. For larger values of $\delta\omega_{\mathrm{th}}$ the perturbative approach described by (5.22) breaks down, as higher order contributions become important. These contributions signify that the reduced but non-zero coherence of the mechanical oscillator still acts as a resonant drive between the MW dressed states.

---

[4] The noise spectral density $S_\perp$ is given by $\frac{1}{2}(S_y + S_{\delta\omega_{\parallel}}) \approx \frac{1}{2}S_{\delta\omega_{\parallel}}$. We then have

$$\tilde{\Gamma}_{\mathrm{spin}} = \frac{2\pi}{\hbar}|\langle f|\tilde{H}'|i\rangle|^2 = \Gamma_{\mathrm{spin}} + \frac{1}{2}S^{\mathrm{th}}_{\delta\omega_{\parallel}}[\Omega_{\mathrm{m}}] = \Gamma_{\mathrm{spin}} + \frac{\delta\omega^2_{\mathrm{th}}}{2\Gamma_{\mathrm{m}}}, \tag{5.21}$$

which is the same expression as above.

Transition from the weak to the strong coupling regime We now study the evolution of the peak height of the central component of the thermal Mollow triplet as the temperature increases. In the coherent case, we have seen that a transition from the weak to the strong coupling regime of the parametric interaction is associated with a decrease of amplitude to half the initial value, see section 3.7.5. Here, we compute spectra of Rabi oscillations at the spin locking condition as above for a wide range of $\delta\omega_{\mathrm{th}}$ and for several Γ_{m}. In Figure 5.10 **(a)** the evolution of $\sigma_z[\Omega_{\mathrm{m}}]$ is shown. Evidently, we see that the central component initially shows the same behavior as in the case of monochromatic modulation (indicated as the $Q = \infty$ trace). However, the steady state value $\sigma_z^{\infty}[\Omega_{\mathrm{m}}]$ at high temperatures strongly depends on the mechanical dissipation. By fitting the data in Figure 5.10 **(a)** to the geometric expression

$$\mathcal{G}(\delta\omega_{\mathrm{th}}) = \mathrm{Constant}\frac{1 + a\delta\omega_{\mathrm{th}} + b\delta\omega_{\mathrm{th}}^2}{1 + c\delta\omega_{\mathrm{th}} + d\delta\omega_{\mathrm{th}}^2}, \tag{5.23}$$

we can extract $\sigma_z^{\infty}[\Omega_{\mathrm{m}}]/\sigma_z^{\infty}[\Omega_{\mathrm{m}}, \delta\omega_{\mathrm{th}} = 0]$ as the ratio b/d. It is plotted in Figure 5.10 **(b)** in dependence of Γ_{m} and compared to the expression

$$\frac{1}{2}\frac{\Gamma_{\mathrm{spin}}}{\Gamma_{\mathrm{spin}} + \Gamma_{\mathrm{m}}},$$

which shows good agreement with the numerically found data for two different values of Γ_{spin}. This verifies the picture of the thermal Mollow triplet being averaged over a range Γ_{m} around Ω_{m}, as was already discussed for the large Q oscillator. Surprisingly, it appears that this picture is even true for the case of low quality factors, when $\Gamma_{\mathrm{spin}} \ll \Gamma_{\mathrm{m}}$. Here higher order contributions of the thermal coupling still create a thermal phonon Mollow triplet, indicating that the spin locking mechanism is still present. Notice also that the temperature necessary to observe the steady state behavior is strongly dependent on Q. Qualitatively, this can be attributed to the fraction of mechanical power $P_{\mathrm{m}}^{\mathrm{spin}}(\Gamma_{\mathrm{m}})$ contained in the range Γ_{spin} around Ω_{m}, which decreases with Γ_{m}, see equation 5.18.

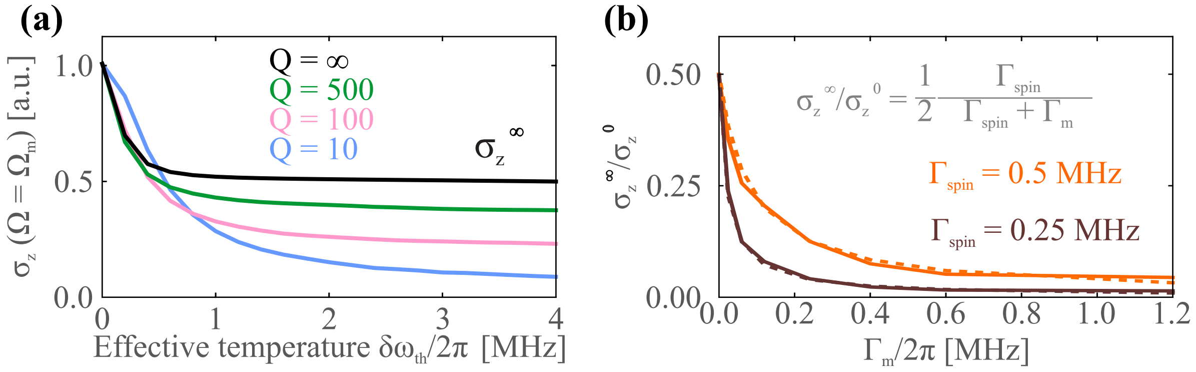

Figure 5.10: Evolution of $\sigma_z[\Omega_{\mathrm{m}}]$ with the temperature $\delta\omega_{\mathrm{th}}$ for various Q. **(a)** The evolution of $\sigma_z[\Omega_{\mathrm{m}}, \delta\omega_{\mathrm{th}}]$ initially resembles the one of $\sigma_z[\Omega_{\mathrm{m}}]$ under monochromatic energy modulation, except in the case of bad mechanical quality factors. **(b)** The steady state value $\sigma_z^{\infty}[\Omega_{\mathrm{m}}]/\sigma_z^{\infty}[\Omega_{\mathrm{m}}, \delta\omega_{\mathrm{th}} = 0]$ (solid lines) falls on the curve $\Gamma_{\mathrm{spin}}/2(\Gamma_{\mathrm{spin}} + \Gamma_{\mathrm{m}})$ for $\Gamma_{\mathrm{spin}} = 0.25$ MHz and $\Gamma_{\mathrm{spin}} = 0.5$ MHz (dashed lines)

.

Experimental verification We test this interesting steady state behavior of the central component experimentally. Again, we inject Brownian modulation at $\Omega_{\mathrm{m}}/2\pi = \Omega_{\mathrm{R}}/2\pi = 6\,\mathrm{MHz}$ for $Q = 500$ and $Q = 10$ and increase the effective temperature $\delta\omega_{\mathrm{th}}$. The results are compared to a measurement with a monochromatic RF signal, using the convention that $\delta\omega_{\mathrm{th}} = \delta\omega_0/\sqrt{2}$. In Figure 5.11 we clearly identify the same tendencies as shown in Figure 5.10 **(a)**. In the bad oscillator limit $Q = 10$ we observe indeed a steady state value $\sigma_z^{\infty}[\Omega_{\mathrm{m}}]$ despite $\Gamma_{\mathrm{m}}/2\pi = 0.6\,\mathrm{MHz}$ being much larger than

$\Gamma_{\mathrm{spin}}/2\pi \approx 0.15\,\mathrm{MHz}$. We also notice that in case of $Q = 500$ as well as monochromatic modulation, $\sigma_z^\infty[\Omega_\mathrm{m}]$ does not fall to the expected value of $0.5 \times \sigma_z[\Omega_\mathrm{m}, \delta\omega_{\mathrm{th}} = 0]$, for which the spin locking mechanism is responsible, which here gradually reduces the influence of a parasitic variation of the Rabi frequency, $\Delta\Omega_\mathrm{R}$. The latter effect renders a more quantitative analysis of the data cumbersome.

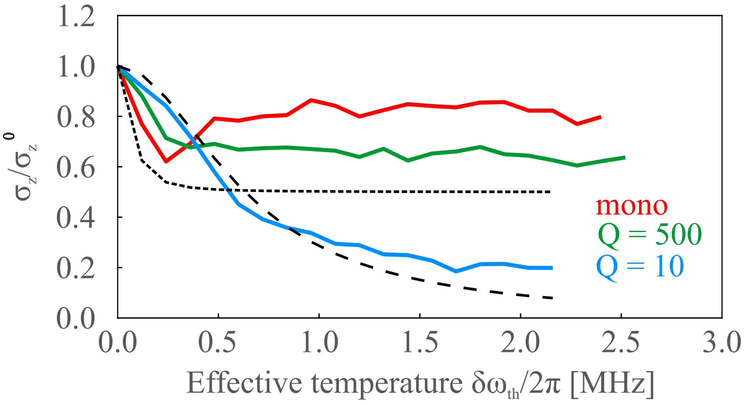

Figure 5.11: Peak evolution of the thermal phonon Mollow triplet. Data is shown for $Q = 10$ (blue), $Q = 500$ (green) and the monochromatic case (red). The qualitative features of the simulation can be recognized. On the one hand, the saturation value σ_z^∞ decreases with increasing mechanical dissipation. On the other hand, this saturation value is reached for higher temperatures as the quality factor decreases. Short-dashed line is the analytic expression 3.94, long-dahsed line is an extrapolation of σ_z assuming $\Gamma_0 \to \Gamma_{\mathrm{spin}} + \delta\omega_{\mathrm{th}}^2/2\Gamma_\mathrm{m}$ for $Q = 10$. The data stays above the curve for large temperatures, indicating that higher order correlations between spin and oscillator start to play an important role.

We have thus seen how the incoherent thermal motion can still create a Mollow triplet signature in the spectra of Rabi oscillations, albeit its phonon distribution being fundamentally different from the coherent state. In the next section we are going to see how the coherent Mollow triplet is perturbed by mixing coherent and incoherent modulation of the spin energy.

5.5 Coherence protection

The preceding section has highlighted two experimental problems for the coupling between a driven spin to a thermal oscillator. First, noise in the drive strength adds to environmental noise and therefore complicates the spin's employment as a spectrum analyzer. Second, operation at $\Omega_\mathrm{R} \approx \Omega_\mathrm{m}$ is aggravated by the fact that the noise spectral density is highest at mechanical resonance: the spin picks up the largest possible amount of noise. This can lead to severe complications when performing a dynamical feedback experiment, which profits from an increase in amplitude by a factor of Q when working at the resonance condition. In Chapter 3, locking the dressed spin by monochromatic energy modulation has been suggested as potential workaround to the first problem. We will now show that it also provides a solution to the second dilemma.

5.5.1 Protection of spin coherence

Again, we start by running a series of numerical simulations using Brownian noise traces with an emulated mechanical frequency[5] at $\Omega_\mathrm{m}/2\pi = 12\,\mathrm{MHz}$ with quality factor $Q = 10$, superposed to coherent energy modulation at $\Omega_\mathrm{d} = \Omega_\mathrm{m}$. While the temperature of the thermal oscillator to the spin is described by the parameter $\delta\omega_{\mathrm{th}}$, the effective coupling strength to the monochromatic energy modulation is denoted by $\delta\omega_0$. Throughout this section we will work at the resonance condition,

---

[5] We are choosing a large value of Ω_m in order to reduce contributions from the Bloch-Siegert shifts.

$\Omega_\mathrm{R} = \Omega_\mathrm{d}$. At this stage we stress that the coherent energy modulation might well be due to additional coherent motion of the mechanical oscillator, for example provided by an electrostatic actuation of the nanowire as in Chapter 4. However, the scheme that we present here is modular in the sense that the signal can also be provided, without loss of validity, by an external RF source, serving as a passive supplementary equipment in order to stabilize the spin drive frequency $\Omega_\mathrm{R}/2\pi$.

In the simulations we sweep the temperature of the thermal oscillator for three different values of $\delta\omega_0$. Figure 5.12 **(a)** recaps the situation in terms of a phase space representation for the mechanical oscillator, which is shifted away from the origin as $\delta\omega_0$ grows. Here, we are interested in isolating the component oscillating at Ω_m. Evolution of the detected width Γ_0 is depicted in Figure 5.12 **(b)**. We make two observations. First, the value of Γ_0 for large $\delta\omega_\mathrm{th}$ seems to be independent of $\delta\omega_0$. Second, a retarded augmentation of the decay rate Γ_0 with increasing coherent amplitude $\delta\omega_0$ is clearly visible. Notice that for initially small values of $\delta\omega_\mathrm{th}$ the situation corresponds to a very prominent coherent Mollow triplet, which is perturbed by the thermal noise. In principle the linewidth of the monochromatic phonon Mollow triplet is independent of the coupling strength $\delta\omega_0$ ($\Gamma_\mathrm{pop} = \Gamma_\mathrm{spin}$ at $\Omega_\mathrm{R} = \Omega_\mathrm{m}$) and so the linewidth Γ_0 is not a function of the monochromatic energy modulation. To explain the effect, we invoke the noise spectral density of the mechanical oscillator, $S^\mathrm{th}_{\delta\omega_\parallel}[\Omega]$, in the dressed state picture.

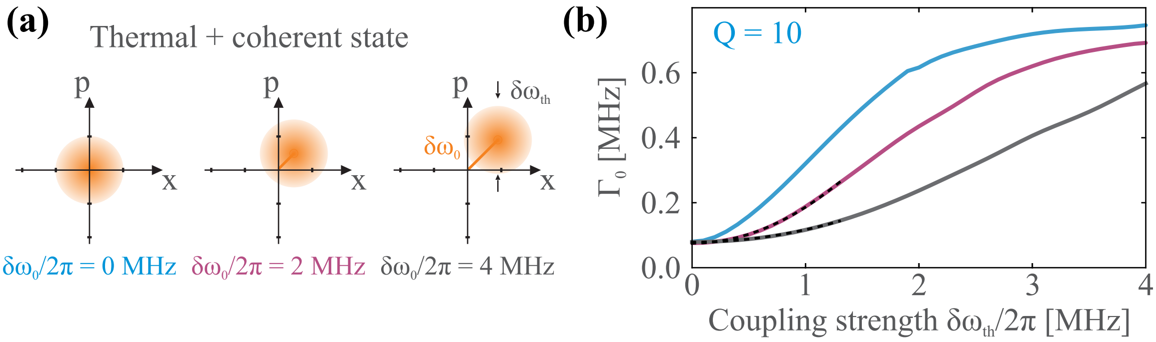

Figure 5.12: Coherent and incoherent energy modulation. **(a)** Phase-space representation of the motional state in the presence of a thermal and coherent drive. **(b)** Linewidth, Γ_0, of the central Mollow triplet peak as a function of temperature $\delta\omega_\mathrm{th}$ for different coherent amplitudes $\delta\omega_0/2\pi = 0$ (blue), 2 (red) and 4 MHz (black).

As explored in Chapter 3, the coherent modulation splits up the MW dressed qubit states with the energy diagram shown in Figure 5.13 **(a)**, creating a splitting $\Delta_\mathrm{d} = \delta\omega_0/2$ in the doubly dressed multiplicities. The Fourier transforms of Rabi oscillations of the spin measure the noise in the environment: the height A_0 of the peak at Ω_m then reflects the relative contribution of scattering processes at Ω_m, while the peak width Γ_pop reflects the processes different from $\hbar\Omega_\mathrm{m}$ and is particularly sensitive to scattering processes $|+\rangle \leftrightarrow |-\rangle$ in the double dressed spectrum. We can rewrite expression (3.85) of the phonon Mollow triplet as

$$\begin{aligned}\langle\sigma_z[\Omega]\rangle = \frac{1}{2} &+ \frac{A_0}{\Gamma_\mathrm{pop} + i(\Omega - \Omega_\mathrm{d})} \\ &+ \frac{A_+}{\Gamma_\mathrm{coh} + i(\Omega - \Omega_\mathrm{d} - \delta\omega_0/2)} \\ &+ \frac{A_-}{\Gamma_\mathrm{coh} + i(\Omega - \Omega_\mathrm{d} + \delta\omega_0/2)},\end{aligned} \tag{5.24}$$

with

$$\Gamma_{\mathrm{pop}} = \Gamma_{+\to-} + \Gamma_{-\to+}, \tag{5.25}$$

$$\Gamma_{\mathrm{coh}} = \frac{1}{2}(\Gamma_{+\to+} + \Gamma_{-\to-} + \Gamma_{+\to-} + \Gamma_{-\to+}) + \sqrt{\Gamma_{+\to+}\Gamma_{-\to-}}. \tag{5.26}$$

All the above rates receive additional contributions via Γ_ν from the mechanical oscillator's noise spectral density, stimulating transitions at the respective frequencies. Therefore, they describe how Rabi oscillations at the spin locking condition $\Omega_{\mathrm{d}} = \Omega_{\mathrm{R}}$ are damped in the presence of additional Brownian motion in the perturbative limit. Notice that the width of the central peak, Γ_{pop}, depends on the noise spectral density at the position of the sidebands $\Omega_{\mathrm{d}} \pm \delta\omega_0/2$. It therefore probes the mechanical oscillator's Brownian motion away from Ω_{m}, where its effect on the induced decoherence is much less. The situation is demonstrated in Figure 5.13 **(b)**, highlighting the importance of the monochromatic energy modulation amplitude for the coherence protection mechanism. Because the noise spectral density is highest at Ω_{m}, a larger value of $\delta\omega_0$ reduces more and more the detected noise spectral density.

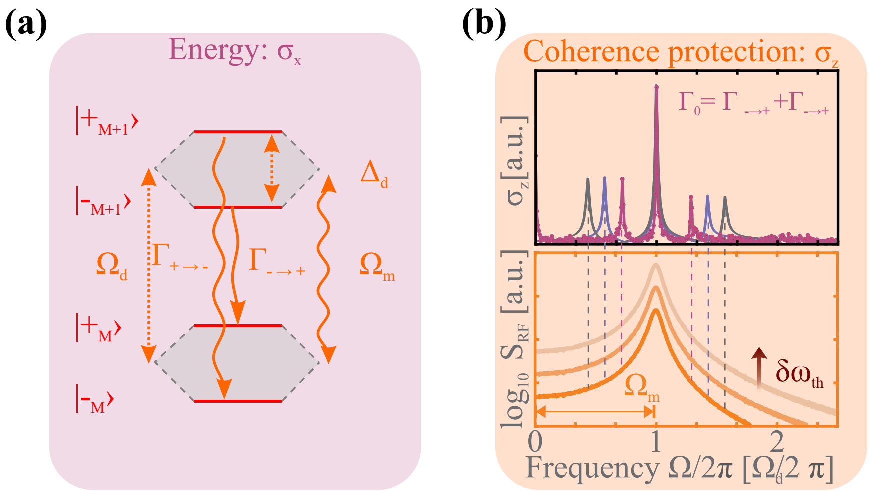

Figure 5.13: Diagrammatic explanation of the coherence protection mechanism. **(a)** The energy diagram in the dressed state basis, showing two multiplicities separated by the drive frequency $\Omega_{\mathrm{d}}/2\pi$. The rates $\Gamma_{+\to-}$ and $\Gamma_{-\to+}$ are associated with transitions at $\Omega_{\mathrm{d}}+\Delta_{\mathrm{d}}$ and $\Omega_{\mathrm{d}}-\Delta_{\mathrm{d}}$, respectively, causing a broadening of the central peak. **(b)** These rates receive additional contributions from the thermal noise with spectral density $S^{\mathrm{th}}_{\delta\omega_\parallel}[\Omega]$, stimulating emission and absorption processes in the dressed state basis. The position of the sidebands of the Mollow triplet (top) indicate at which frequencies $S^{\mathrm{th}}_{\delta\omega_\parallel}[\Omega]$ is probed, showing that the influence of the thermal noise is reduced as the coherent drive strength increases.

Using equation (3.23) and our conventions from Appendix C, $\Gamma_{+\to-}$ receives a contribution from the thermal oscillator, such that

$$\Gamma_{+\to-} = 2\Gamma_{\mathrm{spin}}\sin^4\theta \to 2\left(\Gamma_{\mathrm{spin}} + \frac{1}{2}S^{\mathrm{th}}_{\delta\omega_\parallel}[\Omega_{\mathrm{d}} + \frac{\delta\omega_0}{2}]\right)\sin^4\theta. \tag{5.27}$$

We therefore arrive at the width of the central peak of the phonon Mollow triplet at the resonance condition $\Omega_{\mathrm{R}} = \Omega_{\mathrm{m}}$ ($\theta = \pi/4$):

$$\Gamma_0 = \Gamma_{\mathrm{spin}} + \frac{1}{2}\frac{S^{\mathrm{th}}_{\delta\omega_\parallel}[\Omega_{\mathrm{d}} - \frac{\delta\omega_0}{2}] + S^{\mathrm{th}}_{\delta\omega_\parallel}[\Omega_{\mathrm{d}} + \frac{\delta\omega_0}{2}]}{2}, \tag{5.28}$$

and for the sidebands

$$\Gamma_{\pm} = \frac{3}{2}\Gamma_{\text{spin}} + \frac{1}{2}\frac{S^{\text{th}}_{\delta\omega_{\|}}[\Omega_{\text{d}}] + S^{\text{th}}_{\delta\omega_{\|}}[\Omega_{\text{d}} + \frac{\delta\omega_0}{2}] + +S^{\text{th}}_{\delta\omega_{\|}}[\Omega_{\text{d}} - \frac{\delta\omega_0}{2}]}{2}. \tag{5.29}$$

In the latter expression we have taken into account that both transitions $|+_M\rangle \leftrightarrow |+_{M-1}\rangle$ and $|-_M\rangle \leftrightarrow |-_{M-1}\rangle$ are driven by processes at Ω_{d}. This degeneracy causes the rates $\Gamma_{+\to+}$ and $\Gamma_{-\to-}$ to receive a contribution $S^{\text{th}}_{\delta\omega_{\|}}[\Omega_{\text{d}}]/4$ each instead of $S^{\text{th}}_{\delta\omega_{\|}}[\Omega_{\text{d}}]/2$.

5.5.2 Experimental verification of the coherence protection mechanism

We now verify these relations experimentally. We inject the same traces of Brownian motion into the RF waveguide and supply additional monochromatic modulation at $\Omega_{\text{d}}/2\pi = \Omega_{\text{m}}/2\pi = \Omega_{\text{R}}/2\pi = 6\,\text{MHz}$ and $\delta\omega_0/2\pi = 3.6\,\text{MHz}$ (corresponding to 2 V peak-to-peak RF amplitude). The Brownian signal is chosen to emulate a bad mechanical oscillator. Selecting $Q = 10$, that is $\Gamma_{\text{m}}/2\pi = 600\,\text{kHz}$, ensures that the noise is approximately flat over a range Γ_{spin} but changes considerably over a range $\delta\omega_0$. Brownian motion is then injected at initially low RF voltage and increased over a series of Rabi measurements. A single trace of Rabi oscillations is measured during 14 hours of data acquisition. The protocol applies 1000 MW pulses, from 20 ns to 20 μs in 20 ns steps. The result is shown in Figures 5.14 **(a, b)** and analyzed in **(c, d)**. In **(a)**, the phononic Mollow triplet can easily be identified at the bottom horizontal line in absence of Brownian motion. As the effective temperature of the emulated oscillator is increased, the triplet signatures disappear: the central peak is reduced in amplitude and slightly broadened. The same behavior is visible for the sidebands, but here the process takes place much more rapidly, until eventually only the central peak is visible at $\delta\omega_{\text{th}}/2\pi \approx 1.3\,\text{MHz}$.

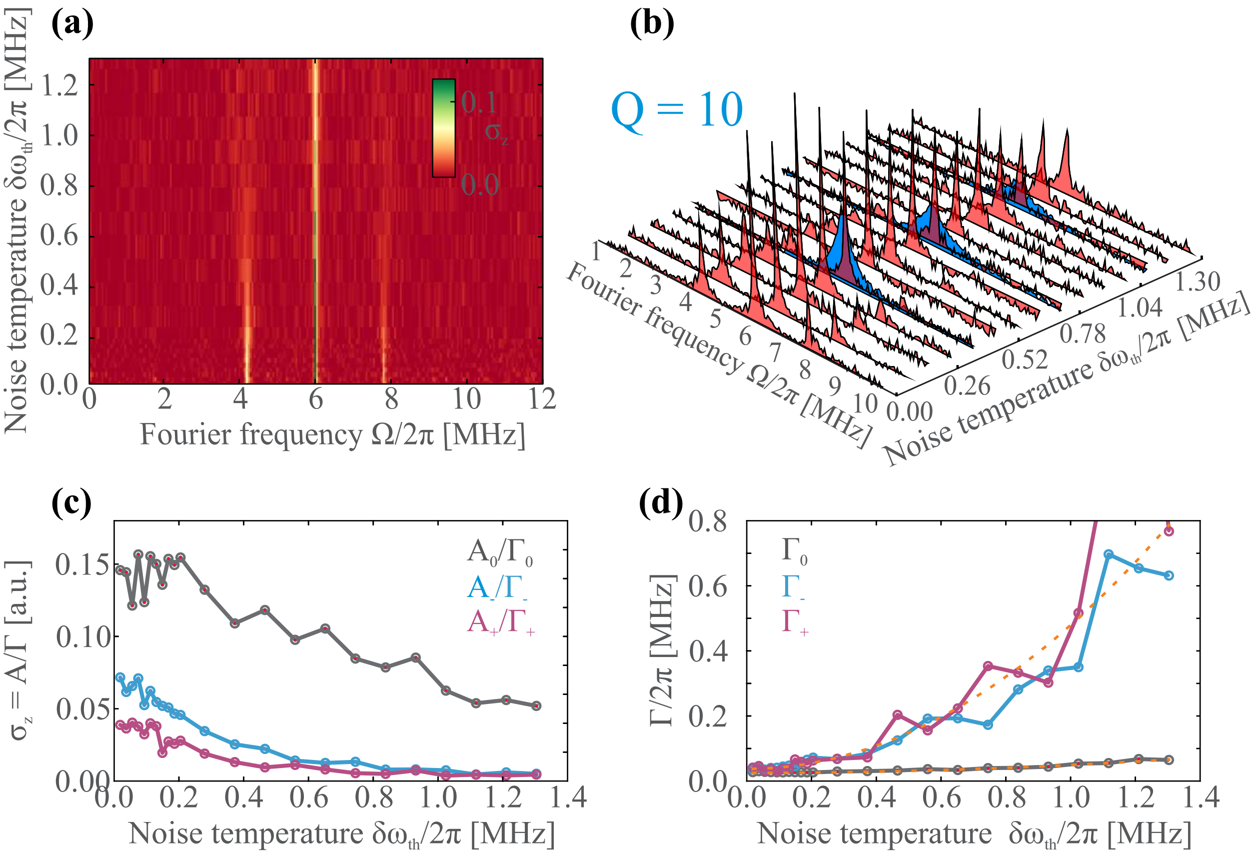

Figure 5.14: Coherence protection. The phonon Mollow triplet ($\Omega_{\mathrm{d}}/2\pi = \Omega_{\mathrm{m}}/2\pi = 6\,\mathrm{MHz}$) due to a coherent drive is measured while the emulated temperature of the Brownian oscillator is increased. **(a)** The Fourier map shows the gradual disappearance of the Mollow triplet. While the sidebands show a large spread already for modest temperatures, the central peak presents an enhanced robustness to the noise. **(b)** The same data as in **(a)** (red traces) compared to the purely thermal Mollow triplet of Figure 5.7 for $Q = 10$ (blue traces). The experimental data clearly shows that the additional coherent drive prevents broadening of the central peak induced by the incoherent thermal motion. **(c)** We fit the Mollow triplets to expression (5.24) and deduce the measured height of the Fourier peaks (as ratios of amplitude to width). The data indicates that the central peak is still a prominent feature of the Fourier spectra while the sidebands have disappeared. **(d)** The widths of the triplet peaks (dots and thick solid lines) are extracted and compared to expressions (5.28) and (5.29) (dashed orange lines), showing excellent agreement between theory and experiment.

In Figure 5.14 **(b)** we compare the data set to the previously obtained Rabi measurements for purely Brownian energy modulation (for the same quality factor Q). These scans are shown in blue and compared to the coherently *plus* incoherently modulated oscillations in red. While the central peak remains clearly visible at large temperatures in presence of a coherent drive, it has almost disappeared in case of pure thermal excitation. This shows that, due to the coherent motion, Rabi oscillations at the mechanical frequency resist the relatively large decoherence effects, offering a convincing demonstration of the protected spin coherence. We fit the red traces using expression (3.85), assuming Lorentzian lineshapes for the central as well as the sideband peaks despite the Brownian noise. We thus extract relative amplitudes of the peaks, shown in Figure 5.13 **(c)**. The amplitudes A_0/Γ_0, A_-/Γ_- and $A_+/\Gamma_=$, reflecting the ratio of transitions at the peak frequency to transitions at different frequencies, show that for larger values of $\delta\omega_{\mathrm{th}}$, the sidebands diminish, favoring expression of the central peak only. In Figure 5.13 **(d)** we plot the evolution of the peak linewidth with increasing temperature $\delta\omega_{\mathrm{th}}$ as solid lines. The dashed lines represent expression (5.28) and (5.29). Here, we have chosen

$\Gamma_{\mathrm{spin}}/2\pi = 17.8\,\mathrm{kHz}$, determined from the analysis of section 3.7.7 in Chapter 3. The theoretical curves are thus free of any fitting parameters and show excellent agreement with the experimental data. The spin locking condition has removed the ambiguity of noise induced by MW power fluctuations. This allows for a sensitive measurement of the mechanically induced noise, which is in clear contrast to the results obtained in Figure 5.5. Moreover, the data shows that, as a further consequence of spin locking, the mechanical noise is probed away from its spectral peak, reducing the destructive impact of the mechanical oscillator's incoherent motion on the spin coherence. Remarkably, the prediction by equation (5.28) is still accurate at relatively large values of $\delta\omega_{\mathrm{th}}$.

To better understand the competition between the coherent and incoherent signals, we continue our experimental study by measuring the emergence of the triplet structure with increasing coherent strength while the spin is experiencing energy modulation due to a Brownian oscillator ($Q = 10$) at constant temperature $\delta\omega_{\mathrm{th}}$. The measurements shown in Figure 5.15 correspond to $\delta\omega_{\mathrm{th}}/2\pi \approx 0.37\,\mathrm{MHz}$ in **(a)** and $\delta\omega_{\mathrm{th}}/2\pi \approx 0.75\,\mathrm{MHz}$ in **(b)**. For low noise temperature **(a)**, the triplet structure can still be identified for coherent amplitudes $\delta\omega_0/2\pi \gtrsim 1\,\mathrm{MHz}$ and linear increase of sideband separation is visible. For larger noise temperature $\delta\omega_{\mathrm{th}}$ **(b)**, the creation of the triplet structure is retarded with respect to $\delta\omega_0$. Due to the increased thermal noise, emergence of the triplet structure, which is a signature of the strong parametric coupling to the coherent oscillations, demands larger amplitudes $\delta\omega_0$. While sidebands are much less visible in **(b)**, they still tend to appear at $\Omega = \Omega_{\mathrm{m}} \pm \delta\omega_0/2$ for large values of $\delta\omega_0$. Evolutions of the central component's strength and linewidth are shown in **(c)** and **(d)**. This analysis is reminiscent of the measurements in section 3.7.5. However, a clear qualitative difference arises due to the colored character of the noise spectral density $S_{\delta\omega_{\|}}[\Omega]$ at $\Omega = \Omega_{\mathrm{R}}$. For a flat $S_{\delta\omega_{\|}}[\Omega]$ we would observe an initial decrease $\sigma_z[\Omega_{\mathrm{m}}]$ with increasing amplitude $\delta\omega_0$ due to the splitting of the Rabi peak into the triplet structure, see Figure 3.45. Here, however, we observe an increase of $\sigma_z[\Omega_{\mathrm{m}}]$ due to the maximum of $S^{\mathrm{th}}_{\delta\omega_{\|}}[\Omega]$ exhibited at $S^{\mathrm{th}}_{\delta\omega_{\|}}[\Omega_{\mathrm{R}} \pm \delta\omega_0/2]$ when $\delta\omega_0 \to 0$.

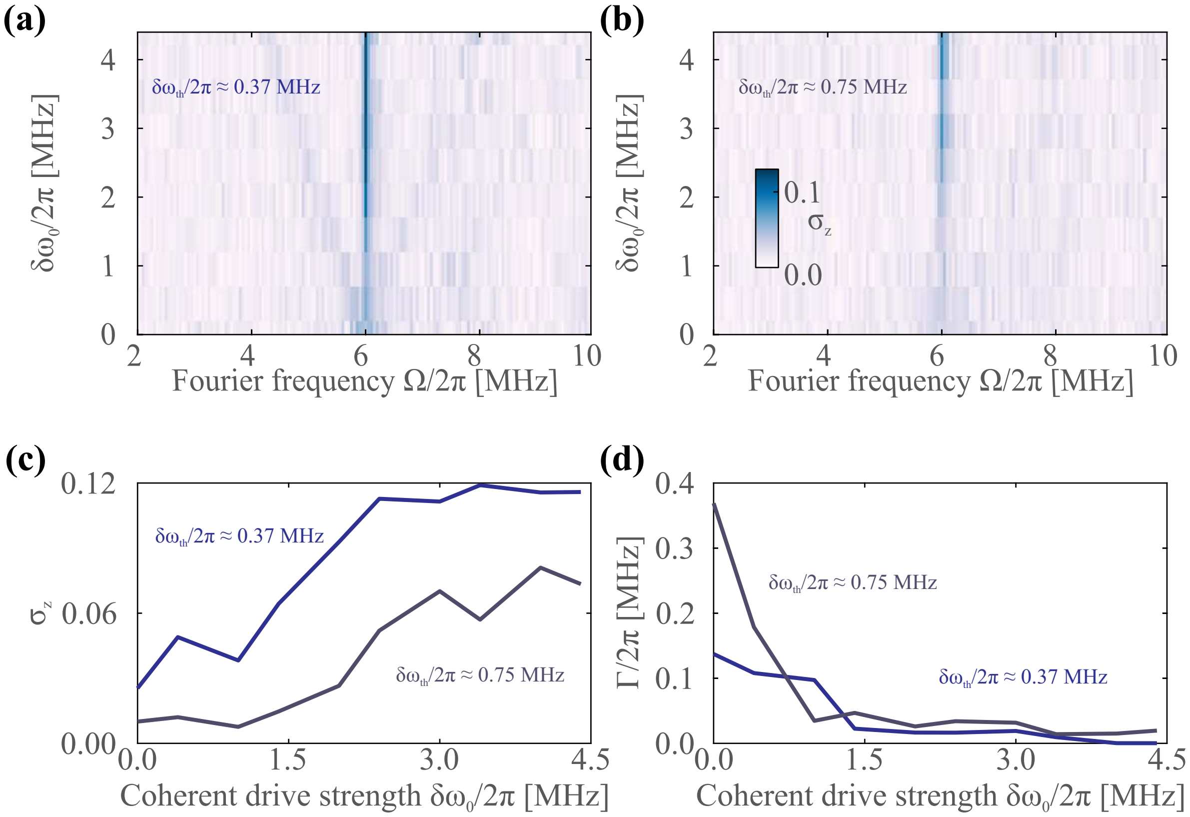

Figure 5.15: Measurement of the emergence of the Mollow triplet in the presence of colored noise. **(a)** Fourier maps of a measurement at $\delta\omega_{\mathrm{th}}/2\pi \approx 0.37\,\mathrm{MHz}$. **(b)** Fourier maps of a measurement at $\delta\omega_{\mathrm{th}}/2\pi \approx 0.75\,\mathrm{MHz}$. **(c)** Peak height of the central component. **(d)** Linewidth Γ_0 of the central component.

To gain further insight, we return to the numerical simulations. We chose a mechanical oscillator at $\Omega_{\mathrm{m}}/2\pi = 12\,\mathrm{MHz}$ with parameters $\delta\omega_{\mathrm{th}}$ and $\delta\omega_0$ similar to the experimental case above. Overall, the numerical data in Figure 5.16 shows good qualitative agreement with the experimental observations. We have marked the onset of sideband separation with a horizontal yellow line, which is consistently lying at values of $\delta\omega_0 > \Gamma_{\mathrm{spin}} + \delta\omega_{\mathrm{th}}$. This is a clear indication that the spin decoherence rate has obtained contributions from the thermal noise, $\Gamma_{\mathrm{spin}} \to \Gamma_{\mathrm{spin}}(\delta\omega_{\mathrm{th}})$. The foregoing inequality can be understood by considering that the width of the pedestal observed in the Rabi spectra for the purely Brownian modulation is approximately linear with respect to $\delta\omega_{\mathrm{th}}$. The monochromatic sidebands, adding incoherently to the Fourier spectra, emerge as distinct features as soon as their separation is larger than the thermal broadening given by $\delta\omega_{\mathrm{th}}$. Comparison of Figures 5.16 **(a)** and **(b)** with **(c)** and **(d)**, respectively, shows that sideband separation is independent of the quality factor Q, as expected from these arguments. Eventually, the sidebands are lying in a range between $\mathrm{Re}\left(\Omega_{\mathrm{m}} \pm \sqrt{\delta\omega_0^2 - \Gamma_{\mathrm{spin}}^2}\right)/2$ (blue dashed line) and $\mathrm{Re}\left(\Omega_{\mathrm{m}} \pm \delta\omega_{\mathrm{th}}/2 \pm \sqrt{\delta\omega_0^2 - (\Gamma_{\mathrm{spin}} + \delta\omega_{\mathrm{th}})^2/2}\right)$ (black dashed line), indicating that the coherent coupling has received contributions from the thermal noise.

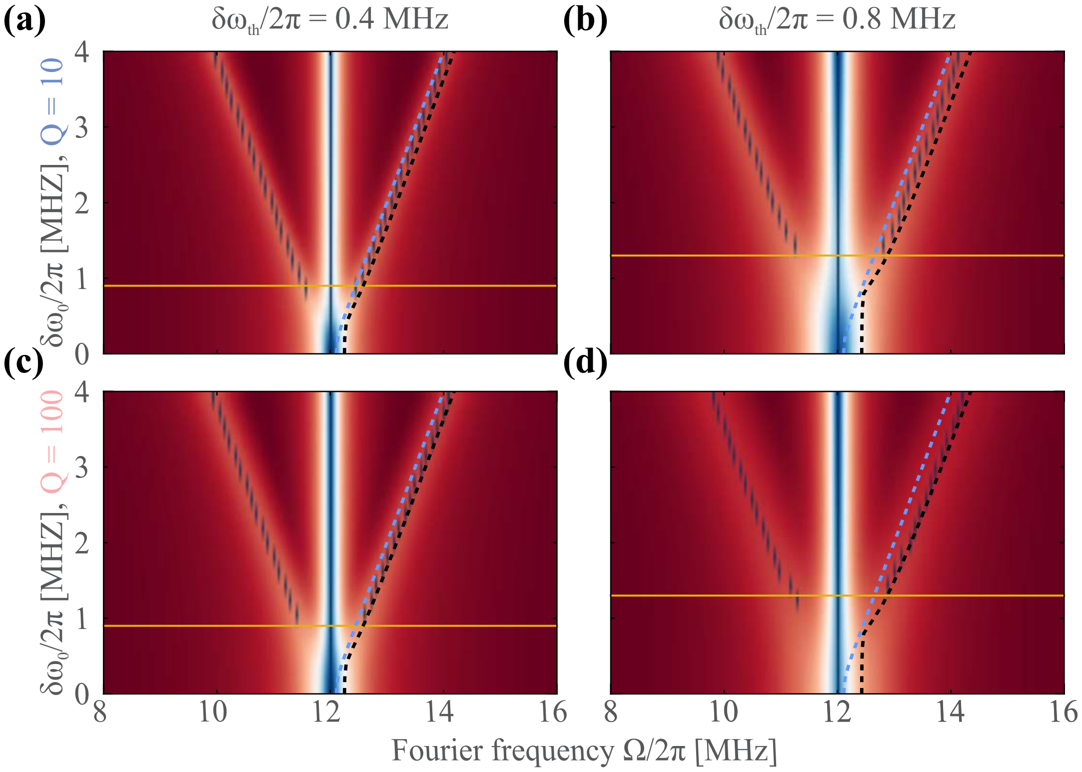

Figure 5.16: Sideband separation in the presence of additional colored noise. The yellow line indicates the value $\delta\omega_0/2\pi$ at which the sidebands emerge. It is consistently found above $\delta\omega_0 > \Gamma_{\text{spin}} + \delta\omega_{\text{th}}$. The sidebands are found in a range given by the two functions $\text{Re}\left(\Omega_\text{m} \pm \sqrt{\delta\omega_0^2 - \Gamma_{\text{spin}}^2}\right)/2$ (blue dashed line) and $\text{Re}\left(\Omega_\text{m} \pm \delta\omega_{\text{th}}/2 \pm \sqrt{\delta\omega_0^2 - (\Gamma_{\text{spin}} + \delta\omega_{\text{th}})^2/2}\right)$ (black dashed line).

5.6 Mollow triplet spectroscopy of colored environmental noise

We summarize our findings by performing one last measurement, in which we now use the Mollow triplet as a measurement of the noise spectral density of the spin environment. The principal noise source will here be provided by a (second) mechanical mode that is thermally driven at $\Omega_\text{m}/2\pi$ and detuned from a coherent drive frequency $\Omega_\text{d}/2\pi$, to which we adjust the MW power, such that $\Omega_\text{R} \approx \Omega_\text{d} \neq \Omega_\text{m}$. This situation is analogous to the Rabi measurement in Chapter 4, where drive and Rabi frequency were swept across the mechanical susceptibility of the nanowire. We inject a Brownian signal of $\Omega_\text{m}/2\pi = 8$ MHz, $\delta\omega_{\text{th}}/2\pi = 1.2$ MHz and $Q = 10$, while driving Rabi oscillations at $\Omega_\text{d}/2\pi = \Omega_\text{R}/2\pi = 6$ MHz. By gradually increasing the modulation amplitude $\delta\omega_0$, the spin dynamics first enter the Mollow triplet regime. Then the central peak becomes sensitive to the noise spectral density at the Mollow sidebands as described above in section 5.5.1. As the sidebands move further apart, the higher frequency component picks up more and more of the mechanically added noise. Consequently, the Mollow triplet is strongly altered as soon as the upper sideband probes the extra noise of thermal origin. This measurement illustrates the stimulated emission induced by the colored noise spectrum. The FFT data is shown in Figure 5.17. In **(c)** we see the evolution of the Mollow triplet with the sidebands diverging from the central component as expected. Moreover, at $\delta\omega_0/2\pi = 4$ MHz, the higher frequency sideband traverses the peak noise spectral density at $\Omega_\text{m}^{\text{BM}}/2\pi = 8$ MHz, which is accompanied by a considerable broadening of the central component. This broadening is presented in Figure 5.17 **(d)** in terms of $\sigma_z[\Omega_\text{d}, \delta\omega_0]$, which is consequently reduced when the thermal noise is detected and which can be expected to evolve as (see equation (5.28)):

$$\sigma_z[\Omega_\mathrm{d},\delta\omega_0]=\sigma_z[\Omega_\mathrm{d},0]\frac{\Gamma_\mathrm{spin}}{\Gamma_\mathrm{spin}+\frac{1}{4}\left(S_{\delta\omega_\mathrm{th}}[\Omega_\mathrm{d}-\frac{\delta\omega_0}{2}]+S_{\delta\omega_\mathrm{th}}[\Omega_\mathrm{d}+\frac{\delta\omega_0}{2}]\right)}. \tag{5.30}$$

We observe good agreement with the above expression, as the decrease of $\sigma_z[\Omega_\mathrm{d},\delta\omega_0]$ appears at the predicted modulation amplitude $\delta\omega_0$. However, proper analysis of the experimental data is difficult because at the present stage of our investigation it is not clear which value to inject for Γ_spin. Initially, Γ_0 represents the noise at the Rabi frequency and an additional inhomogeneous contribution $\Delta\Omega_\mathrm{R}$ due to slow thermal drifts. As $\delta\omega_0$ increases the spin becomes locked to the drive frequency $\Omega_\mathrm{d}/2\pi$ and the inhomogeneous broadening is overcome. In that case Γ_0 reflects the actual noise from the environment, Γ_spin. Moreover, as the spin locking condition is achieved, the central component decreases in amplitude to half its initial value, see Figure 3.45. We compare the experimental data (solid line in Figure 5.17 **(b)**) to an upper and lower limit. For the upper limit we inject $\Gamma_\mathrm{spin}/2\pi=0.187\,\mathrm{MHz}$ into expression (5.30), corresponding to the experimentally measured peak linewidth of the Rabi spectra in absence of RF modulation and therefore including a nonzero $\Delta\Omega_\mathrm{R}$. The lower bound is obtained by injecting $\Gamma_\mathrm{spin}/2\pi=0.073\,\mathrm{MHz}$, which is the linewidth obtained once the spin is locked. We also rectify expression (5.30) by a factor of 0.5, accommodating a decrease of the central peak amplitude to half its initial value. These bounds provide proper limits for the experimental data, signifying that the establishment of spin locking to the coherent modulation plays an important role.

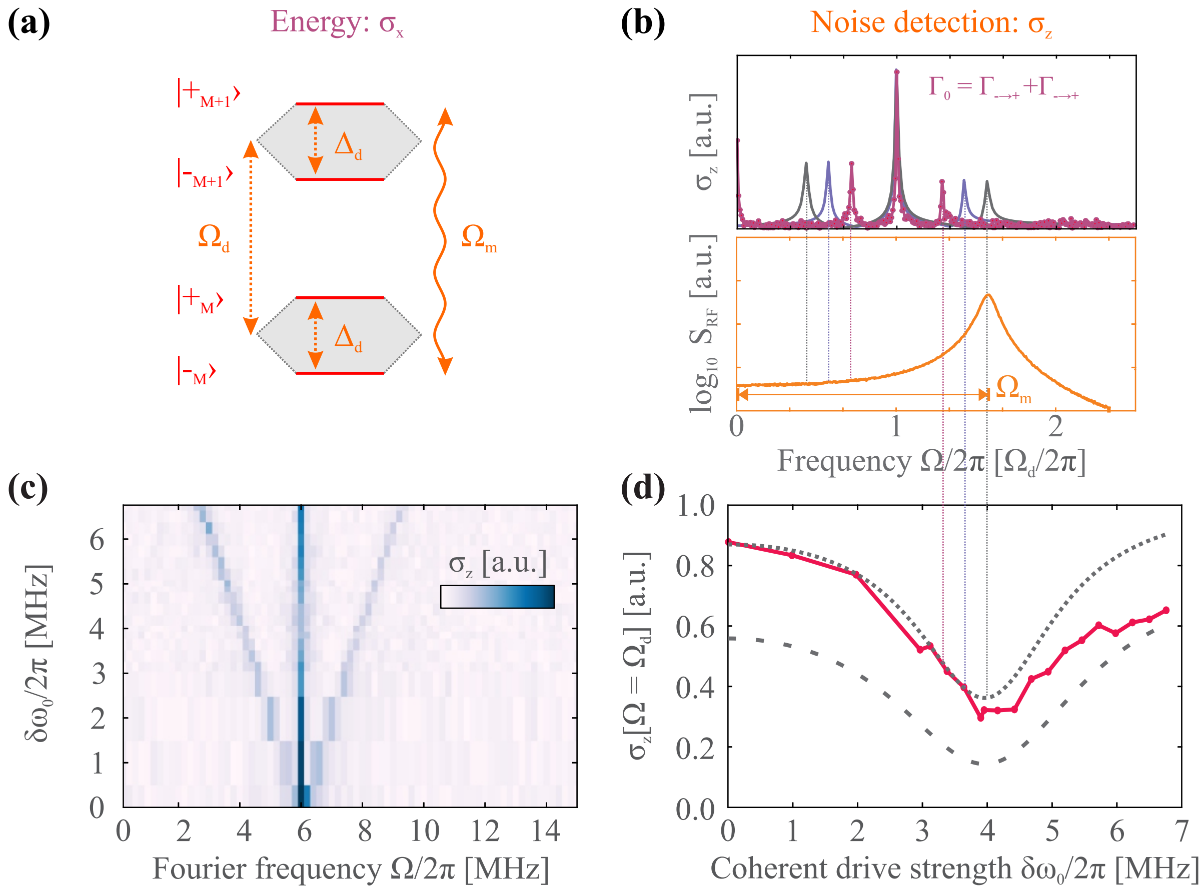

Figure 5.17: Sweep of the coherent Mollow triplet sidebands across the Brownian motion of a second oscillation mode. **(a)** Energy diagram in the dressed state basis. The coherent motion induces an energy gap $\hbar\Omega_\mathrm{d}$ between multiplicities, creating the doubly dressed states. The incoherent thermal motion at Ω_m stimulates emission and absorption between $|+_{M+1}\rangle \leftrightarrow |-_M\rangle$ when $\Omega_\mathrm{d} + \Delta_\mathrm{d} = \Omega_\mathrm{m}$. **(b)** Schematic explanation of the experiment. Increase of the coherent modulation amplitude separates the Mollow triplet sidebands (top), thereby changing the frequency at which the noise spectral density of the thermal motion, $S^{\mathrm{th}}_{\delta\omega_\parallel}[\Omega]$, is probed (bottom). **(c)** Data, $\Omega_\mathrm{d}/2\pi = 6$ MHz, $\Omega_\mathrm{m}/2\pi = 8$ MHz, $Q = 10$, $\delta\omega_\mathrm{th}/2\pi = 1.04$ MHz. **(d)** Central component of the Mollow triplet compared to upper and lower bounds as explained in the text. Red curve: data, top gray curve: (5.30) with $\Gamma_\mathrm{spin}/2\pi = 0.187$ MHz, bottom gray curve: $0.5\times$(5.30) with $\Gamma_\mathrm{spin}/2\pi = 0.073$ MHz. The vertical lines qualitatively compare the central Mollow component to $S^{\mathrm{th}}_{\delta\omega_\parallel}[\Omega]$ and the sideband position indicated in **(b)**.

5.7 Conclusion

In this chapter we have revisited earlier signatures of the spin-oscillator coupling and investigated how the corresponding signatures are influenced by the thermal motion of the mechanical oscillator. Separation of amplitude and frequency distribution of the mechanical motion has been a powerful analytic tool, which has accounted for most of the observed effects.

We have studied the spin dynamics when the spin is intentionally driven at the mechanical frequency where a maximum of thermal noise is found. The experimental data, in agreement with numerical results, show that a thermal Mollow triplet signature can still be obtained in the case of large quality factors and effective temperature. On the one hand, the amplitude distribution is reflected by the washing out of the sidebands, which form a pedestal instead. On the other hand, variation of the mechanical frequency is reflected by a broadening of the central Mollow triplet peak, which is swept over a frequency range given by Γ_{m}. For mechanical oscillators of large quality factors, this regime is easily obtained. In the limit of large mechanical dissipation, the oscillator's thermal motion can be regarded as a source of decoherence to the spin. As long as mechanical amplitudes $\delta\omega_{\mathrm{th}}$ stay low compared to the mechanical decay rate, a Fermi's Golden rule type argument can be used to evaluate their influence on the decay of Rabi oscillations. For larger temperatures, however, the interaction evolves on a timescale at which correlations between the spin and thermal oscillator become important.

Finally, we have studied the effect of thermal Brownian motion on the Mollow triplet created by a separate coherent drive of the mechanical motion. Our data show that the components of the triplet are sensitive to the noise spectral density at different frequencies. This effect can be used in order to exploit the Mollow triplet as a probe of high frequency magnetic noise. Beyond such applications, by showing that the central component of the Mollow triplet is protected from noise at the mechanical frequency, we have established the important relevance of this regime for spin mechanical hybrid systems.

This study finally shades new light on the measurement of Chapter 4. Despite the important parametric modulation imposed by the large Brownian motion of the suspended NV defect, it was possible to observe long-lived Rabi oscillations with the Mollow triplet signature when driving the nanowire at its mechanical resonance frequency. This is a direct consequence of the coherence protection described in section 5.5.

Moreover, the disturbance observed on the Mollow triplet when the lower sideband crosses the mechanical resonance frequency can be explained by the observations of section 5.6. These findings will be investigated in more detail in an upgraded experiment, exhibiting a higher spatial stability and larger coupling strength.

Conclusion

Ground breaking trapped ion and atom experiments have revealed the quantum physical aspects in the behavior of small objects. Ground state cooling, generation of arbitrary quantum states and the creation of quantum correlations between clusters of several particles have become well established experimental techniques. These developments motivate looking for similar signatures in larger, and eventually, macroscopic objects. Hybrid systems between mechanical oscillators and a single quantum system have been suggested as, and already proven to be, potential devices that offer the necessary properties required to achieve such an ambitious goal. By magnetically coupling the motion of a SiC nanowire to a single NV defect electron spin, we here propose to realize a hybrid system that can potentially operate in the resolved sideband regime. SiC nanowires can be engineered to have large aspect ratios. Due to their low masses and the material's very high Young modulus, large oscillation frequencies and amplitudes can be observed. This facilitates the observation of zero point fluctuations on the one hand. On the other hand, these oscillators become very susceptible force sensors, rendering them useful to detect the small forces exerted by a quantum system. NV defects have gained much popularity throughout a wide range of scientific communities due to their exceptional properties as single photon source and solid state qubit. Here we profit from optical preparation and readout and MW control of the spin state together with exceptional coherence times at room temperature.

The experimental feasibility of parametrically coupling the spin's energy to the mechanical motion of the SiC nanowire has been demonstrated by spectroscopy measurements in an effort preceding the here presented work. Here, we have expand on this success by studying the NV spin's dynamics in the resolved sideband regime. A compact but powerful formalism in terms of Bloch equations is provided which, which describes the coupled spin- oscillator- driving field system. This has allowed the theoretical description of the several experimental signatures in terms of numerical simulations as well as an analytic approach.

Experimental signatures of the parametric coupling in the resolved sideband regime were obtained using two setups. On a radio frequency waveguiding system the energy of a single NV spin is modulated using oscillating magnetic fields, emulating the mechanical motion of a spin through a magnetic field gradient. The achieved stability of this device in connection with the wide tunability of the emulated mechanical oscillator allows for a careful study of various coupling regimes. Monochromatic modulation of the spin energy leads to a wide range of consequences. Studying the average spin energy in the steady state regime by measuring ODMR spectra has revealed the existence of an adiabatic regime where the change of energy occurs on a time scale much larger than the spin lifetime and the spin resonances become broadened. Conversely, fast periodic energy variation lead to frequency modulation of the spin, whose spectra thereupon exhibit resolved sidebands.

We have subsequently investigated the dynamics of the MW driven spin. These can be interpreted with the help of an effective field theory, in which a pseudo two level system is created, whose energy splitting is proportional to the frequency of driven evolution (the so called Rabi frequency). In the resolved sideband regime, the spin can be driven at frequency detunings that correspond to integer multiples of the modulation frequency. For small enough strength of the MW drive, the Rabi frequency belonging to each of those resonances is modulated by Bessel functions.

The dynamics of the driven spin become strongly altered when the modulation and drive frequency match, which was studied here at a resonant MW drive. Beating signatures between several frequencies appear in the spin's time evolution and the spectra of Rabi oscillations are marked by a symmetric triplet structure. Remarkably, the central component of the triplet locks the spin dynamics to the modulation frequency of the mechanical oscillator. This phenomenon, which in analogy to experiments from atom physics we refer to as a Mollow triplet, is the result of a twofold dressing of the spin with first the MW and second the RF field. In order to adequately describe these signatures, we have presented two approaches. Both, Bloch equations of the dressed spin irradiated by a resonant field, as well as a study of the time evolution of the doubly dressed eigenstates reproduce the experimental signatures with great accuracy and show that the driven spin– oscillator dynamics can considered to have entered a strong coupling regime.

These effects have important consequences and their observation in a hybrid device would constitute a significant development in this field of physics. On the one hand, reminiscent of a classical phase lock loop, locking of the Rabi frequency to the mechanical oscillator renders the spin evolution insensitive to variations of the Rabi frequency caused by slow noise sources, which shift the spin resonance away from the MW field frequency. On the other hand, this locking phenomenon shows how the spin dynamics can be tuned to evolve at the frequency at which a mechanical oscillator exhibits its maximum mechanical susceptibility. Under these conditions, spin state dependent forces result in spatial displacements of the resonator exceeding those of a static force by the mechanical quality factor.

For these reasons it was important to reproduce these findings on a true mechanical device. Those were demonstrated on the second experimental setup described in this work, a spin-mechanical hybrid system built from a single NV electron spin and a SiC nanowire. Single nanodiamonds can simply be attached to the nanowire tip, whose position is encoded in the spin energy by a magnetic field gradient. While the spatial variation of the spin energy can be complex, we have demonstrated a reliable technique identifying a working point for spin manipulation protocols. Moreover, by directly detecting the energy variation of the spin around the working point, the magnetic gradients along the oscillation directions can be measured. In this much more complex system the experimentally observed spin locking signatures have however gained considerably in richness, due to both, oscillation direction dependent coupling and the introduction of a nonlinearity of energy modulation at large oscillation amplitudes. These consequences open routes for even more advanced spin manipulation protocols and will be subject of forthcoming work.

The latter system comprising an ultrasensitive mechanical force sensor, the oscillator exhibits large thermal amplitudes at room temperature operation. Due to the strong magnetic field gradients that were employed, the incoherent thermal motion couples to the spin additionally. Previous signatures of the spin-oscillator coupling are revisited and the role of the mechanical oscillator's Brownian motion on the spin dynamics were studied on the radio frequency waveguiding device. Emulating such motion with an arbitrary waveform generator offers tunability of all relevant physical parameters such as temperature and quality factor. Our results show in agreement with numerical data that a 'thermal' Mollow triplet can be created for a large enough effective temperature when the Rabi frequency matches the mechanical peak frequency. Then, separation of amplitude and frequency distribution of the emulated mechanical motion proves a powerful analytic tool. On the one hand, the amplitude distribution is reflected by the washing out of the sidebands, which form a pedestal. On the other hand, variation of the mechanical frequency is reflected by a broadening of the central Mollow triplet peak, which is swept over a frequency range given by Γ_{m}. For mechanical oscillators of large quality factors, this regime is easily obtained. In the limit of large mechanical dissipation, the oscillator's thermal motion can be regarded as a source of decoherence to the spin. As long as mechanical amplitudes stay low compared to the mechanical decay rate, a Fermi's Golden rule type argument can be used to evaluate the influence on the decay of Rabi oscillations.

Finally, we have studied the effect of supplemental noise in the form of Brownian motion on the Mollow triplet, which is created by additional coherent mechanical motion. Our data shows that different components of the triple peak are sensitive to the noise spectral density at different frequencies.

This effect can be used in order to exploit the Mollow triplet as a probe of high frequency magnetic noise. Beyond such applications, by showing that the central component of the Mollow triplet is protected from noise at the mechanical frequency, we have established the important relevance of this regime for spin mechanical hybrid systems.

Appendices

Appendix A

List of variables

Symbol	**Variable/ Meaning**
U	Potential energy
x	Position of a particle
x_0	Rest position of a particle
δx	Displacement of a particle, $\delta x = x - x_0$
k_B	Boltzman constant, $k_B = 1.38 \times 10^{-23}$J/K
$\hbar = h/2\pi$	Reduced Planck constant, $h = 6.626 \times 10^{-34}$Js
Θ	Classical temperature of the environment
E	• Electric field • Young modulus • Strain splitting of the NV spin • Energy
B	Magnetic field
b	Magnetic field amplitude
$\Omega_\mathrm{m}/2\pi$	Mechanical resonance frequency
Γ_ion	Dissipation rate of a single ion in a trap potential
$\lvert g\rangle$/ $\lvert e\rangle$	Ground/ excited state of a two level system
$a^\dagger$/ a	Phonon raising/ lowering operators
$\hat{m}$	Phonon number operators, $\hat{m} = a^\dagger a$
$b^\dagger$/ b	Photon raising/ lowering operators
$\hat{n}$	Photon number operators, $\hat{n} = b^\dagger b$
$\lvert n\rangle$/ $\lvert m\rangle$	Photon/ phonon number state
$\lvert\alpha\rangle$	Coherent state with amplitude α
θ	Polar angle (e.g. of a quantum superposition phase or the NV coordinate system)
φ	Azimuthal angle (e.g. of a quantum superposition phase or the NV coordinate system)
Γ_1	Energy dissipation rate in a quantum system
Γ_2	Decoherence rate in a quantum system
Γ_φ	Decoherence due to pure dephasing
Γ_m	Mechanical dissipation rate
Γ_th	Mechanical decoherence rate, $\Gamma_\mathrm{th} = \Gamma_\mathrm{m} k_B \Theta/\hbar\Omega_\mathrm{m}$ oscillator and a quantum system
$\sigma_{x,y,z}$	Pauli matrices
S	Total electronic spin quantum number
m_s	Projection of S along the quantization axis

Symbol	**Variable/ Meaning**
I	Total nuclear spin quantum number
I_z	Projection of I along the quantization axis
$\omega_0/2\pi$	Resonance frequency of a TLS
$\omega/2\pi$	Frequency of a photon field
δ	Detuning between TLS and photon field, $\delta = \omega - \omega_0$
t, τ_c	Time, correlation time
H	Hamiltonian
Z	Partition function
ρ	- Density matrix - Mass density (of the nanowire)
$\mathrm{Tr}\left\{\right\}$	Trace operator
k	Spring constant of a harmonic potential
p	Momentum of a particle
M	Mass
X, P	Position/ Momentum operator
F_ext	External force
f_ext	External force density
F_th	Langevin force
$\chi[\Omega]$	Mechanical susceptibility, $\chi = \frac{1/M}{\Omega_\mathrm{m}^2 - \Omega^2 - i\Omega\Gamma_\mathrm{m}}$
$\hat{F}_\mathrm{th}^\mathrm{q}$	Quantum Langevin force operator
Q	Mechanical quality factor, $Q = \Omega_\mathrm{m}/gm$
$S_a[\Omega]$	Spectral density of quantity a, defined as the Fourier transform of the autocorelation function of a: $S_a[\Omega] = \int\limits_{-\infty}^{\infty} \langle a(t), a(t+\tau)\rangle\, e^{i\Omega\tau}\, \mathrm{d}\tau$
σ	Poisson ratio
E	- Zero field splitting of the NV spin, $D \approx 2.87$ GHz - $D = \frac{Ed^3}{12}(1-\sigma^2)$
y	Spatial coordinate along the resonator axis
d	Diameter of a cylindrical resonator/ nanowire
$\mathbf{u}(y,t)$	Deflection vector
k_n	Wave vector of the n^th vibrational mode
a_n	Amplitude of the n^th vibrational mode
$\mathbf{r_0}$	Three dimensional rest position
$\delta\mathbf{r}$	Three dimensional position fluctuation
g	Landé factor, $g \approx 2$ for the NV spin
μ_B	Bohr magneton, $\mu_B = 9.274 \times 10^{-24}\mathrm{J/T}$
A	Hyperfine coupling tensor
R	Collective coupling to the spin bath
$P_{0/1}$	Ground/ excited state population
$\delta\omega_\parallel$	Longitudinal coupling strength to the spin
$\delta\omega_\perp$	Transverse coupling strength to the spin
$g^{(2)}(\tau)$	Autocorrelation function with delay τ
P_opt	Optical power
P_sat	Optical saturation power
s	Optical saturation parameter, $s \equiv P_\mathrm{opt}/P_\mathrm{sat}$
Γ_p	Optical pumping rate, $\Gamma_\mathrm{p} \equiv \Gamma_\mathrm{p}^\infty \frac{s}{s+1}$
Γ_c	Optical decoherence rate, $\Gamma_\mathrm{c} \equiv \Gamma_\mathrm{c}^\infty \frac{s}{s+1}$

Symbol	**Variable/ Meaning**
$\mathbf{e_m}$	Direction of the mechanical mode
λ_{ij}	Coupling strength due to variation of the magnetic field component i in the direction j, $\lambda_{ij} = \frac{g\mu_B}{\hbar}\partial_j B_i$
τ_ρ	Coherence time of a Schrödinger cat state
$\delta\omega_0/2\pi$	Longitudinal coupling strength of a mechanical oscillator or amplitude of energy modulation of a spin induced by coherent mechanical motion
$\delta\omega_{\mathrm{R}}/2\pi$	Rabi frequency of spin transitions induced by a mechanical oscillator
$\Omega_{\mathrm{R}}/2\pi$	Rabi frequency
Γ_{fluo}	Detected fluorescence rate
η	Fluorescence detection efficiency
$\boldsymbol{\sigma}$	Bloch vector of the NV spin
u, v, w	Components of $\boldsymbol{\sigma}$ $u = \frac{1}{2}\left(\tilde{\rho}_{01} + \tilde{\rho}_{10}\right)$ $v = \frac{1}{2i}\left(\tilde{\rho}_{01} - \tilde{\rho}_{10}\right)$ $w = \frac{1}{2}\left(\tilde{\rho}_{11} - \tilde{\rho}_{00}\right)$
w^{st}	Steady state population difference
C_w	Population contrast
C^{ODMR}	ODMR contrast
μ	Scaling factor: $C^{\mathrm{ODMR}} = \mu C_w$
Γ_{eff}	ESR linewidth
w^{st}_{∞}	Steady state population difference at $\delta = \infty$
$F[\delta]$	Fluorescence detected in an ODMR measurement
$f_{0/1}$	Fluorescence emission rate of the ground/ excited state
J_n	n^{th} order Bessel function of the first kind
ϵ	Label used for the spin ground and excited states in the form ±.
A_n	Area of the n^{th} ODMR sideband
η	Angle between the spin axis and the effective field, $\eta = \arctan(\Omega_{\mathrm{R}}/\delta)$
τ	Delay time/ pulse duration
Γ_ν	Decoherence induced by the longitudinal noise spectral density at the Rabi frequency, $\Gamma_\nu = \pi S_{\delta\omega_\parallel}[\Omega_{\mathrm{R}}^{\mathrm{eff}}]$
Γ_{static}	Amplitude decay of the non-oscillating component in a Rabi measurement, $\Gamma_{\mathrm{static}} = \Gamma_\nu \sin^2\eta + \Gamma_1 \frac{1+\cos^2\eta}{2}$.
Γ_{spin}	Amplitude decay of the oscillating component in a Rabi measurement, $\Gamma_{\mathrm{spin}} = \frac{1}{2}\Gamma_\nu \sin^2\eta + \Gamma_\varphi \cos^2\eta + \Gamma_1 \frac{3-\cos^2\eta}{4}$.
Δ_N	Rabi splitting, $\Delta_N = \sqrt{\delta^2 + N{\Omega_{\mathrm{R}}^{v}}^2}$ and $\sqrt{N}\Omega_{\mathrm{R}}^{v} = \Omega_{\mathrm{R}}$ for a coherent field
$\mathcal{E}_N$	Multiplicity of the singly dressed states, $\mathcal{E}_N = \{\lvert 0, N\rangle, \lvert 1, N-1\rangle\}$
$\mathcal{F}_{N,M}$	Multiplicity of the doubly dressed states, $\mathcal{F}_{N,M} = \{\lvert -_N, M\rangle, \lvert +_N, M-1\rangle\}$
$\theta_N \in [0, \pi/2]$	Mixing angle of the first dressed states, $\arctan 2\theta_N = -\frac{\Omega_{\mathrm{R}}}{\delta}$
$g_{N,M}$	Phonon coupling strength to the dressed states, $g_{N,M} \equiv -\frac{g_z\sqrt{M}}{2}\sin 2\eta_N = -\frac{g_z\sqrt{M}}{2}\frac{\Omega_{\mathrm{R}}^{v}\sqrt{N}}{\Delta_N}$
$\Delta_{N,M}$	Splitting of the doubly dressed states
Δ_{Mollow}	Splitting of the doubly dressed states for a coherent phonon field
Δ_N^{BS}	Bloch-Siegert corrected splitting of the doubly dressed states
$\Omega_{\mathrm{R}}^{\odot}$	Bloch-Siegert corrected position of the anticrossing of the Mollow triplet
Ω_{R}^{*}	Bloch-Siegert corrected position of maximum intensity of the central component

Symbol	**Variable/ Meaning**
$\rho^{(N)}$	Density matrix of the singly dressed states of $\mathcal{E}(N)$
α	Initial oscillator phase with respect to $P_0(0) = 1$.
$A_{0,\pm,\Delta}$	Amplitude of the Mollow triplet peaks: (0) central, (-) lower, (+) upper sideband, (Δ) $\delta\omega_0/2$ -component
$\Gamma_{0,\pm}$	Widths of the Mollow triplet peaks: (0) central, (-) lower, (+) upper sideband
Γ_{pop}	Transition rates of the dressed state populations, $\Gamma_{\text{pop}} = 2\Gamma_{\text{spin}}\left(\sin^4\theta_{N,M} + \cos^4\theta_{N,M}\right)$
Γ_{coh}	Transition rates of the dressed state coherences, $\Gamma_{\text{coh}} = 2\Gamma_{\text{spin}}\left(\frac{1}{2} + \sin^2\theta_{N,M}\cos^2\theta_{N,M}\right)$
$\Delta\omega_0/2\pi$	Variance of the spin resonance frequency (due to experimental imperfections)
Δ_{sl}	Variance of the spin resonance frequency at the spin locking condition
$\Delta\Omega_{\text{R}}/2\pi$	Variance of the Rabi frequency (due to experimental imperfections)
$\boldsymbol{\lambda}$	Dynamical coupling strength, $\boldsymbol{\lambda} = \hbar\boldsymbol{\nabla}\big\vert_{\boldsymbol{r_0}}\omega_0(\boldsymbol{r_0})$
$V_\ominus$	Differential voltage reading of the quadrant photo diode, containing the encoded nanowire displacement
$\boldsymbol{\beta}$	Measurement vector of the optical displacement detection scheme
$\delta\mathbf{r}_\beta$	Mechanical displacement projected along the measurement direction $\mathbf{e}_\beta$
C	Capacitance
$S_{11}/\,S_{12}$	Reflection/ Transmission coefficient of a voltage signal measured with a Vector Network Analyzer
$\mathbf{u}$	Unit vector in the coordinate system defined by the optical axis, which is aligned along $\mathbf{u_z}$
$\delta\omega_{\text{th}}$	Root mean square energy modulation of the spin due to the mechanical oscillator's thermal motion, $\delta\omega_{\text{th}} = 2\pi\lambda\Delta x_{\text{th}}$
$\boldsymbol{\zeta}(\mathbf{r_0})$	Curvature matrix with elements $\zeta_{ij} \equiv \partial^2_{ij}\omega_0\big\vert_{\mathbf{r_0}}$
$X_1(t)$, $X_2(t)$	Quadratures of motion
$r(t)$	Time dependent amplitude of the thermal oscillator motion, $r(t) \equiv \sqrt{X_1^2(t) + X_2^2(t)}$
$p^{\text{th}}(r)$	Circular distribution of the thermal amplitude $r(t)$

Appendix B

Derivation of the Bloch equations

$$H/\hbar = (\omega_0 + \delta\omega_0)|1\rangle\langle 1| + (\Omega_{\mathrm{R}} + \delta\omega_{\mathrm{R}})(|0\rangle\langle 1| + |1\rangle\langle 0|) \tag{B.1}$$

$$\dot{\rho}_{\mathrm{relax}} = \begin{pmatrix} -\Gamma_{\mathrm{p}}\rho_{11} - \frac{1}{2}\Gamma_1(\rho_{11} - \rho_{00}) & -\Gamma_2\rho_{01} \\ -\Gamma_2\rho_{10} & +\Gamma_{\mathrm{p}}\rho_{11} + \frac{1}{2}\Gamma_1(\rho_{11} - \rho_{00}) \end{pmatrix}, \tag{B.2}$$

$$\dot{\rho} = \frac{1}{i\hbar}[H_{\mathrm{tot}}, \rho] + \dot{\rho}_{\mathrm{relax}}, \quad \rho_{ij} = \langle i|\rho|j\rangle \tag{B.3}$$

$$\dot{\rho}_{11} = -i(\Omega_{\mathrm{R}} + \delta\omega_{\mathrm{R}})(\rho_{01} - \rho_{10}) - \Gamma_{\mathrm{p}}\rho_{11} - \frac{1}{2}\Gamma_1(\rho_{11} - \rho_{00}) \tag{B.4}$$

$$\dot{\rho}_{10} = -i(\omega_0 + \delta\omega_0)\rho_{10} - i(\Omega_{\mathrm{R}} + \delta\omega_{\mathrm{R}})(\rho_{00} - \rho_{11}) - \Gamma_2\rho_{10} \tag{B.5}$$

$$\dot{\rho}_{01} = i(\omega_0 + \delta\omega_0)\rho_{01} + i(\Omega_{\mathrm{R}} + \delta\omega_{\mathrm{R}})(\rho_{00} - \rho_{11}) - \Gamma_2\rho_{01} \tag{B.6}$$

We now introduce the time dependence of the MW field

$$\Omega_{\mathrm{R}}(t) = \Omega_{\mathrm{R}}\cos\omega t, \tag{B.7}$$

and go into the MW rotating frame by defining:

$$\rho_{10} \equiv \tilde{\rho}_{10}e^{-i\omega t}, \quad \rho_{01} \equiv \tilde{\rho}_{01}e^{i\omega t}. \tag{B.8}$$

It follows that

$$\frac{d\rho_{10}}{dt} = \frac{d\tilde{\rho}_{10}}{dt}e^{-i\omega t} - i\omega\tilde{\rho}_{10}e^{-i\omega t} \quad \text{and} \quad \frac{d\rho_{01}}{dt} = \frac{d\tilde{\rho}_{01}}{dt}e^{i\omega t} + i\omega\tilde{\rho}_{01}e^{i\omega t}. \tag{B.9}$$

We inject the time dependence in equations (B.4, B.5, B.6) and drop terms rotating at 2ω:

$$\begin{aligned}
\dot{\rho}_{11} = {} & -i\Omega_{\mathrm{R}}\left(\tilde{\rho}_{01}e^{i\omega t} - \tilde{\rho}_{10}e^{-i\omega t}\right)\frac{e^{i\omega t} + e^{-i\omega t}}{2} - i\delta\omega_{\mathrm{R}}(\rho_{01} - \rho_{10}) - \Gamma_{\mathrm{p}}\rho_{11} - \frac{1}{2}\Gamma_1(\rho_{11} - \rho_{00}) \\
\approx {} & \frac{\Omega_{\mathrm{R}}}{2i}(\tilde{\rho}_{01} - \tilde{\rho}_{10}) - i\delta\omega_{\mathrm{R}}(\rho_{01} - \rho_{10}) - \Gamma_{\mathrm{p}}\rho_{11} - \frac{1}{2}\Gamma_1(\rho_{11} - \rho_{00})
\end{aligned} \tag{B.10}$$

$$\begin{aligned}
\dot{\tilde{\rho}}_{10} = {} & \left(\dot{\rho}_{10} + i\omega\tilde{\rho}_{10}e^{-i\omega t}\right)e^{i\omega t} \\
= {} & \dot{\rho}_{10}e^{i\omega t} + i\omega\tilde{\rho}_{10} \\
= {} & \left(-i(\omega_0 + \delta\omega_0)\tilde{\rho}_{10} + i\left(\frac{\Omega_{\mathrm{R}}}{2}\left(e^{i\omega t} + e^{-i\omega t}\right) + \delta\omega_{\mathrm{R}}\right)(\rho_{11} - \rho_{00}) - \Gamma_2\tilde{\rho}_{10}e^{-i\omega t}\right)e^{i\omega t} + i\omega\tilde{\rho}_{10} \\
\approx {} & -i(\omega_0 - \omega + \delta\omega_0)\tilde{\rho}_{10} + i\left(\frac{\Omega_{\mathrm{R}}}{2} + \delta\omega_{\mathrm{R}}e^{i\omega t}\right)(\rho_{11} - \rho_{00}) - \Gamma_2\tilde{\rho}_{10}
\end{aligned} \tag{B.11}$$

$$\dot{\tilde{\rho}}_{01} \approx i(\omega_0 - \omega + \delta\omega_0)\tilde{\rho}_{01} - i\left(\frac{\Omega_{\mathrm{R}}}{2} + \delta\omega_{\mathrm{R}}e^{-i\omega t}\right)(\rho_{11} - \rho_{00}) - \Gamma_2\tilde{\rho}_{01} \tag{B.12}$$

Intorducing the coordinates of the Bloch vector:

$$u \equiv \mathrm{Re}\left(\tilde{\rho}_{01}\right), \qquad v \equiv \mathrm{Im}\left(\tilde{\rho}_{01}\right), \qquad w \equiv \frac{1}{2}(\rho_{11} - \rho_{00}), \tag{B.13}$$

and using that $\rho_{00} + \rho_{11} = 1$ we have

$$\tilde{\rho}_{01} = u + iv \qquad \tilde{\rho}_{10} = u - iv, \qquad \rho_{11} = w + \frac{1}{2}. \tag{B.14}$$

We will use

$$u = \frac{1}{2}(\tilde{\rho}_{01} + \tilde{\rho}_{10}), \qquad v = \frac{1}{2i}(\tilde{\rho}_{01} - \tilde{\rho}_{10}), \qquad \dot{w} = \frac{1}{2}(\dot{\rho}_{11} - \dot{\rho}_{00}) = \dot{\rho}_{11} \tag{B.15}$$

and

$$(u+iv)e^{i\omega t} - (u-iv)e^{-i\omega t} = u(e^{i\omega t} - e^{-i\omega t}) + iv(e^{i\omega t} - e^{-i\omega t}) = 2iu\sin\omega t + 2iv\cos\omega t. \tag{B.16}$$

$$\begin{aligned}
\dot{w} =\ & \Omega_{\mathrm{R}} v - i\delta\omega_{\mathrm{R}}\left((u+iv)e^{i\omega t} - (u-iv)e^{-i\omega t}\right) - \Gamma_{\mathrm{p}}\left(w + \frac{1}{2}\right) - \Gamma_1 w \\
=\ & \Omega_{\mathrm{R}} v + 2\delta\omega_{\mathrm{R}}(u\sin\omega t + v\cos\omega t) - \Gamma_1 w - \Gamma_{\mathrm{p}}\left(w + \frac{1}{2}\right) \qquad (\mathrm{B.17}) \\
\dot{u} =\ & \frac{1}{2}\left(\dot{\tilde{\rho}}_{01} + \dot{\tilde{\rho}}_{10}\right) \\
=\ & \frac{1}{2}\Big(i(\omega_0 - \omega + \delta\omega_0)(\tilde{\rho}_{01} - \tilde{\rho}_{10}) + i\delta\omega_{\mathrm{R}}(e^{i\omega t} - e^{-i\omega t})(\rho_{11} - \rho_{00}) - \Gamma_2(\tilde{\rho}_{10} + \tilde{\rho}_{01})\Big) \\
=\ & -(\omega_0 - \omega + \delta\omega_0)v - 2\delta\omega_{\mathrm{R}}\sin\omega t\, w - \Gamma_2 u \qquad (\mathrm{B.18}) \\
\dot{v} =\ & \frac{1}{2i}\left(\dot{\tilde{\rho}}_{01} - \dot{\tilde{\rho}}_{10}\right) \\
=\ & \frac{1}{2i}\Big(i(\omega_0 - \omega + \delta\omega_0)\left(\tilde{\rho}_{01} + \tilde{\rho}_{10}\right) - i\left(\Omega_{\mathrm{R}} + \delta\omega_{\mathrm{R}}(e^{i\omega t} + e^{-i\omega t})(\rho_{11} - \rho_{00})\right) - \Gamma_2(\tilde{\rho}_{01} - \tilde{\rho}_{10})\Big) \\
=\ & (\omega_0 - \omega + \delta\omega_0)u - \left(\Omega_{\mathrm{R}} + 2\delta\omega_{\mathrm{R}}\cos\omega t\right) w - \Gamma_2 v \qquad (\mathrm{B.19})
\end{aligned}$$

The equations are summarized in matrix form as follows:

$$\begin{pmatrix} \dot{u} \\ \dot{v} \\ \dot{w} \end{pmatrix} = \begin{pmatrix} -\Gamma_2 & \delta - \delta\omega_0(t) & -2\delta\omega_{\mathrm{R}}(t)\sin\omega t \\ -\delta + \delta\omega_0(t) & -\Gamma_2 & -\Omega_{\mathrm{R}} - 2\delta\omega_{\mathrm{R}}\cos\omega t \\ 2\delta\omega_{\mathrm{R}}\sin\omega t & \Omega_{\mathrm{R}} + 2\delta\omega_{\mathrm{R}}(t)\cos\omega t & -\Gamma_1 - \Gamma_{\mathrm{p}} \end{pmatrix} \begin{pmatrix} u \\ v \\ w \end{pmatrix} - \begin{pmatrix} 0 \\ 0 \\ \Gamma_{\mathrm{p}}/2 \end{pmatrix}. \tag{B.20}$$

Appendix C

Analytical expressions for the phononic Mollow triplet

C.1 Time evolution of the populations and coherences

We begin[1] by considering the quantum master equation

$$\dot{\rho} = -\frac{i}{\hbar}[H, \rho] - \frac{\Gamma}{2}(\sigma_+\sigma_-\rho + \rho\sigma_+\sigma_-) + \Gamma\sigma_-\rho\sigma_+ \tag{C.1}$$

for the density matrix ρ representing the coupled atom and light field with Hamiltonian H whose eigenstates are the dressed states

$$\begin{pmatrix} |+_N\rangle \\ |-_N\rangle \end{pmatrix} = \begin{pmatrix} \cos\theta & -\sin\theta \\ \sin\theta & \cos\theta \end{pmatrix} \begin{pmatrix} |0, N+1\rangle \\ |1, N\rangle \end{pmatrix}, \tag{C.2}$$

with energy separation

$$\Delta = \sqrt{\delta^2 + \Omega_{\mathrm{R}}^2}. \tag{C.3}$$

We are interested in the time evolution of

1. the populations $\pi_{\pm,N} = \langle \pm_N|\rho|\pm_N\rangle$
2. the intra-multiplicity coherences $\rho_{+-,N} = \langle +_N|\rho|-_N\rangle$
3. the inter-multiplicity coherences $\rho^q_{ij,N} = \langle i_{N-q}|\rho|j_N\rangle$

which is found by projecting the appropriate states around (C.1). We will make use of the following relations:

$$\langle -_N|\sigma_+|-_{N-1}\rangle = (\sigma_+)_{--} = \sin\theta\cos\theta, \tag{C.4}$$

$$\langle +_N|\sigma_+|+_{N-1}\rangle = (\sigma_+)_{++} = -\sin\theta\cos\theta, \tag{C.5}$$

$$\langle -_N|\sigma_+|+_{N-1}\rangle = (\sigma_+)_{-+} = \cos^2\theta, \tag{C.6}$$

$$\langle +_N|\sigma_+|-_{N-1}\rangle = (\sigma_+)_{+-} = \sin^2\theta, \tag{C.7}$$

in order to define the transition rates

$$\Gamma_{i\to j} = \Gamma|\langle i_N|\sigma_+|j_{N-1}\rangle|^2 = \Gamma|(\sigma_+)_{ij}|^2, \tag{C.8}$$

---

[1] The following section is a summary of Chapter VI D of [122]

which are explicitly written as

$$\Gamma_{-\to-} = \Gamma \sin^2\theta\cos^2\theta, \tag{C.9}$$

$$\Gamma_{+\to+} = \Gamma \sin^2\theta\cos^2\theta, \tag{C.10}$$

$$\Gamma_{-\to+} = \Gamma \cos^4\theta, \tag{C.11}$$

$$\Gamma_{+\to-} = \Gamma \sin^4\theta. \tag{C.12}$$

Populations We find that

$$\dot{\pi}_{\pm,N} = -(\sum_{j=1,2}\Gamma_{i\to j})\pi_{\pm,N} + (\sum_{l=1,2}\Gamma_{l\to i})\pi_{\pm,N+1}. \tag{C.13}$$

The population of the level $|+_N\rangle$ changes due to populations leaving to levels $|\pm_{N-1}\rangle$ and populations arriving from levels $|\pm_{N+1}\rangle$ at the corresponding transition rates. We can introduce the *reduced populations* $\pi_\pm$, which is the sum of the populations of one state over all multiplicities N:

$$\pi_\pm = \sum_N \pi_{\pm,N} \tag{C.14}$$

with the simple dynamics

$$\begin{aligned}\dot{\pi}_- &= \Gamma_{-\to+}\pi_- + \Gamma_{+\to-}\pi_+,\\ \dot{\pi}_+ &= \Gamma_{+\to-}\pi_+ + \Gamma_{-\to+}\pi_-.\end{aligned} \tag{C.15}$$

The solution to these equations is given by

$$\pi_\pm(t) = \pi_\pm^{\text{st}} + (\pi_\pm(0) - \pi_\pm^{\text{st}})e^{-\Gamma_{\text{pop}}t}, \tag{C.16}$$

where $\pi_\pm^{\text{st}}$ is the steady state population of $\pi_\pm$ and Γ_{pop} is the decay rate of the populations

$$\Gamma_{\text{pop}} = \Gamma_{-\to+} + \Gamma_{+\to-}. \tag{C.17}$$

The dynamic equilibrium is reached when population losses are compensated by population gain. In that case

$$\dot{\pi}_\pm = 0. \tag{C.18}$$

leading to steady state populations

$$\pi_+^{\text{st}} = \frac{\Gamma_{-\to+}}{\Gamma_{-\to+} + \Gamma_{+\to-}} = \frac{\cos^4\theta}{\sin^4\theta + \cos^4\theta}, \tag{C.19}$$

$$\pi_-^{\text{st}} = \frac{\Gamma_{+\to-}}{\Gamma_{-\to+} + \Gamma_{+\to-}} = \frac{\sin^4\theta}{\sin^4\theta + \cos^4\theta}, \tag{C.20}$$

obeying $\pi_+^{\text{st}} + \pi_-^{\text{st}} = 1$. In the steady state regime we obtain the *detailed balance condition*, stating that transitions from one to another level are compensated by transition in the opposite direction:

$$\pi_+\Gamma_{+\to-} = \pi_-\Gamma_{-\to+}. \tag{C.21}$$

This balance leads to the symmetric shape of the fluorescence triplet.

Coherences The intra-multiplicity coherences evolve as

$$\begin{aligned}\frac{d}{dt}\langle -_N|\rho|+_N\rangle =& - i\Delta\langle -_N|\rho|+_N\rangle \\ &+ \Gamma_{-+}\langle -_N|\rho|+_N\rangle \\ &+ K_{-+}\langle -_{N+1}|\rho|+_{N+1}\rangle.\end{aligned} \tag{C.22}$$

which presents free evolution, radiative decay and transfer of the coherences from a higher multiplicity, respectively. The decay rate Γ_{-+} is half the spontaneous emission rate

$$\Gamma_{-+} = \frac{1}{2}(\Gamma_{+\to+} + \Gamma_{-\to-} + \Gamma_{-\to+} + \Gamma_{+\to-}) = \frac{\Gamma}{2}, \tag{C.23}$$

while the transfer rate K_{-+} is

$$K_{-+} = \Gamma\langle -_N|\sigma_-|-_{N+1}\rangle\langle +_{N+1}|\sigma_+|+_N\rangle = -\Gamma\sin^2\theta\cos^2\theta. \tag{C.24}$$

The evolution of the inter-multiplicity coherences ρ^q_{ij}, separated by q excitations, is an extension of the above expression:

$$\begin{aligned}\frac{d}{dt}\langle -_N|\rho|+_{N-q}\rangle =& - i(\Delta + q\omega_L)\langle -_N|\rho|+_{N-q}\rangle \\ &+ \Gamma_{-+}\langle -_N|\rho|+_{N-q}\rangle \\ &+ K_{-+}\langle -_{N+1}|\rho|+_{N-q+1}\rangle,\end{aligned} \tag{C.25}$$

with the same rates Γ_{-+} and K_{-+}.

For the intra-multiplicity *reduced coherences* ρ_{-+}

$$\rho_{-+} = \sum_N \langle -_N|\rho|+_N\rangle \tag{C.26}$$

the evolution equation becomes

$$\dot\rho_{-+} = -(i\Delta + \Gamma_{\text{coh}})\rho_{-+} \tag{C.27}$$

with the damping rate

$$\Gamma_{\text{coh}} = \Gamma_{-+} - K_{-+} = \Gamma(\frac{1}{2} + \cos^2\theta\sin^2\theta). \tag{C.28}$$

When considering inter-multiplicity coherences, we distinguish between two cases. For ρ^q_{-+} we have

$$\dot\rho^q_{-+} = \frac{d}{dt}\langle -_{N-q}|\rho|+_N\rangle = (i(q\omega_L - \Delta) + \Gamma_{\text{coh}})\rho_{-+}, \tag{C.29}$$

$$\dot\rho^q_{+-} = \frac{d}{dt}\langle +_{N-q}|\rho|-_N\rangle = (i(q\omega_L + \Delta) + \Gamma_{\text{coh}})\rho_{+-}. \tag{C.30}$$

On the other hand, for $\rho^q_{\pm\pm}$ we find the coupled equations

$$\begin{aligned}\dot\rho^q_{--} &= iq\omega_L\rho^q_{--} - \rho^q_{--}\Gamma_{-\to+} + \rho^q_{++}\Gamma_{+\to-}, \\ \dot\rho^q_{++} &= iq\omega_L\rho^q_{++} - \rho^q_{++}\Gamma_{+\to-} + \rho^q_{--}\Gamma_{-\to+}.\end{aligned} \tag{C.31}$$

The solutions to the differential equations are

$$
\begin{aligned}
\rho^q_{-+}(t) &= \rho^q_{-+}(0)e^{(i(q\omega_L-\Delta)-\Gamma_{\mathrm{coh}})t},\\
\rho^q_{+-}(t) &= \rho^q_{+-}(0)e^{(i(q\omega_L+\Delta)-\Gamma_{\mathrm{coh}})t},\\
\rho^q_{--}(t) &= \frac{e^{i\omega_L t}}{\Gamma_{\mathrm{pop}}}\left(a_1(e^{-\Gamma_{\mathrm{pop}}t}\Gamma_{-\to+}+\Gamma_{+\to-})+a_2(e^{-\Gamma_{\mathrm{pop}}t}-1)\Gamma_{+\to-}\right),\\
&= \frac{e^{i\omega_L t}}{\Gamma_{\mathrm{pop}}}\left(\Gamma_{+\to-}+e^{-\Gamma_{\mathrm{pop}}t}(\Gamma_{\mathrm{pop}}\rho^q_{--}(0)-\Gamma_{+\to-})\right),\\
\rho^q_{++}(t) &= \frac{e^{i\omega_L t}}{\Gamma_{\mathrm{pop}}}\left(b_1(e^{-\Gamma_{\mathrm{pop}}t}-1)\Gamma_{-\to+}+b_2(e^{-\Gamma_{\mathrm{pop}}t}\Gamma_{+\to-}+\Gamma_{-\to+})\right),\\
&= \frac{e^{i\omega_L t}}{\Gamma_{\mathrm{pop}}}\left(\Gamma_{-\to+}+e^{-\Gamma_{\mathrm{pop}}t}(\Gamma_{\mathrm{pop}}\rho^q_{++}(0)-\Gamma_{-\to+})\right).
\end{aligned}
\tag{C.32}
$$

C.2 Fluorescence triplet

Measurement of the fluorescence $F[\Omega]$ emitted by the excited atom corresponds to a measurement of the correlator $\langle\sigma_+(t)\sigma_-(0)\rangle$, s.t.

$$
F[\Omega] = \frac{\Gamma}{\pi}\,\mathrm{Re}\left(\int_0^\infty \langle\sigma_+(t)\sigma_-(0)\rangle\, e^{i\omega t}\,\mathrm{d}t\right), \tag{C.33}
$$

with normalization

$$
I = \int \mathrm{d}\omega F[\Omega] = \langle\sigma_+(0)\sigma_-(0)\rangle = \Gamma\rho_{11}. \tag{C.34}
$$

The analytical form of the spectrum is obtained by using the quantum regression theorem, which states that the time evolution of the correlator $\langle\sigma_+(t)\sigma_-(0)\rangle$ is the same as for $\langle\sigma_+(t)\rangle$ (for $t > 0$). The average of the operator σ_+ is found by expanding σ_+ in the dressed state basis and tracing over the eigenstates. We can express the spin raising operator between the dressed states within the same as well as the lower multiplicity:

$$
\sigma_+|_{\mathcal{E}(\Delta N=0,1)} = \begin{array}{c|cccc}
 & |+_N\rangle & |-_N\rangle & |+_{N-1}\rangle & |-_{N-1}\rangle \\
\hline
|+_N\rangle & 0 & 0 & 0 & 0\\
|-_N\rangle & 0 & 0 & 0 & 0\\
|+_{N-1}\rangle & -\sin\theta\cos\theta & \cos^2\theta & 0 & 0\\
|-_{N-1}\rangle & -\sin^2\theta & \sin\theta\cos\theta & 0 & 0
\end{array} \tag{C.35}
$$

The expansion of the σ_+ operator in terms of dressed states of neighbouring multiplicities associated with radiative jumps is

$$
\sigma_+ = \sum_{i,j,N}(\sigma_+)_{ij}|i_N\rangle\langle j_{N-1}| = \sigma_+^{-+}+\sigma_+^{+-}+\sigma_+^{++}+\sigma_+^{--}, \tag{C.36}
$$

or, in matrix notation,

$$
\sigma_+ = \begin{pmatrix}(\sigma_+)_{++} & (\sigma_+)_{-+}\\ (\sigma_+)_{+-} & (\sigma_+)_{--}\end{pmatrix} = \begin{pmatrix}-\sin\theta\cos\theta & \cos^2\theta\\ -\sin^2\theta & \sin\theta\cos\theta\end{pmatrix}. \tag{C.37}
$$

Form of the sidebands The expansion of σ_+ allows us to directly calculate the different components of the triplet. For the upper frequency sideband, we have

$$\left\langle \sigma_+^{-+} \right\rangle = \mathrm{Tr}\left\{ \sigma_+^{-+} \rho \right\} = (\sigma_+)_{-+} \sum_N \mathrm{Tr}\left\{ |-_N\rangle\langle +_{N-1}|\rho \right\} = (\sigma_+)_{-+} \sum_N \langle +_{N-1}|\rho|-_N\rangle. \tag{C.38}$$

On the right hand side of equation (C.38) the reduced inter-multiplicity coherence ρ^1_{+-} appears, of which the time evolution has been determined in equations (C.32). The correlator $\left\langle \sigma_+^{-+}(t)\sigma_-(0) \right\rangle$ therefore evolves as

$$\left\langle \sigma_+^{-+}(t)\sigma_-(0) \right\rangle = \left\langle \sigma_+^{-+}\sigma_- \right\rangle e^{(i(\omega_L+\Delta)-\Gamma_{\mathrm{coh}})t}, \tag{C.39}$$

whose spectrum[2] is

$$F_\omega^{+1} = \Gamma \left\langle \sigma_+^{-+}\sigma_- \right\rangle \frac{1}{\pi} \frac{\Gamma_{\mathrm{coh}}}{(\omega-\omega_L-\Delta)^2+\Gamma_{\mathrm{coh}}^2}. \tag{C.40}$$

For the same reasons,

$$F_\omega^{-1} = \Gamma \left\langle \sigma_+^{+-}\sigma_- \right\rangle \frac{1}{\pi} \frac{\Gamma_{\mathrm{coh}}}{(\omega-\omega_L+\Delta)^2+\Gamma_{\mathrm{coh}}^2}. \tag{C.41}$$

The weight $\left\langle \sigma_+^{-+}\sigma_- \right\rangle$ is

$$\begin{aligned} \left\langle \sigma_+^{-+}\sigma_- \right\rangle &= (\sigma_+)_{-+} \sum_N \mathrm{Tr}\left\{ |-_N\rangle\langle +_{N-1}|\sigma_-\rho \right\} \\ &= (\sigma_+)_{-+} \sum_N (\cos^2\theta\langle -_N|\rho|-_N\rangle - \sin\theta\cos\theta\langle +_N|\rho|-_N\rangle) \end{aligned} \tag{C.42}$$

Here we have expanded $\langle +_{N-1}\sigma_-|$ to $\cos^2\theta\langle -_N| - \sin\theta\cos\theta\langle +N|$ in order to express $\left\langle \sigma_+^{-+}\sigma_- \right\rangle$ in terms of the reduced coherences and populations found above. For the Mollow triplet the stationary regime ($t \gg 1/\Gamma$) is considered. The coherence $\langle +_N|\rho|-_N\rangle$ has therefore decayed to 0. The steady state populations of each multiplicity are related to the reduced populations of the steady state via the photon distribution $P(N)$ of the coherent laser field:

$$\pi^{\mathrm{st}}_{\pm,N} = P(N)\pi^{\mathrm{st}}_{\pm} \tag{C.43}$$

and inversely,

$$\sum_N P(N)\pi^{\mathrm{st}}_{\pm,N} = \pi^{\mathrm{st}}_{\pm} \tag{C.44}$$

The weight of the upper sideband is thus

$$\Gamma \left\langle \sigma_+^{-+}\sigma_- \right\rangle = \Gamma\cos^4\theta \sum_N \langle -_N|\rho|-_N\rangle = \Gamma\cos^4\theta \sum_N P(N)\pi^{\mathrm{st}}_- = \pi^{\mathrm{st}}_-\Gamma_{-\to+} \tag{C.45}$$

In the same manner, we find the weight of the lower frequency sideband to be

$$\Gamma \left\langle \sigma_+^{+-}\sigma_- \right\rangle = \pi^{\mathrm{st}}_+\Gamma_{+\to-} \tag{C.46}$$

Form of the central line For the central line, we consider that the time evolution of

$$\left\langle (\sigma_+^{--}(t) + \sigma_+^{++}(t))\sigma_-(0) \right\rangle$$

has the general form

$$\left\langle (\sigma_+^{--}(t) + \sigma_+^{++}(t))\sigma_-(0) \right\rangle = Ae^{(i\omega_L-\Gamma_{\mathrm{pop}})t} + Be^{i\omega_L t} \tag{C.47}$$

---

[2] The Fourier transform of a damped oscillation $Ae^{(i\omega_L+\gamma)t}$ is $\frac{1}{2\pi}\frac{1}{\gamma+i(\omega-\omega_L)}$. The real part is then $\frac{1}{2\pi}\frac{\gamma}{\gamma^2+(\omega-\omega_L)^2}$.

corresponding to coherently and incoherently scattered photons. The spectrum thus consists out of a Dirac peak with weight ΓB and a Lorentzian with weight ΓA and width Γ_{pop} centered at ω_L. By considering the initial conditions, we find that

$$\Gamma(A+B) = \Gamma(\langle \sigma_+^{--}\sigma_-\rangle + \langle \sigma_+^{++}\sigma_-\rangle). \tag{C.48}$$

We evaluate the averages as above

$$\begin{aligned} \langle \sigma_+^{--}\sigma_-\rangle &= (\sigma_+)_{--}\sum_N \operatorname{Tr}\{|-_N\rangle\langle -_{N-1}|\sigma_-\rho\} \\ &= (\sigma_+)_{--}\sum_N (\sin\theta\cos\theta\langle -_N|\rho|-_N\rangle - \sin^2\theta\langle +_N|\rho|-_N\rangle) \end{aligned} \tag{C.49}$$

$$\begin{aligned} \langle \sigma_+^{++}\sigma_-\rangle &= (\sigma_+)_{++}\sum_N \operatorname{Tr}\{|+_N\rangle\langle +_{N-1}|\sigma_-\rho\} \\ &= (\sigma_+)_{++}\sum_N (-\sin\theta\cos\theta\langle +_N|\rho|+_N\rangle + \cos^2\theta\langle -_N|\rho|+_N\rangle) \end{aligned} \tag{C.50}$$

We again drop the contributions from the coherences and find for the weight of the central line

$$\Gamma(A+B) = \Gamma(\langle \sigma_+^{--}\sigma_-\rangle + \langle \sigma_+^{++}\sigma_-\rangle) = \pi_-^{\text{st}}\Gamma_{-\to-} + \pi_+^{\text{st}}\Gamma_{+\to+}. \tag{C.51}$$

These results are summarized in Figure C.1.

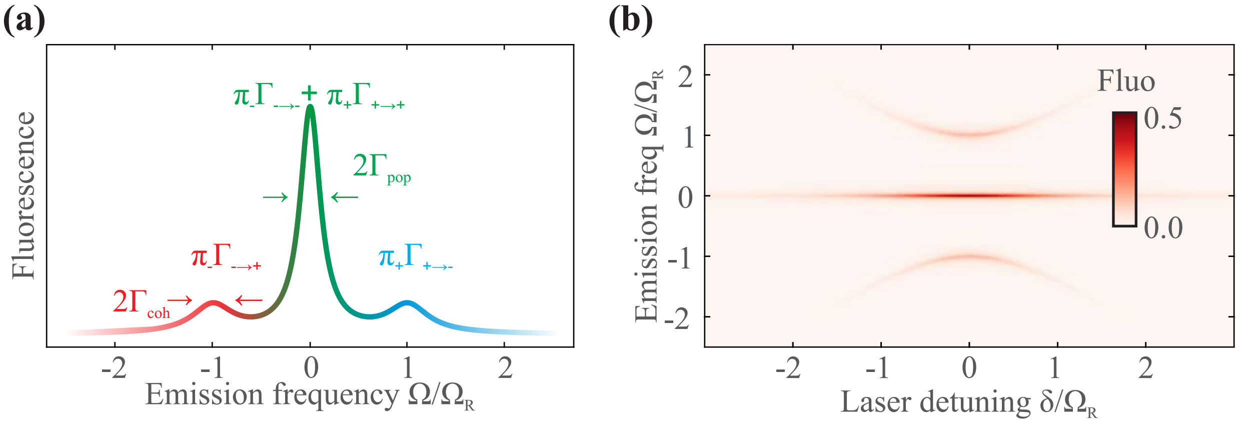

Figure C.1: Fluorescence Mollow triplet. **(a)** Spectrum of the Mollow triplet. **(b)** Fluorescence versus detuning and emission frequency showing the symmetric spectra.

C.3 Phonon Mollow triplet

Measurements of the Fourier spectra of Rabi oscillations are described by[3]

$$\langle \sigma_z[\Omega]\rangle = \int_0^\infty \langle \sigma_z(t)\rangle\, e^{i\omega t}\,\mathrm{d}t, \tag{C.52}$$

We can expand the operator σ_z in terms of the doubly dressed basis, similar as done in the above section. For example,

$$(\sigma_z)_{-+}\sigma_z^{-+} = (\sigma_z)_{-+}|+_{N,M-1}\rangle\langle -_{N,M}|$$

---

[3] See remark at the end of this section.

takes $|-_{N,M}\rangle$ to $|+_{N,M-1}\rangle$ and $(\sigma_z)_{-+} = \langle -_{N,M}|\sigma_z|+_{N,M-1}\rangle$. By considering all the non-zero transitions, we obtain (here we write α and θ for the angles θ_N and $\theta_{N,M}$ of the main text, respectively.)

$$\sigma_z|_{\mathcal{F}(N,\Delta M=0,1)} = \begin{array}{c} \\ |+_{N,M}\rangle \\ |-_{N,M}\rangle \\ |+_{N,M-1}\rangle \\ |-_{N,M-1}\rangle \end{array} \begin{array}{c} \begin{array}{cc} \quad |+_{N,M}\rangle \quad & \quad |-_{N,M}\rangle \quad \end{array} \\ \begin{pmatrix} \# & \# \\ \sin\theta\cos\theta(\cos^2\alpha-\sin^2\alpha) & \# \\ -\sin\theta\cos\theta\sin\alpha\cos\alpha & -\sin^2\theta\sin\alpha\cos\alpha \\ \cos^2\theta\sin\alpha\cos\alpha & \sin\theta\cos\theta\sin\alpha\cos\alpha \end{pmatrix} \end{array} \tag{C.53}$$

C.3.1 MW on resonance

We set $\delta = 0$ to simplify the calculations. In that case the angles α becomes $\alpha = \frac{\pi}{2}$ and $\sin\alpha = \cos\alpha = \frac{1}{\sqrt{2}}$. The transition matrix $\sigma_z|_{\mathcal{F}(N,\Delta M=0,1)}$ is

$$\sigma_z|_{\mathcal{F}(N,\Delta M=0,1)} = \frac{1}{2}\begin{pmatrix} \# & \# & \# & \# \\ 0 & \# & \# & \# \\ -\sin\theta\cos\theta & -\sin^2\theta & \# & \# \\ \cos^2\theta & \sin\theta\cos\theta & 0 & \# \end{pmatrix} \tag{C.54}$$

or, invoking only entries associated with a change of multiplicity,

$$\sigma_z|_{\mathcal{F}(N,\Delta M=1)} = \frac{1}{2}\begin{pmatrix} (\sigma_z)_{++} & (\sigma_z)_{-+} \\ (\sigma_z)_{+-} & (\sigma_z)_{--} \end{pmatrix} = \frac{1}{2}\begin{pmatrix} -\sin\theta\cos\theta & -\sin^2\theta \\ \cos^2\theta & \sin\theta\cos\theta \end{pmatrix}, \tag{C.55}$$

which is the same as for the case of the fluorescence triplet[4], (C.37). We can therefore expect the same transition rates as above. However, to account for the peaks in the spectra of Rabi oscillations, we necessarily have to invoke timescales during which coherence is still present in the system, $t \approx 1/\Gamma_{\text{spin}}$. Thus, we consider the initial conditions of doubly dressed qubit for this transitory regime, $\rho(0) = |m_s = 0\rangle\langle m_s = 0|$, due to the laser induced polarization of the spin in its ground state. To find $\langle\sigma_z[\Omega]\rangle$, we consider

$$\begin{aligned} \langle\sigma_z[\Omega]\rangle = \; & \underbrace{\langle(\sigma_z)_{--}|-_{N,M}\rangle\langle -_{N,M-1}|\rangle + \langle(\sigma_z)_{++}|+_{N,M}\rangle\langle +_{N,M-1}|\rangle}_{\text{central component}} \\ & + \underbrace{\langle(\sigma_z)_{-+}|-_{N,M}\rangle\langle +_{N,M-1}|\rangle}_{\text{lower sideband}} \\ & + \underbrace{\langle(\sigma_z)_{+-}|+_{N,M}\rangle\langle -_{N,M-1}|\rangle}_{\text{upper sideband}} \\ = \; & (\sigma_z)_{--}\mathrm{Tr}\left\{|-_{N,M}\rangle\langle -_{N,M-1}|\rho\right\} + (\sigma_z)_{++}\mathrm{Tr}\left\{|+_{N,M}\rangle\langle +_{N,M-1}|\rho\right\} \\ & + (\sigma_z)_{-+}\mathrm{Tr}\left\{|-_{N,M}\rangle\langle +_{N,M-1}|\rho\right\} \\ & + (\sigma_z)_{+-}\mathrm{Tr}\left\{|+_{N,M}\rangle\langle -_{N,M-1}|\rho\right\} \end{aligned} \tag{C.56}$$

We can make use of equations (C.32) when writing

$$\begin{aligned} \langle\sigma_z[\Omega]\rangle = \; & (\sigma_z)_{--}\rho^1_{--}[\Omega] + (\sigma_z)_{++}\rho^1_{++}[\Omega] \\ & + (\sigma_z)_{-+}\rho^1_{+-}[\Omega] \\ & + (\sigma_z)_{+-}\rho^1_{-+}[\Omega]. \end{aligned} \tag{C.57}$$

---

[4] The two matrices are the same except for a swapping of the off-diagonal entries, which is due to convention: In case of the singly dressed qubit, $|-_N\rangle$ is energetically higher than $|+_N\rangle$, whereas in the doubly dressed qubit $|+_{N,M}\rangle$ is energetically higher than $|-_{N,M}\rangle$.

Inserting the Fourier transform for the damped oscillations first, see footnote 2, and subsequently the trasition rates (C.55), we have

$$\begin{aligned}
\langle\sigma_z[\Omega]\rangle = &+\frac{(\sigma_z)_{--}}{2\pi}\left(\frac{\rho^1_{--}(0)-\Gamma_{+\to-}/\Gamma_{\text{pop}}}{\Gamma_{\text{pop}}+i(\Omega-\Omega_{\text{m}})}+\frac{\Gamma_{+\to-}}{\Gamma_{\text{pop}}}\delta_{\Omega,\Omega_{\text{m}}}\right)\\
&+\frac{(\sigma_z)_{++}}{2\pi}\left(\frac{\rho^1_{++}(0)-\Gamma_{-\to+}/\Gamma_{\text{pop}}}{\Gamma_{\text{pop}}+i(\Omega-\Omega_{\text{m}})}+\frac{\Gamma_{-\to+}}{\Gamma_{\text{pop}}}\delta_{\Omega,\Omega_{\text{m}}}\right)\\
&+\frac{(\sigma_z)_{-+}}{2\pi}\frac{\rho^1_{+-}(0)}{\Gamma_{\text{coh}}+i(\Omega-\Omega_{\text{m}}-\Delta_{N,M})}\\
&+\frac{(\sigma_z)_{+-}}{2\pi}\frac{\rho^1_{-+}(0)}{\Gamma_{\text{coh}}+i(\Omega-\Omega_{\text{m}}+\Delta_{N,M})}\\
= &+\frac{\sin\theta\cos\theta}{2\pi}\left(\frac{\rho^1_{--}(0)-\Gamma_{+\to-}/\Gamma_{\text{pop}}}{\Gamma_{\text{pop}}+i(\Omega-\Omega_{\text{m}})}+\frac{\Gamma_{+\to-}}{\Gamma_{\text{pop}}}\delta_{\Omega,\Omega_{\text{m}}}\right)\\
&-\frac{\sin\theta\cos\theta}{2\pi}\left(\frac{\rho^1_{++}(0)-\Gamma_{-\to+}/\Gamma_{\text{pop}}}{\Gamma_{\text{pop}}+i(\Omega-\Omega_{\text{m}})}+\frac{\Gamma_{-\to+}}{\Gamma_{\text{pop}}}\delta_{\Omega,\Omega_{\text{m}}}\right)\\
&-\frac{\sin^2\theta}{2\pi}\frac{\rho^1_{+-}(0)}{\Gamma_{\text{coh}}+i(\Omega-\Omega_{\text{m}}-\Delta_{N,M})}\\
&+\frac{\cos^2\theta}{2\pi}\frac{\rho^1_{-+}(0)}{\Gamma_{\text{coh}}+i(\Omega-\Omega_{\text{m}}+\Delta_{N,M})}\\
= &+\frac{\sin\theta\cos\theta}{2\pi}\left(\frac{\rho^1_{--}(0)-\rho^1_{++}(0)+(\Gamma_{-\to+}-\Gamma_{+\to-})/\Gamma_{\text{pop}}}{\Gamma_{\text{pop}}+i(\Omega-\Omega_{\text{m}})}+\frac{\Gamma_{+\to-}-\Gamma_{-\to+}}{\Gamma_{\text{pop}}}\delta_{\Omega,\Omega_{\text{m}}}\right)\\
&-\frac{\sin^2\theta}{2\pi}\frac{\rho^1_{+-}(0)}{\Gamma_{\text{coh}}+i(\Omega-\Omega_{\text{m}}-\Delta_{\text{Mollow}})}\\
&+\frac{\cos^2\theta}{2\pi}\frac{\rho^1_{-+}(0)}{\Gamma_{\text{coh}}+i(\Omega-\Omega_{\text{m}}+\Delta_{\text{Mollow}})}.
\end{aligned} \tag{C.58}$$

We explicitly calculate the initial values of the coherences using $\rho(0)=|0\rangle\langle 0|$ and find

$$\begin{aligned}
\rho^1_{+-}(0) &= \langle +_{N,M-1}|\rho|-_{N,M}\rangle = \sin^2\theta\sin\alpha\cos\alpha = \frac{1}{2}\sin^2\theta\\
\rho^1_{-+}(0) &= \langle -_{N,M-1}|\rho|+_{N,M}\rangle = -\cos^2\theta\sin\alpha\cos\alpha = -\frac{1}{2}\cos^2\theta\\
\rho^1_{--}(0) &= \langle -_{N,M-1}|\rho|-_{N,M}\rangle = -\cos\theta\sin\theta\sin\alpha\cos\alpha = -\frac{1}{2}\cos\theta\sin\theta\\
\rho^1_{++}(0) &= \langle +_{N,M-1}|\rho|+_{N,M}\rangle = \cos\theta\sin\theta\sin\alpha\cos\alpha = \frac{1}{2}\cos\theta\sin\theta.
\end{aligned} \tag{C.59}$$

We thus finally arrive at the spectra of Rabi oscillations:

$$\begin{aligned}
\langle\sigma_z[\Omega]\rangle = &+\frac{\sin\theta\cos\theta}{2\pi}\left(\frac{-\sin\theta\cos\theta+(\Gamma_{-\to+}-\Gamma_{+\to-})/\Gamma_{\text{pop}}}{\Gamma_{\text{pop}}+i(\Omega-\Omega_{\text{m}})}+\frac{\Gamma_{+\to-}-\Gamma_{-\to+}}{\Gamma_{\text{pop}}}\delta_{\Omega,\Omega_{\text{m}}}\right) \qquad \text{(C.60)}\\
&-\frac{\sin^4\theta}{4\pi}\frac{1}{\Gamma_{\text{coh}}+i(\Omega-\Omega_{\text{m}}-\Delta_{\text{Mollow}})}\\
&-\frac{\cos^4\theta}{4\pi}\frac{1}{\Gamma_{\text{coh}}+i(\Omega-\Omega_{\text{m}}+\Delta_{\text{Mollow}})}.
\end{aligned}$$

The spectrum is a sum of three Lorentzians, where the sidebands have weights $\cos^4\theta/2$ and $\sin^4\theta/2$ (for the lower component centered at $\Omega_{\text{m}}-\Delta_{N,M}$ and upper component, centered at $\Omega_{\text{m}}+\Delta_{N,M}$, respectively) and width Γ_{coh}. The central peak is composed of a Lorentzian of width Γ_{pop} and a monochromatic component, both centered at Ω_{m}. Their total weight is $\sin^2\theta\cos^2\theta$, see Figure C.2.

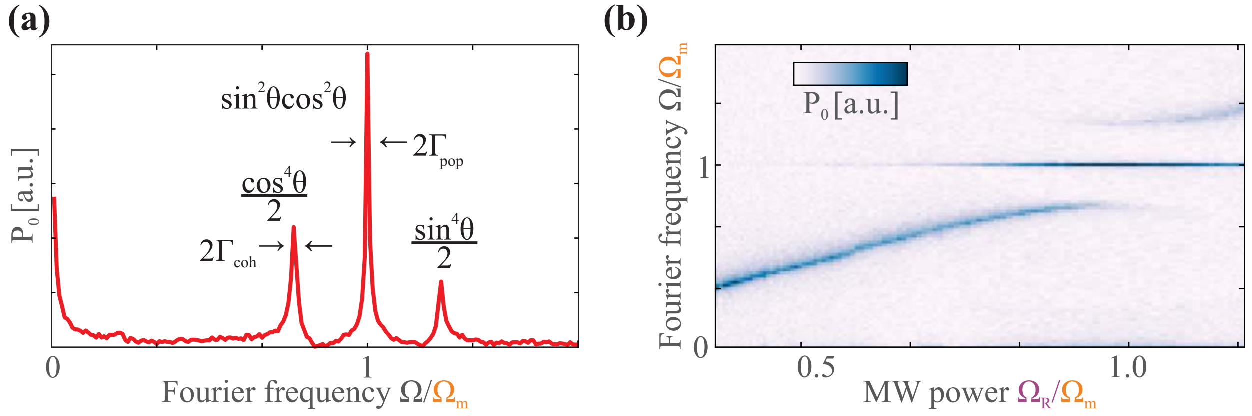

Figure C.2: Measurement of the phononic Mollow triplet. **(a)** Rabi oscillation spectra taken at $\Omega_{\mathrm{R}} = \Omega_{\mathrm{m}}$ showing the triple peak spectra. **(b)** Rabi spectra as a function of the Rabi frequency.

Remark 1: Signs

With our definition of the σ_z matrix

$$\sigma_z = \begin{pmatrix} 1 & 0 \\ 0 & 0 \end{pmatrix}$$

a measurement of the ground state population always yields zero:

$$\langle 0|\sigma_z(t)|0\rangle = 0 \quad \forall t. \tag{C.61}$$

Since the basis is complete,

$$\langle \sigma_z[\Omega]\rangle = P_1, \quad P_0 = 1 - \langle \sigma_z[\Omega]\rangle\,. \tag{C.62}$$

Expression (C.60) therefore reflects the spectra of the excited state population and we find the ground state population by multiplying all oscillating components by -1 and subtracting 1 from the zero frequency component. The value $P_{|0\rangle}(\Omega = 0)$ reflects the steady state population and is $P_{|0\rangle}(\Omega = 0) = 0.5$.

Remark 2: Finite acquisition times

Because in experiment and simulations we have finite measurement times T, spectra of Rabi oscillations

$$\langle \sigma_z[\Omega]\rangle_T \equiv \int_0^T \langle \sigma_z(t)\rangle\, e^{i\Omega t}\,\mathrm{d}t, \tag{C.63}$$

are re-scaled by a common prefactor $\langle \sigma_z[\Omega]\rangle_T = \frac{1}{T}\langle \sigma_z[\Omega]\rangle$. The notation $\langle \sigma_z[\Omega]\rangle_T$ has been dropped and $\langle \sigma_z[\Omega]\rangle$ is written instead throughout the main text. However, the factor $\frac{1}{T}$ is taken into account for the analysis of the simulations.

Remark 3: Cascade and ascension

For the linewidths at $\delta = 0$, we find

$$\Gamma_{\mathrm{pop}} = 2\Gamma_{\mathrm{spin}}\left(\sin^4\theta + \cos^4\theta\right), \tag{C.64}$$

$$\Gamma_{\mathrm{coh}} = 2\Gamma_{\mathrm{spin}}\left(\frac{1}{2} + \sin^2\theta\cos^2\theta\right). \tag{C.65}$$

Here, we have replaced Γ by $2\Gamma_{\mathrm{spin}}$, which reflects the fact that the steady state population of the spin is not 0 but 0.5 and that the spin is not only cascading downwards but also upwards.

Final expression for the Mollow triplet

We finally state the complete analytic expression of the Mollow triplet at $\delta = 0$:

$$\begin{aligned}\langle\sigma_z[\Omega]\rangle_T = \frac{1}{2\pi T}\Bigg(& \frac{\sin^2\theta\cos^2\theta}{2\pi}\frac{1}{\Gamma_{\mathrm{pop}} + i(\Omega - \Omega_{\mathrm{m}})} \\ & + \frac{\sin^4\theta}{4\pi}\frac{1}{\Gamma_{\mathrm{coh}} + i(\Omega - \Omega_{\mathrm{m}} - \Delta_{\mathrm{Mollow}})} \\ & + \frac{\cos^4\theta}{4\pi}\frac{1}{\Gamma_{\mathrm{coh}} + i(\Omega - \Omega_{\mathrm{m}} + \Delta_{\mathrm{Mollow}})} \\ & + 0.5\delta_{\Omega,0}\Bigg),\end{aligned} \tag{C.66}$$

with

$$\begin{aligned}\Delta_{\mathrm{Mollow}} =& \sqrt{(\Omega_{\mathrm{m}} - \Omega_{\mathrm{R}})^2 + \left(\frac{\delta\omega_0}{2}\right)^2}, \\ \theta =& \frac{1}{2}\arctan\left(\frac{\delta\omega_0/2}{\Omega_{\mathrm{m}} - \Omega_{\mathrm{R}}}\right), \\ \Gamma_{\mathrm{pop}} =& 2\Gamma_{\mathrm{spin}}\left(\sin^4\theta + \cos^4\theta\right), \\ \Gamma_{\mathrm{coh}} =& 2\Gamma_{\mathrm{spin}}\left(\frac{1}{2} + \sin^2\theta\cos^2\theta\right).\end{aligned}$$

Appendix D

Higher order couplings of the MW dressed states

D.1 Coupling Hamiltonian

D.1.1 Reduction to the dressed spin picture

We consider a spin dressed by a MW field and parametrically coupled to the motion of a mechanical oscillator, with coupling Hamiltonian

$$H_{\text{int}} = \hbar g_z \sigma_z \left(a^\dagger + a \right). \tag{D.1}$$

The spin evolution is

$$\begin{aligned} \langle \sigma_z(t) \rangle &= \mathrm{Tr}\left\{ \rho \sigma_z \right\} \\ &= \sum_{\substack{\alpha=\pm \\ \beta=\pm \\ M \\ N}} \langle \alpha_N | \rho | \beta_M \rangle \underbrace{\langle \beta_M | \sigma_z | \alpha_N \rangle}_{\text{A}}. \end{aligned} \tag{D.2}$$

All terms in the sum for which $N \neq M$ vanish, such that

$$\begin{aligned} \langle \sigma_z(t) \rangle &= \sum_{\substack{\alpha=\pm \\ \beta=\pm \\ N}} \langle \alpha_N | \rho | \beta_N \rangle \langle \beta_N | \sigma_z | \alpha_N \rangle \\ &= \sum_N \mathrm{Tr} \left\{ \rho^{(N)} \sigma_z \big|_{\mathcal{E}(N)} \right\}, \end{aligned} \tag{D.3}$$

where $\rho^{(N)}$ is the density matrix of the N^{th} multiplicity,

$$\rho^{(N)} = \begin{pmatrix} \rho^N_{++} & \rho^N_{+-} \\ \rho^N_{-+} & \rho^N_{--} \end{pmatrix}. \tag{D.4}$$

In particular, we find that

$$\langle \sigma_z(t) \rangle = \sum_N \cos^2 \theta_N \rho^{(N)}_{--} + \sin^2 \theta_N \rho^{(N)}_{++} - \cos \theta_N \sin \theta_N (\rho^{(N)}_{+-} + \rho^{(N)}_{-+}), \tag{D.5}$$

which reduces to

$$\begin{aligned}\langle \sigma_z(t)\rangle &= \frac{1}{2}\sum_N(\rho_{--}^{(N)}+\rho_{++}^{(N)})-\frac{1}{2}\sum_N(\rho_{+-}^{(N)}+\rho_{-+}^{(N)}) \\ &= \frac{1}{2}(\pi_-+\pi_+)-\frac{1}{2}(\sigma_{+-}+\sigma_{-+}) \qquad \text{(D.6)} \\ &= \frac{1}{2}-\frac{1}{2}(\sigma_{+-}+\sigma_{-+}). \qquad \text{(D.7)}\end{aligned}$$

in case of resonant pumping ($\delta = 0$). Here we have defined the reduced populations $\pi_\pm = \sum_N \rho_{\pm\pm}^{(N)}$ and coherence $\sigma_{+-} = \sum_N \rho_{+-}^{(N)}$, which illustrates that we can introduce an effective two level system which describes the MW dressed qubit.

In the basis of MW dressed states (assuming a coherent state with large MW photon number N, such that $\sqrt{N} \gg 1$), our considerations can be restricted to the reduced density matrix $\rho^{(N)}$, for which H_int is transformed into

$$\begin{aligned}H_{\text{int}}^{(N)} &= \frac{1}{2}\hbar g_z\left(\mathbb{I}^{(N)}-\sigma_x^{(N)}\right)(a^\dagger+a) \\ &= \frac{1}{2}\hbar g_z\Bigg(\underbrace{\mathbb{I}^{(N)}\left(a^\dagger+a\right)}_{\text{Vertical coupling}}-\underbrace{\left(\sigma_+^{(N)}a+\sigma_-^{(N)}a^\dagger\right)}_{\text{Resonant coupling}}-\underbrace{\left(\sigma_+^{(N)}a+\sigma_-^{(N)}a^\dagger\right)}_{\text{Non-resonant coupling}}\Bigg)\end{aligned} \qquad \text{(D.8)}$$

We identify three terms. The resonant coupling terms create the doubly dressed eigenstates $|\pm_M\rangle$. The non-resonant coupling terms occur at an energy penalty of $2\hbar\Omega_\text{m}$ and lead to the Bloch-Siegert shift. The vertical couplings do not change the spin state and correspond to descent or ascent of the phonon ladder. They are marked as the entries D and A in Figure D.1 **(a)**, respectively. However, they also only appear with an energy penalty, $\hbar\Omega_\text{m}$. Here we are interested in their effect on the doubly dressed state. Because of the energy penalty, we consider that they have a higher order effect, perturbing the eigenstates $|\pm\rangle_M$, created by the couplings shown in Figure D.1 **(b)**.

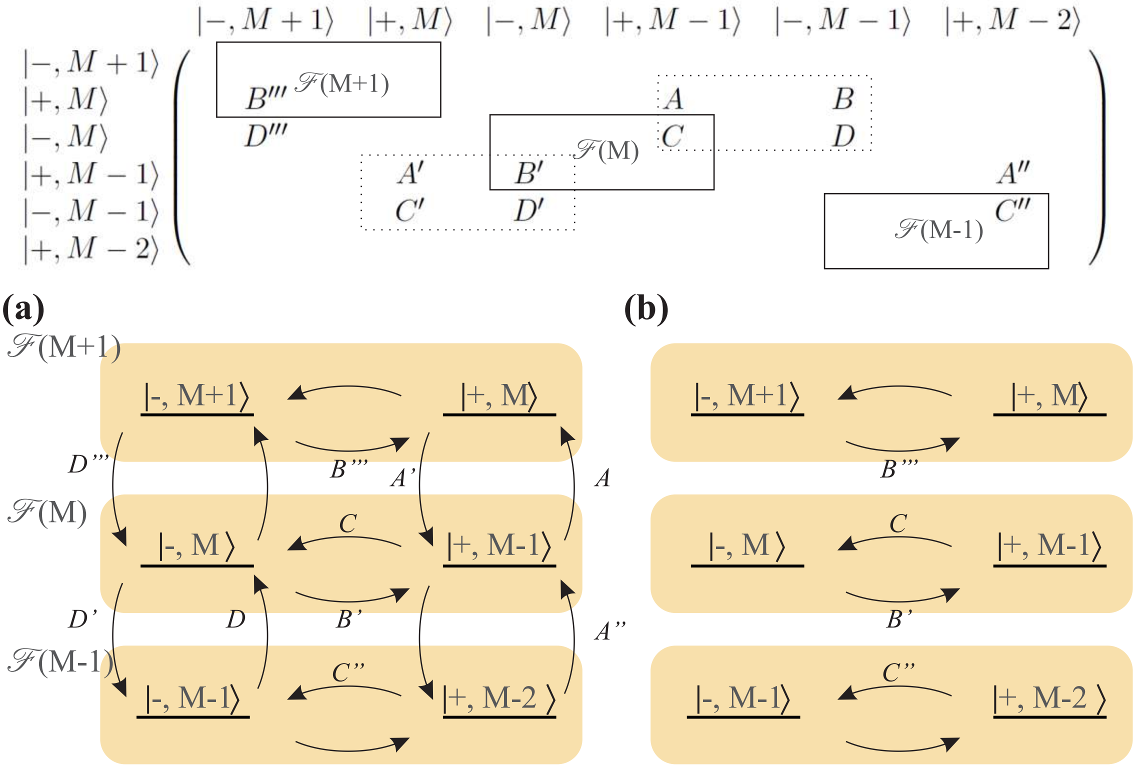

Figure D.1: Effect of the hybrid Hamiltonian ion the $|\pm\rangle$ basis. The above table presents the matrix elements of the $(\hat{a}^\dagger + \hat{a})\sigma_z$ interaction Hamiltonian in the $|\pm\rangle$ basis, underlining the transitions induced inside and outside the $\mathcal{F}(M) = \{|+, M-1\rangle, |-, M\rangle\}$ multiplicities appearing in the second dressing. These transitions are visualized in the energy diagram in **(a)**. Panel **(b)** highlights the intra-multiplicity transitions, which are left after the rotating wave approximation. The label N for the photon number was omitted as there is no coupling between the multiplicities $\mathcal{E}_N$.

D.1.2 Horizontal couplings

The horizontal couplings create the eigenstates for each multiplicity $\mathcal{F}_M$, where we have

$$|+_M\rangle = \cos\theta|+, M-1\rangle + \sin\theta|-, M\rangle, \tag{D.9}$$

$$|-_M\rangle = -\sin\theta|+, M-1\rangle + \cos\theta|-, M\rangle. \tag{D.10}$$

The energy of the dressed states is $E = \pm\Delta_{\text{Mollow}}/2$. Here, we have neglected the term $\left(\sigma_+^{(N)} a + \sigma_-^{(N)} a^\dagger\right)$. We also see, that the vertical coupling can induce transitions between the doubly dressed states of different multiplicities, because the operator $\left(a^\dagger + a\right)$ changes the phonon number.

D.2 Vertical couplings

D.2.1 Perturbation approach

Using a first order perturbation approach, we have new eigenstates $|\widetilde{\pm_M}\rangle$ due to the coupling term $V = \frac{1}{2}\hbar g_z \mathbb{I}^{(N)} \left(a^\dagger + a\right)$. In terms of the old eigenstates $|\pm_M\rangle$:

$$\begin{aligned} |\widetilde{n}\rangle =& |n^{(0)}\rangle + |n^{(1)}\rangle, \\ |n^{(0)}\rangle =& |\pm_M\rangle, \\ |n^{(1)}\rangle =& \sum_{k\neq n} \frac{\langle k^{(0)}|V|n^{(0)}\rangle}{E_n^{(0)} - E_k^{(0)}} |k^{(0)}\rangle. \end{aligned}$$

We consider explicitly $|\widetilde{+_M}\rangle$, with the correction $|\pm_M^{(1)}\rangle$. V couples $|+_M\rangle$ to $\Big\{|-_{M-1}\rangle, |-_{M+1}\rangle, |+_{M-1}\rangle, |+_{M+1}\rangle\Big\}$. It turns out that the coupling elements of transitions changing the dressed state level have evaluate to zero. We have

$$|\pm_M^{(1)}\rangle = \frac{\delta\omega_0}{2\Omega_\mathrm{m}} \left(|\pm_{M-1}\rangle - |\pm_{M+1}\rangle\right) \tag{D.11}$$

$$|\widetilde{\pm_M}\rangle = |\pm_M\rangle + \frac{\delta\omega_0}{2\Omega_\mathrm{m}} \left(|\pm_{M-1}\rangle - |\pm_{M+1}\rangle\right) \tag{D.12}$$

$$\tag{D.13}$$

The energy correction from V in first order is zero:

$$E^{(1)} = \langle \pm_M|V|\pm_M\rangle = 0. \tag{D.14}$$

The second order term is found from

$$E^{(2)} = \sum_{k\neq n} \frac{\|\langle k^{(0)}|V|n^{(0)}\rangle\|^2}{E_n^{(0)} - E_k^{(0)}}. \tag{D.15}$$

It also evaluates to zero. This can be seen by noticing from equation (D.11) that the two contributing terms have opposite energy costs ($\pm\frac{\delta\omega_0^2}{2\Omega_\mathrm{m}}$). Thus, the frequencies of the Mollow triplet do not change. However, the transition rates $\langle\widetilde{\epsilon_M}|\sigma_z|\widetilde{\epsilon_{M+1}}\rangle$ are different to $\langle\epsilon_M|\sigma_z|\epsilon_{M+1}\rangle$, because contributions from the multiplicities $\mathcal{F}_{M\pm 2}$ start to play a role.

D.2.2 Transition rates

Explicit calculation of the transition rates is facilitated by noticing that

$$\sigma_z|_{\mathcal{E}(N)} = \begin{pmatrix} \cos^2\theta_N & -\cos\theta_N\sin\theta_N \\ -\cos\theta_N\sin\theta_N & \sin^2\theta_N \end{pmatrix} \overset{\delta=0}{=} \begin{pmatrix} \frac{1}{2} & -\frac{1}{2} \\ -\frac{1}{2} & \frac{1}{2} \end{pmatrix}. \tag{D.16}$$

We find the following transition rates:

$$\begin{aligned} \|\langle\widetilde{+_M}|\sigma_z|\widetilde{+_{M+1}}\rangle\|^2 &= \#\frac{1}{4}\sin^2\theta\cos^2\theta\left(1 + 2\left(\frac{\delta\omega_0}{2\Omega_\mathrm{m}}\right)^2 + \left(\frac{\delta\omega_0}{2\Omega_\mathrm{m}}\right)^4\right) \\ \|\langle\widetilde{-_M}|\sigma_z|\widetilde{-_{M+1}}\rangle\|^2 &= \#\frac{1}{4}\sin^2\theta\cos^2\theta\left(1 + 2\left(\frac{\delta\omega_0}{2\Omega_\mathrm{m}}\right)^2 + \left(\frac{\delta\omega_0}{2\Omega_\mathrm{m}}\right)^4\right) \\ \|\langle\widetilde{+_M}|\sigma_z|\widetilde{-_{M+1}}\rangle\|^2 &= \#\frac{1}{4}\left(\left(\frac{\delta\omega_0}{2\Omega_\mathrm{m}}\right)^2 + \left(1 + \left(\frac{\delta\omega_0}{2\Omega_\mathrm{m}}\right)^2\right)\sin^2\theta\right)^2 \\ \|\langle\widetilde{-_M}|\sigma_z|\widetilde{+_{M+1}}\rangle\|^2 &= \#\frac{1}{4}\left(\left(\frac{\delta\omega_0}{2\Omega_\mathrm{m}}\right)^2 + \left(1 + \left(\frac{\delta\omega_0}{2\Omega_\mathrm{m}}\right)^2\right)\cos^2\theta\right)^2. \end{aligned}$$

Normalization of these rates yields $\# = 1 + 4\left(\frac{\delta\omega_0}{2\Omega_\mathrm{m}}\right)^2 + 5\left(\frac{\delta\omega_0}{2\Omega_\mathrm{m}}\right)^4$.

Appendix E

Generation of numerical Brownian motion

We describe here how the simulated Brownian motion is generated. Notice that all temporal data is defined with respect to microseconds and all frequency data with respect to megahertz.

E.1 Overhead

The simulated Brownian motion is generated by calculating the discrete Fourier transform of the list $X[\Omega]$, where

$$X[\Omega] = \chi[\Omega]\delta F[\Omega].$$

The Langevin force $\delta F[\Omega]$ is spectrally flat with a random phase and is created with the help of a random number generator from the *GNU Scientific Library* (GSL) package. Both, real and imaginary parts of the mechanical susceptibility are defined according to equation (2.16). The complex product $X[\Omega] = \chi[\Omega]\delta F[\Omega]$ is Fourier transformed and saved as a single column list.

```c
#ifndef BrownianMotion_H_INCLUDED
#define BrownianMotion_H_INCLUDED
#include <stdio.h>
#include <stdlib.h>
#include <math.h>
#include <string.h>
#include <gsl/gsl_rng.h>

//Langevin force genration
double gsl_ran_gaussian_ziggurat (gsl_rng *r, double sigma);
double * f_langevin(int len);

//Mechanical susceptibility
double * f_sus_mech(int len_sus , double gamma, double omega, double dt);

//Multiplying lists with complex data
double * f_multiply_complex_lists(double * a, double * b, int len_signal);

//Calculating Fast Fourier Transforms
double * f_forward_fft(double * complex_signal , int len_signal);
double * f_inverse_fft(double * complex_signal , int len_signal);

//Saving a single column list
void f_save_bm(double * list , char * filename , int length_of_array);
#endif
```

Listing E.1: BrownianMotion.h

E.2 Creation of the Langevin force

The function *f_langevin* returns a list of length *len* with temporal data representing white noise with mean value one and rms value zero, generated using the function *gsl_ran_gaussian_ziggurat*. It is necessary to initialize the random number generator with a seed *r*, which is handled by the functions *gsl_rng* and *gsl_rng_set*.

```c
#include <stdio.h>
#include <stdlib.h>
#include <math.h>
#include <string.h>
#include <gsl/gsl_rng.h>
#include "BrownianMotion.h"

/*Creation of a list containing white noise with mean value 0
and rms 1. */
double * f_langevin(int len){
    int k; //Dummy variable for indexing
    double (*l_force) = malloc(sizeof *l_force *len); //Empty list
    //Initialization of the random number generator
    time_t seconds;
    seconds = time (NULL);
    gsl_rng * r = gsl_rng_alloc (gsl_rng_taus);
    gsl_rng_set(r, seconds);
    //List allocation
    for (k=0; k < len ; k++){
        l_force[k] = gsl_ran_gaussian_ziggurat(r, 1.);
    }
    return l_force;
}
```

Listing E.2: Langevin_Force.c

E.3 Definition of the mechanical susceptibility

The mechanical susceptibility is defined as a list *l_sus* of frequencies *o* taking complex values in the positive and negative domain. The frequency step *d_o* is determined from the length of the list *len_sus* (typically 1.6×10^7 entries) and the time step *d_t* (typically 4 ns).

```c
#include <stdio.h>
#include <stdlib.h>
#include <math.h>
#include <string.h>
#include <gsl/gsl_rng.h>
#include "BrownianMotion.h"

#define PI 3.141592653589793
//Use the following commands to handle real and imaginary entries.
#define REAL(z,i) ((z)[2*(i)])
#define IMAG(z,i) ((z)[2*(i)+1])


/*Generate a table with the response of the oscillator in frequency space.
The complex data is organized by alternatingly sequencing real and imaginary parts
belonging to the same frequency value. Moreover, the data is organized using the
convention of the gsl FFT package, meaning that positive frequencies come first,
ordered from largest to zero.*/

double * f_sus_mech(int len_sus, double gm, double o, double d_t){
    int i;//Dummy variable for indexing
```

```
    double d_o = 2.*PI/(len_sus*d_t);//Frequency step
    double (*l_sus) = malloc(sizeof *l_sus *len_sus*2);
    //Allocate values to the list l_sus in the positive frequency domain.
    for (i=0; i <= len_sus/2; i++){
        REAL(l_sus, i) = (o*o - d_o*d_o*i*i)/(
                              (o*o - d_o*d_o*i*i)*(o*o - d_o*d_o*i*i)
                          +   (gm*i*d_o)*(gm*i*d_o)
                                           );
        IMAG(l_sus, i) = (gm*i*d_o)/(
                              (o*o - d_o*d_o*i*i)*(o*o - d_o*d_o*i*i)
                          +   (gm*i*d_o)*(gm*i*d_o)
                               );
    }
    //Allocate values to the list l_sus in the negative frequency domain.
    for (i= -len_sus/2+1; i< 0 ; i++) {
        REAL(l_sus, len_sus + i) = (o*o - d_o*d_o*i*i)/(
                              (o*o - d_o*d_o*i*i)*(o*o - d_o*d_o*i*i)
                          +   (gm*i*d_o)*(gm*i*d_o)
                                                    );
        IMAG(l_sus, len_sus + i) = (gm*i*d_o)/(
                              (o*o - d_o*d_o*i*i)*(o*o - d_o*d_o*i*i)
                          +   (gm*i*d_o)*(gm*i*d_o)
                                            );
    }
    return l_sus;
}
```

Listing E.3: Mech_susceptibility.c

E.4 Definition of the Fourier transforms

Definition of complex multiplication, forward and backward (inverse) Fourier transforms and saving data in a single column list.

```
#include <stdio.h>
#include <math.h>
#include <gsl/gsl_errno.h>
#include <gsl/gsl_fft_complex.h>
#include "BrownianMotion.h"

#define REAL(z,i) ((z)[2*(i)])
#define IMAG(z,i) ((z)[2*(i)+1])
#define PI 3.141592653589793

//Multiplication of complex valued lists
double * f_multiply_complex_lists(double * a, double * b, int len_signal){
    int i;
    double (*data) = malloc(sizeof *data *2*len_signal);

    for (i = 0; i < len_signal; i++){
        REAL(data,i) = REAL(a,i)*REAL(b,i) - IMAG(a,i)*IMAG(b,i);
        IMAG(data,i) = REAL(a,i)*IMAG(b,i) + IMAG(a,i)*REAL(b,i);
    }
    return data;
}

//Forward Fourier transform using the gsl library
double * f_forward_fft(double * l_complex_input, int len_signal){
    int i; //Dummy variable for indexing
    double (*l_data) = malloc(sizeof *l_data *2*len_signal);//l_data will be the FFT
```

```c
    //gsl convention
    gsl_fft_complex_wavetable * wavetable;
    gsl_fft_complex_workspace * workspace;

    //Copying of complex input list l_complex_input
    for (i = 0; i < len_signal; i++){
        REAL(l_data,i) = REAL(l_complex_input,i);
        IMAG(l_data,i) = IMAG(l_complex_input,i);
    }

    //Memomry allocation for FFT procedure
    wavetable = gsl_fft_complex_wavetable_alloc (len_signal);
    workspace = gsl_fft_complex_workspace_alloc (len_signal);
    //Forward FFT
    gsl_fft_complex_forward (l_data, 1, len_signal, wavetable, workspace);
    //Freeing memory
    gsl_fft_complex_wavetable_free(wavetable);
    gsl_fft_complex_workspace_free(workspace);
    return l_data;
}

//Inverse Fourier transform using the gsl library
double * f_inverse_fft(double * l_complex_input, int len_signal){
    int i;//Dummy variable for indexing
    double (*l_data) = malloc(sizeof *l_data *2*len_signal);//l_data will be the iFFT
    //gsl convention
    gsl_fft_complex_wavetable * wavetable;
    gsl_fft_complex_workspace * workspace;

    //Copying of complex input list l_complex_input
    for (i = 0; i < len_signal; i++){
        REAL(l_data,i) = REAL(l_complex_input,i);
        IMAG(l_data,i) = IMAG(l_complex_input,i);
    }

    //Memomry allocation for iFFT procedure
    wavetable = gsl_fft_complex_wavetable_alloc (len_signal);
    workspace = gsl_fft_complex_workspace_alloc (len_signal);
    //Inverse FFT
    gsl_fft_complex_inverse (l_data, 1, len_signal, wavetable, workspace);
    //Freeing memory
    gsl_fft_complex_wavetable_free(wavetable);
    gsl_fft_complex_workspace_free(workspace);
    return l_data;
}

//Saving real data as a single column list
void f_save_bm(double * l_input, char * filename, int length_of_array){
    int n;//Dummy variable for indexing
    FILE *file_var=NULL;//Pointer to file
    file_var = fopen (filename,"w");//Open file
    //Write into file
    for (n=0; n<length_of_array ; n++){
          fprintf(file_var,"%8.5e\n", REAL(l_input, n));
    }
}
```

Listing E.4: ComplexFFT.c

E.5 Brownian motion generation

The main function generates a temporal trace of Brownian motion with radial frequency *omega*, decay rate *gamma*, time step *d_t* and length *len_output*. A temporal trace of the Langevin force is created and transformed into Fourier space. The result is multiplied with the mechanical susceptibility, yielding position values of the thermal oscillator in frequency space. A temporal trace is obtained by Fourier transformation, which is saved as a single column list.

```c
#include <stdio.h>
#include <stdlib.h>
#include <math.h>
#include <string.h>
#include <gsl/gsl_rng.h>
#include "BrownianMotion.h"

#define len_output 16000000
#define PI 3.141592653589793
#define REAL(z,i) ((z)[2*(i)])
#define IMAG(z,i) ((z)[2*(i)+1])

/*Normalization of Brownian temporal data, such that
the root mean square value is one.*/
void * normalize(double *l_data, int len_l_data){
    int k;//Dummy variable for indexing
    double sum = 0.;//Total value counter for l_data squared
    //Summing squares
    for (k=0; k < len_l_data ; k++){
        sum = sum + REAL(l_data , k)*REAL(l_data , k);
    }
    //Calculating rms
    sum = sqrt(sum/(float) (len_l_data));
    //Normalizing rms to one
    for (k=0; k < len_l_data ; k++){
        REAL(l_data , k)=REAL(l_data , k)/sum;
    }
}

/*BM generation function.*/
void * bm(double omega, double gamma, double dt){
    int i;
    double (*c_langevin) = malloc(sizeof *c_langevin *2*len_output);
    double *l_langevin = f_langevin(len_output);//Generating Langevin force
    double *l_sus = f_sus_mech(len_output , gamma, omega, dt);//Generating chi

    //Turn the real list with langevin forces into a complex list
    for (i = 0; i < len_output; i++){
        REAL(c_langevin,i) = l_langevin[i];
        IMAG(c_langevin,i) = 0.0;
    }
    //Convert Langevin force from a temporal into frqeuency data
    double * fft_c_langevin = f_inverse_fft(c_langevin , len_output);
    //Creating list of positions in frequency space, using linear response.
    double * l_x_omega = f_multiply_complex_lists(fft_c_langevin , l_sus , len_output);
    //Freeing memory
    free(fft_c_langevin);
    free(l_sus);
    //Generating list with position in the time domain
    double * l_x_temp = f_forward_fft(l_x_omega , len_output);
    normalize(l_x_temp , len_output);//Normalizing Brownian motion

    //Save as a single column (save_bm)
```

```
    f_save_bm(l_x_temp, "data//filename.txt", len_output);
    free(l_x_temp);//Freeing memory
}

//Main function to call BM generation function
int main(void){
    double dt = 0.004, omega = 2*PI*6, gamma = 2*PI*6./10;
    bm(omega, gamma, dt);
}
```

Listing E.5: BM_generation.c

Appendix F

Slow spin dynamics in the presence of Brownian modulation in the resolved sideband regime

F.1 Spin dynamics in the presence of incoherent energy modulation

In this section we will once again study spin dynamics in the resolved sideband regime using the test system of Chapter 5, employing mechanical oscillators that experience purely thermal excitation. On the one hand, choosing mechanical frequencies much larger than the spin linewidth and the Rabi drive frequency allows us to make clear comparisons to section 3.6.1, where the energy modulation was monochromatic. On the other hand we aim at understanding modifications of the spin dynamics when the mechanical oscillator is coupled weakly compared to the oscillation frequency, a regime relevant to the nanowire experiment of Chapter 4. In this experimental configuration we can neglect effects similar to those leading to the appearance of the phononic Mollow triplet, which was discussed in Chapters 3 and 5. We begin our discussion in the case of a large mechanical quality factor. Experimentally, Rabi oscillations are averaged over many realizations of the emulated Brownian motion. This is ensured by the data acquisition time on the order of 90 min, which is large compared to the Brownian trace of 64 ms. At maximum simulated Rabi pulse durations of 25 μs, each simulated trace of Rabi oscillations represents an average of more than 2500 different realizations of Brownian motion.

F.1.1 Spin dynamics in the resolved sideband regime of good quality mechanical oscillators

In order to distinguish between good and bad quality mechanical oscillators, we recall that coherence properties of Rabi oscillations are lost on a timescale of $1/\Gamma_{\mathrm{spin}} \approx 1\,\mu\mathrm{s}$. For near monochromatic energy modulation, $\Gamma_{\mathrm{m}} \ll \Gamma_{\mathrm{spin}}$, we expect to see little influence of the Brownian motion on the spin dynamics. For a sufficiently strong coupling strength $\delta\omega_{\mathrm{th}} \gg \Gamma_{\mathrm{spin}}$ it should then still be possible to coherently drive Rabi oscillations on the mechanical sidebands. In our simulations we choose to work with a high $Q = 500$ mechanical oscillator of resonance frequency $\Omega_{\mathrm{m}}/2\pi = 8\,\mathrm{MHz}$ and drive strength $\delta\omega_{\mathrm{th}}/2\pi = 3\,\mathrm{MHz}$, while driving Rabi oscillations at frequency $\Omega_{\mathrm{R}}/2\pi = 3\,\mathrm{MHz}$ for a spin with $\Gamma_{\mathrm{spin}} = 0.5\,\mathrm{MHz}$. In Figure F.1 **(a)** we present simulations of driven Rabi oscillations in the coherently driven case ($\Gamma_{\mathrm{m}} = 0$, $\delta\omega_{\mathrm{th}} = \delta\omega_0/\sqrt{2}$) for the purpose of reference. Simulation results for the thermally driven mechanical oscillator are shown in Figure F.1 **(b)**. As can be seen clearly, sidebands are still visible at MW detunings of $\delta = \pm\Omega_{\mathrm{m}}$. It appears, however, that the coherence properties are strongly altered. Comparison of the temporal traces in **(a)** and **(b)** reveals that indeed Rabi oscillations on both, carrier and sidebands, now show reduced contrast and faster decay rate. On the adjacent Fourier traces reduction of contrast and coherence time present themselves as broader peaks of lower amplitudes. The Fourier plot for the Brownian oscillator furthermore reveals a slight shift of the peak position, which is most visible for the $\Omega/2\pi \approx 3\,\mathrm{MHz}$ peak at $\delta = 0$. Figure F.1 **(c)** compares the Rabi oscillation spectra of the monochromatic oscillator (dashed lines) with those obtained for the thermal oscillator (solid lines) for $\delta = 0$ (black) and $\delta = -\Omega_\mathrm{m}$ (red), bringing into evidence the aforementioned alteration of the Rabi peaks. Because we have employed a spectrally narrow mechanical oscillator, we attempt to understand these effects in terms of the amplitude distribution of the mechanical oscillations, as described in section 5.3.2. We first recall expression (3.19) for the temporal evolution of Rabi oscillations in the absence of mechanically induced energy modulation of the spin:

$$P_0(\tau) = A_1 \exp(-\Gamma_\mathrm{static}\tau) + A_2 \exp(-\Gamma_\mathrm{spin}\tau) \cos\left(\Omega_\mathrm{R}^\mathrm{eff}\tau\right).$$

At $\delta = 0$, amplitude A_1 vanishes and the dynamics are decaying oscillations with Fourier representation

$$P_0[\Omega] = \frac{1}{2}\delta[\Omega] + \frac{1}{T}\frac{A_2}{i(\Omega - \Omega_\mathrm{R}) + \Gamma_\mathrm{spin}}, \tag{F.1}$$

where the effective Rabi frequency $\Omega_\mathrm{R}^\mathrm{eff}/2\pi$ corresponds to the drive strength $\Omega_\mathrm{R}/2\pi$. If the monochromatic energy modulation is turned on[1], the effective Rabi frequency is modified by the zeroth order Bessel function, $\Omega_{\mathrm{R},n=0}^\mathrm{eff} \to \Omega_\mathrm{R} J_0\left(\frac{\delta\omega_0}{\Omega_\mathrm{m}}\right)$, which describes the dashed black line in Figure F.1 **(c)**. We now argue that the Lorentzian peaks

$$\mathcal{L}_n[\Omega_\mathrm{R}, \delta\omega_0] = \frac{1}{T}\frac{A_2}{i(\Omega - \Omega_\mathrm{R} J_n\left(\frac{\delta\omega_0}{\Omega_\mathrm{m}}\right)) + \Gamma_\mathrm{spin}} \tag{F.2}$$

are averaged over the amplitude distribution $p^\mathrm{th}(\delta\omega_0)$, defined in (5.17). In other words, at one realization of Rabi oscillations of amplitude $\delta\omega_0^1$ an effective Rabi frequency $\Omega_{\mathrm{R},n=0}^\mathrm{eff} = J_0\left(\frac{\delta\omega_0^1}{\Omega_\mathrm{m}}\right)\Omega_\mathrm{R}$ will be detected. At another instance the oscillation amplitude has changed to $\delta\omega_0^2$ and an effective Rabi frequency $\Omega_{\mathrm{R},n=0}^\mathrm{eff} = J_0\left(\frac{\delta\omega_0^2}{\Omega_\mathrm{m}}\right)\Omega_\mathrm{R}$ will contribute to the average. This simple picture is compromised by the fact that, depending on the detuning δ, the Rabi frequency might approach 0 for very large ($J_0\left(\frac{\delta\omega_0}{\Omega_\mathrm{m}}\right) = 0$ at $\delta\omega \approx 2.4\Omega_\mathrm{m}$) or very small ($J_1\left(\frac{\delta\omega_0}{\Omega_\mathrm{m}}\right) = 0$ at $\delta\omega \approx 0$) oscillation amplitudes, when $\Omega_{\mathrm{R},n}^\mathrm{eff} \lesssim \Gamma_\mathrm{spin}$ the system is not driven coherently. We therefore compare the Rabi spectra obtained for the mechanical sidebands at $\delta = 0, -\Omega_\mathrm{m}$ to the following expression:

$$\sigma_{z,n}^\mathrm{BM}[\Omega] = \mathrm{Re}\left(\int_0^\infty \mathrm{d}\delta\omega_0\, p^\mathrm{th}(\delta\omega_0) F_n[\Omega_\mathrm{R}, \delta\omega_0]\right), \tag{F.3}$$

where $F_n[\Omega_\mathrm{R}, \delta\omega_0]$ is a filtering function

$$F_n[\Omega_\mathrm{R}, \delta\omega_0] = \begin{cases} \mathcal{L}_n[\Omega_\mathrm{R}, \delta\omega_0] & \text{if } J_n\left(\frac{\delta\omega_0}{\Omega_\mathrm{m}}\right)\Omega_\mathrm{R} \geq \Gamma_\mathrm{spin} \\ 0 & \text{otherwise.} \end{cases} \tag{F.4}$$

Such a filtering function only admits coherent driving at large enough effective Rabi frequencies but ignores contributions to the decay at small effective Rabi frequencies. $\sigma_{z,0}^\mathrm{BM}$ and $\sigma_{z,1}^\mathrm{BM}$ are shown as grey traces in Figure F.1 **(c)**. As can be seen, the averaging procedure very well reproduces the spectra obtained from simulations. While $\sigma_{z,0}^\mathrm{BM}$ appears to be very accurate, $\sigma_{z,1}^\mathrm{BM}$ rather provides a qualitative description of peak position and decreased amplitude. We attribute this fact to two simplifications that we have made here. First, we have ignored spectral components due to small effective drive strength.

---

[1] The amplitude A_2 might become slightly less than 1/2 because of a small component emerging at $\Omega = \Omega_\mathrm{m}$ due to off-resonant driving of the phononic Mollow triplet. We will ignore these effects for simplicity here.

Second, we have ignored the fact that, at small oscillation amplitudes $\delta\omega_0$, Rabi oscillations on the sidebands resemble the unperturbed case in absence of a mechanical oscillator. Then, $P_0(\delta = \Omega_\mathrm{m})$ is described by the one component A_1 describing incoherent decay and one coherent oscillation A_2 due to power broadening. While the latter effect stays negligible at $\Omega_\mathrm{R} \ll \Omega_\mathrm{m}$, the competition of the decay term A_1 and the perturbing drive at $J_1\left(\frac{\delta\omega}{\Omega_\mathrm{m}}\right)\Omega_\mathrm{R}$ is visible here as the initial decay of the red trace. Overall, the simulated data can well be reproduced in terms of averaging the Bessel functions that modify the Rabi frequency in case of monochromatic energy modulation, see Figure F.1 **(d)**.

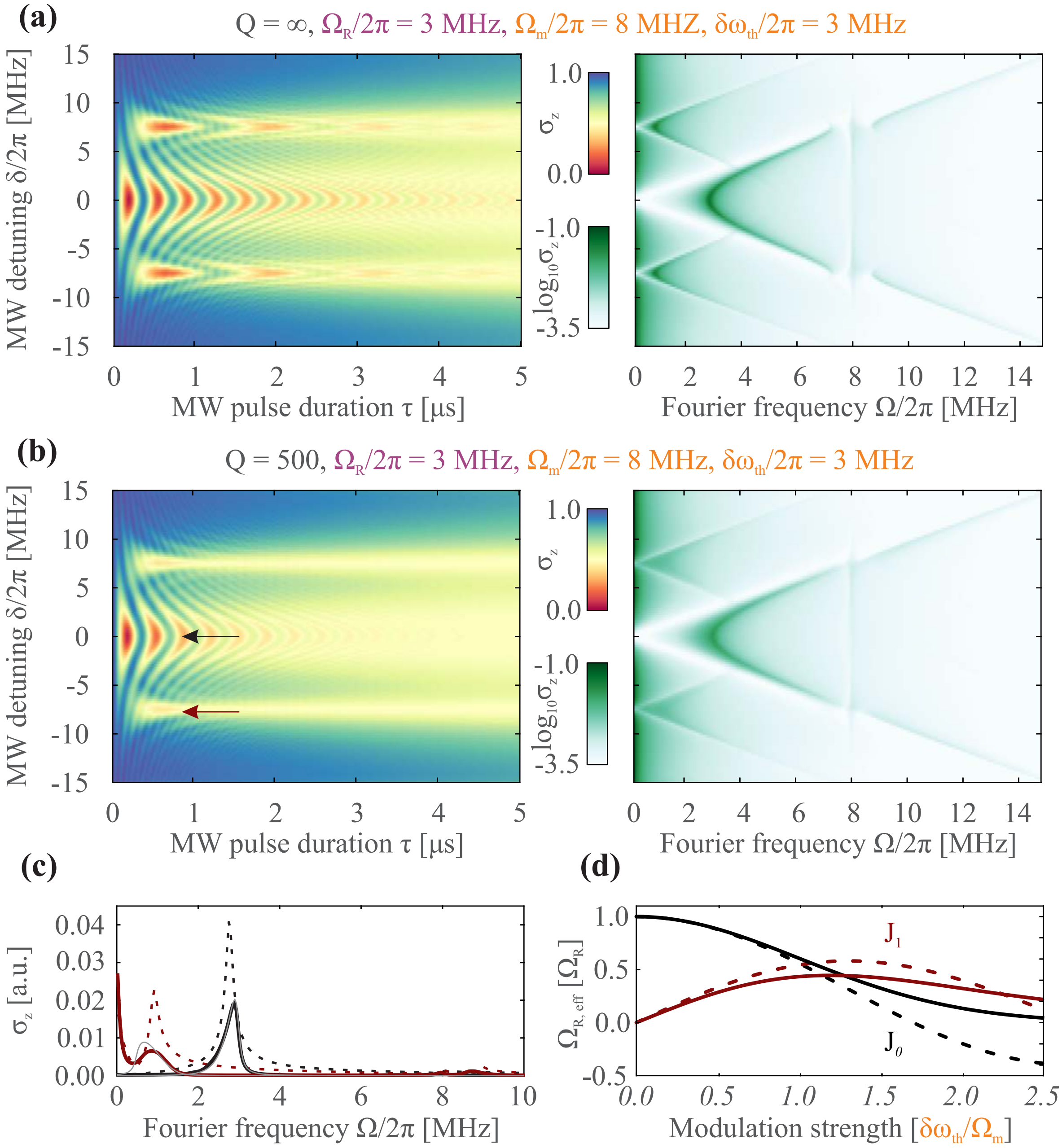

Figure F.1: Simulations of the frequency dependence of Rabi oscillations in the presence of **(a)** coherent and **(b)** large Q thermal modulation. **(c)** Cuts of the Fourier spectra at the sidebands indicated in **(b)** (thick colored lines) compared to the analytic expression (F.3) (gray solid lines). Dashed lines indicate the corresponding Rabi spectra in case of coherent energy modulation as in **(a)**. **(d)** Bessel functions (dashed lines) compared to Bessel functions averaged over $p^{\mathrm{th}}(\delta\omega_0)$.

We verify these findings experimentally by injecting tables of Brownian motion $X(\tau)$, emulating a mechanical oscillator at $\Omega_\mathrm{m}/2\pi = 8\,\mathrm{MHz}$, $\Gamma_\mathrm{m}/2\pi$ ($Q = 500$) into the RF waveguide. With a previously calibrated coupling strength of $\delta\omega_0(\mathrm{V})/2\pi = 4\frac{\mathrm{MHz}}{\mathrm{V}}$ we expect $\delta\omega_\mathrm{th}/2\pi = 3\,\mathrm{MHz}$ at a rms output voltage of $\mathrm{V}_\mathrm{rms} \approx 0.84\,\mathrm{V}$. A preceding measurement of Rabi oscillations yields that a MW output power of 14 dBm produces Rabi oscillations with $\Omega_\mathrm{R}/2\pi = 3\,\mathrm{MHz}$ and $\Gamma_\mathrm{spin} \approx 0.6\,\mathrm{MHz}$ (see the black dashed line in Figure F.2 **(b)**). The measurement is shown in Figure F.2 **(a)** in both, temporal and Fourier representation, demonstrating great qualitative agreement with our numerical data of Figure F.1 **(b)**. Comparisons of the measured Rabi oscillation spectra in **(b)** and **(c)** reveals that expression (F.3) indeed provides a good description of the experimental case: position, height and width of the Fourier peaks are well reproduced for the carrier and both sideband components. Notice that the initial decay that was discussed for the sideband spectra of Figure F.1 **(c)** is absent in F.2 **(c)** due to the reduced resolution of the experimental Fourier traces. Having gained good understanding of the effects related to the amplitude statistics inherent to the thermal drive, we will now discuss consequences of employing low quality mechanical oscillators.

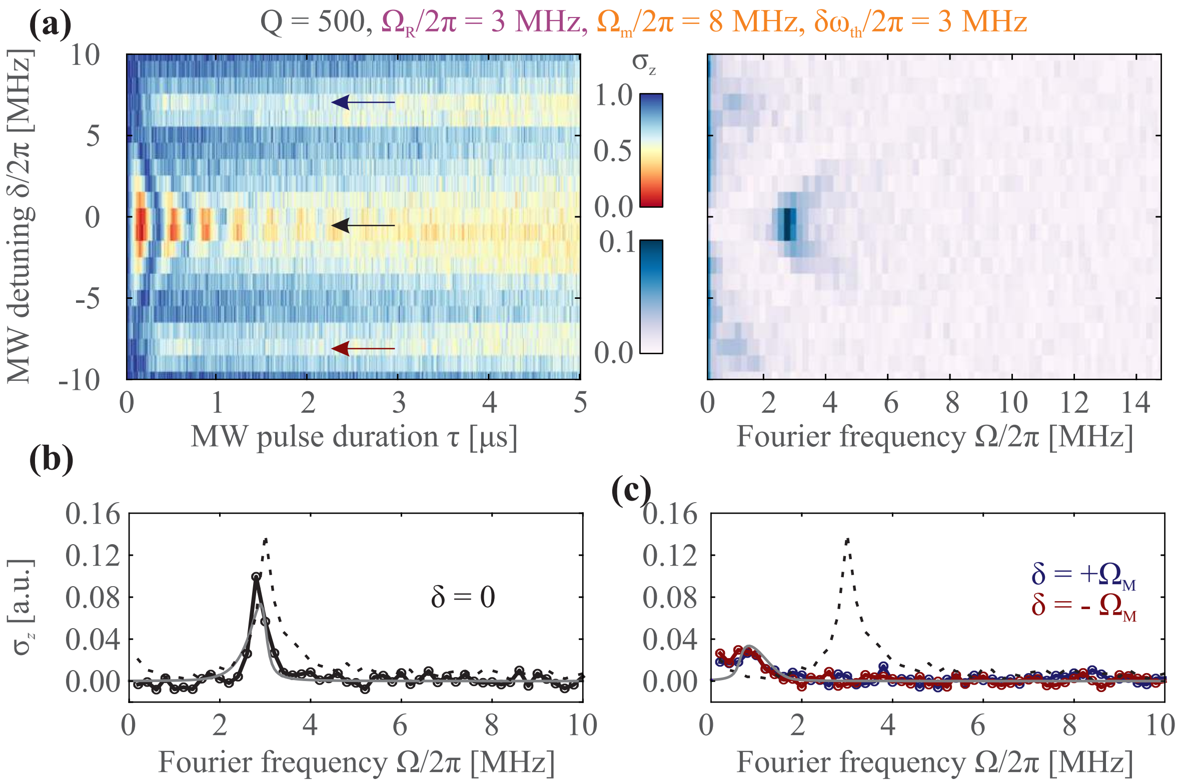

Figure F.2: Rabi detuning experiment in the presence of thermal energy modulation with $Q = 500$. **(a)** Temporal and Fourier data. **(b)** Central Rabi trace ($\delta = 0$) compared to expression (F.3). **(c)** Sideband Rabi traces as indicated in **(a)** compared to expression (F.3). The black dashed line indicates a Rabi measurement at $\delta = 0$ in absence of energy modulation.

F.1.2 Spin dynamics in the resolved sideband regime of bad quality mechanical oscillators

We now simulate Rabi oscillations in the regime of bad mechanical quality factors with the same parameters as above ($\Omega_\mathrm{m}/2\pi = 8\,\mathrm{MHz}$, $\delta\omega_\mathrm{th}/2\pi = 3\,\mathrm{MHz}$, $\Omega_\mathrm{R}/2\pi = 3\,\mathrm{MHz}$). We first compare the temporal traces between realizations for $Q = 100\,(\Gamma_\mathrm{m}/2\pi = 80\,\mathrm{kHz})$ and $Q = 10\,(\Gamma_\mathrm{m}/2\pi = 800\,\mathrm{kHz})$, shown in Figure F.3. Evidently, in both cases spin coherence is preserved, as strong contrast of the oscillations is visible on the carrier as well as the sidebands. However, we see that the perceived decay of Rabi oscillations is slightly enhanced when compared to the large Q case presented in Figures F.1 and F.2. The effect is especially visible on the sidebands, where for $Q = 10$ no full oscillation is observed.

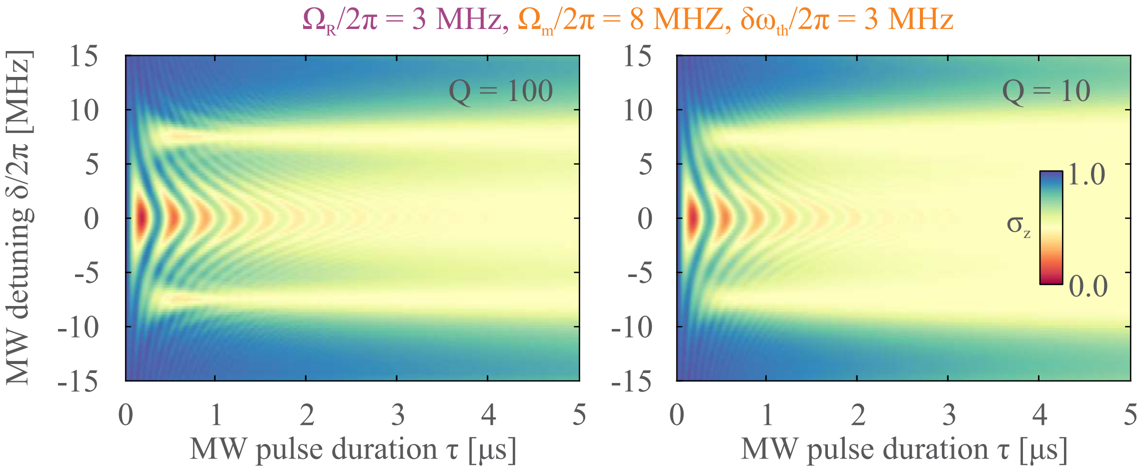

Figure F.3: Distribution of the oscillation amplitude leading to averaged effective Rabi frequencies.

Figures F.4 **(a)** and **(b)** show traces of the spectra taken at $\delta = 0, -\Omega_\mathrm{m}$ compared to the analytic expressions $\sigma_{z,n}^{\mathrm{BM}}$ (F.3). While the overlap between $\sigma_{z,0}^{\mathrm{BM}}$ and the spectrum for Q = 100 is still very high, agreement with $\sigma_{z,1}^{\mathrm{BM}}$ has reduced compared to the large Q case. Further reduction is visible by going to the spectra corresponding to $Q = 10$, where now also $\sigma_{z,0}^{\mathrm{BM}}$ agrees considerably less with the simulation. The numerical spectra are not solely explicable by amplitude averaging, but instead we have to invoke effects of the mechanical linewidth, which becomes comparable here to the decay rate ($\Gamma_\mathrm{spin} = 0.5\,\mathrm{kHz}$). On the one hand we observe a small broadening (along the frequency direction) of the the sidebands in Figure F.3. The effect is however negligible even for bad quality factors as Γ_m stays small compared to Ω_R, which determines the principal width of the Rabi sidebands. On the other hand, the noise spectral density around Ω_R is increased due to the thermal excitation of the mechanical oscillator. Assuming that the mechanical spectral density $S_{\delta\omega_\parallel}^{\mathrm{th}}[\Omega]$ is flat at Ω_R ($\Omega_\mathrm{R} \ll \Omega_\mathrm{m}$), the decay rate of Rabi oscillations increases according to equation (3.23). We have

$$\Gamma_\nu = \pi S_{\delta\omega_\parallel} + S_{\delta\omega_\mathrm{th}}[\Omega_\mathrm{R}^{\mathrm{eff}}], \tag{F.5}$$

with equation (5.2):

$$\begin{aligned} S_{\delta\omega_\parallel}^{\mathrm{th}}[\Omega] &= \frac{\Gamma_\mathrm{m}\Omega_\mathrm{m}^2}{(\Omega_\mathrm{m}^2 - \Omega^2)^2 + \Omega^2\Gamma_\mathrm{m}^2}\delta\omega_\mathrm{th}^2 \\ &= 2\pi\frac{f_\mathrm{m}^2\frac{\Gamma_\mathrm{m}}{2\pi}}{(f_\mathrm{m}^2 - f^2)^2 + f^2\left(\frac{\Gamma_\mathrm{m}}{2\pi}\right)^2}\left(\frac{\delta\omega_\mathrm{th}}{2\pi}\right)^2. \end{aligned}$$

We thus have $\Gamma_\mathrm{spin} \to \Gamma_{\mathrm{spin},n}$, where we define $\Gamma_{\mathrm{spin},n}$ as

$$\Gamma_{\mathrm{spin},n}(\delta = n\Omega_\mathrm{m}) = \Gamma_\mathrm{spin} + \frac{1}{2}S_{\delta\omega_\parallel}^{\mathrm{th}}[\Omega_{\mathrm{R},n}^{\mathrm{eff}}]. \tag{F.6}$$

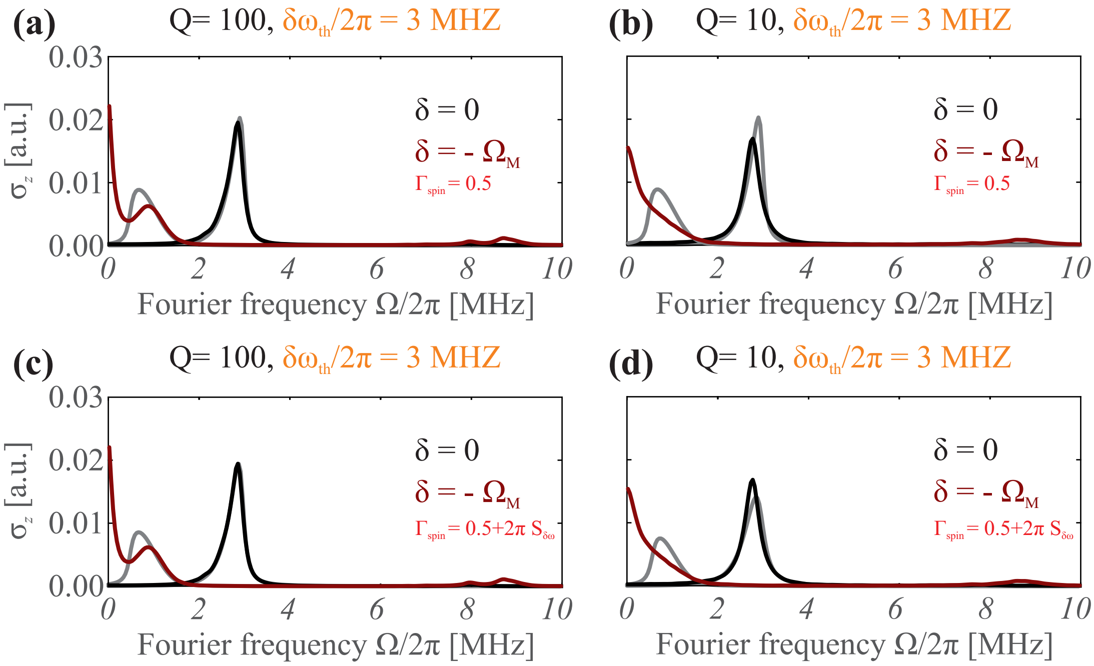

Figure F.4: Improvement of expression (F.3) describing the amplitude averaged Rabi spectra. **(a)** and **(b)** show Rabi spectra (thick solid lines) from the numerical simulations for $Q = 100$ and $Q = 10$, respectively. The gray lines represent expression (F.3). In **(c)** and **(d)** the agreement between numerical data and the analytic expression is improved by injecting $\Gamma_{\text{spin}} \rightarrow \Gamma_{\text{spin},n}$.

The increased noise spectral density leads to enhanced decoherence of Rabi oscillations and therefore to a broadening of the peaks in the Fourier spectra. Injecting $\Gamma_{\text{spin},n}$ in expressions (F.3) and (F.4) we obtain the plots depicted in Figures F.4 **(c)** and **(d)**. The adapted expressions obtained for $\sigma_{z,0}^{\text{BM}}$ now exhibit improved agreement with the simulated data, while the agreement between $\sigma_{z,1}^{\text{BM}}$ and the spectra of the sidebands is still modest[2]. A close look at the evolution of the sideband peak observable when comparing $Q = 100$ with $Q = 10$ shows that the sideband peak is in fact disappearing in the low frequency component with decreasing quality factor. To better understand this effect we repeat the same simulations at increased coupling strength for a value of $\delta\omega_{\text{th}} = 10\,\text{MHz}$.

---

[2] Further improvement of these fits may potentially be obtained by also averaging the Bessel functions $J_n\left(\frac{\delta\omega}{\Omega_{\text{m}}}\right)$ over the spectral density of the mechanical oscillator. The attempt to do so has not been conclusive so far.

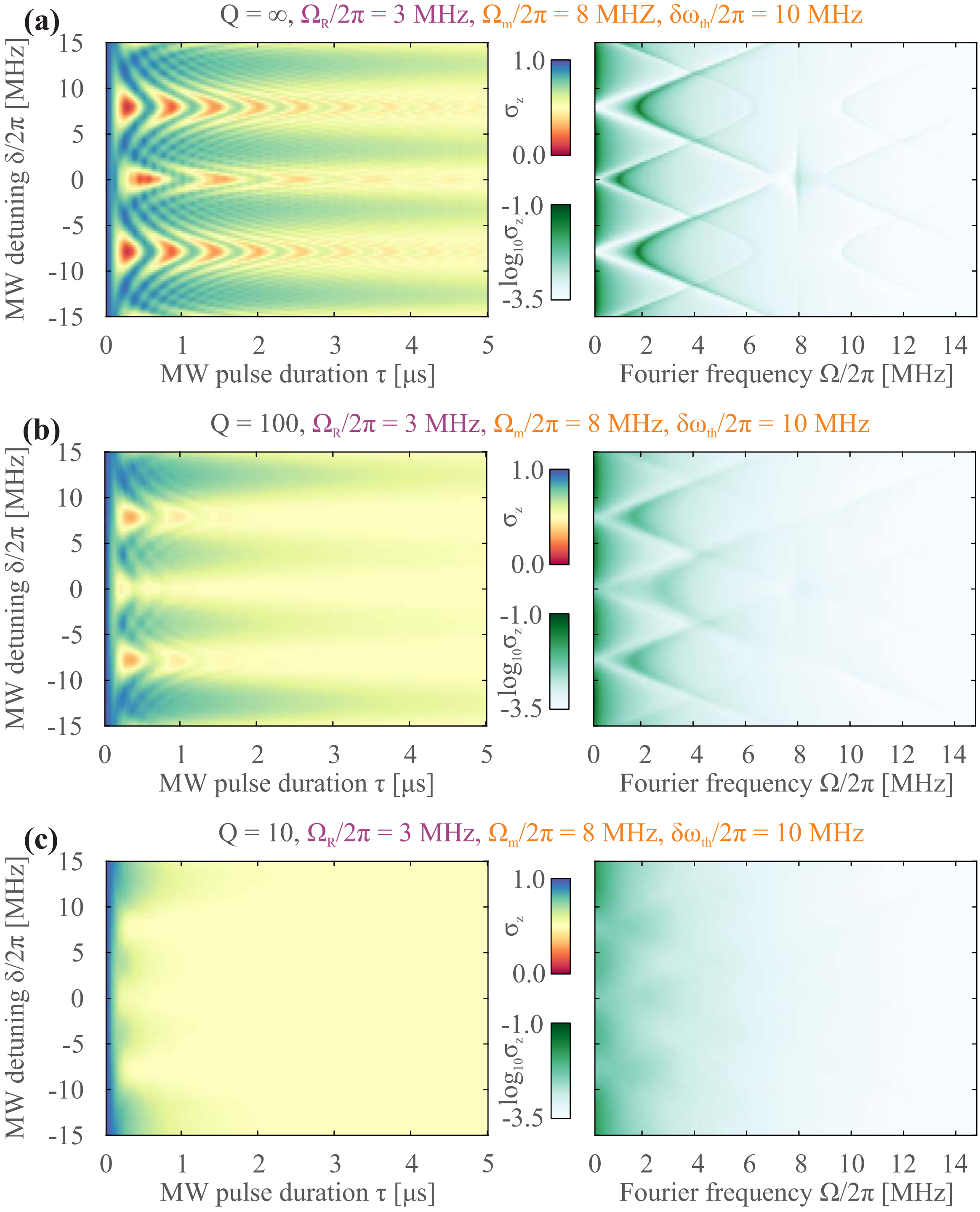

Figure F.5: Distribution of the oscillation amplitude leading to averaged effective Rabi frequencies for lower quality factors in the high temperature regime. **(a)** Coherent modulation. **(b)** $Q = 100$. **(c)** $Q = 10$. For large mechanical dissipation rates, no Rabi oscillations can be driven. The decay observed in **(c)** is much faster than $1/\Gamma_1$.

Comparison of Figures F.3 with Figure F.5 shows that the qualitative difference between the spectra obtained for the two quality factors further increases with $\delta\omega_{\mathrm{th}}$. Both, the temporal as well as the Fourier traces reveal that the driving of coherent oscillations as evidenced in Figure F.6 **(a)** for a moderate quality factor is no longer possible for the strongly coupled bad quality mechanical oscillator in **(b)**. We can understand this difference by considering the noise spectral density $S^{\mathrm{th}}_{\delta\omega_{\parallel}}[\Omega]$ with quadratic dependence on $\delta\omega_{\mathrm{th}}$: for a bad mechanical oscillator the added noise floor at low frequencies is larger compared to a good quality factor by the ratio of the respective mechanical decay rates (see expression (5.2)).

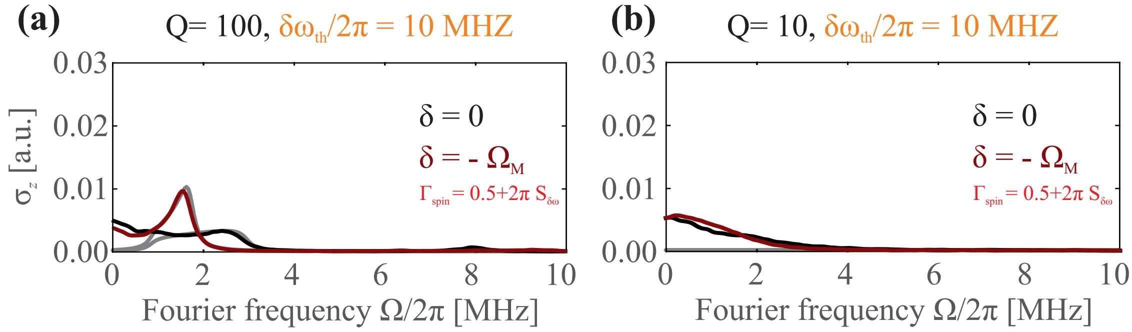

Figure F.6: Rabi spectra in presence of thermal energy modulation the high temperature, low Q regime. The solid lines indicate horizontal cuts taken from Figure F.5 **(b)** and **(c)** for the two quality factors $Q = 100$ (here shown in **(a)**) and $Q = 10$ **(b)**. Grey lines indicate evaluation of expression (F.3). In case of $Q = 10$ pure population decay over a wide range of detunings δ is observed instead of coherent oscillations.

The effect of noise in the system is thus much more severe for larger values of Γ_{m} at the same coupling strength. The case presented in Figures F.3 and F.5 corresponds to power spectral densities shown in Figure F.7 **(a)** and **(b)**, respectively. With the noise level $\Gamma_{\mathrm{spin},n}$ surpassing the drive strength Ω_{R} for $Q = 10$ at $\delta\omega_{\mathrm{th}}/2\pi = 10\,\mathrm{MHz}$, decoherence effects are too strong to drive oscillations coherently.

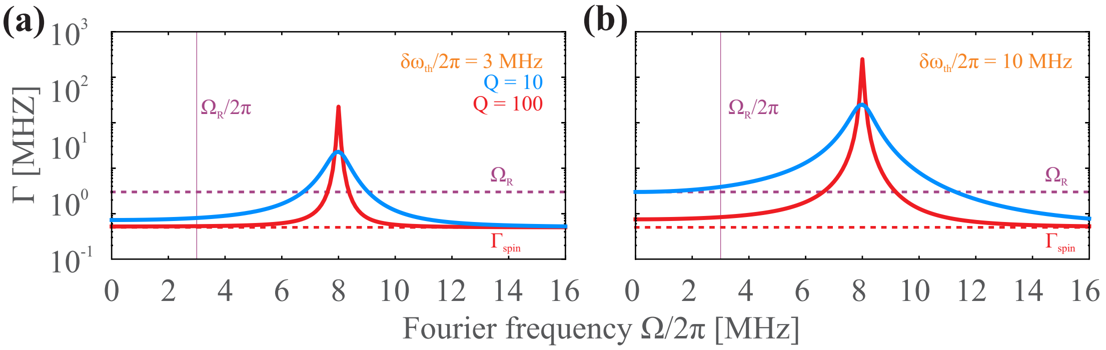

Figure F.7: Noise spectral densities in the low **(a)** and high **(b)** temperature regimes. As the total decay rate Γ surpasses Ω_{R}, no Rabi oscillations can be driven.

The simulation data shows that the coherence properties of the mechanical oscillator directly influence the coherence of the spin. The measurement of Rabi oscillations at constant but sufficiently large coupling strength shows that coherence is lost much more rapidly as the mechanical dissipation increases. We demonstrate this regime experimentally. As before we inject Brownian motion emulated at $\Omega_{\mathrm{m}}/2\pi = 8\,\mathrm{MHz}$ with quality factors $Q = 100$ and $Q = 10$ and drive Rabi oscillations over a large span of detunings δ. The data depicted in Figure F.8 is in very good qualitative agreement with the simulated traces from above. Clearly visible are oscillations at $\Omega^{\mathrm{eff}}_{\mathrm{R},1}/2\pi \approx 2\,\mathrm{MHz}$ and their gradual disappearance as the emulated mechanical oscillator is changed from monochromatic to largely incoherent. In the latter case the spin shows decay to the steady state population of $P_0 = 0.5$ on a time scale much shorter than $1/\Gamma_1$ over a wide range of frequencies. This is characteristic of the weak coupling limit $\Omega_{\mathrm{R}} < \Gamma_{\mathrm{spin}}$, where a monochromatic drive enhances the emission rates of the TLS, leading to accelerated population decay [103]. Notice that we have encountered this regime before in the context of mechanically driving the dressed spin populations, which, for $\delta\omega_0 < \Gamma_{\mathrm{spin}}$, leads to an initial broadening of the oscillating component in Rabi spectra before separation into the Mollow triplet (see section 3.7.5 and Figure 3.45).

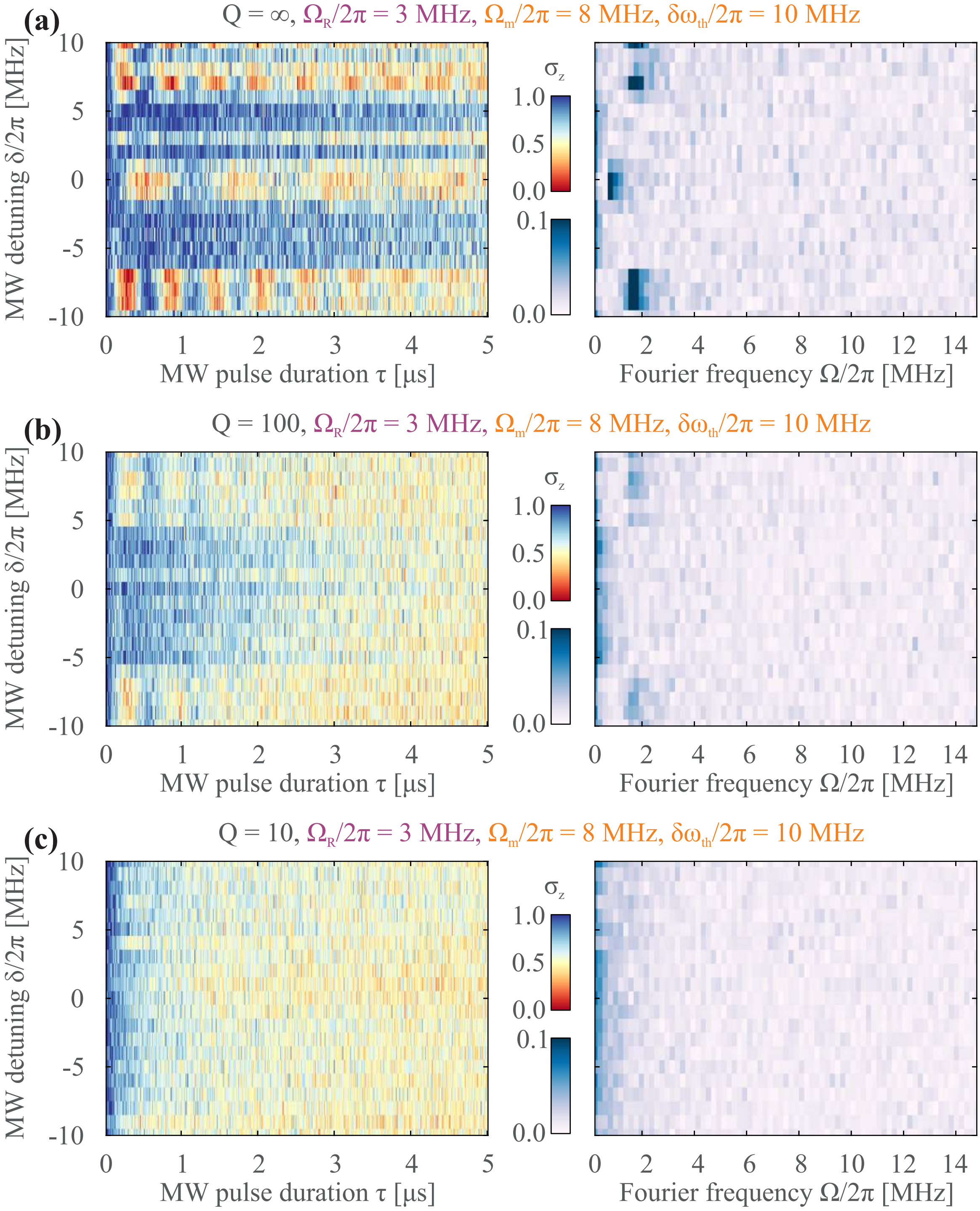

Figure F.8: Experimental measurements. **(a)** The coherent case is presented for comparison. **(b)** $Q = 100$. Rabi oscillations are visibly driven on the mechanical sidebands. At resonance ($\delta = 0$) no contrast is visible, as the effective, averaged Rabi frequency is close to Γ_{spin}. **(c)** $Q = 10$. No Rabi oscillations are visible. The effective decoherence rate is larger than the drive strength and fast population decay is measured, verifying the observation from the numerical data.

In conclusion: In this section we have seen two effects of the mechanical oscillator related to either its amplitude or frequency distribution. First, the temperature dependent amplitude distribution necessitates averaging over $p^{\mathrm{th}}(\delta\omega_0)$, which leads to a shift and broadening of the Rabi peaks in the spectra. The effect is independent of Γ_{m} and Rabi spectra will suffer the temperature related broadening even for very high quality mechanical oscillators. Second, the incoherent energy modulation induces additional decoherence of Rabi oscillations. In extreme cases such coupling can prevent Rabi oscillations when $2\frac{\Gamma_{\mathrm{m}}}{\Omega_{\mathrm{m}}^2}\delta\omega_{\mathrm{th}}^2 \approx \frac{\Omega_{\mathrm{R}}}{2\pi}$.

F.2 ESR spectra with Brownian modulation

We will now extend the above considerations to the steady state regime of the spin dynamics. As we have seen, amplitude averaging of the Brownian oscillator leads to reduction of contrast of the Fourier peaks on the one hand. On the other hand, contrast is decreased due to an increased noise spectral density, which directly depends on the mechanical quality factors Naturally, we expect to find similar signatures in the ODMR spectra of the NV defect. As opposed to the Rabi oscillation protocols, in the ODMR spectra the spin experiences additional decoherence to to optical pumping. For reasonable values of the light intensity, the decoherence rate is on the order of several MHz and is reflected by a linewidth $\delta\nu$. In this sense we are necessarily working with good mechanical oscillators, $\Gamma_{\mathrm{m}} \lesssim \delta\nu$, when operating in the resolved sideband regime of the ODMR measurement: $\Omega_{\mathrm{m}} > \delta\nu$. We start studying the consequences of the Brownian motion on the steady state spin population by performing simulations. We will then turn towards the experimental case, attempting to verify the previously identified signatures.

F.2.1 Simulations

In order to simplify our study and free the simulated ODMR spectra of power broadening effects, we perform the simulations at extremely low values of the MW drive strength. We choose $\Omega_{\mathrm{m}}/2\pi = 8\,\mathrm{MHz}$, $\Omega_{\mathrm{R}} = 0.05\pi\,\mathrm{MHz}$, $\Gamma_1 = 0.1\,\mathrm{MHz}$, $\Gamma_2 = 0.4\,\mathrm{MHz}$, $\Gamma_{\mathrm{c}}^{\infty} = 0\,\mathrm{MHz}$, $s = 0.5$, $\Gamma_{\mathrm{p}} = \Gamma_{\mathrm{p}}^{\infty}\frac{s}{1+s} = 5/3\,\mathrm{MHz}$.

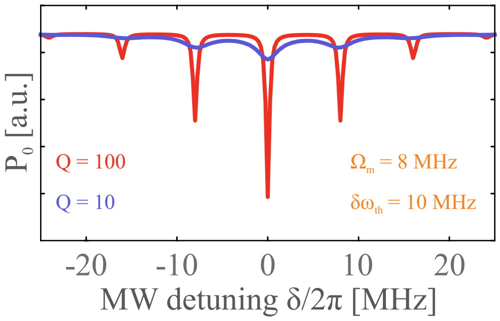

Figure F.9: Simulated spectra showing the ground state population P_0. Sidebands are visibile up to third order for both quality factors $Q = 10$ and $Q = 100$ at $\delta\omega_{\mathrm{th}} = 10\,\mathrm{MHz}$.

As can be seen from Figure F.9, sidebands are visible up to third order for large thermal drive strength $\delta\omega_{\mathrm{th}}$. A significant difference between the two spectra shown for $Q = 100$ and $Q = 10$ is that the increased mechanical linewidth broadens the ODMR peaks and reduces their contrast. We investigate the evolution of both with parameter $\delta\omega_{\mathrm{th}}$ for the central and first order sideband. We fit the numerical spectra with a superposition of Lorentzian lineshapes $\mathcal{L}$ and deduce contrast and linewidth.

$$w(\omega) = 1 - \sum_n \mathcal{L}(\omega - \omega_0 \mp n\Omega_\mathrm{m}, \delta\nu_n, C_n), \tag{F.7}$$

$$\mathcal{L}(\omega_0 \mp n\Omega_\mathrm{m}, \delta\nu_n, C_n) = C_n \frac{\delta\nu_n^2}{(\omega - \omega_0 \mp n\Omega_\mathrm{m})^2 + \delta\nu_n^2}. \tag{F.8}$$

Linewidth

We first inspect the expression for the linewidth (3.6) of the n^th-order sideband, $\delta\nu_n$, in case of monochromatic energy modulation:

$$\delta\nu_n = \frac{1}{2\pi}\sqrt{\tilde{\Gamma}_{2,n}\left(\tilde{\Gamma}_{2,n} + \frac{\Omega_\mathrm{R}^2 J_n^2\left(\frac{\delta\omega_0}{\Omega_\mathrm{m}}\right)}{\tilde{\Gamma}_1}\right)}. \tag{F.9}$$

Since we have chosen a weak drive strength Ω_R, the effects of power broadening can be ignored. Without any dependence on the MW drive strength, amplitude averaging of the Brownian motion has no impact on the linewidth. We are then left with the decoherence rate

$$\delta\nu_n \approx \frac{\tilde{\Gamma}_{2,n}}{2\pi}. \tag{F.10}$$

On the one hand, the decoherence rate $\tilde{\Gamma}_2$ is proportional to the noise spectral density close to zero frequency, which has obtained additional contributions from $S^\mathrm{th}_{\delta\omega_\|}[\Omega]$. We therefore expect an increase of the linewidth due to the thermal motion, such that

$$\tilde{\Gamma}_2 \to \tilde{\Gamma}_2^\mathrm{th} = \tilde{\Gamma}_2 + S^\mathrm{th}_{\delta\omega_\|}[\Omega \approx 0]. \tag{F.11}$$

On the other hand, the position of each sideband depends on the mechanical frequency $\Omega_\mathrm{m}/2\pi$. Due to the mechanical linewidth Γ_m, we can expect that the position of the n^th-order sideband is swept by $n \times \Gamma_\mathrm{m}$. Because $\delta\nu_n$ denotes the HWHM, we assume that

$$\begin{aligned}\tilde{\Gamma}^\mathrm{th}_{2,n} &= \Gamma_2 + \frac{n}{2}\Gamma_\mathrm{m} + S^\mathrm{th}_{\delta\omega_\|}[\Omega \approx 0] + \Gamma_c \\ &\approx \Gamma_2 + \frac{n}{2}\Gamma_\mathrm{m} + \frac{\Gamma_\mathrm{m}}{\Omega_\mathrm{m}^2}\delta\omega_\mathrm{th}^2 + \Gamma_c.\end{aligned} \tag{F.12}$$

Expression (F.12) is compared with the values found from the simulation data in Figure F.10 for the zeroth and first order sideband. We see that the quadratic dependence on $\delta\omega_\mathrm{th}$ is initially well reproduced for the two quality factors $Q = 10$ and $Q = 100$. For large effective temperatures $\delta\omega_\mathrm{th} \gtrsim \Omega_\mathrm{m}$ the predicted behavior (F.12) for $\delta\nu_n$ becomes an underestimate of the values found from simulations. This could be due to the fact that a large $\delta\omega_\mathrm{th}$ strongly modifies the effective Rabi frequency, either due to the off-resonant phonon Mollow triplet or Bloch-Siegert like shifts. In either case, higher order contributions of $\delta\omega_\mathrm{th}$ are not taken into account in the linear dependence of $\tilde{\Gamma}_2$ on $S^\mathrm{th}_{\delta\omega_\|}[\Omega \approx 0]$ originating from a perturbation theoretical approach.

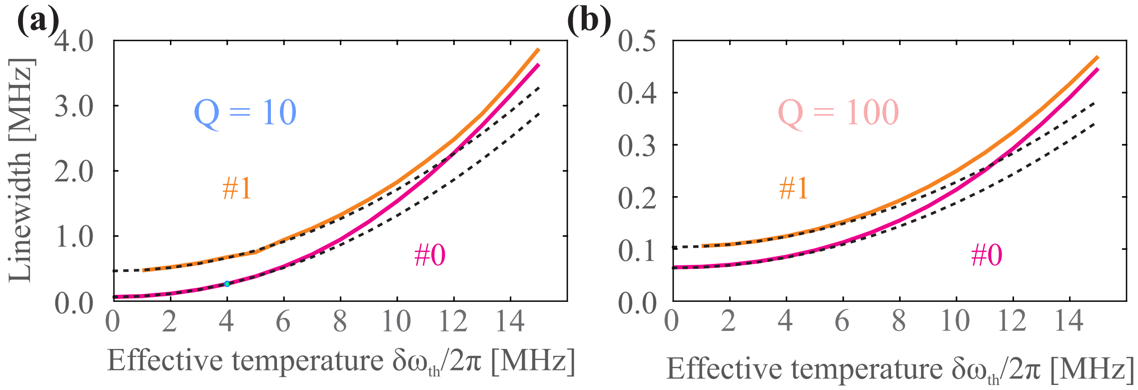

Figure F.10: The linewidth of the zeroth (#0) and first (#1) order sidebands are initially showing quadratic dependence on $\delta\omega_{\mathrm{th}}$ for **(a)** $Q = 10$ and **(b)** $Q = 100$ (indicated by the dashed black lines) until $\delta\omega_{\mathrm{th}} \approx \Omega_{\mathrm{m}}$.

Contrast

As opposed to the linewidth $\delta\nu_n$, the contrast of each sideband, C_n, depends on the Rabi frequency $\Omega_{\mathrm{R},n}$ and will therefore be subject to amplitude averaging. We have, from expression (3.7):

$$C = \frac{\Omega_{\mathrm{R}}^2}{\Omega_{\mathrm{R}}^2 + \tilde{\Gamma}_1\tilde{\Gamma}_2} \rightarrow C_n = \frac{\Omega_{\mathrm{R}}^2 J_n^2\left(\frac{\delta\omega_0}{\Omega_{\mathrm{m}}}\right)}{\Omega_{\mathrm{R}}^2 J_n^2\left(\frac{\delta\omega_0}{\Omega_{\mathrm{m}}}\right) + \tilde{\Gamma}_1\tilde{\Gamma}_2}$$

Taking into account the dependence of $\tilde{\Gamma}_2$ on $\delta\omega_{\mathrm{th}}$, we average C_n over the distribution $p^{\mathrm{th}}(\delta\omega_0)$:

$$C_n^{\mathrm{th}} = \int_0^\infty \mathrm{d}\delta\omega_0\, p^{\mathrm{th}}(\delta\omega_0) \frac{\Omega_{\mathrm{R}}^2 J_n^2\left(\frac{\delta\omega}{\Omega_{\mathrm{m}}}\right)}{\Omega_{\mathrm{R}}^2 J_n^2\left(\frac{\delta\omega}{\Omega_{\mathrm{m}}}\right) + \tilde{\Gamma}_1\tilde{\Gamma}_2^{\mathrm{th}}}. \tag{F.13}$$

The good agreement with the values obtained from simulation data is shown in Figure F.11.

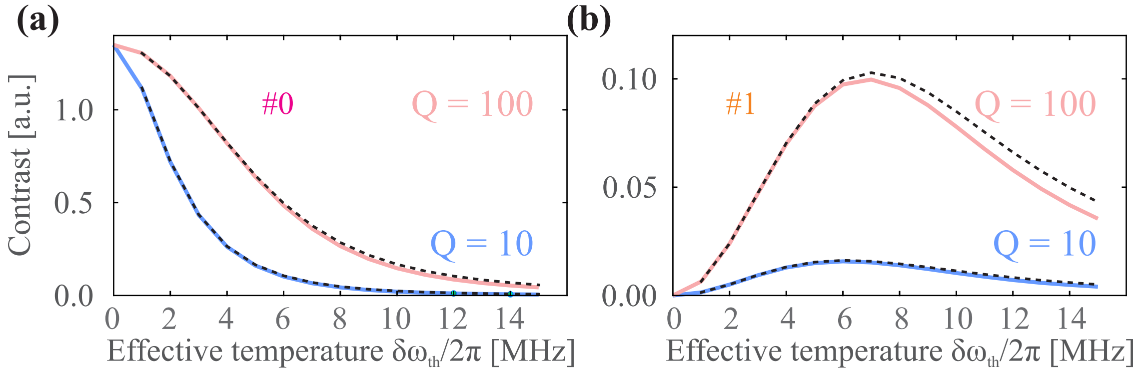

Figure F.11: Contrast of the **(a)** zeroth and **(b)** first order sideband. Expression (F.13), shown as black dashed lines, accurately describes the contrast for small values of $\delta\omega_{\mathrm{th}}$. For larger values of $\delta\omega_{\mathrm{th}}$, (F.13) becomes an overestimate.

Area

To remedy the discrepancy between expressions (F.12) and (F.13) (which give underestimates for the linewidth and overestimates for the contrast, respectively) and the simulation data, we consider the total area of each sideband given by the product $C_n \delta\nu_n$. In the thermal case, we have

$$A_n^{\mathrm{th}} = C_n^{\mathrm{th}} \delta\nu_n^{\mathrm{th}}. \tag{F.14}$$

The above expression (F.14) yields great agreement with the simulations, see Fig. F.12.

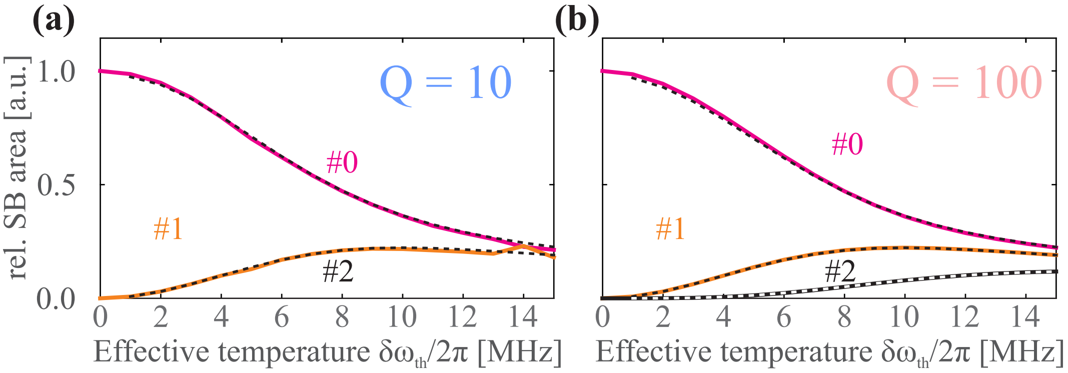

Figure F.12: Area of the sidebands for **(a)** $Q = 10$ and **(b)** $Q = 100$. In case of the larger quality factor fit parameters could be extracted for the second order sideband from the simulations.

Conclusion: While the expressions for contrast and linewidth are very accurate at low temperatures, the total sideband area has to be taken into account in order to precisely describe the simulated ODMR spectra in the high temperature regime.

F.2.2 Experiment

We will now attempt to reproduce the above results experimentally. The mayor challenge in the execution of these measurements lies within the compromise between data acquisition times and the employed optical power. The increased intensity of the light field causes broadening of the ESR spectra. At the same time larger MW power is required for sufficient contrast of the ESR peaks in order to overcome the optical repolarization rate. All of the following measurements were preformed at conditions very similar to those of section 3.6.1, that is at 0 dBm MW output power and optical power corresponding to a detected fluorescence rate between approximately 5500 and 7000 cts/s. While the low optical power reduced optical broadening, it also demands long averaging times to increase the signal-to-noise ratio. This makes the experiment susceptible to drifts in laser power. A series of measurements was performed for quality factors of $Q = 10$ and $Q = 100$, both at $\Omega_{\mathrm{m}}/2\pi = 8\,\mathrm{MHz}$. ODMR measurements are taken over a range of approximately $3V_{\mathrm{rms}}$. Each curve is an average of 5000 frequency sweeps, amounting to data acquisition times of ~ 15 hours per scan. It should be stressed that the optical saturation parameter $s = P_{\mathrm{opt}}/P_{\mathrm{sat}}$ is difficult to control, since small fluctuations of P_{opt} near P_{sat} lead to large variations of s. Despite this problem, several conclusions can be made about the measurements shown in Figure F.13. First order sidebands emerge well separated from the central peak by the emulated mechanical frequency for both quality factors. Generally, it is evident that sidebands in the small Q case are larger and the contrast is reduced. However, the reduced contrast is also explained by lower light intensities in case of $Q = 10$, as evidenced by direct comparison of the two ODMR measurements in absence of the RF field, see the caption of Figure F.13. At a larger quality factor, the spectral density of the RF field at $\Omega = \Omega_{\mathrm{m}}$ is high enough for second order sidebands to be exhibited at $\mathrm{V_{rms}} = \sqrt{2}\,\mathrm{V}$, while they remain absent in the lower Q case.

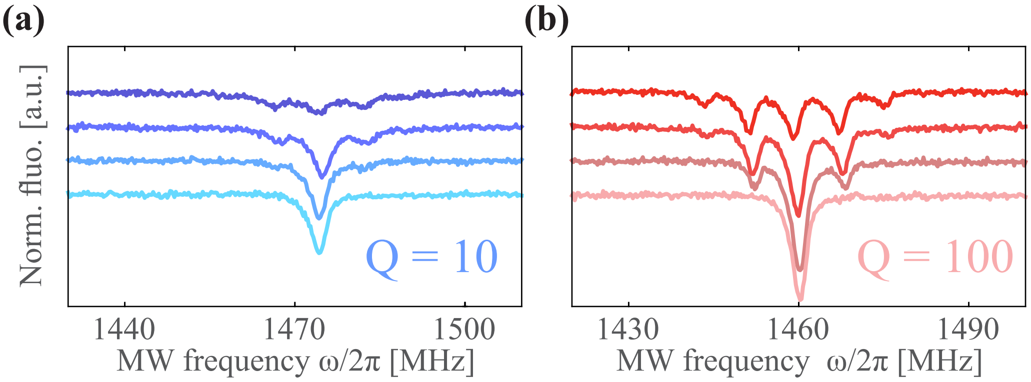

Figure F.13: ODMR measurements with a Brownian oscillator in the resolved sideband regime for $Q = 10$ in **(a)** and $Q = 100$ in **(b)**. Scans are vertically adjusted to match pairs taken at voltages $\mathrm{V}_{\mathrm{rms}} = (0, 2, 4, 6)/\sqrt{2}\,\mathrm{V}$ (bottom to top).

Estimates for the light broadened decay rates $\tilde{\Gamma}_1$, $\tilde{\Gamma}_2$ and Ω_{R} are obtained from a fit to a Lorentzian lineshape of the zero modulation scans. These values are then used to compare the area contained in each sideband to expression (F.14) as presented in Figure F.14. The agreement is reasonably good apart from slight deviations that we attribute to variations in the optical power.

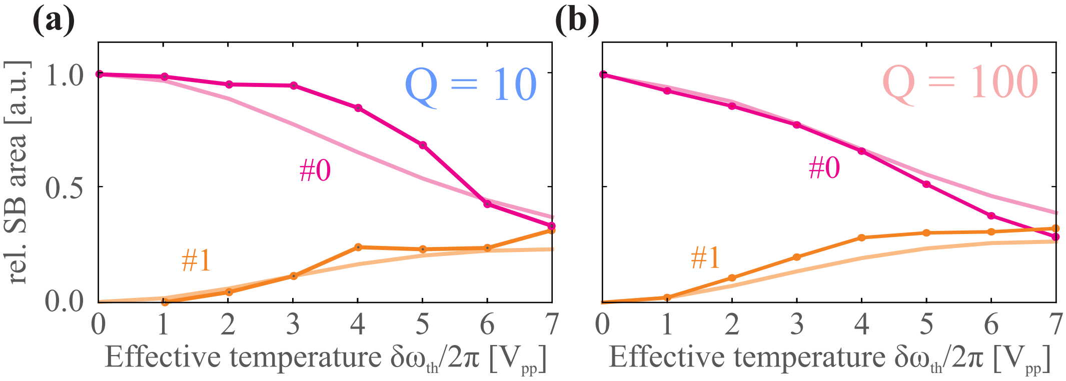

Figure F.14: Area of the sidebands of the ODMR measurements of Figure F.13 compared to expression (F.14) for $Q = 10$ in **(a)** and $Q = 100$ in **(b)**.

By sweeping the applied MW frequency in ODMR measurements we experimentally obtain much larger resolution on the mechanical sidebands than in the Rabi measurements of section F.1. We can therefore expect to be sensitive to the broadening induced by the temperature as well as mechanical dissipation, as in equation (F.12). Qualitative differences of the linewidth evolution compared to the case simulated above are visible in Figure F.15: contributions from MW power broadening cause the central peak to exhibit a larger width than the sidebands, which are sensitive to the mechanical dissipation rate Γ_{m}. Taking non-negligible values of Ω_{R} into account, the expressions for the linewidth of the n^{th} sideband has to be averaged over the amplitude distribution as well:

$$\delta\nu_n^{\mathrm{th}}(\delta\omega_{\mathrm{th}}, \Omega_{\mathrm{R}}) = \frac{1}{2\pi}\int_0^{\infty} \mathrm{d}\delta\omega_0\, p^{\mathrm{th}}(\delta\omega_0)(\delta\omega)\sqrt{\tilde{\Gamma}_{2,n}^{\mathrm{th}}\left(\tilde{\Gamma}_{2,n}^{\mathrm{th}} + \frac{\Omega_{\mathrm{R}}^2 J_n^2\left(\frac{\delta\omega_0}{\Omega_{\mathrm{m}}}\right)}{\tilde{\Gamma}_1}\right)}. \tag{F.15}$$

However, injecting the deduced values for $\tilde{\Gamma}_2$ and Γ_1 into the above expression does not provide sensible agreement with the experimental data. This is probably due to insufficient accuracy of the parameters Θ, $\tilde{\Gamma}_1$ and $\tilde{\Gamma}_2$ and problems arising from varying laser power and drift of the NV spin resonance frequency. Due to long data acquisition times, all these factors add up and render comparison of different ODMR spectra difficult. In order to yet provide a phenomenological description explaining the different evolution of the widths of the central and sideband peaks corresponding to different quality factors, we fit the data with the expression

$$\delta\nu_n^{\mathrm{th,eff}}(\delta\omega_{\mathrm{th}},\Omega_{\mathrm{R}}) = \frac{1}{2\pi}\sqrt{\underbrace{\left(\tilde{\gamma}_2 + \frac{n}{2}\Gamma_{\mathrm{m}} + \frac{\Gamma_{\mathrm{m}}}{\Omega_{\mathrm{m}}^2}\delta\omega_{\mathrm{th}}^2\right)}_{\tilde{\Gamma}_2}\left(\underbrace{\left(\tilde{\gamma}_2 + \frac{n}{2}\Gamma_{\mathrm{m}} + \frac{\Gamma_{\mathrm{m}}}{\Omega_{\mathrm{m}}^2}\delta\omega_{\mathrm{th}}^2\right)}_{\tilde{\Gamma}_2} + \underbrace{\frac{{\Omega_{\mathrm{R},n}^{\mathrm{eff}}}^2}{\tilde{\gamma}_1}}_{\Gamma(P_{\mathrm{MW}})}\right)} \tag{F.16}$$

Here, we average the Rabi frequency over all amplitudes, so that

$${\Omega_{\mathrm{R},n}^{\mathrm{eff}}}^2 = \int_0^\infty \mathrm{d}\delta\omega_0\, p^{\mathrm{th}}(\delta\omega_0)\Omega_{\mathrm{R}}^2 J_n^2\left(\frac{\delta\omega_0}{\Omega_{\mathrm{m}}}\right).$$

We set $\Omega_{\mathrm{R}}/2\pi = 1\,\mathrm{MHz}$, which we retrieve from MW calibration data and choose $\tilde{\gamma}_1$ and $\tilde{\gamma}_2$ to be free fitting parameters summarizing the experimental uncertainties. From (F.16) we obtain the dashed black lines in Figure F.15, which are in qualitative agreement with the experimental data. The free parameters were fitted to $\tilde{\gamma}_1 = 0.63\,(0.36)\,\mathrm{MHz}$ and $\tilde{\gamma}_2 = 1.54\,(0.96)\,\mathrm{MHz}$ for $Q = 10\,(100)$.

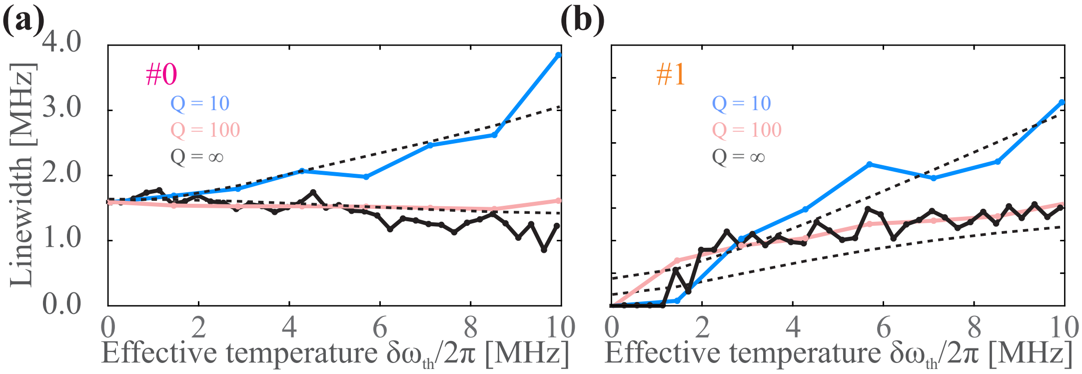

Figure F.15: Evolution of the **(a)** zeroth and **(b)** first order sideband ODMR linewidth with effective temperature $\delta\omega_{\mathrm{th}}$ for $Q = 100$ and $Q = 10$. The solid lines are data, the dashed lines are fits to expression (F.16), which takes into account power broadening. This explains the qualitative difference of the experimental data to the numerical data showing monotonic increase, see Figure F.10. The values determined are $\tilde{\gamma}_1 = 0.63\,(0.36)\,\mathrm{MHz}$ and $\tilde{\gamma}_2 = 1.54\,(0.96)\,\mathrm{MHz}$ for $Q = 10\,(100)$. The measurements are compared to the case of coherent modulation ($Q = \infty$).

F.2.3 Asymmetry of ODMR spectra

So far, we have not discussed the fact that the power spectral density of the mechanical oscillator is asymmetric around the resonance frequency Ω_{m}. For small values of Q ($\Gamma_{\mathrm{m}} \approx \delta\nu/2$) ODMR spectra are more complicated in the fact that the peaks are non-Lorentzian. This is evidenced in the simulated spectra for $Q = 10$ in Figure F.16, where an asymmetry is clearly visible. Because n^{th}-order sidebands are exhibited at $n \times \Omega_{\mathrm{m}}$ from ω_0, their position is sensitive to the frequency distribution of mechanical oscillations. While the central peak is unaffected (its position is not swept), higher order sidebands are dragged towards resonance. In order to take this effect into account, we fit the ODMR spectra from above with a Fano line shape, allowing for an asymmetry of the peaks:

$$\mathcal{F}_n(\delta) = C\frac{(q\delta\nu + \delta + n\Omega_{\mathrm{m}})^2}{(\delta + n\Omega_{\mathrm{m}})^2 + \delta\nu^2}, \tag{F.17}$$

where q and $\delta\nu$ are free parameters.

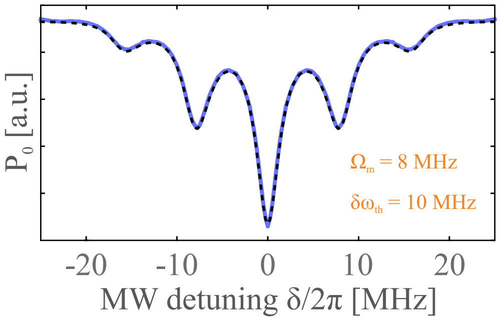

Figure F.16: Spectrum of w at Q = 10. The asymmetric peaks are fitted with a Fano line shape (F.17).

Experimentally, we obtain an ODMR spectrum as shown in Figure F.17 which we compare to an equivalent coherent measurement. Both curves were acquired during long acquisition times and therefore potentially suffer the same problems as encountered above. Qualitatively, a slight asymmetry is visible as indicated by the two arrows: close to the first order sideband peak, the slope to either side of the peak seems different. Divergence from a Lorentzian lineshape is indicated by comparison to a Lorentzian fit traced in black. However, the overall quality of the data is not entirely convincing and requires further investigation.

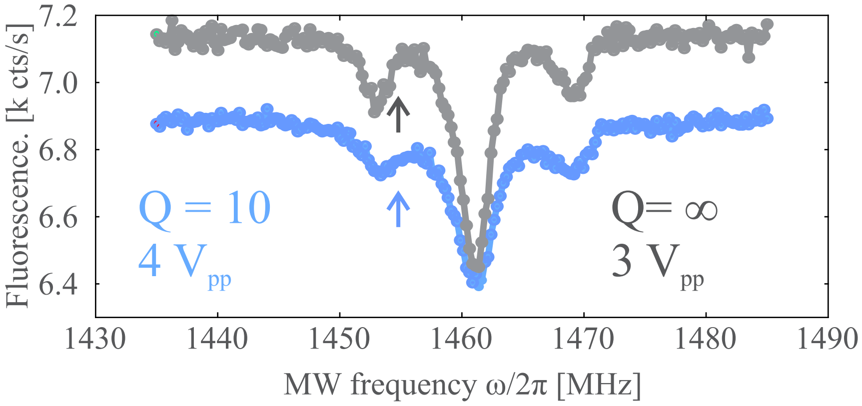

Figure F.17: Comparison between sideband spectra due to monochromatic excitation (black curve) and a bad quality mechanical oscillator. Lorentzian fits are indicated by the black traces. The blue arrows indicate the divergence from the Lorentzian profile at the wings of the sidebands due to the asymmetry of $S^{\mathrm{th}}_{\delta\omega_{\parallel}}[\Omega]$ around Ω_{m}.

Conclusion: We have presented a numerical and experimental study of the steady state spectra of a NV spin parametrically coupled to a thermally excited mechanical oscillator. While both, frequency and amplitude distribution of the modulation are clearly identified in the simulated spectra, experimental signatures suffer from long data acquisition times and various broadening processes, blurring out the effects under investigation. Improvements on the stability will help to clarify interpretation of the various experimental signatures, as for example the asymmetry of the sideband caused by a mechanical noise spectral density $S^{\mathrm{th}}_{\delta\omega_{\parallel}}[\Omega]$ asymmetric around Ω_{m}.

Bibliography

[1] L. D. Landau and E. M. Lifshitz. *Mechanics, Third Edition: Volume 1*. Butterworth-Heinemann; 3 edition, 1976. 1

[2] W. Paul and H. Steinwedel. Ein neues Massenspektrometer ohne Magnetfeld. *Zeitschrift fuer Naturforschung*, 8(Teil A):448, 1953. 2

[3] T. W. Hänsch and A. L. Schawlow. Cooling of gases by laser radiation. *Optics Communications*, 13(1):68–69, January 1975. 2

[4] D. J. Wineland. Proposed $1014\delta\nu/\nu$ laser fluorescence spectroscopy on Tl+ mono-ion oscillator III (side band cooling). *Bulletin of the American Physical Society*, 20:637, 1975. 2

[5] D. J. Wineland, R. Drullinger, and F. Walls. Radiation-Pressure Cooling of Bound Resonant Absorbers. *Physical Review Letters*, 40(25):1639–1642, June 1978. 2

[6] H. S. Lakkaraju. Motional side-band resonances in the microwave spectrum of stored ions. *Journal of Applied Physics*, 53(6):3967, 1982. 2

[7] V. Vuletić and S. Chu. Laser Cooling of Atoms, Ions, or Molecules by Coherent Scattering. *Physical Review Letters*, 84(17):3787–3790, April 2000. 2

[8] F. Diedrich, J. Bergquist, W. M. Itano, and D. J. Wineland. Laser Cooling to the Zero-Point Energy of Motion. *Physical Review Letters*, 62(4):403–406, January 1989. 2, 51

[9] M. G. Raizen, J. Gilligan, J. Bergquist, W. M. Itano, and D. J. Wineland. Ionic crystals in a linear Paul trap. *Physical Review A*, 45(9):6493–6501, May 1992. 2

[10] B. King, C. Wood, C. Myatt, Q. Turchette, D. Leibfried, W. M. Itano, C. Monroe, and D. J. Wineland. Cooling the Collective Motion of Trapped Ions to Initialize a Quantum Register. *Physical Review Letters*, 81(7):1525–1528, August 1998. 2, 3

[11] Rainer Blatt and David J. Wineland. Entangled states of trapped atomic ions. *Nature*, 453(7198):1008–15, June 2008. 3, 5

[12] A. D. O'Connell, M. Hofheinz, M. Ansmann, C. Radoslaw Bialczak, M. Lenander, E. Lucero, M. Neeley, D. Sank, H. Wang, M. Weides, J. Wenner, J. M. Martinis, and A. N. Cleland. Quantum ground state and single-phonon control of a mechanical resonator. *Nature*, 464(7289):697–703, April 2010. 3, 4, 7, 8, 9, 54

[13] P.-F. Cohadon, A. Heidmann, and M. Pinard. Cooling of a Mirror by Radiation Pressure. *Physical Review Letters*, 83(16):3174–3177, October 1999. 3

[14] M. Poggio, C. Degen, H. Mamin, and D. Rugar. Feedback Cooling of a Cantilevers Fundamental Mode below 5 mK. *Physical Review Letters*, 99(1):017201, July 2007. 3

[15] D. Kleckner and D. Bouwmeester. Sub-kelvin optical cooling of a micromechanical resonator. *Nature*, 444(7115):75–8, November 2006. 3, 4

[16] C. Höhberger Metzger and K. Karrai. Cavity cooling of a microlever. *Nature*, 432(7020):1002–5, December 2004. 3

[17] O. Arcizet, P.-F. Cohadon, T. Briant, M. Pinard, and A. Heidmann. Radiation-pressure cooling and optomechanical instability of a micromirror. *Nature*, 444(7115):71–4, November 2006. 3, 4

[18] S. Gigan, H. R. Böhm, M. Paternostro, F. Blaser, G. Langer, J. B. Hertzberg, K. C. Schwab, D. Bäuerle, M. Aspelmeyer, and A. Zeilinger. Self-cooling of a micromirror by radiation pressure. *Nature*, 444(7115):67–70, November 2006. 3, 4

[19] C. A. Regal, J. D. Teufel, and K. W. Lehnert. Measuring nanomechanical motion with a microwave cavity interferometer. *Nature Physics*, 4(7):555–560, May 2008. 3

[20] A. Schliesser, P. DelHaye, N. Nooshi, K. J. Vahala, and T. J. Kippenberg. Radiation Pressure Cooling of a Micromechanical Oscillator Using Dynamical Backaction. *Physical Review Letters*, 97(24):243905, December 2006. 4

[21] A. Naik, O. Buu, M. D. LaHaye, A. D. Armour, A. A. Clerk, M. P. Blencowe, and K. C. Schwab. Cooling a nanomechanical resonator with quantum back-action. *Nature*, 443(7108):193–6, September 2006. 4

[22] K. Brown, J. Britton, R. Epstein, J. Chiaverini, D. Leibfried, and D. J. Wineland. Passive Cooling of a Micromechanical Oscillator with a Resonant Electric Circuit. *Physical Review Letters*, 99(13):137205, September 2007. 4

[23] J. D. Thompson, B. M. Zwickl, A. M. Jayich, F. Marquardt, S. M. Girvin, and J. G. E. Harris. Strong dispersive coupling of a high-finesse cavity to a micromechanical membrane. *Nature*, 452(7183):72–5, March 2008. 4

[24] T. Corbitt, Y. Chen, E. Innerhofer, H. Müller-Ebhardt, D. Ottaway, H. Rehbein, D. Sigg, S. Whitcomb, C. Wipf, and N. Mavalvala. An All-Optical Trap for a Gram-Scale Mirror. *Physical Review Letters*, 98(15):150802, April 2007. 4

[25] A. Vinante, M. Bignotto, M. Bonaldi, M. Cerdonio, L. Conti, P. Falferi, N. Liguori, S. Longo, R. Mezzena, A. Ortolan, G. a. Prodi, F. Salemi, L. Taffarello, G. Vedovato, S. Vitale, and J.-P. Zendri. Feedback Cooling of the Normal Modes of a Massive Electromechanical System to Submillikelvin Temperature. *Physical Review Letters*, 101(3):033601, July 2008. 4

[26] F. Marquardt, J. Chen, A. A. Clerk, and S. M. Girvin. Quantum Theory of Cavity-Assisted Sideband Cooling of Mechanical Motion. *Physical Review Letters*, 99(9):093902, August 2007. 4

[27] I. Wilson-Rae, N. Nooshi, W. Zwerger, and T. J. Kippenberg. Theory of Ground State Cooling of a Mechanical Oscillator Using Dynamical Backaction. *Physical Review Letters*, 99(9):093901, August 2007. 4

[28] C. Genes, D. Vitali, P. Tombesi, S. Gigan, and M. Aspelmeyer. Ground-state cooling of a micromechanical oscillator: Comparing cold damping and cavity-assisted cooling schemes. *Physical Review A*, 77(3):033804, March 2008. 4

[29] A. Dantan, C. Genes, D. Vitali, and M. Pinard. Self-cooling of a movable mirror to the ground state using radiation pressure. *Physical Review A*, 77(1):011804, January 2008. 4

[30] O. Arcizet, P.-F. Cohadon, T. Briant, M. Pinard, A. Heidmann, J.-M. Mackowski, C. Michel, L. Pinard, O. Français, and L. Rousseau. High-Sensitivity Optical Monitoring of a Micromechanical Resonator with a Quantum-Limited Optomechanical Sensor. *Physical Review Letters*, 97(13):133601, September 2006. 4

[31] A. Schliesser, O. Arcizet, R. Rivière, G. Anetsberger, and T. J. Kippenberg. Resolved-sideband cooling and position measurement of a micromechanical oscillator close to the Heisenberg uncertainty limit. *Nature Physics*, 5(7):509–514, June 2009. 4, 51, 81

[32] R. Rivière, S. Deléglise, S. Weis, E. Gavartin, O. Arcizet, a. Schliesser, and T. J. Kippenberg. Optomechanical sideband cooling of a micromechanical oscillator close to the quantum ground state. *Physical Review A*, 83(6):063835, June 2011. 4

[33] J. Chan, T. P. Mayer Alegre, A. H. Safavi-Naeini, J. T. Hill, A. Krause, S. Gröblacher, M. Aspelmeyer, and O. Painter. Laser cooling of a nanomechanical oscillator into its quantum ground state. *Nature*, 478(7367):89–92, October 2011. 4

[34] J. D. Teufel, T. Donner, D. Li, J. W. Harlow, M. S. Allman, K. Cicak, A. J. Sirois, J. D. Whittaker, K. W. Lehnert, and R. W. Simmonds. Sideband cooling of micromechanical motion to the quantum ground state. *Nature*, 475(7356):359–63, July 2011. 4

[35] E. Verhagen, S. Deléglise, S. Weis, A. Schliesser, and T. J. Kippenberg. Quantum-coherent coupling of a mechanical oscillator to an optical cavity mode. *Nature*, 482(7383):63–7, February 2012. 4, 8

[36] D. Meekhof, C. Monroe, B. King, W. M. Itano, and D. J. Wineland. Generation of Nonclassical Motional States of a Trapped Atom. *Physical Review Letters*, 76(11):1796–1799, March 1996. 5

[37] D. Leibfried, R. Blatt, C. Monroe, and D. J. Wineland. Quantum dynamics of single trapped ions. *Reviews of Modern Physics*, 75(1):281–324, March 2003. 5

[38] T. Sleator and H. Weinfurter. Realizable Universal Quantum Logic Gates. *Physical Review Letters*, 74(20):4087–4090, May 1995. 5

[39] C. Monroe, D. Meekhof, B. King, W. M. Itano, and D. J. Wineland. Demonstration of a Fundamental Quantum Logic Gate. *Physical Review Letters*, 75(25):4714–4717, December 1995. 5

[40] F. Schmidt-Kaler, H. Häffner, S. Gulde, M. Riebe, G. P. T. Lancaster, T. Deuschle, C. Becher, W. Hänsel, J. Eschner, C. F. Roos, and R. Blatt. How to realize a universal quantum gate with trapped ions. *Applied Physics B: Lasers and Optics*, 77(8):789–796, December 2003. 5

[41] J. D. Jost, J. P. Home, J. M. Amini, D. Hanneke, R. Ozeri, C. Langer, J. J. Bollinger, D. Leibfried, and D. J. Wineland. Entangled mechanical oscillators. *Nature*, 459(7247):683–5, June 2009. 5

[42] J. I. Cirac and P. Zoller. Quantum Computations with Cold Trapped Ions. *Physical Review Letters*, 74(20):4091–4094, May 1995. 5, 8

[43] D. Deutsch. Quantum Theory, the Church-Turing Principle and the Universal Quantum Computer. *Proceedings of the Royal Society A: Mathematical, Physical and Engineering Sciences*, 400(1818):97–117, July 1985. 5

[44] D. Deutsch. Quantum Computational Networks. *Proceedings of the Royal Society A: Mathematical, Physical and Engineering Sciences*, 425(1868):73–90, September 1989. 5

[45] D. Leibfried, E. Knill, S. Seidelin, J. Britton, R. B. Blakestad, J. Chiaverini, D. B. Hume, W. M. Itano, J. D. Jost, C. Langer, R. Ozeri, R. Reichle, and D. J. Wineland. Creation of a six-atom 'Schrödinger cat' state. *Nature*, 438(7068):639–42, December 2005. 5

[46] L. Tian and P. Zoller. Coupled Ion-Nanomechanical Systems. *Physical Review Letters*, 93(26):266403, December 2004. 6

[47] I. Wilson-Rae, P. Zoller, and a. Imamolu. Laser Cooling of a Nanomechanical Resonator Mode to its Quantum Ground State. *Physical Review Letters*, 92(7):075507, February 2004. 6, 20

[48] P. Rabl. Cooling of mechanical motion with a two-level system: The high-temperature regime. *Physical Review B*, 82(16):1–11, October 2010. 6, 51, 59, 85

[49] C. Law and J. H. Eberly. Arbitrary Control of a Quantum Electromagnetic Field. *Physical Review Letters*, 76(7):1055–1058, February 1996. 6

[50] M. Hofheinz, H. Wang, M. Ansmann, R. C. Bialczak, E. Lucero, M. Neeley, A. D. O'Connell, D. Sank, J. Wenner, J. M. Martinis, and A. N. Cleland. Synthesizing arbitrary quantum states in a superconducting resonator. *Nature*, 459(7246):546–9, May 2009. 6, 54

[51] D. Rugar, R. Budakian, H. J. Mamin, and B. W. Chui. Single spin detection by magnetic resonance force microscopy. *Nature*, 430(6997):329–32, July 2004. 7, 51, 143

[52] A. Pályi, P. Struck, M. Rudner, K. Flensberg, and G. Burkard. Spin-Orbit-Induced Strong Coupling of a Single Spin to a Nanomechanical Resonator. *Physical Review Letters*, 108(20):206811, May 2012. 7

[53] P. Rabl, P. Cappellaro, M. V. G. Dutt, L. Jiang, J. Maze, and M. D. Lukin. Strong magnetic coupling between an electronic spin qubit and a mechanical resonator. *Physical Review B*, 79(4):041302, January 2009. 7, 20, 85

[54] T. A. Palomaki, J. W. Harlow, J. D. Teufel, R. W. Simmonds, and K. W. Lehnert. Coherent state transfer between itinerant microwave fields and a mechanical oscillator. *Nature*, 495(7440):210–4, March 2013. 8

[55] P. Rabl, S. J. Kolkowitz, F. H. L. Koppens, J. G. E. Harris, P. Zoller, and M. D. Lukin. A quantum spin transducer based on nanoelectromechanical resonator arrays. *Nature Physics*, 6(8):602–608, May 2010. 8

[56] J.-M. Pirkkalainen, S. U. Cho, J. Li, G. S. Paraoanu, P. J. Hakonen, and M. A. Sillanpää. Hybrid circuit cavity quantum electrodynamics with a micromechanical resonator. *Nature*, 494(7436):211–5, February 2013. 8, 13, 25

[57] S. Camerer, M. Korppi, A. Jöckel, D. Hunger, T. W. Hänsch, and P. Treutlein. Realization of an Optomechanical Interface Between Ultracold Atoms and a Membrane. *Physical Review Letters*, 107(22):223001, November 2011. 9, 10

[58] D. Hunger, S. Camerer, T. W. Hänsch, D. König, J. P. Kotthaus, J. Reichel, and P. Treutlein. Resonant Coupling of a Bose-Einstein Condensate to a Micromechanical Oscillator. *Physical Review Letters*, 104(14):143002, April 2010. 10

[59] M. D. LaHaye, J. Suh, P M. Echternach, K. C. Schwab, and M. L. Roukes. Nanomechanical measurements of a superconducting qubit. *Nature*, 459(7249):960–4, June 2009. 10, 11

[60] S. D. Bennett, L. Cockins, Y. Miyahara, P. Grütter, and A. A. Clerk. Strong Electromechanical Coupling of an Atomic Force Microscope Cantilever to a Quantum Dot. *Physical Review Letters*, 104(1):017203, January 2010. 11, 12

[61] I. Yeo, P.-L. de Assis, A. Gloppe, E. Dupont-Ferrier, P. Verlot, N. S. Malik, E. Dupuy, J. Claudon, J.-M. Gérard, A. Auffèves, G. Nogues, S. Seidelin, J.-P. Poizat, O. Arcizet, and M. Richard. Strain-mediated coupling in a quantum dot-mechanical oscillator hybrid system. *Nature Nanotechnology*, 9(2):106–10, February 2014. 12, 13

[62] S. Koizumi, C. Nebel, and M. Nesladek, editors. *Physics and Applications of CVD Diamond.* Wiley-VCH Verlag GmbH & Co. KGaA, Weinheim, Germany, August 2008. 14

[63] A. M. Zaitsev. *Optical Properties of Diamond: A Data Handbook.* Springer-Verlag Berlin and Heidelberg GmbH & Co. K, 2010. 14

[64] R. Mildren and J. R. Rabeau. *Optical Engineering of Diamond.* Wiley, 2013. 14

[65] L. Rondin, G. Dantelle, a. Slablab, F. Grosshans, F. Treussart, P. Bergonzo, S. Perruchas, T. Gacoin, M. Chaigneau, H.-C. Chang, V. Jacques, and J.-F. Roch. Surface-induced charge state conversion of nitrogen-vacancy defects in nanodiamonds. *Physical Review B*, 82(11):115449, September 2010. 15

[66] A. Dréau. *Spins individuels dans le diamant pour l'information quantique.* PhD thesis, Ecole Normale Superieur Cachan, 2013. 15

[67] A. Gruber, A. Dräbenstedt, C. Tietz, L. Fleury, J. Wrachtrup, and C. von Borczyskowski. Scanning Confocal Optical Microscopy and Magnetic Resonance on Single Defect Centers. *Science*, 276(5321):2012–2014, June 1997. 15, 45, 47, 48

[68] R. Brouri, A. Beveratos, J.-P. Poizat, and P. Grangier. Photon antibunching in the fluorescence of individual color centers in diamond. *Optics letters*, 25(17):1294–6, September 2000. 15

[69] C. Kurtsiefer, S. Mayer, P. Zarda, and H. Weinfurter. Stable Solid-State Source of Single Photons. *Physical Review Letters*, 85(2):290–293, July 2000. 15

[70] A. Beveratos, R. Brouri, T. Gacoin, A. Villing, J.-P. Poizat, and P. Grangier. Single Photon Quantum Cryptography. *Physical Review Letters*, 89(18):187901, October 2002. 15

[71] R. Alléaume, F. Treussart, G. Messin, Y. Dumeige, J.-F. Roch, A. Beveratos, R. Brouri-Tualle, J.-P. Poizat, and P. Grangier. Experimental open-air quantum key distribution with a single-photon source. *New Journal of Physics*, 6:92–92, July 2004. 15

[72] A. Cuche, A. Drezet, Y. Sonnefraud, O. Faklaris, F. Treussart, J.-F. Roch, and S. Huant. Near-field optical microscopy with a nanodiamond-based single-photon tip. *Optics express*, 17(22):19969–80, October 2009. 15

[73] D. Redman, S. Brown, R. Sands, and S. Rand. Spin dynamics and electronic states of N-V centers in diamond by EPR and four-wave-mixing spectroscopy. *Physical Review Letters*, 67(24):3420–3423, December 1991. 15, 47

[74] J.-P. Tetienne, L. Rondin, P. Spinicelli, M. Chipaux, T. Debuisschert, J.-F. Roch, and V. Jacques. Magnetic-field-dependent photodynamics of single NV defects in diamond: an application to qualitative all-optical magnetic imaging. *New Journal of Physics*, 14(10):103033, October 2012. 15, 78

[75] F. Jelezko, T. Gaebel, I. Popa, A. Gruber, and J. Wrachtrup. Observation of Coherent Oscillations in a Single Electron Spin. *Physical Review Letters*, 92(7):1–4, February 2004. 15

[76] G. Balasubramanian, P. Neumann, D. Twitchen, M. L. Markham, R. Kolesov, N. Mizuochi, J. Isoya, J. Achard, J. Beck, J. Tisler, V. Jacques, P. R. Hemmer, F. Jelezko, and J. Wrachtrup. Ultralong spin coherence time in isotopically engineered diamond. *Nature Materials*, 8(5):383–7, May 2009. 15, 20, 46

[77] M. V. Gurudev Dutt, L. Childress, L. Jiang, E. Togan, J. Maze, F. Jelezko, A. S. Zibrov, P. R. Hemmer, and M. D. Lukin. Quantum register based on individual electronic and nuclear spin qubits in diamond. *Science (New York, N.Y.)*, 316(5829):1312–6, June 2007. 15

[78] P. Neumann, N. Mizuochi, F. Rempp, P. R. Hemmer, H. Watanabe, S. Yamasaki, V. Jacques, T. Gaebel, F. Jelezko, and J. Wrachtrup. Multipartite entanglement among single spins in diamond. *Science (New York, N.Y.)*, 320(5881):1326–9, June 2008. 15

[79] E. Togan, Y. Chu, A. S. Trifonov, L. Jiang, J. Maze, L. Childress, M. V. G. Dutt, A. S. Sø rensen, P. R. Hemmer, A. S. Zibrov, and M. D. Lukin. Quantum entanglement between an optical photon and a solid-state spin qubit. *Nature*, 466(7307):730–4, August 2010. 15

[80] F. Dolde, I. Jakobi, B. Naydenov, N. Zhao, S. Pezzagna, C. Trautmann, J. Meijer, P. Neumann, F. Jelezko, and J. Wrachtrup. Room-temperature entanglement between single defect spins in diamond. *Nature Physics*, 9(3):139–143, February 2013. 15

[81] J. M. Taylor, P. Cappellaro, L. Childress, L. Jiang, D. Budker, P. R. Hemmer, A. Yacoby, R. L. Walsworth, and M. D. Lukin. High-sensitivity diamond magnetometer with nanoscale resolution. *Nature Physics*, 4(10):810–816, September 2008. 15, 16

[82] J. R. Maze, P. L. Stanwix, J. S. Hodges, S. Hong, J. M. Taylor, P. Cappellaro, L. Jiang, M. V. Gurudev Dutt, E. Togan, A. S. Zibrov, A. Yacoby, R. L. Walsworth, and M. D. Lukin. Nanoscale magnetic sensing with an individual electronic spin in diamond. *Nature*, 455(7213):644–7, October 2008. 15, 46

[83] M. S. Grinolds, S. Hong, P. Maletinsky, L. Luan, M. D. Lukin, R. L. Walsworth, and A. Yacoby. Nanoscale magnetic imaging of a single electron spin under ambient conditions. *Nature Physics*, 9(4):215–219, February 2013. 15

[84] L. Rondin, J.-P. Tetienne, T. Hingant, J.-F. Roch, P. Maletinsky, and V. Jacques. Magnetometry with nitrogen-vacancy defects in diamond. *Reports on progress in physics. Physical Society (Great Britain)*, 77(5):056503, May 2014. 15

[85] F. Dolde, H. Fedder, M. W. Doherty, T. Nöbauer, F. Rempp, G. Balasubramanian, T. Wolf, F. Reinhard, L. C. L. Hollenberg, F. Jelezko, and J. Wrachtrup. Electric-field sensing using single diamond spins. *Nature Physics*, 7(6):459–463, April 2011. 15, 16

[86] G. Kucsko, P. C. Maurer, N. Y. Yao, M. Kubo, H. J. Noh, P. K. Lo, H. Park, and M. D. Lukin. Nanometre-scale thermometry in a living cell. *Nature*, 500(7460):54–8, August 2013. 15, 16

[87] L. Rondin. *Réalisation d'un magnétomètre à centre coloré NV du diamant*. PhD thesis, Ecole Normale Superieure de Cachan, 2012. 16, 46, 64, 143

[88] J.-P. Tetienne, T. Hingant, L. Rondin, S. Rohart, A. Thiaville, J.-F. Roch, and V. Jacques. Quantitative stray field imaging of a magnetic vortex core. *Physical Review B*, 88(21):214408, December 2013. 17

[89] L. Robledo, L. Childress, Ha. Bernien, B. Hensen, P. F. A. Alkemade, and R. Hanson. High-fidelity projective read-out of a solid-state spin quantum register. *Nature*, 477(7366):574–578, September 2011. 17, 19

[90] W. Pfaff, T. H. Taminiau, L. Robledo, H. Bernien, M. L. Markham, D. J. Twitchen, and R. Hanson. Demonstration of entanglement-by-measurement of solid-state qubits. *Nature Physics*, 8(1):29–33, October 2012. 17, 19

[91] J. Teissier, A. Barfuss, P. Appel, E. Neu, and P. Maletinsky. Strain Coupling of a Nitrogen-Vacancy Center Spin to a Diamond Mechanical Oscillator. *Physical Review Letters*, 113(2):020503, July 2014. 20, 25, 86

[92] Y. Tao, J. M. Boss, B. A. Moores, and C. L. Degen. Single-crystal diamond nanomechanical resonators with quality factors exceeding one million. *Nature Communications*, 5:3638, January 2014. 20

[93] D. M. Toyli, C. D. Weis, G. D. Fuchs, T. Schenkel, and D. D. Awschalom. Chip-scale nanofabrication of single spins and spin arrays in diamond. *Nano letters*, 10(8):3168–72, August 2010. 20

[94] J. P. Hadden, J. P. Harrison, A. C. Stanley-Clarke, L. Marseglia, Y.-L. D. Ho, B. R. Patton, J. L. OBrien, and J. G. Rarity. Strongly enhanced photon collection from diamond defect centers under microfabricated integrated solid immersion lenses. *Applied Physics Letters*, 97(24):241901, 2010. 20

[95] S. Perisanu, P. Vincent, A. Ayari, M. Choueib, S. T. Purcell, M. Bechelany, and D. Cornu. High Q factor for mechanical resonances of batch-fabricated SiC nanowires. *Applied Physics Letters*, 90(4):043113, 2007. 20, 133

[96] S. Perisanu, V. Gouttenoire, P. Vincent, a. Ayari, M. Choueib, M. Bechelany, D. Cornu, and S. Purcell. Mechanical properties of SiC nanowires determined by scanning electron and field emission microscopies. *Physical Review B*, 77(16):165434, April 2008. 20, 133

[97] A. Gloppe, P. Verlot, E. Dupont-Ferrier, A. Siria, P. Poncharal, G. Bachelier, P. Vincent, and O. Arcizet. Bidimensional nano-optomechanics and topological backaction in a non-conservative radiation force field. *Nature nanotechnology*, (September):1–7, September 2014. 21, 34, 52, 136, 138

[98] J. M. Nichol, E. R. Hemesath, L. J. Lauhon, and R. Budakian. Nanomechanical detection of nuclear magnetic resonance using a silicon nanowire oscillator. *Physical Review B*, 85(5):054414, February 2012. 21, 162

[99] O. Arcizet, V. Jacques, A. Siria, P. Poncharal, P. Vincent, and S. Seidelin. A single nitrogen-vacancy defect coupled to a nanomechanical oscillator. *Nature Physics*, 7(11):879–883, September 2011. 22, 79

[100] S. Rohr, E. Dupont-Ferrier, B. Pigeau, P. Verlot, V. Jacques, and O. Arcizet. Synchronizing the Dynamics of a Single Nitrogen Vacancy Spin Qubit on a Parametrically Coupled Radio-Frequency Field through Microwave Dressing. *Physical Review Letters*, 112(1):010502, January 2014. 25

[101] B. Pigeau, S. Rohr, L. Mercier de Lépinay, E. Dupont-Ferrier, P. Verlot, and O. Arcizet. Observation of a phonon dressed Mollow triplet on a hybrid spin-mechanical system. *in preparation.* 25

[102] A. Gloppe. *Nano-optomécanique au coeur dun faisceau laser focalisé : cartographie du champ de force optique et action en retour bidimensionnelle.* Phd thesis, Grenoble University, 2014. 25, 136

[103] C. Cohen-Tannoudji, B. Diu, and F. Laloe. *Quantum Mechanics.* Wiley-VCH; 2 Volume Set edition, 1992. 28, 226

[104] R. Kubo. The fluctuation-dissipation theorem. *Reports on Progress in Physics*, 29(1):255–284, January 1966. 31

[105] S. Reynaud, A. Heidmann, E. Giacobino, and C. Fabre. Quantum fluctuations in Optical Systems. In E. Wolf, editor, *Progress in Optics*, pages 11, 12, 22, 42, 106. North-Holland, xxx edition, 1992. 31

[106] A. N. Cleland. *Foundations of Nanomechanics.* Advanced Texts in Physics. Springer Berlin Heidelberg, Berlin, Heidelberg, 2003. 33, 34

[107] A. Gloppe. *High sensitivity readout of nano-resonator dynamics.* Master thesis, Grenoble INP, 2011. 34

[108] M. Pinard, Y. Hadjar, and A. Heidmann. Effective mass in quantum effects of radiation pressure. *The European Physical Journal D - Atomic, Molecular, Optical and Plasma Physics*, 7(1):107–116, 1999. 35, 36

[109] A. Lenef and S. Rand. Electronic structure of the N-V center in diamond: Theory. *Physical Review B*, 53(20):13441–13455, May 1996. 37

[110] A. Lenef, S. Brown, D. Redman, S. Rand, J. Shigley, and E. Fritsch. Electronic structure of the N-V center in diamond: Experiments. *Physical Review B*, 53(20):13427–13440, May 1996. 37

[111] P. Neumann, R. Kolesov, V. Jacques, J. Beck, J. Tisler, A. Batalov, L. J. Rogers, N. B. Manson, G. Balasubramanian, F. Jelezko, and J. Wrachtrup. Excited-state spectroscopy of single NV defects in diamond using optically detected magnetic resonance. *New Journal of Physics*, 11(1):013017, January 2009. 37

[112] M. W. Doherty, F. Dolde, H. Fedder, F. Jelezko, J. Wrachtrup, N. B. Manson, and L. C. L. Hollenberg. Theory of the ground-state spin of the NV- center in diamond. *Physical Review B*, 85(20):1–21, May 2012. 38

[113] A. Gali, M. Fyta, and E. Kaxiras. Ab initio supercell calculations on nitrogen-vacancy center in diamond: Electronic structure and hyperfine tensors. *Physical Review B*, 77(15):155206, April 2008. 39

[114] A. Gali. Hyperfine tensors of nitrogen-vacancy center in diamond from ab initio calculations. *ArXiv*, page 4, May 2009. 39

[115] J. R. Rabeau, P. Reichart, G. Tamanyan, D. N. Jamieson, S. Prawer, F. Jelezko, T. Gaebel, I. Popa, M. Domhan, and J. Wrachtrup. Implantation of labelled single nitrogen vacancy centers in diamond using [sup 15]N. *Applied Physics Letters*, 88(2):023113, 2006. 39

[116] B. Smeltzer, J. McIntyre, and L. Childress. Robust control of individual nuclear spins in diamond. *Physical Review A*, 80(5):050302, November 2009. 39, 72

[117] V. Jacques, P. Neumann, J. Beck, M. L. Markham, D. Twitchen, J. Meijer, F. Kaiser, G. Balasubramanian, F. Jelezko, and J. Wrachtrup. Dynamic Polarization of Single Nuclear Spins by Optical Pumping of Nitrogen-Vacancy Color Centers in Diamond at Room Temperature. *Physical Review Letters*, 102(5):7–10, February 2009. 39

[118] S. Felton, A. M. Edmonds, M. E. Newton, P. M. Martineau, D. Fisher, D. J. Twitchen, and J. M. Baker. Hyperfine interaction in the ground state of the negatively charged nitrogen vacancy center in diamond. *Physical Review B*, 79(7):1–8, February 2009. 39, 48

[119] M. Steiner, P. Neumann, J. Beck, F. Jelezko, and J. Wrachtrup. Universal enhancement of the optical readout fidelity of single electron spins at nitrogen-vacancy centers in diamond. *Physical Review B*, 81(3):1–6, January 2010. 39

[120] L. J. Rogers, R. L. McMurtrie, M. J. Sellars, and N. B. Manson. Time-averaging within the excited state of the nitrogen-vacancy centre in diamond. *New Journal of Physics*, 11(6):063007, June 2009. 39, 47

[121] G. Ithier, E. Collin, P. Joyez, P. Meeson, D. Vion, D. Esteve, F. Chiarello, A. Shnirman, Y. Makhlin, J. Schriefl, and G. Schön. Decoherence in a superconducting quantum bit circuit. *Physical Review B*, 72(13):134519, October 2005. 43, 93, 164

[122] C. Cohen-Tannoudji, J. Dupont-Roc, and G. Grynberg. *Atom - Photon Interactions: Basic Process and Appilcations.* Wiley Science Paperback Series, 1998. 43, 109, 120, 125, 154, 198

[123] C.P. Slichter. *Principles of magnetic resonance.* Number 3 in Solid-State Sciences 1. Springer; 3rd enlarged and updated ed. 1990. Corr. 3rd printing 1996 edition (March 21, 1996), Berlin, March 1996. 44, 92, 124

[124] I. L. Chuang, L. M. K. Vandersypen, X. Zhou, D. W. Leung, and S. Lloyd. Experimental realization of a quantum algorithm. *Nature*, 393(6681):143–146, May 1998. 45

[125] R. Hanson, J. R. Petta, S. Tarucha, and L. M. K. Vandersypen. Spins in few-electron quantum dots. *Reviews of Modern Physics*, 79(4):1217–1265, October 2007. 45

[126] J. J. Pla, K. Y. Tan, J. P. Dehollain, W. H. Lim, J. J. L. Morton, D. N. Jamieson, A. S. Dzurak, and A. Morello. A single-atom electron spin qubit in silicon. *Nature*, 489(7417):541–5, September 2012. 45

[127] R. Hanson, V. V. Dobrovitski, A. E. Feiguin, O. Gywat, and D. D. Awschalom. Coherent dynamics of a single spin interacting with an adjustable spin bath. *Science (New York, N.Y.)*, 320(5874):352–5, April 2008. 45

[128] Y. Kubo, C. Grezes, A. Dewes, T. Umeda, J. Isoya, H. Sumiya, N. Morishita, H. Abe, S. Onoda, T. Ohshima, V. Jacques, A. Dréau, J.-F. Roch, I. Diniz, A. Auffèves, D. Vion, D. Esteve, and P. Bertet. Hybrid Quantum Circuit with a Superconducting Qubit Coupled to a Spin Ensemble. *Physical Review Letters*, 107(22):220501, November 2011. 45

[129] J. Maze Rios. *Quantum manipulation of nitrogen-vacancy centers in diamond : from basic properties to applications.* PhD thesis, Harvard University, 2010. 45

[130] A. M. Tyryshkin, S. Tojo, J. J. L. Morton, H. Riemann, N. V. Abrosimov, Peter Becker, H.-J. Pohl, T. Schenkel, M.L. W. Thewalt, K. M. Itoh, and S. A. Lyon. Electron spin coherence exceeding seconds in high-purity silicon. *Nature Materials*, 11(2):143–7, February 2012. 45

[131] A. Jarmola, V. M. Acosta, K. Jensen, S. Chemerisov, and D. Budker. Temperature- and Magnetic-Field-Dependent Longitudinal Spin Relaxation in Nitrogen-Vacancy Ensembles in Diamond. *Physical Review Letters*, 108(19):1–5, May 2012. 45, 90

[132] J. H. N. Loubser and J. A. van Wyk. Electron spin resonance in the study of diamond. *Reports on Progress in Physics*, 41(8):1201–1248, August 1978. 45

[133] F. Reinhard, F. Shi, N. Zhao, F. Rempp, B. Naydenov, J. Meijer, L. T. Hall, L. C. L. Hollenberg, J. Du, R.-B. Liu, and J. Wrachtrup. Tuning a Spin Bath through the Quantum-Classical Transition. *Physical Review Letters*, 108(20):200402, May 2012. 45

[134] T. Gaebel, M. Domhan, I. Popa, C. Wittmann, P. Neumann, F. Jelezko, J. R. Rabeau, N. Stavrias, A. D. Greentree, S. Prawer, J. Meijer, J. Twamley, P. R. Hemmer, and J. Wrachtrup. Room-temperature coherent coupling of single spins in diamond. *Nature Physics*, 2(6):408–413, May 2006. 45

[135] L. Childress, M. V. Gurudev Dutt, J. M. Taylor, A. S. Zibrov, F. Jelezko, J. Wrachtrup, P. R. Hemmer, and M. D. Lukin. Coherent dynamics of coupled electron and nuclear spin qubits in diamond. *Science (New York, N.Y.)*, 314(5797):281–5, October 2006. 45

[136] T. A. Kennedy, J. S. Colton, J. E. Butler, R. C. Linares, and P. J. Doering. Long coherence times at 300 K for nitrogen-vacancy center spins in diamond grown by chemical vapor deposition. *Applied Physics Letters*, 83(20):4190, 2003. 45

[137] G. de Lange, Z. H. Wang, D. Ristè, V. V. Dobrovitski, and R. Hanson. Universal dynamical decoupling of a single solid-state spin from a spin bath. *Science (New York, N.Y.)*, 330(6000):60–3, October 2010. 45, 46

[138] G. Uhlenbeck and L. Ornstein. On the Theory of the Brownian Motion. *Physical Review*, 36(5):823–841, September 1930. 45

[139] J. Klauder and P. Anderson. Spectral Diffusion Decay in Spin Resonance Experiments. *Physical Review*, 125(3):912–932, February 1962. 45

[140] A. Tallaire, A. T. Collins, D. Charles, J. Achard, R. Sussmann, A. Gicquel, M. E. Newton, A. M. Edmonds, and R. J. Cruddace. Characterisation of high-quality thick single-crystal diamond grown by CVD with a low nitrogen addition. *Diamond and Related Materials*, 15(10):1700–1707, October 2006. 46

[141] F. P. Bundy, H. T. Hall, H. M. Strong, and R. H. Wentorf. Man-Made Diamonds. *Nature*, 176(4471):51–55, July 1955. 46

[142] K. Schmetzer. High pressure high temperature treatment of diamonds a review of the patent literature from five decades (1960-2009). *The Journal of Gemmology*, 32(1):52, 2010. 46

[143] B. K. Ofori-Okai, S. Pezzagna, K. Chang, M. Loretz, R. Schirhagl, Y. Tao, B. A. Moores, K. Groot-Berning, J. Meijer, and C. L. Degen. Spin properties of very shallow nitrogen vacancy defects in diamond. *Physical Review B*, 86(8):081406, August 2012. 46

[144] G. Uhrig. Keeping a Quantum Bit Alive by Optimized π-Pulse Sequences. *Physical Review Letters*, 98(10):100504, March 2007. 46

[145] J.-M. Cai, B. Naydenov, R. Pfeiffer, L. P. McGuinness, K. D. Jahnke, F. Jelezko, M. B. Plenio, and A. Retzker. Robust dynamical decoupling with concatenated continuous driving. *New Journal of Physics*, 14(11):113023, November 2012. 46, 125

[146] G. de Lange, D. Ristè, V. V. Dobrovitski, and R. Hanson. Single-Spin Magnetometry with Multipulse Sensing Sequences. *Physical Review Letters*, 106(8):1–4, February 2011. 46

[147] M. Loretz, T. Rosskopf, and C. L. Degen. Radio-Frequency Magnetometry Using a Single Electron Spin. *Physical Review Letters*, 110(1):017602, January 2013. 46

[148] G. Davies. Vibronic spectra in diamond. *Journal of Physics C: Solid State Physics*, 7(20):3797–3809, October 1974. 47

[149] A. Batalov, C. Zierl, T. Gaebel, P. Neumann, I.-Y. Chan, G. Balasubramanian, P. R. Hemmer, F. Jelezko, and J. Wrachtrup. Temporal Coherence of Photons Emitted by Single Nitrogen-Vacancy Defect Centers in Diamond Using Optical Rabi-Oscillations. *Physical Review Letters*, 100(7):077401, February 2008. 47

[150] A. S. Barnard. Diamond standard in diagnostics: nanodiamond biolabels make their mark. *The Analyst*, 134(9):1751–64, September 2009. 47

[151] L. Robledo, H. Bernien, T. van der Sar, and R. Hanson. Spin dynamics in the optical cycle of single nitrogen-vacancy centres in diamond. *New Journal of Physics*, 13(2):025013, February 2011. 47

[152] X.-F. He, N. B. Manson, and P. Fisk. Paramagnetic resonance of photoexcited N-V defects in diamond. II. Hyperfine interaction with the N14 nucleus. *Physical Review B*, 47(14):8816–8822, April 1993. 47

[153] L. J. Rogers, S. Armstrong, M. J. Sellars, and N. B. Manson. Infrared emission of the NV centre in diamond: Zeeman and uniaxial stress studies. *New Journal of Physics*, 10(10):103024, October 2008. 48

[154] V. M. Acosta, A. Jarmola, E. Bauch, and D. Budker. Optical properties of the nitrogen-vacancy singlet levels in diamond. *Physical Review B*, 82(20):2–5, November 2010. 48

[155] P. Neumann, R. Kolesov, B. Naydenov, J. Beck, F. Rempp, M. Steiner, V. Jacques, G. Balasubramanian, M. L. Markham, D. J. Twitchen, S. Pezzagna, J. Meijer, J. Twamley, F. Jelezko, and J. Wrachtrup. Quantum register based on coupled electron spins in a room-temperature solid. *Nature Physics*, 6(4):249–253, February 2010. 48

[156] A. Dréau, M. Lesik, L. Rondin, P. Spinicelli, O. Arcizet, J.-F. Roch, and V. Jacques. Avoiding power broadening in optically detected magnetic resonance of single NV defects for enhanced dc magnetic field sensitivity. *Physical Review B*, 84(19):1–8, November 2011. 48, 70, 76

[157] M. W. Doherty, N. B. Manson, P. Delaney, F. Jelezko, J. Wrachtrup, and L. C. L. Hollenberg. The nitrogen-vacancy colour centre in diamond. *ArXiv*, 528(1):101, February 2013. 49

[158] W. Gerlach and O. Stern. Das magnetische Moment des Silberatoms. *Zeitschrift für Physik*, 9(1):353–355, December 1922. 51

[159] S. Haroche and J.-M. Raimond. *Exploring the Quantum: Atoms, Cavities, and Photons.* Oxford Graduate Texts, 2006. 51, 101, 102

[160] W. H. Zurek. Decoherence and the Transition from Quantum to Classical Revisited. *Los Alamos Science*, (27):86–109, 2002. 52

[161] A. Venugopalan. Decoherence and Schrödinger-cat states in a Stern-Gerlach-type experiment. *Physical Review A*, 56(5):4307–4310, November 1997. 52

[162] Keith C. Schwab and Michael L. Roukes. Putting mechanics into Quantum mechanics. *Physics Today*, 58(7):36–42, July 2005. 52

[163] P. Ovartchaiyapong, K. W. Lee, B. A. Myers, and A. C. Bleszynski-Jayich. Dynamic strain-mediated coupling of a single diamond spin to a mechanical resonator. *Nature communications*, 5:4429, January 2014. 54

[164] G.N. Milstein and M.V. Tretyakov. Stochastic Numerics for Mathematical Physics, 2004. 61

[165] M. Berthel, O. Mollet, G. Dantelle, T. Gacoin, S. Huant, and A. Drezet. Photophysics of single nitrogen-vacancy centers in diamond nanocrystals. *in preparation*, pages 1–13. 78

[166] N. Polonsky and C. Cohen-Tannoudji. Interprétation quantique de la modulation de fréquence. *Journal de Physique*, 26(7):409–414, 1965. 81, 126

[167] E. Jones, T. Oliphant, and P. Peterson. {SciPy}: Open source scientific tools for {Python}. 97

[168] B. Mollow. Power Spectrum of Light Scattered by Two-Level Systems. *Physical Review*, 188(5):1969–1975, December 1969. 101

[169] C. Cohen-Tannoudji, J. Dupont-Roc, and C. Fabre. A quantum calculation of the higher order terms in the Bloch-Siegert shift. *Journal of Physics B: Atomic and Molecular Physics*, 6(8):L214–L217, August 1973. 107, 154

[170] V. R. Horowitz, B. J. Alemán, D. J. Christle, A. N. Cleland, and D. D. Awschalom. Electron spin resonance of nitrogen-vacancy centers in optically trapped nanodiamonds. *Proceedings of the National Academy of Sciences of the United States of America*, 109(34):13493–7, August 2012. 133

[171] J. Li, M. P. Silveri, K. S. Kumar, J.-M. Pirkkalainen, A. Vepsäläinen, W. C. Chien, J. Tuorila, M. A. Sillanpää, P. J. Hakonen, E. V. Thuneberg, and G. S. Paraoanu. Motional averaging in a superconducting qubit. *Nature Communications*, 4:1420, January 2013. 164

[172] Piotr Szakowski, M. Trippenbach, and Y. B. Band. Spin decoherence due to fluctuating fields. *Physical Review E*, 87(5):052112, May 2013. 164

[173] J. F. Kenney and E. S. Keeping. *Mathematics of Statistics*. Mathematics of Statistics. Van Nostrand, 1947. 170

Abstract

Summary Exploring the quantum properties of macroscopic objects has been a core challenge for research in physics during the past decades. Proposed systems to reach this goal include hybrid devices that couple a nanomechanical resonator to a single qubit. In particular, the implementation of spin dependent forces represents a fundamental objective towards the creation of non-classical states of motion. In this manuscript, we investigate a hybrid system coupling a nanomechanical oscillator and a single electronic spin of a NV defect in magnetic interaction. We focus on the parametric interaction case, when the mechanical motion modulates the qubit energy, and in particular when the driven qubit and mechanical oscillators evolves on similar timescales. In that situation a synchronization of the qubit dynamics onto the mechanical motion is observed. The phenomenon is first explored on a test experiment where mechanical motion is replaced by a parametrically coupled RF field. It allows to establish the main properties of the phenomenon, which is subsequently investigated on the core experiment involving a true hybrid spin-mechanical system. It consists of a NV defect attached at the vibrating extremity of a silicon carbide nanowire, immersed in a strong magnetic field gradient. The spin state is hence coupled to the nanowire vibrations via Zeeman effect. The bidimensional character of the nanowire deformations is responsible for novel vectorial signatures in the synchronization mechanism, which can also be viewed as a phononic Mollow triplet as observed in early quantum electrodynamics experiments. We finally explore the robustness of the synchronization against the Brownian motion of the resonator and demonstrate the possibility to protect the qubit against this additional decoherence source by applying a small coherent mechanical drive.

Keywords: Hybdrid spin-nanomechanical systems, NV defects, Electron spin, Nanomechanics, Spin locking, Dressed states, Coherence protection

Resumé L'exploration des propriétés quantiques d'objets macroscopiques constitue l'un des défis centraux de ces dernières décennies pour la recherche en physique. Parmi les stratégies proposées pour atteindre cet objectif, les systèmes hybrides couplant un résonateur nanomécanique à un qubit unique font figure de paradigme. En particulier, la mise en œuvre de forces dépendant de l'état du qubit représente un objectif fondamental ouvrant la voie à la création d'états non-classiques du mouvement. Dans ce manuscrit, nous considérons un système hybride constitué d'un oscillateur nanomécanique et du spin électronique d'un unique centre NV, couplés entre eux par une interaction magnétique. Nous nous concentrons sur leur couplage paramétrique, dans lequel la vibration mécanique module l'énergie du qubit, et plus précisément sur le cas où la précession du qubit, générée par un champ externe, et l'oscillation mécanique évoluent sur des échelles de temps comparables. Dans cette situation, nos observations mettent en évidence une synchronisation de la dynamique du qubit sur l'oscillation mécanique. Le phénomène est dans un premier temps abordé dans une expérience-test qui remplace le mouvement mécanique par un champ radiofréquence en couplage paramétrique avec le spin. Cette première implémentation permet de dégager les propriétés essentielles de l'effet paramétrique, qui est dans un second temps observé sur un vrai système mécanique hybride. Dans cette seconde expérience, un centre NV est attaché à l'extrémité oscillante d'un nanofil de carbure de silicium, immergé dans un fort gradient de champ magnétique couplant ainsi par effet Zeeman l'énergie du qubit aux vibrations du nanorésonateur. Le caractère bidimensionnel des déformations du nanofil octroie alors un caractère vectoriel au mécanisme de synchronisation, qui peut aussi être interprété comme la manifestation d'un triplet de Mollow phononique, en analogie avec le phénomène observé dans les premières expériences d'électrodynamique quantique. Pour terminer, nous explorons la robustesse de la synchronisation vis-à-vis du mouvement Brownien du résonateur, et démontrons la possibilité de protéger le qubit de cette source de décohérence additionnelle grâce à une excitation mécanique cohérente de faible amplitude.

Mots clés : Systèmes hybrides spino-mécaniques, Centre NV, Spin électronique, Nanomécanique, Synchronisation de spin, Etats habillés, Protection contre la décohérence